IAEA-TECDOC-1036

Advances in fuel pellet technology for improved performance at high burnup

Proceedings of a Technical Committee meeting held in Tokyo, Japan, 28 October – 1 November 1996

INTERNATIONAL ATOMIC ENERGY AGENCY IAEA

The originating Section of this publication in the IAEA was:

Nuclear Fuel Cycle and Materials Section
International Atomic Energy Agency
Wagramer Strasse 5
P.O. Box 100
A-1400 Vienna, Austria

ADVANCES IN FUEL PELLET TECHNOLOGY FOR IMPROVED PERFORMANCE AT HIGH BURNUP
IAEA, VIENNA, 1998
IAEA-TECDOC-1036
ISSN 1011–4289

Printed by the IAEA in Austria
August 1998

The IAEA does not normally maintain stocks of reports in this series. However, microfiche copies of these reports can be obtained from

INIS Clearinghouse
International Atomic Energy Agency
Wagramerstrasse 5
P.O. Box 100
A-1400 Vienna, Austria

Orders should be accompanied by prepayment of Austrian Schillings 100,— in the form of a cheque or in the form of IAEA microfiche service coupons which may be ordered separately from the INIS Clearinghouse.

FOREWORD

In the nuclear field, as in many others, improved performance is an important economic aim Improved fuel fabrication is one means of raising the performance of nuclear fuel in reactor plants These focal points, fuel fabrication and performance, were widely covered by the Technical Committee Meeting on Advances in Fuel Pellet Technology for Improved Performance at High Burnup

In connection with improving performance, a reliable estimate of fuel behaviour constitutes a basic demand for safety based calculations, for design purposes and for fuel assessments Close observation of fuel at high burnup is necessary to improve the safety codes and capabilities of predicting fuel behaviour in both normal and abnormal conditions

The IAEA has recently completed two Co-ordinated Research Programmes (CRPs) on The Development of Computer Models for Fuel Element Behaviour in Water Reactors, and on Fuel Modelling at Extended Burnup Through these CRPs it became evident that there was a need to obtain data on fuel behaviour at high burnup Data related to thermal behaviour, fission gas release and pellet to clad mechanical interaction were obtained and presented at the Technical Committee Meeting on Advances in Fuel Pellet Technology for Improved Performance at High Burnup which was recommended by the International Working Group on Fuel Performance and Technology (IWGFPT)

The 34 papers from 10 countries were grouped into 6 sessions The first two sessions covered fuel fabrication of both UO_2 fuel and additives and MOX fuel Sessions 3 and 4 covered the thermal behaviour of both types of fuel. The remaining two sessions dealt with fission gas release and the mechanical aspect of pellet to clad interaction

The IAEA wishes to thank the Japan Atomic Research Institute and the Nuclear Power Engineering Corporation of Japan for hosting the meeting and all the participants for their contributions to this publication The IAEA officer responsible for the organization of the meeting was P M Chantoin of the Division of Nuclear Power and the Fuel Cycle P J Menut of the same division compiled and completed this publication

EDITORIAL NOTE

In preparing this publication for press, staff of the IAEA have made up the pages from the original manuscripts as submitted by the authors. The views expressed do not necessarily reflect those of the IAEA, the governments of the nominating Member States or the nominating organizations.

Throughout the text names of Member States are retained as they were when the text was compiled.

The use of particular designations of countries or territories does not imply any judgement by the publisher, the IAEA, as to the legal status of such countries or territories, of their authorities and institutions or of the delimitation of their boundaries.

The mention of names of specific companies or products (whether or not indicated as registered) does not imply any intention to infringe proprietary rights, nor should it be construed as an endorsement or recommendation on the part of the IAEA.

The authors are responsible for having obtained the necessary permission for the IAEA to reproduce, translate or use material from sources already protected by copyrights.

CONTENTS

FUEL THERMAL BEHAVIOUR — THERMAL CONDUCTIVITY DEGRADATION OF GADOLINIA DOPED AND MOX FUEL (Session 4)

FISSION GAS RELEASE (Session 5)

PELLET–CLAD MECHANICAL INTERACTION (Session 6)

SUMMARY

1. INTRODUCTION

The aim of the Technical Committee Meeting on Advances in Fuel Pellet Technology for Improved Performance at High Burnup was to present an overview and a synthesis on advances made in pellet design and technology during recent years.

Sixty-six participants from 17 countries and international organizations attended the presentations and panel discussions. The 34 papers presented were grouped into 6 sessions covering fuel fabrication and outcome from high burnup of both UO_2 fuel (additives or not) and MOX. Sessions 1 and 2 are related to the new development of UO_2 fabrication and MOX. Sessions 3 and 4 covered the thermal behaviour of both types of fuel. The remaining two sessions dealt with fission gas release and the mechanical aspect of pellet to clad interaction. The technical discussions were conducted in four panels under the headings Fuel Fabrication, Fuel Thermal Behaviour, Fission Gas Release and Pellet–Clad Mechanical Interaction.

It is too early to reach conclusions about advanced fuels compared to conventional UO_2 fuel which has a history of 20 to 30 years with the resulting experience. The main findings of this meeting are that in spite of a great number of new data related to high burnup additional data about characteristics and behaviour are still missing. Research and development is still required, especially irradiation tests to check fuel performance at high burnup are to be carried out.

The technical discussions are summarized here.

2. FUEL FABRICATION

2.1. UO_2

As the fission gas release rate increases with the burnup, the structural influence on this topic will be studied. Some tests of different grain size fabrication are reported.

It is necessary to obtain more knowledge on the structural evolution related to the additives which should have a harmful effect on the diffusion of the fission gases.

The creep rate is important for PCI behaviour, but it is not the only parameter. The creep rate could be improved by reducing the grain size. A small grain size at the outside area and a large grain size inside could be the best method. However, the grain size only affects the creep rate when the mechanism is the grain boundary diffusion, i.e. the stress is low. Consequently, it is clear that the main future research work on fuel fabrication would be related to the grain size.

2.2. UO_2+Additives

It is difficult to say definitively which additives are available and useful. Niobia doped fuel experience exhibits a reliability to promote grain. Other additives are promising (Al, Si).

Manufacturing reliability and quality control could be improved by additives. Additional information about irradiation behaviour of doped UO_2 fuels is necessary to come to a conclusion about the benefit of additions (as doping) on fission gas release and PCI.

2.3. Burnable absorber

Gadolinia doped fuel is already used commercially. No new fuel, as composite fuel or duplex fuel, is required today. So, power generation from the poisoned fuel initiated a new approach consisting in the absence of degradation of the thermal conductivity and retention of fission gas.

In this case, composite or duplex fuels should be an innovative solution. Duplex fuel could be of interest to avoid gadolinia contamination in the manufacture of MOX fuel.

Irradiation of defect rods will induce a degradation of the composite or duplex fuel because there is a dissolution of gadolinia by water. Some studies on a new material like (Zr, Gd)O_2 would lead to avoiding this phenomenon of dissolution.

2.4. MOX

Pu homogeneity is a current aspect of MOX manufacturing. Homogeneity means fine dispersion of Pu, and reprocessing aspects must also be taken into account with regard to this local Pu content. Homogeneity is expected to be better for fission gas release which would be an important specific behaviour of MOX fuel. Regardless of the fission gas release, homogeneity could improve.

Today, the MIMAS process pellet or COCA-process pellet provide a similar fission gas release rate at 45 GWd/t. Linear power at the 3rd or 4th cycle seems to be the major parameter regarding the fission gas release rate. Experimental irradiation with rods, including thermocouples, could be performed with an accelerated evolution of parameters.

Advanced MOX fuels are required in a second stage while the main result will be essential for advanced UO_2 fuels.

3. FUEL THERMAL BEHAVIOUR

3.1. Thermal conductivity - reliability of data available

Reasonable agreement exists between the data obtained from in-pile fuel temperature measurements at Halden and that obtained from out-of-pile post irradiation measurements of Thermal Diffusivity and Specific Heat - which indicates the reliability of the available data. However, more data are required in the following areas:

(a) Effects of stoichiometry on specific heat
(b) Measurement of thermal conductivity of the RIM zone
(c) Measurement of thermal conductivity of Gd_2O_3 fuels
(d) Measurement of thermal conductivity under conditions relevant to transients and RIA
(e) Examination of effects of additives under RIA conditions.

Attempts should be made to collect the data available on fuel thermal properties in the form of a database. A benchmarking exercise and error analysis would have to be carried out in the laboratories where these measurements are made.

3.2. Microstructural changes

In addition to the need to complement the database on porosity measurement, there is a need to identify the location of fission product gases. The electron backscatter technique seems to offer a possible solution; however, data are required in the RIM zone.

3.3. Fuel performance modelling

The models are very sensitive to the values of thermal conductivity used, e.g. 5% on thermal conductivity can give rise to a variation in fission gas release of between 4 and 10%.

The question of microcracking and its impact on thermal conductivity was raised. It appears that much of the degradation of this property is influenced not only by "microcracking", but by the structural evolution of the fuel as RIM and porosity which can have an effect on gas behaviour.

3.4. Chemical form of fission products

Information on the chemistry at fuel clad gap is important in terms of gap conductivity. However, little work appears to be focused in this area. The importance of the volatile fission products I, Te and Cs with respect to SCC was pointed out. Work has been done on this topic jointly by TUI and EDF but more attention could be given to the aspect of fuel rod performance.

The RIM zone might have a major impact on the performance of fuel, particularly under transients and/or RIA conditions.

4. FISSION GAS RELEASE

The first topic to be discussed was the dependence of threshold temperature for 1% integral gas release. Two kinds of curves were shown displaying this dependency. The first one is Vitanza's curve. The second one is Manzel's curve, which is derived from data given in this meeting, but was first given at the last ANS topical meeting on LWR fuel performance held at Avignion, in April 1991. It was noted that the threshold temperature for 1% integral gas release is higher in the former curve than in the latter one in the high burnup region.

This work continues at Halden now, but the threshold temperature does not drop to the extent of temperature difference shown in Manzel's curve in the high burnup region. Based on the data recently obtained at Halden, the threshold temperature drops by 50 at the most.

The difference between the two curves results from the fact that in the Manzel curve, the degradation of the thermal conductivity of the fuel has not been taken into account. Contribution of the RIM to FGR at high burnup is not clearly identified. More experimental data are needed in order to settle different interpretations. A comparison between commercial LWR UO_2 and MOX fuel fission gas release versus burnup, grain size and linear heat rating was beginning. CEA experiments on UO_{2+x} fuels exhibit a reduced fission gas release in

transient conditions in case of large grained slightly hyperstoichiometric fuels. Diffusion is not the only parameter but solubility of the gas into the UO_2 matrix has to be taken into account. The only undoped and silicate doped large grain fuel shows the better than standard UO_2 under transient operating conditions. Contrarily, the Nb_2O_5 and TiO_2 doped large grain UO_2 showed a high fission gas release under transient heating. In addition, the dependence of fission gas release on the burnup and linear heat rating was compared between BWR-MOX and UO_2 fuel. It seems to be conclusive that there is not such a big difference between BWR–MOX and UO_2 fuels. It will be confirmed by further data from many irradiation experiments.

EPMA diametral scan of Xe in UO_2 and MOX fuels after the first, second and third irradiation cycles were presented and discussed. Compared to UO_2 fuel, a depletion of Xe was observed in the matrix in the central region of the MOX fuel due to the higher linear heat rating. The concentration of total fission products attains about 50% in the outermost rim region of the extended burnup fuel. This fact is very important for understanding the relationship of fission gas release with the rim effect.

5. PELLET–CLAD MECHANICAL INTERACTION

The technique being used or developed for measuring detailed fuel pellet mechanical properties may constitute a valuable complement to measurements performed during irradiation (e.g. diameter profilometry) or in PIE. Their development is encouraged as useful for modelling. The work carried out characterizing the composition and properties of the pellet-cladding bonding layer and the mechanism leading to bonding are considered to be important both for normal operation and for transients (e.g. RIA) fuel behaviour. There is a question as to whether the bonding layer may even protect the cladding from fission products damage. The use of barrier cladding as one of the means of protecting the fuel against PCI failure was emphasized. The continuation of studies aimed at characterizing mechanisms and properties of the bonding layer is necessary. Regarding the effectiveness of annular pellets in mitigating PCI, it was observed that, apart from economical considerations, the question remains on the consequences of, for instance, unrestrained swelling in the centre hole. Annular pellet may be considered for reducing the gas release of MOX fuel, however the centre hole dimensions should be properly optimized.

The need for experimental data on MOX fuel for PCI modelling was noted. While ramp data on MOX fuel show a good ability of MOX fuel to withstand PCI failure, property data of irradiated MOX fuel suitable for modelling are lacking. Compensative measurements of pellet-cladding interaction in MOX and UO_2 operated at the same conditions (e.g. in power ramps) were needed. The existing and available data on MOX fuel behaviour must be collected in a systematic databank.

The use of additives in UO_2 fuel for PCI mitigation constitutes an alternative or supplement to barrier fuel. Work in this direction should aim at providing data proving the improved performance of novel fuels. In particular, efforts should be made in validating the use of additives in the high burnup ranges.

6. RECOMMENDATIONS

(1) Further studies on fabrications of Gd203/UO_2 composites (using alternative methods/compounds for Gd203 dispersion) should be carried out.

(2) Duplex–MOX Gadolinia seems to be an attractive concept to overcome many of the problems of this system. The neutronic behaviour of Gd in the central location of the pellet has to be studied and hence further work and irradiation experiments are highly recommended.

(3) A sound energy policy and a sound environmental policy call for utilization of Pu for power production. Hence, development of MOX fuel technology and Pu recycling should be encouraged.

(4) It would appear that significant benefit could be gained by further exchange of ideas, and possibly, of data, so that the best features of the available models might be established.

(5) A workshop on modeling of thermal conductivity, and comparison with experimental data, might be worthy of consideration.

(6) A better knowledge of the basic physical phenomena; for instance, is PCI rupture governed by stress corrosion mechanisms?

(7) It is necessary to obtain codes with PCI modelization. They have to be provided with precise and detail models. These codes have to contain the right local material properties. One dimensional and three dimensional thermomechanical codes are necessary to describe the local deformations.

(8) It is necessary to perform both of "out of pile" and "in pile" international experiments in transient conditions. For these experiments, we must know the initial fuel condition (gap size and so on) and the experimental parameters (temperature, pressure and so on) very accurately during the tests. An effort must be done to measure cladding deformations during the experiments.

(9) We need a better characterization of mechanical properties (visco–plasticity) of cladding, fuel matrix and fuel cladding interface (rim and so on). Also a better knowledge of the bonding layer structure and chemical composition is necessary. For instance, soft compounds in the gap tend to uniform the azimuthal stress distribution on the cladding.

(10) For decreasing PCI, efforts must be made in increasing cladding ductility, in manufacturing fuel pellets with advanced structures in order to decrease FGR and increase creep rate.

(11) More MOX fuel ramp tests should be performed with different kinds of MOX route fabrication.

FUEL FABRICATION — UO_2 FUEL, UO_2 AND ADDITIVES

(Session 1)

CHARACTERISTICS OF FUEL PELLET WITH ADDITIVE OF Al AND Si

T. MATSUDA, Y. YUASA, S. KOBAYASHI, M. TOBA
Nuclear Fuel Industries Ltd,
Osaka, Japan

XA9847840

Abstract

The large grain pellet is a candidate for a high burnup fuel pellet. We have investigated the large grain pellet in which Al and Si are added within the impurity limits. These additives promote the grain growth of uranium dioxide during sintering and modify the characteristics of the grain boundary. It is expected to reduce fission gas release and pellet cladding mechanical interaction. We have already confirmed that there is a slight difference in the out of pile properties of the UO_2 pellet except for creep behavior. The additive enhances the creep rate over a wide range of creep conditions.

To precisely understand the effect of additives on the fabrication conditions and properties of the pellet, we investigated a UO_2 pellet in which an excess of Al and Si is added. As for grain growth only small amount of additives is needed to cover the grain boundary of UO_2. An excess of additive does not promote further grain growth but leads to suppression of pellet densification by volatilization of the additives. So, an excess of Al and Si is not necessary to improve the microstructure of the pellet and creep behavior, while thermal expansion and diffusivity are not significantly affected by the amount of additive.

1. INTRODUCTION

Coarsening the grain of a UO_2 pellet is considered an effective method to reduce fission gas release. In order to change the microstructure of the UO_2 pellet, various methods are used such as the use of sintering aid and changing the sintering conditions [1]. It is known that some kinds of additives can promote grain growth of the UO_2 pellet during sintering. One is the matrix modification type such as TiO_2 and/or Nb_2O_5 [2.3] which enhances the diffusion in the UO_2 lattice. Another type of additive modifies the grain boundary characteristics such as silicate which forms a glassy phase in the grain boundary and promotes sintering.

In general, it is known that impurities such as silicates easily form a glassy phase. These materials are believed to form glassy phase so that an intergranular phase acts as a rapid diffusion path during the sintering. There are many proposals for the mechanisms of grain growth in the presence of a liquid phase. Also, diffusion or an interface-reaction is considered to be the rate controlling step.

We have investigated a large grain pellet in which Al and Si are added within the impurity limits [4]. The solubility of Al and Si in UO_2 is considered to be limited to a low level and this form an intergranular phase. That phase is considered to promote the grain growth of UO_2 during sintering. But the total amount of the additives is too small to determine how the additives behave in the compacts during sintering. Furthermore, it is important to understand the effect of additive content on sintering behavior and the UO_2 characteristics. In this paper, we describe the behavior of additives in case of a high concentration and the effect of additive content. The microstructure of a sintered UO_2 pellet containing various amounts of Al and Si are presented. The sintering behavior of these compacts are discussed.

2. SINTERING BEHAVIOR

In the presence of additives, which is believed to form a liquid phase such as a silicate, the sintering mechanism differs from that of the solid state shown Fig. 1. But the information for U-Al-Si-O is limited and amount of additive is not sufficient in order to understand the sintering behavior. To understand the behavior of additives during sintering, an excess of Al and Si were added to UO_2.

The ADU process powder was used as UO_2 in this study. Fig. 2 shows a schematic diagram of the manufacturing process. Al_2O_3 and SiO_2 were used as the source of Al and Si, respectively. These powders and UO_2 were mechanically blended and then formed into a pellet using a press. Sintering tests were performed in cracked NH_3 using a dilatometer or batch type furnace.

2.1 Basic behavior of additives during sintering

The sintering kinetics of UO_2 compacts containing various kinds of oxides have been investigated in a dilatometer. Each compact contains a total of 0.5wt% additives. Fig.3 shows the sintering curves of the compacts. The compact with no additives shows a higher shrinkage than the compacts with additives up to 1300°C. By increasing, temperature, the $Al_2O_3SiO_2$-added compact rapidly densifies at about 1400°C. It indicates that the additives inhibit densification of the UO_2 compact during the early stage of sintering and some kinds of additives such as $Al_2O_3SiO_2$ act as a sintering promoter near 1400°C.

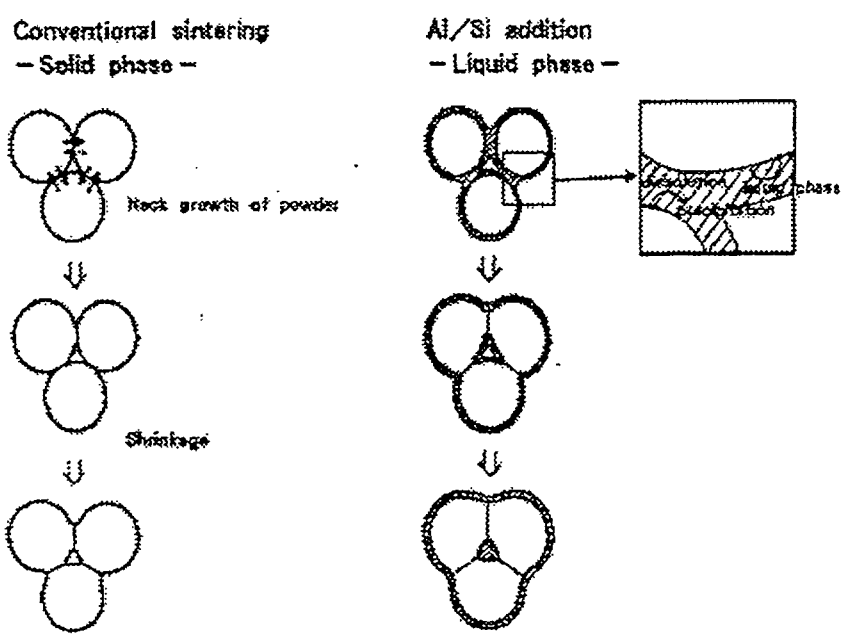

FIG. 1. Sintering behaviour in the presence of Al and Si

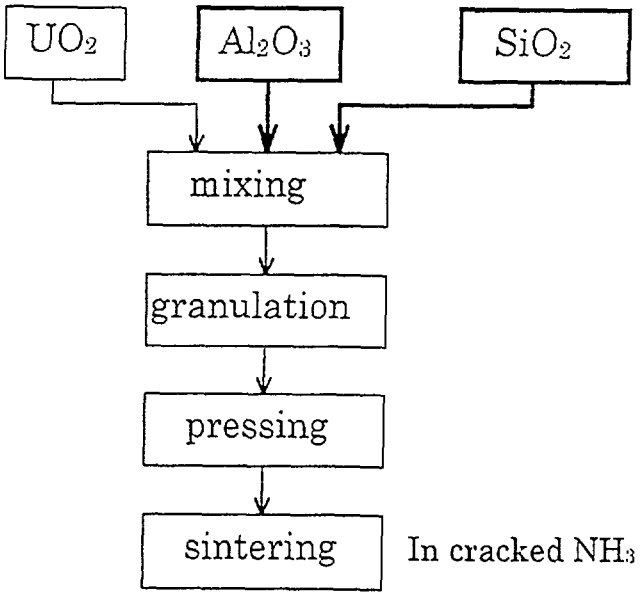

FIG. 2. *Schematic diagram of manufacturing process (Al/Si added pellet)*

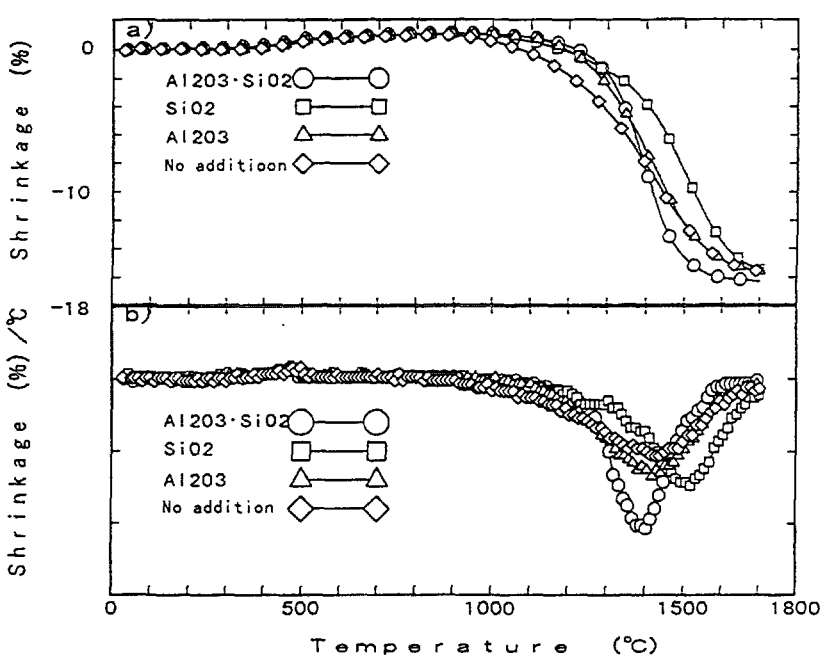

FIG. 3. *Effect of additives on sintering behaviour: a) shrinkage curve b) shrinkage rate*

Fig. 4 shows SEM photographs of the polished surface of UO_2 pellets sintered for 4h. at 1500°C. Only the $Al_2O_3SiO_2$-added pellet shows an apparent grain boundary phase which forms a low dihedral angle. The dihedral angle in the sintered body of pure UO_2 is approximately 90° [5]. Strictly speaking, the dihedral angle seems to depend on the number of faces and pore size. Fig. 4 indicates the existence of the boundary phase which has a low interfacial energy with UO_2. The SEM photographs of the $Al_2O_3SiO_2$-added compacts show

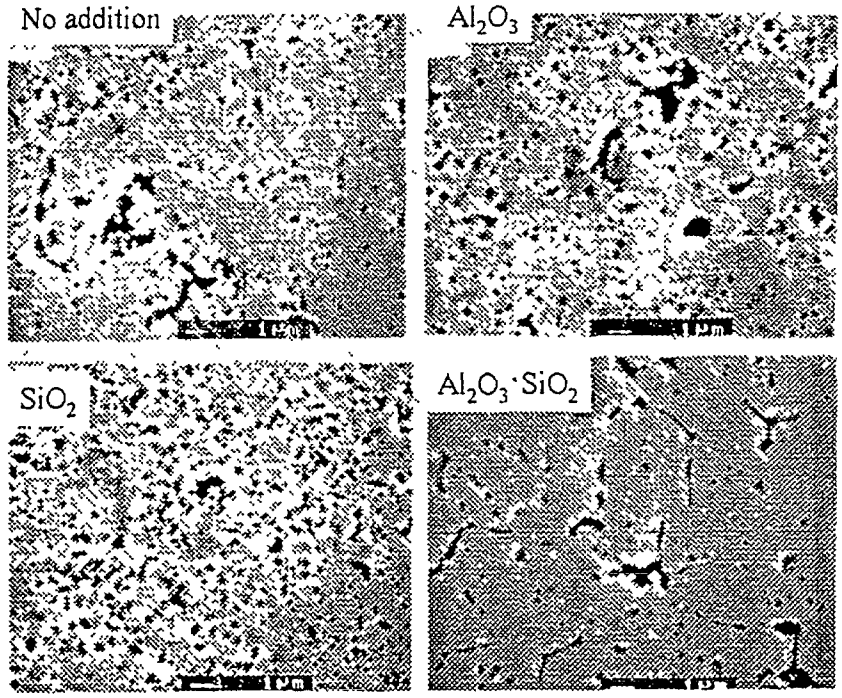

FIG. 4. *SEM image of polished surface of sintered UO_2 with 0.5wt% of additives (at 1500 °C, 4h, in cracked NH_3)*

that the UO_2 grain form a low dihedral angle in the range of 1400 ~ 1500 °C (Fig. 5). The intergranular phase composed of Al-Si compounds are shown in Fig.6. It is known that SiO_2 easily forms a glass phase during its coexistence with other metal oxides. The intergranular phases are believed to be the liquid phase during the sintering.

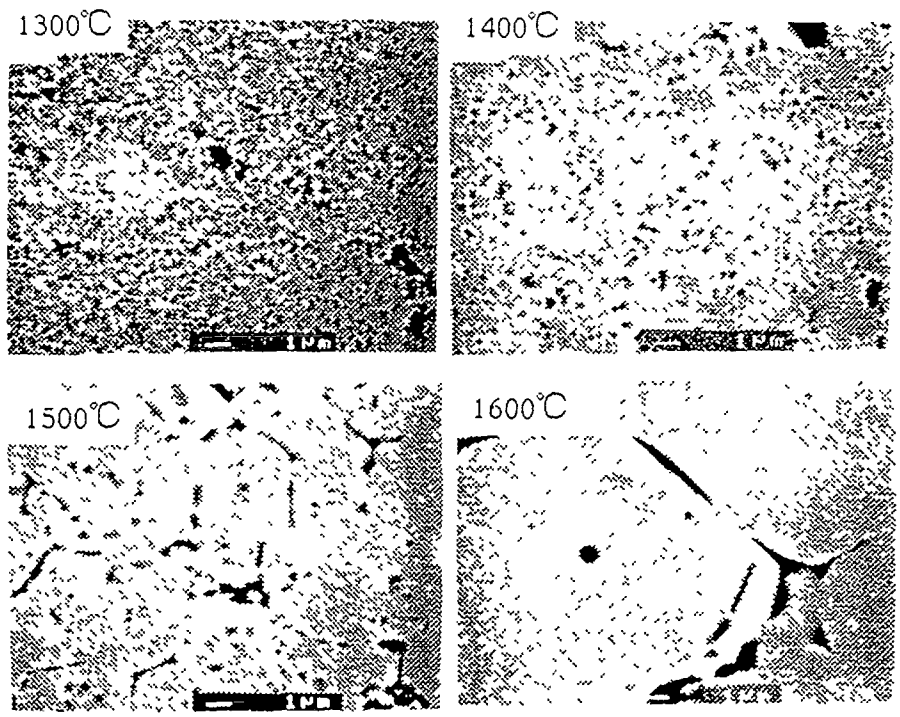

FIG. 5. *SEM image of polished surface of sintered UO_2 with 0.5wt% of Al_2O_3 and SiO_2. (for 4h, in cracked NH_3, at various temperature)*

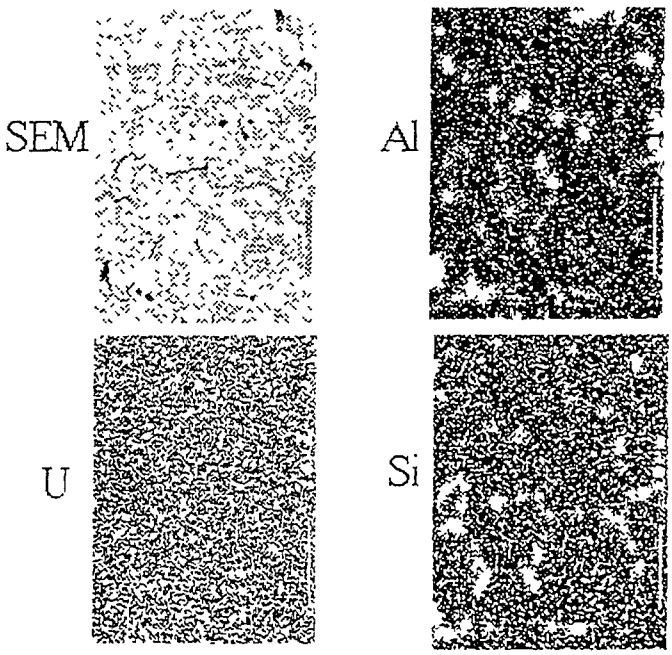

FIG. 6. *SEM image of sintered UO_2 pellet*
Polished surface of sintered UO_2 with 0.5wt% of Al_2O_3 and SiO_2. (for 4h, in cracked NH_3, at various temperature)

As for the compacts manufactured in the same lot, the weight change of the compacts during sintering were measured using thermogravimetry. Fig. 7 shows the weight change of the compact, during heating. The weight of the $Al_2O_3SiO_2$-added and SiO_2-added compacts gradually decrease above 1400°C while the no- added and Al_2O_3-added compacts are almost stable. This suggests that volatilization of the additives from the compacts has a higher vapor pressure under this condition. Fig. 8 shows the vapor pressure over Al_2O_3 and SiO_2 in the equilibrium state, which is calculated from the Gibbs free energy [6]. Each pressure shows the pressure of the gas phase having a maximum partial pressure over the metal oxide. By lowering the oxygen pressure, the partial pressure is higher over the oxide. This supports the results of the weight change of the compacts during sintering.

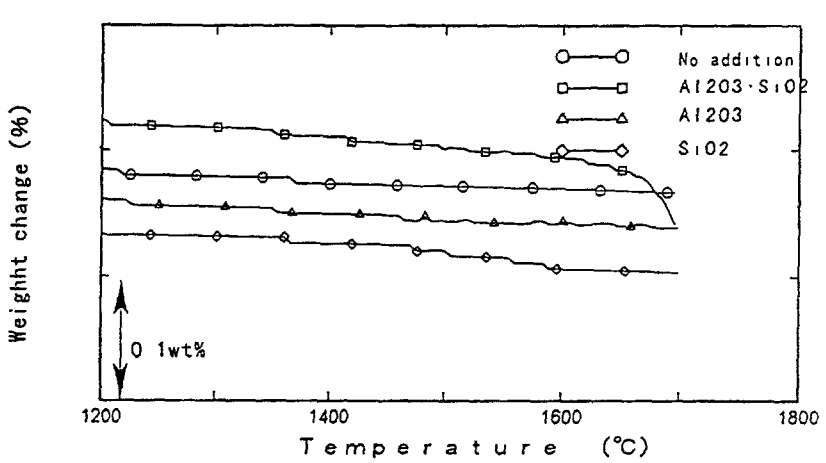

FIG. 7. *Weight change of UO_2 compacts during sintering (sintered rate of 6 °C/min in cracked NH_3)*

Above 1600°C, the rate of weight change for the $Al_2O_3SiO_2$-added compact is apparently higher than that with SiO_2. This indicates that there is a more volatile phase than SiO_2. The rapid weight loss suggests the existence of a liquid phase during sintering.

2.2 Sintering with Al_2O_3·SiO_2

Fig. 9 shows the effects of additive content on sintering behavior. These pellets were sintered for 4h in a batch type furnace. The higher the amount of additive, the lower the density of the pellets, because volatilization of the additives prevents the pellets from densification. This is consistent with the fact that vapor pressures from Al_2O_3 and SiO_2 oxides are quite high in a reducing atmosphere from a thermodynamically viewpoint as shown in Fig. 8. The grains of the pellet have coarsened with only a small amount of additive, but an excess of additive did not cause any further grain growth. This means that only a small amount of additives are needed for grain growth in order to cover the grain boundary of UO_2. An excess of additive leads to suppression of pellet densification by volatilization of the additives.

3. CHARACTERIZATION

UO_2 compacts with various $Al_2O_3SiO_2$ contents were sintered for 10h at 1650°C to evaluate their thermal expansion and thermal conductivity.

Thermal expansion of the pellets were examined using differential dilatometer in cracked NH_3. Fig. 10 shows the results of the thermal expansion with additives up to O.Gwt%. It indicates that the UO_2 pellet is not significantly affected by additives. This is consistent with the summation of the theoretical expansion of each UO_2,Al_2O_3 and SiO_2 component.

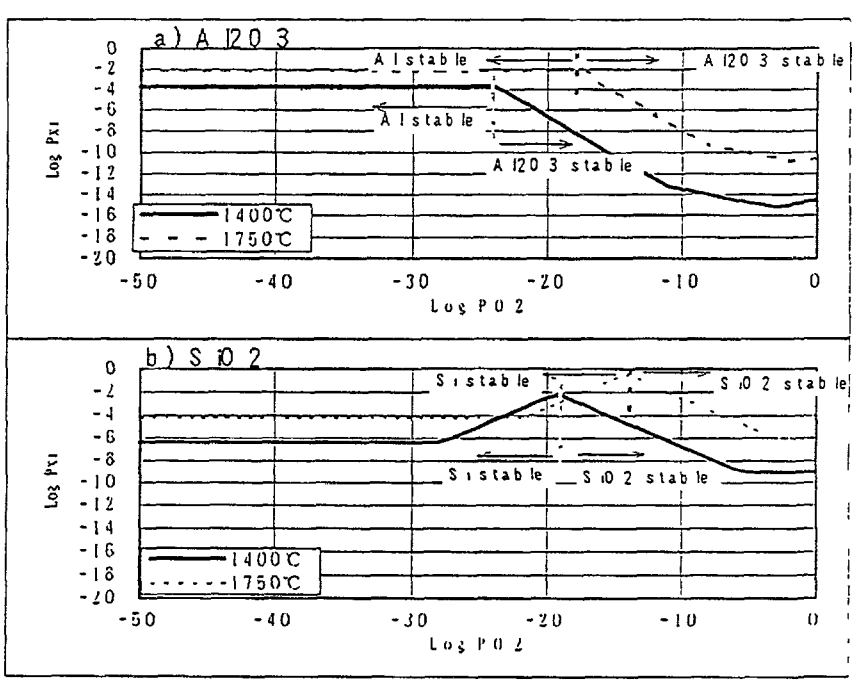

FIG. 8. Maximum vapor pressure for vapor species over oxides in atmospheres with various PO_2 at 1400 and 1750 °C

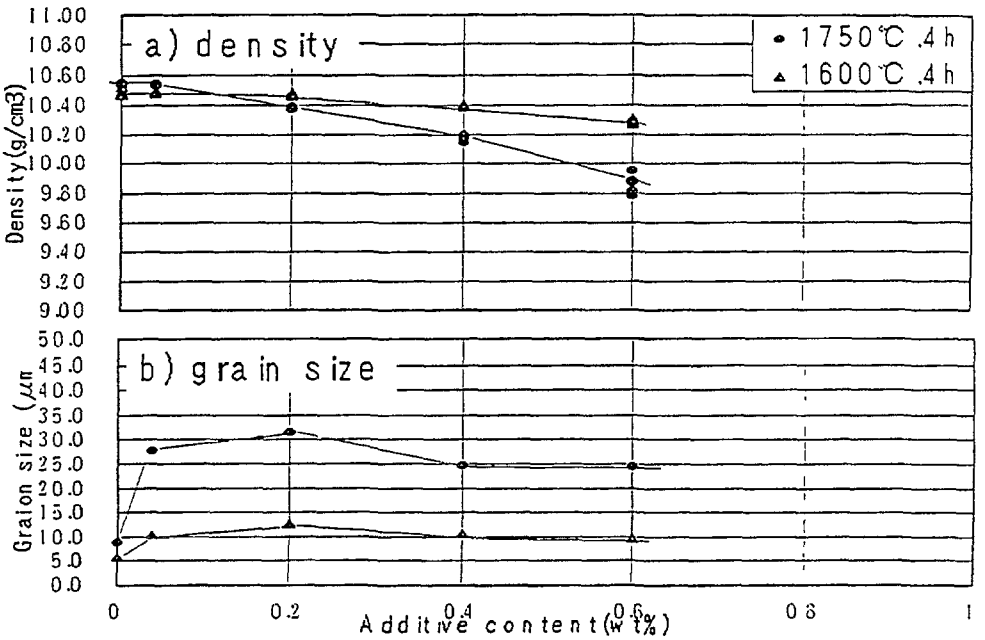

FIG. 9. *Effect of additive content on sintering*
Each compact is sintered for 4 hrs at prescribed temperature in cracked NH_3

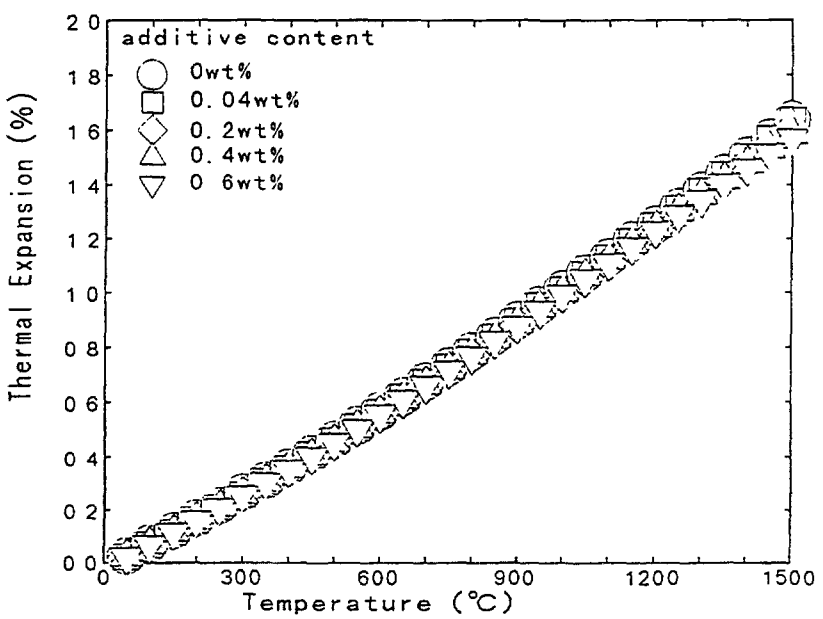

FIG. 10. *Thermal expansion of UO_2 pellet containing various amount of Al_2O_3 and SiO_2*

Thermal conductivity was calculated from the thermal diffusivity, specific heat and density. Thermal diffusivity was determined using the laser flash technique. In regard to specific heat and density of the pellet, published data were used. Fig. 11 shows the results that the thermal conductivity is not dependent on additives. So, thermal conductivity of the UO_2 pellet with additives within the specified impurity levels is almost the same as that for UO_2.

Fig. 12 shows the effects of additives on the high temperature creep of a UO_2 pellet in a vacuum. These pellets were all sintered for 4h at 1760°C. All the tests were carried out in

a vacuum using a compressive creep apparatus under constant load. Initial stress was set to be 45Mpa. Small amounts of additives can enhance the creep rate of the UO_2 pellet. The UO_2 pellet with 50ppm Al and Si shows a higher creep rate than pure UO_2.

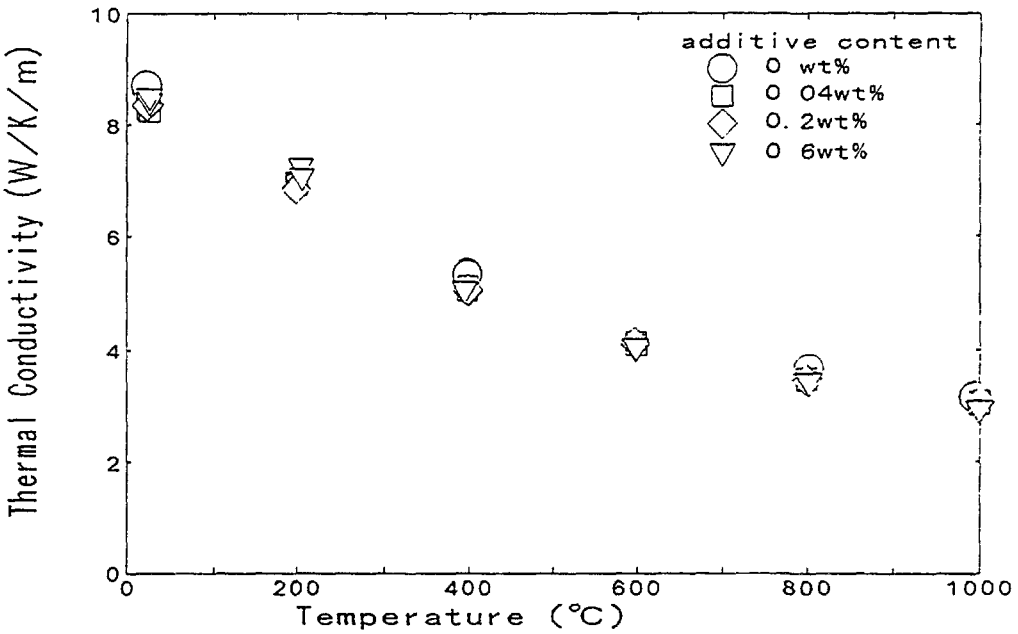

FIG. 11. *Thermal conductivity of UO_2 pellet containing various amount of Al_2O_3 and SiO_2*

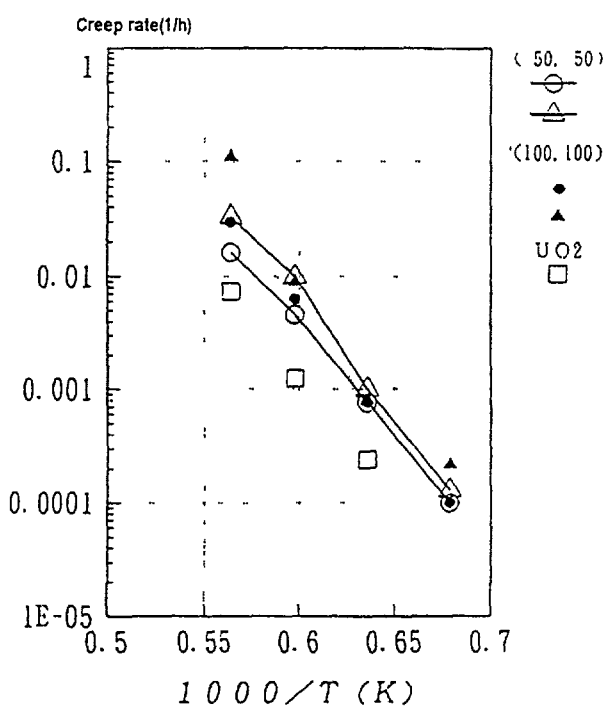

FIG. 12. *Creep rate of UO_2 pellets containing Al and Si compressive creep, 45MPa*

4. CONCLUSIONS

In order to understand the sintering behavior of the UO_2 compacts containing Al and Si, the compacts in which an excess of Al and Si is added have been sintered and evaluated. The microstructure having a low dihedral angle at the grain boundary intersection was observed after sintering above 1500° C. The intergranular phase rapidly volatilized above 1600°C.

From the results of the sintering tests, we confirmed that only a small amount of additives were needed to cover the grain boundary of UO_2. An excess of additive did not promote further grain growth but lead to suppression of pellet densification by volatilization of the additives.

As for the properties of the UO_2 pellet, thermal expansion and diffusivity were not sufficiently affected by the amount of additive. Also UO_2 the creep rate easily increase by the addition of small amount of Al and Si.

REFERENCES

[1] KAWANISHI, K. WATARUMI, K.,"Control of U02 microstructure by oxidation -reduction sintering method" Proc. 4th International Symposium on Advanced Nuclear Energy Research, Mito, Japan, Feb. 5-7, 1992 p151-157.

[2] AMATO, I. et al, "Grain Growth in Pure and Titania-doped Urania Dioxide, J. Nucl. Mater. 18 (1966) 252.

[3] RADFORD, K. C. POPE, J. M. "UO_2 Fuel Pellet Microstructure Modification Through Impurity Additions", J. Nucl. Mater. 116 (1983) 305.

[4] KAWANISHI, K., et al, Proc. 1994 Fall Meeting of the Atomic Energy Society of Japan. Sep. 2830,J14 Atomic Energy Society of Japan, Tokyo(1996).

[5] KINGERY, W. D. et al., "Introduction to ceramics", chapter 10, John Wiley & Sons. Inc. (1976)

[6] YOKOKAWA, H., "On Work for Establishing a Thermodynamic Data Base for Inorganic Compounds", Netsu Sokutei, 12(3) 144- 148 (1985).

DISCUSSION

(Questions are given in italics)

As a result of potential volatility of the additives under sintering conditions: Is there any evidence for this in terms of a difference in grain size between the center and surface of pellets doped with alumina silicate ?

No, the microstructure is uniform in the pellet.

Since the Al and Si is concentrated at the grain periphery, what is the influence on the melting point of the resulting fuel?

We think there is no impact on the melting point because of its low content. Our goal is low contents of Al_2O_3 and SiO_2. These contents are under 50 ppm for each element.

What steps have you taken to irradiate UO_2 fuel with additives and, in your view, when could such fuel be loaded in commercial reactors?

The lead test fuel assemblies, which contain Al/Si additives, will be loaded in a commercial reactor in 1997. But the amount of the additives is as small as the current UO_2 impurities limit.

Swelling occurs in Nb_2O_5 fuel according to our experience in the HBR-project. Can you please comment on this with respect to PCMI though PCI behavior seems favorable.

Although the PCI resistance of Nb doped fuel appears promising, the ramp test results cannot be characterized as a "demonstration." The joint DOE/Commonwealth Edison/GE demonstration of the PCI resistance of Zr barrier fuel involved many tens of ramp tests and other tests as well as a control blade pull on a quarter core of barrier fuel in the Quad Cities reactor.

NIOBIA-DOPED UO_2 FUEL MANUFACTURING EXPERIENCE AT BRITISH NUCLEAR FUELS LTD

G. MARSH, G.A. WOOD, C.P. PERKINS
British Nuclear Fuels International Group,
British Nuclear Fuels Ltd,
Salwick, Preston,
United Kingdom

Abstract

BNFL Fuel Division has made niobia doped fuel for over twenty years in its Springfields Research and Development facilities. This paper reviews this experience together with feedback from successful in-reactor and laboratory tests. Recent experience in qualifying and manufacturing niobia doped fuel pellets for a European PWR will be described.

INTRODUCTION

BNFL's original interest in niobia doped fuel stems from the early 1970's and it's use as a grain growth promoter leading to a more fission gas retentive, large grained fuel. Niobia, together with other materials, was investigated and the work led to the publication of patent GB 2 020641 B. BNFL's patent prescribes a sintering regime in which the oxygen potential of the sintering atmosphere is controlled within fairly well defined limits in order to achieve a large grain size fuel. Outside this region, grain size decreases (more reducing conditions) or large grain sizes are achieved and sintered density control is problematic (more oxidising conditions).

The work covered both laboratory scale investigations and pilot scale operations using full scale production equipment. Thus from an early stage, BNFL Research and Development Department developed a manufacturing capability for niobia doped fuel.

By 1982 BNFL had manufactured quantities of niobia doped fuel for irradiation in the Dodewaard BWR, Netherlands [1]. The different quantities required for these campaigns, 4 rods and 40 rods for reloads 8 and 10, respectively, necessitated the use of equipment of different scale with the latter (approximately 100 kg) comparable to a continuous, full scale manufacturing process.

Contemporaneously with these studies, laboratory scale work continued leading to the preparation of material for several irradiation experiments as part of national and international collaborative programmes. Details of the experiments and the quantities involved are given in Table I.

Irradiation trials have confirmed that large grain size niobia doped fuel does have a slightly enhanced fission gas retention capability. However, the fission gas retention benefit is now seen as secondary to the realisation of a much greater benefit from improved resistance to pellet clad interaction (PCI) failure, arising from the significantly enhanced thermal creep rate of niobia doped fuel. During an increase in reactor power, thermal expansion of fuel pellets can generate large tensile stresses in the cladding, which, in the presence of corrosive fission products, can result in stress corrosion cracking. Rapid creep of doped fuel pellets

TABLE I. NIOBIA-DOPED FUEL MANUFACTURING EXPERIENCE

EXPERIMENT/ ORGANISATION	REACTOR	QUANTITY	NIOBIA CONTENT (wt%)
IE591	WAGR		0.5
IE585	SGHWR		0.5
IFA 512	HALDEN	3 x 50 pellets	0.5
IFA 512	HALDEN	3 x 50 pellets	0.25
DEMO RAMP 1	STUDSVIK	5 rods	0.3
BATELLE	HALDEN	6 rods	0.5
BNFL/GKN	DODEWAARD RELOAD 8	4 rods	0.3
BNFL/GKN/ CEGB	DODEWAARD RELOAD 10	40 rods	0.5

under these thermally generated loads leads to relaxation and a corresponding reduction of clad stresses and hence diminished propensity for clad failure.

Recently this enhanced performance has been confirmed in power ramp tests for irradiated, solid niobia doped BNFL IDR/CONPOR fuel. A fuel rod, containing niobia doped pellets, forming part of the charge for Dodewaard reload 8, was refabricated into rodlets, and subsequently ramp tested in the Petten HFR [2]. An undoped rod from the same reload and power history formed a control sample. The rodlets were tested under simulated PWR conditions (14.5 MPa system pressure and 340 C rodlet surface temperature).

During ramp testing, none of the rodlets containing doped pellets failed despite being ramped to significantly higher power levels than the undoped counterparts. The rodlets containing undoped fuel behaved as expected from empirically derived failure threshold criteria. Thus the superior resistance to PCI failure of niobia doped fuel was clearly demonstrated.

In IDR/CONPOR solid fuel, the voidage into which material is displaced during relaxation is provided by crack and dimple volumes and the induced porosity. During pellet manufacture a fugitive pore former (CONPOR) is added at the powder processing stage. The amount of CONPOR added controls the sintered density of the pellet through generation of thermally stable porosity.

In countries where PCI failures due to reactor faults are evaluated as part of the operating safety case, particularly the United Kingdom, France and Japan, the need to develop a fuel resistant to PCI failure is recognised and niobia doped IDR/CONPOR fuel represents a means of achieving this.

To add to the experience base of niobia doped fuel a further programme is underway involving BNFL and ENUSA as members of the European Fuel Group (EFG) and Electricite de France (EdF). This covers the loading of niobia doped fuel in a commercial PWR. Pellets, produced by BNFL Springfields Research and Development Department, have been loaded into 8 fuel rods and assembled as a component of advanced demonstration assemblies by ENUSA. The assemblies have now been loaded into Belleville 1.

COMPARISON WITH EARLIER, RAMP TESTED, PRODUCT

Following on from the successful ramp testing of the refabricated fuel from the Dodewaard BWR, the philosophy was adopted to produce the current fuel with characteristics as close as possible to those of the earlier fuel. This approach placed increased demands on the production process used through the need to maintain tight control of processing conditions as manufacturing limits are artificially narrowed relative to the specification limits, and, in the case of sintered density, resinter densification and grain size, the inter-relationship of these parameters further restricts the manufacturing window. The extent to which we were successful in achieving the above aim is exemplified, with respect to these, and some other parameters, in Table II.

Figure 1 shows a typical pellet microstructure obtained during recent doped fuel manufacture.

QUALIFICATION

Due to the relatively extended period between the present and previous niobia doped manufacturing campaigns, a formal qualification of the production process was deemed appropriate. The qualification process involved defined data collection and analysis both during manufacture of the enriched product material and during a similar production exercise, carried out earlier, on depleted feedstock. An identical production route was employed for both depleted and enriched stages, and also on similar quantities of material such that equipment loadings were, in both cases, comparable.

DOCUMENTATION

An overall description of the project was contained in the Project Plan which outlined the responsibilities of individual groups contributing to the project, the scope of the work and the document structure. Documents specific to the project included those covering pellet

TABLE II. COMPARISON OF CURRENT AND EARLIER PRODUCT

Parameter	Present Work	Dodewaard Reload 8
Density (g cm^{-3})	10.502	10.485
sigma (g cm^{-3})	0.0164	0.021
mean grain size (microns)	40.1	36.0
sigma (microns)	1.48	2.2
Nb:U (w/o)	0.24	0.23
Resinter densification(g cm^{-3})	+0.026	+0.028
sigma (g cm^{-3})	0.006	0.012
O/U ratio	1.9981	2.0005

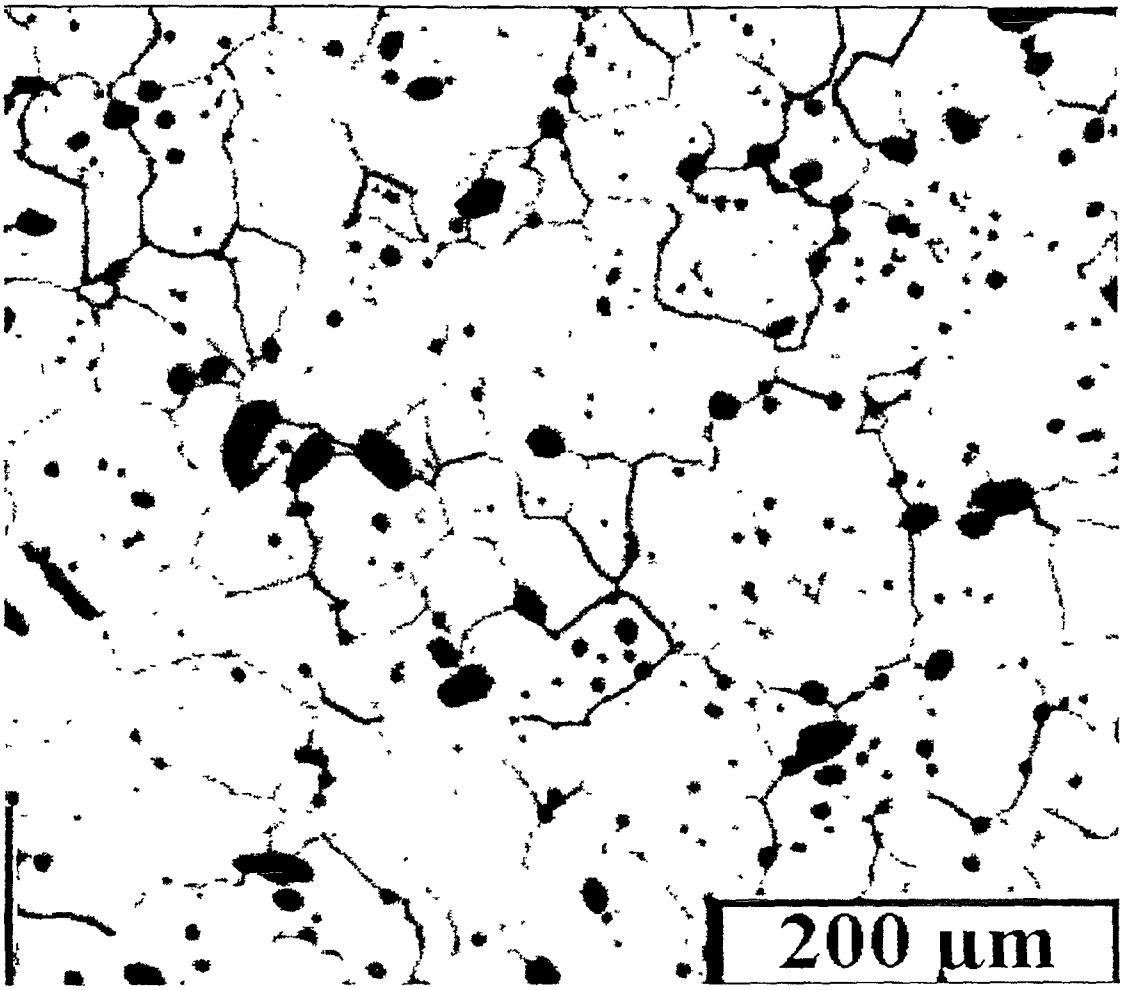

FIG. 1. Typical microstructure of a large grain niobia doped fuel pellet

design and customer requirements, the Quality Assurance System and Route Definition, including the qualification document structure. Additional, generic documentation included the Divisional Quality Assurance Manual, individual Department and Division Procedures and Instructions and data sheets.

All documentation was made available to both EdF and ENUSA on the occasion of audits carried out on BNFL Fuel Division by representatives of both organisations. Figure 1 shows a typical microstructure obtained during recent fuel pellet manufacture.

MANUFACTURE

The outline production route for the manufacture of niobia doped pellets was as follows:

(a) Manufacture U_3O_8
(b) Produce Master Blend
(c) Blend Master Blend, UO_2 and U_3O_8
(d) Add and Blend Pore Former
(e) Granulate, Condition and Lubricate

(f) Press
(g) Sinter
(h) Grind
(i) Screen
(j) Pack

With the exception of sintering, which employed a small (4 kg capacity) batch furnace, all the above process stages are directly scaleable to the production of larger quantities, in some instances using the same equipment employed for this project. As far as sintering is concerned, the experience of sintering niobia doped fuel is directly transferable to large scale production in a continuous sintering furnace. Indeed, the conditions employed during sintering of niobia doped fuel are, nominally, in terms of temperature, atmosphere and cycle, those employed during production of undoped fuel.

Manufacture U_3O_8

A quantity of IDR UO_2 powder, approximately 30 kg of 3.9% U-235, was diverted from a 2 te production batch for the manufacture of the niobia doped pellets. The remaining powder was supplied to the customer to manufacture undoped pellets for the same reactor loading. Although prepared following a qualified, customer approved, route and of acceptable quality standards, additional chemical analysis was carried out on the parent batch prior to release of the powder for doped pellet manufacture. A small quantity, approximately 3.5 kg, of powder had previously been removed from the parent batch and converted to U_3O_8 by oxidation in air, following a pelleting and sintering exercise. Testing of the U_3O_8 was limited to determination of the density depression at the 10% level when added to a standard batch of powder and sintered under standard conditions.

Master Blend Production and Blending

The relatively low concentration of niobium in the sintered pellets coupled with the requirement to achieve a high degree of niobium homogeneity prescribed a two stage blending process, comprising production of a high niobia content niobia/urania masterblend subsequently blended with the appropriate quantity of urania and U_3O_8. Qualification of the blending processes covered both masterblend production and the final blending stage, with verification of achieved homogeneity by chemical analysis on the final blend. Additional chemical analysis at the powder blending stage confirmed compliance with customer requirements. Blending also included addition and homogenisation of CONPOR pore former. The latter is added to achieve the required sintered density and the quantity is determined following a sintering test on the blended powders.

Granulation, Conditioning, Lubrication and Pressing

Granulation was performed with a roll-compactor with process parameters adjusted to produce a free flowing granulate of appropriate pour and tap density. Following conditioning and lubrication, the granulate was characterised in terms of pressing load versus green density and green density versus sintered density, together with radial and axial shrinkage ratios. These ratios were used to derive a target green density for the chosen die diameter and green length, respectively. All test pellet sintering was carried out in the same furnace under the same conditions employed during manufacture. These conditions were established previously during a qualification exercise involving niobia doped pellets of the same composition.

Sintering

Sintering was carried out in a batch furnace over 9 runs (lots) in a controlled atmosphere and the resulting product sampled for acceptability in terms of grain size and density at the lot and batch scale. These sintered density data, presented in Table III, show both small within lot and between lot variations.

Density control was achieved by the addition of BNFL CONPOR pore former, added at the powder blending stage, and employing a sintering cycle derived for niobium doped fuel. In addition to achieving the specified sintered density, the sintering cycle was constructed to produce pellets having grain size and resinter densifications values similar to those of the ramp tested material (Table II).

TABLE III. LOT TO LOT VARIATION IN SINTERED DENSITY OF NIOBIA-DOPED FUEL

lot	mean	sigma	lot	mean	sigma
1	10.500	0.015	6	10.499	0.014
2	10.510	0.008	7	10.502	0.013
3	10.497	0.017	8	10.507	0.012
4	10.498	0.032	9	10.501	0.015
5	10.497	0.021	overall	10.502	0.016

Grinding, Inspection and Packing

Sintered pellets were centreless ground to diameter using a bronze bonded diamond grinding wheel prior to 100% diameter measurement using a laser micrometer and screening, against subjective standards, for visual defects. Following final inspection, and sampling for chemical and physical analysis, a release certificate was issued by Springfields Quality Assurance department to confirm compliance with the pellet specification. The required number of pellets, were packed, according to an agreed drawing and despatched to ENUSA, on time and in full compliance with the specification. Collated data was provided to the customers in the form of qualification and pre-irradiation characterisation reports.

CONCLUSIONS

Ramp testing of solid niobia doped IDR/CONPOR fuel has confirmed the material as a remedy for Pellet Clad Interaction failure.

BNFL Springfields Research and Development Department has produced niobia doped pellets for loading into a commercial PWR having almost identical characteristics to pellets produced earlier and successfully ramp tested in the Petten test reactor.

The manufacture of niobia doped fuel employed equipment and processing representative of a full scale production route. The only exception to this was the use of a batch sintering

furnace However, the employed conditions, in terms of the sintering atmosphere, temperature and cycle times are directly transferable to a continuous sintering process

BNFL has demonstrated a current capability to manufacture niobia doped fuel to the satisfaction of a major European reactor operator

REFERENCES

[1] TURNER, E , VAN ENGEN ,W R , and CORDALL, D The post irradiation examination of Niobia-Doped Fuel Irradiated in the Dodewaard BWR, ANS-ENS International Topical Meeting on LWR Fuel Performance, Avignon, 1991

[2] HOWL, D. A , PALMER, I .D , and TOPLISS, I R , Niobia Doped Fuel as a PCI Remedy ANS-ENS International Topical Meeting on LWR Fuel Performance, Palm Beach, 1994

DISCUSSION

(Questions are given in italics)

Can you comment on the fact that large grain fuel does not retain fission gas any more than standard fuel?

Diffusion of fission gas during ramps from the grain boundaries is higher than for standard fuel. Therefore, the global result (diffusion from the grains + diffusion from the grain boundaries) is at a level similar to the case of doped and standard UO_2.

Comment of a modeler:

Not convinced on PCI improvement because ramp tests presented are not representative of power rates in power plant. Pre-conditioning is 24 kW/m instead of 10 kW/m (Representative of a long time at low power before return to 100% power of the reactor). In that case a power increase from 10 kW/m to 30 kW/m is more problematic because fuel creep is not activated.

There is the same relationship between homogeneity of Nb_2O_5 in UO_2 and safety in reactor accidents How can you have the confidence of homogeneity of Nb_2O_5 in UO_2 by manufacturing?

(a) Niobia homogeneity tests are carried out at the powder blending stage of manufacture. EPMA examination of pellets shows no segregation.

(b) BNFL's experience is that there are no significant safety problems due to the presence of niobium.

The Belleville experimental fuel is sub-stoichiometric, while the Dodewaard fuel was close to stoichiometry. What was the purpose of this change? What could be the effect of this change?

Fission gas release benefits are not realized due to increased cation diffusion rates.

The O:U ratio of EDF demonstration assembly fuel is lower than that power ramp tested due to slight difference in the UO_2 of the sintering atmosphere. During irradiation, the O:U will equilibrate with the atmosphere POxyen2 in the fuel rod.

NEW UO_2 FUEL STUDIES

Ph. DEHAUDT, C. LEMAIGNAN, L. CAILLOT,
A. MOCELLIN, G. EMINET
Nuclear Reactor Directorate,
Service for Fuel Behaviour Studies,
Grenoble, France

Abstract

With improved UO_2 fuels, compared with the current PWR, one would enable to : retain the fission products, rise higher burn-ups and deliver the designed power in reactor for longer times, limit the pellet cladding interaction effects by easier deformation at high temperatures.

Specific studies are made in each field to understand the basic mechanisms responsible for these improvements. Four programs on new UO_2 fuels are underway in the laboratory: advanced microstructure fuels (doped fuels), fuels containing Er_2O_3 a burnable absorber, fuels with improved caesium retention, composite fuels.

The advanced microstructure UO_2 fuels have special features such as : high grain sizes to lengthen the fission gas diffusion paths, intragranular precipitates as fission gas atoms pinning sites, intergranular silica based viscoplastic phases to improve the creep properties. The grain size growth can be obtained with a long time annealing or with corundum type oxide additives partly soluble in the UO_2 lattice. The amount of doping element compared with its solubility limit and the sintering conditions allows to obtain oxide or metallic precipitates.

The fuels containing Er_2O_3 as a burnable absorber are under irradiation in the TANOX device at the present time. Specific sintering conditions are required to improve the erbium solubility in UO_2 and to reach standard or large grain sizes.

The improved caesium retention fuels are doped with SiO_2 + Al_2O_3 or SiO_2 + ZrO_2 additives which may form stable compounds with the Cs element in accidental conditions.

The composite fuels are made of UO_2 particles of about 100 μm in size dispersed in a molybdenum metallic (CERMET) or $MgAl_2O_4$ ceramic (CERCER) matrix. The CERMET has a considerably higher thermal conductivity and remains "cold" during irradiation. The concept of double barrier (matrix + fuel) against fission products is verified for the CERMET fuel.

A thermal analysis of all the irradiated rods shows that the thermal conductivity of the standard UO_2 is not lowered with small amounts of doping elements (< 1 vol. %, advanced microstructure fuels with or without Er_2O_3) but decreases when the volume fraction of additives increases (> 5 vol. %, improved caesium retention fuels).

1. INTRODUCTION

Conventional UO_2 fuel, currently used in PWR type power reactors, is renowned for its quality and performance. Nevertheless two main aims motive current research of an enhanced UO_2 fuel : optimisation of fuel management cost and extension of safety margins. This has led to the following requirements in terms of properties expected of the fuel :

- capability of withstanding high burnups (65000 MWd/t_U) ;
- better reactivity control to extend in-pile cycle time ;

- enhanced capacity to retain fission products ;
- high capacity for hot plastic strain in order to minimise pellet-cladding interaction effects.

Research into new UO_2 fuels is focused around four programmes, each of which meets one or several of the specific requirements indicated above :

- advanced microstructure fuels ;
- fuels containing erbium ;
- fuels with enhanced caesium retention capacity ;
- composite fuels.

In each programme great care is taken to control microstructure changes in order to understand and explain the basic mechanisms responsible for the desired improvement in a property. Care is also taken to ensure that the improvement in a particular property is not achieved to the detriment of other properties, with every effort being made to strike the right balance between conflicting effects.

This article presents the four research programmes on new UO_2 fuels and some early results obtained so far. The first part will be devoted to explaining the general approach made for conducting such a study.

2. IMPLEMENTATION OF A NEW FUEL STUDY

In the light of observations made on fuels irradiated in a PWR or an experimental reactor for analysis, advantageous changes in fuel microstructure could be considered and solutions proposed to obtain such changes. The first stage would involve determining the optimum conditions for preparing this new product. The new product is characterised by density, thermal stability and grain size measurements taken during ceramographic examinations, and by its chemical and uranium isotope composition.

As soon as the manufacture is controlled, small size fuel pellets (about 5 mm in diameter and height) are prepared and designed for analytical irradiation in an experimental reactor. The TANOX device which allows to test a lot of different products is used for this purpose [1]. This irradiation cycle provides important data on the thermal behaviour of the rods and on the thermal conductivity of the fuels but the main aim is to accumulate fission gases within the fuel rods over relatively short durations. Consequently, the post-irradiation examination stage is of particular importance : among other things, this examination enables fuels to be tested with regard to fission gas release, during high-temperature annealing. This examination also includes detailed observation of the irradiated fuels before and after heat treatment by optical and scanning electron microscopy. In this way, it is possible to identify changes in microstructure linked to the retention or release of fission gases.

Figure 1 shows the complete organisation chart of post-irradiation examinations that are likely to be carried out on new UO_2 fuels.

3. ADVANCED MICROSTRUCTURE FUELS

The envisaged microstructural changes must contribute to achieving better fission gas retention by:

- increasing the grain size to extend diffusion paths;
- the presence of nanometric intragranular precipitates promoting the nucleation of bubbles and trapping gas atoms in the grain.

The introduction of additives in the fuel is also aimed at improving its plasticity to reduce the effects of pellet-cladding interaction : the presence of silica-based viscoplastic phases at the grain boundaries makes a significant contribution in this respect.

Grain enlargement can be achieved by annealing at 1800°C for 100 hours or by the addition of crystal growth activators. The latter solution is the only to consider industrially to increase significantly the grain size. For UO_2, it has been shown that crystal growth activators are small trivalent cations, the oxides of which are of the corundum type M_2O_3 with M = Al, Cr, Ti, V, etc (Fig. 2). In order for these activators to work efficiently, the thermodynamic sintering conditions (oxygen potential and temperature) must be such that the right cation valency is maintained : the sintering atmosphere will consist of hydrogen with varying water vapour content depending on the element used (Fig. 3) [2]. These oxides, which are partially soluble in the UO_2 lattice at the sintering temperature (1700°C), are found in the form of intragranular precipitates in the sintered product. By varying the oxygen potential at the end of sintering, or during subsequent annealing, metallic precipitates can be obtained from these additives [3].

Doped fuels such as these, with large grain size and containing discrete inclusions (Fig. 4), are of great interest for their creep properties [4]. For example, the simultaneous addition of silica, to obtain a quasi-continuous intergranular phase, cannot be systematically justified. However, it leads to a further increase in creep rate.

4. FUELS CONTAINING ERBIUM

The addition of erbium as a neutron poison UO_2 can be used as a means of limiting the fuel reactivity at start of life. The consumption of the efficient isotope of the poison ^{167}Er as neutron capture takes place gradually restores the reactivity, thereby allowing in-pile cycles to be extended (18 to 24 months). Neutronic studies have indicated that a small amount of Er_2O_3 (0.5 wt % in all rods or 1 wt % in half of the core) must be added to a UO_2 enriched with 4.5% of ^{235}U [5].

Er_2O_3 forms a solid solution with UO_2 on condition that the atom diffusion in the bulk is sufficiently fast. This is not generally the case during conventional sintering at 1700°C under dry or wet hydrogen atmosphere, which leads to a very fine-grained microstructure ($< 5\ \mu m$), as the movement of grain boundaries is blocked by Er_2O_3 precipitates [5]. Consequently, special sintering conditions are used to obtain a standard or large grain size with solubility of the additive in the UO_2.

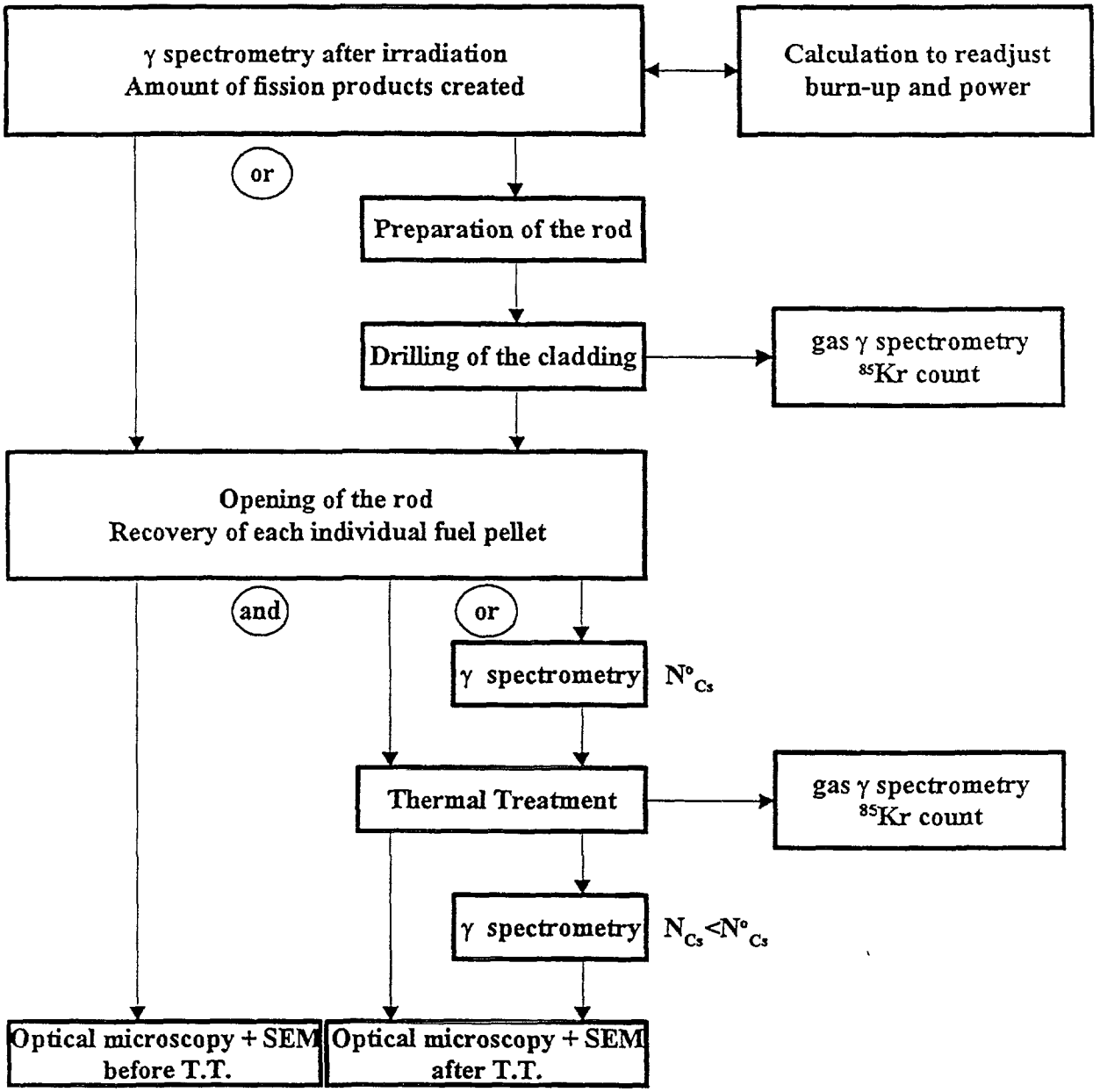

FIG. 1 : Post-irradiation examinations synoptic

In order to keep the benefit of advanced microstructures even in the presence of erbium, studies are being carried out on fuels containing several additives in oxide form to improve the transport properties and to allow simultaneous crystal growth and solution of the rare-earth oxide. A corundum-type oxide - which is a crystal growth activator - can be taken together with another oxide likely to form a low-melting point eutectic compound with the first additive. During preparation, all the oxides are mixed together, including the rare earth oxide, before being added to the UO_2. In this way homogeneous microstructures are obtained (Fig. 5).

Such UO_2 fuels containing 1% by weight of Er_2O_3 are currently being irradiated in the TANOX device in the SILOE experimental reactor.

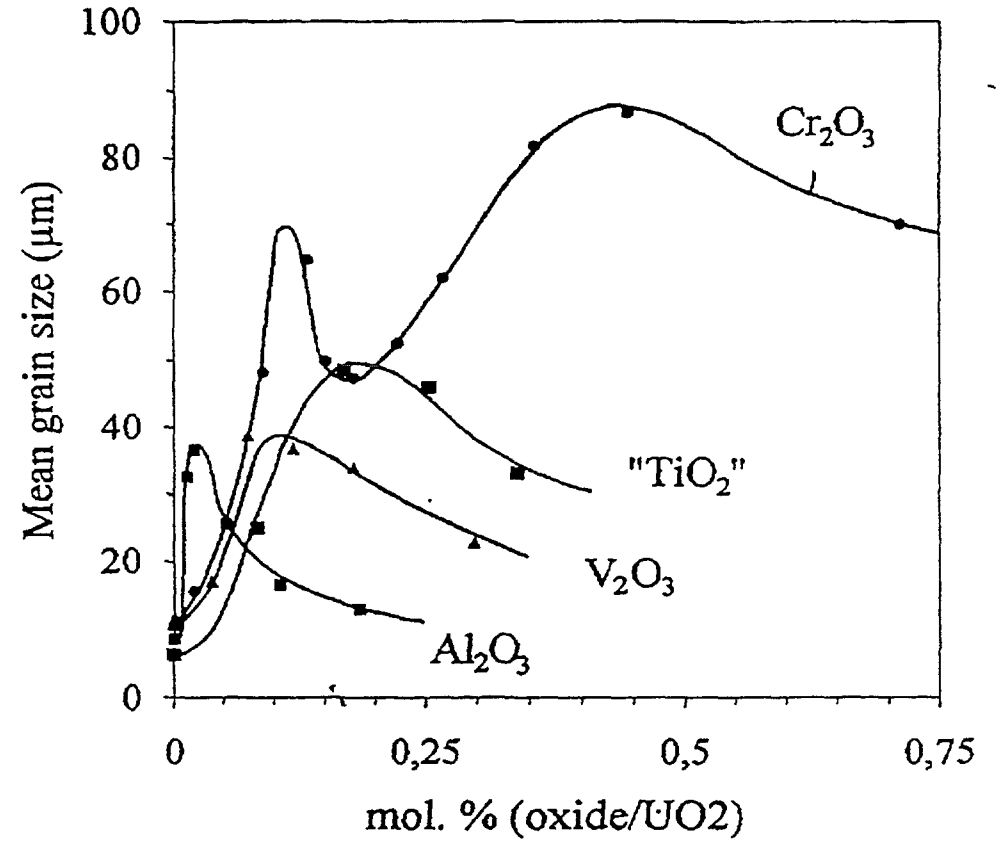

FIG. 2 : Influence of a corundum type oxide addition on grain growth

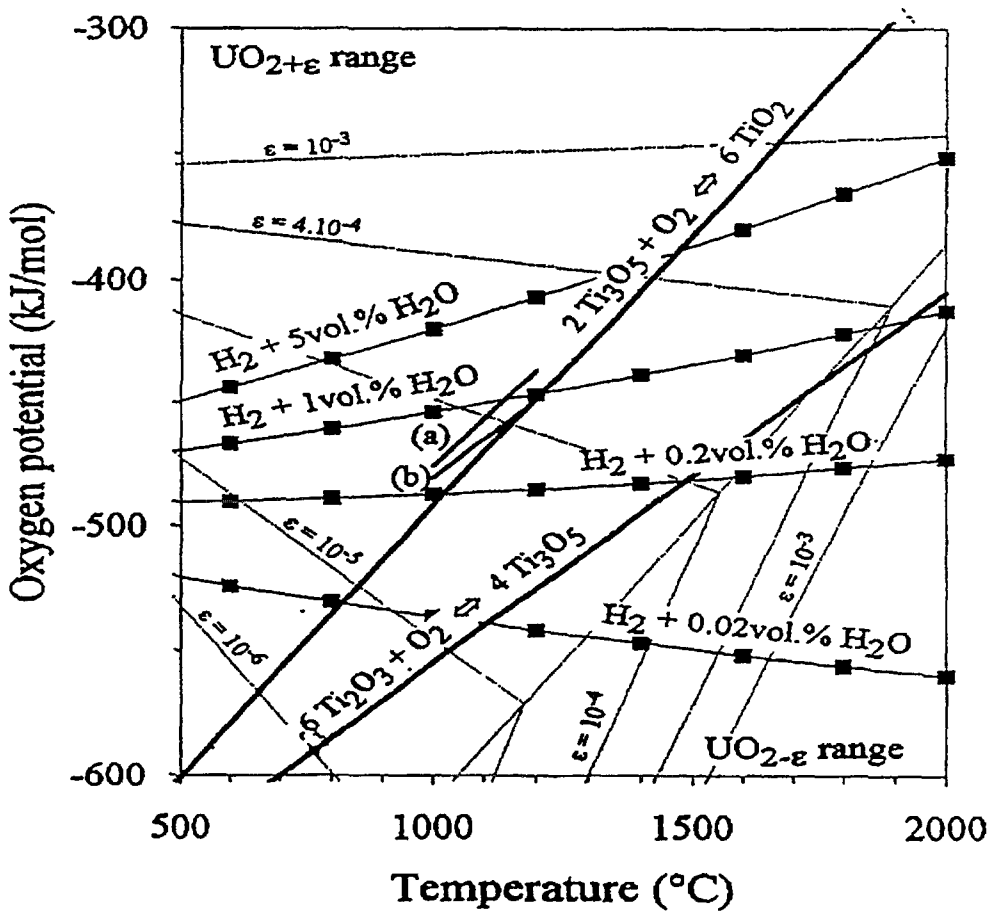

FIG. 3 : Free enthalpy diagram to define sintering parameters with the TiO_2 addition

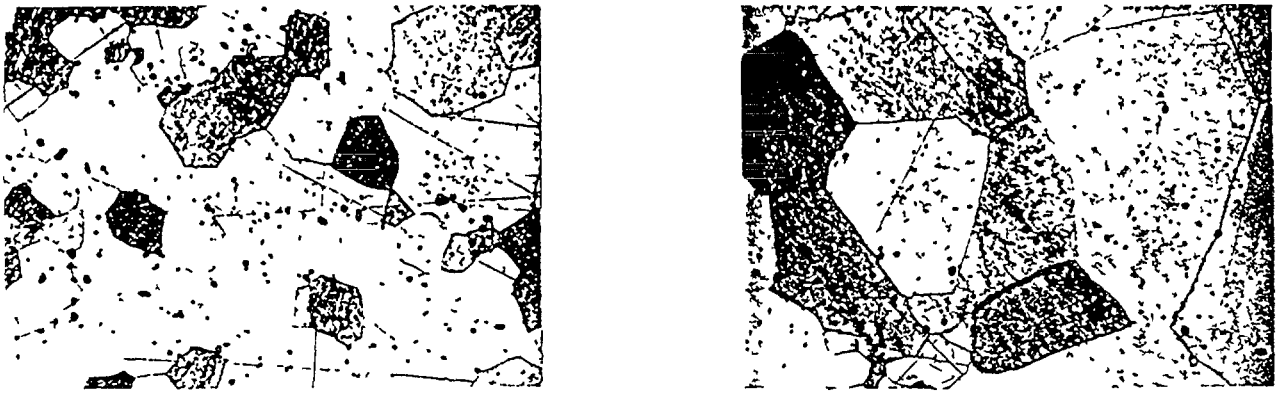

$UO_2 + Cr_2O_3$ (two different contents)

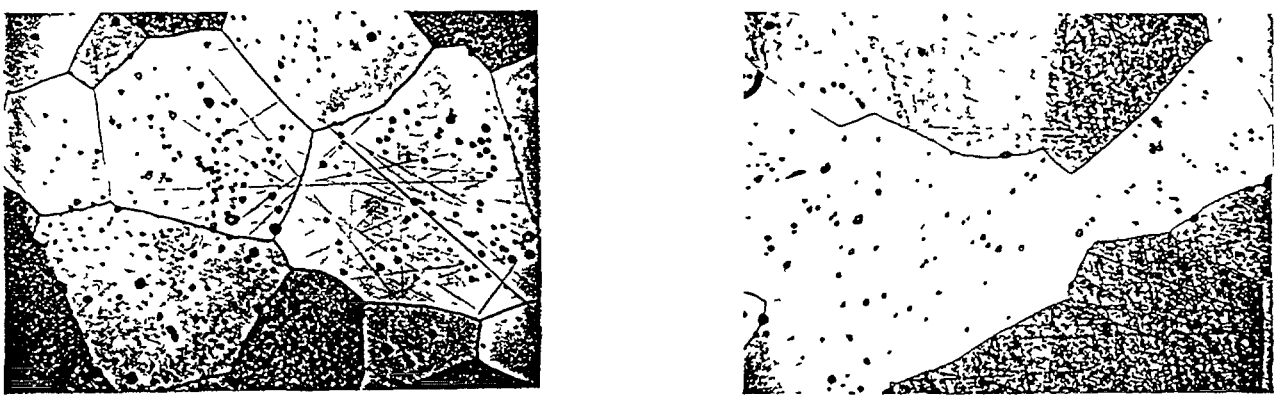

$UO_2 + Cr_2O_3$ after reduction thermal treatment

$UO_2 + Cr_2O_3 + SiO_2$

FIG. 4 : Microstructure of advanced doped fuels

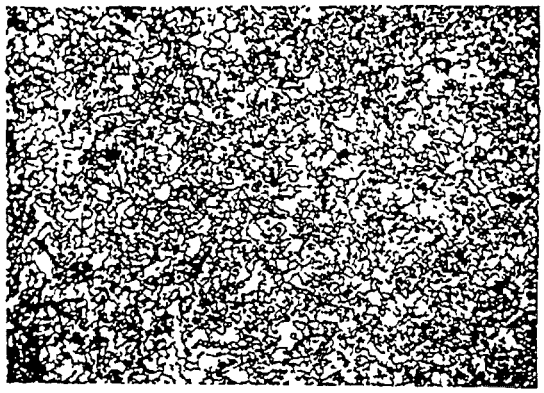

$UO_2 + Er_2O_3$
Standard sintering

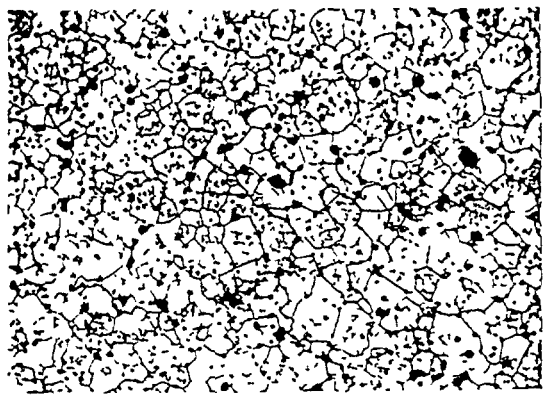

$UO_2 + Er_2O_3$
Non standard sintering

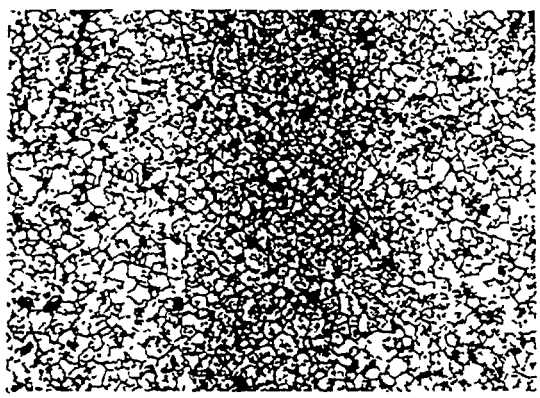

$UO_2 + Er_2O_3 + MgO$

$UO_2 + Er_2O_3 + M_2O_3$

$UO_2 + Er_2O_3 + M_2O_3$ 40 µm

FIG. 5 : Microstructure of UO_2 fuels containing Er_2O_3 as a burnable neutron absorber

5. FUELS WITH ENHANCED CAESIUM RETENTION CAPACITY

Of the gaseous volatile fission products which migrate with ease outside the fuel, caesium is probably the most highly contaminating element for the environment in the event of an accident. Special microstructures are being studied with a view to slowing down the kinetics of caesium release outside the fuel. The aim is to trap the caesium atoms chemically at the grain boundaries in silica, alumina or zirconia-based secondary phases. Relatively stable caesium compounds, $CsAlSi_2O_6$ (pollucite) and $Cs_2ZrSi_6O_{15}$, are likely to form in the presence of these elements during irradiation. The caesium zirconosilicate $Cs_2ZrSi_6O_{15}$ was not known before and has been investigated in detail [6]. The kinetics of caesium release outside these compounds, taken separately or introduced in the fuel deliberately, is much slower than that observed for standard fuel [7].

Three kinds of fuels of this type, with $SiO_2 + Al_2O_3$ or $SiO_2 + ZrO_2$ additives, have been prepared for analytical irradiation in TANOX : the intergranular phase represents a 5 to 6% volume fraction, estimated to be sufficient to trap all caesium that may form at 45000 $MWd.t_U^{-1}$. In the case of $SiO_2 + Al_2O_3$ addition a melting phase is formed during sintering under an hydrogen atmosphere which allows the grain growth (Fig. 6) : the intergranular phase obtained is continuous. In the case of $SiO_2 + ZrO_2$ addition sintering under an oxidising atmosphere has to be performed to avoid ZrO_2 solubility in UO_2 : inclusions are formed at the grain boundaries and the grain growth is hindered (Fig. 6).

The irradiation covered a period corresponding to six operating cycles of the SILOE experimental reactor for a total duration of 78 to 92 equivalent full power days. The burnup reached by the three rods vary from 17170 to 19580 $MWd.t_U^{-1}$.

Post-irradiation annealings and microstructural examinations are in progress. Burst release is measured throw two thermal treatments at 1580°C and 1700°C for 30 minutes ; temperatures have been chosen below and above the melting points of the caesium based compounds. The ^{85}Kr release fractions give data about the role of the secondary phase on fission gas release. The Cs release fractions are determined by a γ spectrometry count of the pellet before and after annealing.

6. COMPOSITE FUELS

The composite is made up of an inert matrix in which the fuel is dispersed in granular form. This concept is the most innovative and its introduction in nuclear reactors is still far. Its potential advantages are nonetheless undeniable and attractive. With regard to safety, for example, the matrix could promote thermal transfer so that the fuel temperature and the specific fission gas release would be lowered ; the matrix also forms a second barrier (after the fuel itself) to the migration of fission products.

Our study [8] concerns CERMET-type composite (Fig. 7) with a molybdenum metallic matrix and a CERCER-type composite with a $MgAl_2O_4$ ceramic matrix. They contain 36 vol. % of UO_2 particles with a 19.6 wt % of ^{235}U enrichment.

The CERMET fuel stays cold during irradiation (§ 7, Fig. 8). The irradiated pellets are not cracked and remain as they were before irradiation. The fraction of ^{85}Kr released during

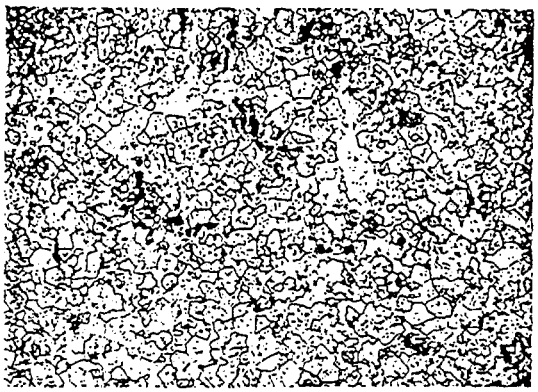

Standard UO_2 — 40 µm

After chemical etching

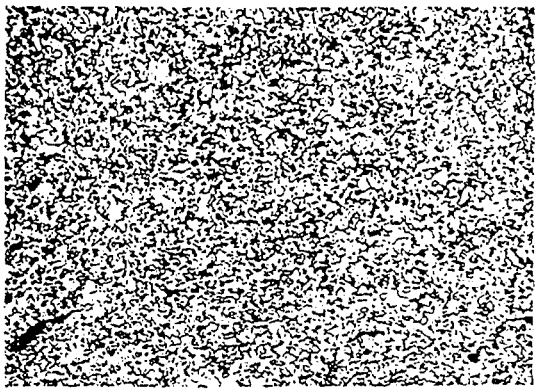

$UO_2 + ZrO_2 + SiO_2$ — 40 µm

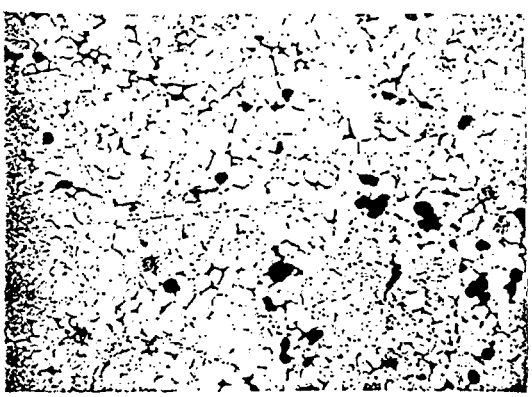

$UO_2 + Al_2O_3 + SiO_2$ — 40 µm

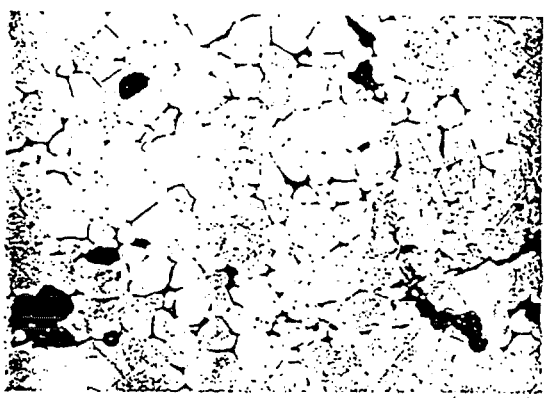

$UO_2 + Al_2O_3 + SiO_2$ — 15 µm
S.E.M. picture

Before chemical etching

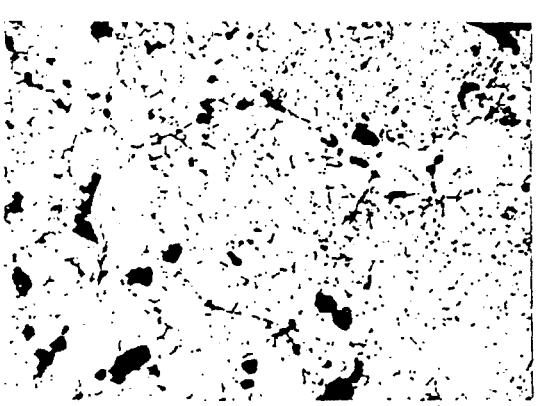

$UO_2 + Al_2O_3 + SiO_2$ — 40 µm
(with an other Si/Al ratio)

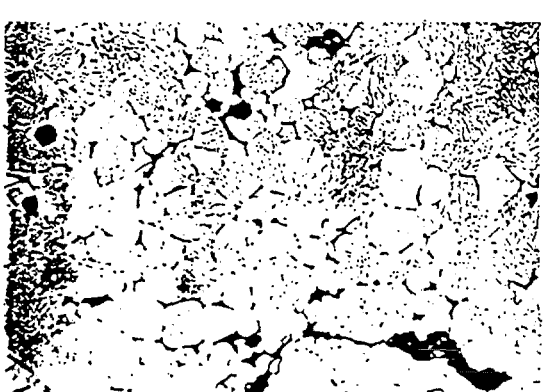

$UO_2 + Al_2O_3 + SiO_2$ — 15 µm
(with an other Si/Al ratio)
S.E.M. picture

FIG. 6 : Microstructure of improved cesium retention fuels

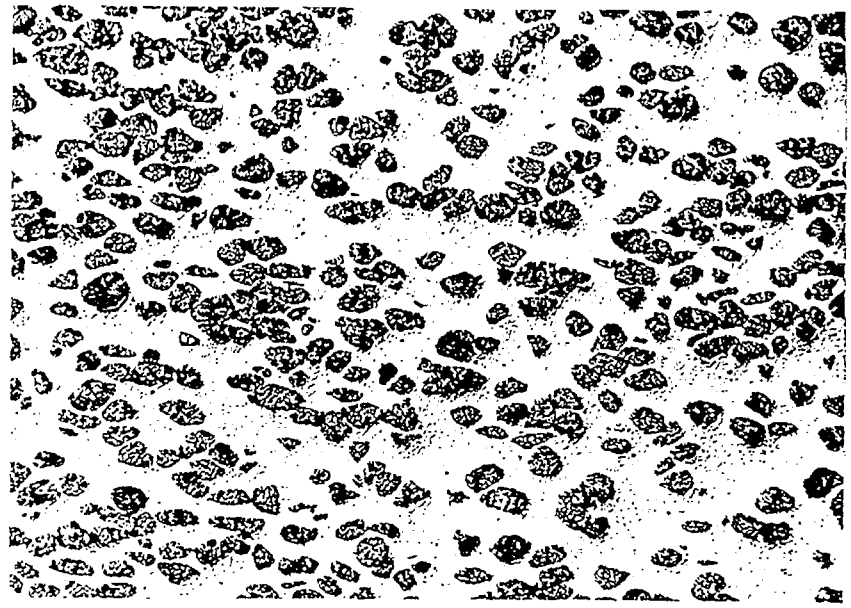

General aspect

200 µm

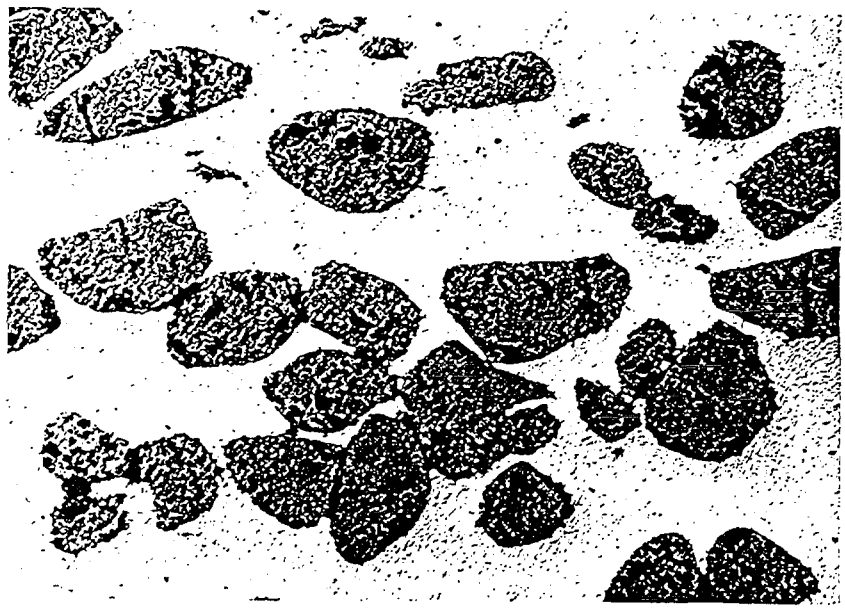

Morphology of UO_2 particles

50 µm

UO_2/Mo interface

10 µm

FIG. 7 : Microstructure of the UO_2/Mo CERMET fuel

irradiation is 2.1% due to ejection and recoil from UO_2 granules emerging at the pellet surface. The fission gas release during post-irradiation annealings is very low in view of the high burnup, close to 50000 $MWd.t_U^{-1}$, and the temperatures that it would never reach under irradiation.

The CERCER fuel behaves like a standard UO_2 for the thermal (§ 7, Fig. 8). The fraction of ^{85}Kr released during irradiation is only 0.7% due to the existence of a strong contact between fuel and cladding during most of the irradiation period. This swelling seems to be caused by the transformation of the matrix around UO_2 particles on the edge of the pellets. The fission gas release during post-irradiation annealings is rather high because the CERCER cracks during the irradiation period and subsequent post-irradiation relief annealing and no longer forms a tight barrier with respect to fission products.

7. THERMAL ANALYSIS

The thermal analysis was performed on the basis of the experimental and calculated relationships between centre-line temperature and power, as represented on Figure 8.

In view of the low contents of additives introduced in the advanced microstructure fuels with or without Er_2O_3, their thermal conductivities may be considered to be equivalent to that of standard UO_2. The thermal response of a given fuel rod changes during the irradiation cycle

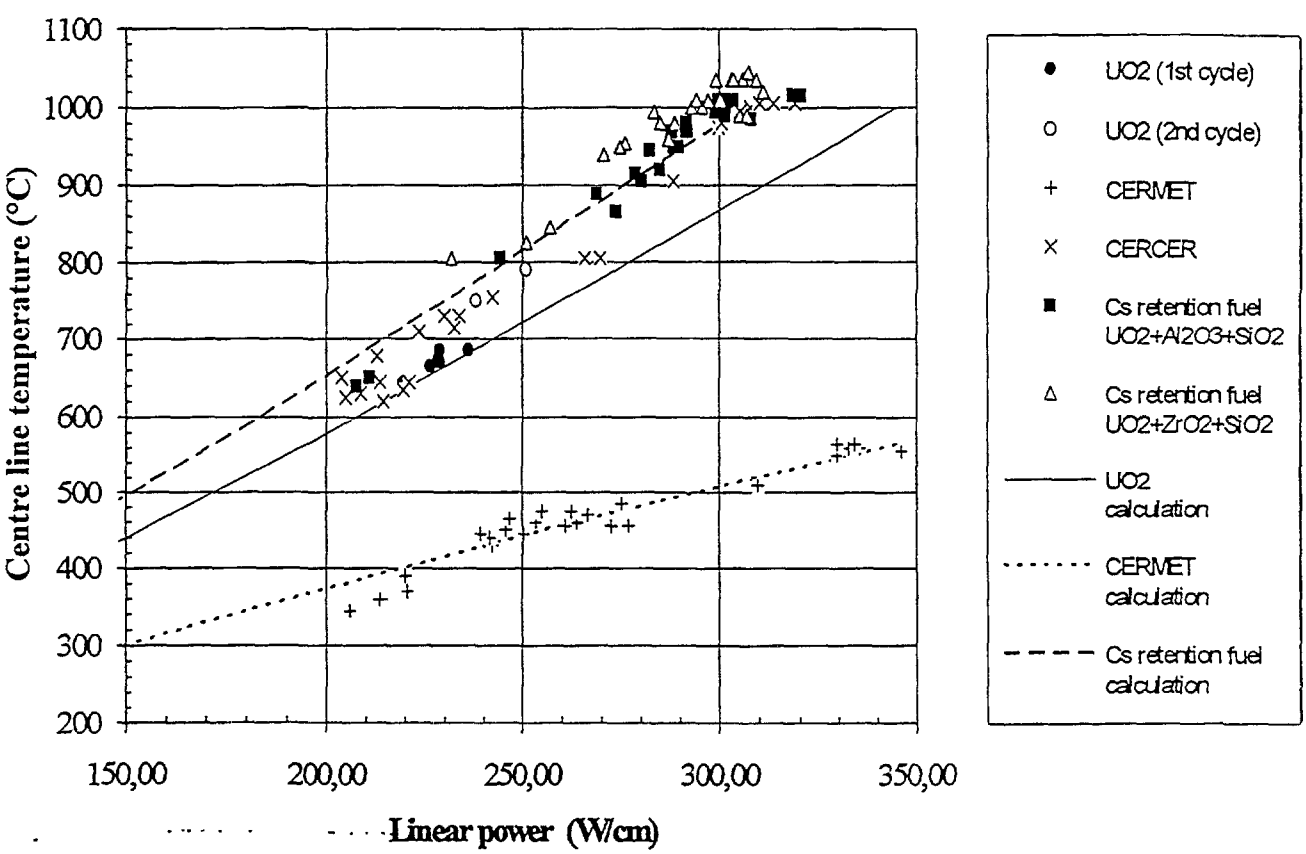

FIG. 8 : Centre line temperature versus linear power diagram

when the power exceeds a certain limit (as can be seen for the reference UO_2 fuel) : the thermal conductivity reduces from an "out-of-pile" value to an "in-pile" value ; this is indicative of the degree of fuel fragmentation.

For the fuels with enhanced caesium retention capacity, the high proportion of additives contributes to a reduction in UO_2 thermal conductivity of about 5% estimated according to the Maxwell-Eucken's law of mixtures. The rods effectively tend to be much hotter than the reference UO_2 fuel.

Experimental data show that the thermal conductivity of the CERCER is the same as the UO_2 one. The calculation with the Maxwell-Eucken law does not confirm that : either the knowledge of the thermal conductivity of the $MgAl_2O_4$ spinel is insufficient or the heat tranfert between UO_2 particles and matrix is not good enough.

The thermal conductivity of the CERMET is much higher than the UO_2 one and in good agreement with calculation with Maxwell-Eucken law.

8. CONCLUSION

Given the diversity of this research on innovative UO_2 fuels, coupled with the originality and efficiency of the experimental procedure, the authors are able to propose solutions to meet the stated requirements for improved fission product retention at high burnups, extension of irradiation durations and minimisation of pellet-cladding interaction effects.

Thanks to the relationships which exist or that can be made between the various studies presented in this article, progress has been made in the definition of a UO_2 fuel in which the maximum number of properties are improved.

Fuel with a low doping agent content would seem to hold out most promise and its use is being continued in order to optimize compositions and microstructures.

The composite fuel concept is interesting as a study tool ; for example, it can be used to obtain UO_2 at very high burnups having been subject to special irradiation conditions such as low temperatures in the CERMET case.

These basic studies are supported by the FRAMATOME and EDF companies and will be followed by numerical calculation on the behaviour in reactor and irradiations in PWR.

REFERENCES

[1] DEHAUDT, Ph., CAILLOT, L., DELETTE, G., EMINET, G., MOCELLIN, A., Irradiation of UO_{2+x} fuels in the TANOX device, TCM IAEA Tokyo, these Proceedings.

[2] BOURGEOIS, L., Effect of additives on enhanced sintering and grain growth in uranium dioxide, Thesis, 17 june 1992.

[3] PEREZ, V., Contribution to the study of second phases particles dispersion in polycristalline uranium dioxide, Thesis, 17 dec. 1993.

[4] DUGUAY, C., DEHAUDT, Ph., SLADKOFF, M., MOCELLIN, A., High temperature mechanical tests performed on doped fuels, TCM IAEA Tokyo, these Proceedings.

[5] ASOU, M., DEHAUDT, Ph., PORTA, J., Assessment of erbium as candidate burnable absorber for future PWR operating cycles : a neutronic and fabrication study, International KTG/ENS TOPical Meeting on Nuclear Fuel, Würzburg, Germany, 12-15 march 1995, vol. II, p. 79-84.

[6] JOLICART, G., LEBLANC, M., MOREL, B., DEHAUDT, Ph., DUBOIS, S., Hydrothermal synthesis and structure determination of $Cs_2ZrSi_6O_{15}$, Eur. J. Solid State Inorg. Chem., t 33, n°7, p. 647-657, 1996.

[7] GAMAURY, S., MOREL, B., DEHAUDT, Ph., Advanced fuel with improved cesium retention, a study using simulated fuel, International KTG/ENS TOPical Meeting on Nuclear Fuel, Würzburg, Germany, 12-15 march 1995, vol. II, p. 85-90.

[8] DEHAUDT, Ph., MOCELLIN, A., EMINET, G., CAILLOT, L., DELETTE, G., Composite fuels behaviour under and after irradiation, IAEA TCM on Research of Fuel Aimed at Low Fission Gas Release, Moscow, Russia, 1-4 october 1996.

DISCUSSION

(Questions are given in italics)

Do you have any plans to test the Cs retentive fuel in steam, which must be the proper condition?

Cs release is provoked by annealing. Today, experiments are in progress on as-irradiated pellet in inert gas or vacuum. Then, the same experiment will be performed after a pre-oxidation of the fuel.

The additives to Er fuel have 2 effects:

- *to increase sinterability. But are densities of 98-99% TD, to be compensated by pore-former additions, a desirable feature?*

- *to enhance uniform dispersion of Er within the fuel. But, since lower neutron cross-section of Er than Gd makes self-shielding less of a problem and since a low consumption rate of the burnable absorption is a reason to select Er rather than Gd, is homogeneous dispersion of Er in the fuel of any benefit?*

High densities are achieved with additives which are introduced first to enhance Er solubility and grain growth. Perhaps, homogeneous dispersion of Er is not absolutely indispensable, it is useful for grain growth and in pile behavior. Such an improvement can easily be achieved.

ON THE SINTERING KINETICS IN UO_2

A. MARAJOFSKY
Argentine Atomic Energy Commission,
Buenos Aires, Argentina

Abstract

The fabrication process of UO_2 pellets from powders involve pressing and a sintering anneal at high temperature (1650°C to 1750°C) during two or more hours in a hydrogen atmosphere. An alternative method is the oxidative sintering , made at lower temperature (1000°C to 1300°C) in a CO_2 or CO/CO_2 atmosphere. The sintering phenomena consist in the densification of the material by a thermal treatment below the fusion point. For a compact made by pressing a powder, sintering is the process of annulation of the porosity present in the compact or pellet. Several theories describe the sintering phenomena dividing it in three stages, initial, intermediate and final: in all of them the densification is a continuous growing function of time.

Nevertheless it has been experimentally reported that a reduction of the density occurs in the third step of the sintering. The phenomena has been called solarization.

Solarization has been attributed to the effect of the evolved gases from additives or to the CO_2 atmosphere in oxidative sintering. Thus, it is convenient to distinguish between solarization in oxidative or reducing conditions.

Reducing solarization is a consequence of the tendency towards equilibrium of intergranular pores. In oxidative sintering it occurs in the reducing anneal after the sintering and is due to the change in the lattice parameter.

This work shows examples of both types of solarization and qualitative interpretation of this phenomena. Both situations show the need of strict control of the sintering and powder production conditions.

1. Solarization

Solarization phenomena were observed and discussed by Amato *et al.* [1,2,3] and defined as a decrease in density of sinterized bodies, resulting from increasing time or temperature treatments. These authors attributed such phenomena to organic additives pressure within pores. Assmann *et al.*[4] attribute solarization to (i) volume transfer from closed fine to coarse pores through gas diffusion into the matrix according to concentration gradients which depend on the pore radius; (ii) transport from fine to coarse pores through grain-boundary diffusion, entailing both a decrease in density. In the case of oxidative sintering, these authors attribute solarization to the action of CO_2.

2. Solarization during normal sintering

UO_2 pellet manufacture is carried out through two-plateaus annealing, the first one between 400°C and 800°C, with a view to additive sublimation and/or stoichiometric uniformity; and the second one at approximately 1700°C for sintering itself (Fig 1).

Figure 2 shows the hydrostatic density of UO_2 pellets sinterized at 1760, 1700, and 1650 °C for different periods, pressed from ex-AUC (uranyl ammonium tricarbonate) powders

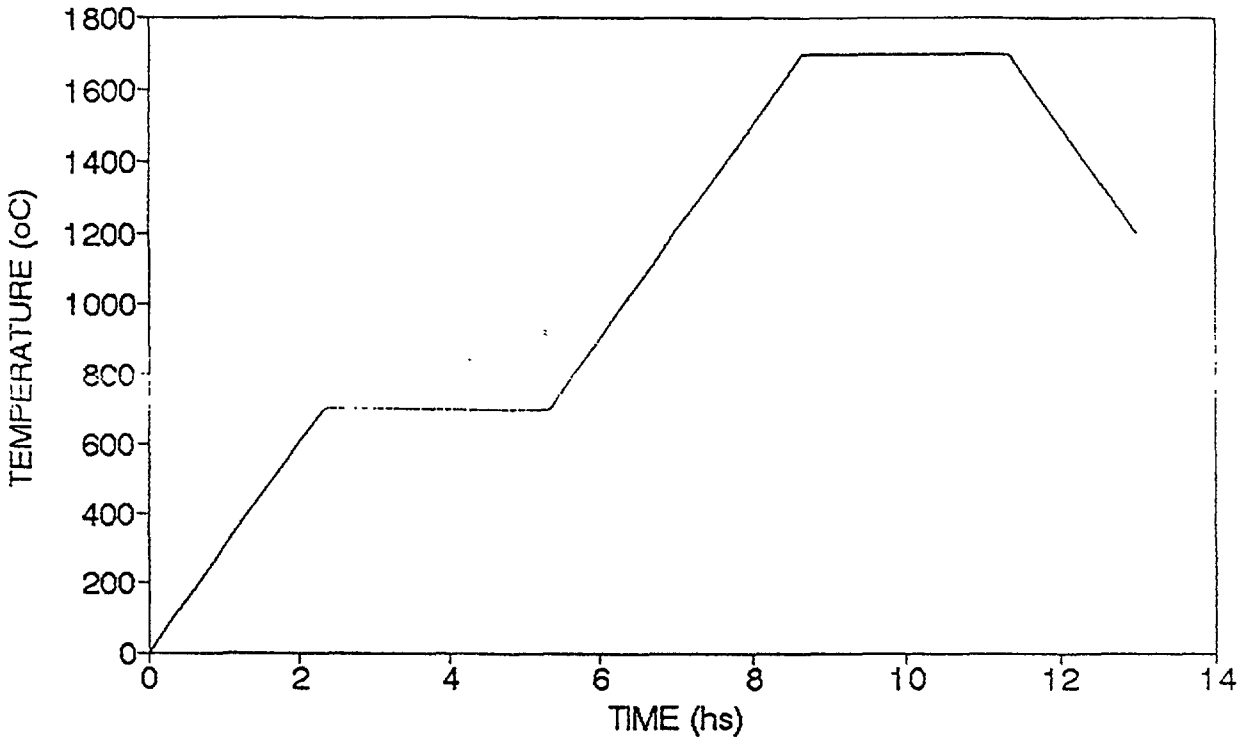

FIG. 1. *Profile of the production sintering anneal*

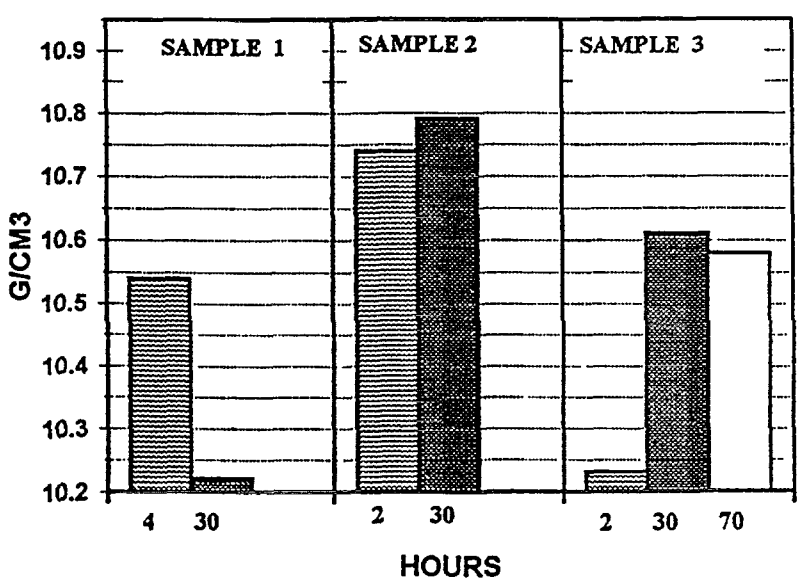

FIG. 2. *Hydrostatic density vs period of anneal of samples 1,2 and 3*

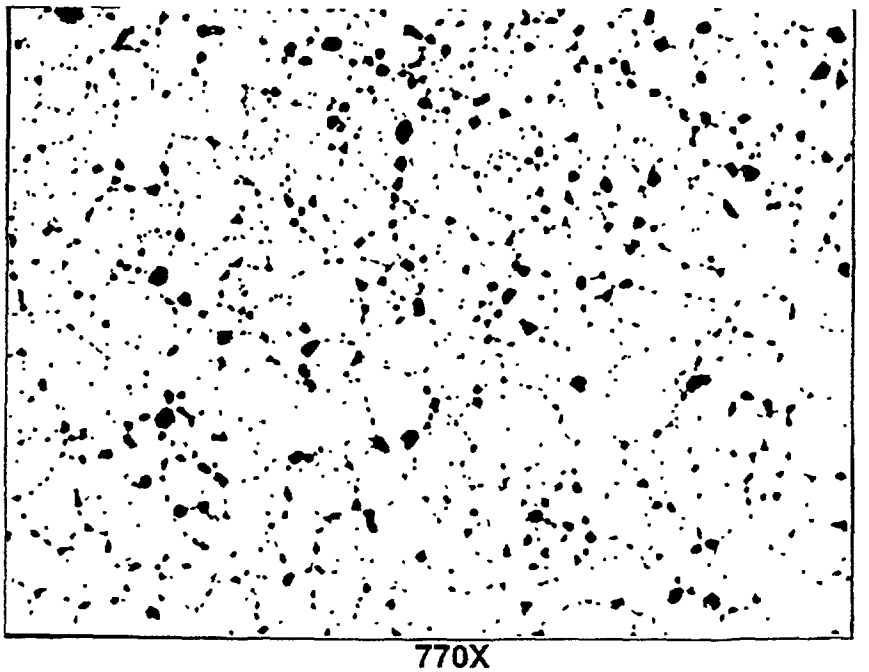

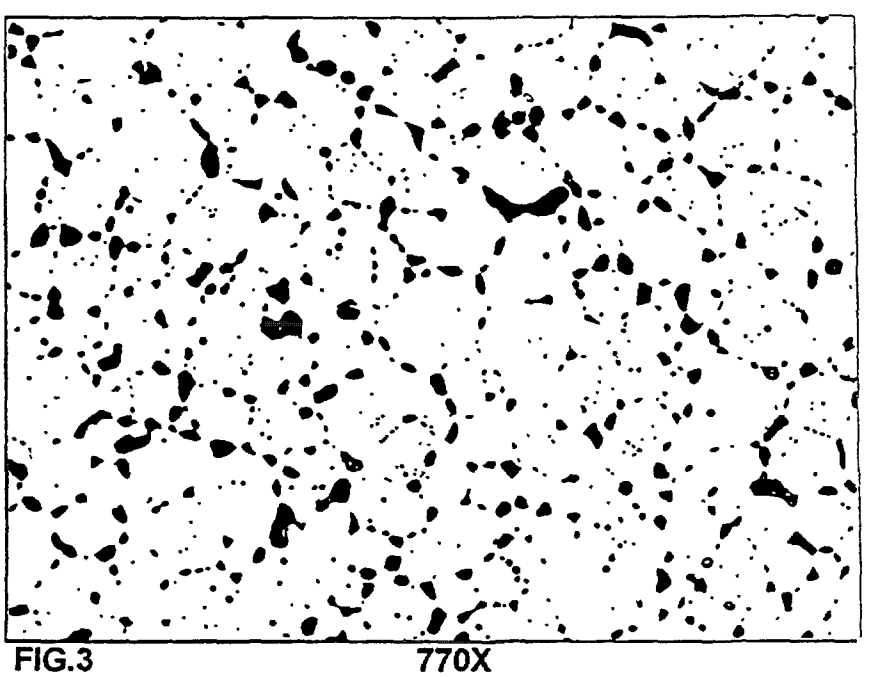

FIG. 3. *Center zone porosity of sample 1 :*
upper photo: after 4 hours sintering anneal, magnification x 770 .
lower photo: after 30 hours sintering anneal , magnification x 770.

free from additives. The effect of solarization after 30 hours is evident in the annealing at the highest temperature.

Figure 3 shows the microstructure of the central area of solarized pellets after 4 and 30 hours respectively. A qualitative increase in intergranular pore size may be observed.

In Table 1, the average of maximum and minimum of intergranular pore diameters may be seen, obtained from 3 micrographies derived with a quantitative image analysis program. [5], confirms quantitatively the affirmation of growing pores.

This type of porosity has been discussed by W.D. Kingery et al. [6] and I.V. Nicolaescu and F. Glodeanu [7], who showed that the intergranular pore may grow if it is big enough and thus decrease pellet density. This conclusion derives from considerations about pore geometry, surface and intergranular tension, as well as on the contact angle.

Sintering itself [4] operates simultaneously through (a) annihilation of intragranular porosity through vacancy flow; (b) spheroidization and closure of pores by surface diffusion; and (c) grain growth. Fig 3, sample 1, shows that after two hours intragranular pores are few, and that after 30 hours they are practically nonexistent. The same can be observed in sample 2 corresponding to 1700°C though in sample 3, 1650°C intragranular pores still persist, especially (either inter- or intra-granular) macropores generated in pressing derived from the spaces between ex-AUC particles and not from the pores inside this particles (mean diameter:0 .1 micrometer).

Sample 1 and 2 pellets correspond to PHWR reactors. Their sizes are greater than those of sample 3: 14mm and 8.5mm respectively (in green). Both are not completely homogenous and show two zones, but in sample 1 pellets there is a gradual inhomogeneity from the center to the border, while sample 2 pellets are also inhomogeneous but only in the peripheral 500 micrometer. Sample 3 microstructure is practically uniform. Therefore, the measured hydrostatic density is in fact an average of the different zones.

Considering this, Table II results, containing figures which correspond to densities by zone, shows that there is solarization in both sample 1 zones (the central one and the peripheral one), and in the central zone of sample 2 (32 hours).

In contrast, sample 3 (30 hours) does not show a decrease in density, although their spherical pores have grown, there is an incipient quantity of triangular intergranular pores, and poligonization has started in a great number of macropores derived from pressing (72 hours).

TABLE I. AVERAGE OF MAXIMUM AND MINIMUM DIAMETERS OF INTERGRANULAR PORES WITH THREE OR MORE SIDES. SAMPLE 1

	2 HOURS	30 HOURS
DIAM.MAX	7.16	10.9
DIAM.MIN.	4.79	6.63

TABLE II. RELATIVE DENSITY MADE WITH QUANTITATIVE IMAGE ANALYSIS IN CENTER ZONE AND BORDER ZONE IN SAMPLES 1, 2 AND 3.

	HOURS 2		HOURS 30		HOURS 70	
SAMPLE	CENTER	BORDER	CENTER	BORDER	CENTER	BORDER
1	9.9	10.51	9.62	10.17	-----	-----
2	10.78	10.7	10.56	10.8	-----	-----
3	10.26	10.34	10.37	10.4	10.56	10.53

These are precisely the pores that shrink and contribute to density decrease together with the annihilating smaller pores. The homogeneity of this sample has to do with his lower diameter and consequently his facility to be reduced faster.

Either solarization will not take place or its value will be small in so far as porosity may be eliminated before big enough intergranular pores are formed. The annealing profile should be slow enough so as to prevent the formation of sufficiently big intergranular pores.

Conversely, steep profiles contribute to fast grain growth, thus sweeping out small porosity and giving rise to intergranular porosity. Kingery and Francois [8] observed this phenomenon in UO_2 using a steep slope annealing profile up to 1700°C.

The same type of porosity may be seen in sintering under oxidative atmosphere (CO_2) after one hour at 1500°C (Fig.4).

Differences in porosity between the central zone and the border may be due to:

- overstoichiometry in the powders (samples 1 and 2) , and the presence of U_3O_8 as additive (sample 1), both involving a gradual reduction from the external part of the pellet towards the center. This entails a pseudo-oxidative sintering at the center (let us recall that this type of process involves a dramatic increase of the U self-diffusion coefficient [4, 9] and, as a consequence, the growth of the grain), thus yielding the beginning of the big intergranular pores.

- differences in green density due to pressure gradients within the pellet.

If differences between zone densities increase, pellets may even break down (Fig. 5) when the first plateau in the sintering (Fig. 1) is not enough to homogenize the stoichiometry of the pellet. Rupture is a consequence of differences in density: from the external, denser zone and the inner zone, less dense because of the porosity derived from solarization.

Premature growing of intergranular pores, as in sample 1 , my be due also to the use of powders ex-AUC with excessive quantity of intraparticle pores, of the order of 0.1 micrometers.

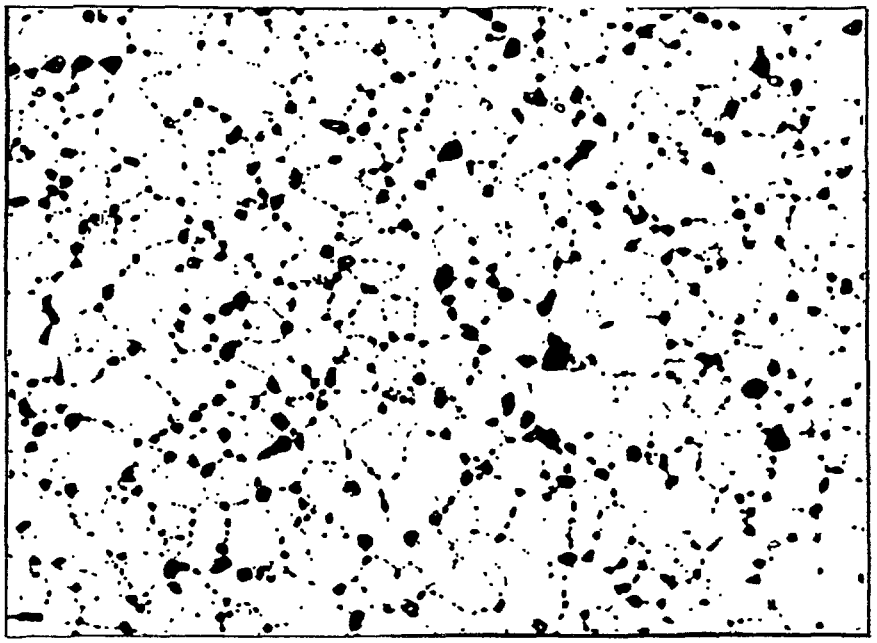

FIG. 4. *Porosity of a sintered pellet annealed in CO_2 atmosphere 1 h at 1500 °C magnification x770*

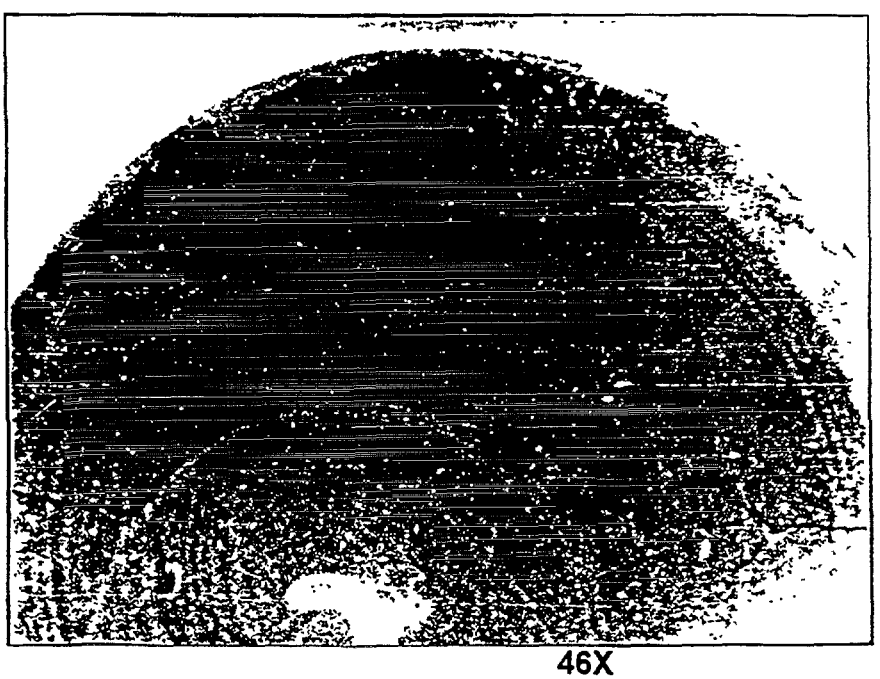

FIG. 5. *Broken pellet due to differences in density between central and border zone*

3. Solarization in oxidative sintering

Oxidative sintering (at low temperature, i.e 1100 to 1300°C) properly carried out, with the first plateau acting as normalizer of the intergranular porosity, yields pellets with normal porosity. In order to bring pellets to stoichiometric values, annealing in H_2 atmosphere is

needed. Although solarization is also observed, in this case, (Fig.6) decrease in density should be attributed to a lower lattice parameter after oxidative annealing than after reductive annealing [10]. That is why the annealing carried out at lower ppO_2 involves less decrease in density.

Δ Density/density = $\Delta m/m - 3\Delta a/a$

$\Delta m/m - 3\Delta a/a \approx -0.47\ \% - 3 \times 0.15\ \% \approx -0.9\%$

The porcentual variation of density is calculated for a stoichiometry of 2.08 , where $\Delta m/m$ is the fractional variation of mass in the unit cell due to the change in stoichiometry and $\Delta a/a$ is the change in lattice parameter due to the change in stoichiometry. This figures gives a variation of the order of magnitude as observed.

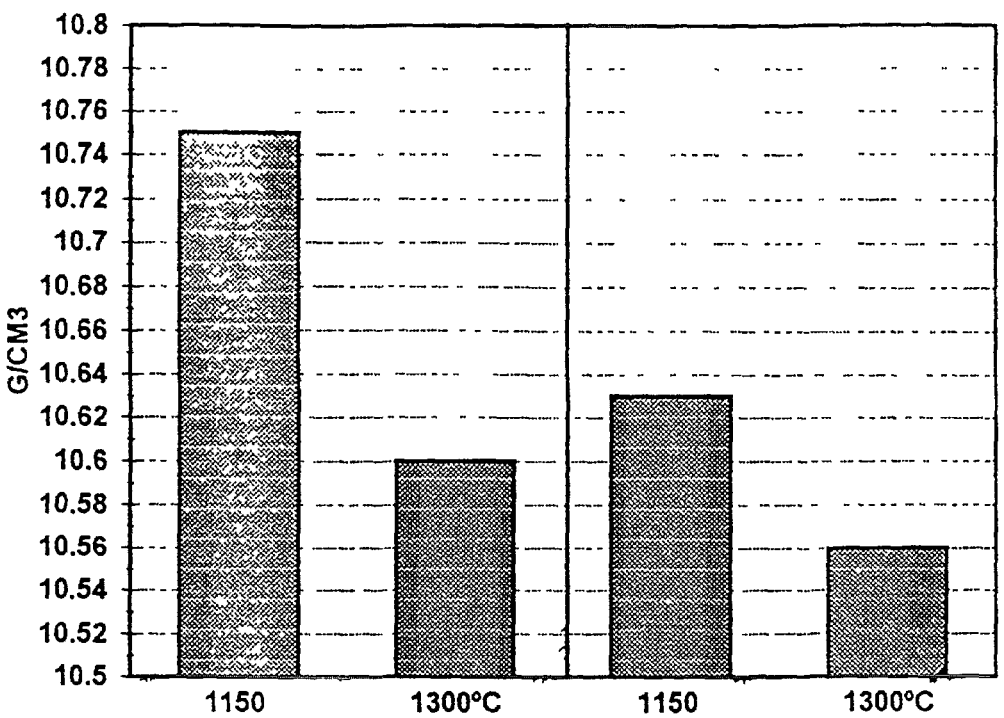

FIG. 6. *Density after oxidative and reduced anneal : 1st. oxidative CO/CO_2 = 1/1000, reduced at 1150 °C, 2nd oxidative CO/CO_2 = 1/100 , reduced at 1300 °C.*

CONCLUSIONS

Solarization in UO_2 pellets is a consequence of the growth of coarse pores in grain boundaries. The growth of such coarse pores occurs in the third stage of sintering and is a general result of the tendency to equilibrium of intergranular pores. Incomplete reduction of the pellet at the beginning of sintering and the consequent activation of cation diffusion yields a fast grain growth that sweeps out the smaller porosity into coarser intergranular pores in the central zone of the pellet at lower temperatures. Such grain growth may also occur in a reduced pellet through a fast arrival to a high enough sintering temperature. In order to prevent excessive solarization, slower slopes and not too high sintering temperatures are recommended.

Differences in density between the center of the pellet and the periphery, due to solarization, may produce its rupture.

In oxidative sintering, after the reducing annealing, solarization occurs due to the change in the lattice parameter.

ACKNOWLEDGEMENTS

To A. Benitez for the ceramographies and useful discussions and G. Thern for the termogravimetries.

REFERENCES

[1] AMATO, R. COLOMBO, A.M. PROTTI, On a case of solarization during steam sintering of UO_2 pellets. JMN,8, No. 2 (1963) 271-272.

[2] AMATO, R. COLOMBO,A.M. PROTTI, Pore growth during solarization of sintered UO2. JMN 13, No.2 (1964), 265-267

[3] AMATO, R. COLOMBO, The influence of organic additions on the solarization and grain growth of sintered UO2. JMN 11,3 (1964) 348-351

[4] ASSMANN,H. DORR W. AND PEEHS. N. JMN 140(1986)1-6. Control of UO2 microstructure by oxidative sintering.

[5] LAVAGNINO, CARLOS, Sistema para Análisis cuantitativo de imágenes. Asociación Arg. de Tecnología Nuclear.Cordoba 1995.

[6] KINGERY,W.D., BOWEN H.K., y UHLMANN D.R., Introd. to Ceramics. John Wiley and Sons(1976)

[7] NICOLAESCU I.V. and GLODEANU F.. Pore Geometry and interfacial energy. JMN 113 (1983) 253-255

[8] KINGERY W.D. and FRANCOIS B., Grain growth in porous compacts. J. of The Am. Cer. Soc. Vol 48 No. 10 546-547

[9] MATZKE HJ.,On Uranium self-diffusion in UO2 and UO2+x. JMN 30 (1969) 26-35

[10] Uranium dioxide. Ed. J. Belle. 1962.Naval Reactor Dept.

DISCUSSION

(Questions are given in italics)

The presentation illustrates the necessity to properly handle the results of the thermal resinter test specified as QC in the fabrication of fuel. It is not sufficient to specify a maximum densification limit: a densification (increase in volume of the pellet) limit must also be considered, as well as a modification of the O/U ratio during the test.

I agree that a scale test would be necessary. Under hydrogen atmosphere, measuring of O/M will not be necessary. The oxidative sintering, yes.

GRAIN SIZE DISTRIBUTION IN SEEDED LARGE GRAIN SIZE UO_2

G.A. WOOD, C.P. PERKINS
British Nuclear Fuels International Group,
British Nuclear Fuels Ltd,
Salwick, Preston,
United Kingdom

Abstract

A large grain size fuel is seen as desirable for the reduction of fission gas release. Conventional techniques to obtain a large grained UO_2 include the use of dopants, elevated temperatures, oxidising atmospheres (with or without dopants) and greatly increased cycle times. Although each approach may, ultimately, result in a large grain size fuel, manufacturing considerations may outweigh performance benefits. Similarly performance benefits of doped material, in terms of an improved fission gas retention, may also not be realisable.

Seeding is a novel technique for obtaining a large grain sized UO_2 in which preferential growth of introduced seed crystals results in a large grain microstructure. By selecting the appropriate size and concentration of seeds, a large grain size fuel is obtained using conventional plant and standard processing cycles. Such grain sizes could only be achieved in a similar time in undoped material by sintering at 2000 °C. Additionally, as the seed crystals comprise UO_2 there can be no implications, for fuel chemistry, of adopting the approach.

Grain size distributions are presented on seeded material sintered in production furnaces for one and two conventional cycles. These show that a fully recrystallised microstructure, comprising a large grain size, can be obtained after one process cycle. Where the seed size is larger and the quantity of nuclei is correspondingly reduced, the time to achieve full recrystallisation is longer, necessitating a second pass through the sintering furnace. However the grain size that could potentially be achieved in these circumstances is larger.

2. INTRODUCTION

A large grain size in uranium dioxide based Light Water Reactor (LWR) Fuel is considered desirable from the standpoint of fission gas release and various methods are available to achieve this including:

(a) Use of dopants.
(b) Use of extended times at conventional sintering temperatures.
(c) Use of higher temperatures (above 2000 °C).
(e) Use of oxidising atmospheres.
(f) Use of oxidising atmospheres in conjunction with a dopant.
(g) By seeding grain growth, using single crystal UO_2, to achieve a "recrystallised" large grain size microstructure.

Of the above techniques items (1) to (5) can be considered as "conventional" methods for obtaining large grain sizes in sintered UO_2 fuel pellets, though for the most part both plant and/or processing parameters may have to be adjusted to achieve the required product and, although each approach may, ultimately, result in a large grain size fuel, manufacturing

considerations may outweigh performance benefits. In the case of high temperature sintering, oxidative sintering and oxidative sintering in conjunction with a dopant, alternative sintering technology to the almost universal approach of sintering in reducing conditions in the temperature range 1700 °C to 1800 °C must be employed. Additionally, where dopants are employed in conjunction with conventional sintering, performance benefits, in terms of an improved fission gas retention, may not be realisable, as enhanced diffusivity, which gives rise to the increased grain size may only result in a modest increase in fission gas retention [1]. Furthermore, as grain growth kinetics in stoichiometric undoped UO_2 follow the general form

$$G_t^3 - G_0^3 = kt, \qquad (1)$$

where G_t is the grain size at time t and G_0 is the grain size at time t_0, and k is the rate constant which varies exponentially with temperature , the time, at constant temperature, required to achieve, for example, a doubling of the grain size, is considerable with a corresponding adverse effect on plant throughput.

Seeding, on the other hand, represents a novel approach to producing large grain size fuel without recourse to alternative manufacturing technology. In comparison to most alternative techniques for enhancing grain growth, seeding enhances the driving force for grain boundary motion as opposed to increasing grain boundary mobility (via enhanced diffusivity) and as such, a seeded large grain size material will have an improved fission gas retention. It is achieved in UO_2 [2] by the addition of single crystals of uranium dioxide, of appropriate size, to UO_2 powder at the blending stage. Processing then proceeds as per conventional practice employing standard equipment and nominal production conditions. A large grain size UO_2 then results on sintering from the preferential growth of the seed crystals into the matrix material. The process is best exemplified with respect to fig.1 which shows the deliberately generated interface between seeded and unseeded regions of a conventionally sintered uranium dioxide pellet. Growth of grains in the seeded region is clearly seen to be considerably greater than in the unseeded region.

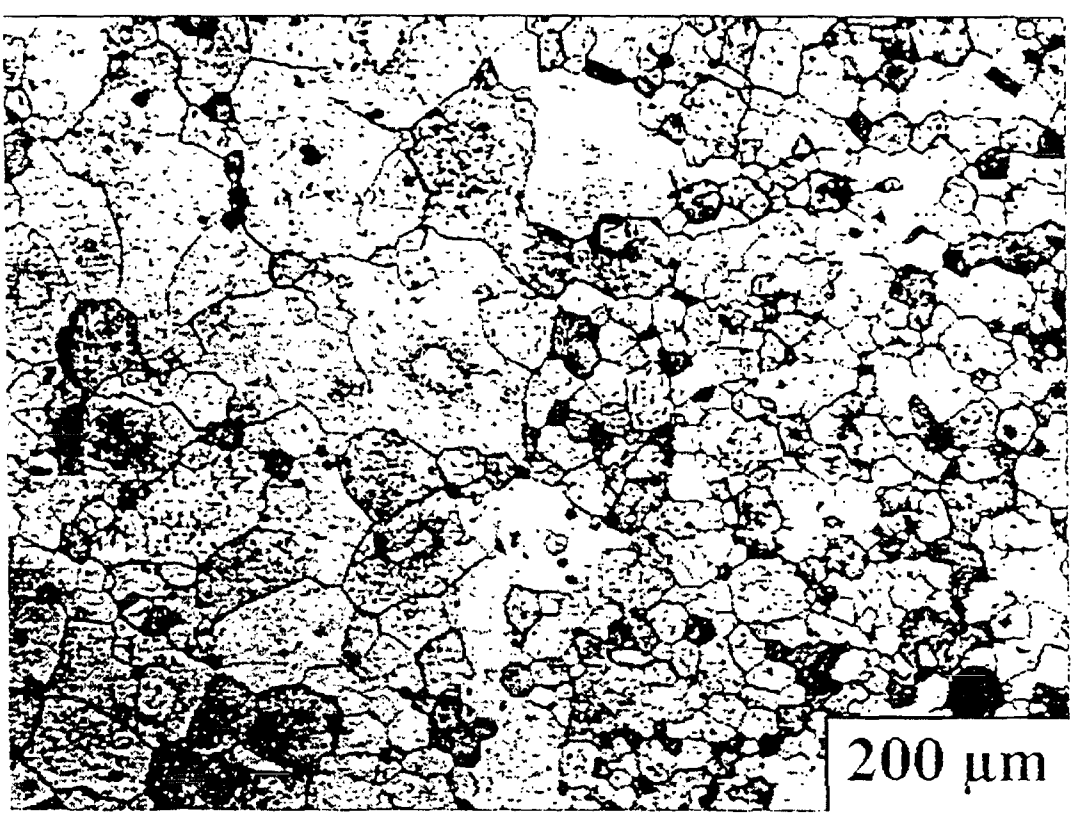

FIG. 1. Created interface between seeded and unseeded regions in a sintered pellet

During sintering, microstructural development passes through stages until a fully recrystallised large grain structure is achieved. Up to this time the microstructure comprises both large and small grains originating from the seed material and the matrix powder, respectively. For a given weight fraction of seeds the number of seeds per unit volume is uniquely defined by the seed size. In the case of a large number of seeds per unit volume (small seed size for a given weight percentage addition) average seed centre to centre distances are small thus limiting the maximum amount of growth that can occur before recrystallising grains impinge on one another and the growth rate is reduced. On the other hand, a small number of seeds per unit volume (larger seed size for the same weight fraction addition) results in the potential to achieve very large grains from considerations of seed separation. However, very large grains are unlikely to be achieved for the following reasons:

(a) The timescale required to achieve a fully recrystallised microstructure will be long when this relies on the large growth of a small number of seeds.
(b) The extended timescale during sintering will result in appreciable growth of matrix grains and a reduction in the driving force for seed growth (proportional to 1/matrix grain size [3]). The larger matrix grains will then be stabilised with respect to consumption by the recrystallising grains during growth of the latter.

Thus, the size of seeds and their concentration together with the thermal cycle employed during sintering will be the factors which determine the final grain size of sintered pellets.

In order to assess the extent to which a material has recrystallised it is necessary to obtain three-dimensional grain size distributions on seeded sintered pellets. These enable not only the relationship (if any) between the two-dimensional grain size and the three-dimensional grain size to be explored but reveal the required sintering times to achieve full or near full recrystallisation and the effects such factors as seed size and concentration have on microstructural development. These are important variables in that they have a direct bearing on the viability or otherwise of seeding as a means of achieving large grain size fuel on a production scale.

To date seeded grain growth in Integrated Dry Route (IDR) UO_2 has been successfully achieved using single crystal seeds obtained by the disintegration of sintered pellets at high temperatures in dry hydrogen [2] and by comminution of sintered pellets [4]. It is also considered possible to employ chemical methods to obtain seed crystals of the appropriate size for example by precipitation and subsequent calcination [5]. In the present work, three-dimensional grain size distributions were measured on large grained samples of uranium dioxide obtained through seeding with crushed sintered scrap of two size fractions and at two weight percent additions. The effect of seed size and concentration and sintering cycle on microstructural development was investigated.

3. EXPERIMENTAL

3.1 Sample Preparation

Sintered pellets of approximately 15 micron grain size were crushed in a uranium percussion mortar and sieved into two size fractions, (<37 μm and 37-53 μm). These seeds were added to IDR powder at 2% and 5% by weight. A binder technique was employed to

facilitate preparation of green pellets. These seeded green pellets were debonded in production debonding furnaces before being sintered in a hydrogen sintering furnace employed in the manufacture of pellets for the British Civil Advanced Gas Cooled Reactor (CAGR) programme. Unseeded control samples accompanied the seeded pellets. After passing through the furnace once, corresponding to a nominal production sintering cycle, at maximum temperature of 1730°C and a residence time in the hot zone of approximately 5 hours, samples of both seeded and unseeded pellets were removed and the remaining pellets cycled a second time through the furnace.

3.2 Analysis

Two-dimensional grain sizes were obtained on polished etched samples by the linear intercept method (ASTM E112). Three-dimensional grain size distributions were obtained via image analysis, with Saltakov correction [6], of tracings of micrographs from several fields, totalling approximately 1000 grains. Seed size distributions were obtained optically, using the same equipment employed for the determination of grain size distribution.

4. RESULTS AND DISCUSSION

4.1 Seed Size Distributions

Figure 2 shows the size distributions of the two size fractions of seeds. The data represents average diameter obtained from projected area and results in an over estimation of diameter. The distribution of the small seed size fraction extends to fine particle sizes where approximately 6% of the total volume is represented by particles of size less than 10 microns. This contrasts with the situation for the larger seed size fraction where about 0.5% of the material is less than 10 microns in diameter. The very fine material, in the region of 1 micron diameter, corresponds to dust attached to the larger particles. It is formed during crushing of sintered pellets and is of a size comparable to the matrix powder. As such, it is considered too small to generate large recrystallised grains. Slightly larger seeds, however, of approximately 10 microns in size have been shown to generate a large grain size via recrystallisation [7].

The large seed size fraction contains material of a size exceeding that of the grains present in the pellets crushed to provide the seeds. This arises from the formation of polycrystal seeds usually comprising two grains, which are still found to recrystallise and generate a large grained sintered material.

4.2 Grain Size

Table 1 compares two and three-dimensional mean grain sizes of conventional and seeded samples; in all instances the grain size of the seeded samples exceed those of the unseeded samples. An optimum seeding effect appears to have been achieved with the smaller seed size (<37 μm) added at the 2% level and sintered for one cycle. On this basis, a large grained product is potentially achievable following conventional (single cycle) sintering with a minimum addition of seeding material.

As larger quantities of small size seeds do not result in a larger grain size than material containing 2% of the same size seeds, sintered for both one and two cycles, the conclusion can

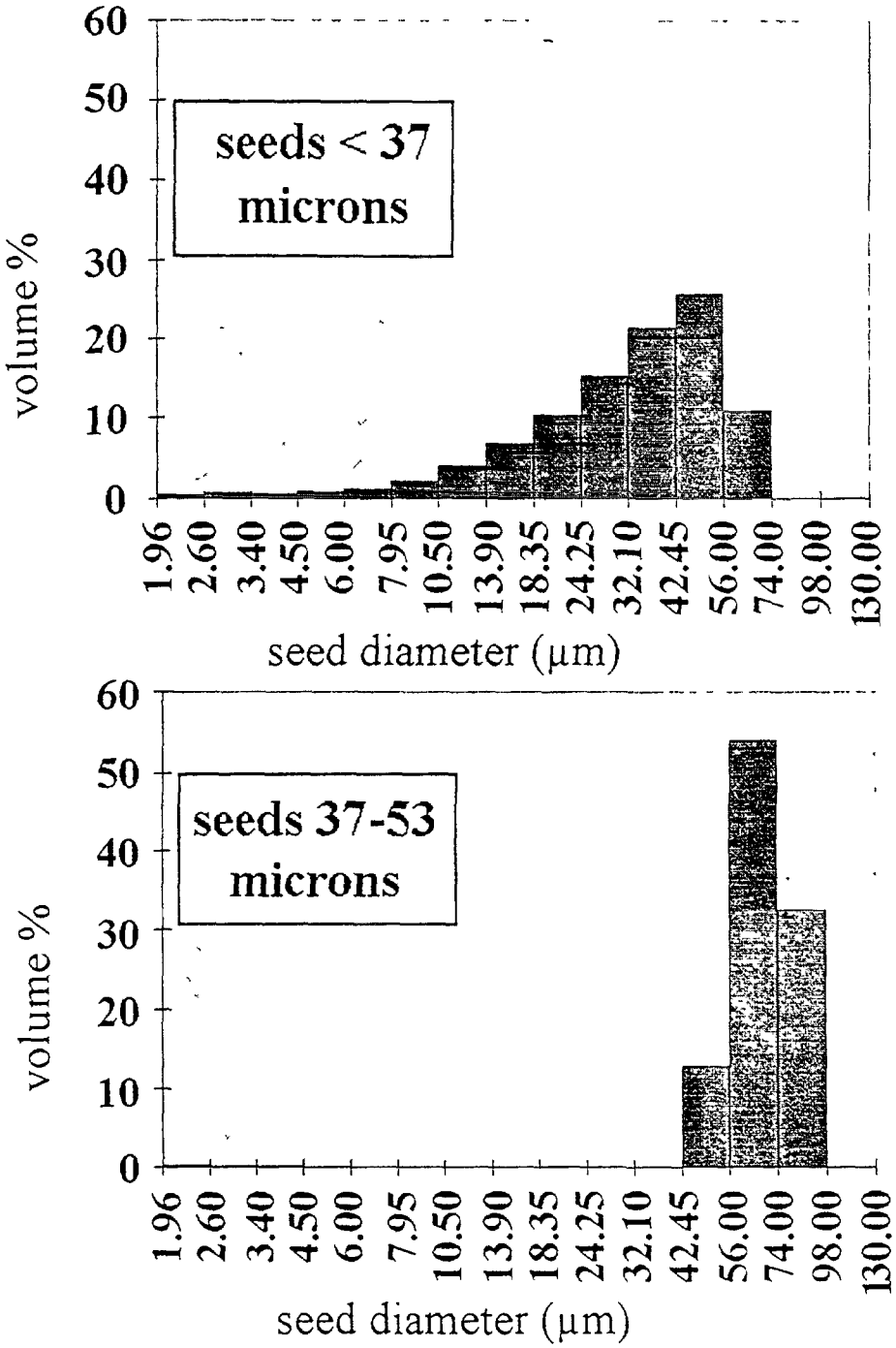

FIG. 2. Seed size distributions. Top, seed size fraction < 37 microns, bottom, seed size fraction 37-53 microns.

be drawn that interference between recrystallising grains in the case of 5% seeded material, with the associated decrease in grain boundary velocity has occurred during the first sintering cycle.

For samples containing the smaller seed size, irrespective of seed content, the increase in grain size during the second sintering cycle is fairly limited, which is also the case for the unseeded material. This contrasts with the situation for material containing the larger size fraction of seeds where greater increases in grain size have been recorded during the second sintering cycle, yielding the largest overall grain sizes.

After the second sintering cycle all seeded samples are thus expected to have fully or nearly fully recrystallised large grained microstructures. This is also predicted to be the case after one sintering cycle for pellets seeded with the smaller size fraction of seeds. For samples containing the larger seeds, incomplete recrystallisation would, therefore, be expected which would be revealed in the three-dimensional grain size distributions obtained on samples.

4.3 Grain Size Distributions

Figure 3 shows the three-dimensional grain size distributions for seeded and unseeded samples after one furnace cycle. A single peak in the distribution is present for all samples with the exception of that containing 2% of the larger seed size fraction (37-53 microns). In this instance, the peak in the size range 32.1-42.5 microns corresponds to the growth of grains following conventional growth kinetics, whereas the peak at 74-98 microns represents the growth of seeds. This sample has, therefore, a partially recrystallised microstructure comprising approximately 50% large grains and 50% conventionally sized grains.

For the remaining seeded samples, after one sintering cycle the degree of recrystallisation is for the most part total with little presence of grains of a size associated with conventional growth.

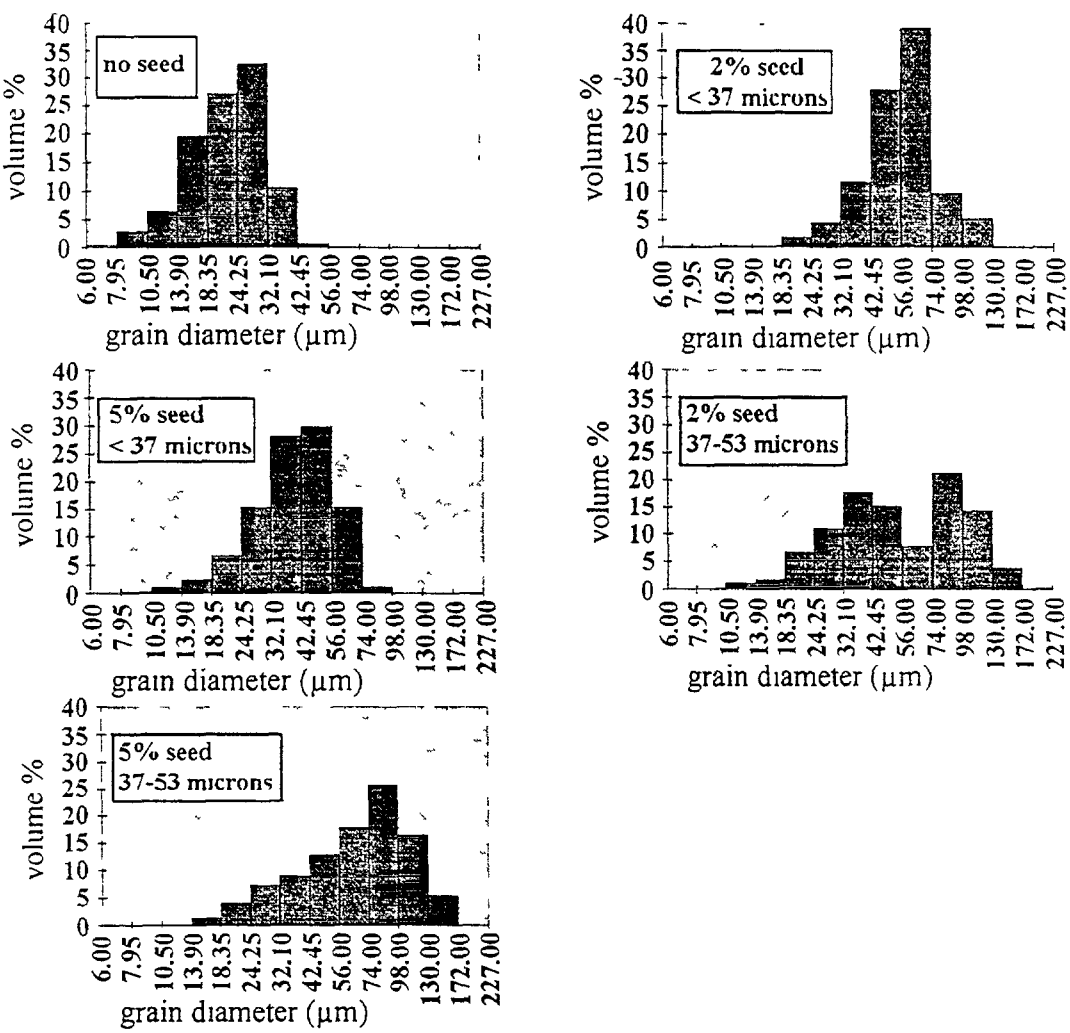

FIG 3 *Three-dimensional grain size distributions on seeded and unseeded samples after one furnace cycle.*

The peak in the distribution of the sample containing 5% of small seeds occurs at a smaller grain size than for the remaining samples. This confirms the incidence of seed-seed interference with a subsequent reduction in grain size increase as the growth then proceeds according to conventional kinetics. In this instance the reduction of seed to seed distance as the number of seeds has been increased, has limited the growth of the seeds, resulting in a smaller mean grain size.

Figure 4 shows the three-dimensional grain size distributions obtained after the second sintering cycle. All distributions of seeded samples comprise a single peak showing that full recrystallisation has been achieved, together with additional grain growth, during the second cycle.

4.4 Comparison With High Temperature Sintered Large Grain Size Fuel

Figure 5 compares the size distribution of the seeded sample containing 2% of small seeds, obtained after a single sintering cycle, with that of an undoped sample sintered for 4 hours at 2000°C in reducing conditions [8]. Differences between the distributions are characterised by a higher narrower peak for the seeded sample and correspondingly reduced volumes of the very smallest and largest sizes of grains. Reduction in the volume of small

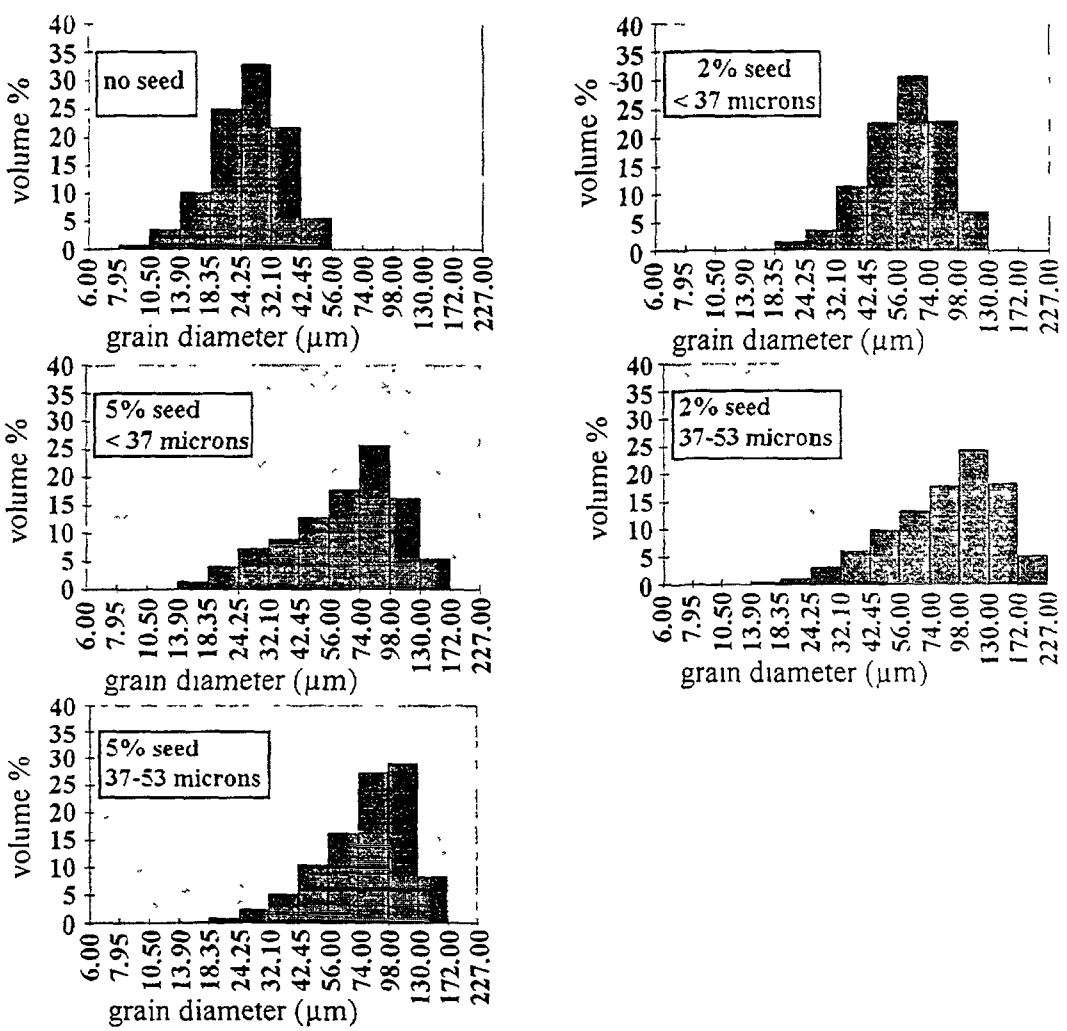

FIG. 4. Three-dimensional grain size distributions on seeded and unseeded samples after two furnace cycles.

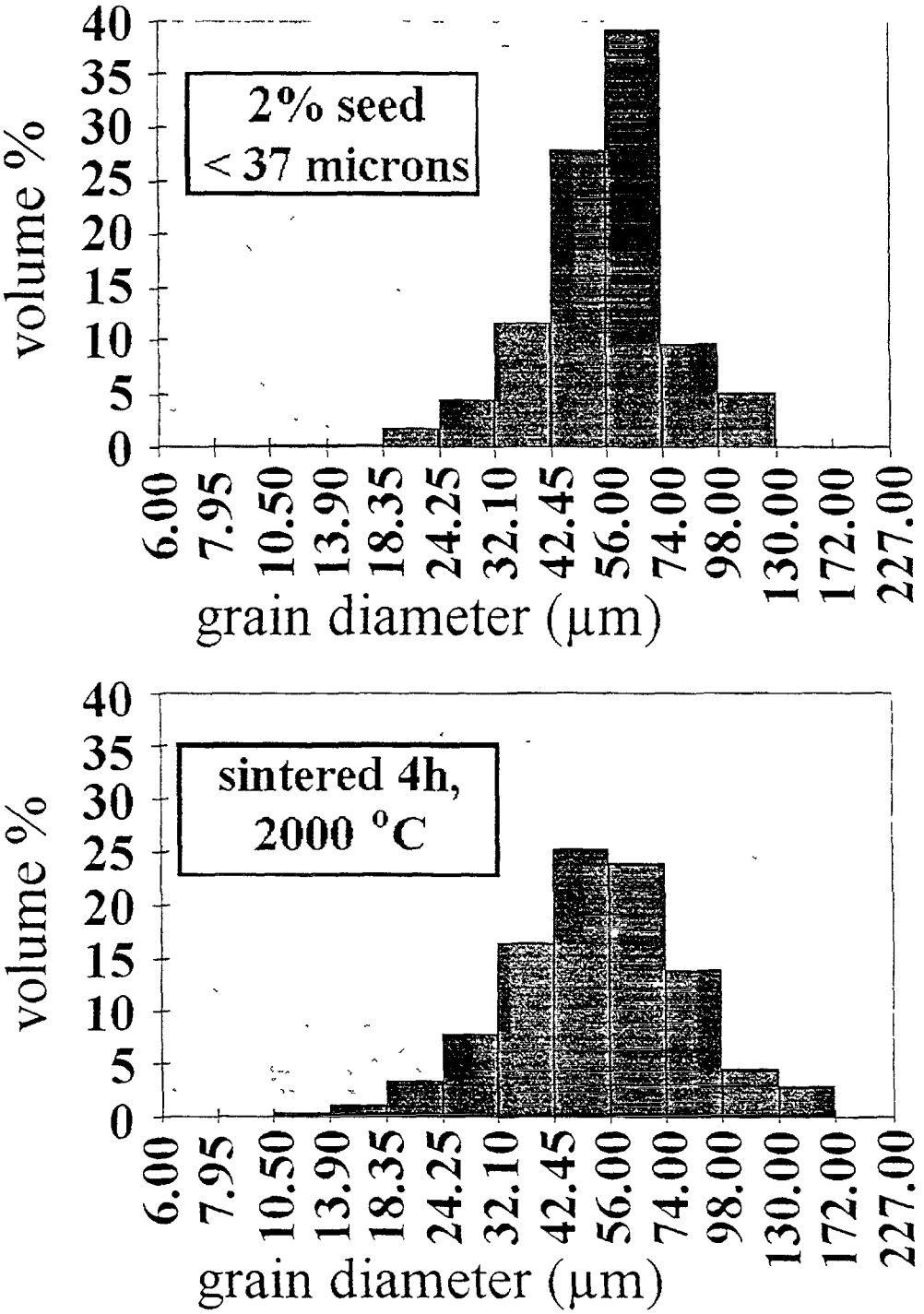

FIG 5 *Comparison of three-dimensional grain size distribution on seeded sample containing 2 % of seeds (< microns) after one sintering cycle with unseeded sample sintered for 4 hours @ 2000 °C.*

grains is considered desirable as these grains would have a disproportionate contribution to the overall fission gas release and would be an expected result from a recrystallised microstructure where grain growth has occurred by the consumption of small grains on the growth of larger grains. At the same time, a reduction in the volume of larger grains is not considered detrimental as the increased benefit of a large grain size decreases as the grain size increases.

TABLE I. INTERCEPT AND THREE-DIMENSIONAL GRAIN SIZE ON SEEDED AND UNSEEDED SAMPLES

Seed Size (μm)	% Seed	Furnace Cycles	Intercept Grain Size (μm)	Mean 3-dimensional Grain Size (μm)
-	0	1	13.7	18.3
<37	2	1	38.1	44.1
<37	5	1	30.3	30.7
>37<53	2	1	44.4	33.8
>37<53	5	1	38.1	41
-	0	2	18.6	21.9
<37	2	2	43.5	48.7
<37	5	2	33.1	41.5
>37<53	2	2	51.6	54.9
>37<53	5	2	55.6	57.3

The high temperature sintered sample has a linear intercept grain size of 34.7 m which represents the mean value obtained on samples sintered under the above conditions. This grain size is similar to that obtained on the seeded sample (38.1 m) though the mean three-dimensional grain size of 52.6 m is larger than the corresponding value of the seeded sample (44.1 m). Never the less, seeding has resulted in comparable grain sizes to those achieved in a similar time at a temperature nearly 300°C greater.

To achieve a comparable grain size by extended sintering at conventional processing temperatures would require a considerable residence time in the furnace hot zone (equivalent to cycling material through the furnace between 10 and 20 times, from equation 1) which could only be achieved at the expense of a considerable reduction in plant throughput and increase in capital and production costs. Similarly, sintering at 2000°C in either batch or continuous mode demands alternative, expensive, furnace technology.

5. CONCLUSIONS

(1) Large grains have been achieved in UO_2 by seeding uranium dioxide powder with single crystals and sintering under standard conditions.

(2) A 2% addition of seeds of size less than 37 microns results in a fully recrystallised, large grain structure after one cycle through a production sintering furnace.

(3) Similar grain sizes to those achieved by seeding techniques can only be achieved after similar times on undoped uranium dioxide by sintering above 2000°C or by considerable multiple cycling through a sintering furnace at conventional temperatures.

(4) Seeded large grain size UO_2 is achieved through the enhancement of the driving force for grain boundary motion as opposed to, where dopants are employed, increasing grain boundary mobility. This material can be considered as undoped and as such fission gas release will be comparable to large grained, undoped, fuel produced by alternative techniques.

REFERENCES

[1] BROWN, C., HESKETH, K., PALMER, I. D., BNFL Assessment of Methods of Attaining High Burnup MOX Fuel, IAEA Conference on Advances in Pellet Technology for Improved Performance and High Burnup, Tokyo 1996.

[2] UK Patent, GB 2177249 B, 1988.

[3] KINGERY, W.D., BOWEN, H.K., UHLMANN, D.R., Introduction to Ceramics, 2nd Edition, John Wiley & Sons, New York (1976) 448-468.

[4] WOOD, G. A., Unpublished Work; The Use of Sintered Scrap to Produce Large Grain Size UO_2.

[5] WOOD, G. A., Unpublished Work; Preliminary Investigation of the Use of High Temperature Calcined UO_3 as a Possible Grain Growth Seeding Agent.

[6] The Determination of Size Distribution. (Proc 2nd Int Congress For Stereology, New York, 1967), Springer Verlag (1967).

[7] WOOD, G. A., Unpublished Work; Seeding Using Small Seed Crystals

[8] WATSON, R. H., HOWARD, R. J., WOOD, G. A., BNFL MEMO 865(S), Evaluation of High Temperature Stoichiometric Sintering of Undoped UO_2 for Large Grain Fuel Manufacture.

DISCUSSION

(Questions are given in italics)

Are you going to perform evaluation in these seeded UO_2?

(1) Could you indicate experimental evidence that the results through a binderless route would be similar?

(2) In industrial fabrication, not only seeds and pure IDR powder will need to be used but also scrap recycle. What will be the effect?

(1) Seeding has been carried out using a binderless technique. Large grained fully recrystallized microstructures have been produced with no discernable differences between binder route material.

(2) U_3O_8 as scrap recycle does not cause seeding as the ultimate particle size is small even though there may be some agglomeration of the U_3O_8. U_3O_8 derived UO_2 in the matrix will not affect recrystalization of seeds.

The grain size distribution exhibits volume fraction of size class. Do you measure or calculate the volume fraction?

Volume fraction distribution gives a major role to the seeds. Could you present us a number fraction distribution?

Grain size distribution was measured. Samples were sectioned and images of several fields were analysed using an optical technique and connected to give a 3-dimensional distribution, Alfen Soliykov. A volume fraction distribution is preferable as it easily demonstrates the degree to which recrystalization has occurred. It does not weight the results in favor of the seeds as the volume of seeds is small (2 or 5%) and the samples are fully recrystallized. This shows that the seeds have increased 20 or 50 times respectively in volume for 2 and 5% seed additions. The data is available for the generation of a number fraction distribution but the distribution would be less readily interpreted as the extent to which recrystalization has occurred would not be as evident.

How to make seeds of single crystal?

Seeds can be made by:

* Crushing sintered pellets and sieving the crush to obtain desired size of seed.

* Disintegration of UO_2 at high temperature at >2000C in dry hydrogen UO_2 sintered pellet disintegrate into essentially single grains which can be used to seed grain growth.

FUEL FABRICATION — GADOLINIA AND MOX FUEL

(Session 2)

A STUDY OF THE UO_2/Gd_2O_3 COMPOSITE FUEL

D. BALESTRIERI
Centre des études nucléaires,
Saint-Paul-lez-Durances,
France

Abstract

Composite fuels or targets are considered as possible candidates for use in various applications (advanced fuels, burnable poisons, minor actinide incineration, increased plutonium consumption...). This paper summarizes the results of studies performed on UO_2/Gd_2O_3 composite fuels.

The use of a burnable poison present within the fuel is being considered in order to increase the length of irradiation cycles beyond 12 months in French PWRs without increasing the concentration of soluble boron in the coolant. Furthermore, to extend the efficiency of the poison by slowing its gadolinium consumption down, a study was led using gadolinia in the shape of 300 μm diameter macrospheres, dispersed within the UO_2 fuel.

The first stage of the studies involved manufacturing and characterizing the microstructure and sinterability of a UO_2 matrix 12 wt% gadolinia composite, with Gd_2O_3 macrospheres 300 μm in diameter. The second stage consisted in comparing the conductivity of the composite to that of stoichiometric UO_2 and a gadolinia-doped UO_2 containing the same proportion of gadolinium. Furthermore, composite reaction with water under PWR conditions has been studied.

1. INTRODUCTION

In order to achieve irradiation cycles exceeding 12 months in French PWRs, it is planned to use burnable poisons within the fuel, such as for example gadolinium oxide. Moreover, in order to prolong the efficiency of the poison, a study was conducted using gadolinia in the shape of 300 μm diameter macrospheres, homogeneously dispersed within the urania matrix.

This paper presents the work carried out on a composite fuel containing 12 wt% of gadolinia macrospheres, the objective being to study the properties such as its sinterability, its thermal conductivity and its reaction with water under PWR conditions, compared both to pure UO_2 and gadolinia-doped UO_2 containing the same proportion of gadolinium .

2. DESCRIPTION OF THE BATCHES STUDIED

The gadolinia macrospheres were manufactured by a granulation process [1]. All the composite batches were elaborated using the same UO_2 powder which constitutes the matrix, and using similar forming and sintering conditions (uniaxial pressing at 350 MPa-1700°C for 2 hours in H_2 + 2 vol. $\%H_2O$).

The manufacturing objectives consisted on the one hand in obtaining a high density material free of any cracks likely to affect its intrinsic properties, and on the other hand, to preserve the initial quasi-spherical shape of the inclusions after pressing.

In order to avoid distorting the shape of the Gd_2O_3 macrospheres during pressing, it was found useful to consolidate them by a preliminary heat treatment before mixing them with the UO_2 powder. Three different batches were characterized in order to study the effects of the preliminary consolidation of the macrospheres on the final microstructure, the sinterability and the thermal conductivity of the composite structure.

The various batches studied are described in Table 1.

3. CHARACTERIZATION OF THE BATCHES

3. 1. Density

The relative densities (d/d_{th}) are shown in Table 2. The density of the composite pellets decreases as the preliminary consolidation temperature of the Gd_2O_3 macrospheres increases.

3. 2. Porosity

The main results are shown in Table 2. The open porosity increases significantly with the consolidation temperature of the macrospheres. As stated in the literature [2-9], batch C, initially containing dense macrospheres, appears to be the worst from the point of view of density as well as open porosity.

TABLE 1

Batch	Conditions of the preliminary heat treatment of macrospheres	Diameter of macrospheres before pressing (μm)
A	none	360
B	1200°C-1 hour in air atmosphere	360
C	1700°C-2 hours in (H_2+2vol% H2O) atmosphere	300

TABLE 2

Batch	Sintering Temperature (°C)	Gd_2O_3 content (%)	Density		Porosity	
			d/d_{th} (%) before sintering	d/d_{th} (%) after sintering	*Open* P_o(%)	*Total* P(%)
A	1700	12	53,75	94,2 ± 0,3	0,41 ± 0,10	5,81 ± 0,27
B	1700	12	54,19	94,0 ± 0,2	0,63 ± 0,13	5,95 ± 0,17
C	1700	12	56,38	93,6 ± 0,4	2,48 ± 0,21	6,39 ± 0,45
pure UO_2	1700	-	51,9	95,7 ± 0,2	0,10 ± 0,05	4,30 ± 0,13

3. 3. Dilatometric analyses

In order to compare the densification kinetics for pure UO_2 and the UO_2 matrix of batches A and C, the density of the matrix was calculated in the 800°C-1600°C temperature range using the following equation :

$$\frac{1}{d_{m/c}} = \frac{1}{d_c(1-\eta)} - \frac{\eta}{d_{Gd_2O_3}(1-\eta)}$$

where η is the weight fraction of Gd_2O_3 (= 12 wt%),

$d_{m/c}$ is the density of the UO_2 matrix within the composite,

d_c is the density of the composite (measured),

$d_{Gd_2O_3}$ is the density of Gd_2O_3 (measured).

The densification kinetics for pure UO_2 and UO_2 matrix of batches A and C are compared in Fig. 1. The results show that the Gd_2O_3 macrospheres significantly hinder the densification of the matrix.

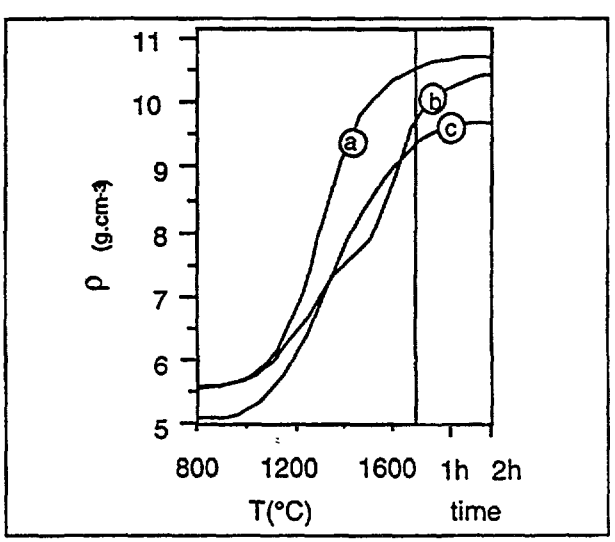

FIG. 1. Density as a function of temperature and time

3. 4. Microstructural Observations

The observations performed using optical and scanning electron microscopes reveal how the macrospheres are distorted during the pressing stage, the appearance of microcracks and heterogenous density zones within the matrix, as well as the interconnected porous zones around the macrospheres.

- *Shape of macrospheres*

  Batch A contained Gd_2O_3 macrospheres which showed extensive flattening in a direction perpendicular to the pressing axis (Fig. 2a). This clearly indicates that the cohesion is inadequate. In batches B and C, the shape of the macrospheres is improved due to the preliminary consolidation by heat treatment of the Gd_2O_3 macrospheres at 1200°C and 1700°C respectively for batches B and C (Fig. 2b).

- *Cracking of the UO_2 matrix*

- Contrary to batches B and C, microcracks were observed in the matrix of batch A (Figs. 2a, 3a, 3b).

- *Macrosphere-matrix interface*

  Although absent from batch A, an interconnected porous zone was observed around the macrospheres in the batches B and C. This zone was larger for batch C than for batch B (Figs 3c and 3d). Examination of polished samples indicated a diffusion zone at the macrosphere-matrix interface (Fig. 3a). The thickness of the diffusion zone was evaluated at approximately 20 μm using a electron probe microanalyser.

  Figure 4 represents the macrosphere-matrix interface structure. Two different phases have been identified using a electron probe microanalyser at the macrosphere-matrix interface. The first phase, adjacent to the macrosphere exhibits a 4 μm grain size. According to the phase diagram established by Beals [10] (Figure 5), it appears very probable that this phase is UGd_6O_{11}. The second phase, consisting mainly of submicronic grains, corresponds to the $(U_{1-x}, Gd_x)O_{2-y}$ solid solution, the concentration of gadolinium decreasing steadily down to 0% (UO_2 matrix).

- *Heterogenous density in the matrix*

  The density of the matrix is not homogeneous. As stated in the literature, certain very dense zones were observed in the matrix particularly between the closely spaced macrospheres, especially for batch C, and often adjacent to porous zones [11, 12]. Additionally, dense regions of the matrix often presented a large grain microstructure (Fig. 3e) [11, 13-15].

3. 5. Discussion

The dilatometric analyses show in all cases that the presence of macrospheres hinders the densification of the matrix. This hindrance is frequently attributed to the density variations noted in the matrix. Moreover, the differential thermal expansions between the two constituents during cooling can generate thermal stresses which are the cause of the microcracks in the matrix. The specimens including non consolidated macrospheres (batch A) exhibit a microcracked UO_2 matrix due to the difference between the thermal expansion coefficients of the two phases below 600°C. On the other hand, in the specimens including Gd_2O_3 macrospheres previously consolidated or even densified, a porous zone was observed around the macrospheres.

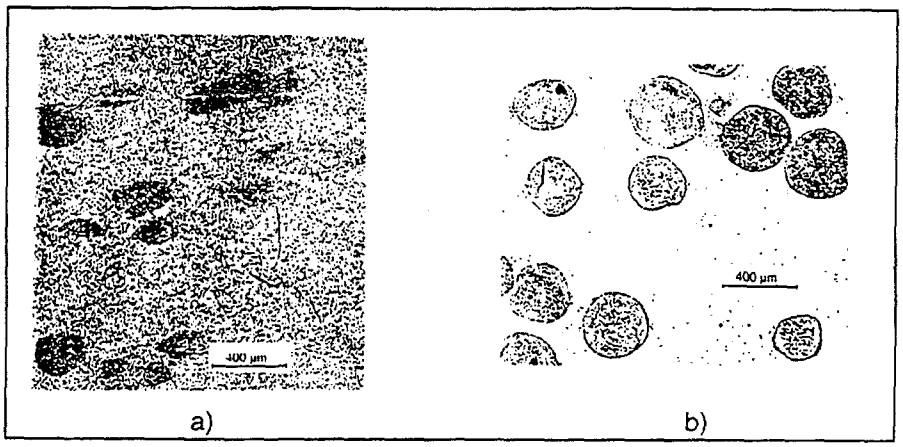

FIG. 2. Shape of macrospheres in the sintered pellets: a) batch A, b) batch B

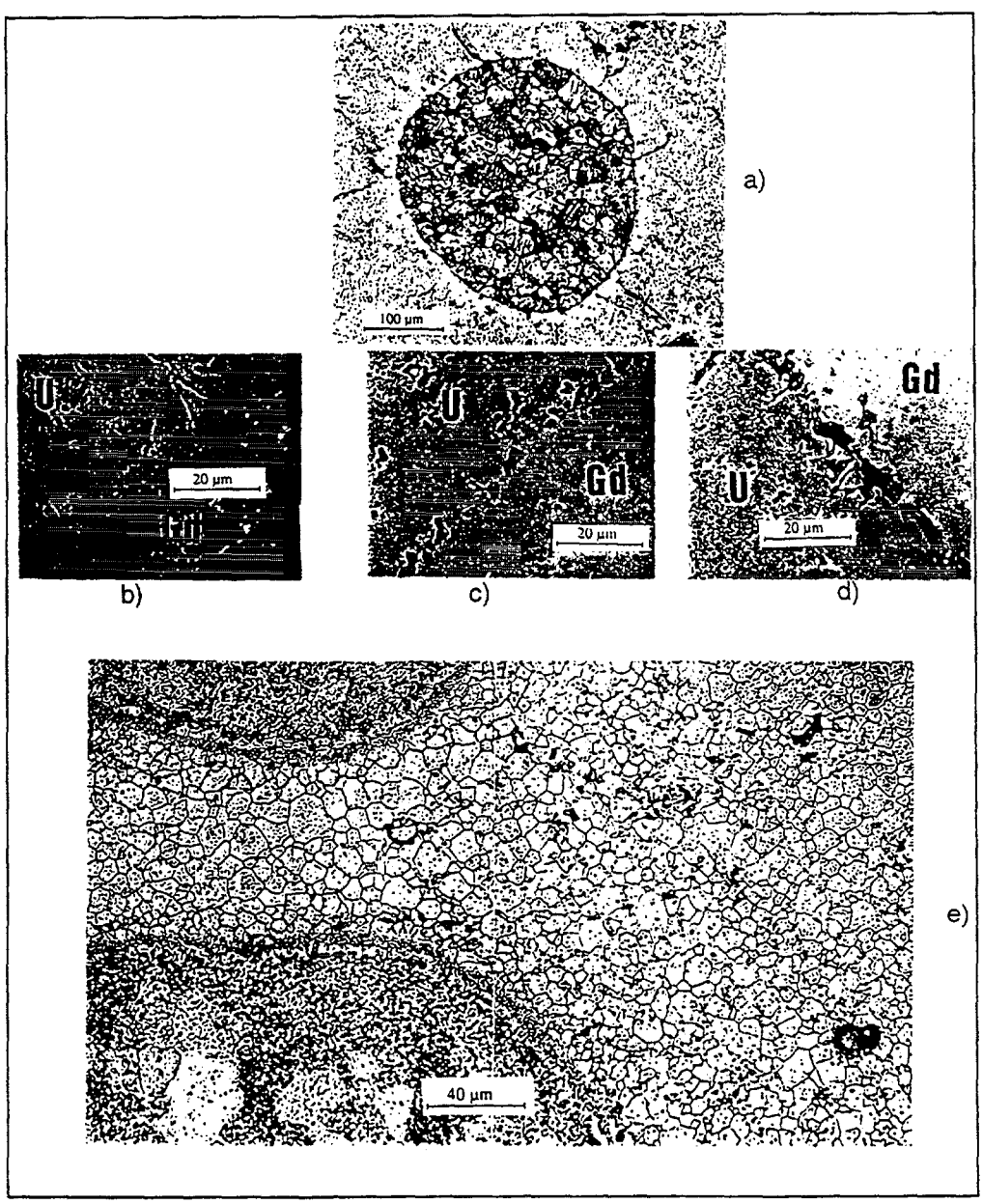

FIG. 3. a) Cracking of the matrix (batch A); b), c), d) macrospheres - matrix interface for batches A, B, C; e) microstructure of UO_2 matrix.

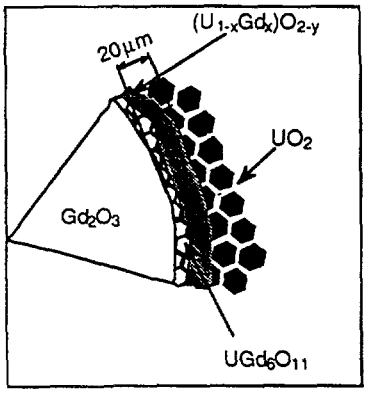

FIG. 4. Schematic representation of macrosphere - matrix interface.

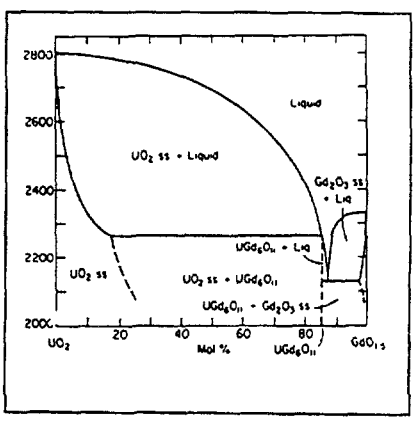

FIG. 5. UO_2-Gd_2O_3 phase diagram [15].

The effect of inclusions and heterogeneities on the sintering process has been the subject of many theoretical and experimental studies [2-9]. It has been widely observed that the sinterability of a polycristalline ceramic powder used as the matrix can be reduced significantly by the presence of a rigid inclusion phase. In fact, during the uniaxial pressing stage, heterogeneities are produced in the matrix, particularly between the closely spaced macrospheres. During the sintering process, these prematurely dense regions form, with the near-touching macrospheres, a rigid, continuous network which can substantially reduce the overall densification of the composite matrix, this hindrance is all the more marked if the macrospheres are unable to densify (batch C).

4. THERMAL CONDUCTIVITY

The thermal properties of stoichiometric UO_2 and gadolinia-doped UO_2 are relatively well known [16-19]. The same cannot be said for the UO_2/Gd_2O_3 composite fuel. The objective is therefore to calculate the thermal conductivities of the composite batches A and B, in order to be able to compare them with the gadolinia-doped UO_2 including 12 wt % of Gd_2O_3.

The thermal conductivity (λ) is obtained from the product of the thermal diffusivity (a), the density (ρ) and the specific heat (Cp).

It is known that the addition of gadolinia to UO_2 has a negative effect on the thermal conductivity. Figure 6 shows that the thermal conductivity of the gadolinia-doped UO_2 is in fact lower than that of pure UO_2.

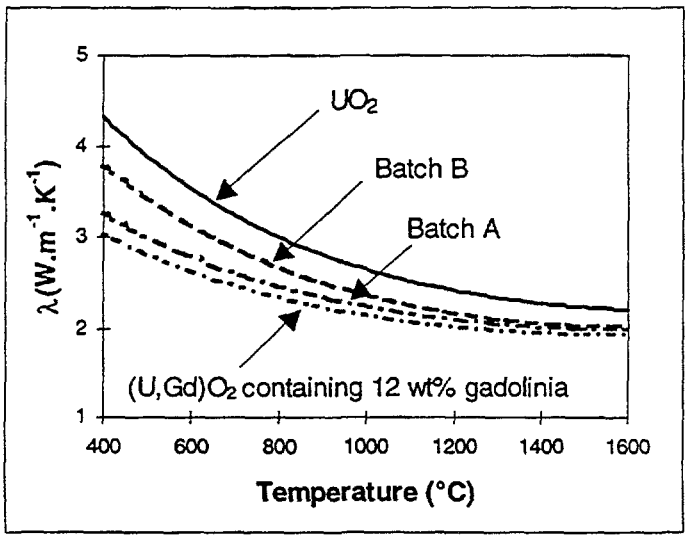

FIG. 6. Comparison of the thermal conductivities.

The measurements taken using UO_2/Gd_2O_3 are similar. The addition of Gd_2O_3 macrospheres, with a lower thermal conductivity than UO_2, within the 400°C-1600°C temperature range, reduces the overall conductivity of the fuel. To illustrate this, it can be seen that the conductivities of composite batches A and B are respectively 10% and 14% lower than for stoichiometric UO_2 with the same density at 1000°C.

Within the temperature range investigated (400°C-1600°C) and for the same proportion of gadolinium, our measurements show on the one hand that in all cases, for the same gadolinium content, the thermal conductivity of the UO_2/Gd_2O_3 composite is better than that of a stoichiometric gadolinia-doped UO_2 (i.e. 10% increase at 1000°C), and on the other hand that the thermal conductivity of batch A is lower than that of batch B. This result therefore shows the high sensitivity of thermal conductivity to the presence of microcracks in the matrix, compared with porosity located around the macrospheres.

5. REACTION WITH WATER

Preliminary tests show that gadolinia reacts with water under PWR conditions (i.e. 350°C and 155 bar) to produce a gadolinium hydroxide $Gd(OH)_3$ which results in a considerable swelling of the material [1]. The same can be said for the UO_2/Gd_2O_3 composite fuel. Tests performed on the composite show a strong affinity to water which leads to a destruction of the pellets. This incompatibility with water under PWR conditions for the composite pellets can be explained by the reaction of the peripheral gadolinia macrospheres with water to produce a hydroxide which in turn causes the macrospheres to swell and the matrix to crack (Fig. 7).

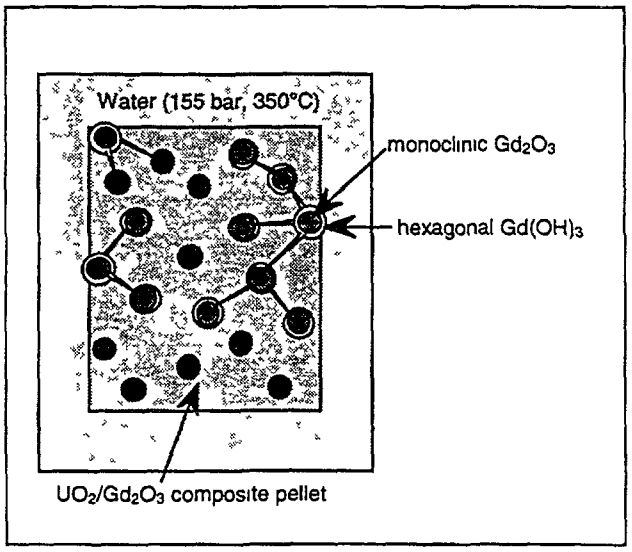

FIG 7 Schematic representation of the pellet destruction

In order to suppress composite affinity to water whilst keeping gadolinium as the burnable poison in the form of macrospheres, it could be interesting to find another gadolinium-based compound which can withstand aqueous corrosion. Gadolinium orthoaluminate ($AlGdO_3$) would seem to be a likely candidate.

The Al_2O_3-Gd_2O_3 phase diagram in fact shows the existence of this orthorhombic structured compound (a = 525.0 pm, b = 530.2 pm, c = 744.7 pm) with a theoretical density of 7.44:

$$Al_2O_3 + Gd_2O_3 \quad 2\ AlGdO_3\ .$$

6. CONCLUSIONS

The composite fuel consisting of 12 wt % gadolinia macrospheres (300 μm in diameter) homogeneously dispersed within urania matrix, certainly presents some advantage from a neutron point of view, but presents a certain number of problems in its elaboration. For example, it has been seen that the UO_2 matrix could crack under the effect of the differential thermal expansions between UO_2 and Gd_2O_3. But the essential problem is the distortion of the Gd_2O_3 macrospheres during the pressing process. In order to avoid this problem, the macrospheres were subjected to a preliminary heat treatment in order to increase the cohesion before the pressing stage.

The results show the influence of the preliminary consolidation of the macrospheres by heat treatment. It was observed that:

- the density of the composite decreases slightly,
- the open porosity increases significantly,
- the size of the diffusion zone between the UO_2 and Gd_2O_3 remains constant and equal to 20 μm,

- the cracking of the matrix disappears,
- the thermal conductivity increases,
- an increasingly large interconnected porous zone appears around the macrospheres,
- more zones of varying density are observed ; a large grain microstructure is observed in the dense regions located between the closely spaced macrospheres.

The thermal conductivity measurements showed the improved thermal behaviour of the UO_2/Gd_2O_3 composite compared to the gadolinia-doped UO_2 containing the same gadolinium content. However, the strong affinity to water under PWR conditions revealed the limits of this fuel. An alternative solution, however, could consist in elaborating macrospheres of $AlGdO_3$, for example, as that compound does not react with water.

REFERENCES

[1] BALESTRIERI, D., "Study and optimization of the composite nuclear fuel with burnable poison UO_2/Gd_2O_3", Thesis : INSA, Lyon, No.95, ISAL 0061 (1995) 159 p.

[2] SCHERER, G. W., "Sintering with Rigid Inclusions", *J. Amer. Ceram. Soc.*, Vol. 70, N° 10 (1987) 719-25.

[3] EVANS, A. G., "Considerations of Inhomogeneity Effects in Sintering". *J. Amer. Ceram. Soc.*, Vol. 65, N° 10 (1982) 497-501.

[4] HSUEH, C. H., "Sintering Behavior of Powder Compacts with Multiheterogeneities". *J. Mater. Sci.*, Vol. 21 (1986) 2067-72.

[5] REEVE, K. D., "Non-Uniform Shrinkage in Sintering". *Am. Ceram. Soc. Bull.*, Vol. 42, N° 8 (1963) 452

[6] LANGE, F. F., "Constrained Network Model for Predicting Densification Behavior of Composite Powders". *J. Mater. Res.*, , Vol. 2, N° 1 (1987) 59-65.

[7] BORDIA, R. K.; Scherer, G. W., "Constrained Sintering: III. Rigid Inclusions". *Acta Metall.*, Vol. 36, N° 9 (1986) 2411-16.

[8] WEISER, M. W.; De Jonghe, L. C. . "Inclusion Size and Sintering of Composites Powders"., *J. Amer. Ceram. Soc.*, , Vol. 71, N° 3 (1988) 125-127.

[9] SUNDARESAN, S.; AKSAY, I. A., "Sintering with Rigid Inclusions : Pair Interactions". *J. Amer. Ceram. Soc.*, Vol. 73, N° 1 (1980) 54-60.

[10] BEALS, R. J.; HANDWERK, J. H. - WRONA, B. J., "Behaviour of Urania-Rare Earth Oxides at High Temperatures". *J. Amer.Ceram. Soc.*, , Vol. 52, N° 11 (1969) 578-81.

[11] SUDRE, O.; BAO, G.; FAN, B.; LANGE, F. F.; EVANS, A. G., "Effect of Inclusions on Densification: II, Numerical Model" *J. Amer. Ceram. Soc.*, Vol. 75, N° 3 (1992) 525-31.

[12] SUDRE, O.; LANGE, F. F., "The Effect of Inclusions on Densification: III, The Desintering Phenomenon".*J. Amer. Ceram. Soc.*, Vol. 75, N° 12 (1992) 3241-51.

[13] CAMERON, C. P.; RAJ, R., "Grain-Growth Transition During Sintering of Colloidally Prepared Alumina Powder Compacts". *J. Amer. Ceram. Soc.*, Vol. 71, N° 12 (1988) 1031-35.

[14] BROOK, R. J., "Pore-Grain Boundary Interactions and Grain Growth". *J. Amer. Ceram. Soc.*, Vol. 52, N° 1 (1969) 56-57.

[15] LAM, D. C.; LANGE , F. F., "Microstructural Observations on Constrained Densification of Alumina Powder Containing a Periodic Array of Sapphire Fibers". *J. Amer. Ceram. Soc.*, Vol. 77, N° 7 (1994) 1976-78.

[16] HIRAI, M. "Thermal diffusivity of UO_2-Gd_2O_3 pellets" *J. Nucl. Mat.*, Vol. 173 (1990) 247-254.

[17] FUKUSHIMA, S., "The Effect of Gadolinium content on the Thermal Conductivity of Near-stoichiometric (U,Gd)O_2 solid solutions". *J. Nucl. Mat.*, Vol. 105 (1982) 201-210.

[18] HIRAI, M.; ISHIMOTO, S. "Thermal Diffusivity and Thermal Conductivities of UO_2-Gd_2O_3". *J. Nucl. Mat.*, Vol. 28, N° 11 (1991) 995-1000.

[19] CHOTARD, A. ; MELIN, P. ; BRUET, B. ; FRANÇOIS, B., "Out of pile physical properties and in pile thermal conductivity of (U,Gd)O_2" IAEA - meeting Vienne 13-17/10/86.

DISCUSSION

(Questions are given in italics)

Comments

Corrosion test perhaps too conservative because in the case of a failed fuel rod exposure to H_2O restricted by the cladding. Also the ex-reactor results that homogeneous (U,Gd)O_2 is resistant to corrosion does not apply to in-reactor, because of radiolytic oxidizing species. In the context of 12-18 month cycles, difference between composite and homogeneous corrosion may not be so great.

Besides the successful irradiation of this type of fuel more than 10 years ago in the BR3, was more recent irradiation performed?

Composite fuel has already been irradiated, but there is a very long time.

EFFECT OF PARTICLE SIZE AND OXYGEN POTENTIAL ON UO_2/Gd_2O_3 PELLET SINTERING

T. NISHIDA
Japan Nuclear Fuel Company Ltd,
Kanagawa-ken

R. YUDA
Nippon Nuclear Fuel Development Company Ltd,
Ibaraki-ken

Japan

Abstract

Effects of the powder mixing condition and the oxygen potential of the sintering atmosphere on the characteristics of UO_2-Gd_2O_3 fuel pellet were evaluated. The effective inter diffusion length of U and Gd ions was estimated to be approximately 2μm in the normal commercial sintering condition through the evaluation of the effective diffusion coefficient of U and Gd ions by means of a UO_2-Gd_2O_3 diffusion couple examination. Powder mixing condition, sintered density, grain growth and solid solubility of actual UO_2-Gd_2O_3 pellets made from the different powder mixing conditions and the sintering atmosphere were also evaluated. As a result of the examination, more uniformly mixed powder was concluded to be preferable to enhance UO_2-Gd_2O_3 solid solubility as well as grain growth. On the other hand, higher oxygen potential of the atmosphere was also concluded to be effective to enhance grain growth, while sintered density decrease was observed in the oxygen potential higher than approximately -350 kJ/mole. Moreover, especially in less uniformly mixed powder, slight suppression of solid solubility in terms of the FWHM of X-ray diffraction peak was observed in the oxygen potential higher than approximately -350 kJ/mole.

1. INTRODUCTION

Gadolinia, a burnable absorber, has been employed as UO2-Gd2O3 fuel pellets for compensating reactivity of the light water reactor. In UO2-Gd2O3 pellet characteristics, homogeneity of UO2-Gd2O3 solid solution and grain size are recognized as notable characteristics, thereupon it is substantial for commercial fuel fabricators to enhance UO2-Gd2O3 pellets as uniform in solid solution and large in grain size as possible in reasonable fabrication cost. Recently, moreover, Gd2O3 concentration tends to become higher with extension of burnup of fuels, it is useful to understand the effects of manufacturing parameters on solid solution formation and grain growth.

It is generally known that the UO2-Gd2O3 pellet microstructure after sintering as well as sintering behavior are considerably influenced by the mixed condition of UO2 and Gd2O3

powders and the oxygen potential of the sintering atmosphere. There have been several studies on sintering behavior of UO_2-Gd_2O_3 powder compacts. [1]-[5] But most of those were mainly with respect to the effect of the oxygen potential of the sintering atmosphere. H. Assmann et al. [6] evaluated the difference in the microstructure of the UO_2-Gd_2O_3 pellets made from the mechanical blended powder and the coprecipitated powder, while so far there have been little studies that evaluated the effect of the mixing condition of powders on the microstructure of UO_2-Gd_2O_3 pellets.

In this study, the effects of the powder mixing condition as well as the oxygen potential of the sintering atmosphere on solid solubility and grain growth were evaluated. In evaluation of the effect of the mixing condition, firstly the effective diffusion length to form a homogenized solid solution was estimated by measuring the effective inter diffusion coefficient of U and Gd ions using UO_2-Gd_2O_3 diffusion couple, secondary the mixing condition of actual UO_2-Gd_2O_3 powder compacts made of different mixing processes as well as the characteristics of the sintered pellets were evaluated. On the other hand, in evaluation of the effects of the oxygen potential, UO_2-Gd_2O_3 green compacts made of the powder through the dry process were sintered in three(3) different oxygen potential atmospheres and examined.

2. EFFECT OF UO_2/Gd_2O_3 AGGLOMERATE PARTICLE SIZE

2.1. Experimental Procedure

2.1.1. Measurement of the effective inter Diffusion Coefficient of U and Gd Ions

Evaluation of the effective inter diffusion coefficient of U and Gd ions was made by means of a UO_2-Gd_2O_3 diffusion couple examination method. The sketch of the sample diffusion couple prior to heat treatment is shown in Fig. 1. The sample diffusion couple prior to heat treatment was prepared by uni axial pressing the UO_2 powder in which an already pressed Gd_2O_3 green compact had been embedded. Each sample was heated at 1700 °C or 1800 °C for 100 h. in the atmosphere of N_2(92%)+H_2(8%) gas with the dew point of 21 °C, respectively.

After heat treatment, each specimen was cut in axial direction followed by polishing, then the cross section was observed by means of SEM. Gd concentration and U concentration were also evaluated by measuring intensity of Mα and Lα1 lines of U and Gd atoms by means of EDX on twenty(20) to thirty(30) spots which were located near and across perpendicularly the boundary between UO_2 phase and Gd_2O_3 phase.

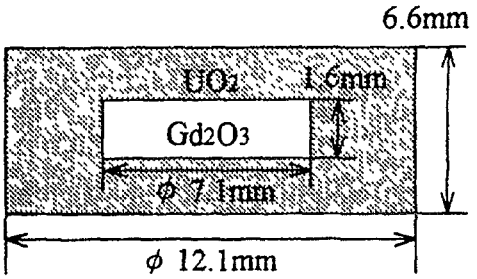

FIG. 1. Sketch of diffusion couple prior to heat treatment.

2.1.2 Examination on Actual UO_2-Gd_2O_3 Pellets

For evaluation of the effect of the powder mixing condition on the characteristics of the actual UO_2-Gd_2O_3 pellet, sample UO_2-Gd_2O_3 pellets were prepared using UO_2/Gd_2O_3 mixed powder with different mixing conditions. In order to obtain the UO_2/Gd_2O_3 mixed powders, powders were submitted to two(2) different preparation processes such as wet ball milling and dry hammer milling For the powder processed in the wet process, UO_2 and Gd_2O_3 powders were milled and mixed in carbon tetrachloride (CCl_4) for 1 h. by means of a centrifugal ball mill For the powder processed in the dry process, UO_2 and Gd_2O_3 powders were mixed in a pot for 5 min. by shaking, then milled by means of a hammer mill. Two(2) different Gd_2O_3 concentration powders such as 4.5 wt%-Gd_2O_3 and 10.0 wt%-Gd_2O_3 were prepared for each powder preparation process, five(5) legs of powders including UO_2 powder as reference were submitted to the test. The flow chart of powder preparation processes is shown in Fig 2 and the powders used in this study are summarized in Table 1.

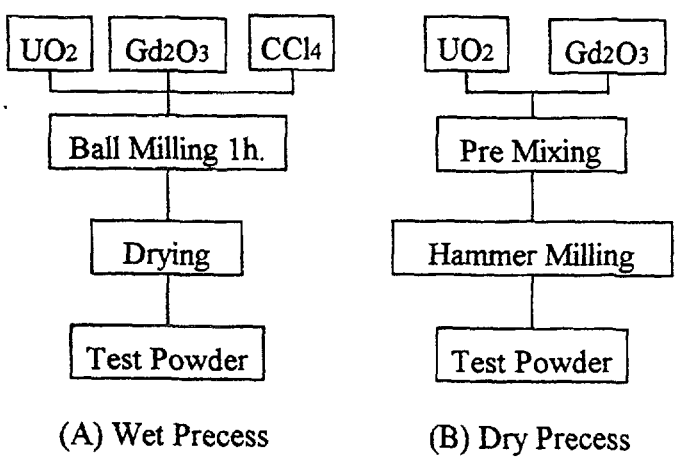

FIG. 2. Flow chart of powder preparation process.

TABLE I. POWDERS USED IN THIS STUDY.

Identification of Powder	UO2	DUG45	WUG45	DUG10	WUG10
Gd_2O_3 Concentration	0	4.5	4.5	10.0	10.0
Preparation Process		Dry	Wet	Dry	Wet

Each powder was pressed into green compacts with diameter of 7 mm, height of 14 mm, and density of 51.5 %TD. In order to evaluate the particle size as well as mixing uniformity of UO_2 and Gd_2O_3 prior to sintering, the green compacts molded by resin were polished of their end surfaces, then submitted to mapping analysis of Gd distribution by means of EDX. Intensity of the characteristic X-ray of Gd was also measured on ten(10) SEM images sampled randomly on the end surface. Other green compacts were sintered at 1750 °C for 4 h. in the atmosphere of N_2(92%)+H_2(8%) gas with the dew point of 1 °C. Evaluation of homogeneity of the solid solution of the sintered pellets was made by measuring the full width at half maximum(FWHM) of (620) peak of X-ray diffraction. Grain size of the sintered pellets was evaluated by ceramographic observation.

2.2. Results and Discussion

2.2.1. Measurement of the effective inter Diffusion Coefficient of U and Gd Ions

Microstructure of the specimen heated at 1800 °C observed by SEM is shown in Fig. 3. Formation of the third phase is observed between UO_2 phase and Gd_2O_3 phase. Measured U concentration was fitted in accordance with the formula (1) described below by taking the origin of the coordinate axis at the interface between Gd_2O_3 phase and the third phase so that we could obtain the effective inter diffusion coefficient of U ion in UO_2-Gd_2O_3 "Deff".

$$C(x,t)=C_0\ \frac{(C_1-C_0)}{2}\ \operatorname{erfc}\ \frac{x}{2\sqrt{Deff \cdot t}} \qquad (1)$$

$$x=X-x_r$$

where

C(x,t) : UO_2 concentration at the measuring point

x : Distance between initial UO_2/Gd_2O_3 boundary and the measuring point

X : Distance between the origin of the coordinate axis and the measuring point

x_r : Distance between the origin of the coordinate axis and the initial UO_2/Gd_2O_3 boundary

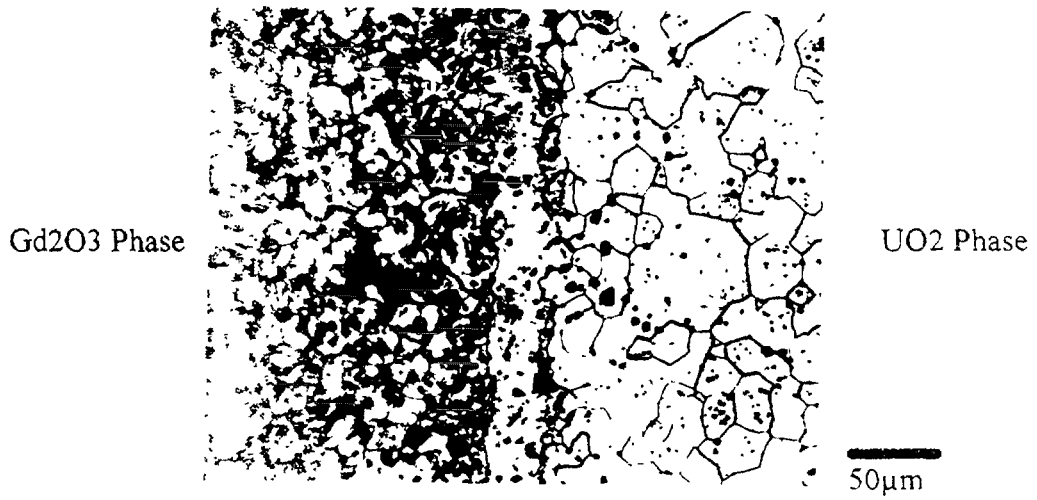

FIG. 3. Microstructure of the specimen heated at 1800°C for 100 h.

The fitting curve was calculated on the assumption that discontinuity due to the phase boundary was neglected and the Deff was constant regardless of concentration For the specimen heated at 1700 ℃ for 100 h. and the specimen heated at 1800 ℃ for 100 h, measurement results of U and Gd concentrations and the fitted curve are shown in Fig 4 (A) and Fig 4 (B), respectively In this figure, the horizontal axis indicates the distance from the interface between Gd_2O_3 phase and the third phase to the measuring point, and the vertical axis indicates the relative mol concentration of U and Gd According to these figures, U concentration is zero for X<0, changes discontinuously from zero to approximately 20 % at X=0, and increases exponentially for X>0 This indicates that the area of X<0 is identified as Gd_2O_3 single phase, the area between X=0 and X=25μm for heated at 1700 °C and the area between X=0 and X=40μm for heated at 1800 °C are identified as UO_2-Gd_2O_3 solid solution phase and the area of X>25 and the area of X>40 are identified as UO_2 single phase. Arrhenius plot of Deff derived from this study is shown in Fig. 5. According to Fig. 5, Deff was expressed as the following formula (2)

$$Deff = 1.0 \times 10^{-5} \exp\left(-2.6 \times 10^{5} (J/mol) / RT \right) (cm^2/s) \qquad (2)$$

Deff obtained in this study is larger than the lattice diffusion coefficient of U ions in UO_2 by Reimann and Lundy [7], and is smaller than the grain boundary diffusion coefficient of U ions in UO_2 by Reynolds and Burton [8]. This suggests that both lattice diffusion and grain boundary diffusion contribute to formation of the UO_2-Gd_2O_3 solid solution during sintering.

Diffusion length of U ion is $\sqrt{Deff \cdot t}$ for sintering time t Therefore, considering adjacent UO_2 agglomerate particle and Gd_2O_3 agglomerate particle with radius of R

(R>$\sqrt{}$Deff • t), U ion is scarcely possible to permeate the Gd_2O_3 agglomerate particle deeper than $\sqrt{}$Deff • t from the surface of the Gd_2O_3 agglomerate particle, and the core with radius of (R - $\sqrt{}$Deff • t) may remain as Gd_2O_3 shingle phase. According to the formula (2), the diffusion length of U ions is estimated to be approximately 2μm for the normal commercial sintering temperature and time of 1750 ℃ for 4 h.. Similarly, the diffusion length of Gd ions is also estimated to be approximately 2μm.

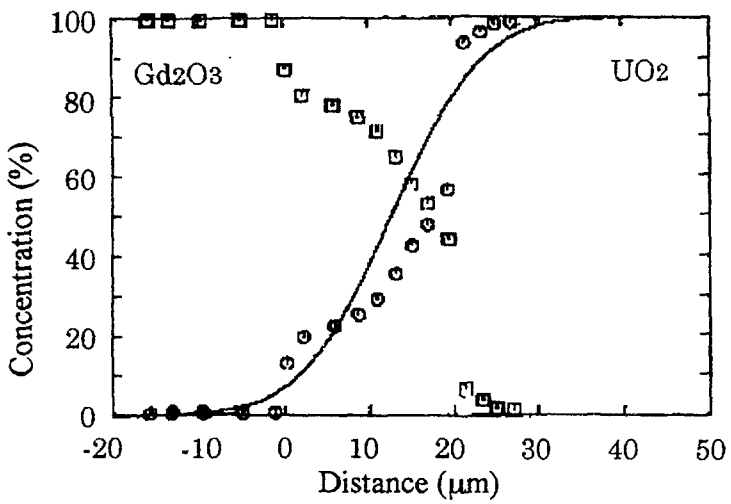

FIG. 4. *Measures value of U and Gd concentration and fitting curve (heated at 1700°C for 100 h).*

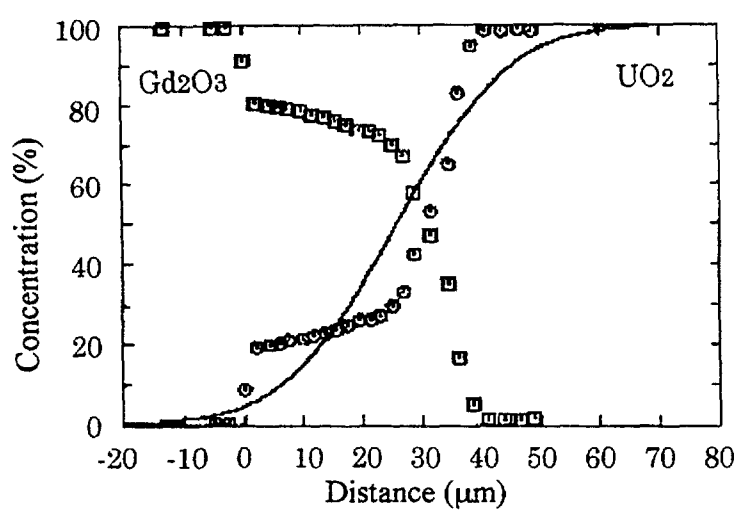

FIG. 4(B) *Measures value of U and Gd concentration and fitting curve (heated at 1800°C for 100 h).*

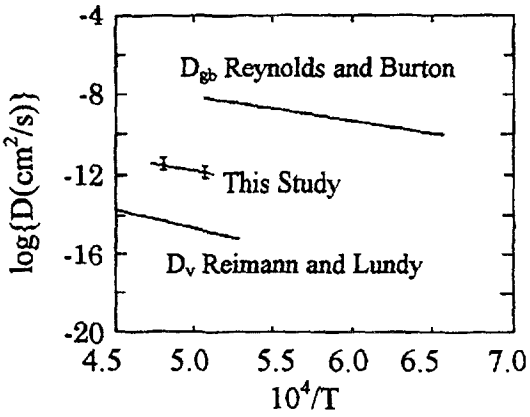

FIG. 5. Arrhenius plot of inter diffusion coefficient.

2.2.2. Examination on Actual UO2 Gd2O3 Pellets

The Gd distribution maps of DUG10 and WUG10 are shown in Fig. 6. According to Fig. 6, Gd_2O_3 and UO_2 agglomerate size in the powder compacts of the dry process powder prior to sintering were estimated to 5 μm and 70 μm, respectively, and those of the wet process powder prior to sintering were estimated to 5 μm and 10 μm, respectively. In addition, uniformity of UO_2 and Gd_2O_3 mixture in the green compact was confirmed by magnitude of standard deviation of ten(10) measured values of intensity of characteristic X-ray of Gd. The results are shown in Table 2. The figures described in Table 2 do not indicate the absolute Gd concentration but the intensity of characteristic X-ray of Gd. According to Table 2, the wet process powder is more superior than the dry process powder with respect to uniformity of UO_2-Gd_2O_3 mixture.

The FWHM of (620) peak of X-ray diffraction of the sintered pellets is shown in Table 3. The lattice parameter of UO_2-Gd_2O_3 solid solution varies according to Gd concentration[3], thus the diffraction angle of (620) of UO_2-Gd_2O_3 solid solution is slightly shifted. Therefore, imperfect solid solution having Gd concentration gradation makes the FWHM broader. The results indicate the uniformly mixed powder with smaller agglomerate particle size enhances solid solution formation. The reason why good solid solution was formed in the WUG powder with approximately 10 μm agglomerate while the estimated agglomerate size to form solid solution by the diffusion couple experiment was approximately 4 μm was considered as follows. The Deff was measured by 100 h. heat treatment in the diffusion couple experiment, and it was recognized that both grain boundary diffusion and lattice diffusion contributed to formation of solid solution. However, those diffusions do not occur simultaneously but the grain boundary diffusion with higher diffusion coefficient is dominant in the early stage of heat treatment. Therefore, the effective diffusion length in the actual pellet

sintering such as 4 h sintering time is longer than as estimated by the diffusion couple experiment.

Measured grain size is shown in Table 4. With respect to grain growth, smaller agglomerate particle size is also preferable, especially in high Gd concentration.

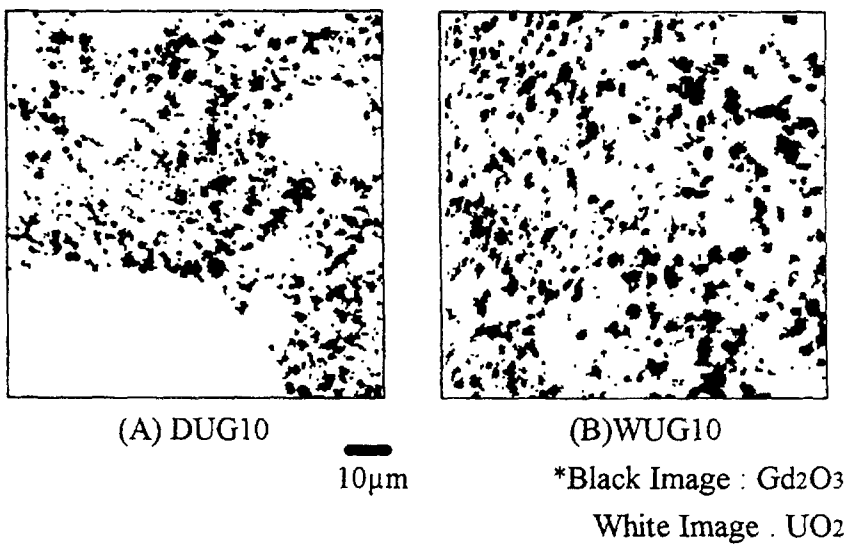

FIG. 6. Gd distribution map in the green compact.

TABLE II. DISTRIBUTION OF GD IN THE GREEN COMPACT

	DUG45	WUG45	DUG10	WUG10
Number of Data	10	10	10	10
Average	0.0259	0.0278	0.0626	0.0655
Standard Deviation (σ)	0.0040	0.0019	0.0115	0.0039
σ/Average (%)	15.4	6.8	18.4	6.0

TABLE III. FWHM OF (620) PEAK OF X-RAY DIFFRACTION OF THE SINTERED PELLET (UNIT: DEGREE)

	Gd_2O_3 concentration		
Powder Process	0 wt%	4.5 wt%	10.0 wt%
Dry	0.1641	0.3397	0.3405
Wet	-	0.2300	0.1750

TABLE IV. GRAIN SIZE OF THE SINTERED PELLET (UNIT: μm)

	Gd_2O_3 concentration		
Powder Process	0 wt%	4.5 wt%	10.0 wt%
Dry	18.2	11.0	9.1
Wet	-	8.7	15.1

3. EFFECT OF OXYGEN POTENTIAL

3.1. Experimental Procedure

Evaluation of the effect of the oxygen potential on UO_2-Gd_2O_3 pellet microstructure was made using actual UO_2-Gd_2O_3 pellet made from the dry hammer milling process powder. Green compacts were prepared in the same manner as described in paragraph 2.1.2.. In order to evaluate the sintered pellet microstructure, the green compacts were sintered at 1750 °C for 4 h. in three (3) different oxygen potential atmospheres. The atmospheres applied to this study are shown in Table 5. Evaluation of homogeneity of the solid solution and grain growth were made in the same manner as described in paragraph 2.1.2..

TABLE V. ATMOSPHERE GAS AND OXYGEN POTENTIAL

	Atmosphere 1	Atmosphere 2	Atmosphere 3
H_2 (vol%)	75	8	8
N_2 (vol%)	25	92	92
Dew Point (°C)	10	1	20
Oxygen Potential (at 1700°C:kJ/mol)	-408	-356	-312

3.2. Results and Discussion

Sintered density, grain size and FWHM of (620) peak of X-ray diffraction of the sintered pellets are shown in Fig. 7, in Fig. 8, and in Table 6, respectively. The grain size enlarged according to the oxygen potential, while the sintered density declined in the atmosphere3 (higher oxygen potential), that qualitatively corresponded with the previous study [5]. On the other hand, the FWHM of (620) peak showed broadening in both the atmosphere 1 and the atmosphere 3 as opposed to [5].

It is well recognized that the diffusion rate of U ions in UO_2 and UO_2-Gd_2O_3 depends on the oxygen to metal ratio (O/M ratio) [9],[10] and the O/M depends on the oxygen potential of the atmosphere.[4],[11],[12] Therefore, grain growth was enhanced in the higher oxygen potential atmosphere where the diffusion rate of cations became greater.

On the other hand, in the higher oxygen potential atmosphere, sintered density decrease was introduced due to closed porosities formation resulted from rapid densification of UO_2 phase in the early stage of sintering [5]. With respect to broadening of the FWHM as an indicator of poor homogeneity of the solid solution, the following reason is possibly considered. Diffusivity of U and Gd ions is enhanced corresponding with the oxygen potential. However, in the oxygen potential more than approximately -350 kJ/mol, the effective diffusion length necessary to form solid solution is slightly elongated due to a barrier effect of closed porosities formation which results in sintered density decrease also. The previous study [5] was made using the uniformly mixed UO_2-Gd_2O_3 powder, therefore no influence on elongation of the effective diffusion length necessary to form solid solution was introduced. On the contrary, in this study using less uniformly mixed powder, enhancement of diffusivity could not compensate elongation of the effective diffusion length necessary to form solid solution Possibly, in more excessively high oxygen potential atmosphere, enhancement of diffusivity overcomes the influence on elongation of diffusion length necessary to form solid solution because formation of porosities will be saturated gradually.

Though the higher oxygen potential atmosphere will be required to sinter higher Gd_2O_3 concentration pellets because the oxygen potential equivalent to a certain O/M ratio corresponds to Gd_2O_3 concentration, it can be concluded that the oxygen potential as high as atmosphere 2's is preferable for sintering UO_2-Gd_2O_3 pellets up to 10 % Gd_2O_3 concentration considering sintered density decrease.

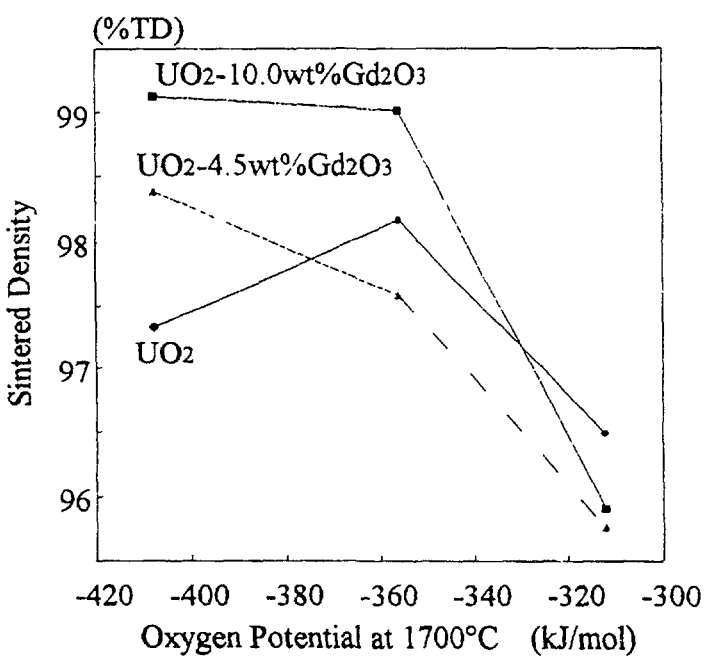

FIG. 7. Effects of the oxygen potential on the sintered density.

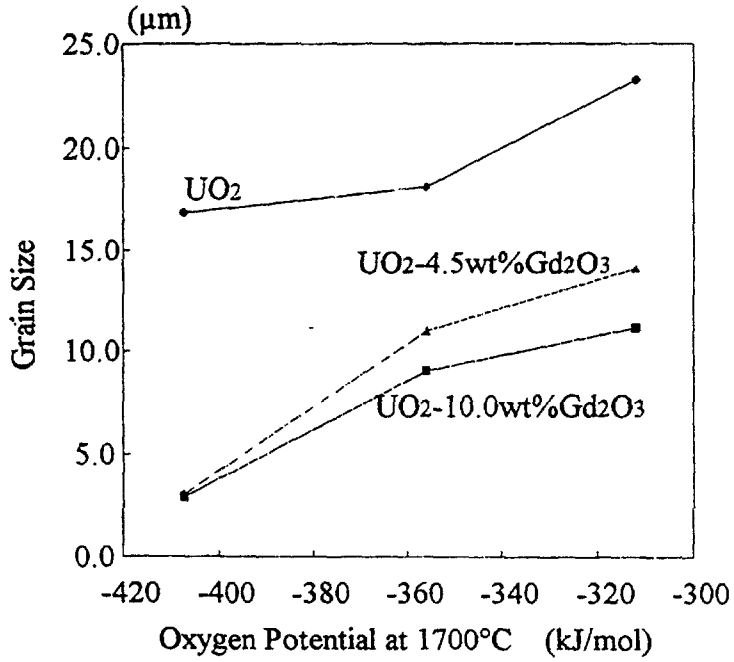

FIG. 8. Effects of the oxygen potential on the pellet grain size.

TABLE VI. FWHM OF (620) PEAK OF X-RAY DIFFRACTION OF THE SINTERED PELLET (UNIT: DEGREE)

Oxygen Potential	Gd_2O_3 concentration		
(at 1700°C:kJ/mol)	0 wt%	4.5 wt%	10.0 wt%
- 408	-	0.5609	-
- 356	0.1641	0.3397	0.3405
- 312	-	0.4036	0.4548

4. CONCLUSION

In order to improve UO_2-Gd_2O_3 pellet microstructure, the effect of the UO_2/Gd_2O_3 mixing condition prior to sintering as well as the oxygen potential of the atmosphere during sintering was evaluated. The effective diffusion length was estimated to be approximately 2 μm through the basic study using a UO_2-Gd_2O_3 diffusion couple. In addition, through the study using actual UO_2-Gd_2O_3 pellets, the following observations were concluded. More uniformly mixed UO2-Gd2O3 powder is preferable to enhance UO_2-Gd_2O_3 solid solubility as well as grain growth. On the other hand, higher oxygen potential of the atmosphere was also effective to enhance grain growth, while sintered density decreased in the oxygen potential higher than approximately -350 kJ/mole. Moreover, especially in less uniformly mixed powder, solid solution formation was slightly suppressed due to the effect to elongate the diffusion length necessary to form solid solution by formation of closed porosities in the oxygen potential higher than approximately -350 kJ/mole.

REFERENCE

(1) J E Littlechild, G G. Butler and G W. Lester, Pro Int Conf Nucler Fuel Performance, London, paper 65 (1973) BNES.
(2) H H Davis and R A Potter, Mater Sci Res., 11 (1978) 515
(3) R Manzel and W O Dorr, Am Ceram Soc Bull., 59 (1980) 601
(4) K Une and M Oguma, J Nucl Mater , 131 (1985) 88
(5) R Yuda and K Une, J Nucl Mater , 178 [213] 195-203 (1991)
(6) H Assmann, W Doerr and M Peehs, J Am Ceram Soc , 67 [9] 631-636 (1984)
(7) Reimann, D K. Lundy, T S J Am Ceram Soc , 52, 511 (1969)
(8) Reynolds, G.L Burton, B J Nucl Mater , 82, 22 (1979)
(9) Hj Matzke J Phys C9, 34, 317 (1973)
(10) D Glasser-Leme and Hj Matzke J Nucl Mater , 106, 211(1982)
(11) Terrence B Lindemer and Alfred L Sutton, Jr J Am Ceram Soc., 71 [7] 553-61 (1988)
(12) K Une and M Oguma : J Nucl. Mater 110, 215-222 (1982)

DISCUSSION

(Questions are given in italics)

Table 4 shows an opposite result between 4 5wt% and l0.0wt% Why?

Uniformity of mixing condition enhance the grain growth and higher Gd_2O_3 content ofl0.0wt% was more enhanced the grain growth And the result was 1 case of the examination, not the general tendency

Comment on "Why is grain size of 10% Gd_2O_3 larger than 4.5%?"

One explanation is that 10% Gd_2O_3 is more homogeneous than 4.5% by wet process and heterogeneity prevents grain growth under that sintering condition. Therefore, grain size of 10% Gd_2O_3 became larger than 4.5%. However, dry process, 10% is more heterogeneous.

Do you think higher oxygen potential is better for pellet sintering?

Yes, especially in higher Gd_2O_3 content pellet. But in heterogeneous blended powder, now uniform sintering make sintered density decrease and decrease the homogeneity of solid solution.

DEVELOPMENT OF DUPLEX TYPE MOX–Gd_2O_3 FUEL FOR WATER REACTORS

M. KATO, S. KOHNO, K. KAMIMURA
Power Reactor and
Nuclear Fuel Development Corporation,
Ibaraki, Japan

Abstract

Duplex type fuels of MOX-Gd_2O_3 were fabricated. They were the complex that Gd_2O_3 or Gd_2O_3 -ZrO_2 rods were inserted into a stack of annular MOX pellets. Phase diagram and stability of Gd_2O_3 -ZrO_2 system was investigated by the measurements of melting temperature, X-ray diffraction and TG-DTA. It was confirmed that the rods of Gd_2O_3 and $Gd_{0.405}Zr_{0.595}O_y$ had no phase transformation, no change of the weight and the shape in the temperature range up to 1700°C, which was a foreseen maximum fuel temperature of design. Melting temperature of both Gd rods are over 2300°C. Two types of annular MOX pellets were fabricated with the accuracy of inner diameters of 1.886 ± 0.018 mm and 2.667 ± 0.005 mm. An irradiation test in Halden Boiling Water Reactor will be carried out to investigate duplex type fuels of MOX- Gd_2O_3 and MOX-(Gd_2O_3 -ZrO_2) behaviors for thermal reactor.

1. INTRODUCTION

In order to reduce the nuclear fuel cycle cost, maximum fuel discharge burn up for light water reactors (LWRs) has been gradually extended. The burn up of LWRs UO_2 fuels has been increased more than 50GWd/tU. According to the requirement of increasing burn up, the development of fuels with Gd_2O_3 as a burnable poison has been needed to suppress the initial excess reactivity of the core. A solid solution type fuels of UO_2-Gd_2O_3 [1-3] has been used practically as a high burn up fuel in most LWRs. On the other hand, MOX-Gd_2O_3 fuels have not yet been irradiated in power reactors. But, MOX-Gd_2O_3 fuels have such attractive characteristics as longer reacting time and smaller reactivity swing with burning of Gd than UO_2-Gd_2O_3 fuels.

A duplex type fuel of MOX-Gd_2O_3 has other advantages compared to the solid solution type fuels as follows.

(i) The present MOX fabrication facility can be used for the fabrication of the duplex type fuel. (It is not necessary to construct a new independent MOX-Gd_2O_3 fuel fabrication line).
(ii) Centerline temperature of the fuel and the F.P. gas release rate can be lowered by using annular MOX pellets.
(iii) Thermal conductivity of the fuel is not degraded because of Gd-free in MOX matrix.
(iv) Power range can be easily tuned by adjusting quantity of Gd_2O_3.

This paper describes the result of the fabrication tests of the duplex type fuels of MOX-Gd_2O_3, phase stability of Gd_2O_3 and Gd_2O_3-ZrO_2 rods and an irradiation test program.

The schematic of the duplex type fuel is shown in Fig.1. The duplex type fuel consists of annular MOX pellets and Gd_2O_3 rods or Gd_2O_3-ZrO_2 rods. The rods are inserted into a stack of annular MOX pellets.

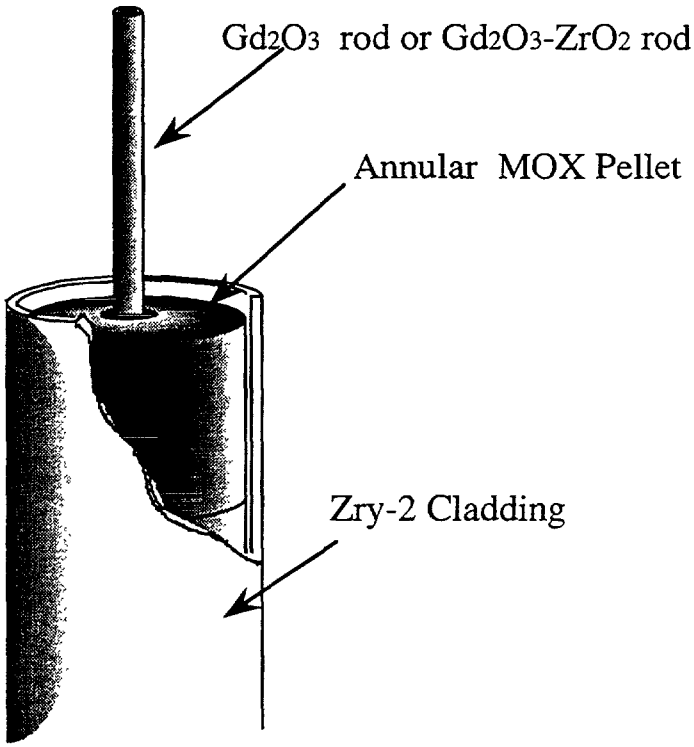

FIG. 1. Schematic of duplex type MOX-Gd_2O_3 fuel rod

R. Collongues et al. reported the phase diagram of Gd_2O_3-ZrO_2 system [4], but the melting temperature of that is not clear. Therefore, we evaluated phase diagram and stability of Gd_2O_3-ZrO_2 system experimentally, and confirmed to be able to fabricate Gd_2O_3 rod and Gd_2O_3-ZrO_2 rods with the sufficient accuracy required by the fuel design. Then the rods and annular MOX pellets with Pu content 8.5% were assembled.

The irradiation test program of the duplex type fuels of MOX-Gd_2O_3 is planned as a part of joint research program between PNC and JAERI with the participation in the OECD Halden Reactor Project since 1997 until 2004.

2. PHASE STABILITY OF GD-ZR OXIDE AND FABRICATION OF GD_2O_3 AND GD_2O_3-ZRO_2 RODS

2.1 Experiment

Sintered pellets of Gd_2O_3, $Gd_{0.405}Zr_{0.595}O_y$ and $Gd_{0.5}Zr_{0.5}O_y$ were prepared to investigate the phase stability of Gd_2O_3-ZrO_2 system. The powders of Gd_2O_3 and ZrO_2 were mixed and pressed to pellets. These pellets were sintered in air for several hours at 1600°C. The sintered pellets were observed on a ceramograph. Melting temperature, X-ray diffraction and TG-DTA were measured. Melting temperature was measured by a thermal arrest method [5], which had an accuracy within ±50°C in this work and TG-DTA were measured up to 1500°C in air.

Rods of Gd_2O_3 (Gd rod) and $Gd_{0.405}Zr_{0.595}O_y$ (Gd-Zr rod) were prepared by an extrusive compacting method. They have 1.24±0.02 mm and 2.3±0.23 mm diameter, respectively.

They were around 170 mm long, and their axial deflection were less than 0.3 mm. The diameter of the Gd and Gd-Zr rods were determined to give the same Gd contents as in a stack. Then the rods were annealed at 1700°C for 2hr in He gas. Thermal cycle tests were performed on both rods 3 times in He atmosphere with temperature range of R.T. - 1500°C. Heating and cooling rates were more than 30°C/min. The amount of impurities were as most same as specifications of MOX fuel as shown in Table I.

TABLE I. RESULT OF CHEMICAL ANALYSIS FOR GD AND GD-ZR RODS

Element	Gd rod	Gd-Zr rod
N	60 ppm	65 ppm
H2O	12 ppm	13 ppm
vaperized element	5 μ l/g	9 μ l/g
Eu	< 10 ppm	< 10 ppm
Sm	< 10 ppm	< 10 ppm
Tb	< 10 ppm	< 10 ppm
Yb	< 10 ppm	< 10 ppm
Dy	< 10 ppm	< 10 ppm
B	< 1 ppm	< 1 ppm
Cd	< 10 ppm	< 10 ppm
Cl	< 20 ppm	< 20 ppm
F	< 20 ppm	< 20 ppm
C	< 50 ppm	< 50 ppm
Al	< 200 ppm	< 200 ppm
Cd	< 10 ppm	< 10 ppm
Ca	< 10 ppm	< 10 ppm
Mg	< 10 ppm	< 10 ppm
Fe	< 100 ppm	< 100 ppm
Ni	< 10 ppm	< 10 ppm
Si	< 250 ppm	< 250 ppm
Th	< 1 ppm	< 1 ppm

2.2 Results and Discussion

In $Gd_{0.5}Zr_{0.5}O_y$ samples, a small amount of precipitates were observed on ceramograph. The average size of precipitates was about 100μm. X-ray diffraction patterns of $Gd_{0.405}Zr_{0.595}O_y$ and $Gd_{0.5}Zr_{0.5}O_y$ are shown in Fig.2. The diffraction pattern of $Gd_{0.405}Zr_{0.595}O_y$ sample is from fluorite-type cubic structure. In $Gd_{0.5}Zr_{0.5}O_y$ sample, small peaks of pyrochlore structure of $Gd_2Zr_2O_7$ are observed. The results of ceramograph and X-ray diffraction show the existence of $Gd_2Zr_2O_7$ phase in the $Gd_{0.5}Zr_{0.5}O_y$ sample. The peaks of diffraction pattern of fluorite structure of $Gd_{0.5}Zr_{0.5}O_y$ sample shift to lower angle compared with that of the $Gd_{0.405}Zr_{0.595}O_y$ sample. It is suggested that the shift is due to increasing lattice parameter by doped Gd.

The measurements of TG-DTA were conducted to investigate a phase transformation up to 1500°C in air. TG curve had no change on both samples, but a peak of DTA curve on both samples was observed at 1462°C. The peak suggests the existence of a phase transformation without a change of oxygen content at that. R.Collongues has reported that the transformation from a $Gd_2Zr_2O_7$ phase to fluorite phase occurs at about 1550°C. In the sample

of $Gd_{0.5}Zr_{0.5}O_y$, a small amount of $Gd_2Zr_2O_7$ phase are observed by X-ray diffraction analysis. The sample was sintered at 1600°C which fluorite phase was stable. Therefore, $Gd_2Zr_2O_7$ phase might appear during cooling. The peak of DTA suggests to be appeared by the transformation from pyrochlore structure of $Gd_2Zr_2O_7$ to fluorite structure. We think that the difference of the transformation temperature between both studies is caused by the heterogeneity of samples.

Melting temperature was measured and the data were plotted in the phase diagram [4] shown in Fig.3. Melting temperature of $Gd_{0.405}Zr_{0.595}O_y$ and $Gd_{0.5}Zr_{0.5}O_y$ samples was over 2300°C. On the other hand, melting temperature of Gd_2O_3 was reported to be in the range of 2330 to 2350°C[6]. We have estimated that a maximum center temperature of fuel would reach about 1700°C during irradiation. Melting temperature of $Gd_{0.405}Zr_{0.595}O_y$ sample were much higher than that of $Gd_{0.5}Zr_{0.5}O_y$ sample and $Gd_{0.405}Zr_{0.595}O_y$ sample kept a stable fluorite structure up to the melting temperature of about 2520°C. Therefore, we selected the composition of $Gd_{0.405}Zr_{0.595}O_y$ for the Gd-Zr rod.

Appearance of the fabricated Gd rods is shown in Fig.4. Density of Gd and Gd-Zr rods are more than 95%TD. Gd and Gd-Zr rods had no change of weight and dimension in the annealing test at 1700°C and the thermal cycle test. We confirmed that the rods could be used in the irradiation test by the phase stability evaluation, the annealing test and the thermal cycle test results.

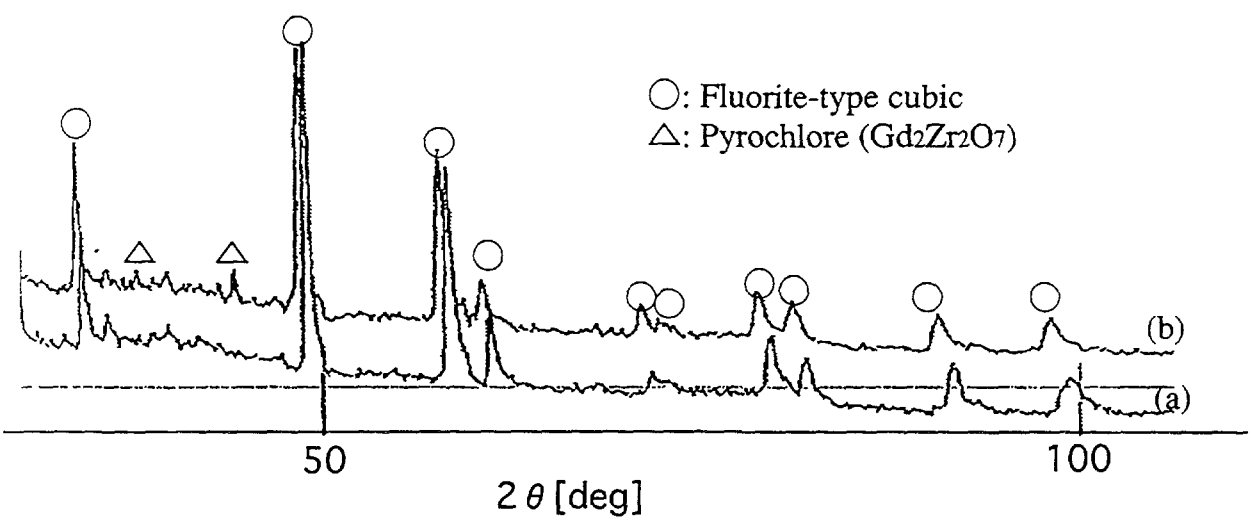

FIG. 2. X-ray diffraction pattern of samples (a)$Gd_{0.405}Zr_{0.595}O_y$ (b)$Gd_{0.5}Zr_{0.5}O_y$

3. IRRADIATION TEST PLAN

The irradiation test of the duplex type fuels is planned to evaluate the irradiation behavior of the fuels, and to investigate the influence of the pellets/cladding gap on the irradiation behavior. The duplex type fuels are MOX-Gd, MOX-(Gd-Zr) and UO_2-Gd fuels. The specification of the Gd, Gd-Zr rod and the test fuel are shown in Tables II and III. Both rods contain the same Gd content in one rod. Solid and annular MOX pellets have three levels

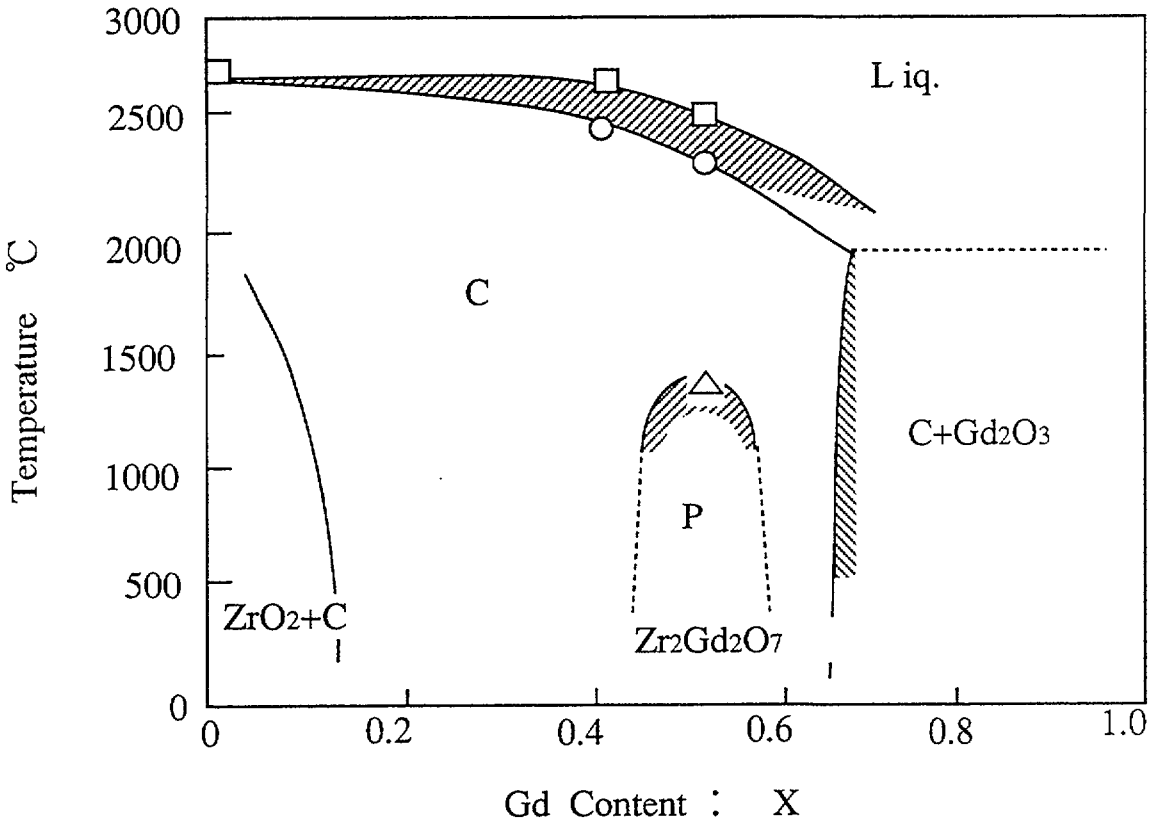

FIG.3. *Phase diagram of $Zr_{(1-X)}\ Gd_xO_{(2-y)}$.[4]*
C:fluorite-type cubic , P: Pyrochlore structure

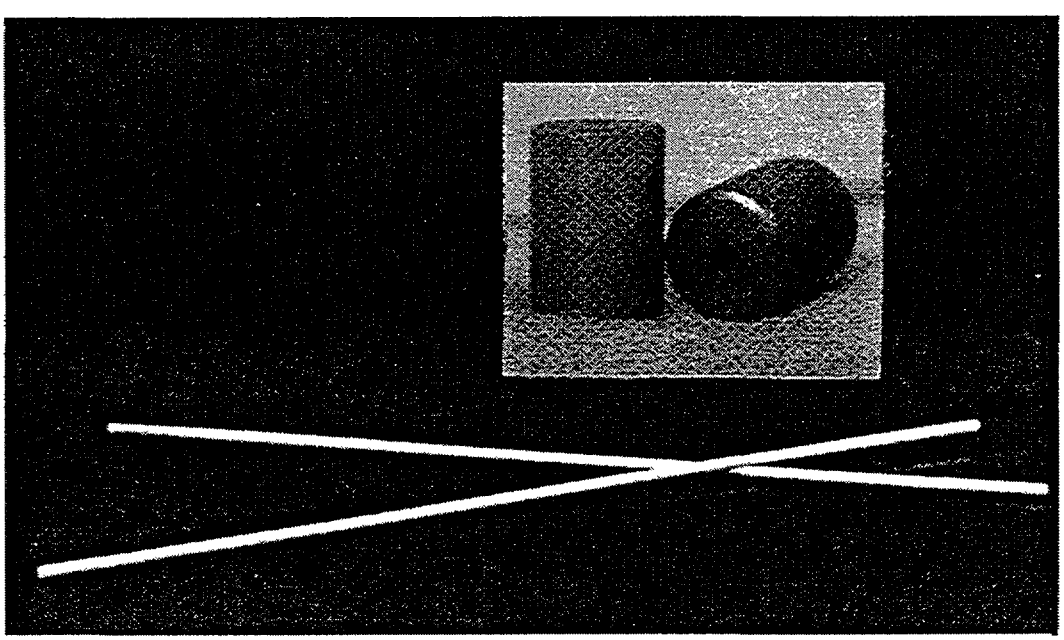

FIG.4. *Appearance of Gd_2O_3 rods and annular MOX pellets*

of 150, 200 and 250μm as a parameter of pellet/cladding gap. Stack length is about 340mm. Plutonium content of MOX pellets is 8.5%. Each fuel rod is equipped with instruments in either or both ends as shown in Table III. The irradiation conditions are shown in Table IV. 8 fuel rods in lower cluster and 8 fuel rods to be exchanged will be irradiated by 15GWd/t and 25GWd/t respectively. 8 fuel rods in upper cluster will be irradiated by about 40GWd/t for 8 years in HBWR. PIE of all 24 rods will be carried out.

TABLE II. SPECIFICATION OF GD ROD AND GD-ZR ROD

Nominal coposition	Diametere	Length	Theoretical density	Axial deflection
Gd_2O_3 $Gd_{0.405}Zr_{0.595}O_y$	1.2mm 1.8mm	169mm	$\geqq$95%	$<$0.3mm

TABLE III. SPECIFICATION OF FUEL RODS FOR IRRADIATION TEST

Type of Fuel	Dimension of Pellets [mm]			Pellet /Cladding gap [μm]	Number of Rod	Instruments*
	Height	Diameter	Innner diameter			
Solid MOX	13.0±2.0	9.05±0.02 9.10±0.02 9.15±0.02	———	150 200 250	1 3 1	PF
Annular MOX	13.0±2.0	9.05±0.02 9.10±0.02 9.15±0.02	1.9±0.19	150 200 250	1 5 1	ET PF + ET, ET ET
Duplex type MOX-Gd rod	13.0±2.0	9.10±0.02	1.9±0.19	200	4	PF + EC PF + EF PF EC
Duplex type MOX- (Gd,Zr) rod	13.0±2.0	9.10±0.02	2.7±0.27	200	4	PF + EC PF + EF PF EC
Duplex type UO_2- Gd rod	13.0±2.0	9.10±0.02	1.9±0.19	200	4	PF + EC PF + EF PF EC

* PF:Plenum Pressure, ET:Expansion Thermometer,
EC:Cladding Elongation, EF:Fuel Stack Length Elongation

TABLE IV. CONDITION OF IRRADIATION TEST

Maximum linear heat rate	Burn-up	Coolant temp.	Coolant press.	Irradiation Time
439 W/cm	40 GWd/t	240 ℃	35.5 kg/cm^2	8 years

4. FABRICATION OF ANNULAR MOX PELLETS AND ASSEMBLY OF DUPLEX TYPE FUEL

One of the subjects for developing duplex type fuel is to fabricate annular MOX pellets. The pellets are fabricated from PuO_2 and UO_2 powder by a mechanical mixing method. Two types of annular MOX pellets had 1.886 ± 0.018 mm and 2.667 ± 0.005 mm inner diameter. Appearance of the annular MOX pellets is shown in Fig.4. The pellets had $95 \pm 2\%$ TD and the average crystal grain size of $13.5 \mu m$. Maximum plutonium spot detected by α-autoradiography was $180 \mu m$.

In assembly of duplex type fuels, Gd or Gd-Zr rod was installed into the annular MOX pellets placed in a row by a manual operation. Then they were loaded into a cladding with lower end plug. The fuel rod was sealed with $5 kg/cm^2$ He gas.

5. SUMMARY

Phase stability of Gd_2O_3-ZrO_2 system was evaluated. It was confirmed that $Gd_2Zr_2O_7$ phase of pyrochlore structure was stable under about 1500°C in the sample of $Gd_{0.5}Zr_{0.5}O_y$ and fluorite structure was also stable up to the melting temperature in the sample of $Gd_{0.405}Zr_{0.595}O_y$. Melting temperature of both samples was over 2300°C.

Rods of Gd and Gd-Zr for the duplex type fuels of MOX-Gd_2O_3 were fabricated by an extrusion method. They were 1.24 ± 0.02 mm and 1.84 ± 0.18 mm diameter respectively. The rods were approximately 170 mm length and less than 0.3 mm axial deflection. The rods were confirmed to be kept stable shape, weight and crystal structure under 1700°C, which was a maximum foreseen fuel temperature of design. Two types of annular MOX pellets were fabricated with an accuracy of 1.886 ± 0.018 mm and 2.667 ± 0.005 mm inner diameter. The duplex type fuels of MOX-Gd, MOX-(Gd-Zr) and UO_2-Gd are planned to be irradiated in Halden Reactor up to burn-up of 40Gwd/t.

ACKNOWLEDGEMENT

The authors are pleased to acknowledge Mr. Carlo Vitanza of Halden Project for his valuable advice in planning of the irradiation test program.

REFERENCES

[1] BEALS, R.J., HANDWERK, J.H., WRONA, B.J., Behavior of Urania-Rare-Earth Oxides at High Temperature, J. Amer. Ceram. Soci. 52,11(1969), 578-581.

[2] TSUCHIE, T., KODAMA, T., PIE of Turuga Fuel Part-2, IAEA Specialists Meeting, Tokyo, (1984).

[3] MORI, K., et. al., Development of Gd Fuel for PWR, IAEA Specialists Meeting, Tokyo, (1984).

[4] ROBERT, C., et. al., Sur les diagrammes d'equilibre des systems Zircone-Oxyde de terrres rares, Memories presentes a la societe chimique, France (1960).

[5] YAMAMOTO, K., HIROSAWA, T., YOSHIKAWA, K., MOROZUMI, K., NOMURA, S., Melting temperature and thermal conduvtivity of irradiated mixed oxide fuel, J. Nucl. Mater., 204(1993)85-92.
[6] WISNYI, L. G., PIJANOWSKI, U. S., Atomic Energy Comission Rept., KAPC-1564, 10-11(1956).

DISCUSSION

(Questions are given in italics)

Comment

The use of center hole also has the merit of reducing the fuel temperature In addition, the pressure of the center Gd_2O_3 core would eliminate the problem of water ingress. As to the neutronics, the S/V ratio is lower, thus one needs the duplex gadolinia in more rods, but the effect will hopefully be the best

Why did you perform your irradiation at 400W/cm (high) linear heat rating?

The initial poisoning effect of a Gd containing rod is proportional to the diameters it is contained within. This means that your concept will have a 5–10 smaller poisoning effect This can of course be compensated by a large proportion of Gd containing rods Is it your intention to introduce Gd in all rods in MOX fuel assemblies for BWRs?

Our concept was designed for ATR (Advanced heavy water moderated thermal reactor). In a core of ATR, neutronics are so thermalized and reactor is so soft that the poisoning effect of Gd is larger than in cores of BWRs Thus only 6 to 24 out of 54 fuel rods per one assembly contain Gd I suppose that for the case of BWRs, more fuel rods need to contain Gd. I don't have the exact value yet We have a plan to do a design research and to evaluate the duplex type Gd fuel for BWRs in future

DEVELOPMENT OF MOX MANUFACTURING TECHNOLOGY IN BNFL

P.G. BUCHAN, D.J. POWELL, J. EDWARDS
Thorp Division,
British Nuclear Fuels Ltd,
Risley, United Kingdom

Abstract

BNFL is successfully operating a small scale MOX fuel fabrication facility at its Sellafield Site and is currently constructing an advanced, commercial scale MOX facility to complement its existing LWR UO_2 fabrication capability. BNFL's MOX fuel capability is fully supported by a comprehensive technology development programme aimed at providing a high quality product which is successfully competing in the market. Building on the experience gained over the last 30 years, ie from the production of both thermal and fast reactor MOX fuels, BNFL's development team set a standard for its MOX product which is targeted at exceeding the performance of UO_2 fuel in reactor. In order to meet the stringent design requirements the product development team has introduced the Short Binderless Route (SBR) process that is now used routinely in BNFL's MOX Demonstration Facility (MDF) and which forms the basis for BNFL's large scale Sellafield MOX Plant. This plant not only uses the SBR process for MOX production but also incorporates the most advanced technology available anywhere in the world for nuclear fuel production.

A detailed account of the technology developed by BNFL to support its MOX fuels business will be provided, together with an explanation of the processes and plants used for MOX fuel production by BNFL. The paper also looks at the future needs of the MOX business and how improvements in pellet design can assist the MOX fabrication production process to meet the user demand requirements of utilities around the world.

1. INTRODUCTION

BNFL has been involved in all aspects of the nuclear fuel cycle for over 40 years. Recycling has long been an important feature of BNFL's portfolio during this time and is currently being extended further with the introduction of new facilities for manufacture of recycle uranium fuel at BNFL's Springfield site and commencement of MOX fuel production at Sellafield. These advanced facilities will provide BNFL with a fully integrated recycling capability to meet the requirements of the next century which has demanded the introduction of new technology. As a result BNFL has been undertaking a comprehensive development programme aimed at introducing the latest technology for the manufacture of high quality products in an increasingly competitive market. The advances made by BNFL in the MOX manufacturing area is the main focus of this paper which will describe some of the key developments and the steps taken to introduce these into BNFL's facilities.

In establishing its development programme, BNFL has utilised the many years of experience gained from production of MOX fuel for both fast reactor and thermal applications which dates back to the early 1960s. Since this time the development of MOX manufacturing technology particularly in the area of powder processing has been recognised as an important factor in establishing and maintaining high quality products. BNFL's development programme has not only been directed at implementing successful developments in its MOX manufacturing

facilities but has also had to take into consideration other factors. In particular there have been a number of developments that have been made in the UO_2 fuels area which has placed increasing demands on MOX manufacturers to produce fuels with higher enrichments which can be irradiated to higher burn ups. MOX fuel must be fabricated to cater for these advances and BNFL's development programme has been geared to establishing plants and processes which are aimed at not only satisfying the current technical requirements of fuels irradiated in reactor, but which also have the flexibility to produce the next generation of MOX fuel which will be equal to or better than an advanced uranium equivalent. One of the ways this will be achieved is through increasing the plutonium content of MOX, advances in MOX fuel pellet design and the increased homogeneity of MOX powder used to produce the pellets which will ultimately lead to better in reactor performance of the fuel. BNFL has paid particular attention to this area through development of its Short Binderless Route (SBR) process.

Following on from the advances in the UO_2 fuel areas, BNFL's development programme has also taken into consideration the need to handle PuO_2 separated from high burn up uranium fuel which contain lower levels of Pu-239 but high levels of Pu-241 and the even numbered plutonium isotopes. Furthermore the technical challenges associated with scaling up fabrication and inspection processes from the demonstration size to full scale plant facilities without compromising the quality of fuel produced is another factor that has been considered.

It is through approaching the issues outlined above in dedicated development programmes that BNFL has been able to achieve the introduction of advanced MOX fuel fabrication facilities which can successfully compete in the global market.

2. DEVELOPMENT OF THE SHORT BINDERLESS ROUTE

One of the key elements in the successful development of BNFL's MOX capability has been the short binderless route process for mixing U and Pu powders to produce an excellent product.

During the 1970s and 1980s fast reactor fuel in the UK was produced using the binder route, but after it was found that UO_2 fuel pellets could be successfully manufactured without the aid of a binding agent, the initiative for a new programme of work on MOX fuels was initiated. Initially this work concentrated on the conventional binderless route with which BNFL had extensive experience from UO_2 fuels, but development studies showed that high energy attritor milling instead of ball milling yielded a powder which could be converted directly to a free flowing press feed by a simple, single stage spheroidisation process. This two stage process replaced the traditional ball mill, precompaction and granulation stages. This new flowsheet developed by BNFL is referred to as the Short Binderless Route (SBR) process and the advantages associated with using the route ensured that it was chosen as the basis for MOX powder production in BNFL's MOX fabrication facilities.

The SBR process uses an attritor mill to blend the UO_2 and PuO_2 powders and a spheroidiser to condition the powder to convert it into a suitable press feed. The attritor mill is a high energy stirred ball mill, which efficiently breaks down powder agglomerates and produces a fine intimately mixed UO_2 /PuO_2 powder in a very short time. The milling times

used in the SBR process are substantially less than one hour, compared with more than 10 hours in a conventional tumbling mill.

The spheroidiser operates at a much slower speed, gently tumbling the attritor milled powder. This tumbling process causes the finely divided powder particles to agglomerate and produce a granular type material with good flow characteristics which is an excellent feed to an automatic press. By carefully controlling the conditions used in the attritor mill and spheroidiser good quality press feed is consistently produced. During the subsequent sintering process, the finely divided particles making up the MOX powder diffuse to form an almost completely solid solution of uranium-plutonium dioxide.

In the MOX Demonstration Facility (MDF) the SBR process is carried out on a 25kg batch scale. In the Sellafield MOX Plant (SMP) the process has been scaled up to accommodate the larger batch sizes required for a commercial scale plant. In this plant a 50kg mixture of UO_2 /PuO_2 powder is prepared in the first attritor mill before it is blended with two other 50kg lots to form a 150kg MOX powder batch of identical composition. This MOX powder batch is then subdivided into three 50kg sub-batches, for processing through a second attritor mill and spheroidiser to produce the granular press feed.

The SBR process has several significant advantages from an engineering and safety point of view which can be summarised as follows:

- Reduced milling times enable the desired plant throughput to be achieved using small batch sizes. This increases operational flexibility and supports the inherent safety of the plant.
- The shape and size of the process vessels used in SMP are such that a criticality incident cannot occur when processing reactor grade plutonium through the plant.
- The process allows the equipment used for powder milling and conditioning to remain connected during loading and discharge of powder which has obvious benefits for containment and dose reduction in the plant.
- The relatively small size of the equipment in SMP, together with the minimum inventory and enlarged containment, greatly assists equipment maintainability. Operating the equipment in MDF has shown it to be extremely reliable with only minimum maintenance requirements.

3. DEVELOPMENT OF BNFL'S MOX FABRICATION PLANTS

BNFL commenced the design and construction of a small MOX fuel production facility known as the MOX Demonstration Facility (MDF) in 1989. This was the first stage in plans which also encompass the design and construction of a commercial scale plant known as the Sellafield MOX Plant (SMP).

In defining this strategy BNFL recognised the importance in enhancing the commercial irradiation experience for SBR fuel through irradiation in a variety of different reactors. To this end MDF was constructed on a fast track basis as a single production line facility with small throughput. The facility was created by modifying and extending an existing building which had previously been used for the fast reactor fuel development work. This fast track

approach, coupled with ongoing R&D programmes covering key plant items, helped gain the necessary fabrication and irradiation experience in a short timescale.

The MDF consists of four main areas of plant:

a) fuel pellet production
b) fuel rod production
c) fuel rod inspection
d) fuel assembly manufacture and inspection

The heart of the process is the pelleting plant which consists of a single line of key equipment for production of high quality MOX fuel pellets. In this area the UO_2 and PuO_2 feed materials are weighed out in the correct proportions and processed to press feed by the SBR. In MDF the press feed granules are pressed using a single punch press to green pellets which are then transferred by a cushion transfer conveyor to the furnace boat load station. Here the pellets are carefully loaded by a pick and place machine into sinter furnace boats which are then charged to the furnace. Pellets are sintered at 1650°C over a cycle time of 24 hours before being discharged from the furnace for dry grinding and subsequent inspection. After inspection, pellets of acceptable quality are loaded into an in line pellet store pending loading into fuel rods.

Fully inspected pellets are manually loaded in lm long sub stacks into pre-dried fuel tubes in which the bottom end plug has been actually welded. Each pellet sub stack is weighed and when the complete fuel column has been loaded into the rod it is processed through various workstations to have the spring and top end plug inserted and welded before final pressurisation with helium and eventual seal welding. The rod is then checked to ensure that there is no contamination on its surface before it is transferred to the rod inspection area. Each fuel rod is uniquely identified with a bar code which is entered into a computer based traceability system at each workstation in the rod production and inspection areas.

The fuel rod inspection area contains shielded workstations to inspect and check that the rods meet the specification requirements. Certified rods are manually transferred to the rod store where they are loaded into magazines in the same location as in the finished fuel assembly.

The MDF fuel assembly and inspection area has been designed for PWR fuel assemblies although it could be modified to accommodate BWR designs. In this part of the plant certified magazines are removed from the rod store and brought adjacent with the rod loading machine which transfers rods into the fuel assembly skeleton. After fitting the top and bottom nozzles, assemblies are then inspected to check they meet the specification requirements following which the finished fuel assemblies will be stored awaiting despatch to the customers.

There are major differences in the design of conventional uranium and MOX fuel manufacture due largely to safety and radiation dose uptake requirements. Due to the presence of plutonium, MOX fuel has to be manufactured in fully contained gloveboxes shielded for gamma and neutron radiation. The level of gamma and neutron radiation is dependent on the source of PuO_2 and the burn up of the UO_2 fuel from which the plutonium has been separated,

the reactor type and the time between reprocessing and using the PuO_2 for MOX production. To reduce operator dose as far as practicable operations are carried out in gloveboxes with appropriate lead/steel shielding to remove gamma radiation and moderator (e.g. polythene or wood) to reduce neutron dose. Operations in MDF are a mixture of hands on and automatic carefully evaluated to ensure that operator dose does not exceed a target of 5mSv/year (internal and external) which is set by BNFL.

4. FROM DEMONSTRATION TO COMMERCIAL SCALE

The next stage in BNFL's plans has already taken shape at BNFL's Sellafield Site with the completion of construction of the Sellafield MOX Plant (SMP). The SMP is the most up to date, flexible and automated MOX fuel fabrication plant in the world. The plant incorporates a mixture of proven and advanced technologies developed and used by BNFL in the MDF, other plutonium facilities at Sellafield and in its UO_2 fuel fabrication plants at its Springfields Site. SMP is co-located and integrated with the Thermal Oxide Reprocessing Plant (Thorp) to provide the first truly integrated recycling capability in the world which will allow BNFL to receive irradiated fuel into Thorp and despatch finished MOX fuel assemblies from the SMP without the need for any intermediate transport of separated plutonium.

The SMP which will have a throughput of 120 tonnes/year (HM) of MOX, has been designed to produce both PWR and BWR fuels using the most up to date technology. The plant adopts the same principle flowsheet as MDF but incorporates a number of additional design features to achieve the higher throughput rate and enable the plant to produce MOX fuel of the quality that will be required by customers through to the next century. The features included in the design are discussed below.

The powder and pelleting operations in SMP are fully automated with limited maintenance requirements to ensure that operator radiation dose is minimised. The scale of the SBR process in the plant has been optimised so that a number of 150kg MOX powder batches made from the same feed powders can be produced with almost identical isotopic composition. This design feature will allow the MOX fuel loaded into a group of fuel assemblies to have almost identical isotopic composition, thus helping to minimise the impact of any nuclear design issues (e.g. power peaking) on the safety of using MOX in the reactor core.

In SMP there are two identical powder processing and pelleting lines and four identical furnaces for sintering the MOX pellets. The SMP sintering furnaces are designed to operate at temperatures of 1750-1800°C using atmospheres of controlled oxygen content. The experience gained so far in MDF shows that although excellent quality, homogeneous fuel can be obtained using sintering temperatures of about 1650°C, the quality could be further enhanced by using higher sintering temperatures. In addition, it is envisaged that the drive towards higher burn up fuel will result in the need to increase the grain size in the MOX fuel pellet during the next few years. The technology incorporated into the SMP furnaces should allow BNFL to produce larger grained MOX fuel and fuel of even better homogeneity than that made at present in MDF, thus helping BNFL to meet the future demands of customers.

Finally in the pelleting area, the plant incorporates two centreless grinding machines for dry grinding of the MOX pellets and an in line pellet store allowing the finished pellets to be stored in the plant before they are loaded into fuel rods. Experience in MDF has shown that dry grinding produces fuel with surface roughness characteristics that are easily able to meet the needs of the tight BWR and PWR vendor specifications. The SMP grinding facilities have been designed with features capable of producing excellent quality pellets with special dust offtake systems so that the powder removed during grinding can be recycled and not spread about the glovebox containment or disposed of in the plant waste streams.

Fuel rod production in SMP is carried out in one of two duplicate lines. Stacks of finished pellets are automatically prepared and weighed before they are loaded into a pre-dried fuel tube with welded bottom end plug. Following pellet loading the spring and end plug are inserted to enable circumferential welding to be completed. In the plant Tungsten Insert Gas Welding is carried out using equipment specially designed for this purpose.

The finished fuel rods are immediately leak tested before they are processed through automatic inspection stations. The rods are inspected for the normal characteristics, weld quality, pellet enrichment, straightness and surface finish using automatic techniques that have been developed by BNFL. The data collected from this inspection is available for viewing by QA/QC inspectors in a central control room and where appropriate is stored on computer for use as part of the records for the fuel. The acceptable fuel rods are taken automatically from the inspection area of the plant and loaded into magazines where they will reside until required for fuel assembly production.

The operations associated with fuel assembly building and inspection are carried out automatically and remotely in one of two purpose built fuel assembly caves dedicated to PWR or BWR fuel. The operation in the caves is monitored from the plant central control room with the inspection data viewed by QA/QC inspectors and where appropriate stored on computer. Following inspection the finished fuel assemblies are automatically transferred to a fuel assembly store awaiting despatch to the customers.

5. THE QUALITY OF BNFL'S MOX FUEL

The most important features of thermal reactor MOX fuel pellets from the fuel performance point of view are:

- the geometrical and surface features
- the impurity content
- the microstructural properties

The geometrical and surface features of BNFL's MOX pellets are excellent. The control of these features is dependent on the equipment used for fabrication such as tooling used for pelleting, the grinding system used to grind the pellets to the correct diameter as well as the plant operational and quality control systems being correctly adhered to.

The impurity content of the fuel is controlled by materials used to construct the plant, the process conditions and the purity of the feed powders. Whilst it is of great importance to

minimise all impurities, the most important impurities are those that can migrate within the fuel and have the potential to interact with the clad. i.e. Cl, F and H_2 and those which can absorb neutrons and limit the performance of the MOX fuel pellets, e.g. Gd, Eu and all elements with a high neutron cross section. The impurity content of MOX fuels made by BNFL has been extremely low with the levels of neutron absorber, hydrogen and other gases significantly lower than customers specification limits.

The microstructural properties of the fuel, notably the grain size and homogeneity, are important factors that are controlled during fabrication. The grain size of the fuel which in turn impacts on the thermal creep rate and fission gas release rate is controlled during the sintering process. The homogeneity which is important from the point of view of fuel properties (creep rate, thermal conductivity) is controlled by the powder preparation stage as well as the sintering process.

The SBR process has been specially developed by BNFL to produce homogeneous MOX fuel. The function of the high energy attritor mill is to reduce the particle size of the PuO_2 and UO_2 feed powder particles and agglomerates and to generate a completely homogeneous mixture of MOX powder. During the subsequent sintering process the finely divided particles making up the MOX powder inter-diffuse to form an almost complete solid solution of uranium-plutonium dioxide.

BNFL has successfully produced more than 10 tonnes of MOX fuel in the MDF using the SBR without any problems being experienced with the plutonium homogeneity of the fuel. The homogeneity has been measured using colour autoradiography on routine samples of sintered pellets produced in MDF. The results show that the average plutonium content of any plutonium rich regions in the fuel pellets is ofthe order 15-20% with the occasional small region identified with a plutonium content of about 30%.

To confirm the results of autoradiography, samples have been subjected to electron probe microanalysis. The results of the analysis show that the maximum %Pu/(U+Pu) of more than 300 measurement areas (each 1 μm diameter), selected at random throughout an SBR MOX pellet, was 32% and that the majority of plutonium rich regions had plutonium contents of 12-15%. The Pu/(U+Pu) ratio of the fuel pellet was 5.5%. The results confirm the conclusions made from the autoradiography data that SBR MOX fuel is very homogeneous.

From this commercial production experience, BNFL has been able to successfully demonstrate that SBR MOX fuel contains no significant plutonium rich regions of more than 20 μm diameter containing more than about 30% plutonium.

6. DEVELOPMENT WORK IN SUPPORT OF SMP

One key point of BNFL's current development programme is aimed at supporting the successful construction, commissioning and qualification of the SMP involving the following:

- development work to demonstrate the scale up of the process
- testing under uranium active conditions to assess the performance of key equipment.
- testing of prototype equipment at manufacturers' works.

- on site testing of equipment when installed in SMP.
- comprehensive programmes for uranium/plutonium commissioning and qualification.

To demonstrate the scale up of the processes and assess the performance of key items of equipment BNFL has invested in special facilities at its Springfields Site to undertake comprehensive demonstration programmes. These programmes will provide information to support commissioning of the plant, allowing it to be completed in the shortest possible timescale. The key items of equipment included in these programmes are:

- the powder processing facilities where a full scale replica of the SMP equipment has been constructed to prove reliability, maintainability and operational capability of the key plant items.
- the welding facilities where a prototype welder has been procured for tests using actual fuel rod components.
- the pellet inspection equipment where one of the actual inspection systems to be used in SMP is being fully tested with UO_2 pellets.
- the pellet grinding equipment and dust offtake system which have already been satisfactorily demonstrated.

In the case of fuel assembly building special arrangements have been made to test the key items of equipment in SMP at the earliest timescale, so that any issues can be resolved well in advance of the schedule for delivery of the first fuel from the plant.

7. THE FUTURE OF MOX FUEL IN BNFL

BNFL's commitment to continuously improve its products and processes is borne out by the extent of its investment in R&D and the fact that the company has recently endorsed a proposal to build a new R&D facility at Sellafield costing of the order of £100 million. The focus of the longer term MOX fuel R&D programmes in BNFL is towards reducing the cost of production, improving fuel quality and providing its customers with advanced fuel designs to meet their future requirements. To this end the long term R&D programmes are focused around:

- improving manufacturing processes to produce competitive product
- producing new MOX fuel designs and proving their performance
- reducing waste volumes and maximising the use of recycle
- improving the quality of SBR MOX fuel.

One key component of BNFL's MOX business has been the development of strong links with its international customers to ensure that the end user, the utility is fully satisfied. This has resulted in a close working relationship and a good understanding of the requirements and capability to quality and the reliability of supplying MOX fuel.

Finally, another key development area for BNFL's MOX business is with disposition/utilisation of ex-weapons grade plutonium via the use of thermal reactor MOX fuel. Although all of BNFL's MOX fuel fabrication facilities are designed solely for the conversion of civil plutonium into MOX fuel, the technical, production and engineering expertise

developed since the early 1960s can be fully utilised in developing programmes with the USA and Russia to use plutonium separated from dismantled weapons. BNFL supported by the UK Government is currently in discussion with interested parties world-wide to identify how today's MOX technology can be used to promote world peace on the shortest achievable timescales.

8. CONCLUSIONS

During the last ten years, BNFL has developed MOX fuel technology to enable the provision of a recycling service to reprocessing customers. The technology developed includes:

- the development of the Short Binderless Route for MOX powder production
- the provision of the MOX Demonstration Facility
- the provision of the Sellafield MOX Plant.

The technology developed has so far resulted in the provision of excellent quality fuel to our customers which will continue when SMP is successfully brought on line and further enhances BNFL's MOX fuel capability. This paper has outlined the scope of development being carried out to support SMP and the future direction of the company's MOX development programme.

DISCUSSION

(Questions are given in italics)

How is PuO_2 particle size distribution (Pu spot size)? Do you have FGR data, say above 40 GWd/t? A presentation by NOK at the INE meeting (Windermere) in July 1996 indicated that 5.4 t had been fabricated by MDF for and delivered to Beznau. In your presentation, you indicated that a total of 10 t has been fabricated up to now. Are you at liberty to indicate for which reactor the other 5 t have been fabricated?

Do you have any quantitative data on the Pu particle size in BNFL MOX fuel?

In manufacturing MOX fuel BNFL has a customers specification for Pu particle size to meet. This specification has been considered achieved in fuel supplied to BNFL's customers.

Do you have experience of fission gas release at fuel irradiation of >40000 MWd/t?

This information will be contained in a paper presented by Dr.C.Braun - In-reactor performance of prototype SBR MOX fuel.

BNFL presented a paper jointly with NOK saying that 5 tons of MOX fuel had been fabricated. Are you at liberty to say the name of the customer for whom you have made the remaining MOX fuel (up to the 10 tons).

Without discussing with the customer, I am not at liberty to disclose their name. I can just confirm that BNFL have made MOX fuel for other customers.

DEVELOPMENTS IN MOX FUEL PELLET FABRICATION TECHNOLOGY: INDIAN EXPERIENCE

H.S. KAMATH, S. MAJUMDAR, D.S.C. PURUSTHOTHAM
Bhabha Atomic Research Centre,
Trombay, Mumbai,
India

Abstract

India is interested in mixed oxide (MOX) fuel technology for better utilisation of its nuclear fuel resources. In view of this, a programme involving MOX fuel design, fabrication and irradiation in research and power reactors has been taken up. A number of experimental irradiations in research reactors have been carried out and a few MOX assemblies of "All Pu" type have been loaded in our commercial BWRs at Tarapur. An island type of MOX fuel design is under study for use in PHWRs which can increase the burn-up of the fuel by more than 30% compared to natural UO_2 fuel. The MOX fuel pellet fabrication technology for the above purpose and R & D efforts in progress for achieving better fuel performance are described in the paper.

The standard MOX fuel fabrication route involves mechanical mixing and milling of UO_2 and PuO_2 powders. After detailed investigations with several types of mixing and milling equipments, dry attritor milling has been found to be the most suitable for this operation. Neutron Coincident Counting (NCC) technique was found to be the most convenient and appropriate technique for quick analysis of Pu content in milled MOX powder and to know Pu mixing is homogenous or not. Both mechanical and hydraulic presses have been used for powder compaction for green pellet production although the latter has been preferred for better reproducibility. Low residue admixed lubricants have been used to facilitate easy compaction.

The normal sintering temperature used in Nitrogen-Hydrogen atmosphere is between 1600°C to 1700°C. Low temperature sintering (LTS) using oxidative atmospheres such as carbon dioxide, Nitrogen and coarse vacuum have also been investigated on UO_2 and MOX on experimental scale and irradiation behaviour of such MOX pellets is under study.

Ceramic fibre lined batch furnaces have been found to be the most suitable for MOX pellet production as they offer very good flexibility in sintering cycle, and ease of maintainability under glove box conditions.

Pellets of different geometry, from simple cylindrical to chamfered, dished and annular pellets have been fabricated and irradiated in research reactors although plain cylindrical pellets with L/D less than 1.2 have been used for MOX fuel loading in power reactors. Fully automated wet centreless grinding of MOX pellets using composite diamond wheel and subsequent ultrasonic cleaning has been used in the fabrication flowsheet. The MOX pellets undergo vacuum degassing at 400°C to ensure low hydrogen content prior to loading of pellets into zircaloy clad fuel tubes.

A novel sol-gel microsphere pelletisation route (SGMP) combined with LTS has also been developed and is briefly discussed.

1. INTRODUCTION

The Indian Nuclear Power Programme is mainly based on Pressurised Heavy Water Reactors (PHWRs) with the exception of two Boiling Water Reactors (BWRs) at Tarapur. The PHWRs use indigenous natural uranium oxide (NU) as fuel whereas the fuel for the BWRs is

imported low enriched uranium oxide (LEU). India has only modest reserves of uranium and in order to make maximum use of its nuclear resources it has adopted a closed fuel cycle strategy which involves plutonium (Pu) utilisation in thermal and fast reactors [1]. This strategy calls for development of mixed oxide (MOX) technology and hence a programme involving MOX fuel design, fabrication and irradiation in research and power reactors has been taken up. This paper discusses Indian experience in MOX fuel fabrication technology with particular reference to developments in pellet fabrication for improved safety, performance and economics. Although the major emphasis at present is mixed uranium-plutonium oxide fuel for BWRs, the developments in pellet technology are generally applicable to $(UPu)O_2$ and $(Th\text{-}Pu)O_2$ fuels which are of interest for use in PHWRs.

2. MOX FUEL DESIGN FOR PHWRs AND BWRs

The MOX fuel design both for BWRs and PHWRs is done in such a way that it retains the original hardware structure, same geometry and clad material etc. with no major changes in nuclear, mechanical and thermohydraulic parameters of respective reactor systems.

The MOX fuel bundle proposed for PHWRs is of island type consisting of 12NU rods in the outer periphery and 7 inner MOX rods instead of 19 NU rods used in standard fuel bundle. The main strategy is to increase the average burnup of the core from the present 6700 MWD/T to about 10,700 MWD/T (30% increase) in an equilibrium core consisting of 44 central channels of natural UO_2 and remaining 262 channels with MOX. Experimental irradiations in pressurised water loop (PWL) of our research reactors have been taken up as the first stage of development prior to MOX introduction in commercial PHWRs.

The MOX fuel assembly designed for use in our BWRs is "All Pu" type consisting of 36 rods in 6 x 6 square array. The main difference between the standard LEU and MOX assembly, (apart from fuel material) is the water rod in the spacer capture rod position. The MOX assembly incorporates fuel rods of 3 enrichments of UO_2-PuO_2 and the reactor employs 3-batch cycling of 18 months with average MOX bundle burn-up of about 15,000 MWd/Te [2]. The main emphasis is of indigenous fuel and optimum use of nuclear fuel resources. A number of experimental MOX fuel irradiations have been carried out [3] and a few MOX fuel assemblies are undergoing irradiation in commercial BWRs.

3. MOX PELLET FABRICATION FLOWSHEET

The MOX fuel fabrication flowsheet used in India involves mechanical mixing of UO_2 and PuO_2 powders as in most of the industrial scale production flowsheets today. The UO_2 powder is obtained through Ammonium Di-Uranate (ADU) route and PuO_2 is obtained through oxalate route. The powders are non-flowable and hence are precompacted at about 75 MPa, granulated and finally compacted at 300 MPa to a green density of 54% to 56% of T.D. The pellets are then sintered at temperatures between 1600°C to 1700°C in N_2 -- 7% H_2 atmosphere. The sintered pellets are centrelessly ground to the exact diameter using resin bonded silicon carbide grinding wheels. The ground pellets are cleaned, dried, inspected, stacked and degassed at temperatures around 400°C in vacuum better than 1 m bar. The pellet stacks are then loaded into zircaloy tubes and TIG/Resistance welded in case of BWR/PHWR fuel rods respectively. The work on development of MOX pellet fabrication flowsheet was

started in the late 70s at Radlometallurgy Division at BARC and has undergone several improvements/modifications for reasons of safety, performance and economics. Fig. 1 shows the basic flow sheet of pellet fabrication and broad areas in which development work was carried out in the last 25 years some of which are briefly discussed below.

4. IMPROVEMENTS IN PELLET FABRICATION FLOWSHEET

4.1 Powder Mixing

From the very beginning mechanical mixing/milling was selected for production of MOX powder as a reference process though R&D efforts on development of co-conversion route using sol-gel technique was started at a later date [4].

At the very early stage it was realised that simple mixing of UO_2 and PuO_2 powders in V or twin shell blenders is not satisfactory for meeting the micro-homogeneity and dissolution test specifications. Hence for laboratory scale operations planetary ball mills with progressive mixing of UO_2 in PuO_2 was used successfully. For larger scale work conventional centrifugal ball mills have not been found satisfactory as separation of milled product from the grinding balls resulted in dust raising in glove boxes. Dry attritor milling has been found to be the most satisfactory technique.

An attritor is a grinding mill containing internally agitated media and can be termed as "stirred ball mill". In the attritor the power input is used directly for agitating the media to achieve grinding and not for rotating a heavy tank in addition to media as in case of a ball mill. This ensures excellent micro-homogeneity in the product and the operation is completely contained as the grinding media is automatically retained during discharge of product. Additionally, attritor grinding does not take place against the tank walls so there is little or no wear of the walls and consequent contamination of the product. Attritor milling has been satisfactorily demonstrated for industrial scale manufacture of MOX fuel for use in our BWRs at Tarapur [5]. Neutron coincident counting (NCC) was found to be the most appropriate technique for quick analysis of Pu content in the milled powder and to confirm uniformity of Pu mixing [6]. Use of MOX gels for manufacture of pellets could be an alternative to mechanical milling route and described separately.

4.2 Pellet Compaction

The milled MOX powder is non-free flowing and hence is precompacted and granulated to make it flowable and improve its apparent density. Development work on alternate agglomeration techniques are under development. The free flowing granules are compacted at pressures of the order of 300 MPa either in hydraulic or mechanical presses using single or multiple punches. In general, it has been found hydraulic presses give green pellets of highly reproducible density even when powder/granule characteristics vary from batch to batch.

It is well known that during compaction of powder in a die, the die-wall friction and the inter particle friction affect the density, uniformity, die wear and ease of ejection of the pellet. Hence die-wall/granule lubrication is of prime importance and over the years extensive studies [7] have been carried out to select an optimum lubricant and the lubrication technique. In the recent past these studies have concentrated on admixed synthetic lubricant formulation

which is "stainless" (low residue on ignition) and permits green pellets to be sintered without prior dewaxing in a separate furnace. The lubricant addition does not result in unacceptable levels of metallic/non metallic impurities in the pellet. This admixed lubricant is added to the MOX powder during the attritor milling stage which ensures homogeneous lubricant distribution and easy discharge of the MOX powder from the attritor mill.

Another important area that needs attention from the point of view of radiation safety in MOX pellet compaction is the powder/granule feeding mechanism used in the compaction press. Most compaction presses use vibratory feeders for die filling which lead to spillage of the powder on the die table as well as airborne activity in the glove box. Afzal [8] has developed a volumetric granule feeding device using a directional screw that feeds the powder in two dies exactly to a pre-determined volume. This die-filling device is completely free from vibrations and clean in operation.

4.3 Sintering

The conventional sintering of UO_2 and MOX fuels is carried out at temperatures between 1550°C to 1700°C in reducing atmosphere. For MOX pellets the non-explosive reducing gas mixture of A-7%H_2 or N_2-7%H_2 is used. The latter is less expensive but is likely to give higher nitrogen contamination if the MOX composition contains more than 6 wt% of PuO_2 in UO_2 [9]. As MOX fuels presently being used have PuO_2 content less than about 6 wt% in MOX, N_2 - 7%H_2 is used as standard sintering atmosphere.

Both batch type and continuous pusher type of furnaces have been used for manufacture of MOX/UO_2 pellets respectively. It is generally believed that continuous sintering furnaces are more energy efficient than batch furnaces and are invariably used in the UO_2 fuel fabrication industry. However use of advanced ceramic fibre insulation and control electronics has made most batch furnaces used in the nuclear fuel industry equally energy efficient. In our experience batch furnaces are also easier to maintain under glove box conditions.

In any case high temperature sintering in reducing atmosphere is the most energy intensive and expensive step in pellet fabrication. There have been attempts even during the late 50s for lowering the sintering temperature but lack of full understanding of the sintering mechanisms has restricted such developments to only laboratory scale experiments.

In the 80s systematic investigations of Matzke [10] clearly indicated that sintering and solid-solution formation in UO_2 /MOX are primarily diffusion phenomenon and the rate controlling diffusion of cation (U/Pu) can be enhanced under higher oxygen potential conditions during sintering. Based on this principle a two step low temperature sintering technique for UO_2 involving sintering at 1100 -- 1200°C in CO_2 and later reduction in hydrogen have been developed in Germany and is known as "NIKUSI" process [11]. We have also carried out such LTS studies of UO_2/MOX in oxidative atmospheres like CO_2, Argon-Oxygen, Nitrogen-Oxygen, and coarse vacuum [12]. In these studies enhanced diffusion of PuO_2 into MOX matrix was confirmed at 1200°C in CO_2 atmosphere but to meet the o/m specification of less than 2.02, a post sintering reduction treatment in A-H_2, is required [13]. MOX pellets sintered in Argon and Nitrogen at 1250°C in single stage in optimum conditions to meet the O/M specifications have been successfully irradiated in research reactors. UO_2 pellets fabricated by LTS in CO_2 using two stage [NIKUSI] technique

have also been irradiated in power reactors. At present an indigenous continuous type LTS furnace with oxidising and reducing zones separated by inert gas curtain is under commissioning for pilot plant scale demonstration on UO_2 fuel.

The LTS work has also been extended on ThO_2 pellets where Nb_2O_5 is used as an additive in the range of 0.125 to 0.25 wt%. The sintering temperature used is 1150°C to 1200°C in air atmosphere [14].

4.4 Centreless Grinding

Centreless grinding is an important step in MOX pellet fabrication for diametral and surface finish control. However, this step generates Pu bearing dust/sludge which is generally termed as dirty rejected oxide (DRO). While "sintering to size" is ideal and must be aimed at, it is not always easy to meet the right diametral tolerance of the order of 25 microns on pellets of nominal size 10mm or above. Some MOX fuel fabricators have used dry grinding which minimises problems associated with solid-liquid separation during handling of sludge in wet grinding. Till the early 80s, resin bonded silicon carbide grinding wheels were most commonly used for wet grinding but the MOX sludge used to contain unacceptable levels of metallic and non-metallic impurities. Hence expensive wet recovery methods had to be adopted for recycling this material back into fabrication stream.

Composite diamond grinding wheels show low wear and bring down the sludge volume significantly. The sludge in most cases is sufficiently pure to be used in dry recycle. Since metal bonded diamond wheels have excellent shock resistance and good mechanical strength, they can be employed for larger cuts up to 400 microns though all efforts should be made to minimise the extent of cuts. Another development worth mentioning is the use of synthetic coolants which are oil free and hence ease pellet cleaning operations as no-oil films are formed on the pellet. The coolant in the centreless grinding machine is used in a recirculatory system consisting of a settling tank and hydroclone [15].

A novel pellet feeding system using rotary bowl feeder has been developed [8] to feed the pellets into the grinder and a pellet transport system for conveying the pellets to the next stage of ultrasonic cleaning. The entire operation of MOX pellet grinding has been fully automated.

4.5 Dry recycling

During MOX pellet fabrication most of the scrap generated is chemically pure and can be dry recycled if acceptable quality pellets could be produced using this scrap. In an effort to develop a fabrication route using sintered scrap various blends containing up to 30 wt% of such material pulverised by mechanical [16] and thermal methods were prepared. Thermal pulverisation method involving oxidation of UO_2 to U_3O_8/MO_2 to M_3O_8 was found to give good acceptable microstructure and density if used to the extent of 20 wt%. It was also noticed that MOX pellets produced using 20 wt% oxidised scrap showed better dimensional regularity [17].

4.6 Sol-gel micro-sphere pelletisation (SGMP) technique

The SGMP technique is one of the most promising techniques being developed in BARC for the fabrication of UO_2 /MOX pellets. UO_2/MOX gels containing carbon black are prepared by internal or external gelation technique. These gels after washing and drying are air calcined to get porous microspheres [18]. These are easily crushable and amenable for direct compaction without requiring powder processing steps. The green pellets are sintered either at high temperature under reducing atmosphere or by LTS technique [19]. As gel microspheres are free flowing and dust free, they minimise the risks of Pu contamination/deposition on equipment/glove box surfaces and thereby reduce the toxicity and radiation hazards to the operators. UO_2/MOX fuel rods made by SGMP technique has been successfully test irradiated in our reactors.

5. DEVELOPMENTS FOR HIGH PERFORMANCE

5.1 Pellet Geometry

Pellets of different geometry, from simple cylindrical to chamfered, dished, tapered and annular pellets have been fabricated as per design specifications and requirements. It is well known that the diametral gap and pellet shape play an important role in PCMI/PCI behaviour. In BWRs using standard LEU fuels, the pellet geometry was modified to "short height-chamfered" with no dish on end surfaces since the mid 80s. The pellet to clad gap was also optimised (2% of dia.) and the above changes have resulted in general improvement in performance of BWR fuel [20].

However MOX pellets used for loading in BWRs at present have a simple cylindrical shape in order to reduce the grinding cut and also to have longer life of compaction plungers. Pellets of different enrichment are identified by depression rings of various sizes.

MOX pellets with annular holes of 3.8mm $\pm$ 0.2mm (o.d. 12.26 mm) have been irradiated in research reactors as part of the development [13] of BWR MOX fuel as they seem to have safety and performance advantages over solid pellets. The annular MOX fuel will have lower central temperature resulting in lower fission gas release and stored energy. The transient behaviour of such pellets have also been reported to be superior [21].

The PHWR fuel uses collapsible clad and hence here the pellets are relatively immobile. In view of this thermal expansion space is provided on each pellet in the form of dish on one end-face in the present day natural UO_2 pellets. Double end dishing is also under consideration and investigation for future use. Tapered pellets are proposed for reducing end pellet interaction with end plugs [22].

5.2 Controlled porosity

It is well known that the amount, type, size and distribution of pores in ceramic nuclear fuel plays an important role in determining its performance in the reactor. The amount of porosity which is inverse of density can be controlled by various means such as (i) characteristics of powders (ii) compaction parameters [23] (iii) sintering temperature (iv) thermal treatment [24] of powders (v) addition of poreformers.

The ideal pore structure should have minimum open porosity and pore distribution such that most of it is in the range of 2-5 microns to avoid in-reactor densification. Controlled porosity MOX pellets fabricated by addition of oxidised (U_3O_8/M_3O_8) sintered scrap have been irradiated successfully in research reactors and are presently planned for irradiation in BWRs.

5.3 Larger grain size

The UO_2/MOX fuel pellets made by conventional high temperature sintering have grain size of the order of 5-15 microns. There is considerable interest in the use of larger grain sized (30-40 microns) pellets for high burn-up applications as it is reported that fission gas release is lower for such fuels. Larger grain sized MOX pellets (25-40μ) have been prepared by doping with small amounts of TiO_2 (0.1 wt%). It is also noticed that addition of TiO_2 helps in spherodisation of pores leading to very desirable microstructure of 2-5 μ size pore and 25-40 micron grain size which are ideal for better fuel performance [25]. MOX pellets of such controlled microstructure have been irradiated in research reactors.

6. IRRADIATION EXPERIENCE

Since the beginning of the 80s a number of MOX fuel experimental clusters have been irradiated in pressurised water loop (PWL) of our research reactor CIRUS as part of the programme for development and testing of MOX fuel for power reactors. Table I gives the summary of these MOX fuel irradiation experiments. MOX fuel characteristics representing advanced technologies/design/techniques have all been included in these irradiation experiments. These experiments have helped in selecting the manufacturing flowsheet, finalisation of fuel specifications and formulating quality control plan/procedures.

TABLE I. MOX FUEL IRRADIATION EXPERIENCE IN RESEARCH REACTORS

Designation	**Fuel Mat. Comp.**	**Linear rating W/cm**	**Burnup MWd/T**	**Remarks/design intent**
A-C-2	UO_2-4%PuO_2	414	16265	Dev. of std MOX fuel (BWR)
A-C-3	UO_2-4%PuO_2	490	16000	Higher linear rating (BWR)
A-C-4	UO_2-4%PuO_2	490	2000	Gap size, grain size, LTS, annular pellets. etc.(BWR)
A-C-6	ThO_2-4%PuO_2	-	20767	Thorium irradiation
A-C-8	ThO_2-6.75%Pu UO_2-3%PuO_2	-	7000 Continuing	PHWR MOX Fuel development

A few "All Pu" MOX fuel assemblies have been loaded in two of our commercial BWRs at Tarapur. Two of the MOX fuel assemblies have completed one cycle of operation and found to be defect free in sip testing.

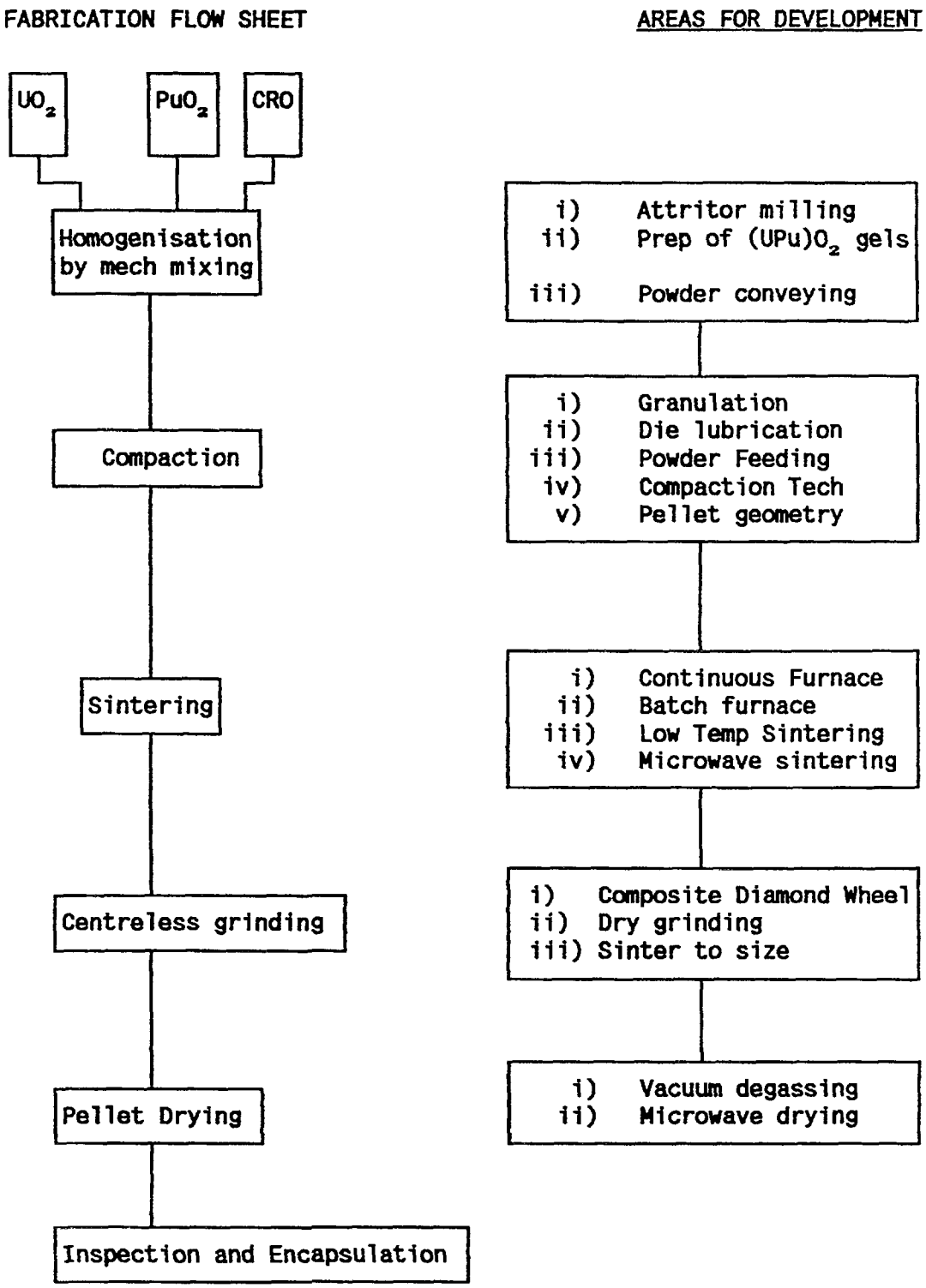

FIG. 1. MOX pellet fabrication flow sheet and areas identified for development.

7. CONCLUSIONS

MOX pelletising technology has been under development since the 80s in India and the emphasis has been on improvement of fuel performance, economics and safety.

Some of the developments related to performance and fabrication technology have now been routinely used for manufacture of MOX fuels for use in commercial power reactors. The R&D work is continuing in many areas with the aim of achieving higher levels of automation and protection to personnel and the environment.

ACKNOWLEDGEMENTS

The paper is based on several years of work done at Radiometallurgy division and Advanced Fuel Fabrication Facility of Bhabha Atomic Research Centre in India and the authors wish to thank all the members of the divisions who participated in this programme. The authors sincerely thank Shri M S Ramkumar, Director, Nuclear Fuels Group and Shri Anil Kakodkar, Director, BARC for the constant encouragement and the permission to present the paper.

REFERENCES

[1] KAKODKAR, A., "Indian Nuclear Power Programme' -- Facets of Nuclear science and technology, Appreciation course by DAE, BARC, Mumbai (1996) 1 -5.

[2] ANANTHARAMAN, K., et al., "MOX fuels for reduced actinide generation" IAEA-TCM on Advanced fuels with reduced actinide generation, Vienna, (1995).

[3] KAMATH, H.S., et al., "Some aspects of plutonium recycling in thermal reactors" -- IAEA specialists meeting on improved utilisation of water reactor fuel with special emphasis on extended burn-up & Pu recycling, CEN/SCK, Mol Belgium (1984).

[4] SOOD, D D., VAIDYA, V.N., "Experience in BARC on the preparation of gel microspheres of uranium, thorium and plutonium fuels" NUFAB-88 Proceedings, DAE, India (1988) 245-255.

[5] PURUSHOTHAM, D.S.C., KAMATH, H.S., "Mixed oxide fuel development for Indian nuclear power programme" -- IAEA TCM on Recycle of Pu & U in water reactor fuels, Newbybridge, U. K. (1995).

[6] PRADEEP KUMAR, et al., "A rapid NDA method (NWCC) for determination of Pu content in MOX powders" -- Nucl. and Radiochem. symp, NUCAR-95, IGCAR, Kalpakkam (1995).

[7] MAJUMDAR, S., et al., "Choice of proper powder lubricant for the production of ceramic nuclear fuel pellets" -- Trans. of the PMAI, Vol 10, (1983) 15-18.

[8] AFZAL, M., "Personal communication"

[9] ROY, P.R., et al., "Fabrication of MOX fuel element clusters for irradiation in PWL" CIRUS, BARC, (1983) 1203.

[10] MATZKE, HJ., "Application of diffusion results in technology: Increased uranium self diffusion in UO_2 and $(UPu)O_2$" EUR-7700 (1982).

[11] ASSMANN, H., "Advantages of oxidative UO_2 sintering process "NIKUSI" -- Proc. of European Nucl. Soc. Meeting, Geneva (1986).

[12] KAMATH, H.S., ROY, P.R., "Sintering technology in the manufacture of nuclear fuels" -- Int. Conf. on sintering in multiphase and ceramic systems, New Delhi (1989).
[13] KAMATH, H.S., et al., "CO_2 -- a low temperature sintering atmosphere for oxide fuels" -- Trans. of Powder Met Assn. of India, 10, (1983) 8-14.
[14] BALAKRISHNAN, P., "Low Temperature Sintering of Thoria -Jnl. of Material Science letters, 7(1988) 657-660.
[15] KAMATH, H.S., ROY, P.R., "Recent developments in P/M techniques used in fabrication of plutonium bearing ceramic nuclear fuels" -- Key Engg. Materials. Vol 29-31 (1989).
[16] KAMATH, H.S., et al., "Development of a dry recycling route for rejected UO_2 and UO_2-4% PuO_2 sintered pellets" BARC -1188 (1983).
[17] SOMAYAJULU, P.S., et al., "Dry recycling of scrap in MOX fuel fabrication proc." of PMAI, Bangalore (1996).
[18] GANGULY, C., et al., Proc of 3rd Int. Conf. on CANDU Fuel, Chalk River, Canada (1992).
[19] GANGULY, C., and BASAK, U., Jnl. of Nucl. Mater. 178 (1991) 179-183.
[20] CHAUDHARY, V.N., et al., "Improvements in fuel performance design and operating practices at Tarapur" -- WANO -- TC seminar on core management and fuel performance, NPC, Bombay (1995).
[21] Plutonium utilisation in BWR -- Phase II -- Semi-Annual report, Jan-June 1970, NEDC-12152, General Electric Company (1970).
[22] PRASAD, P., et al., "A parametric study of Indian PHWR fuel bundles to reduce failure at the clad-end capjunction", BARC (1991).
[23] RAJGOPALAN, P.P., et al., "Effect of pre-compaction on sintered UO_2 pellets -- Proc. of the symposium on sintering and sintered products" October 29-31, BARC, Bombay (1979).
[24] KAMATH, H.S., et al., "Thermal treatments for sinterability control Trans. of PMAI, Vol 5 (1978) 49-55.
[25] GANGULY, C., and KAMATH, H.S., "Fabrication and characterisation of ceramic nuclear fuels in BARC -- Proc of Indo-FRG seminar on trends and techniques in modern research, (1987) IGCAR, Kalpakkam.

DISCUSSION

(Questions are given in italics)

How much is the open porosity of the samples?

In ordinary cases, when you add sintered scrap to pellets, you will get the higher open porosity ratio.

FUEL THERMAL BEHAVIOUR — THERMAL CONDUCTIVITY DEGRADATION OF UO_2 FUEL

(Session 3)

THERMAL CONDUCTIVITY DETERMINATIONS FOR IRRADIATED FUEL

T.L. SHAW, J.C. CARROL, R.A. GOMME
Fuel Performance Group,
AEA Technology plc,
Windscale, Cumbria,
United Kingdom

Abstract

In evaluating fuel performance, the fuel thermal conductivity is considered a key parameter due to its influence on operating temperature, and hence important processes such as fission gas release. Fuel thermal conductivity is known to increase with burnup, and as operators push to reduce operating costs by extending fuel life to higher burn-ups, there is a need to ensure that such degradation will not compromise safety margins. Direct measurement of thermal conductivity, k, is not straightforward, however, it may be derived from measurements of thermal diffusivity, β, specific heat, C_p and density, d, via the relationship: $k = \beta.d.C_p$.

Irradiated ceramic fuel is heavily cracked due to the large thermal stresses generated in-reactor, with the result that sample preparation is difficult, and often only relatively small fragments can be obtained. Despite their size, however, these samples are typically very active, necessitating the use of shielded facilities, with sample handling and equipment operation having to be carried out remotely.

At AEA Technology, Windscale, a laser flash rig for the measurement of thermal diffusivity has now been operating successfully in a shielded facility for a number of years. To complement this, a Netzsch DSC-404 differential scanning calorimeter has recently been installed in an adjacent shielded cell, for which a robotic system under operator control via a closed circuit TV surveillance system has been developed to enable precise sample placement. This provides a *unique* capability of being able to perform *both* thermal diffusivity and specific heat measurements on irradiated fuel samples. This paper describes this capability, together with an example of measurements on fuel irradiated to ca. 40 GWd/tU.

INTRODUCTION

In assessments of nuclear fuel performance, the fuel thermal conductivity is a key parameter since for a given power rating it controls the operating fuel temperature, which in turn influences all other aspects of fuel behaviour, such as fission gas release and fuel swelling. Fuel conductivity is known to degrade with increasing burnup and as operators push to reduce costs by extending fuel life to higher burnup a knowledge of the conductivity of irradiated fuel is crucial. As direct measurement of thermal conductivity is not straightforward thermal conductivity values, k, are commonly derived from measurements of thermal diffusivity, β, specific heat, C_p, and density, d, through the relationship:

$$k = \beta.d.C_p \quad (1)$$

Irradiated ceramic fuel is extensively cracked due to large thermal stresses generated in-reactor, and the amount of cracking increases progressively with fuel burn-up, with the result that sample preparation is difficult and often only relatively small fragments can be obtained. However, although the typical size of samples available is relatively small, they are typically very active, which means that thermal property measurements must be performed

using equipment designed to operate in specially shielded facilities, both sample handling and equipment operation have to be carried out remotely.

At AEA Technology Windscale a laser flash rig for the measurement of thermal diffusivity has now been operating successfully in a shielded facility for a number of years. To complement this a Netzsch DSC-404 differential scanning calorimeter has recently been installed in an adjacent shielded cell, for which a robotic system under operator control has been developed to enable precise crucible placement. This provides a unique capability of being able to perform *both* thermal diffusivity and specific heat measurements on irradiated fuel samples.

This paper describes the Windscale thermal property measurement capabilities (shown in schematic form in Figure 1) together with an example of such measurements on fuel irradiated to ~40 GWd/tU in the Halden BWR, using the laser flash method for thermal diffusivity and differential scanning calorimetry for specific heat.

SPECIFIC HEAT MEASUREMENTS

Equipment

The basic equipment comprises a standard Netzsch DSC-404 high temperature Differential Scanning Calorimeter (DSC), as described by Kaiserberger et al (1989) and shown schematically in Figure 1. However, in order to allow measurements to be made on irradiated samples the operation of the calorimeter has been adapted for remote use inside a shielded cell.

The main innovation is a robotic "pick and place" system which has been developed to allow the precise positioning of sample crucibles to be performed remotely by an operator with the aid of Closed Circuit TV (CCTV) surveillance equipment. The furnace, robotic system and camera surveillance equipment are all located inside the cell, with the temperature control equipment and computerised data acquisition system outside. Sample crucible(s) are placed in a special carrier and transported to an adjacent cell, where the carrier is then loaded into the rig sample transfer system and driven into position using a motorised slide. The robot "pick and place" system is then used to transfer the crucibles from the carrier onto the measurement stem of the DSC-404.

The robot pickup head essentially comprises a nozzle which can be pressurised and when located on top of a standard Netzsch platinum crucible (with its lid in place), it is able to lift and move it. The nozzle can also can be raised and lowered so that the crucible can be positioned precisely (with the aid of an overhead CCTV camera) onto the measurement head.

Platinum crucibles are used, with their bases coated with a thin layer of aluminium oxide. This coating is to prevent the crucibles bonding to the measurement head during runs to high temperature (up to 1400°C), which would make them difficult for the robot to remove. No significant loss in performance has been observed using coated crucibles.

A gas supply (either pure argon or an argon/4% hydrogen mixture) is available and is designed to deliver modest flow rates of between 50-100cm^3/minute through the furnace.

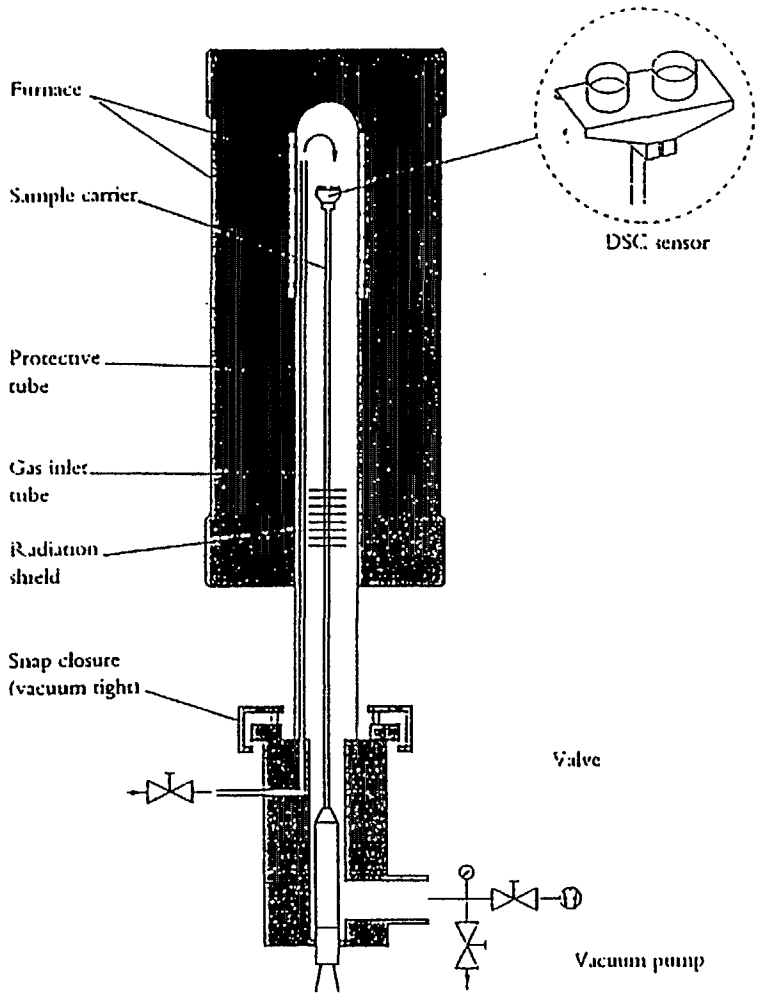

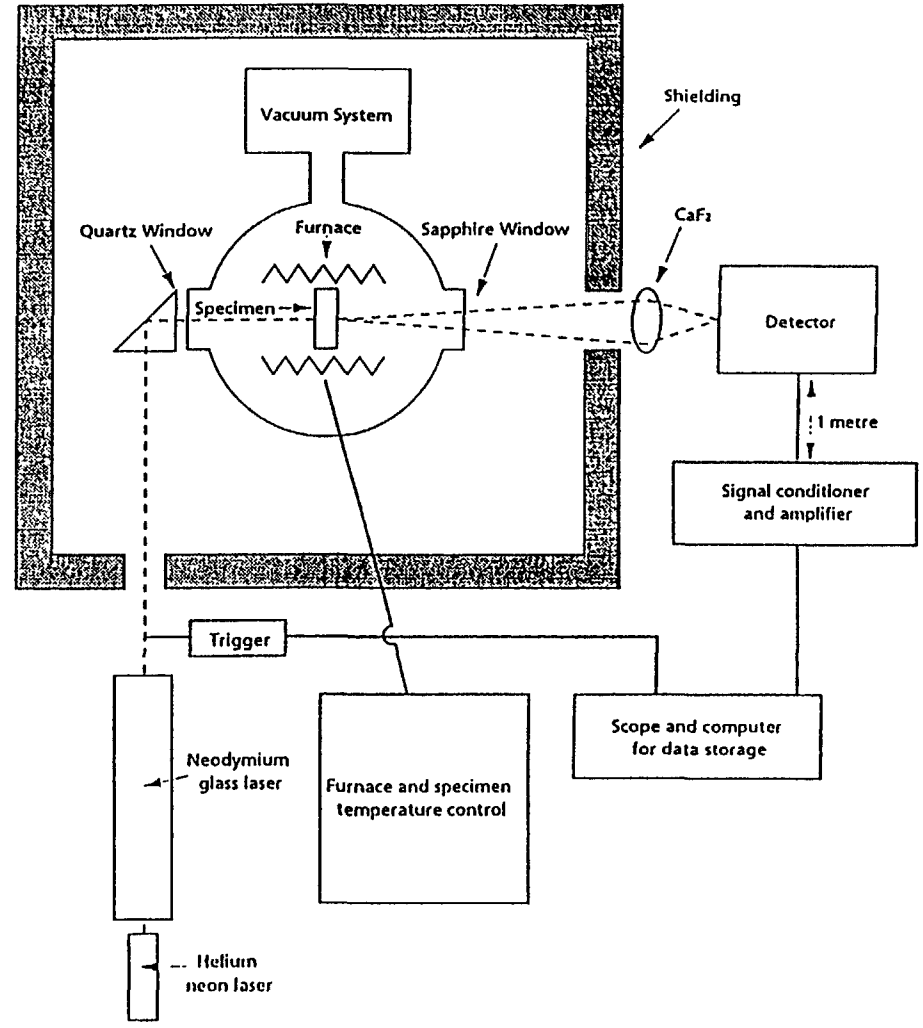

FIG. 1. Schematic diagrams of specific heat and thermal diffusivity measurement apparatus

MEASUREMENT PROCEDURE

DSC is a method by which the heat input into a sample as compared to a known reference material is measured while the sample and reference material are subjected to a controlled temperature programme with constant heating and/or cooling rates (or constant temperatures). The differential heat flux into both the sample and the reference results in temperature differences which are measured as a function of temperature and time.

When applied to the measurement of specific heat, three separate runs with the same crucibles are performed using identical temperature programmes:

- a "baseline" run with two empty crucibles (to establish a baseline);
- a "reference" run using a standard material with known properties (usually Sapphire);
- a "sample" run using the material of interest (for irradiated samples this will be the last stage to avoid contamination of the reference standards, which may be used again).

The temperature differential (expressed in micro-volts) between the two crucible thermocouples is measured during all three temperature scans and the data stored by the controlling computer. The sample specific heat, C_p^s (in J/kg/K), is then given by the following expression

$$C_p^S = \frac{W_R}{W_S}\frac{\Delta V_S}{\Delta V_R}.C_p^R \qquad (2)$$

where:

C_p^R is the specific heat of the reference standard (J/kg/K)
W_R is the weight of the standard (mg)
W_S is the weight of the sample (mg)
ΔV_R is the voltage difference between the reference curve and the baseline (μV)
ΔV_S is the voltage difference between the sample curve and the baseline (μV)

RESULTS

The following measurement procedure was adopted:

- a pre-conditioning cycle comprising an isothermal hold at 800°C for half an hour to anneal out "low temperature" irradiation damage (irradiated fuel only).
- a temperature programme (see Figure 2) comprising a series of cycles to progressively higher temperatures with isothermal holds at the top of each up-ramp, each of 30 minutes duration, at 1000, 1200 and 1400°C to simulate the times that were spent at those temperatures during the thermal diffusivity measurement sequence. A ramp rate of 20°C/minute was used for the three heating and two cooling ramps defined.

In order to validate the technique an unirradiated sample of UO_2 (of mass 140 mg) was prepared and subjected to the above temperature programme, and the results are shown in

Figure 3. Agreement between the up and down ramp data is excellent and the mean values plotted (U-1) are within 5% of the MATPRO recommendation.

Following the U-1 measurement a fragment of UO_2, irradiated to 40 GWd/tU and with a mass of around 100 mg, was prepared and the above measurement sequence run. Figure 4(a) shows the effect of cycling the sample to progressively higher temperatures in the first set of heating cycles, T-1, while Figure 4(b) shows measurements on the same sample during the repeated temperature programme, T-2. Both show the tendency for the specific heat of irradiated UO_2 to be slightly higher for the unirradiated sample (U-1), although to within the experimental uncertainties the differences are not considered significant.

More importantly however, Figure 4(a) shows interesting changes in the specific heat during the progression of the heating cycle programme. On the first up-ramp (to 1000°C) there is a steady increase in the specific heat up to ~800°C (at which temperature the pre-conditioning isothermal hold was performed), whereupon there is a marked decrease in its value - indicative of an exothermic process. On the second up-ramp (to 1200°C), a similar decrease is seen, but does not start until ~900°C. Such a temperature dependence of the change in behaviour is indicative of the annealing processes previously observed in the

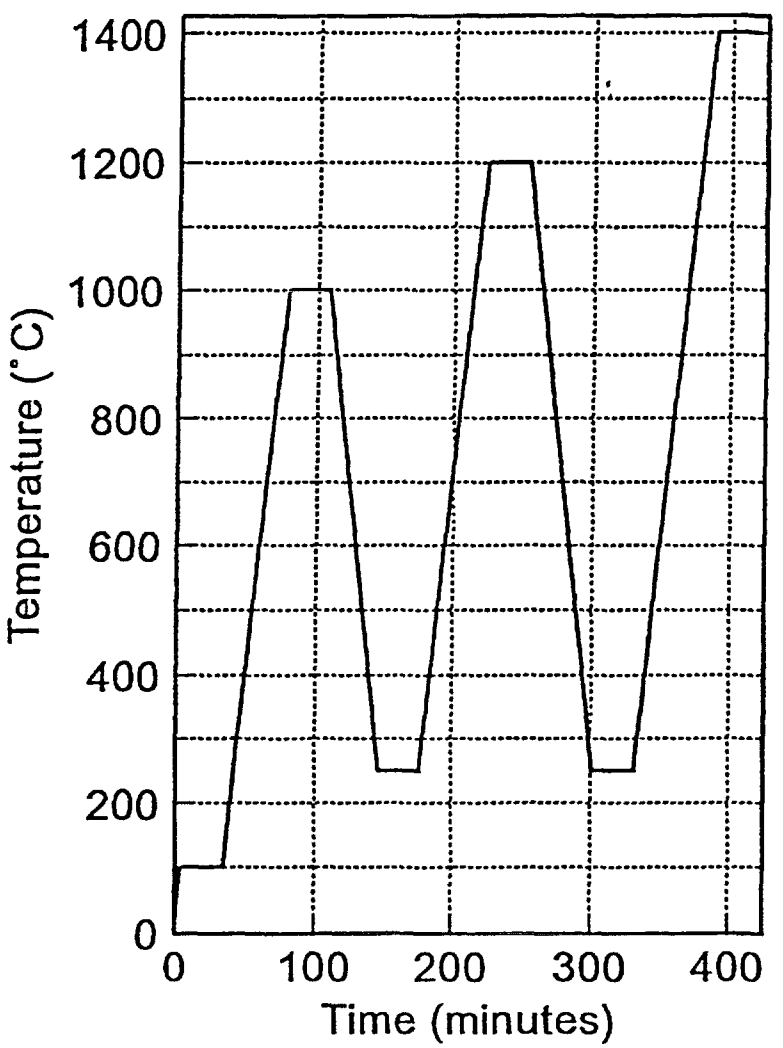

FIG. 2. Temperature programme for tests on Urania fuel

measurement of thermal diffusivity, and referred to in the next section. On the third ramp (to 1400°C) there is no evidence for this pattern of behaviour to be repeated, which may indicate that the earlier half hour hold at 1200°C proved sufficient to complete the annealing process(es) seen at the lower temperatures. However, such a conclusion can only be tentative based on the data presented in Figure 4(a); above 1200°C a sharp increase in "apparent" specific heat is seen, but this is believed to be spurious and to result from a small amount of sample fragmentation (a small amount of particulate was found at the bottom of the crucible after the measurements).

The damage annealing hypothesis is further supported by Figure 4(b) showing the repeat temperature cycle, T-2, performed after the sample has already been taken to a maximum temperature of 1400°C (with a 30 minute hold), and in which the features ascribed to annealing effects are not observed. Within the experimental scatter, a consistent behaviour is observed between each part of the temperature programme. The scatter is largely ascribable to the small sample size which was necessitated in this case due to the annular nature of the fuel being studied.

From Figure 4(a) it is clear that in a temperature up-ramp following an isothermal hold a decrease in "apparent" specific heat, due to exothermic process(es), is observed. The

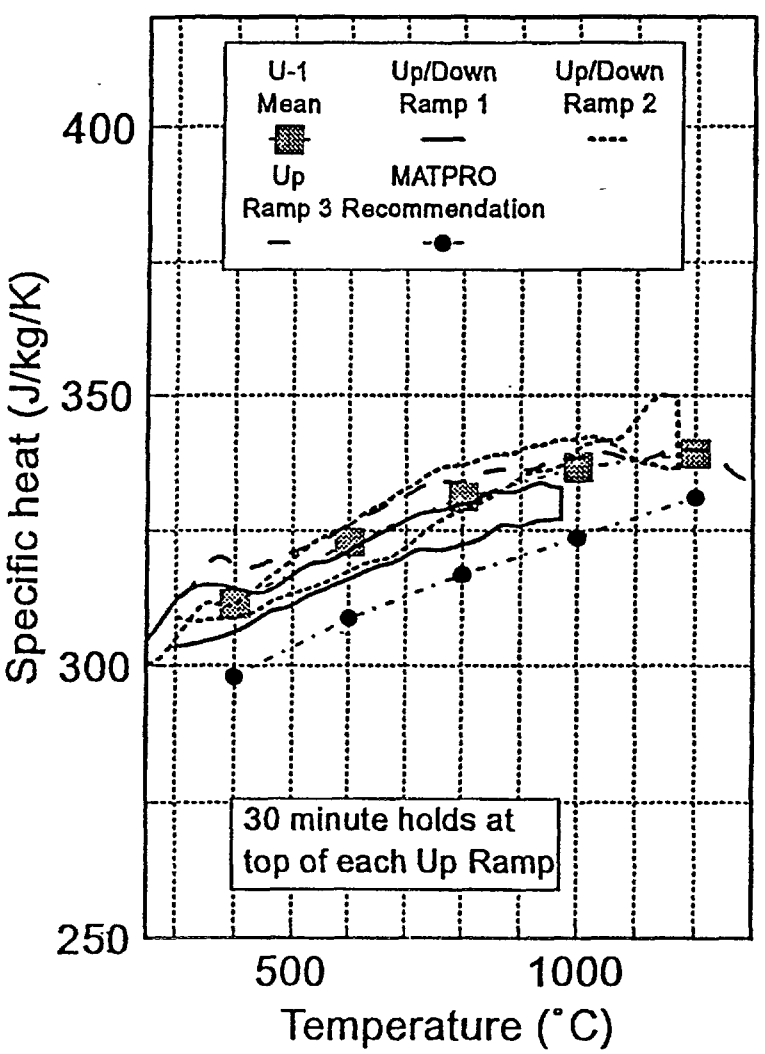

FIG. 3. Specific heat determinations for unirradiated Urania (U-1)

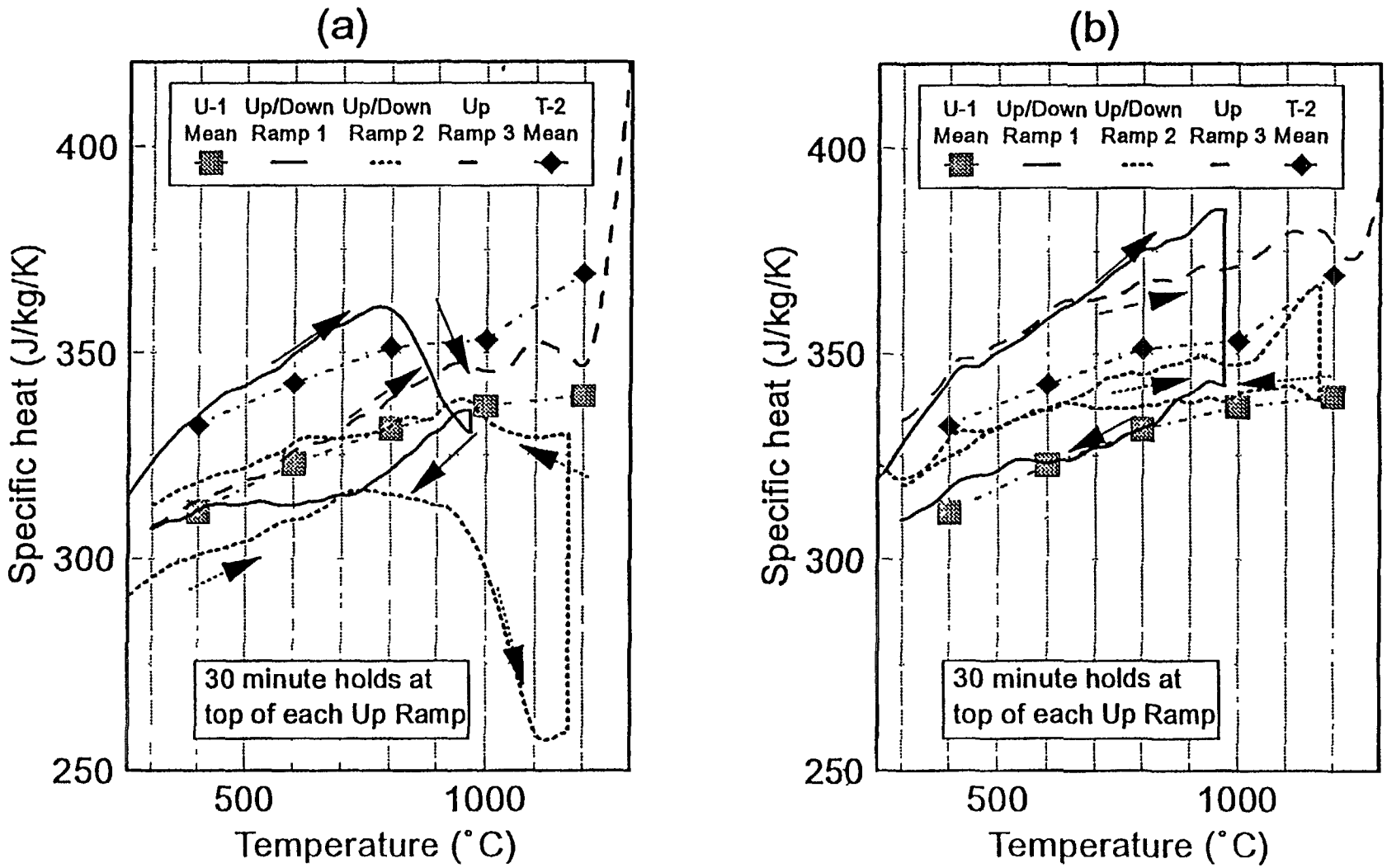

FIG. 4. *Specific heat determinations for irradiated Urania for*
(a) the initial temperature programme, T-1, and
(b) the same programme repeated, T-2

implication for in-reactor performance (e.g. in a transient) will depend upon how the "equilibrium" irradiation damage changes as a function of temperature, and also upon how fast the damage present can anneal (at that temperature) to reach a new equilibrium value.

THERMAL DIFFUSIVITY MEASUREMENTS

Equipment

Thermal diffusivity measurements are performed using the laser flash apparatus illustrated schematically in Figure 1. For the measurements reported here the back surface of the sample was monitored by an In-Sb infra-red detector, with its field of view restricted to the central 2 mm of the sample. A germanium filter was placed immediately before the detector to prevent the possibility of the detector being damaged by the direct 'shine through' of laser light.

Measurement Technique

Irradiated ceramic fuel is extensively cracked making sample preparation difficult. Often only relatively small fragments can be obtained, which do not allow the "standard" analysis techniques to be applied with any degree of confidence. As a consequence of recent work at AEA Technology Windscale a modified version of the standard logarithmic method has been developed to include a heat loss correction term, which was derived empirically from fits to idealised data over the temperature range of interest. The thermal diffusivity data reported here have been obtained using this "Windscale Corrected Logarithmic'' method.

Results

Figure 5 shows in graphical form, the data obtained from the measurement of thermal diffusivity on a fragment of UO_2 irradiated to 40 GWd/tU, over a temperature cycle 400-1400-400°C. For comparison purposes, data from a fragment of unirradiated UO_2 is also shown. Figure 5 shows two clearly distinctive features: (i) the depression of the diffusivity values of the irradiated material compared with the unirradiated; (ii) a hysteresis, or recovery effect, following heating to 1400°C.

The degradation compared with the unirradiated value is now a well known feature and is considered to arise from the presence of dissolved fission products, fission gas bubbles and irradiation damage (e.g. vacancies, interstitials and dislocation loops). The recovery effect seen following annealing is believed ascribable to different processes at different temperatures, although the exact mechanisms are still to be elucidated.

At temperatures of ~600-900°C, it is postulated that recovery occurs via the annealing out of irradiation damage, whereas at higher temperatures, recovery occurs as a result of fission products coming out of solution into bubbles, with subsequent coarsening leading to a reduction in the number of scattering centres and hence diffusivity recovery. Although such restructuring may be expected to occur in-reactor, where changes in bubble characteristics/ populations will occur during temperature transients, such large recoveries are not expected since an equilibrium concentration of irradiation damage is maintained by the presence of a neutron flux. Some confirmation of such hypotheses could be obtained by quantitative

microstructural characterisation of the fuel, before and after annealing. To date, however, no such characterisation has been performed on the fuel studied here.

THERMAL CONDUCTIVITY DETERMINATION

As described in the introduction, measurements of thermal diffusivity and specific heat may be used (along with values of density) to determine values of thermal conductivity. The most meaningful determination of this parameter from the data presented is from the 'annealed' values (i.e. data from the 'down-ramp' shown in Figure 5, and data from the second specific heat heating cycle given in Figure 4(b)).

Figure 6 plots the derived conductivity (based on a density value of 95% theoretical), and compares the values with those given by a UK recommendation. This figure would suggest that the recommendation for irradiated fuel is highly conservative, with the values derived from these measurements being some 30% higher (although still depressed compared with the recommendation for unirradiated fuel). However, it is generally believed that the 'fully annealed' thermal diffusivity values *are not comparable to in-reactor values*, where the effects of an irradiation flux on microstructure must be taken into account.

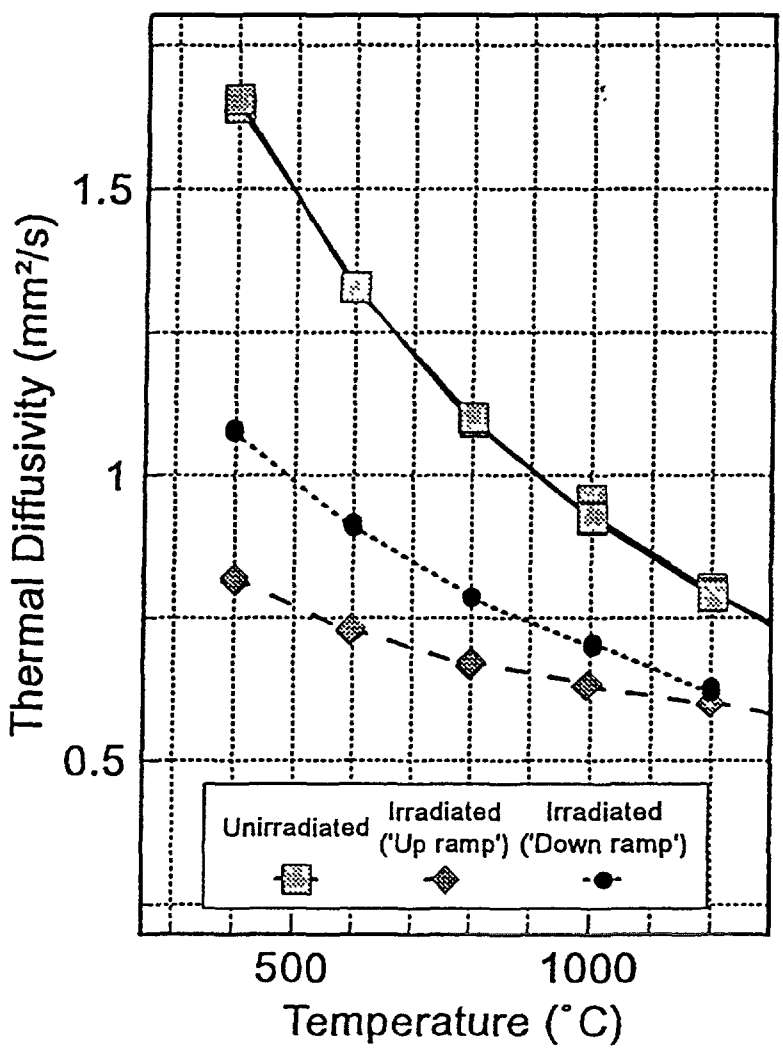

FIG. 5. Thermal diffusivity results for Urania fuel

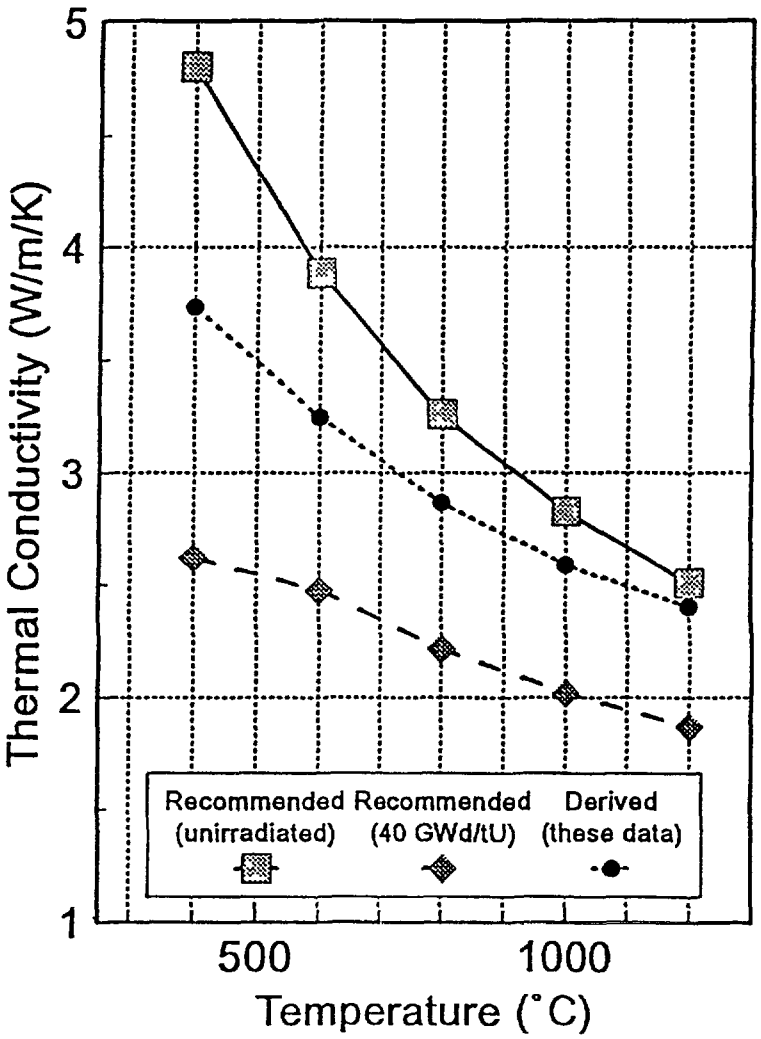

FIG. 6. Comparison of derived thermal conductivity with UK recommendation

CONCLUSIONS

Experimental facilities have been developed at AEA Technology Windscale for the measurement of the thermal diffusivity and the specific heat of irradiated fuel, and an example of such measurements on fuel irradiated to ~40 GWd/tU has been reported here and values of thermal conductivity derived.

Thermal diffusivity values of the irradiated material are depressed compared with the unirradiated, while specific heat values are comparable with unirradiated values and perhaps slightly enhanced.

Both the diffusivity and specific heat data suggest there to be restructuring processes occurring during the heating cycles associated with the measurement techniques; the specific heat data suggest that these processes are exothermic. These effects have been attributed to the removal of irradiation damage and re-distribution of fission products, although the exact mechanisms are still to be confirmed, and ideally require quantitative microstructural characterisation for their elucidation.

A clear feature is the decrease in "apparent" specific heat observed in a temperature up-ramp following an isothermal hold. The implication for in-reactor performance will depend upon how the "equilibrium" irradiation damage changes as a function of temperature, and also upon how fast the damage present can anneal (at that temperature) to reach a new equilibrium value.

References

JAMES H M, 1980. Some extensions of the flash method of measuring thermal diffusivity. J Appl Phys. 51 4666-4672.
KAISERBERGER E, JANOSCHEK J and WASSMER E, 1989. A heat flux DSC for enthalpy and specific heat determinations to 1700K. Thermochimica Acta 148 499-505.
HAGRMAN D L, REYMANN G A and MASON R E. MATPRO - Version 11 (Revision 2). A handbook of materials properties for use in the analysis of light water reactor fuel rod behaviour. NUREG/CR-0479.

DISCUSSION

(Questions are given in italics)

How are your specific heat measurements corrected for the self-heat of the irradiated fuel?

At present the specific heat values are not corrected for self-heating. The need for this correction will be examined.

Why do you believe that the "annealed" data are the correct values to deduce thermal conductivity under irradiation. You indicate that "annealing" results at low temperature from annealing out of irradiation damage and at high temperatures from FPs migrating into the bubbles. I would add modifications of the FP inventories at the grain boundaries due to the vacuum in the chamber. Are those 3 "annealing" factors representative of irradiation conditions?

We comment in the written paper that the use of the "annealed" values are not necessarily representative of in-reactor values, where a dynamic equilibrium will result in irradiation damage and FP bubble formation processes. From the measured data available, however, we believe the annealed values to be closer to the real in-reactor conditions than either the unirradiated or as-irradiated but removed-from-reactor values.

THERMAL DIFFUSIVITY OF HIGH BURNUP UO_2 PELLET

J. NAKAMURA, M. UCHIDA,
H. UETSUKA, T. FURUTA
Japan Atomic Energy Research Institute,
Ibaraki-ken, Japan

Abstract

Thermal diffusivity of high burnup UO_2 (63MWd/kgU) irradiated at HBWR was measured from 290 to 1794 K by laser flash method. The thermal diffusivity of high burnup UO_2 was lower than the half of that of unirradiated UO_2 at room temperature and the difference between them decreased as the measurement temperature increased. The thermal diffusivity gradually increased when the measurement was repeated. It was estimated that the increase of thermal diffusivity was mainly caused by the recovery of radiation damage. The thermal diffusivity data of four samples were separated into two groups. The difference of these groups was mostly explained by the effect of density difference.

The present thermal diffusivity measurement results on high burnup UO_2 after the recovery between 700 and 1300K were a little smaller than those of SIMFUEL, which chemically simulated the effects of burnup by adding solid FPs.

1. INTRODUCTION

The thermal conductivity of UO_2 is estimated to degrade with burnup increase due to FP accumulation, radiation damage, density change and so on. The degradation of thermal conductivity of pellet results in the increase of fuel center temperature and affects strongly fuel behavior such as FP gas release and PCMI. Therefore, the evaluation of thermal conductivity degradation of fuel pellet is very important especially at high burnup.

The effect of solid FP accumulation on thermal conductivity was evaluated by the thermal diffusivity measurement of simulated high burnup UO_2 , added with solid FPs [1,2]. The inpile measurements of thermal conductivity of irradiated fuel were tried in the 60's, but the burnup of the fuel was relatively low [3]. Recently, the Halden Project has performed some in-pile measurement on fuel center temperature during irradiation to high burnup level, and the results showed gradual increase of fuel center temperature with burnup increase at the same power level [4].

The thermal conductivity can also be derived from the thermal diffusivity data combined with heat capacity and density data. However, the thermal diffusivity measurement on high burnup fuel has not been conducted because of the difficulty of sample preparation and delicate nature of the measurement method. JAERI has developed an equipment to measure the thermal diffusivity of high burnup pellet [5,6]. This paper summarizes the measurement results of thermal diffusivity on high burnup fuel irradiated at HBWR up to 63 MWd/kgU.

2. EXPERIMENT

2.1 Samples

The UO_2 disk samples were prepared from a fuel pin (rod 201) irradiated at HBWR up to 63 MWd/kgU. The pre-irradiation characterization of the rod is shown in Table I. The initial density of the pellet was 94.5%TD. The fuel rod was sliced with diamond wheel slicing machine to obtain disk shaped specimens about 1mm. thickness. There were many cracks in the pellet and it was difficult to get a large size sample. The shape of the disk specimens was irregular and four specimens of about 3x3 mm size were obtained. These specimens were washed in acetone to remove the oil used for cooling during cutting. Visual inspection was carried out to check free of cracks. The weight and thickness of the specimen were measured by balance and dial gauge.

2.2 Measurements and analysis method

The thermal diffusivity of irradiated UO_2 was measured over the temperature range from 290 to 1794 K by the laser flash method. The specimen was installed in the apparatus developed by JAERI [5,6]. Figure 1 shows the block diagram of the apparatus. The apparatus is composed of specimen holder, heating furnace, laser oscillator, vacuum pumps, infra-red detector for sample temperature measurement, radiation shielding, transfer cask and data acquisition systems. The specimen is prepared and set in the specimen holder in a lead cell and transferred to the apparatus in the transfer cask. The sample holder is automatically set into the heating furnace with remote control systems. Ruby laser (6J/pulse) is used as heat source. The rear surface temperature of the sample is measured by In-Sb infra-red detector.

The thermal diffusivity was determined by "logarithmic method" [7] instead of the conventional "half time method". The logarithmic method has an advantage to reduce the experimental error even under non-ideal boundary conditions compared with the half time method [7].

TABLE I. PRE-IRRADIATION CHARACTERIZATION OF FUEL ROD 201

Fuel pellet		Cladding	
composition	UO_2	material	Zry-2
enrichment	7.0 %	outer diameter	14.29 mm
density	94.5 %TD	inner diameter	12.67 mm
diameter	12.35 mm		
length	15.0 mm	Fuel rod	
dish depth	0.6 mm	gap	0.35 mm
shoulder width	1.0 mm	filler gas	He
sintering temp.	1600 ℃	fill pressure	0.1 MPa
sintering time	5 h	free volume	20.2 cc
grain size	25 μm	stack length	226 mm

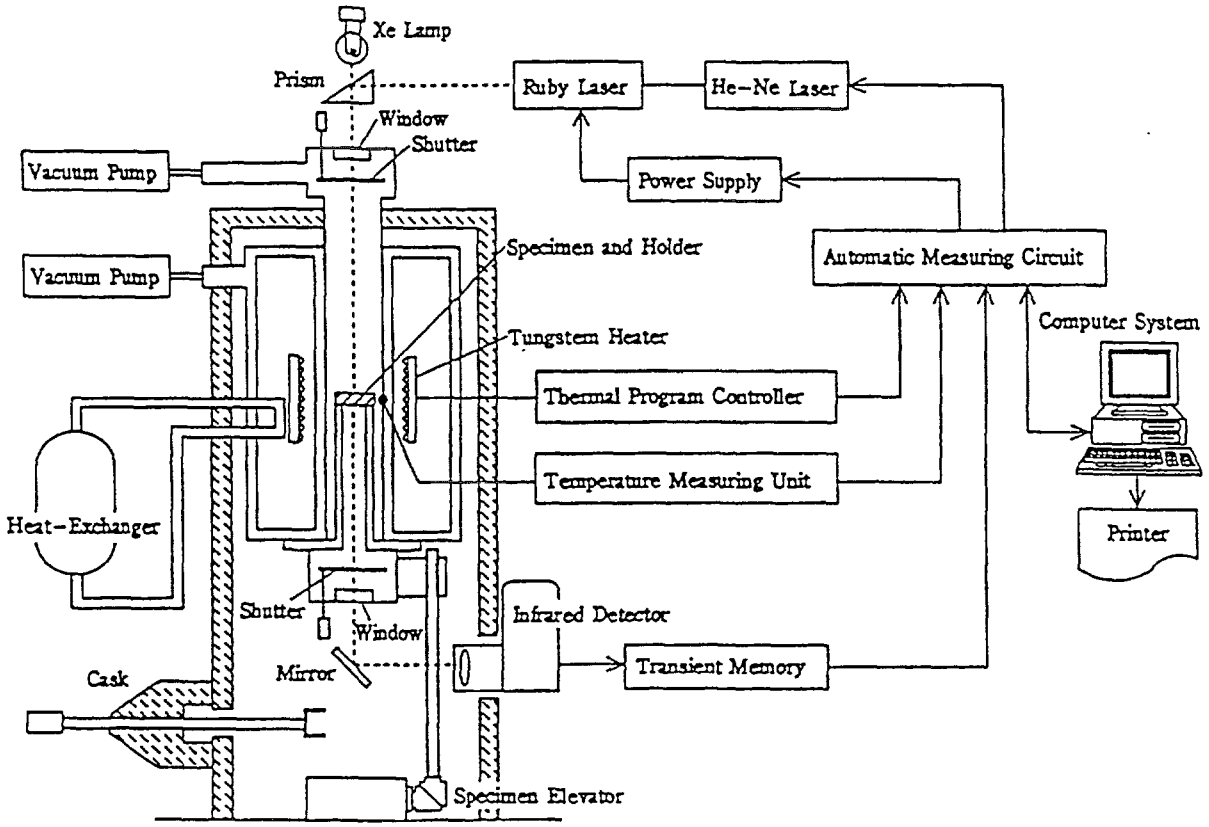

FIG. 1. Block diagram of the pellet thermal diffusivity measurement apparatus.

3. EXPERIMENTAL RESULTS

Thermal diffusivity of four samples was measured. The weight, thickness and the measured temperature range of each sample are shown in Table II. The thickness and weight of the samples are about 1mm. and about 100mg respectively. The measured temperature range of the samples is from room temperature up to max. 1794K.

As an example of the experimental results, the measured thermal diffusivity of sample No.3 is depicted in Fig.2 together with the data of SIMFUEL [I], which simulates high burnup UO_2 chemically by adding soluble FPs. Four runs were repeated as increasing the maximum temperature of measurement. The thermal diffusivity of high burnup UO_2 is lower than the half of that of unirradiated UO_2 at room temperature and the difference of them decreased as temperature increased. The thermal diffusivity increased gradually as the experienced maximum temperature increased from about 870K up to about 1300K. The data measured in

TABLE II. SAMPLE SIZE AND MEASURED TEMPERATURE RANGE

Sample No.	Thickness(mm)	Weight(mg)	Measured temperature range(K)
No.1	1.119	113.4	292-1288
No.2	0.955	100.9	291-1496
No.3	0.925	103.5	290-1794
No.4	0.947	83.1	290-1590

the fourth run at room temperature is only a little larger than that in the third run at room temperature. These data suggest that the recovery of thermal diffusivity between 1300 K and 1793K is relatively small. The temperature dependency of thermal diffusivity of the third run of sample No.3 after having experienced about 1300K is very similar to that of 8 at% SIMFUEL.

The thermal diffusivity of sample No.2 is shown in Fig.3. The tendency of recovery of thermal diffusivity is very similar to that of sample No.3. However, the absolute value of thermal diffusivity is much smaller than that of sample No.3, and it is about three-fourths of that of the sample No.3 at room temperature.

The thermal diffusivity data of four measured samples were classified into two group, although all four samples showed quite similar tendency of the recovery of the thermal diffusivity between 700K and 1300K. Fig.4 shows the thermal diffusivity data of 4 different samples after heating up to about 1300K, which correspond to the data after the recovery. The data of sample No.1 are a little bit higher than that sample No.3. On the other hand, the data of sample No.4 are almost same as that of sample No.2. These samples were obtained from 10 cm-long segment in the same rod, therefore the difference of the thermal diffusivity may be attributed to the radial structure difference in each sample because of small power history change in axial direction.

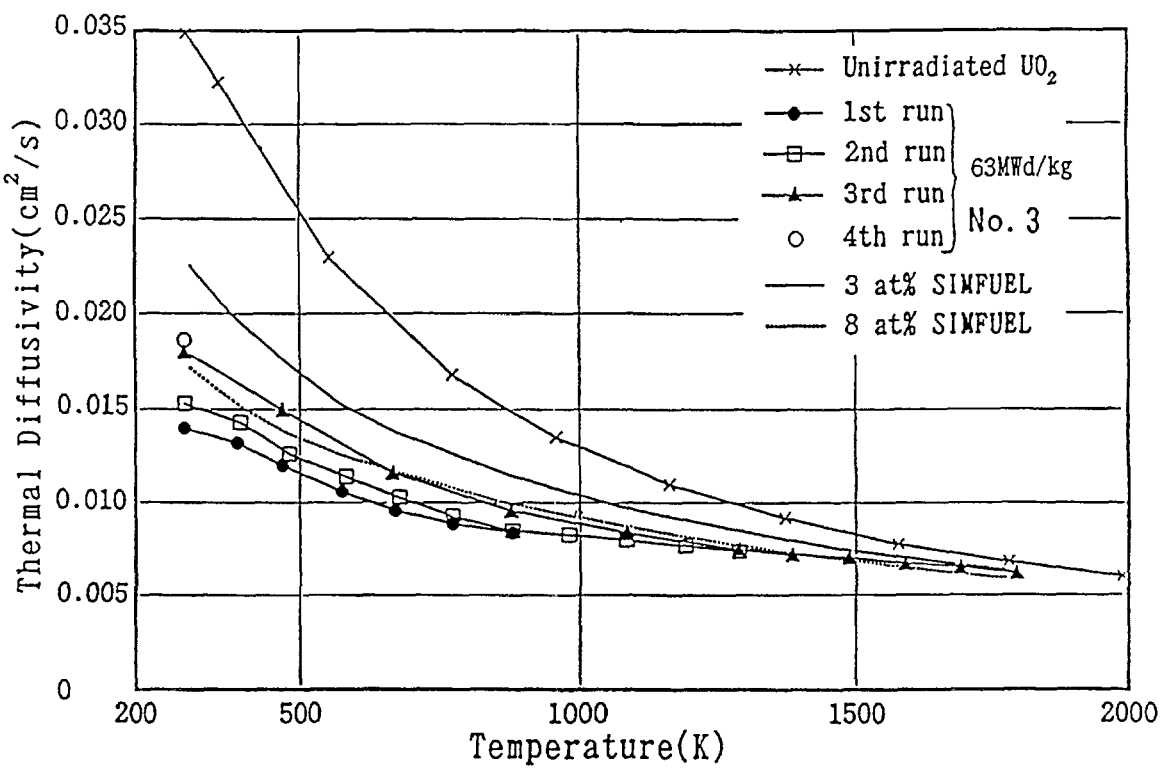

FIG. 2. Thermal diffusivity of sample No. 3 (63MWd/kgU).

4. DISCUSSIONS

4.1 Recovery of the thermal diffusivity of irradiated UO_2

Many factors affect thermal diffusivity and conductivity, for example, soluble FP, precipitated metallic FP, FP gas bubble, O/U ratio, density/porosity and radiation damage.

In these factors, only precipitated metallic FP increase the thermal diffusivity and other factors decrease it.

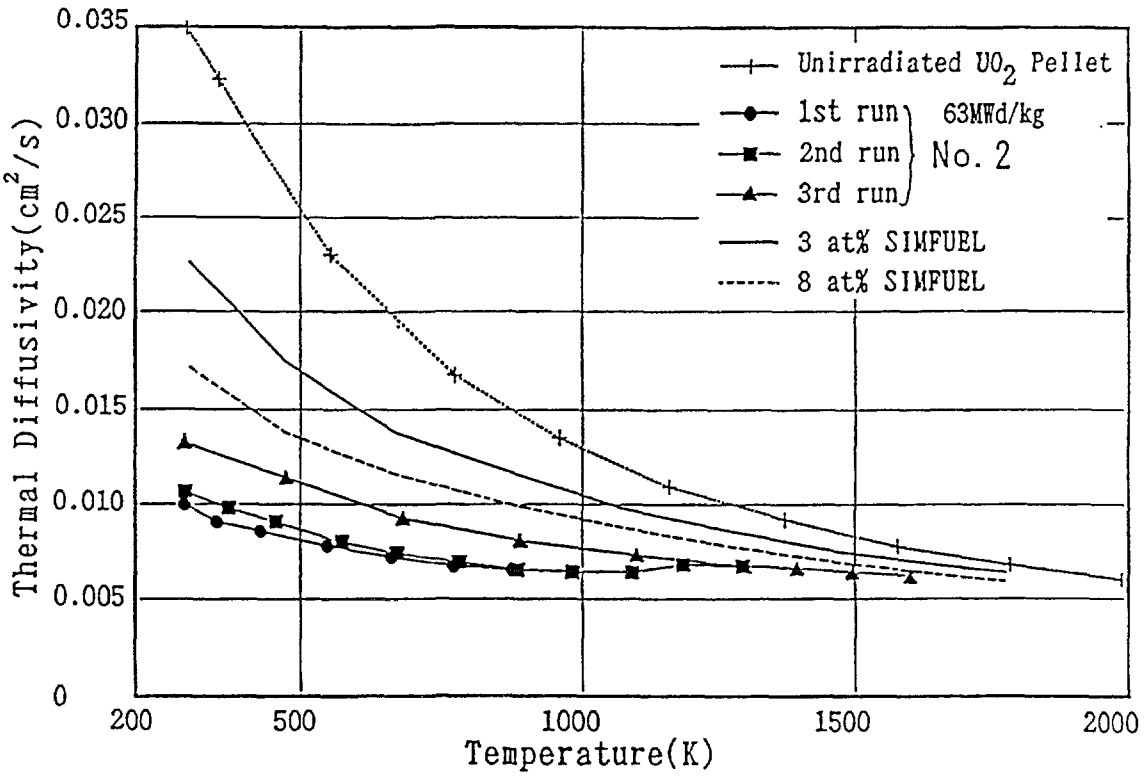

FIG. 3. Thermal diffusivity of sample No. 2 (63MWd/kgU).

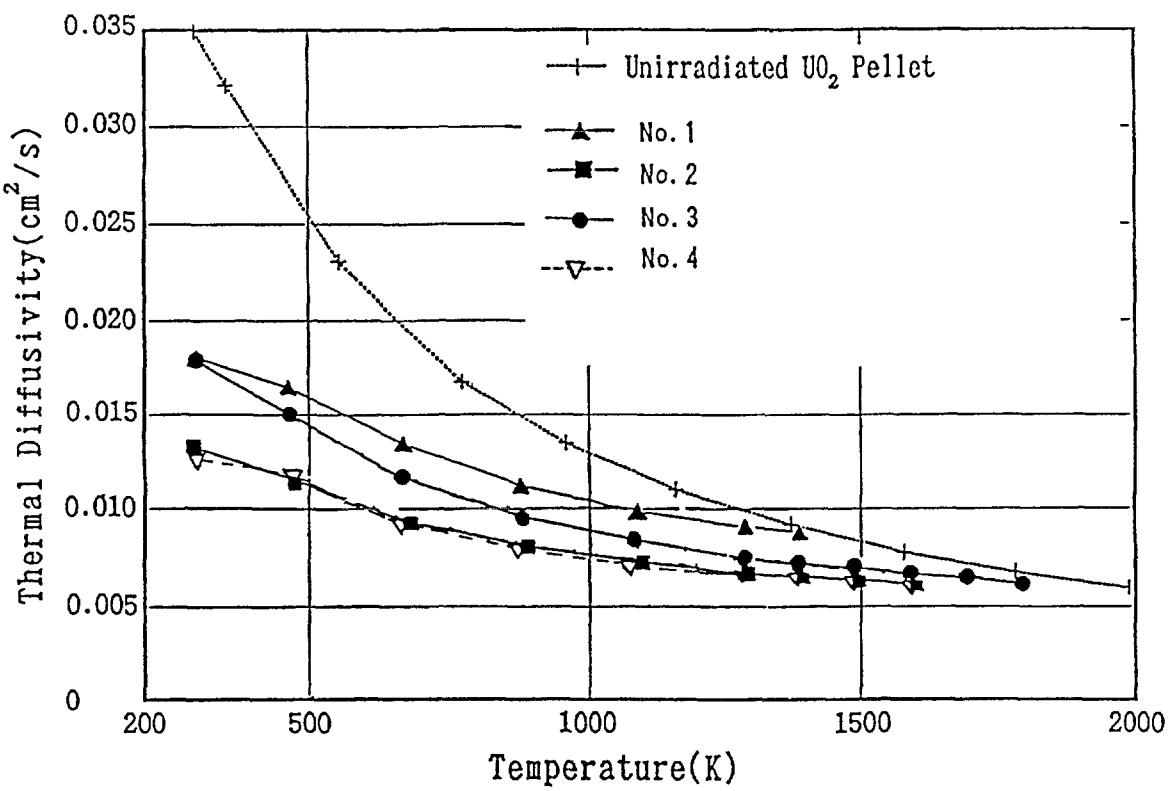

FIG. 4. Thermal diffusivity of different samples after heating up to 1276K.

The O/U ratio has strong effects on thermal diffusivity. However, the O/U ratio of UO_2 irradiated under LWR condition is reported to remain close to stoichiometry even at relatively high burnup [8,9]. This suggests that the effect of O/U ratio can be small in the present measurement.

The present results showed the increase of the thermal diffusivity when the measurement was repeated, especially in the temperature range between 700K and 1300K. The possible reasons for such a recovery of thermal diffusivity are recovery of irradiation damage (point defects or defect cluster) and/or the change of FP gas bubbles in the matrix or on the grain boundary.

Nogita et al. [10] measured the recovery of irradiated UO_2 by means of X-ray diffraction and TEM observation. They observed the recovery of lattice parameter at 723-1123 K, recovery of broadening of X-ray reflection peak above 1423 K and the coalescence of small bubble above 1873K. They estimated the possible point defect recovery for the lattice parameter at this stage is U-vacancy and the recovery of the defect cluster is responsible for that of broadening of X-ray reflection peak.

Matzke and Turos [11) have observed the recovery of the UO_2 implanted with Xe ion between 600 and 1900K depending on the doses of Xe ions, and they attributed the recovery to U-vacancy and the defect cluster.

The increase of thermal diffusivity in the present test was observed between 700K and 1300K, which almost corresponds to the temperature range of the recovery of lattice parameter reported by Nogita et al.[10]. This suggests that the increase of the thermal diffusivity between 700 K and 1300 K is caused by the recovery of radiation damages (perhaps, uranium vacancy and may include the effects of defect cluster and the change of fission gas bubble). Based on Nogita et al.'s observation, it is suggested the recovery of defect cluster and the coalescence of small gas bubbles occurs at high temperature than that of U-vacancy. However, differences of the irradiation history of the samples used in the present study and Nogita et al.'s study make it difficult to compare the recovery behavior directly.

4.2 Effect of microstructure and density

The thermal diffusivity data of four samples were separated into two groups. No.3 and No.1 samples showed relatively high thermal diffusivity, and No.2 and No.4 samples showed low thermal diffusivity.

To clarify the cause of scatter of thermal diffusivity among the samples, micro structure of the samples was examined. Fig.5 shows the microstructure of sample No.3 which showed higher thermal diffusivity. Extensive columnar grain growth and some metallic FP were observed in this sample. On the other hand, neither columnar grain growth nor metallic FP was observed in sample No.2. The cross section of the rod 201, from which samples are derived, is shown in Fig.6. Extensive columnar grain growth is observed in the area $r/r_o \leq 0.6$. The power history of the rod 201 is depicted in Fig.7. The rod power was very high about 510W/cm at the beginning of the irradiation, and it decreased almost linearly with burnup. The rod power at the end of the irradiation was below 170W/cm. From this power history, the columnar grain growth in rod 201 was estimated to have occurred during the high power

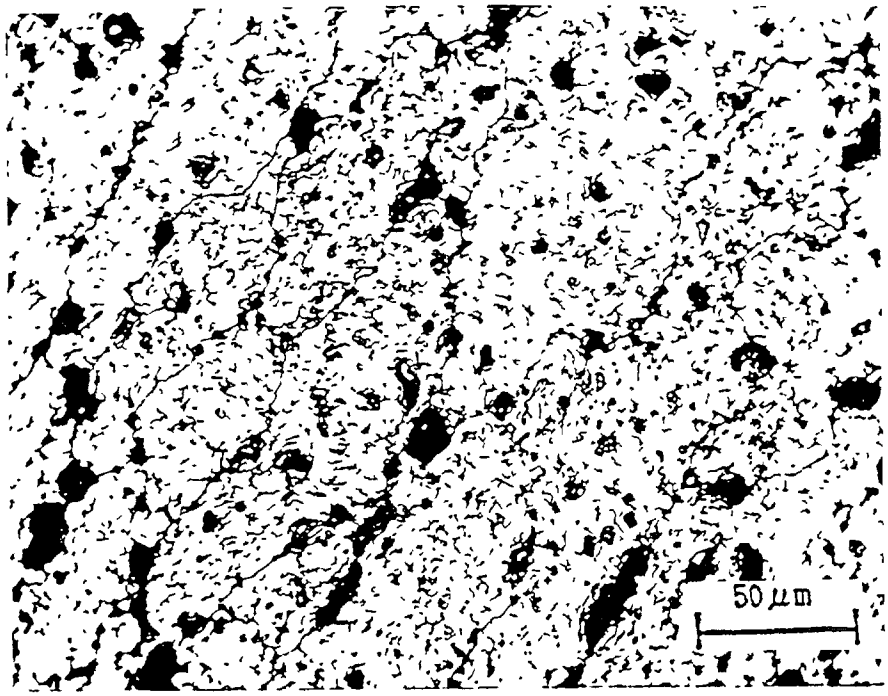

FIG. 5. Micro structure of sample No. 3 (after measurement).

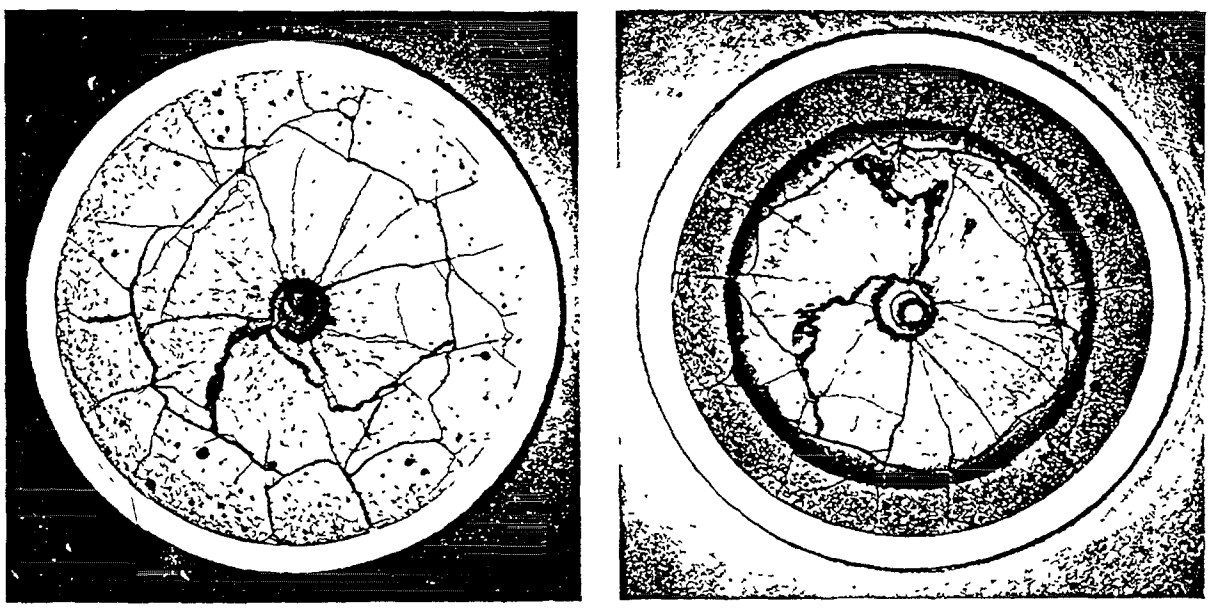

(a)Before etching (b)After etching

FIG. 6. Cross section of Rod 201.

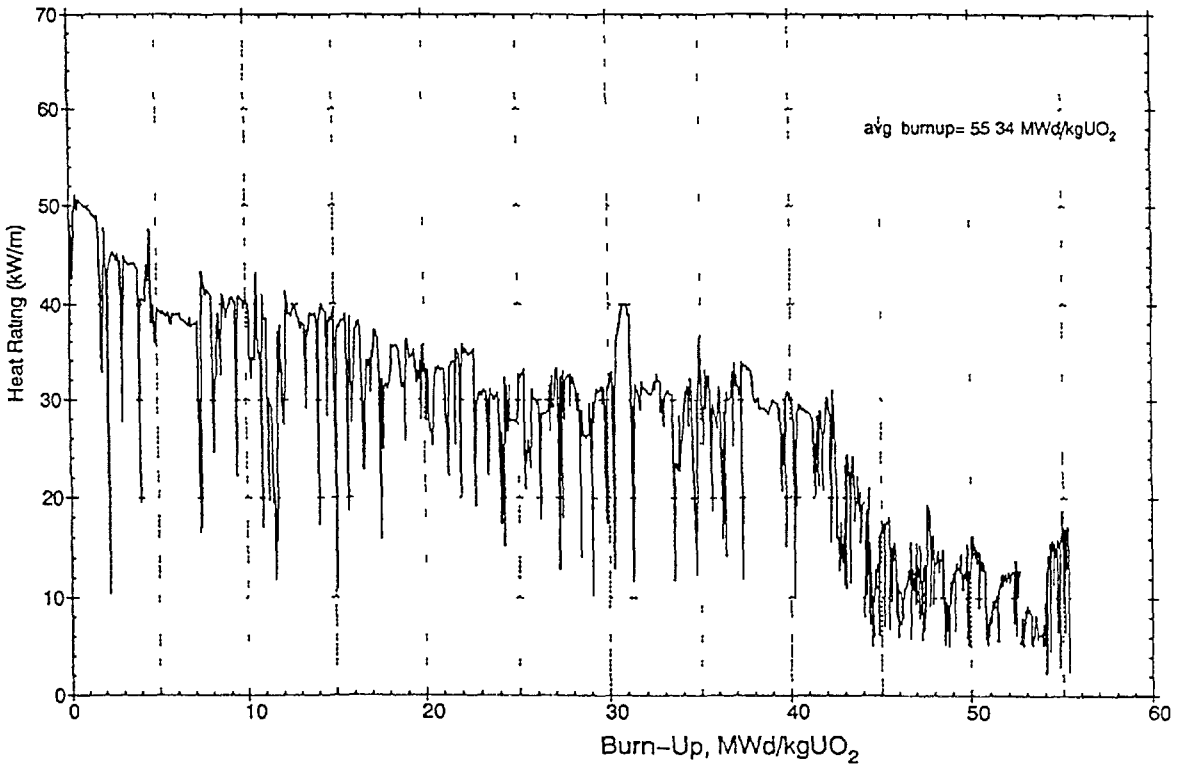

FIG. 7. Power history of Rod 201.

operation period at the beginning of the irradiation. After the columnar grain growth, the density of the columnar gain region is estimated to increase to nearly 100%TD, because the pore in the columnar grain region migrated to center and formed the center hole.

From these data, it is estimated that the pellet of rod 201 is consisted of two regions with different density, i.e. columnar grain region and non-columnar grain region. The initial density of rod 201 was 94.5%TD and the final density measured by PIE was 91.4%TD. These data indicate swelling has occurred during irradiation after the columnar grain growth.

To estimate the local density, porosity measurement and density measurement of small size sample were performed. The scatter of the density and porosity were relatively large, but it is observed that the density at the columnar grain region is generally higher than that of the non-columnar grain region. Based on these observations and the density of 91.4%TD for a whole pellet determined by PIE, the density of the columnar and non-columnar regions are estimated to be 92-96%TD and 83-89%TD, respectively.

To see the effect of the density on thermal diffusivity, the thermal diffusivity corrected to 95%TD of the samples No.2 and No.3 was estimated by the following procedures.

The relation between the thermal diffusivity and thermal conductivity is as follows:

$$k_m = \alpha_m \, Cp \, \rho_m \quad (1)$$

$$= \alpha_m Cp \, \rho_{th} \, (1\text{-}P) \quad (2)$$

k_m : thermal conductivity of sample,
α_m : thermal diffusivity of sample,
Cp: specific heat capacity,
ρ_m : density of sample with porosity of P,
ρ_{th} : theoretical density,
P : porosity.

On the other hand, the relation of the thermal conductivity and porosity is as follows:

$$k_m = k_{th} (1 - \eta P) \tag{3}$$

k_{th} : thermal conductivity of sample with theoretical density,
η : an experimental parameter, [MATPRO: $\eta = 2.6\text{-}5\text{x}10^{-4}(T\text{-}273.15)$]

The thermal conductivity normalized to 95%TD, k_{95} is given by,

$$k_{95} = k_m(1\text{-}0.05\eta)/(1\text{-}\eta P) \tag{4}$$

From equations,(1),(2),(3) and (4), the thermal diffusivity normalized to 95%TD, α_{95} is given by,

$$\alpha_{95} = \alpha_m [(1\text{-}0.05\ \eta)(1\text{-}P)]/[(1\text{-}\ \eta P)(1\text{-}0.05)] \tag{5}$$

The thermal diffusivity normalized to 95%TD of samples No.3 and No.2 is depicted in Fig. 8 on the assumption that the densities of samples No.3 and No.2 are 94%TD and 86%TD, which are the average values of the estimated densities at columnar grain region and at non-columnar grain region, respectively.

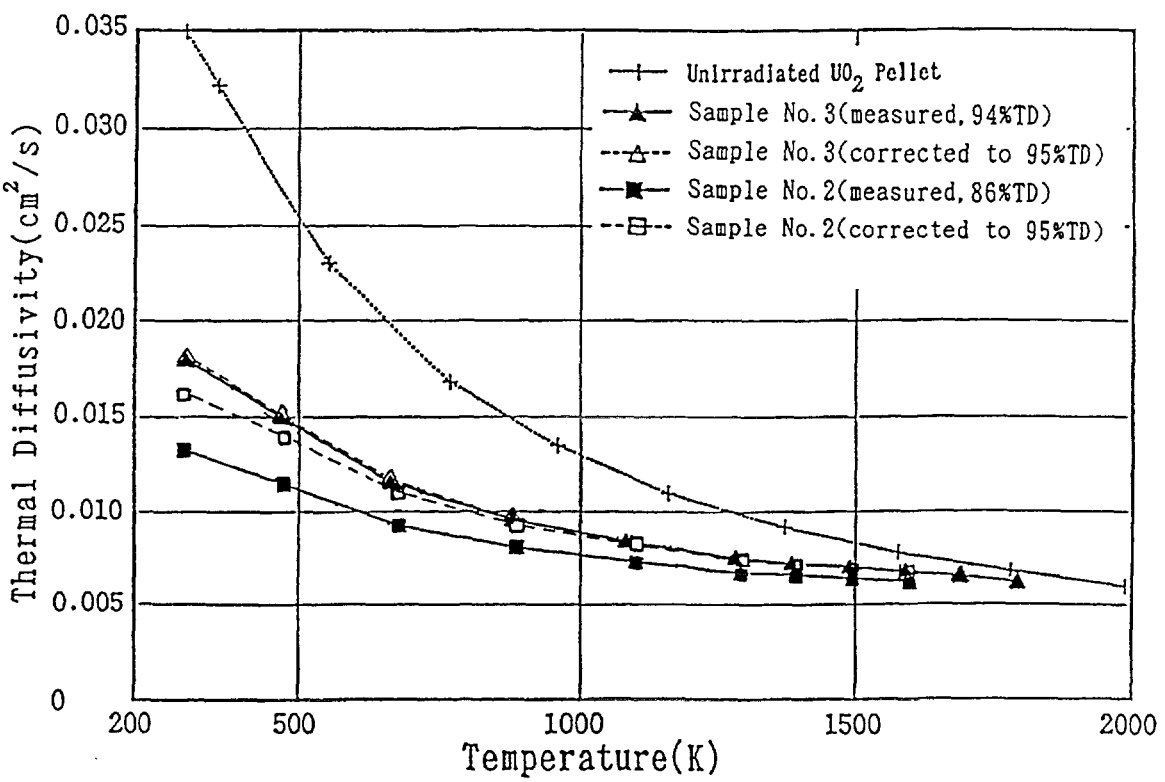

FIG. 8. Thermal diffusivity of samples Nos. 3 & 4 corrected to 95%TD.

The thermal diffusivity of the two samples normalized to 95%TD agreed well each other, and the differences between the samples can be explained mainly by the difference in the sample density.

4.3 Thermal conductivity of irradiated UO_2

The thermal conductivity is derived from thermal diffusivity, density and heat capacity using equation (1). The heat capacity of the irradiated UO_2 is not clarified yet, and the effects of soluble FPs or single-component additives were investigated by several authors [12,13.14]. However, the measured results show different tendencies at high temperature region. Recently, Verrall and Lucuta [14] reported the heat capacity measurement of SIMFUEL. Their results did not show any anomalous increase relative to UO_2 . Therefore, we adopted the heat capacity value of unirradiated UO_2 evaluated by Kellisk and Clifton [15] for the calculation of thermal conductivity of irradiated UO_2. Figure 9 shows the thermal conductivity of sample No.3 calculated from thermal diffusivity data using the estimated density (94%TD) and heat capacity of unirradiated UO_2. The general tendency of the temperature dependence of thermal conductivity is similar to that of thermal diffusivity. The thermal diffusivity data show small peak around 400K. This peak is caused by the large increase of heat capacity in this temperature region.

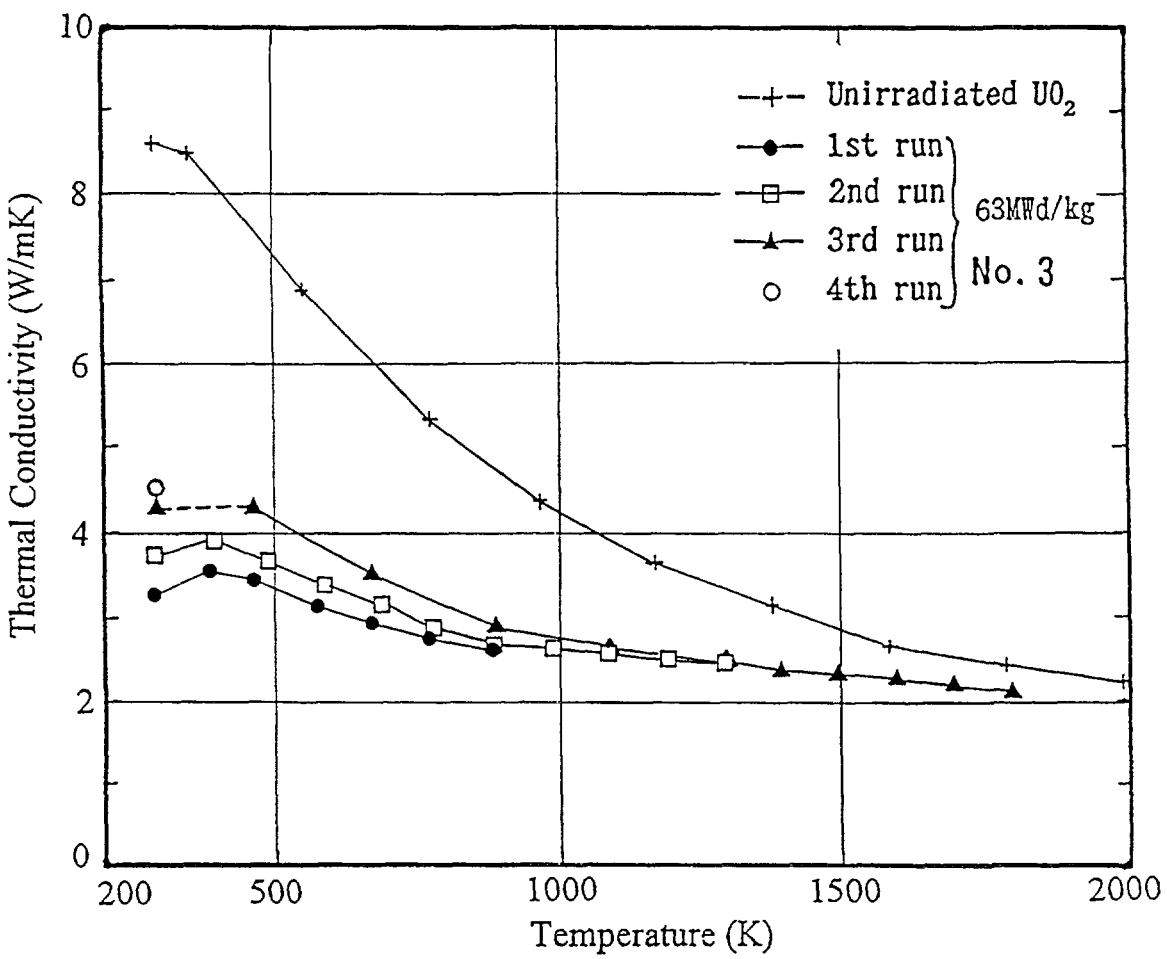

FIG. 9. Thermal conductivity of sample No. 3 calculated from thermal diffusivity data using the heat capacity of unirradiated UO_2 in literature.

To evaluate precisely the thermal conductivity of irradiated UO_2, the heat capacity data of irradiated UO_2 is necessary.

5. CONCLUSION

- The thermal diffusivity of high burnup UO_2 was lower than the half of that of unirradiated UO_2 at room temperature and the difference between them decreased as the measurement temperature increased .
- The thermal diffusivity increased gradually with temperature increase between 700K and 1300K. These increases were estimated to be mainly caused by the recovery of radiation damage. The thermal diffusivity data of four samples were separated into two groups. The difference of thermal diffusivity of these groups was mostly explained by the effect of density difference.
- It was estimated that the reduction of thermal diffusivity of irradiated UO_2 in this study was caused mainly by soluble FP, density reduction, radiation damage (point defect and defect cluster) and may be also affected by FP gas bubbles .

ACKNOWLEDGEMENTS

The authors would like to thank Mr. I. Owada and Mr. S. Miyata for their experimental work, and also the Halden Project for offering the high burnup fuel.

REFERENCES

[1] LUCUTA P.G. et al. J.Nucl.Mater.188(1992)198.
[2] ISHIMOTO S. et al., J.Nucl. Sci. Technol.,31(1994)796
[3] IAEA Tech.Rep.Ser.No.59, (1966) "Thermal Conductivity of Uranium Dioxide"
[4] KOLSTAD E. and VITANZA C. J.Nucl.Mater.188(1992)104.
[5] OWADA I. et al. JAERI-M 93-244(1994)
[6] YAMAHARA T. et al.,IAEA Technical Committee Meeting on Recent Development on PIE Techniques for Water Reactor Fuel, Cadarache, France,1994
[7] TAKAHASHI Y. et al., Netsu Sokutei, 15(1988)103.
[8] UNE K. et al. J.Nucl.Sci.Technol.,28(1991)409.
[9] MATZKE,Hj. J.Nucl.Mater.208(1994)18.
[10] NOGITA K. and UNE J.Nucl.Sci.Technol.,30(1993)900.
[11] MATZKE Hj. and TUROS A. J.Nucl.Mater.,188(1992)285.
[12] MATSUI T. et al. J.Nucl.Mater.,188(1992)205.
[13] TAKAHASHI Y. and ASOU M. J.Nucl.Mater.,201(1993)108.
[14] VERRALL R.A. and LUCUTA P.G. J.Nucl.Mater.,228(1996)251.
[151 KENISK J.F. and CLIFTON D.G.,Nucl.Technol.,16(1972)531.

DISCUSSION

(Questions are given in italics)

Is the laser flash method applicable for measuring diffusivity of rim region in a pellet with Zircaloy cladding?

To prepare the sample is difficult, even though the principle to apply the laser flash method to two-layer component materials exists. High burnup Rim project proposed by Dr. Kinoshita uses disk type pellet, and the result of this test may give the thermal conductivity of rim structure.

Comment:

High Burnup Rim Project (HBRP) uses 1 mm thick discs irradiated to high burnup. It contains rim structured specimen. However, it is a simulation of LWR fuel rim.

To answer how to measure the thermal diffusivity of the rim in LWR fuel specimen preparation is the question. The cladding could be mechanically thinned and trial could be done to etch out chemically.

How is the alpha damage in your specimen?

We used Heavy Water Reactor irradiated fuel, so that the Pu/TRU content and the alpha damage is very small.

The density correction formula is derived from typical porosity shapes and distribution in the flesh fuel. The porosity increase due to irradiation has different shapes and distribution. Uncertainty resulting from applying the formula to irradiated fuel?

I think the correlation can be applicable to irradiated UO_2 as far as the density of the irradiated UO_2 is not so low.

On fission gas threshold mobility, 1500 C is a very high value. We are more used to 1000 C as the temperature for the first fission gas coalescence.

With regard to the temperature, I referred to Nogita and Une's data obtained from TEM observation. Concerning small size bubbles, it may be possible to coalescence at lower temperatures.

THERMAL DIFFUSIVITY MEASUREMENTS OF IRRADIATED UO_2 PELLETS

M HIRAI, M. AMAYA, Y. WAKASHIMA
Nippon Nuclear Fuel Development Co., Ltd,
Ibaraki

T. NOMATA
Toshiba Corporation,

H. HAYASHI, M. KITAMURA
Nuclear Power Engineering Corporation,
Tokyo

Japan

Abstract

Thermal diffusivity was measured with a laser flash method up to 2000 K for UO_2 pellets irradiated in a commercial reactor. Measurements were done on micro samples of disks (2 mm diameter) or regular prisms (1.5 or 2 mm square cross sections). Thermal diffusivity degraded on extending burnup in agreement with reported values for UO_2 irradiated in test reactors, and it showed hysteresis during the laser flash experiments. Thermal diffusivity began to recover above 750 K and almost completely recovered above 1400 K, which corresponded with the reported radiation damage recovery. The obtained data were in agreement with predictions applying the thermal conductivity expression for irradiated UO_2 proposed by Amaya and Hirai. The sample experiencing power ramp showed higher thermal diffusivity than that of the base irradiated sample and had no obvious hysteresis. This suggested that the radiation damage which degraded thermal conductivity accumulated mainly during irradiation and not after it.

1. INTRODUCTION

Thermal conductivity of the UO_2 pellets has been the key factor to evaluating fuel behavior during irradiation in light water reactors (LWRs). By extending fuel burnup, many lattice defects such as fission products (FPs) and radiation damage are accumulated in UO_2 fuel pellets [1-3]. It is well known that thermal conductivity of UO_2 decreases with increasing amounts of point defects such as soluble impurities and also with accumulation of defect dusters. The thermal conductivity of fuel pellets, therefore, is expected to degrade with burnup due to the accumulation of FPs and radiation damage. Thermal conductivity has been measured by the laser flash method for $(U,Gd)O_2$ [4-6] and SIMFUELs [7,8], and was shown to decrease with increasing impurity contents. Many investigators [9-19] have studied the thermal conductivity change by irradiation and reported results supporting the above expectation at lower temperatures. Vitanza [20] indicated from in-reactor measurements of the fuel center temperature at the Halden reactor that the fuel thermal conductivity was degraded during irradiation. Some workers [9,10,14,19] have reported thermal conductivity recovery by excursion at higher temperatures and it was considered that this thermal conductivity recovery was due to radiation damage recovery. Nogita and Une [3] reported that the lattice dilation mainly due to fission induced point defects was completely recovered by annealing at about 1150 K and the heterogeneous lattice strain due to defect clusters of dislocations and small intra-granular bubbles began to recover around 1450 to 1900 K.

In this study, the thermal diffusivity was measured for irradiated UO_2 pellets by the laser flash method up to 2000K in order to evaluate the effect of burnup on UO_2 thermal conductivity. Since the UO_2 pellets irradiated in a commercial reactor generally have many radial cracks (and sometimes circumferential cracks) and high radio activity, using micro samples has advantages of limiting the crack effects on the thermal diffusivity and of easier sample handling. Therefore, the experimental method for thermal diffusivity measurements was developed for small samples.

2. EXPERIMENTAL

2.1 Apparatus

The apparatus (HT-7000S; produced by Shinku-riko Co., Ltd.) used in this work employs the laser flash method. It is shielded by iron and lead and modified to allow operation by a remote control system. A schematic diagram of the apparatus is shown in Fig. 1 and that of a sample assembly is shown in Fig. 2. In a hot cell, a small specimen is mounted into the sample cell. The sample cell is put on a handling table within the radiation shield area and then loaded onto the sample stand by the remote sample loading system. The loading procedure which is done within the shield area is monitored with four TV cameras. The sample is isolated by a Ta tube from the heaters to prevent contamination of the high temperature assembly. Inside and outside of Ta tube and the high temperature assembly are kept in a vacuum of less than 2×10^{-4} Pa during experiments by their respective turbo molecular and oil rotary pumps. The heat source is a ruby laser, the maximum energy of which is above 6 J. The laser power level used in this work was considered to be about 2.5 to 3.8 $J \cdot cm^{-2}$. The specimen is heated by heat radiation from the tungsten mesh heater. The sample temperature is monitored by a W-5%Re/W-26%Re thermocouple located near the sample

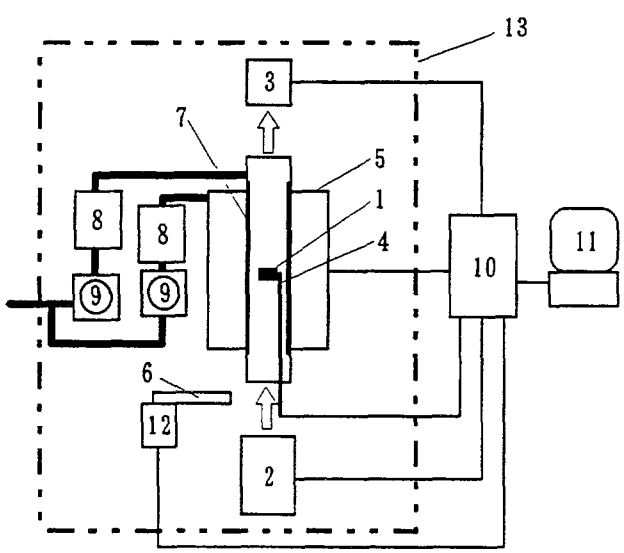

FIG. 1. Schematic diagram of thermal diffusivity measurement system for irradiated samples.

1: Specimen 2: Laser oscillator 3: Infrared detector 4: Thermocouple
5: High temperature assembly 6: Handling table 7: Isolation tube
8: Turbo molecular pump 9: Oil rotary pump 10: Control system
11: Personal computer 12: Sample loading system 13: Radiation shield

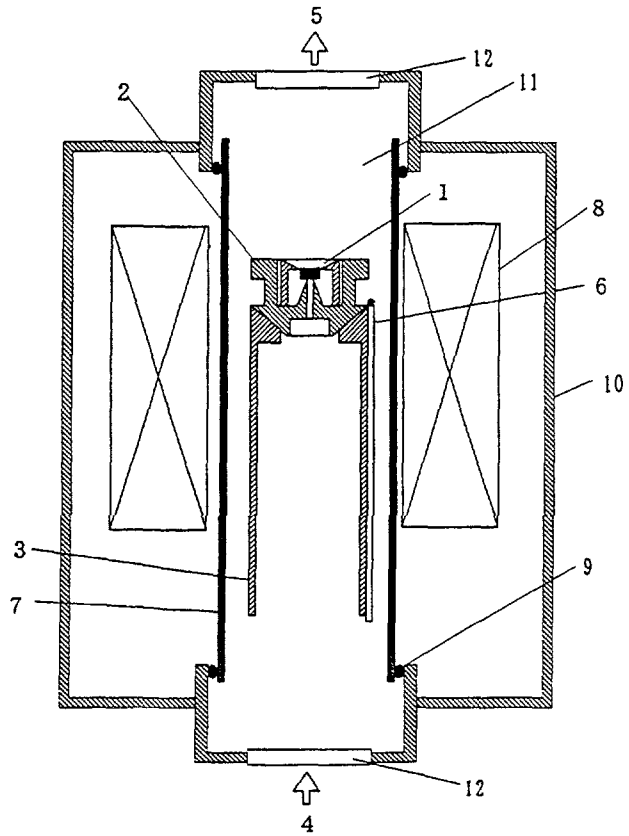

FIG. 2. Schematic diagram of sample assembly.

1: Specimen 2: Sample cell 3: Sample stand
4: Laser oscillator 5: Infra-red detector
6: Thermocouple 7: Isolation tube 8: Heater
9: O-ring 10: High temperature assembly
11: Sample assembly area 12: Windows

holder as shown in Fig. 2. Since the thermocouple is located outside of the Ta sample stand, the indicated values deviated from sample temperatures. Therefore, prior to thermal diffusivity measurements, another thermocouple of Pt/Pt-Rh was inserted at the sample position to obtain a calibration curve for the temperature deviation. The temperature response on the rear surface after the laser flash of about 500 μs was measured by an In-Sb infra-red detector and was recorded digitally by the personal computer. Data sampling was made at a desired rate between 50 and 250 μs for analyzing thermal diffusivity and at 5 ms for estimating heat loss.

2.2 Samples

2.2.1 System characterization

UO_2 powder was pressed into green pellets, which were sintered at about 2000 K in a stream of 100% H_2. The sintered pellets were about 10 mm in diameter, and they were then sliced into thin disks of 0.7 to 1.2 mm in thickness. From the disks, small disk shape (or cylindrical) specimens of 2 to 10 mm in diameter (U1 to U6) were obtained with an ultrasonic cutter. These were used for the system characterization test. Also small regular prismatic specimens of 1.5 and 2.0 mm square cross sections (U7 and U8) were obtained with a diamond cutter. The characteristics of the specimens are summarized in Table I .

2.2.2 Irradiated materials

The fuel pellets irradiated in a commercial reactor for 2 to 5 reactor cycles were sliced into disks of about 1 mm in thickness. From the disks, disk shape or regular prismatic specimens were micro sampled in the same way as unirradiated materials. Their characteristics are summarized in Table II. Specimens I-1 and I-2 were sampled from the top region of a fuel rod and their burnups were about 8.5 GWd/tU. Their irradiated temperature was evaluated as about 750 K. Specimens I3 and I4 were sampled near the highest power position, and their burnups were 39.3 and 44.7 GWd/tU, respectively. Their irradiation temperatures was evaluated as about 1100 K. Specimen R-1 was sampled from power ramped fuel after a base irradiation of 43.1 GWd/tU. The power ramp level was 512 W/cm and duration of this power level was 4 hours. The irradiation temperature during the power ramp test was about 1300 K. For samples I-2, I-4 and R-1, thickness after the thermal diffusivity measurements was measured and porosity change was estimated. The theoretical density of the fuel pellet at each burnup $\rho_{th,E}$ was estimated by considering the mean mass reduction in the matrix.

TABLE I. CHARACTERISTICS OF UNIRRADIATED UO_2 SAMPLES

Sample	Shape	Dimensions (mm)	Density (g/cm^3)	Porosity (%)
U1	disk	$1.048^t \times 2.0^\phi$	10.74_4	1.97
U2	disk	$1.040^t \times 3.0^\phi$	10.74_4	1.97
U3	disk	$1.040^t \times 5.0^\phi$	10.74_4	1.97
U4	disk	$1.040^t \times 9.9^\phi$	10.74_4	1.97
U5	disk	$0.694^t \times 2.9^\phi$	10.74_4	1.97
U6	disk	$1.248^t \times 3.0^\phi$	10.74_4	1.97
U7	regular prism	$0.997^t \times 1.5^w \times 1.5^d$	10.65_1	2.82
U8	regular prism	$1.016^t \times 2.0^w \times 2.0^d$	10.65_1	2.82

TABLE II. CHARACTERISTICS OF IRRADIATED UO_2 SAMPLES

Sample	Burnup (GWd/tU)	Sample characteristics before experiment			Sample characteristics after experiment			Theoretical
		Thickness (mm)	Density (g/cm^3)	Porosity (%)	Thickness (mm)	Density*4 (g/cm^3)	Porosity*4 (%)	Density (g/cm^3)
I-1	8.5	1.099*1	10.45	4.39	-	-	-	10.93
I-2	8.5	1.070*1	10.45	4.39	1.084	10.05	8.05	10.93
I-3	39.3	1.009*2	10.41	3.60	-	-	-	10.80
I-4	44.7	1.175*1	10.28	3.11	1.197	9.72	9.88	10.79
R-1*5	43.1	1.194*3	10.27	4.73	1.225	9.51	11.78	10.78

*1: Disk shape specimen of 2 mm diameter
*2: Regular prismatic specimen of 2 mm square
*3: Regular prismatic specimen of 1.5 mm square
*4: Value estimated from the thickness change during experiment
*5: Power ramp to 512 W/cm for 4 hours

2.3. Measurement and Analytical Methods

Prior to all measurements, the sample was heated to the required temperature by the tungsten mesh heater to reach a state of equilibrium with the ambient temperature. The thermal diffusivity measurements were made as mentioned elsewhere [5]. They were mainly carried out four times at every temperature step, three times for the thermal diffusivity analysis and once for the heat loss estimation. The thermal response data on the rear surface after laser flashing were reduced to thermal diffusivity by the logarithmic method [21-23] and/or by the half time method.

Thermal conductivity was calculated by using the obtained thermal diffusivity, measured density and reported specific heat capacity. Here, molar specific heat capacity of unirradiated UO_2 was used for the value of irradiated materials, since the specific heat capacity change of UO_2 due to FP solution was quite small [24] and was estimated to be about 2 % at 100 GWd/tU, excluding the excess heat capacity [25].

3. RESULTS AND DISCUSSIONS

3.1 Characterization Test

Thermal diffusivities were measured for unirradiated UO_2 specimens with various dimensions and they are shown in Fig. 3. The obtained thermal diffusivities were independent of sample size and shape, and agreed well with the reported values [5, 6] above 400 K. The experimental error was estimated for a micro specimen to be within ± 6 % in the temperature range from 400 to 2000 K.

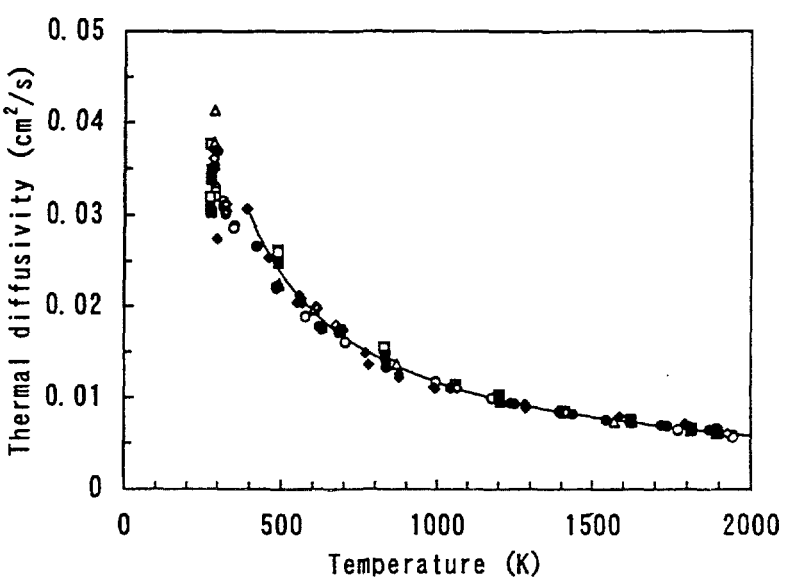

FIG. 3. Measured thermal diffusivity for unirradiated UO_2 with various dimensions.

○: U1 (2mm dia. - 1mm thick), □: U2 (3mm dia. - 1mm thick), △: U3 (5mm dia. - 1mm thick), ◇: U4 (10mm dia. - 1mm thick), ■: U5 (3mm dia. - 0.7mm thick), ▲: U6 (3mm dia. - 1.2mm thick), ◆: U7(1.5mm square - 1mm thick), ●: U8 (2mm square. - 1mm thick), ——— : Previous work [5,6]

3.2 Thermal Diffusivity of Irradiated UO_2

The results are shown in Fig. 4 for UO_2 samples irradiated up to 39.3 GWd/tU (I-3). Solid line represents reported values for unirradiated UO_2 [5, 6] and broken line is calculated

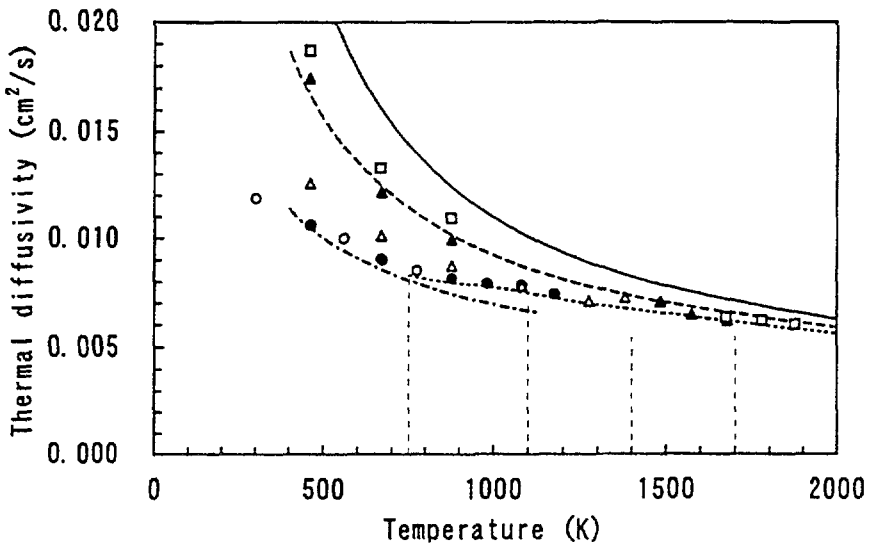

FIG. 4. Thermal diffusivity for UO_2 irradiated up to 39.3 GWd/tU.

○: 1st Run, ●: 2nd Run, △: 3rd Run, ▲: 4th Run, □: 5th Run
———: Unirradiated UO_2[5,6], --------: SIMFUEL corresponding to 39.3 GWd/tU[8], ·-·-·-·-: eq.(2), ·····:eq.(3).

values for simulated burnup fuel (SIMFUEL) [8]. According to reference [8], thermal diffusivity of SIMFUEL α_{FP} was expressed by

$$\alpha_{FP} = \lambda_{FP} / (C_p \rho) \quad (1)$$

where

$$\lambda_{FP} = \lambda_o \arctan(x) / x + CT^3,$$
$$x = [y_{Gd} D_{Gd}^2 + y_{FP} D_{FP}^2]^{1/2} \lambda_o^{1/2}.$$

Here, λ_{FP} and λ_o is thermal conductivity of SIMFUEL and pure UO_2 , respectively, C_p, heat capacity; ρ, density; T, temperature in K; y_{Gd}, atomic fraction of gadolinium; D_{Gd} coefficient; y_{FP}, atomic fraction of simulated fission products; D_{FP}, coefficient.

Thermal diffusivity decreased with increasing burnup. The first run data (○ in Fig. 4: below 750 K) for all samples were lower than the values calculated for SIMFUEL. Assuming that this deviation of thermal conductivity from SIMFUEL data was due to point defects induced by irradiation, k x y_{FP} was substituted for y_{FP} in eq.(1) to express the data as

$$\alpha_{FP+pd} = \lambda_{FP+pd} / (C_p \rho) \quad (2)$$

where

$$\lambda_{FP+pd} = \lambda_o \arctan(x') / x' + CT^3,$$
$$x' = [y_{Gd} D_{Gd}^2 + k \times y_{FP} D_{FP}^2]^{1/2} \lambda_o^{1/2}.$$

Here, α_{FP+pd} and λ_{FP+pd} is thermal diffusivity and thermal conductivity taking account of the effects of impurities and point defects induced by irradiation, respectively.

The calculated value was shown as a chain line in this figure at k = 5 and this agreed well with the data at the first run. This agreement was confirmed for the other samples (I-1, I- 2 and I-4). The second run data (•) for samples experiencing below 750 K agreed well with the first run data, showing that thermal diffusivity recovery did not occur below 750 K. Above 750K, thermal diffusivity deviated from the line by eq.(2) shown as a chain line. After experiments above 750 K, thermal diffusivity (△) recovered and had the same values as the SIMFUEL values after excursion above 1400 K (□). While thermal diffusivity decrease slightly by excursion above 1700 K.

According to Nogita and Une [3], point defects began to recover above 750 K, were almost recovered completely above 1100 K, and above 1400 K micro-bubbles grew to 8 to 10 nm. In this temperature range, no obvious swelling was observed. Above 1700 K, bubbles coarsened rapidly with swelling. This radiation damage recovery coincided with the thermal diffusivity recovery. Based on the results of Nogita and Une, Amaya and Hirai [26] proposed the thermal conductivity expression for irradiated UO_2 by using Klemens' theory and the assumption that thermal conductivity (or thermal diffusivity) was degraded by

(1) fission product dissolved in the UO_2 matrix,

(2) point defects induced by irradiation, which recover completely above 1100 K, and

(3) micro-bubbles, which grow above 1400 K.

According to them, thermal diffusivity for irradiated UO_2 , α_{irrad} could be expressed by

$$\alpha_{irrad} = \lambda_{irrad}/(C_p\rho) \tag{3}$$

where

$$\begin{aligned}
\lambda_{irrad} &= \lambda_o K [\theta_1 \arctan(1/\theta_1) - \theta_2 \arctan(1/\theta_2)] + CT^3 \\
K &= 1 / (1- 4\chi_o^2 x^2)^{1/2} \\
\theta_1 &= [(1/2 + \chi_o x)^{1/2} + (1/2 - \chi_o x)^{1/2}]/(2 x^2)^{1/2} \\
\theta_2 &= [(1/2 + \chi_o x)^{1/2} - (1/2 - \chi_o x)^{1/2}]/(2 x^2)^{1/2} \\
x &= [y_{Gd} D_{Gd} + E (1-y_{Gd}) D_{FP} \{1 + A \exp(-(T-273.15)^n/t_r^n)\}]^{1/2}\lambda_o^{1/2} \\
\chi_o &= [3 \alpha_o/(u L)]^{1/2}
\end{aligned}$$

Here, λ_{irrad} is thermal conductivity of irradiated UO_2; E is burnup; A and t_r are coefficient; α_o is thermal diffusivity of pure UO_2 ; u, the group velocity of phonons in UO_2; L, the mean free path of phonons in UO_2. By using eq.(3), thermal diffusivity of irradiated UO_2 was calculated and plotted as the dotted line in Fig. 4. The calculated value agrees with the obtained data successfully below 1700 K. Above 1700 K, data were slightly lower than the expected values. This decrease in thermal diffusivity can be explained by the porosity change during experiments.

The thermal conductivities were derived from measured thermal diffusivities and were plotted in Fig. 5 for I-3 sample with the values reported by several authors [9, 10, 18, 19]. Ross [9] and Daniel et al. [10] evaluated thermal conductivity by heat flow method and reported thermal conductivity hysteresis during the experiment. Recently, Nakamura et al. [19] measured thermal conductivity by the laser flash method and found similar behavior. Daniel and Cohen [18] evaluated the 'effective' thermal conductivity under irradiation by measuring fuel center temperature. They reported no thermal conductivity hysteresis, but they had data scattered within the hatched region in Fig. 5. The present results were within these reported values. In particular, the tendency for thermal conductivity recovery agreed well with data of Nakamura et al. From the results, it was confirmed that thermal conductivity of UO_2

irradiated in a commercial reactor was consistent with the previous data measured for samples irradiated in a test reactor.

Thermal diffusivity is shown in Fig. 6 for the R-1 sample after being power ramped up to 512 W/cm. Thermal diffusivity in Fig. 6 was higher than the values expected by eq.(3) and does not show obvious hysteresis, contrary to the results for base irradiated samples.

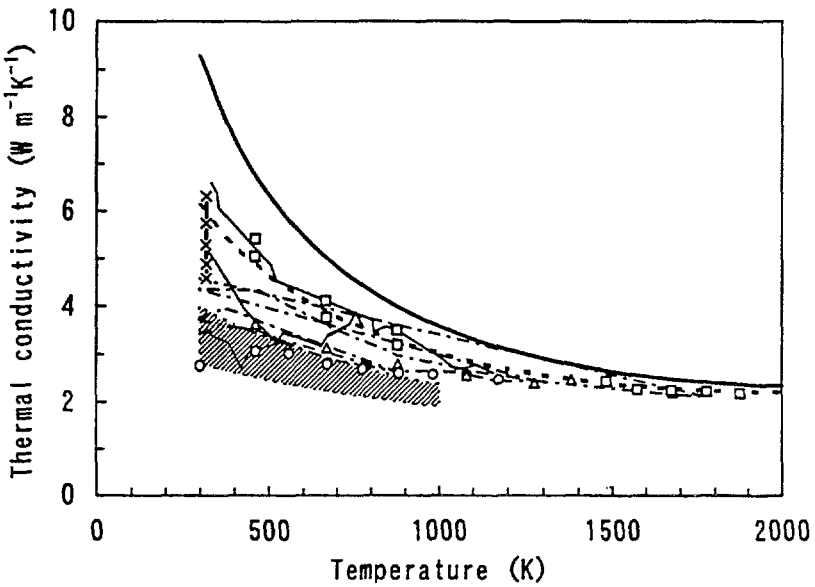

FIG. 5. Thermal conductivity for UO_2 irradiated up to 39.3 GWd/tU.

○: 1st and 2nd Run, △: 3rd Run, □: 4th and 5th Run
——: Unirradiated UO_2[5,6], - - - -: SIMFUEL corresponding to 39.3 GWd/tU [8], —×—: Ross [9], ——: Daniel et al. [10]
– – – –: Nakamura et al. [19], ▨: Daniel & Cohen [17].

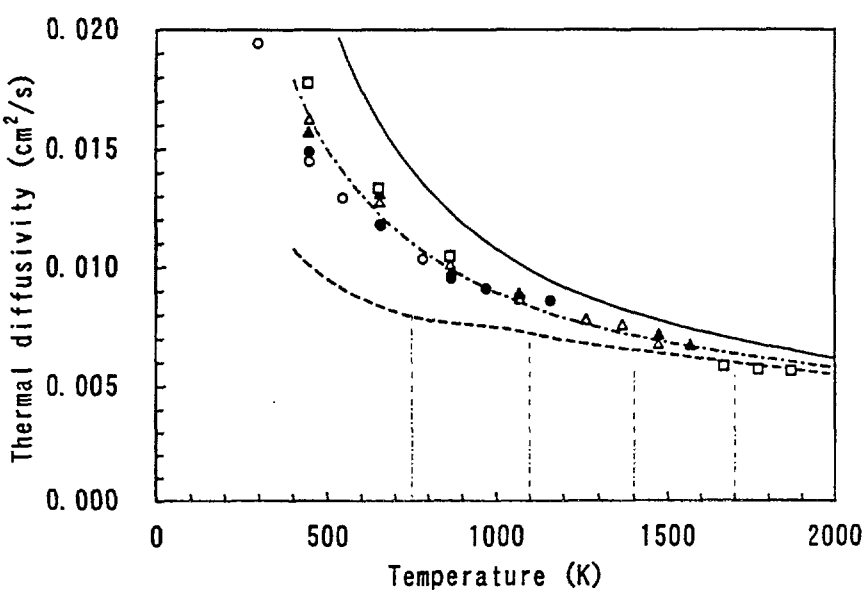

FIG. 6. Thermal diffusivity for UO_2 ramped to 512 W/cm for 4 hours after base irradiation up to 43.1 GWd/tU.

○: 1st Run, ●: 2nd Run, △: 3rd Run, ▲: 4th Run, □: 5th Run
——: Unirradiated UO_2[5,6], – · – · –: SIMFUEL corresponding to 43.1 GWd/tU [8], – – – –: eq. (3).

Thermal diffusivity estimated for base irradiated sample experiencing a temperature above 1100 K was quite similar to that for the power ramped sample. The latter was prepared from a position with a relative radius (R / R_o) of 0.6 to 0.9 and was estimated to experience a temperature up to 1300 K. The base irradiated samples I-1 to I-4 were estimated to have experienced temperatures below 1100 K. Nogita and Une [3] reported that the lattice dilation mainly due to fission induced point defects was recovered completely by annealing at about 1150 K and also that the lattice parameters of power ramped samples in this region were smaller than those of base irradiated samples because of higher irradiation temperature during the ramp test. Therefore, radiation damage recovery during the power ramp test was considered to cause higher thermal diffusivity than obtained for the samples as base irradiated. In other words, thermal diffusivity degradation was suggested to be due to solution of fission products into the matrix and accumulation of radiation damage during irradiation and not after it.

4. CONCLUSIONS

Thermal diffusivity was measured by a laser flash method for micro samples prepared from UO_2 pellets irradiated in a commercial reactor. Thermal diffusivity decreased with increasing burnup at lower temperature, which began to recover above 750 K, and recovered completely above 1400 K, becoming quite similar to the value for SIMFUEL. The recovery stage of thermal diffusivity corresponded with that of the radiation damage. Good predictions were made by using the thermal conductivity expression considering the radiation damage effect by Amaya and Hirai. Obtained thermal conductivity was consistent with reported values for samples irradiated in test reactors. The power ramped sample showed higher thermal diffusivity than base irradiated sample and the former had no obvious thermal diffusivity hysteresis. From these results, thermal diffusivity degradation was suggested to be caused mainly by solution of fission products and accumulation of radiation damage during irradiation and not after it.

ACKNOWLEDGEMENTS

This study was sponsored by the Ministry of International Trade and Industry (MITI). The authors wish to acknowledge the aid of the many persons who co-operated in this study. They would particularly like to thank Dr. Katsumi Une and Mr. Kazuhiro Nogita for many valuable suggestions and helpful discussions.

REFERENCES

[1] UNE, K., TOMINAGA, Y. and KASHIBE, S., J. Nucl. Sci. Technol. 28 (1991) 409.
[2] UNE, K., NOGITA, K., KASHIBE, S. and IMAMURA, M., J. Nucl. Mater. 188 (1992) 65.
[3] NOGITA, K. and UNE, K., J. Nucl. Sci Technol. 30 (1993) 900.
[4] HIRAI, M., MASUDA, H., ITO, K. and ISHIMOTO, S., Proceeding of 10th Japan Symposium on Thermophysical Properties, (1989) 115.
[5] HIRAI, M., J. Nucl. Mater. 173 (1990) 247.

[6] HIRAI, M. and ISHIMOTO, S., J. Nucl. Sci. Technol. 28 (1991) 995.
[7] LUCUTA, P.G., VERRALL, R.A., MATZKE, Hj. and PALMER, B.J., J. Nucl. Mater. 178 (1991) 48.
[8] ISHIMOTO, S., HIRAI, M., ITO, K. and KOREI, Y., J. Nucl. Sci. Technol. 31 (1994) 796.
[9] ROSS, A.M., AECL-1733 (CRDC-1143) (1963).
[10] DANIEL, J.L., MATOLICH, J., Jr. and DEEN, H.W., HW-69945 (1962).
[11] HAWKINGS, R.C. and ROBERTSON, J.A.L., AECL-1733 (CRDC-1143) (1963).
[12] HAWKINGS, R.C. and BAIN, A.S., AECL-1790 (1963).
[13] COHEN, I., LUSTMAN, B. and EICHENBERG, J.D., WAPD-228 (1960).
[14] CLOUGH, D.J. and SAYERS, J.B., AERE-R 4690 (1964).
[15] STORA, J.P., De SIGOYER, B. deB., DEIMAS, R., DESCHAMPS, P., LAVAND, B. and RINGOT, C., CEA-R2586 (1964).
[16] ROBERTSON, J.A.L., AECL-1123 (1960).
[17] DANIEL, R.C. and COHEN,,I., WAPD-246 (1964).
[18] LOKKEN, R.O. and COURTRIGHT, E.L., BNWL-2270 (1977).
[19] NAKAMURA, J., OWADA, I., MIYATA, S. and FURUTA, T., Proceeding of 1995 Fall Meeting of Atomic Energ. Soc. Japan (1995) 590 (in Japanese)
[20] VITANZA, C. and WIESENACK, W., Kakunenryo 17 (1992) 6.
[21] JAMES, H.M., J. Appl. Phys. 51 (1980) 4666.
[22] TADA, Y., HARADA, H., TANIGAKI, M. and EGUCHI, W., Rev. Sci. Instr. 49 (1978) 1305.
[23] TAKAHASHI, Y., YAMAMOTO, K. and OSATO, T., Nestu Sokutei 15 (1988) 103.
[24] VERRALL, R.A. and LUCUTA, P.G., J. Nucl. Mater. 228 (1996) 251.
[25] MATSUI, T., ARITA, Y. and NAITO, K., J. Nucl. Mater. 188 (1992) 205.
[26] AMAYA, M. and HIRAI, M., Proceeding of 14th IUPAC Conference on Chemical Thermodynamics (ICCT-96), August 25-30, 1996, Osaka, Japan (1996), to be published in J. Nucl. Mater.

DISCUSSION

(Questions are given in italics)

For clarification, you mentioned 1100K as base irradiation temperature. Is this temperature calculated at the micro-sample location? Does it take into account modifications of diametrical gap and thermal conductivity during base irradiation? What is the best estimation of the temperature evolution of this 1100K average temperature with burnup?

That temperature is the right specimen temperature.

For modeling purpose it is necessary to have the lowest curve with the maximum degradation. But this is depending upon the fuel power history. The condition is to have a low power irradiation in order to accumulate the maximum of damage and gases in the matrix.

The average irradiation power is bout 250W/cm. I agree with you that the effect depends on power history.

THE EFFECTS OF IRRADIATION ON THE THERMAL CONDUCTIVITY OF HIGH BURNUP UO_2 FUEL

K. BAKKER, R.J.M. KONINGS
Netherlands Energy Research Foundation,
Petten, Netherlands

Abstract

The parameters that may influence the thermal conductivity of high burnup UO_2 fuel are discussed and the thermal conductivity of UO_2 fuel with a burnup of approximately 39 MWd/kgUQ has been analyzed. The parameters that are discussed are changes in the pore structure, dissolution of fission products in the matrix, formation of precipitates, formation of cracks, changes in the O/U-ratio, irradiation damage in the UO_2 lattice and formation of the rim region. The influence of dissolution or precipitation of fission products can be approximated using data for SIMFUEL [1]. The influence of porosity can be estimated using the Finite Element Method. The influence of cracks depends strongly on the width of the fuel-to-cladding gap. Changes in the O/U ratio do probably hardly occur with burnup. Irradiation damage in the UO_2 -lattice is likely to give its main contribution to the change of the thermal conductivity for very low burnup. The influence of the above mentioned parameters on the thermal conductivity in the rim region is also discussed.

1. INTRODUCTION

The thermal conductivity of UO_2 is low [2] and decreases even further during burnup. This may influence the safety and economy of nuclear power plants. Understanding the causes of this decrease is important to optimize the fuel design. In the next paragraphs the potential causes of the decrease of the thermal conductivity will be discussed. They include:

(a) the dissolution of fission products in the fuel matrix,
(b) the formation of fission product precipitates,
(c) changes in the pore structure,
(d) the formation of cracks,
(e) changes in the O/U-ratio,
(f) irradiation damage in the UO_2 -lattice.

The influence of the formation of the rim region on the thermal conductivity will also be discussed. The rim region is a local maximum of the burnup at the pellet edge, in which the above mentioned effects are thought to contribute more strongly to a decrease of the local thermal conductivity. The rim effect is analyzed using the above mentioned properties.

2. PARAMETERS THAT INFLUENCE THE THERMAL CONDUCTIVITY OF UO_2

2.1 The dissolution and precipitation of fission products

The influence on the thermal conductivity of those solid fission products that dissolve in the UO_2 matrix has been measured by various authors using the laser-flash technique [1,3,4]. The influence on the thermal conductivity of the fission products that dissolve as

oxides in the UO_2 matrix and of the fission products that form precipitates has been studied by Lucuta et al. [1,5] by preparing simulated high burnup fuel (SIMFUEL). They mixed eleven elements using high-energy grinding, spray drying and sintering. Characterization of this eleven element mixture showed not only that fission-product atoms dissolve in the UO_2 matrix, but also a Mo-Ru-Pd-Rh compound and a ceramic phase. This microstructure represents that of high-burnup UO_2 fuel, except for the porosity structure. Good agreement exists between the data of Ishimoto et al.[4], Fukushima et al.[3] and that of Lucuta et al.(1994) [1]. Since the microstructure produced by Lucuta et al.[1,5] gives the best representation of the microstructure of high-burnup fuel, their result is used in section 3 for further calculations.

2.2 Porosity changes

The local porosity structure of UO_2 depends strongly on the burnup, the temperature and the thermal gradient. Experimental studies to quantify the influence of these porosity changes on the thermal conductivity are not available but an analytical technique to compute the influence of a complex porosity structure on the thermal conductivity has recently been developed [6]. The Finite Element Method (FEM) is used to compute the two dimensional (2D) thermal conductivity (f_{2D}) of the fuel, based on an analysis of a photograph of the fuel. f_{2D} is the thermal conductivity in the 2D porous plane of the photograph, divided by the thermal conductivity of the fully dense material. f_{2D} is a lower limit of the real (3D) thermal conductivity (f_{3D}), which makes f_{2D} a useful parameter. f_{3D} is calculated from f_{2D} and the porosity [6]. The photograph in Fig. 1 shows a pore structure in high burnup UO_2. The marked areas are used for the FEM calculations. Fig. 2 shows the distribution of the y-component of the 2D thermal flux. From the y-component of the 2D thermal flux f_{2D} can be obtained, which is used to compute f_{3D}.

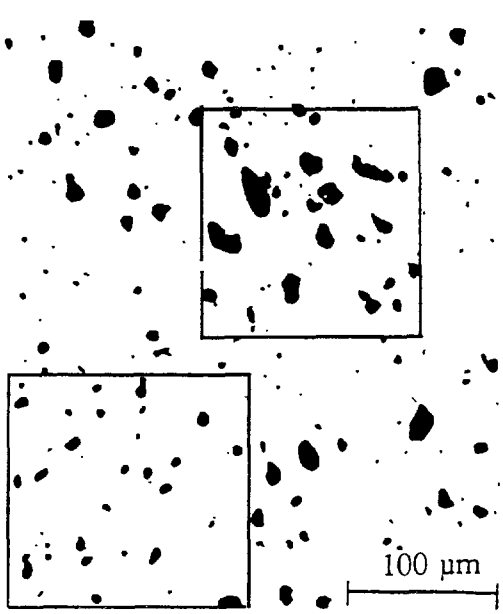

FIG. 1 *A photograph of the centre of the fuel rod. The marked regions are used for FEM computations. A result of the FEM computations on this figure is shown in Fig. 2.*

A potential source of inaccuracy in the thermal conductivity calculations is an irregular spatial distribution of the pores. As a result the porosity of the area that is used for the FEM computations, might be different from the porosity on the full pellet. In order to diminish this inaccuracy, the 3D thermal conductivity and the porosity (p), that are obtained from the FEM, are used to calculate the parameter β (eq. 1), that characterises the influence of the shape of the pores on f_{3D}.

$$f_{3D} = (1-p)^{\beta} \quad (1)$$

Using β, as obtained from eq. 1, and the porosity as obtained from image analysis of a large area, a value of f_{3D} is computed that is corrected for the irregular distribution of the porosity.

2.3 Formation of cracks

Cracks form in a fuel rod that is operated under normal conditions in a nuclear power plant. Cracking of the pellets can significantly decrease the thermal conductivity of UO_2 pellets [7,8]. In fuel rods with a narrow as-fabricated gap compressive forces on the pellet fragments strongly reduce the influence of cracks and the influence of the gap on the central temperature.

2.4 Changes in the O/U-ratio

The thermal conductivity of UO_{2+x} depends strongly on the O/U-ratio [2]. An increase of the O/U-ratio with burnup might be induced by the lower valence state of many fission products compared with that of uranium. However, several mechanisms buffer the oxygen potential, e.g. oxidation of the fission product Mo and oxidation of the zircaloy cladding, which prevents a substantial change of the O/U-ratio [9,10].

2.5 Irradiation damage in the UO_2-lattice

The influence of lattice defects on the thermal conductivity of UO_2 was considered to be significant only at temperatures below approximately 500°C [11,12]. Recently however, Shaw et al. [13] performed thermal diffusivity measurements using the laser flash technique and specific heat measurements on UO_2 fragments irradiated to 40 MWd/kgU. Their measurements show a depression of the conductivity values of the irradiated material compared with unirradiated UO_2, and a recovery effect of the thermal conductivity following heating to 1400 °C. Shaw et al. [13] mention that the exact mechanisms of the recovery effect still have to be elucidated. At temperatures of ~600-900°C the recovery occurs via the annealing of irradiation damage. At higher temperatures Shaw et al. claim that the recovery occurs as a result of fission products coming out of the solution into the bubbles, which causes a reduction of the number of scattering centres. It is likely that in the beginning of the irradiation the irradiation damage will increase rapidly and saturate quickly at a constant value. The main contribution of the irradiation damage is likely to take place for a burnup lower than 1 MWd/kg UO_2, a further increase of the burnup is likely to have a negligible influence on the thermal conductivity.

3. COMPARING THE MEASURED AND THE CALCULATED CONDUCTIVITY

3.1 Halden IFA-432 fuel rod

In order to study quantitatively the effects that were described in section 2, a comparison was made of the as-measured [14] and the calculated thermal conductivity of a irradiated UO_2 fuel rod, from the Halden IFA-432 experiment. This fuel rod was part of a programme to investigate the behaviour of LWR fuel rods under normal operating conditions [15]. This programme was sponsored by the fuel behaviour research branch of the U.S. Nuclear Regulatory Commission and designed and managed by Battelle Pacific Northwest Laboratories. The fuel rod (IFA 432-3) was fabricated with a small fuel to cladding gap (75μm) and contained a central thermocouple. The small fuel to cladding gap makes this rod very suitable to analyze the influence of burnup on the thermal conductivity of the UO_2 pellet. The rod achieved a burnup of approximately 39 MWd/kg UO_2. The fuel rod was filled with helium gas at 0.1 MPa and contains identical UO_2 pellets that are stable with respect to in-reactor densification. Light microscopy photographs from the centre, the mid radius and the edge of fuel pellets in the fuel rod were made by AEA Technology [16]. A photograph of the centre of the fuel is shown in Fig. 1. Using immersion density measurement an average porosity volume of 4.4 % was observed, while quantitative microscopy yields an average porosity volume of 6.7 % [17].

3.2 Thermal conductivity measurements

The conductance of the fuel-to-cladding gap is high throughout the entire irradiation and the major part of the temperature increase is ascribed to the decrease of the thermal conductivity of UO_2. The temperature increase corresponds to a linear reduction of the UO_2 conductivity of 6-7% per 10 MWd/kg UO_2 [14]. The influence of irradiation damage in the UO_2 -lattice on the thermal conductivity takes place on a short time scale and cannot be detected from the temperature versus burnup curve, and is consequently not taken into account.

3.3 Thermal conductivity calculations

The effect of dissolution and precipitation of fission products on the thermal conductivity is calculated using data of Lucuta et al. [1], as discussed in section 2.1. The thermal conductivity at a burnup of 39 MWd/kg UO_2 and at a temperature of 550°C was found to be 76 % of that of fresh fuel.

Parts of the photographs of the centre, the mid-radius and the edge of both fuel rods were analyzed with the FEM method. The results of the FEM computations and the image analysis results are shown in Table I. The irregular distribution of the amount of porosity is demonstrated by the difference between the porosity found in the FEM computations in the two areas in the centre. The f_{3D} values obtained for the centre, the mid-radius and the edge are averaged, yielding a f_{3D} value that describes the overall influence of the porosity on the thermal conductivity of the irradiated fuel. The average porosity, as obtained from image analysis, equals 8.4%, which causes the thermal conductivity to be 85.7% of that of the fully dense material.

In addition to the variation of the thermal conductivity with burnup, the influence on the thermal conductivity of the porosity initially present in the unirradiated fuel should be taken

Table I The FEM results and the image analysis results on various positions in the pellet. The FEM computations yield f_{2D} and p(FEM), from these two values f_{3D} is obtained [6]. f_{3D} and p(FEM) combined with eq. 1 yields β. β and p(image) are combined using eq. 1 in order to obtain a f_{3D} value that is corrected for the porosity obtained from image analysis. Two different areas of the centre photograph were used.

position	f_{2D}	p(FEM)	f_{3D}	β	p(image)
centre	0.7193	0.1356	0.7837	1.672	0.101
centre	0.8922	0.05386	0.9162	1.581	0.101
mid radius	0.7714	0.1092	0.8245	1.670	0.084
edge	0.7879	0.09445	0.8402	1.755	0.068

into account. Using quantitative microscopy Hahn et al. [17] found an average porosity volume of 6.7% in this fuel before irradiation. The porosity in unirradiated UO_2 is essentially spherical, for which shape β equals 1.5 [18]. Using eq. 1 it is found that the thermal conductivity of the porous unirradiated fuel is approximately 90% of that of fully dense unirradiated material. Thus it can be concluded that the change in the porosity structure causes the thermal conductivity to decrease 5% ((90-85.7)/90)%.

The influence of the cracks on the thermal conductivity can be ignored for a burnup of 39 MWd/kg UO_2, due to the compressive force of the cladding. No rim formation has occurred in the fuel due the combination of the pellet average burnup of 39 MWd/kg UO_2 and the relatively soft neutron spectrum in the Halden reactor.

3.4 Comparing the calculated and the measured conductivity

The calculated and the measured thermal conductivity can be compared. The thermal conductivity of SIMFUEL at a burnup of 39 MWd/kg UO_2 is 76% of that of UO_2 . The change of the porosity structure causes an additional decrease of the thermal conductivity of 5%. Combining these numbers yields a relative thermal conductivity of 72% ((100%-5%)*76%). The inaccuracy in the calculated thermal conductivity is estimated to be 5%.

The experimentally determined thermal conductivity for the narrow gap fuel, at a burnup of 39 MWd/kg UO_2, is 72.7-76.6 % of the original thermal conductivity, which is in good agreement with the change in the calculated thermal conductivity. It can therefore be concluded that combining SIMFUEL data and FEM results yields an accurate estimation of the thermal conductivity of UO_2 pellets that are irradiated in a narrow gap fuel rod. A more detailed discussion on the calculated and the measured thermal conductivity of both this narrow gap rod and a wide gap rod has recently been presented [19].

4. THE RIM EFFECT

In recent years the rim effect has gained considerable attention. Above a local burnup of approximately 65 MWd/kgUO_2, recrystallisation of the UO_2 grains takes place [20]. This recrystallisation is accompanied by a strong increase of the porosity. The recrystallisation and the pore formation are thought to have a negative influence on the thermal conductivity. Bagger et al. [21] reconstructed radial temperature profiles using grain growth and Xe diffusion data during a power transient at high burnup. They suggested that the thermal conductivity of the rim region is 3-10 times smaller than that of normal UO_2 fuel. Due to the indirectness of this measuring technique and the fact that the rim region is relatively thin, it is very difficult to determine the actual decrease of the thermal conductivity in the rim region. Scanning electron microscopy images of fracture surfaces suggest a porosity up to 40 % at the most outer part of the pellet edge [21]. Recently Spino et al. [22] performed detailed measurements of fuel porosity, volume pore density and pore size distributions as a function of the radial position for specimens with average burn-ups between 40 and 67 GWd/tM. They observed in these samples a maximum porosity value at the pellet edge in the range 15-17%.

The local increase in the porosity in the rim region contributes strongly to the decrease of the thermal conductivity. Most pores in the rim region are essentially spherical [21], for which case β (see eq. 1) is equal to 1.5. For a randomly ordered spherical porosity of 40 %, the thermal conductivity of the porous material divided by that of the fully dense material (f_{3D}) equals 0.46, while for an initial porosity of 5 % f_{3D} equals 0.93. Hence, an increase of the porosity up to 40% decreases the thermal conductivity by approximately 50 %, while an increase up to 15% decreases the conductivity by approximately 15%. Non-spherical or non-randomly ordered porosity yields a larger decrease of the thermal conductivity. The influence of the thermal conductivity of the fission-gas in the pores is negligible, in the case that the grain-boundaries are not fully covered by fission-gas.

The concentration of fission products in the rim region is also higher than the pellet average concentration. Using the SIMFUEL data of Lucuta et al. [1] (see section 2.1) to calculate the thermal conductivity due to dissolution and precipitation of fission-products at a burnup of 70 MWd/kg UO_2 and a temperature of 673 K, a decrease of 40% is observed, compared to unirradiated fuel. Combining the SIMFUEL and the porosity data yields a local thermal conductivity decrease at the outer edge of the rim region of 70% (40% porosity) or 51% (15% porosity) compared to the thermal conductivity of fresh fuel.

The influence of the formation of the rim region on the thermal conductivity can be modelled assuming a rim width of 100 μm in which the burnup decreases linearly from 70 MWd/kg UO_2 to 39 MWd/kg UO_2 and in which the porosity decreases linearly from 40% to 5%. In this computation an approximation of the burnup and porosity data of Bagger et al. [21] were used. As a first approximation the thermal conductivity of the SIMFUEL at 673 K is used in the calculations. This yields:

$$\lambda(W/mK) = 1.393 + (19770*(0.0001-r)) \qquad 0 \le r \le 0.0001 \tag{3}$$

where r is the distance from the edge of the rim region in meters. Assuming a linear heat rate (P) of 30 kW/m and a pellet radius of 5 mm, which determines the surface (A), the following equation can be used to estimate the temperature step over the rim:

$$\Delta T = \int_{0}^{0.0001} \frac{P}{\lambda A} dr \qquad (4)$$

Equation 4 yields a temperature difference of 42.6 K over the 100 μm of the rim region. In the absence of the rim formation (burnup 39 MWd/kg UO_2, porosity 5%) the temperature increase over 100 μm is 28.3 K, assuming identical conditions as used in eq. 4. This yields a temperature difference of 14.3 K. The value 42.6 K for the temperature difference over the rim is approximately double that computed for unirradiated fuel, and is smaller than the 3-10 times suggested by Bagger et al. [21]. The above mentioned doubling is likely to be a lower limit of the temperature step since randomly ordered spherical porosity is assumed. Pores in the rim region that are positioned on the grain-boundaries or non-spherical pores yield a larger thermal resistance and consequently a larger temperature step over the rim region is induced. Performing the above mentioned computations with the porosity data of Spino et al. [22] yields a slightly smaller temperature step.

Further information on the distribution of porosity can be obtained from Nogita and Une [23], who have performed tunnelling electron microscopy on the rim region. They observed micrometer-sized coarsened bubbles, nanometer-sized intragranular bubbles and nanometer-sized interconnected bubbles positioned on the grain-boundaries of the recrystallized grains. Porosity that is mainly positioned on the grain-boundaries can have a large influence on the thermal conductivity since it creates thermal barriers between the grains. The information on the spatial distribution of these ports in the rim region is not sufficiently accurate to compute the thermal conductivity using finite element computations. Fig. 3 shows a photograph of a piece of UO_2 (non-rim region) in which a considerable part of the grain-boundaries is covered by fission-gas. Finite element computations were performed on the marked region in order to determine the influence of this porosity shape on the thermal conductivity. For this porosity shape and distribution β equals 1.9. When the temperature step computations over the rim region are repeated for β equals 1.9, a temperature step of 53 K is obtained, which yields a temperature step that is 2.8 times that of unirradiated fuel. The FEM computations performed on Fig. 3 suggest that the fraction of fission-gas bubbles on the grain-boundaries must be much higher than that shown in Fig. 3 in order to obtain a thermal conductivity in the rim region that is 310 times smaller than that of unirradiated UO_2. It is not clear if such a high fraction of fission-gas bubbles on the grain-boundaries can be mechanically stable.

Not taken into account in the present analysis are the influence of cracks and the influence of irradiation since there is insufficient data to quantify their magnitude.

5. EXPERIMENTAL RESEARCH AT ECN

Recently, we have started research to mitigate the rim effect by fabricating UO_2 pellets with an inhomogeneous enrichment distribution [24]. The outer 250 μm of these pellets has a lower enrichment than the central part of the fuel. Burnup and power computations have shown that this configuration causes a considerable depression of the burnup in the outer ring of the fuel, which might prevent the rim formation. The low enrichment ring should be thin since it increases the fuel temperature compared with homogeneous fuel at the same linear heat

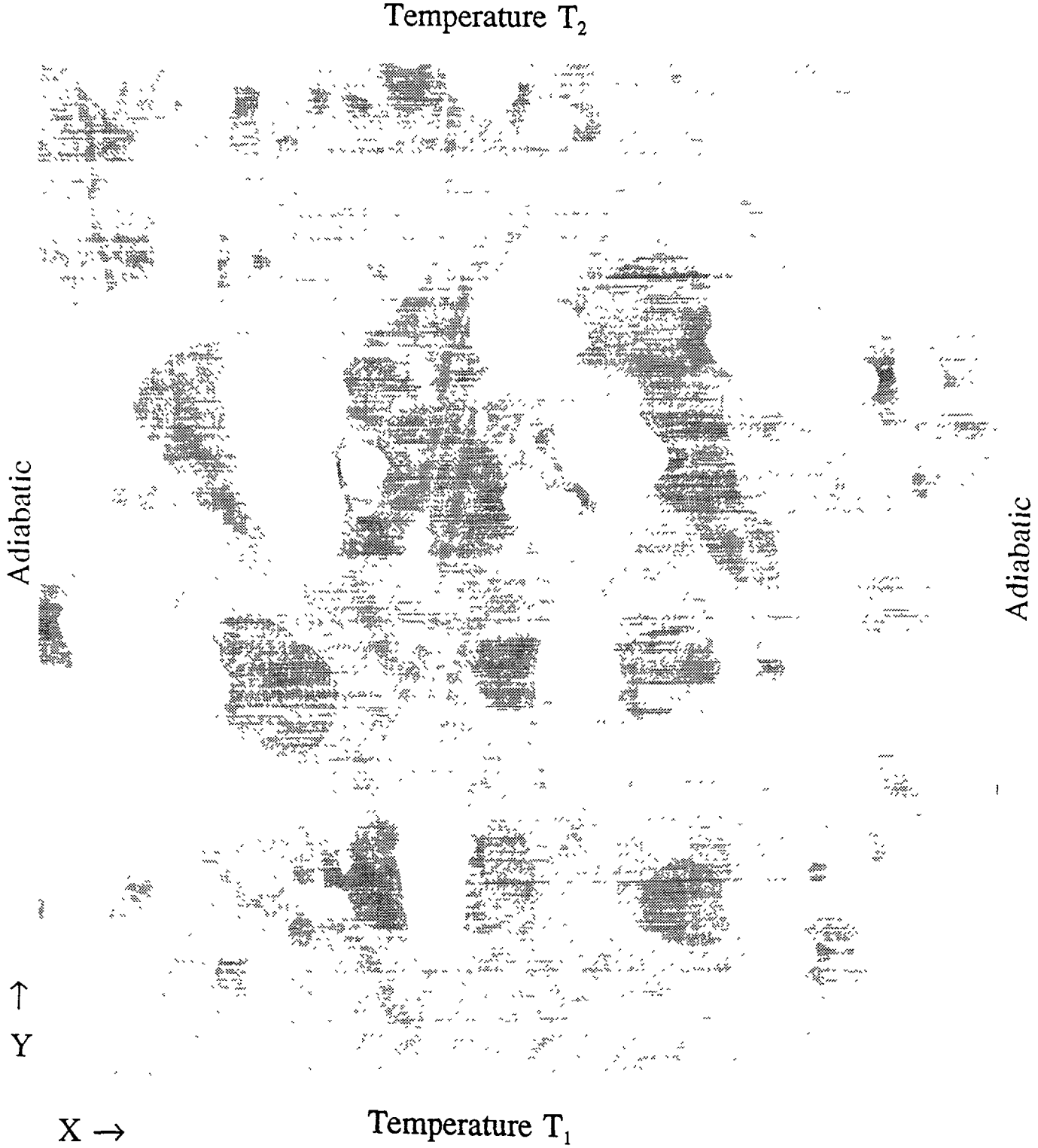

FIG. 2 *The distribution of the y-component of the thermal flux as obtained from FEM calculations on one of the marked areas in Fig. 1. The left and the right boundary are adiabatic. The lower and the upper boundaries of the areas have the arbitrary temperatures T_1 and T_2, respectively. The dark regions represent a larger flux than the light regions. The 2D thermal conductivity in the y-direction equals 0.6234 and the porosity equals 0.1585.*

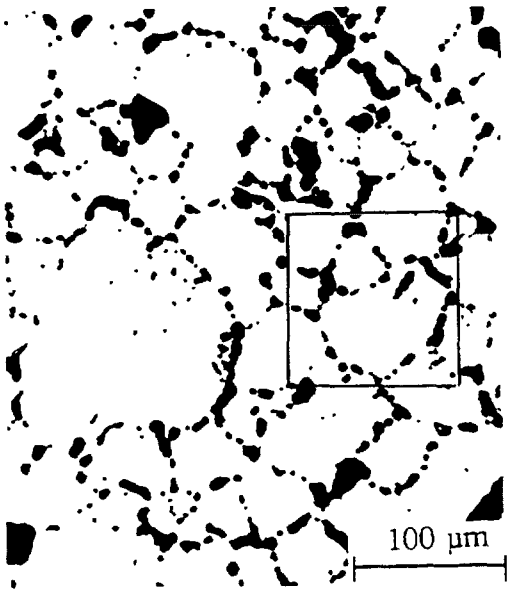

FIG. 3 A photograph of fuel in which a relatively large fraction of the grain boundary is covered by fission gas.

rate. Temperature computations show that this temperature difference between both pellet types decreases with increasing burnup. For a pellet average burnup over 40 MWd/kg UO_2 the temperature of the inhomogeneous fuel can be lower than that of the homogeneous fuel due to the prevention of the formation of the rim region, which acts as a thermal barrier.

ACKNOWLEDEGEMENTS

The authors wish to thank Battelle Pacific Northwest Laboratories for the permission to use the photographs of the fuel pellets and AEA Technology for acting as an intermediary in this.

REFERENCES

[1] LUCUTA, P.G., MATZKE, Hj., VERRALL, R.A., Modelling of UO_2 -based SIMFUEL thermal conductivity, The effect of the burnup, J. Nucl. Mater. 217 (1994) 279-286.

[2] MARTIN, D.G., A re-appraisal of the thermal conductivity of UO_2 and mixed (U,Pu) oxide fuels, J. Nucl. Mater. 110 (1982) 73-85.

[3] FUKUSHIMA, S., OHMICHI, T., HANDA, M., The effect of rare earths on thermal conductivity of uranium, plutonium and their mixed oxide fuels, J. Less Comm. Met. 121 (1986) 631-636.

[4] ISHIMOTO, S., HIRAI, M., ITO, K., KOREI, Y., Effects of soluble fission products on thermal conductivities of nuclear fuel pellets, J. Nucl. Sci. Technol. 31 (1994) 796-802.

[5] LUCUTA, P.G., VERRALL, R.A., MATZKE, Hj., PALMER, B.J., Microstructural features of SIMFUEL - Simulated high-burnup UO_2 based nuclear fuel., J. Nucl. Mater. 178 (1991) 48-60.

[6] BAKKER, K., KWAST, H., CORDFUNKE, E.H.P., Determination of a porosity correction factor for the thermal conductivity of irradiated UO_2 by means of the finite element method, J. Nucl. Mater. 226 (1995) 128-143.

[7] KITAJIMA, S., KINOSHITA, M., Evaluation of measured high burnup fuel at Risø project phase 3. 1992 IAEA report IAEA TECDOC 697 page 205, Proceedings of the IAEA Technical Committee Meeting, Pembroke Canada .

[8] MACDONALD, P.E., SMITH, R.H., An empirical model of the effects of pellet cracking on the thermal conductivity of UO_2 light water reactor fuel, Nucl. Eng. Design 61 (1990) 163-177.

[9] MATZKE, Hj., Oxygen potential in the rim region of high burnup UO_2 fuel, J. Nucl. Mater. 208 (1994) 18-26.

[10] MATZKE, Hj., Oxygen potential measurements in high burnup UO_2 fuel, J. Nucl. Mater. 223 (1995) 1-5.

[11] DANEL, J.L., MATOLICH, J., DEEM, H.W., Thermal conductivity of UO_2, report HW-69945, Hanford Laboratories, Richland, U.S.A. (1962).

[12] CLOUGH, D.J., SAYERS, J.B., The measurement of the thermal conductivity of UO_2 under irradiation in the temperature range 150°-1600°C, report AERE-R 4690, U.K. Atomic Energy Authority, Harwell, U.K. (1964).

[13] SHAW, T.L., CARROL, J.C., GOMME, R.A., The Characterisation of the Thermal Properties of High Burn-up Fuel, paper presented at the Annual Meeting of the European Working Group 'Hot Laboratories and Remote Handling', Petten, The Netherlands, May 14-15 1996.

[14] KOLSTAD, E., DEVOLD, H., TEMPEST, P., LÖSÖNEN, P., In-reactor thermo-mechanical measurements on LWR fuel rods in the high burnup range. 1990 IAEA report IWGFPT-36 page 140, Proceedings of the IAEA Techn. Com. Meeting, Studsvik, Sweden.

[15] LANNING, D.D., Irradiation History and Final Postirradiation Data for IFA-432 report NUREG/CR-4717, report PNL-5971, Pacific Northwest Laboratory, Richland, WA (1986).

[16] CLARK, P.A.E., CLOUGH, D.J., SMITH, R.C., Final report on the post irradiation examination of fuel rods irradiated in the Halden IFA 432 experiment, report AERE G 4190, U.K. Atomic Energy Authority, Harwell, U.K. (1986).

[17] HAHN, C.R., BATES, J.L., BRITE, D.W., DANIEL, J.L., DAVIS, N.C., HART, P.E., MARSHALL, R.K., MELLINGER, G.B., WILLIFORD, R.E., Test design, precharacterization, and fuel assembly fabrication for instrumented fuel assemblies IFA-431 and IFA-432, report NUREG/CR-0332, report BNWL-1988, Pacific Northwest Laboratory, Richland, U.S.A. (1977).

[18] SCHULZ, B., Thermal conductivity of porous and highly porous materials, High Temp.-High Pressures 13 (1981) 649-660.

[19] BAKKER K.and KONINGS R.J.M., The thermal conductivity of high burnup UO_2; the effects of irradiation, to be published in the proceedings of the 14th European conference on thermophysical properties.

[20] MATZKE, Hj., BLANK, H., COQUERELLE, M., LASSMANN, K., RAY, I.L.F., RONCHI, C., and WALKER, C.T., Oxide fuel transients, J. Nucl. Mater. 166 (1989) 165-178.

[21] BAGGER, C., MOGENSEN, M., WALKER C.T.. Temperature measurements in high burnup UO_2 nuclear fuel: Implications for thermal conductivity, grain growth and gas release, J. Nucl. Mater. 211 (1994) 11-29.

[22] SPINO, J., VENNIX, K., COQUERELLE, M., Detailed characterisation of the rim microstructure in PWR fuels in the burn-up range 40-67 GWd/tM, J. Nucl. Mater. 231 (1996) 179-190.

[23] NOGITA, K., UNE, K., Irradiation-induced recrystallization in high burnup UO_2 fuel, J. Nucl. Mater. 226 (1995) 302-310.

[24] BAKKER, K., HEIN, H., KONINGS, R.J.M., Using inhomogeneously enriched UO_2 fuel to reduce the rim effect. To be presented at the 1997 International Topical Meeting on LWR Fuel Performance, Portland, U.S.A.

DISCUSSION

(Questions are given in italics)

Comment:

Effect of Xe/Kr should be eliminated from the degradation. SIMFUEL data do not contain the rare gas effect.Effect of grain boundary should be included.

How do your results compare with the prediction of MATPRO for the same amount of possibility?

I do not have the data with me, but I can communicate them to you.

MICROSTRUCTURE AND FRACTURE TOUGHNESS CHARACTERIZATION OF IRRADIATED PWR FUELS IN THE BURNUP RANGE OF 40–67 GWd/tM

J. SPINO, M. COQUERELLE
Institute for Transuranium Elements,
EC Joint Research Centre,
Karlsruhe, Germany

D. BARON
Direction des études et recherches,
Electricité de France,
Moret-sur-Long, France

Abstract

The radial variation of porosity, pore density, pore size distributions and fracture toughness parameter (K_{IC}) was characterised for several PWR-UO_2 fuel samples in the burnup range 40-67 GWd/tM. In all cases, the formation of a porous zone at the pellet periphery was confirmed, the thickness of which increases with the average burnup. Within this zone, an exponential growth of the fuel porosity and pore density towards the pellet edge was measured, while the mean pore size remaining constant at about 1μm. At the pellet edge both porosity and pore density appeared to reach a saturating value, almost independently on the average burnup considered, which in the case of porosity was in the range 15-17%.

Accompanying this porosity increase, also a structure modification of the original fuel is evidenced, leading to a band of completely grain subdivided material at the pellet edge, with a grain size of 0.29 $\pm$ 0.14 μm, compared to the as-fabricated grain sizes of 5-10 μm. As increasing the distance from the pellet edge, a characteristic of this grain subdivision is that it becomes unambiguously concentrated around pores, first at both intragranular and intergranular positions, and then clearly located at the boundaries of the original matrix grains.

The resistance of the material to crack propagation (K_{IC}), showed an increase of 80 to 100 % in the rim zone, compared to the rest of the fuel. This unexpected improvement is supposed to be caused by a type of Hall-Petch strengthening mechanism, due to the grain refinement occurring in the rim region. The positive contribution of this effect apparently overrides the detrimental influence of the porosity in the material toughness. In this paper, also the influence of the local burnup on the above results is discussed.

1. INTRODUCTION

When PWR-UO_2 fuels are irradiated at average burnups above about 40 GWd/tM, a particularly porous and fine grained microstructure, i.e. the so-called 'rim structure', develops at the pellet periphery [1-3]. The onset and growth of this structure coincides also with observation of a slope change in the gas release rate of these fuels, which increases from a base level of about 1 % of the inventory at 40 GWd/tM to values of several percents at about 70 GWd/tM [4-5]. Due to the in general detrimental influence on an excessive gas release in the fuel performance, interest appeared to elucidate the real contribution of the rim zone to the integral gas release. Two main possibilities for this influence had been considered by different authors, namely a potential increase of the fuel temperatures through the formation of an additional thermal barrier at the fuel-cladding gap [6-8], and or a direct release from the cold fuel periphery via pore venting under postulated intense microcracking [9].

To confirm these hypothesis, a good characterisation of the material properties of the rim zone is needed. With respect to the first point, knowledge of the porosity gradients and related pore features is important for the assessment of the thermal conductivity degradation of the fuel due to matrix voids [10,11], together with that caused by the increase of the fission products concentration [11]. On the other hand, determination of the propensity to cracking of the rim material appears to be relevant, to evaluate the possibility of athermal pore channeling formation during power changes [9].

In a recently published work by the authors, a thorough study of the porosity and other microstructure details within the rim and adjacent zones for a wide range of commercial PWR-UO_2 fuels had been presented [12]. In the present paper, a summary of these results is given, together with new data of the radial dependence of the Vickers hardness, H_v, and the fracture toughness K_{IC}, for the same kind of fuels. As a complement, an evaluation of the results as function of the local burnup is given, according to calculations performed with the APPOLO code [13].

2. EXPERIMENTAL

2.1. Fuel characteristics

Fuel samples treated in this paper were taken from standard PWR fuel rods which were irradiated in a commercial power reactor for several cycles. The cross sections considered correspond to the maximum power positions of different fuel rods, being the assigned burnups to be interpreted as the average peak pellet burnup in each case. Cladding and fuel materials were zirconium base alloys and UO_2 respectively. The initial fuel enrichment was 3.5-4.2 w/o U-235. The nominal fuel rod diameter was 10.75 mm, the fuel density 10.40 g/cm^3 and the fabrication grain size of UO_2 7-10 μm.

2.2. Sample preparation

Ceramographic cross sections were carefully prepared in several grinding and polishing steps with hard abrasives (SiC and diamond) up to a surface roughness of about 1 μm, with two final polishing steps with submicron oxide suspensions to eliminate as much as possible the created surface stresses during grinding. In addition, two intermediate vacuum reimpregnations were made between the coarsest grinding steps in order to avoid artificial pore coarsening and grain fragmentation during preparation.

For SEM examinations, fresh fracture surfaces along the pellet diameter were produced by bending rupture of impregnated pellet discs of 3 mm in thickness, which were previously notched them from both sides to a depth of 0.5 mm.

2.3. Quantitative metallography

Quantitative image analysis was performed with a fully automatic equipment Quantimet 520. The analysis was done using optical micrographs originally taken at magnification 500 x, with an additional enlargement of about 3.4 times through a video camera system. The feature resolution limit on the monitor screen was about 0.2 μm. Photographs were subdivided in bands of 40 μm in width in the fuel radial direction enclosing a measuring area of about 4000 μm^2, and a number of features per frame between 200 and 400. Setting of the detection

threshold (i.e. level of grey colour detected or ignored) was done according to standard methods recommended in the specific literature [14,15]. Manual retouching of the detected field was also performed, to eliminate all artificial pore interconnections and to add all remaining small pores which were not detected automatically [12]. The surface to spatial conversion of the measured two-dimensional pore densities and pore size distributions was done by application of the Saltykov method for spherical particles with logarithmic size classification [12,16].

2.4. Microindentation tests

Room temperature microindentation tests at the loads 20, 50 and 100 g were performed with the indentation device of a remote controlled microscope in the ITU hot cells, using a Vickers diamond pyramid with an edge angle of 136°. Tests were performed with loading and unloading rates of 10 g/s, and with a hold-time at load of 5 s. The load was determined on the calibrated scale of an incorporated load cell with a precision of $\pm$ 2 %. The resulting imprint diagonals and wedge crack lengths were measured on the transferred video image of the imprint, with a precision of about $\pm$ 0.5 μm. Determinations of imprint diagonals and crack lengths were done 24 h after the tests, to allow possible strain-relaxation and post-test crack growth processes to be stabilised. Detailed post-test analysis of the imprint areas was performed by optical microscopy and SEM examinations.

For all samples studied, measurements were done on four orthogonal radii at intervals of 50 μm, with a separation between indentations of about 8 print diagonals at 20 g load, and of about 3 print diagonals at 100 g load. The results given are thus the average of four separated measurements, the error bands being placed at 95 % confidence level. The hardness was calculated with the expression [17]

$$H_v = 1854.4.\ P/d^2 \text{ kg/mm}^2,$$

where P (g) is the indentation load and d (μm] the print diagonal. The fracture toughness was calculated via the relationship [18]

$$K_{IC} = 0.057.H.a^{1/2}.\ (E/H)^{0.4}.\ (c/a)^{-3/2} \text{ (Mpa.m}^{1/2}),$$

where E (MPa) is the Young modulus, a (m) the half print diagonal and c(m) the crack length measured from the imprint centre. The Young modulus was calculated in each case via the relationship [19]

$$E \text{ (MPa)} = 2.20 \cdot 10^5 - 5.10 \cdot 10^3.\ P\ (\%),$$

which takes into account the variation of the elasticity modulus with the local porosity.

For crack counting no rejection criterion was applied. Rather, all the cracks were counted according to their largest projection onto any of the two diagonal axes. In case of lateral crack formation and path branching, like in most of the present indentations on high burnup UO_2 fuels, the so-derived (effective) crack lengths tend to underestimate the true crack extensions, leading to comparatively higher K_{IC} values than in the case of straight crack propagation under the same energy dissipation. This is consistent with the intuitive concept that crack path deviation and branching may contribute to an increased material toughness [17].

3. RESULTS

3.1 Porosity, pore density and pore size distributions within the rim and adjacent zones

The radial variation of the porosity and other relevant microstructure features in the radial range $0.5 < r/r_o < 1$ had been determined for various PWR-UO_2 fuels with average burnups between 40 and 67 GWd/tM [12]. For the present study three fuels with average burnups 40.3, 56.9 and 66.6 GWd/tM were selected. As shown in Figs. 1 and 2, the results of the quantitative porosity and pore density determinations indicate that within a range of few tenths of microns to several hundreds of microns from the pellet edge (this width increasing with burnup), an exponential growth of the fuel porosity and the pore density takes place towards the position $r/r_o = 1$, resulting in 3 to 4 times larger porosities, and typically one order of magnitude larger pore densities at the pellet edge, compared to the values measured at the onset of the rim zone.

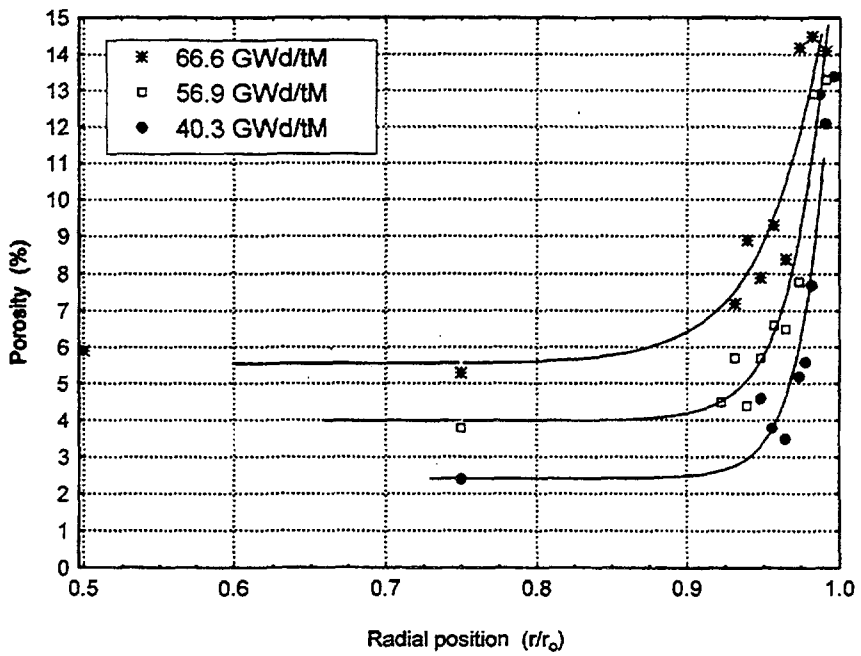

FIG. 1. Variation of the fuel porosity with the radial position and burnup.

A particular finding of these determinations is that the average pore size within the rim zone remains fairly constant around the value of approximately one micron, independently on the average burnup of the sample and the radial position examined (Fig. 3). Interesting to note is also the fact that independently of the average burnup of the fuel, a similar saturating value of porosity and pore density seem to be reached at the pellet edge, corresponding to a maximum of about 15-17 % pore fraction, and a maximum of roughly $1 \cdot 10^8$ pores per mm^3 (Figs.1-2). The concluding remark is that the local swelling (void volume) at the pellet edge extends gradually towards the pellet centre with increasing burnup, without leading to exaggerated pore coalescence and growth as in the case of the Pu-rich agglomerates in heterogeneous MOX fuels [20].

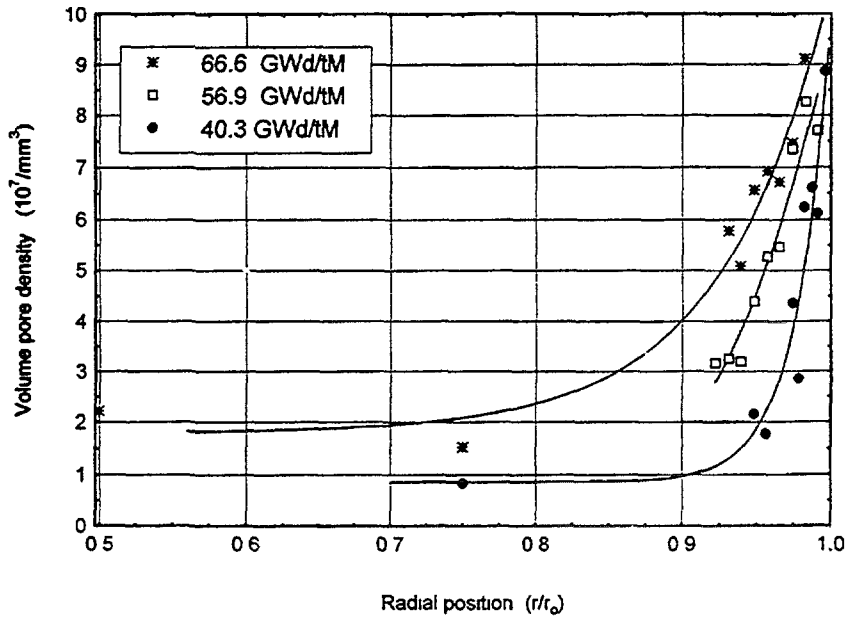

FIG. 2. Variation of the pore density with the radial position and burnup.

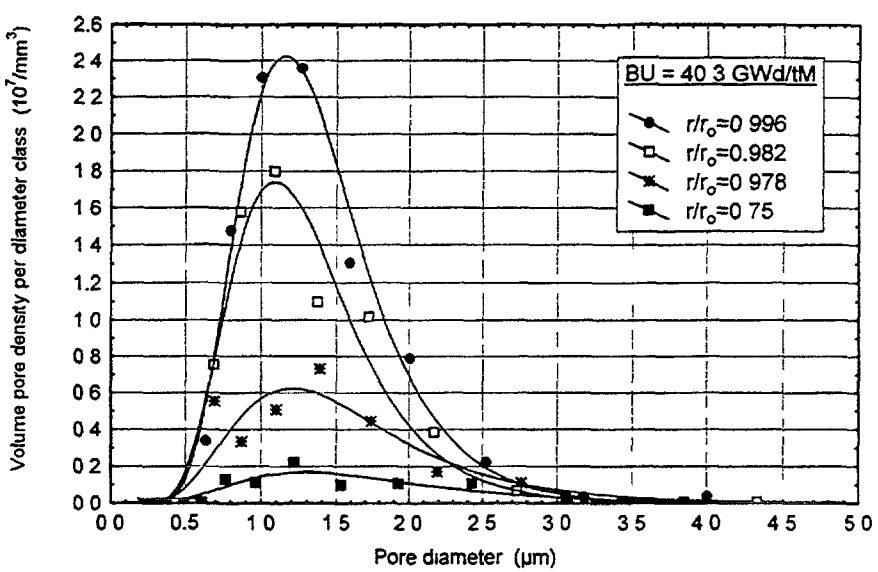

FIG. 3. Pore size distributions at various radial positions. (Average burnup: 40.3 GWd/tM

3.2 Influence of the local burnup

The increase of the local burnups due to the fissioning of Pu isotopes at the pellet periphery was calculated for all fuel samples examined with the APPOLO code [13]. Input data needed for these calculations were the average burnups, the initial enrichments and the pellet diameter [13]. The results obtained were then used to convert the previously determined radial porosity profiles in 'porosity vs. local burnup' profiles. Results of this conversion are compiled in Fig. 4, for the three samples described in the above section and another one with average burnup 50.3 GWd/tM.

Intuitively, since both the local porosity and the local burnup show similar exponential growths towards the pellet edge, one would infer a monotonous increase of the fuel porosity with the local burnup, once certain threshold burnup would have been exceeded [12]. As shown in Fig. 4, this was in general the case of all the samples examined, when local burnups in the range 50-65 GWd/tM were exceeded. As estimated mainly from the EMPA measurements of retained Xe, other threshold burnups mentioned in the literature were 60-65 GWd/tM (pellet edge burnup) [2] and 60-75 GWd/tM (local burnup) [21].

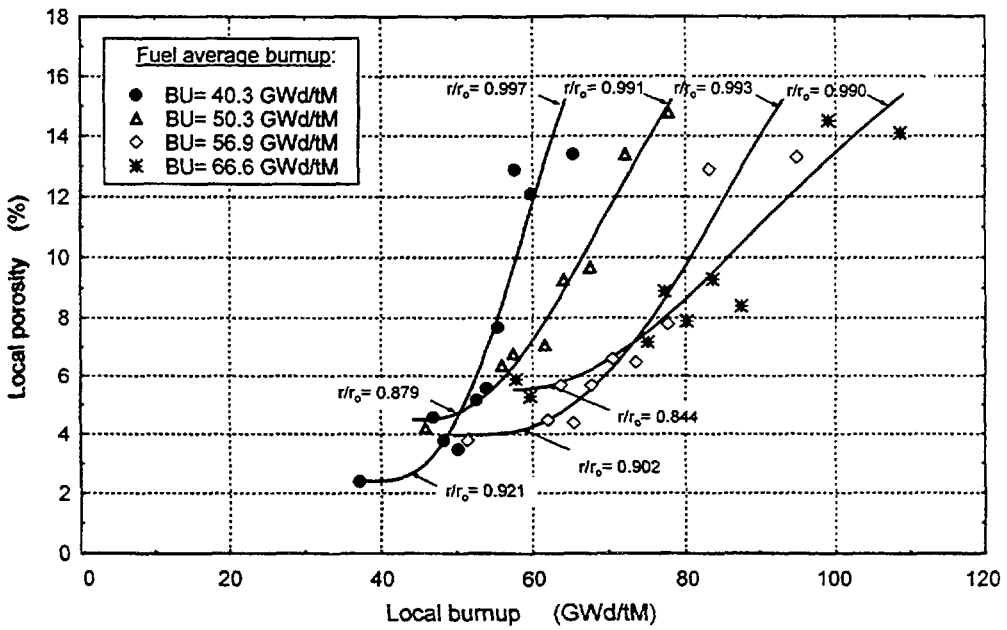

FIG. 4. Variation of the local porosity with the local burnup.

Once this threshold burnup range is surpassed, different trends in the porosity growth with the local burnup are established, the higher the average burnup the lower the slope (Fig.4). This behaviour indicates obviously that the local burnup is not the unique parameter determining the porosity level at a given radial position, and is compatible also with the fact that a saturating level of porosity is reached at the pellet edge independently on the average burnup (upper part of Fig 4 and Fig.1). If on the contrary the local porosity would have depended only on the local burnup, the maximum porosity level at the pellet edge would have shown a continuous growth with the average burnup, which is clearly not the case of the present findings.

3.3 SEM examinations

Accompanying the above described porosity and pore density increase, a grain subdivision process is also verified in the rim and adjacent zones, leading to a typical 'submicron' grain structure after irradiation, in contrast with the relatively large grain size of the as-fabricated material (7-10 μm) [12]. Characteristic of this 'in-reactor' grain subdivision is that it appears as a homogeneous structure only in a narrow band of material near the pellet edge, while as the distance towards the pellet centre increases, the grain subdivided areas are observed only locally concentrated around pores, first at indistinctly intragranular and intergranular positions, and then unambiguously located at the grain boundaries of the original fuel matrix [12].

SEM micrographs of Figs. 5 and 6 illustrate this microstructure evolution for the sample with average burnup of 66.6 GWd/tM. As shown in Fig.5A, the fully recrystallised porous band formed in this case extended only up to position r/ro = 0.97 (~135 μm from the pellet edge). Deeper into the fuel a transition region appeared, with a mixture of unmodified and restructured areas, these last with progressively decreasing amounts towards the pellet centre (Figs.5B and 5C). Fig. 5 C shows also that rather apart from the pellet edge (0.8 < r/ro < 0.9), the restructured areas were found primarily located on the grain boundaries of the original matrix. For this particular sample, vestiges of fuel restructuring were observed on some grain boundaries and intergranular cavities up to r/r_o ~ 0.5. Finally, the localisation of the grain subdivision around pores is shown in Figs. 6A and 6B, for two different radial positions inside the transition region. Within the fully restructured rim (Fig. 5A), the measured average grain size was 0.29 μm $\pm$ 0.14 μm. At other radial positions, no substantial variation of the subdivided grain sizes was found.

3.4 The idealised representation of the rim material

According to the above results, in the outermost (colder) parts of the pellet where still the burnup induced restructuring does not appear concentrated on the grain boundaries of the prior fuel matrix, the rim structure can be characterised by a population of basically non-interconnected quasi-spherical pores, whose average size remains fairly constant (~1μm) *along the irradiation, independently on the stadium (extension) of the restructuring process* (i.e. the average burnup reached). Based on that, an idealised representation of this structure can be attempted as in Fig. 7, subdividing the material in so many cubic cells as pores in the volume are measured, with the centre of each cell occupied by a single pore with its associated recrystallised surrounding [12]. Disregarding recrystallisation, a similar representation of a porous irradiated fuel has been considered by Ronchi [22], taking into account spherical cells. With this approach, if one considers for simplicity reasons a unique mean pore diameter at each radial position, other parameters as the cell size and the average pore-to-pore distance, this last defined as the distance between the surfaces of two nearest neighbour pores, can be easily calculated from the porosity and the volumetric pore density data [12,22].

Fig.8 shows the variation of the calculated pore-to-pore distances within the outer rim regions of three fuels with different discharge burnups. The figure shows that for a given radial position this typical distance decreases as average burnup increases, and, for a given burnup, as the distance to the pellet edge decreases. The slope of the curves indicates also that the separation between pores decreases less markedly towards the pellet centre as the average burnup increases. This is only one indication more that the porous rim zone growths progressively towards the pellet interior as increasing the irradiation time (burnup).

By introducing in Fig. 8 the radial position at which for the sample with burnup 66.6 GWd/tM a fully recrystallised material was observed (r/r_o ~ 0.97), a minimal pore-to-pore distance of about 1.5 μm results [12]. Since at this position this distance would be approximately twice the average thickness of the recrystallised shells around the pores (Fig. 7), a value of about 0.75 μm results for this thickness. This value is well consistent with the experimental observations (Figs. 6A and 6B). Further, if the same critical pore-to-pore distance to observe recrystallisation (~ 1.5 μm) is extended to other samples, the results of Fig. 8 would predict fully recrystallised widths of about 45 μm and 75 μm for the samples with burnups 40.3 GWd/tM and 56.9 GWd/tM respectively, and much more than 150 μm for

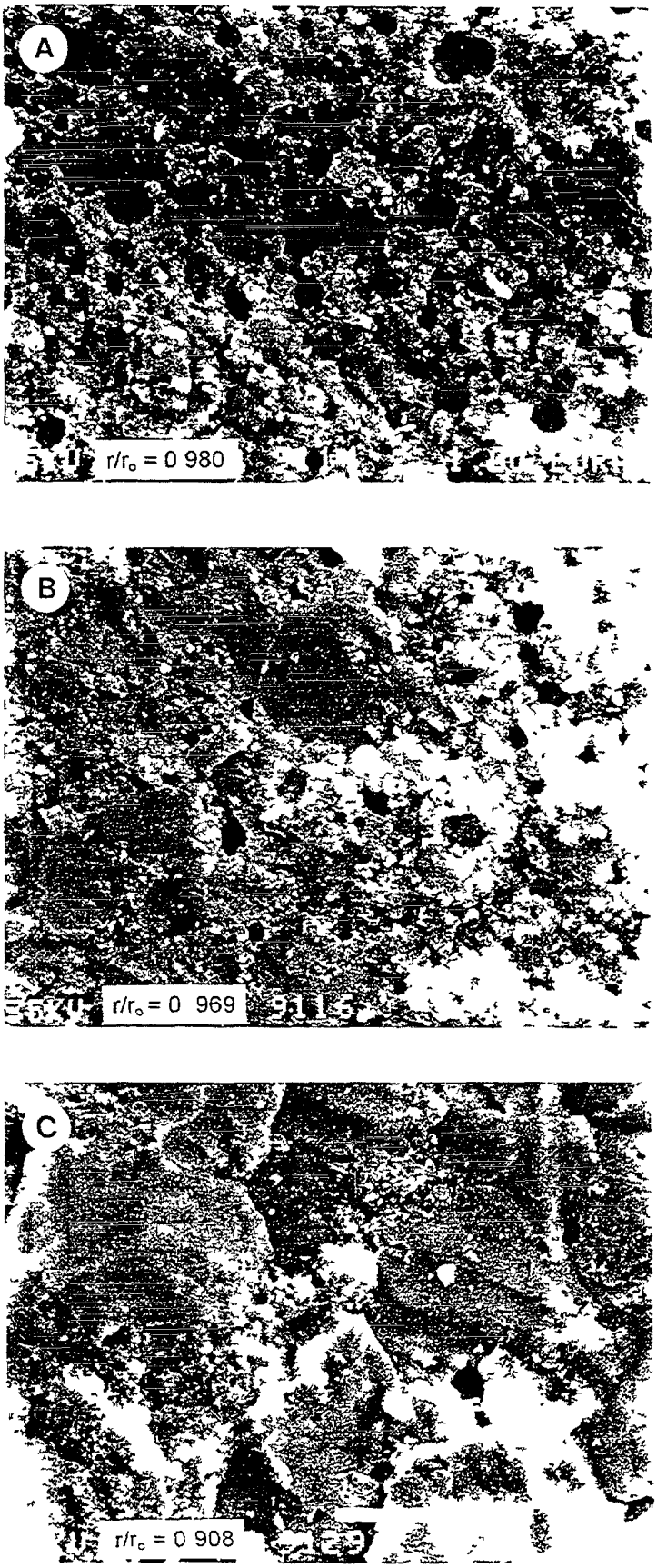

FIG. 5. *Microstructural changes along the pellet radius. (Average burnup: 66.6 GWd/tM. (A) Fully restructured rim. (B) Beginning of the transition zone. (C) Localisation of the fuel restructuring at grain boundaries*

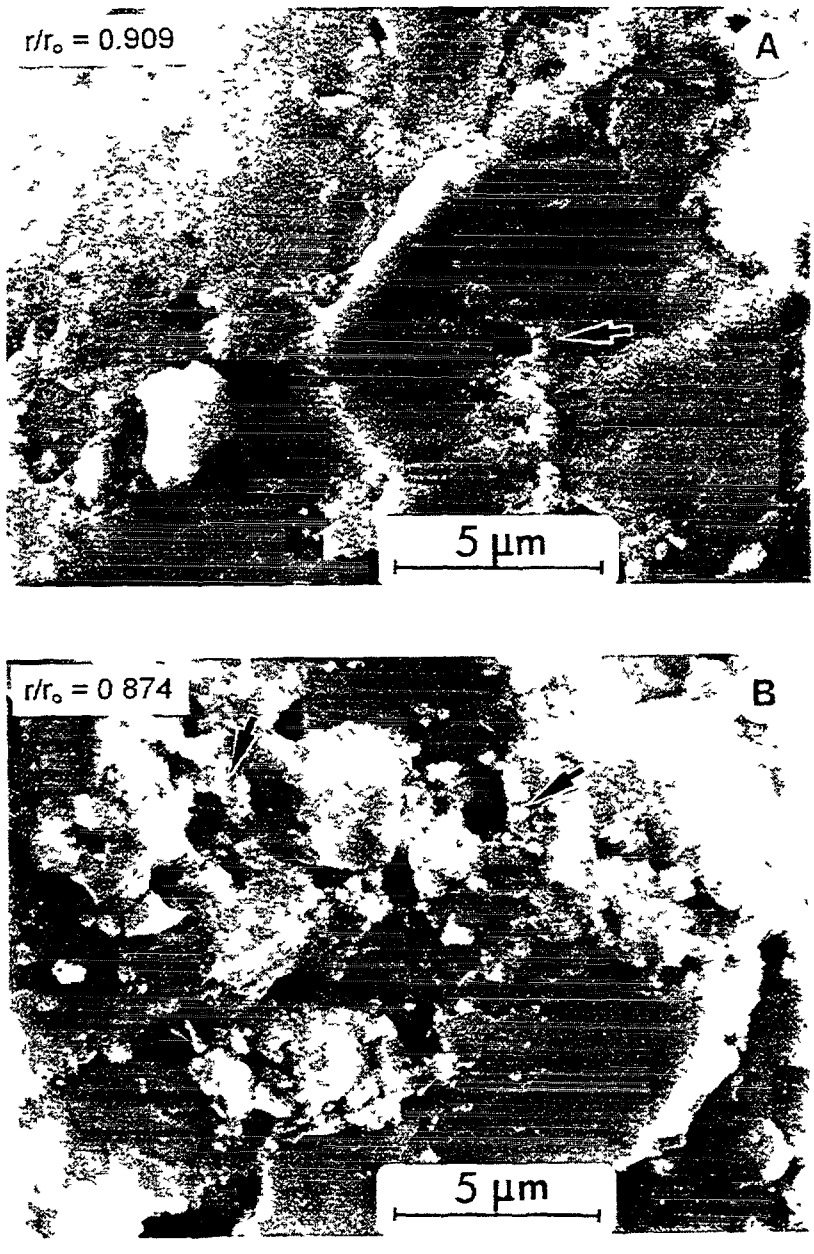

FIG. 6. *Grain subdivision around pores at different radial positions. (A) Intragranular pore (B) Intergranular pores*

the burnups above 66.6 GWd/tM. Preliminary SEM observations of samples with average burnups above 70 GWd/tM confirm this trend.

3.5 Microhardness

For all three fuel samples examined in this work the hardness remained relatively constant along most of the pellet radius, with exception of the peripheric region showing the rim structure. At these positions, a reduction of up to 30 % of the average occurred towards the pellet edge, independently on the indentation load applied and the average burnup examined. This can be appreciated in Fig. 9 where the radial variation of the relative

hardness, i.e. the ratio between the local hardness and the average hardness in the region $0 \leq r/r_o \leq 0.8$, is shown for different average burnups at constant load. Interesting to note is that the width of the region within which the hardness decrease is observed coincides rather well with that region where an enhanced porosity of these fuels region was measured (Fig. 1, rim region).

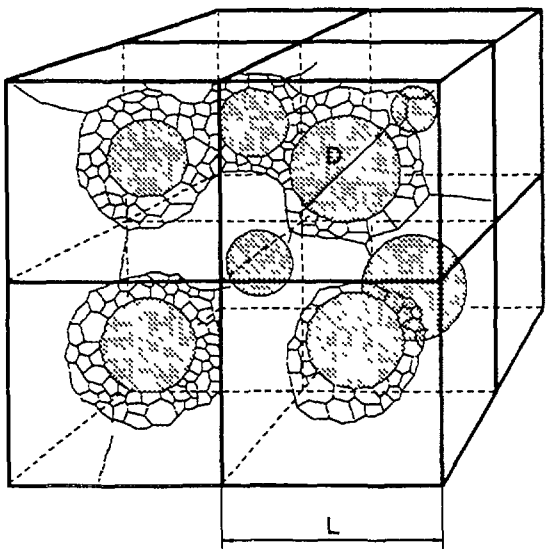

FIG. 7. *Cellular representation of the rim and adjacent zones.*
$D = (6P/\pi N_v)^{1/3}$ $L = N_v^{-1/3}$
P = *Porosity* N_v = *Volume pore density*

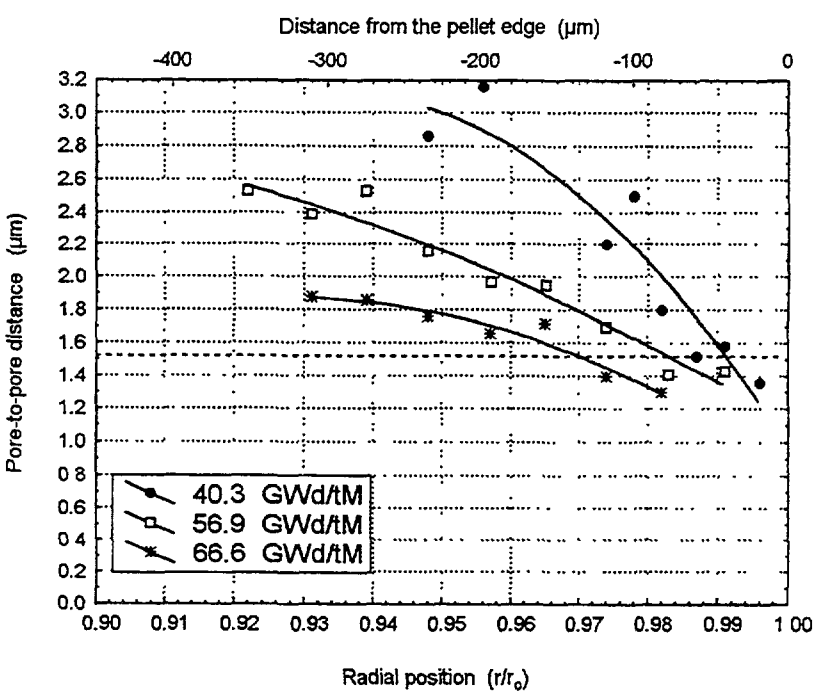

FIG. 8. *Pore-to-pore distance as function of the radial position for different burnups. Dashed line: critical pore-to-pore distance below which a fully recrystallised material might be expected.*

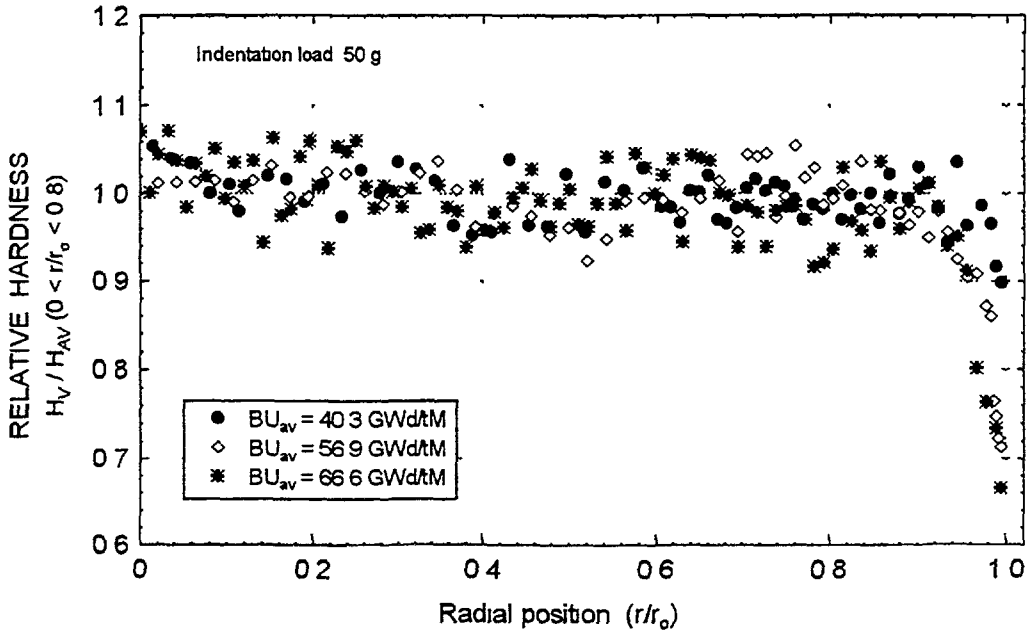

FIG. 9. *Variation of the fuel hardness with the radial position at different burnups. (H_v-data are normalised respective to the average values in the range 0 < r/ro < 0.8)*

A general remark has to be done that with decreasing the indentation load a systematic increase of the fuel hardness was observed, as it is normally the case of the Vickers tests when low loads are applied [17]. This dependence can be eliminated using an expression of the type $H \propto (P-W)/d^2$, where P and d have the usual meaning given in Section 2.4 and W represents a critical load below which no indentation is produced [17]. Applying this correction, a load independent hardness can be assigned to each fuel for the region below $r/r_o = 0.8$ ('plateau' of Fig.9), showing a roughly linear increase with the average burnup [23].

3.6 Crack length and fracture toughness

As with the Vickers hardness, H_v, the radial dependence of the indentation crack lengths, c, was determined for all three samples examined. Fig. 10 shows these results for the sample with 66.6 GWd/tM average burnup, together with the corresponding diagonal lengths at the same indentation load (50 g). Similarly to the hardness profile (Fig. 9), the crack lengths remain relatively constant along most of the pellet radius ($r/ro \leq 0.8$), until they start to decrease on approaching the outer parts of the fuel. This indicates obviously a smaller propensity to crack propagation of the outer fuel regions, which in combination with the observed hardness decrease (Fig. 9) results in a clear improvement of the fracture toughness of the zone, i.e. the rim region. It is noteworthy that on approaching the pellet edge, the shortening of the measured crack lengths clearly starts before any hardness decrease is noticeable (Figs.9,10), and thus before any significant porosity increase is measured (Fig. 1). This effect, which was observed in all three fuel samples examined, is at present not completely understood.

Differently to the case of the hardness, the derived K_{IC} values were rather independent of the indentation load used, allowing direct comparison of the results without any normalisation. Fig. 11 shows the derived fracture toughness (K_{IC}) profiles for the three fuels

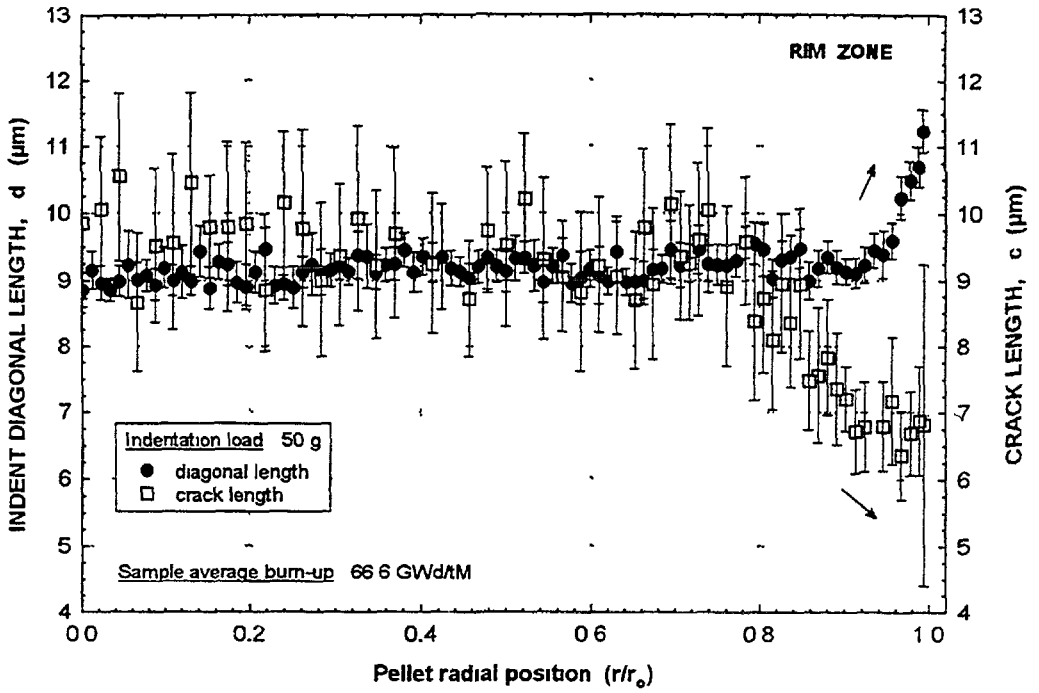

FIG. 10. *Radial variation of the Vickers diagonal lengths and crack lengths at constant indentation load. (Average burnup: 66.6 GWd/tM).*

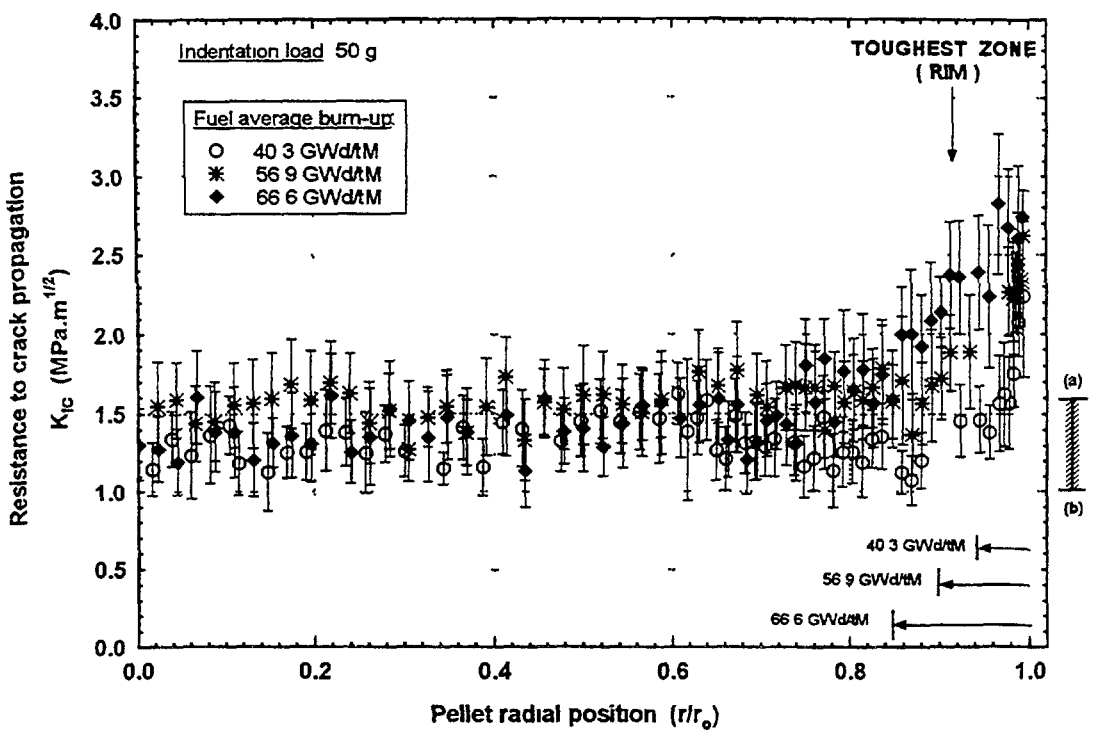

Fig. 11. *Radial variation of the fracture toughness, K_{IC}, at different average burnups. The bar on the right side indicates the differences in the K_{IC} values for unirradiated UO_2 as determined in this work (a) (low loads) and as given in the literature (b) (high loads).*

tested, at the indentation load 50 g. As it becomes evident from the plots, a toughening effect can be associated with the rim zone, whose width of influence clearly increases with the average burnup (Fig. 11). As mentioned before, comparison of Fig. 11 with Figs. 9-10 shows that the 'toughened' rim extends further into the fuel than the corresponding 'softened' region defined by the hardness profile.

In Fig. 11, also the range of K_{IC} values for unirradiated UO_2 is given, according to measurements by other authors at higher loads [19] and the control measurements performed in our case under the same conditions as for the irradiated fuels. As mentioned in point 2.4, the higher K_{IC} value derived in our case is due to the abundant lateral crack formation. Within the scatter of both measured and reference results, the plots of Fig. 11 show primarily that the fracture toughness of the central parts of the irradiated fuels roughly compares to the range of values for unirradiated UO_2, while the fracture toughness of the rim zone can be twice as large.

4. DISCUSSION

It has been shown that the rim region of high burnup fuels is characterised by a steep increase of the porosity and pore density towards the pellet edge, within a peripheral band of the fuel whose thickness increases with the average burnup. This evolution is labelled also with two other important features, namely that the loci of the pore size distributions remain placed at around almost the same median pore size for all radial positions, and that a saturating level of both porosity fraction and pore density is reached at the pellet edge, independently of the average burnup of the fuel. The experimental data show that the porous rim extends progressively into the fuel, without leading to pore interconnections or exaggerated cavity growth, as it is the case of the Pu-rich agglomerates in heterogeneous MOX fuels when very high local burnups are reached (> 250 GWd/tM) [20]. This has a certain positive impact on the thermal properties, since for a given void fraction, smaller and well distributed pores tend to deteriorate less the thermal conductivity than larger and irregularly distributed cavities [11]. Also, the fact that the pores in the rim zone remain basically 'non-interconnected' ensures the retention of the fission gases, so long as no pore connection is provoked under non steady state conditions.

The high burnup effects in the rim zone lead also to a remarkable grain size reduction, typically from 7-10μm in the as-fabricated condition to about 0.2 - 0.3 μm after grain subdivision. Characteristic of this grain subdivision is that it affects uniformly only in a narrow band of material at the pellet edge, and that as the distance from the pellet edge increases, it is observed preferentially concentrated around pores. Further, at deeper positions into the pellet, the restructuring process (i.e. enhanced porosity plus associated grain subdivision) appears localised at the prior grain boundaries, before it vanishes completely in the hotter regions of the fuel. Thus, whichever were the entities causing the restructuring process, when the temperature increases, they appear to deplete first from the grain interiors and then from grain boundaries, falling their concentration to a level below which no restructuring process can be induced. Several kind of physical parameters have been assumed to play a role in the initiation of the grain subdivision process, i.e. the lattice defect concentration, the dislocations density, the bubble overpressure, etc., [12]. However, among them, mainly the fission gases can follow an evolution inside the grains like the above described. Because of that, it appears plausible to consider that the bubble overpressure could play a decisive role in the initiation of the grain restructuring.

It has been described that the rim zone is associated with a hardness decrease of about 30% and with a fracture toughness increase of about 100% compared to the values in the centre of the fuel (Figs. 9,11). It was noted also that the variation of hardness correlates well with the porosity growth inside the rim zone (Figs.1 ,9). This is in agreement with the general observation in ceramic materials [24], and also with data of unirradiated UO_2 and $(U,Pu)O_2$ [25], showing a monotonous decrease of the hardness with the increase of the porosity fraction. However, the behaviour is different in the case of the K_{IC} values, since instead of a reduction of the fracture toughness with increasing porosity, like normally observed in porous ceramics [24, 26-28], the results in the rim zone show just the opposite trend, i.e. higher K_{IC} values towards the regions with higher porosities (Fig. 11). It must be then noted that towards the pellet edge, not only the porosity but also the amount of recrystallised or grain subdivided areas increases. In that sense, it is to remark that the main characteristic of the superplastic ceramics, showing improved ductility and increased toughness, is precisely their submicron grain size [29]. Therefore, the increased K_{IC} values of the rim zone are to be attributed to the submicron grains of the region, whose positive effects on toughness apparently override the detrimental effect of porosity [12]. On that base, a pore venting of the region due to microcracking during moderate power changes [9], appears to be improbable.

5. CONCLUSIONS

Above average burnups of about 40 GWd/tM, the porous rim zone increases gradually its thickness towards the pellet centre, showing a saturating maximum void fraction (porosity) at the pellet edge, with decreasing values of porosity and pore density towards the pellet interior. Also, another feature relevant for the thermal and gas release properties of the fuel, is that the average pore size across the rim region remain more or less constant around 1 μm, with basically no evidence of pore interconnection and cavity growth at any radial position.

With respect to the mechanical integrity of the rim zone, no evidence of deterioration is found. On the contrary, an improved resistance to crack propagation within this zone is observed, precluding in principle a friable behaviour during steady state operation and probably under moderate operational power ramps.

Vestiges of the high burnup fuel restructuring starting at the pellet edge can be found rather deep into fuel (r/ro ~0.5, at ~67 GWd/tM. From intermediate radial positions (r/r_o > 0.9, at ~67 GWd/tM) towards the pellet centre, this restructuring process is observed with decreasing amounts and progressively concentrated on the grain boundaries of the original matrix, until it finally vanishes at the hotter parts of the fuel. This indicates clearly that thermally activated processes, like most probably the gas migration and pore depressurisation, may contribute to the extinction of this athermally initiated fuel restructuring.

References

[1] MATZKE, Hj., BLANK, H., COQUERELLE, M., LASSMANN, K., RAY, I.L.F., RONCHI, C., WALKER, C.T., J.Nucl.Mater. 166 (1989) 165.

[2] PATI, S.R., GARDE, A.M., CLINK, L.J., Proc.Int.Topical Meeting on LWR Fuel Performance, Williamsburg, Virginia, USA, (ANS,1988) 204.

[3] CUNNINGHAM, M.E., FRESHLEY, M.D.,LANNING, D.D., J.Nucl.Mater.188 (1992)19.

[4] MOREL, M., MELIN, P., DUPONT, A., Proc. Int.Topical Meeting on Light Water Reactor Fuel Performance, West Palm Beach, Florida, April 17-21, 1994, p. 15.
[5] VESTERLUND, G., CORSETTL L.V., Proc. Int.Topical Meeting on Light Water Reactor Fuel Performance, West Palm Beach, Florida, April 17-21, 1994, p. 62.
[6] WALKER, C.T., COQUERELLE, M., Int.Topical Meeting on LWR Fuel Performance, Avignon, France, April 21-24, 1991, p.506.
[7] MANZEL, R., EBERLE, R., Int.Topical Meeting on LWR Fuel Performance, Avignon, France, April 21-24, 1991, p.528.
[8] BAGGER, C.,MOGENSEN, M., Proc. of Technical Committee Meeting on Fission Gas Release and Fuel Rod Chemistry Related to Extended burnup, Pembroke, Ontario, Canada, 28 April-1 May 1992, IAEA-TECDOC-697, p.38.
[9] BILLAUX, M R., VAN SWAM, L.F., SHANN, S.H., Int.Topical Meeting on Light Water Reactor Fuel Performance, West Palm Beach, Florida, April 17-21, 1994, p. 242.
[10] BAKKER, K.,KWAST, H., CORDFUNKE, E.H.P., J.Nucl.Mater. 223 (1995) p.135.
[11] LUCUTA, P.G., MATZKE, Hj., HASTINGS, I.J., J.Nucl.Mater. (1996), in press
[12] SPINO, J., VENNIX, K., COQUERELLE, M., J.Nucl.Mater. 231 (1996) p. 179
[13] CEA-EdF, France.
[14] FISHER, C., Praktische Metallographie, Special Issue 1, February 1970, p 21.
[15] QUANTITATIVE IMAGE ANALYSIS OF MICROSTRUCTURE, A practical guide to techniques, instrumentation and assessment of materials, (EXNER, H.E., HOUGARDY, H.P., Eds.), DGM-Informationsgesellschaft Verlag, Oberursel, Germany, 1988.
[16] METALS HANDBOOK 9TH ED., VOL. 9, Metallography and Microstructures, Quantitative Metallography (ASM, METALS PARK, OHIO, USA, 1985) p 13.
[17] JAIN, A., RAZDAN, A.K., KOTRU, P.N., WANKLYN, B.M., J.Mater.Sci.29 (1994) p. 3847.
[18] MATZKE, Hj. (Ed), Indentation Fracture and Mechanical Properties of Ceramic Fuels and of Waste Ceramics and Glasses, (HARDWOOD ACADEMIC PUB, CHUR), special issue of Eur. Ann. Res. Reports: Nucl. Sci.Tech. 7 (1987).
[19] KUTTY, T.RG., SENGUPTA, A K., CANGULY, C., European Appl.Res.Rept.-Nucl.Sci.Technol., (MATZKE, Hj., TOSCANO, E., Eds.), Hardwood Academic Publishers, 1990, p. 1473.
[20] WALKER, C.T., GOLL, W., MATSUMURA, T., J.Nucl.Mater. 228 (1996) p. 8
[21] LASSMANN, K., WALKER C.T., VAN DE LAAR, J., LINDSTRÖM, F., J.Nucl.Mater. 226 (1995) p. 1
[22] RONCH[, C., J.Nucl.Mater. 84 (1979) 55.
[23] SPINO, J., et al, to be published in the J.Nucl.Mater.
[24] RICE, R., Microstructure dependence of mechanical behavior of ceramics, Treatise of Materials Science and Technology, Vol 11, ed R.K.MacCone (Academic Press, 1977) pp 200-369
[25] ENGELHARDT,G., HOFMANN,H., Mechanische Eigenschaften von UO_2, KFK Rep.729, 1968
[26] RICE, R., et al., J.Am.Ceram.Soc.77(10)2539-53 (1994)
[27] RICE,R.,FREIMAN,S.W.,Ceramic Microstructures 76, 6th Int.Material Conf., Berkeley, California, 1976, Ed R.Fulrath., p 800.
[28] RICE, R.W., Materials Science and Engineering, A112 (1989) pp 215-224.
[29] MAYO, M., Mech.properties and deformation behaviour of materials having ultrafine Microstructures, M.Natasi et al (eds), Kluwer Academic Publisher, The Netherlands, 1993,pp 361-380.

DISCUSSION
(Questions are given in italics)

What do you think about original grain size effects (Large grain effects) on the formation of RIM structure? You showed RIM structure was developed from original grain boundary to inside by SEM fractograph. Is any connection with grain size effect?

My impression is that large grains will show relatively less restructuring than smaller ones; however, not at the outermost rim where full restructuring of the original matrix is observed, but at radial positions somewhat apart from the pellet edge. Indeed, we have observed in some fuels with heterogeneous grain size distributions, that the larger grains show much less restructuring at the grain inside than the smaller ones.

Please explain the quality of the signal related to the new sub-grain boundary.

Kikuchi pattern shows parallel line. And/or standard deviation of Intensity Increases.

EXAMINATION OF SUB-GRAIN FORMATION IN HIGH BURNUP UO_2 FUEL USING THE EBSP METHOD

S. BENGTSSON
Hot Cell Laboratory,
Studsvik Nuclear AB,
Nykoping, Sweden

Abstract

The orientation of individual grains was measured by use of electron backscattering patterns (EBSP). By moving the beam and observing the pattern it was possible to measure the extension of different grains. When the beam moves into a grain with a different orientation, the pattern changes. The resolution in orientation is approximately 0,5°.

UO_2 fuel irradiated to a burnup of 65 MWd/kgU was examined. The fuel had developed a high burnup structure near the periphery. The high burnup structure is characterised by numerous small bubbles causing a high porosity at the periphery, decreasing towards the centre of the pellet. Another phenomenon associated with the high burnup structure is the formation of sub grains. This manifests itself as a loss of electron channelling contrast (ECC) near the periphery. The normal ECC is caused by different orientations of the crystal lattice of the UO_2 grains. However, some of the grains at a small distance from the periphery exhibit a changing ECC within itself. This change indicates a disturbance of the crystal lattice. If this behaviour is severe different grains can not be separated.

At the periphery the high burnup structure is fully developed. The sub-grain formation is complete in this region and the original grains have disappeared completely. Further into the pellet the sub-grains are located near the original grain boundaries. The size of the sub-grains are of the same order of magnitude as the beam resolution (0,2 μm). This means that in an area with sub-grains the pattern changes quickly for small movements of the beam. Sometimes two patterns appear at the same time. The extension of the sub-grain zones and the sub-grain free zones was mapped by correlating the beam position and the pattern changes.

1. INTRODUCTION

The prospect of increasing the burnup is driving the fuel manufacturers to investigate the behaviour of high burnup fuel. The occurrence of new (degradation) phenomena at high burnup is especially important since it introduces new limits to the performance. One such phenomenon is the formation of a "high burnup structure" near the periphery that starts at a (local) burnup above approximately 50 MWd/kgU [1-4]. This structure is characterised by the presence of small bubbles and the formation of sub-grains near the bubbles [see e.g. 3-6]. Both the bubbles and the sub-grain boundaries are potential paths out from the pellet for the noble fission gas formed there. The escape of Xe and Kr gas into the rod free volume decreases the thermal conductivity of the gap and increases the pressure inside the fuel rod. The decreased thermal conductivity causes the fuel temperature to increase and will eventually cause further fission gas release from the centre of the pellet. The investigations concerning fission gas release from the outer region of the pellet does not provide a clear picture as regards the mechanisms for the release [1].

An understanding of the nature of the sub-grain formation can give some insight into the possibility of severe fission gas release from the rim. It appears that the precipitation of fission gas bubbles on the grain boundaries are the first step in the formation of the "high burnup

structure". The sub-grains are formed near these bubbles. This procedure is repeated until the original grain is consumed. The driving force for the restructuring is the high pressure in the bubbles [3], lattice defect accumulation [7] and the supersaturation of the solid fission products in the UO_2 lattice. Near the periphery a large part of the fissions come from ^{239}Pu [8]. The Pu was formed by resonance absorption of neutrons in ^{238}U creating ^{239}Np and subsequently ^{239}Pu. The neutrons causing the resonance are epithermal and have a very short range in UO_2 and the Pu build-up is concentrated to near the periphery. The Pu is present in solid solution in the UO_2 lattice substituting U positions. However, the lattice spacing is 5,47 Å for UO_2 and 5,39 Å for pure PuO_2, thus creating a mismatch strain of up to 1,5%. The above mentioned driving forces for recrystallisation can be observed as an increase in dislocation density during irradiation.

Microstructural changes that rely on diffusion are hampered by the relatively low temperature ($T/T_m \approx 0,2$). However, the neutron flux combined with the fission fragments cause the diffusion rate to increase. It has been shown that the material near the periphery can exhibit some plasticity, especially at high fluxes [3]. At low temperature the bulk diffusion is less important while the grain boundary-, pipe- and other alternative diffusion mechanisms are of a higher relative importance. If for example grain boundary diffusion is involved in the transport of noble fission gases, the introduction of 0,1 μm sub-grains, in a 10 μm grain structure, increase the grain boundary surface by two orders of magnitude.

The goal of the present investigation is to examine the extent of the sub-grain formation into the pellet interior.

2. EXPERIMENTAL

2.1 The EBSP method

The electron backscattering pattern (EBSP) is a pattern formed on a phosphor screen located near a highly tilted specimen that is bombarded by electrons. The electrons are diffracted inside the specimen crystal and escape from the crystal with varying intensities in different planes. This variation in intensity forms a pattern similar to a Kikuchi pattern on the phosphor screen. The screen is observed by a CCD TV camera and the signal is improved by a background subtraction before it is transferred to the computer. The computer automatically detects a number of bands. These bands are compared with a simulated set of bands by using an assumed crystal type. The simulation with the smallest mismatch (mean angular deviation) is used. The location of the point, the contrast in the image (band contrast), the orientation of the crystal (three angles) and the mean angle deviation between the detected bands and the best fitting simulated crystal orientation are stored.

The band contrast, which can be imagined as the standard deviation of the grey scale in the pattern, is a measure of the perfection of the crystal lattice that causes the diffraction. A polishing sequence that leaves a cold deformed layer causes a low band contrast (blurred pattern). Lattice strain causes the pattern to become more blurred also. Another factor that can cause a weak contrast is the occurrence of two patterns at the same beam position. This is the case on a grain boundary and more frequently in the areas of a high burnup fuel that is subjected to sub-grain formation. The image formed by using the band contrast shows the areas with a high lattice disturbance, notably the grain boundaries and the zones with sub-grains.

The orientation of the grain is defined by the three Euler angles. In the present case the co-ordinate system is chosen arbitrarily. A convenient way of representing the orientation is to assign a colour to an area in the pole figure. Each colour represents a unique orientation. The number used fore this colour code is called the true Euler angle. This means that all measurements within one grain will have the same colour since the measurements are clustered together in the pole figure. The image formed by using such a colour scheme shows an image with grain field contrast, i.e. an image which is similar to the image formed by electron channelling contrast (also caused by diffraction).

By comparing the orientation of two (neighbouring) measurements a map of misorientations can be found. If the misorientation is above a certain level it is considered to be a grain boundary. By using appropriate threshold levels, high-angle, low-angle and twin grain boundaries can be outlined.

2.2 Specimen preparation

The specimen used was originally prepared for SEM/EPMA analysis. The surface was covered by a thin layer of gold using an Emithech gold sputter apparatus. According to the manufacturer the gold layer should be around 4 nm thick at the current settings. The EBSP method usually demands uncoated surface so a careful manual polishing of the specimen was performed. The polishing is not thought to have removed the coating completely. An accelerating voltage of 20 kV was used since it was not possible to operate the instrument at low accelerating voltages, due to the remaining coating. A specimen tilt of 70° was used. After calibrating the system, the beam control mode was used performing measurements in a grid pattern of 100x100 or 150x150 points at 0,2 μm spacing.

A reference sample was prepared using a piece of an unirradiated fuel pellet. Since this sample was uncoated an accelerating voltage of 12 kV could be used. The lower accelerating voltage produces patterns with wider bands, making the detection and simulation more accurate.

The results were analysed using a mapping program where the properties of each measuring point is used to form an image. The available properties are the band contrast, the mean angle deviation, the three Euler angles, the true Euler angle and the degree of misorientation (relative to the neighbours). In some cases pole-figures were constructed.

3. RESULTS AND DISCUSSION

The maps of band contrast and the true Euler angle can be seen in Figures 1 to 4 for the locations 0,34 and 1 mm from the periphery respectively. The band contrast and true Euler angle maps from an unirradiated specimen can be seen in Figures 5 and 6. The {001} pole figures from the locations 0,34, 1 mm from the periphery and for the unirradiated specimen can be seen in Figures 7 to 10. The secondary and backscattered electron images from the location 1 mm from the periphery can be seen in Figures 11 to 12.

The areas containing sub-grains can easily be identified using the EBSP. In these areas, the grain size is of the same order or smaller than the beam spot size (actually: beam interaction volume). Two patterns are visible simultaneously on the phosphor screen, which

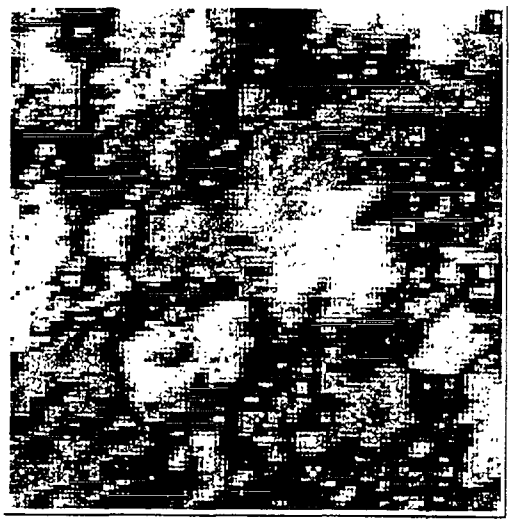

Fig. 1 Band contrast image. 100x100 measurements. Image side length is 20 micron. Image is located 0,34 mm from the periphery.

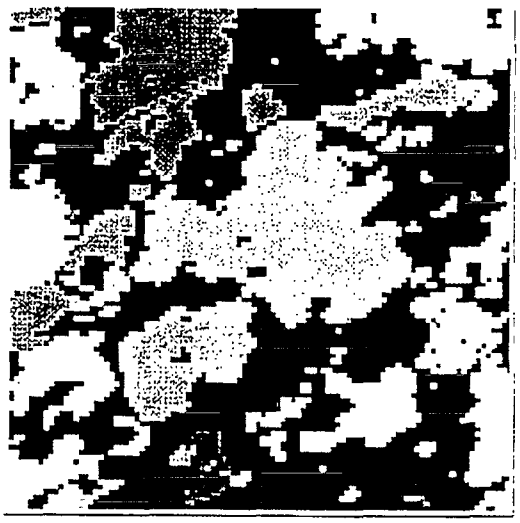

Fig. 2 True Euler angle image. 100x100 measurements. Image side length is 20 micron. Image is located 0,34 mm from the periphery

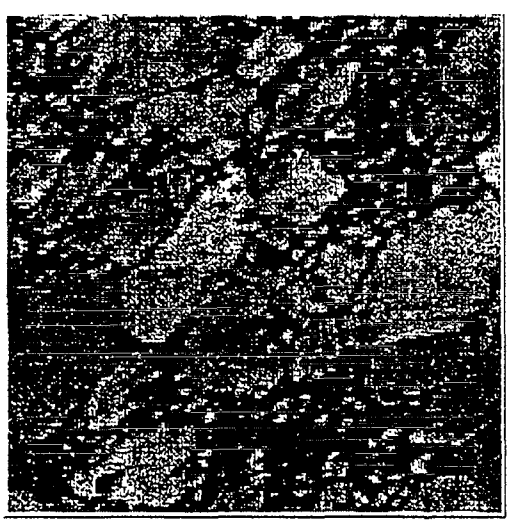

Fig. 3 Band contrast image. 150x150 measurements. Image side length is 25 micron. Image is located 1 mm from the periphery.

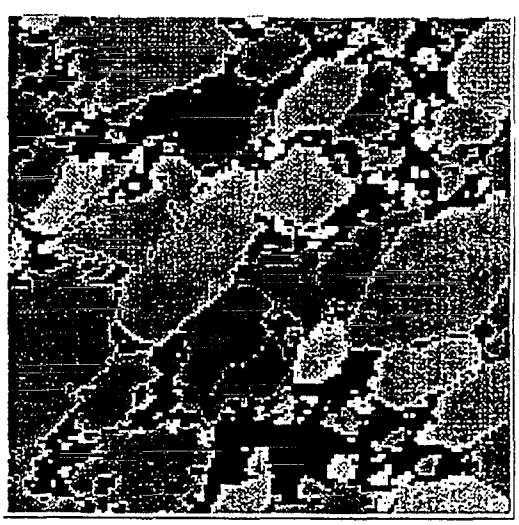

Fig. 4 True Euler angle image. 150x150 measurements. Image side length is 25 micron. Image is located 1 mm from the periphery.

means that it is not possible to automatically index the patterns. In the automatic measurement these points show up as not indexed and having a relatively low band contrast. Pores are also not indexed, but have an even lower band contrast (close to 0). The orientation of the sub grains appear to be completely random, see Figure 9.

In parts of the specimen where the sub grain formation has not yet started, the lattice is strained but the orientation remains approximately the same, see Figures 1 to 4. Points measured in these areas show up as having the same or only slightly distorted orientation as

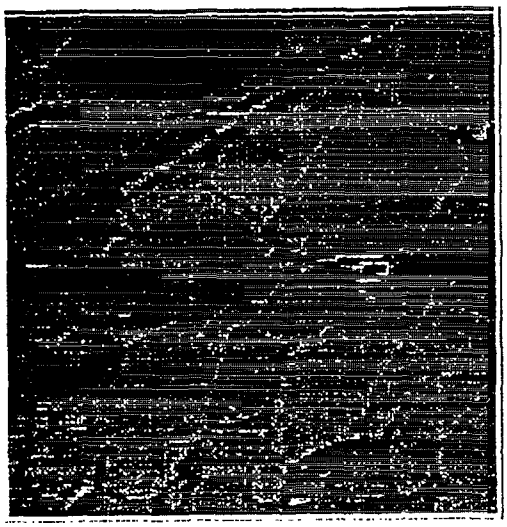

Fig. 5 Band contrast image. 150x150 measurements. Image side length is 25 micron. Unirradiated specimen. Notice image mismatch between the upper and lower halves due to charging during the measurement.

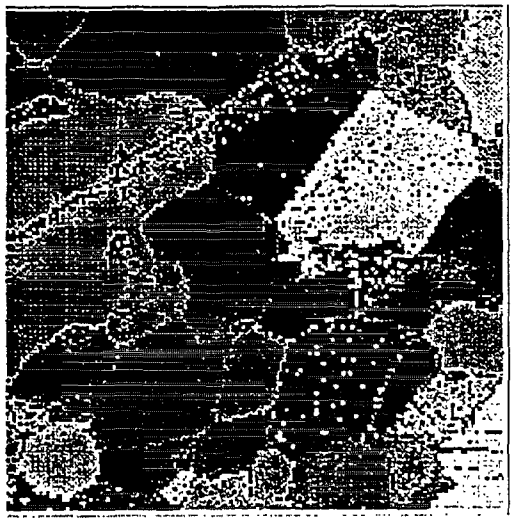

Fig. 6 True Euler angle image. 150 x 150 measurements. Image side length is 25 micron. Unirradiated specimen.

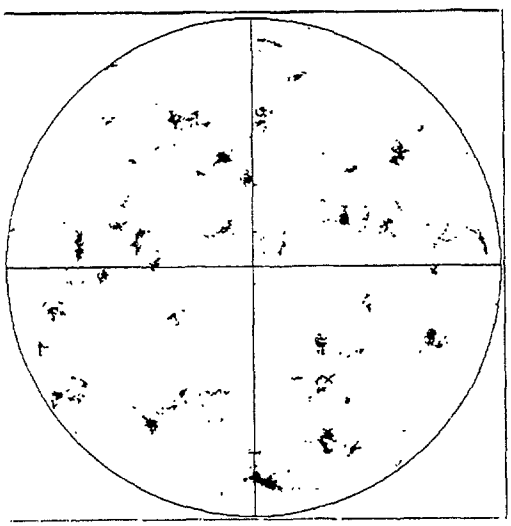

Fig. 7 {001} pole figure. Measurements are performed in a 100x100 grid pattern approximately 0,34 mm from the periphery resulting in 5218 valid data points.

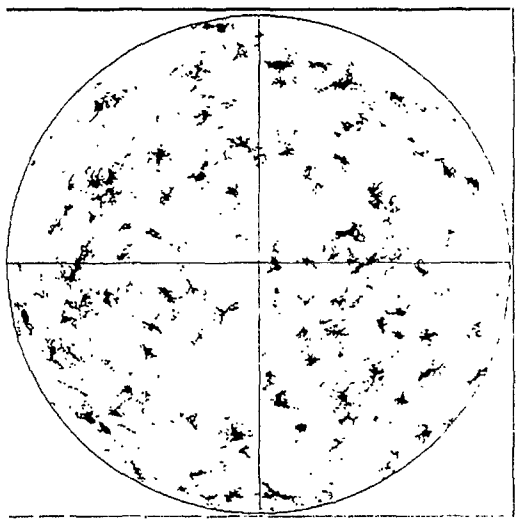

Fig. 8 {001} pole figure. Measurements are performed in a 150x150 grid pattern approximately 1 mm from the periphery resulting in 17059 valid data points.

the rest of the grain it belongs to and a band contrast that is decreasing towards the grain edge. The difference in orientation between positions on one side of a grain to the other can be as large as 9.

Figure 1 shows the band contrast map of a measurement performed 0,34 mm from the periphery. In this map not many "normal" grain boundaries can be found. Typical grain boundaries can be seen in the band contrast map from the unirradiated specimen, see Figure 5. The sub grains has caused the band contrast to be lower and the automatic indexing has not

been successful in large parts, see Figure 2. Further into the pellet, at 1 mm from the periphery, the extent of the sub grain formation is not so severe. It can also be seen that the sub grain formation starts at some grain boundaries, while others are left unaffected.

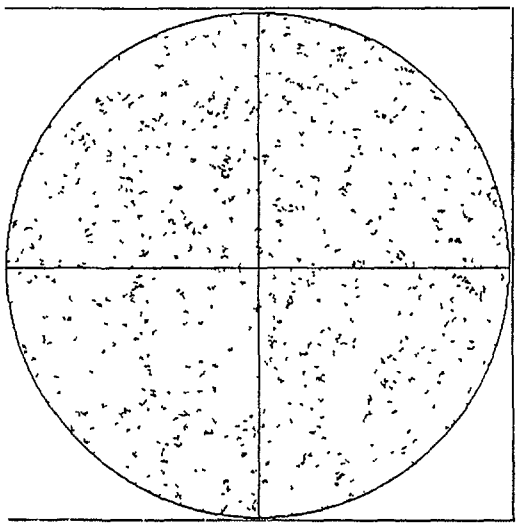

Fig. 9 {001} pole figure. Measurements are performed in a 150 x 150 grid adjacent to the periphery resulting in 1910 valid data points.

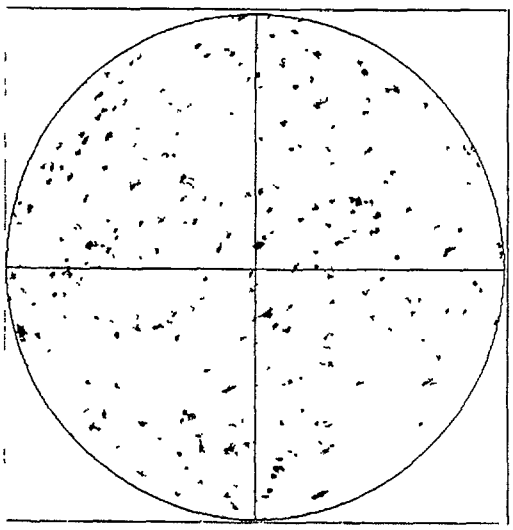

Fig. 10 {001} pole figure. Measurements are performed in a 150 x 150 grid on an unirradiated fuel sample resulting in 20309 valid data points.

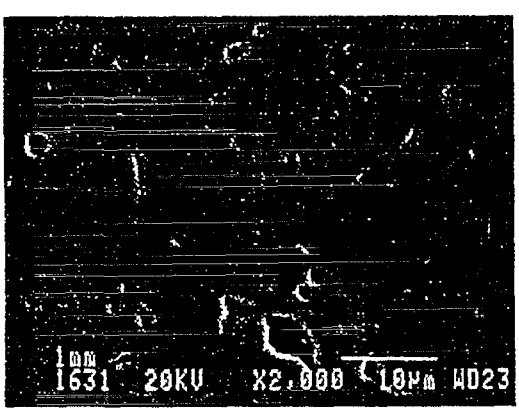

Fig. 11 Secondary electron image. Image is located approximately 1 mm from the periphery.

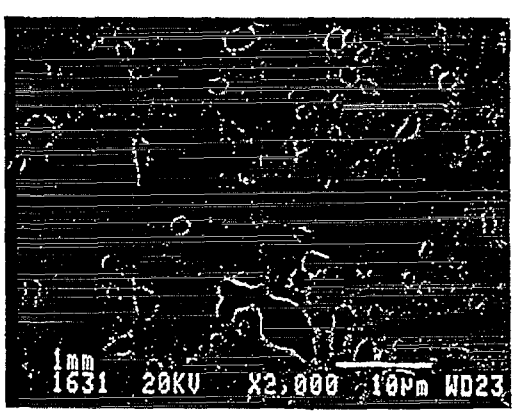

Fig. 12 Backscattered electron image. Image is located approximately 1 mm from the periphery.

Near the periphery the pole figure shows a random orientation, see Figure 9. However, the measurement was not completely successful with only 8% indexed patterns. The difficulty in indexing the patterns are caused by the size of the sub grains, the porosity (≈15%) and poor preparation. The sample was coated with gold for a previous experiment and the removal of the coating was not completely successful in all positions.

As a measure of the surface sensitivity and inherent properties of the EBSP method it can be noted that in Figure 6 a trace of a polishing (or grinding) scratch can be found. This trace cannot be seen in the optical microscope or in the secondary electron image. The trace consists of cold deformed material below the surface of the polished pellet.

4. CONCLUSIONS

- The EBSP method is capable of identifying the sub-grains. Qualitative information on the strain in the lattice can also be obtained. Maps of orientation and pattern quality information can be used to correlate diffraction parameters to specific locations in the microstructure.
- The development of the high burnup structure in the examined sample is complete at periphery. The orientation of the restructured grains is completely random.
- At 0,34 mm from the periphery the HBS formation is only partial. However, almost all grain boundaries are affected
- At 1 mm from the periphery the HBS has only developed on certain grain boundaries. It is estimated that approximately 50% of the grain boundaries are affected.

REFERENCES

[1] BARNER, J.O., CUNNINGHAM, M.E., FRESHLEY, M.D., LANNING, D.D., Evaluation of fission gas release in high-burnup light water reactor fuel rods, Nuclear Technology 102 (1993) 210-231.

[2] LASSMANN, K., WALKER, C.T., VAN DE LAAR, J., LINDSTRÖM, F., Modelling the high burnup UO2 structure in LWR fuel, Journal of Nuclear Materials 226 (1995) 1-8

[3] MATZKE, HJ. On the rim effect in high burnup UO_2 LWR fuel, Journal of Nuclear Materials 189 (1992) 141-148.

[4] SPINO, J., VENNIX, K., COQUERELLE, M., Detailed characterisation of the rim microstructure in PWR fuels in the burnup range 40-67 MWd/kgU, Journal of Nuclear Materials 231 (1996) 179-190

[5] REST, J., HOFMAN, G.L., Dynamics of irradiation-induced grain subdivision and swelling in U3Si2 and UO2 fuels, Journal of Nuclear Materials 210 (1994) 187-202

[6] WALKER, C.T., KAMEYAMA, T., KITAJIMA, S., KINOSHITA, M., Concerning the microstructure changes that occur, at the surface of UO_2 pellets on irradiation to high burnup, Journal of Nuclear Materials 188 (1992) 73-79

[7] NOGITA, K., UNE, K. Irradiation-induced recrystallisation in high burnup UO_2 fuel, Journal of Nuclear Materials 226 (1995) 302-310

[8] LASSMANN, K., O'CARROLL, C., VAN DE LAAR, J., WALKER, C.T., The radial distribution of plutonium in high burnup UO_2 fuels, Journal of Nuclear Materials 208 (1994) 223-231

AN ATTEMPT TO SIMULATE THE POROSITY BUILDUP IN THE RIM AT HIGH BURNUP

D. BARON
Direction des études et recherches,
Electricité de France,
Moret-sur-Long

B. HERMITTE
University of Marseilles,
Marseilles

J.P. PIRON
CEA Centre d'Etudes de Grenoble,
Grenoble

France

Abstract

The "rim effect" was identified fifteen years ago with the examination of the first rods irradiated over 45 GWd/tU (pellet average burnup) in test reactors as well as in power plants. Detailed PIE have shown a progressive disappearance of the grain structure in the fuel periphery, in relation with a strong increase of the porosity.

A scenario for the rim buildup at high burnup is proposed. Regarding the role of the porosity on the evolution of the physical properties, the first step has been an attempt to simulate the fission gas behaviour in the rim. In the proposed model, bubble growing is related to the volume fraction of the fuel restructured. An assumption is made on the creation of short cuts, increasing the average Xenon diffusion rate at very short distances. This model allows to evaluate the pore volume fraction in the fuel, the mean size of these pores and the fission gas volume repartition within the bubbles and the fuel matrix.

The model presented herein was issued in the framework of a PhD, held on May 31st. 1996 in the Marseille II University by Dr. Bruna HERMITTE.

1. INTRODUCTION

The "rim effect" was identified fifteen years ago with the examination of the first rods irradiated over 45 GWd/tU (pellet average burnup) in test reactors as well as in power plants. Detailed PIE have shown a progressive disappearance of the grain structure in the fuel periphery, in relation with a strong increase of the porosity. Radial fission products profiles obtained in EPMA revealed an apparent Xenon depletion at the pellet edge. The trend was confirmed on the HBEP fuel rods examined within the task 2. This singular behaviour enable to expect a drastic modification of the fuel properties in this region and could explain part of the fission gas release enhancement observed above 45 GWd/tU, even for rods operating at very low power during the 4^{th} and the 5^{th} cycles [1].

Further and more accurate investigations were conducted since 1986, firstly within the HBEP task 3, then in the TUI and in NFD, but also in our national laboratories. Many of these

works have been since published, owing a better understanding of the mechanisms involved in the rim buildup. For instance, MEB investigations have shown that over a local burnup threshold, a low temperature fuel restructuring is activated, leading to a grain subdivision and a final "cauliflower" aspect, with an average grain size of 0,1 to 0,3 μm [17]. At the same time the fuel restructuring starts, a large amount of coarsened voids of about 0,5 to 1μm size appear. Bubbles of such a size are theoretically unexpected regarding the very low fission gases diffusion rate at rim temperature and the permanent resolution process induced by the irradiation. It has been pointed out by J.SPINO [17] that these voids are the germs around which restructuring propagates.

Based on these observations we propose a scenario for the rim buildup over a local burnup of 58 GWd/tU. Regarding the role of the porosity on the evolution of the physical properties, the first step was to elaborate a simulation of the fission gas behaviour in the rim. In the proposed model, bubble growing is related to the volume fraction of the fuel restructured. An assumption is made on the creation of short cuts, able to increase the apparent Xenon diffusion rate at short distances. This model allows to evaluate the pore volume fraction in the fuel, the mean size of these pores and the fission gas volume repartition within the bubbles and the fuel matrix.

2. RIM FORMATION

At the beginning of the eighties, EDF and FRAMATOME decided to reload four standard fuel assemblies for a fourth and fifth cycle in the FESSENHEIM 2 nuclear plant. These four assemblies contained a low initial enrichment fuel (3,2 %) and were located at the center of the core during these two additional cycles. The power rate was then quite low : respectively 160 and 140 W/cm at the fourth and fifth cycle. Despite these low power rates, puncturings pointed out an enhancement of the fission gas released with 0,45 % FGR at 45 Gwd/tM rod average burnup and 1,2 % FGR at 55 Gwd/tM. This indicates that a physical threshold was passed. Furthermore, the ceramographic examinations exhibited a high density of inter and intragranular thin porosity in the 100 last micrometers of the pellet periphery [1].

The presentation of such observations in a HBEP (High Burnup Effect Program) steering committee in WENGEN in June 1985 led to change partially the objectives of the program. A great number of investigations were then conducted to better characterize this phenomena induced in the pellet periphery at high burnup and low temperature (<850°C). The rim effect was detected above 45 GWd/tM. The highest peak pellet burnup was reached in a CEA-FRAMATOME rod of the HBEP program (rod BK365), irradiated in the BR3 test reactor in Mol, with a pellet average burnup of 83 GWd/tM. Many communications refer to this fuel rod : [2], [3], [4] and [5].

2.1 Observations

Two stages have been determined in rim formation. The first can be observed on an optical ceramography, characterised by the onset of a high density of thin porosities with a size about 0,5 to 2 μm, giving a dark aspect to the pellet outer rim. At the same time, a radial Xenon profile obtained from an EPMA exhibits a Xenon depletion in this zone. Obviously, that doesn't mean that all the Xenon missing is released but that part of the Xenon is not detectable by EPMA. Indeed the EPMA investigation depth, about 1μm is not enough to detect the Xenon located in buried bubbles.

The evaluation of the relative porosity volume obtained by image analysis gives different values depending on the laboratories. S.PATI [10] gives an average value of 22% porosity measured in the rim region for several fuel pellets got from different rods. On Framatome standard 5 cycles PWR rods, the average rim width optically evaluated was about 250 μm [12]. This is consistent with the value of 300 μm found from EPMA. The limit of the rim region is defined from the Neodymium and the Xenon profiles, where the two profiles intercept. The relative porosity measured in the 30 first rim micrometers where the local burnup is very similar to those reported by Dr. PATI, was about 15 %.

With increasing burnups, a disparity of the granular texture is observed. A scanning electronmicrograph observation reveals a cauliflower aspect with an apparition of subgrains with an average size about 100-300 nm and polygonal pores about 0,5 to 1μm diameter (figure 1A). This is representative of the "advanced rim stage", with a complete local restructuring of the fuel. *It has been shown by SPINO [8,17] that in the partially restructured zone, the porosities are* already formed and restructuring seems to propagate around these porosities (figure 1B).

Furthermore, these porosities look like cavities, more than spherical porosities. Indeed, the SEM pictures published by Dr. UNE [3] (figure 2) confirm a presence of coarsened bubbles in the rim. Dr. UNE has also shown that, as expected, the dislocation density increases sharply with burnup [2] in the low temperature fuel periphery, forming clusters at very high burnup, besides small bubbles of several nanometers and around precipitates of 15-30 nm. This leads to a dislocation density evaluated at 4.2 10^{15} m/m^3 at 83 GWd/tM, nearly 8 times the value measured at 44 GWd/tM. Nevertheless, this value has to be confirmed.

The average UO_2 lattice parameter reported by Dr. UNE and al [4], (figure 3) is increasing linearly with burnup up to 50 GWd/tU. Then the value measured seems to decrease between 50 and 60 GWd/tU and to stabilize above 60 GWd/tU. Such values, 50 to 60 GWd/tU, are the local burnup for which first rim restructuring appears. One can assume the subgrain lattice parameter to be partially restored. After restructuring, diffraction patterns done by THOMAS et al [9] indicate random grain orientations. It was confirmed by NOGITA [2]. In the diffraction pattern, besides the main spots of [2,2,0] of the UO_2 single crystal from [1,1,1] orientation, extra spots were seen. Each spot tends to streak and to form Debye rings. This is interpreted by the authors as a disorientation of the new subgrains, but could also be related to a partial UO_2 phase change.

Just after restructuring a TEM observation doesn't seem to reveal any more dislocation lines or gaseous pores within the new grains formed. That makes one consider that the defects are pushed out of the matrix during the restructuring process.

The last observation that can be related to rim formation is the deformation of the chanfrein reported by P.GUEDENEY [15] in Framatome PWR fuel rods, containing 4.5 % enriched UO_2 pellets and irradiated for 5 cycles in the GRAVELINE 2 plant (figure 4). One may expect an axial creep flow of the fuel in the rim region which requires a dislocation mobility at very high burnup. Obviously it must be representative of a long term creep.

2.2. Scenario for rim formation

Several interpretations of rim formation have been published. From Xenon implant experiments Dr MATZKE [14] concluded that the grain subdivision can be explained by the formation of highly pressurized Xenon bubbles at high local burnup (7 to 8 % FIMA). Indeed, it was demonstrated that an implant of Xenon at high dose promotes a cleavage fracture of UO_2

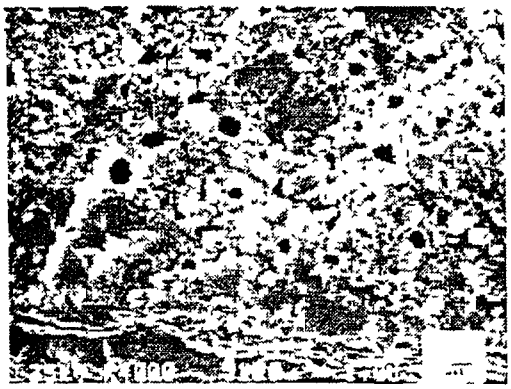

FIG. 1A. *SEM of the rim of a PWR fuel pellet with average burnup of 4.7 % FIMA (from [11])*

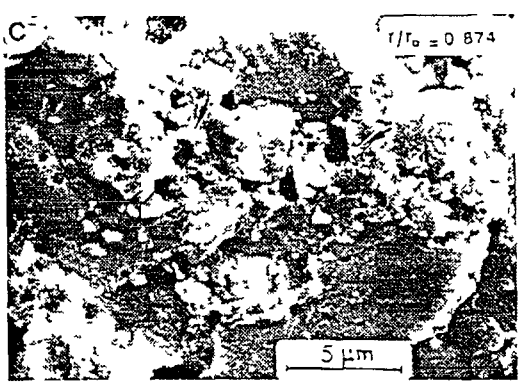

FIG. 1B. *Rim inner zone. Propagation of the restructuring around the porosities (from [17])*

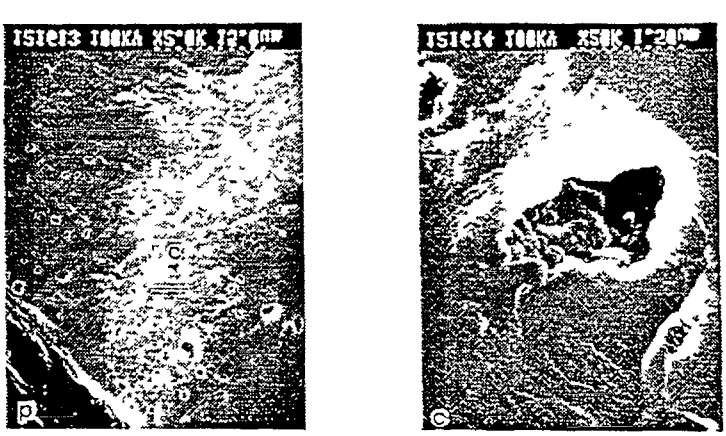

FIG. 2. *SEM images showing coarsened bubbles in the rim (from [3])*

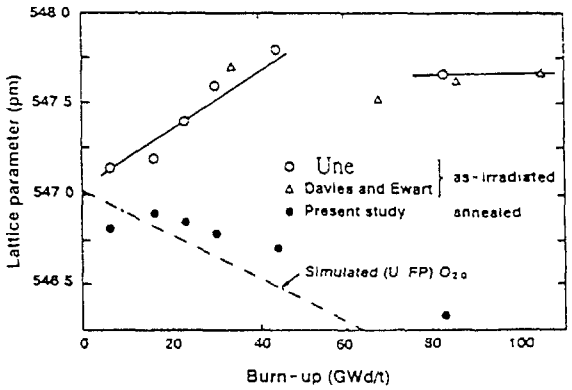

FIG. 3. *Burnup dependence of lattice parameter at the fuel periphery (r/r_0 = 0.8-1.0) of irradiated UO_2 (from [4])*

FIG. 4. *Deformation of the chanfrein at very high burnup (60 GWd/tU pellet average) (from [15])*

grains Nevertheless, the sub-grains lenticular shape obtained by this technique is somehow different of the coarsened sub-grains in the rim From TEM examinations and AUGER electron spectrometries, THOMAS [9] conclude to a burnup-induced instability of the UO_2, driven by the stored energy of fission products in solution

This phenomenon should be able to propagate with increasing burnup Widening this interpretations, UNE [2],[16] suggests that rim formation is directly related to the accumulation of radiation damage below 850°C. Above this temperature, the point defects can be almost recovered In the following paragraphs we propose a scenario for the rim formation not very far from Dr UNE and NOGITA's interpretation

Accounting for the low temperature in the fuel periphery, the Xenon diffusion coefficient is not sufficient for the gas atoms to move at long distance (from the average distance between nanobubbles the Xe atom free path can be assumed about 50 nanometers at rim temperature). Two or three atoms can join together in some preferential low energy sites and form nanometer

bubbles. These tiny bubbles are in perpetual creation and destruction due to the high density fission rate in this zone of the fuel (consequence of Uranium 238 self shielding effect and the formation of fissile plutonium nucleus).

Before the rim formation, apart the stable initial porosities, only numerous nanometer bubbles are able to accommodate gas atoms. Therefore, most of the gas is spread in interstitial and tri-vacancies sites in the lattice. Progressively these gas atoms, besides the other interstitial fission products and the great amount of vacancies, increase the lattice energy. When the lattice energy locally reaches a certain energy threshold, the mobility of the point defects increases, allowing their grouping in preferential sites at short distance, leading to a local stress relaxation of the lattice.

With the arrival of vacancies, located next to them, a certain number of nano-bubbles can reach a size of 6 to 8 nanometers, enough to stabilize. These stabilized bubbles, or more precisely cavities, are then able to pin dislocations, which moving at short distance are activated by the local stresses accumulated in the lattice. The surrounding of the bubble becomes a very perturbed zone where the binding energies are weakened. In these zones, point defects as the Xenon can diffuse more easily than in the matrix and be drained as well as the vacancies toward the central bubble. These zones act as "diffusion short-cuts" and the central polygonal cavities can therefore grow.

Dislocation clusters are able to form in the surrounding, creating progressively dislocation walls, subdividing locally the grain in the neighbourhood next to the cavity. These dislocation clusters drain then continuously the point defects, allowing a local purification of the matrix between this dislocation walls. After a while, the local lattice is able to rotate in order to relax the stresses along the dislocation walls. A new subgrain appears subsequently, with the creation of new sub-grain boundaries.

Once again, these subgrain boundaries are able to drain in their direct neighbourhood the point defects. New Xenon and vacancies can diffuse again more easily and feed the central cavity. With the repetition of such a process, the restructuring can propagate around these cavities as far as all the grain volume is not completely restructured.

2.3 Basis for the modelling

Following this interpretation, the model proposed is based on the local description of the fuel in two zones, the original matrix, where the Xenon diffusion coefficient is negligible (classic diffusion), the restructured zone characterized by a higher Xenon diffusion coefficient (preferential diffusion).

Before the grain subdivision, Xenon is located in interstitial position or tri-vacancies sites. It can agglomerate to form nanometric bubbles (5-10 nm). The lattice energy increases with defects accumulation. An energy threshold is defined above which restructuring can operate in order to relax the internal stresses. Two bubble populations are to be considered: the nano-bubbles in the original matrix, able to be completely destroyed by fission spikes, and the bubbles on dislocation surfaces able to grow, thanks to the preferential diffusion in this zones.

The model accounts only for the second population. The first population is integrated in the gases spread in the original matrix. The average bubble radius is then growing with the expansion of the dislocation surfaces. An apparent diffusion coefficient is defined as :

$$D_{app} = (1 - f_s). D_{vol} + f_s. D_{sc}$$

where D_{vol} is the Xenon volumic diffusion coefficient in the original crystal,
D_{sc} is the Xenon diffusion coefficient in diffusion "short-cuts",
f_s is the fraction of Xenon present in the restructured surfaces.

3 - DESCRIPTION OF THE MODEL

3.1 - Diffusion coefficient used in the model

3.1.1 - Vacancy diffusion coefficient in the UO_2 matrix

The expression used [18] is very close to the formulation developped for the Uranium atom autodiffusion coefficient. The displacement of an atom A in the sub-lattice A create a vacancy site. Therefore, the migration of the defect is indeed equivalent to the autodiffusion of the atomic specie. The expression retained for the vacancy diffusion coefficient is then :

$$D_v = 1.09.10^{-4}.\exp\left[-\frac{52900}{T}\right] \qquad (1)$$

with D_v in m^2/s, and the temperature T in Kelvin. Nevertheless, if the thermal activation is preponderant in the hottest part of the fuel pellet, it must be different in the rim. Unfortunately, no athermal term or mixed term are clearly available in the open literature.

3.1.2 - Xenon volumic diffusion coefficient

The Xenon diffusion coefficient in the fuel matrix under irradiation can be described with three terms representing the temperature contribution, the activation by fission fragments collidings (athermal term) and the influence of the vacancies creation under irradiation (mixed term) [19],[20] and [21] :

$$D_{Xe} = D_{th} + D_{ath} + D_{mix}$$

with the temperature contribution :

$$D_{th} = 7.6.10^{-10}.\exp\left[-\frac{35225}{T}\right] \qquad (2)$$

the athermal contribution :

$$D_{ath} = 6.10^{-40}.\dot{F} \qquad (3)$$

and finally the mixed term for vacancies :

$$D_{mix} = 1.39.10^{-24}.\frac{\sqrt{\dot{F}}}{2}\exp\left[-\frac{13870}{T}\right] \qquad (4)$$

D_{th}, D_{ath} and D_{mix} are in m^2/s, $\dot{F}$ is the local instantaneous number of fissions in the fuel per volume unit

3.1.3 - Xenon diffusion coefficient in the perturbed fuel zone

No works are presently available to evaluate the diffusion coefficient in the restructured zone. Therefore the assumption made is that this coeffient is the previous coefficient D_{xe} multiplied by a fitting factor λ :

$$D_{Xes} = \lambda . D_{Xe} \tag{5}$$

Where D_{Xes} is the diffusion coefficient in the perturbed zone (m^2/s) and λ is fitted to 100.

3.2 - Detailed steps in the resolution

3.2.1 - Evaluation of the lattice energy

The average lattice energy is assumed to evolve linearly with the local burnup. It is obviously strongly related to the local temperature, depending on the capacity of the defects to be recovered. The lattice energy is formulated as follow :

$$E^* = Cte * BU * f(T) \tag{6}$$

Where Cte is a constant, presently fitted at 10^4 and f(T) represents the ratio between the steady state bubble volumic concentration at a temperature T and the same at 573.15 K. This reference temperature is representative of the average cladding temperature at which the defects can be considered quasi motionless. So, f(T) can be formulated :

$$f(T) = \frac{g_\infty^T}{g_\infty^{573.15}} = \frac{D_{Xe}^T}{D_{Xe}^{573.15}} * \frac{\left(k_e . z_{nvv} . D\right)^{573.15}}{\left(k_e . z_{nvv} . D\right)^T} \tag{7}$$

The different terms in this expression are detailed further in the presentation when the evaluation of the bubble volumic concentration versus time is needed.

3.2.2 - Evaluation of the subdivided area

Assuming the fuel partly restructured with an intact zone and a zone where grains are subdivided, the global energy per volume unit can be written as follow :

$$E = E_f * \frac{V_r}{V_0} + E^* \left(1 - \frac{V_r}{V_0}\right) \tag{8}$$

where V_0 and V_r are respectively the total volume (stressed zone with an energy E^* + restructured zone with an energy E_f) and the volume restructured where stresses are relaxed. As far as the lattice energy E is below the threshold energy E_s (for an initiation of the restructuration), then $E = E^*$, the lattice accomodate the distortions generated by the fission spikes. E is a fonction of the temperature and cumulated burnup. When E is higher than E_s, the fuel fraction restructured is evaluated as follow :

$$\frac{V_r}{V_0} = \frac{a_s * S}{3} \tag{9}$$

where a_s is the average subgrain size after relaxation and S the surface by volume unit concerned by the relaxation (subdivided area). The energy threshold, E_s is experimentally fitted (a value of 6.0 10^8 $J.m^3$ have been fixed). Using the standard expression of the energy formation of a spherical cavity :

$$E_{cf} = 2 * S * \gamma \tag{10}$$

with γ as the surface tension parameter taken equal to 0,626 $J.m^{-2}$. One can then estimate the energy variation related to the formation of the S surface, writting the difference between the zone energy before and after the subdivision :

$$d\left\{E^*(1-\frac{V_f}{V_0})-E_f*(1-\frac{V_f}{V_0})\right\}=2.\gamma.dS \qquad (11)$$

then

$$2.\gamma.dS=\left(1-\frac{a_s.S}{3}\right)dE^*+\frac{a_s}{3}\left(E_f-E^*\right).dS \qquad (12)$$

after integration it comes :

$$S=\frac{3}{a_s}.\left\{1-\frac{Cte}{2\gamma+\frac{a_s}{3}.(E^*-E_f)}\right\} \qquad (13)$$

if S=0, $E^*=E_s$ and Cte = $2\gamma+\frac{a_s}{3}(E_s-E_f)$; one can then establish the following expression for $E \geq E_s$:

$$S=\frac{3}{a_s}.\left\{1-\frac{2\gamma+\frac{a_s}{3}.(E_s-E_f)}{2\gamma+\frac{a_s}{3}.(E^*-E_f)}\right\} \qquad (14)$$

The lattice energy after relaxation must be lower than the threshold energy E_s. Nevertheless there is presently a lack in the data provided, for an accurate evaluation of this energy level. Then, in first approximation, the problem can be simplified assuming $E_f = E_s$ The expression of S becomes (in m^2/m^3) :

$$\boxed{S=\frac{3}{a_s}.\left\{1-\frac{2\gamma}{2\gamma+\frac{a_s}{3}.(E^*-E_s)}\right\}} \qquad (15)$$

The surface fraction subdivided f_s is deducted as follow :

$$\boxed{f_s=S.\frac{a_s}{3}} \qquad (16)$$

a_s the average subgrain size is assumed about 7.5 10^{-8} m

3.2.3 - Determination of the bubble volumic concentration

The evolution of the volumetric concentration g of the gas bubble, in the rim zone, can be written with three components : the bubble creation term T_1, the bubble thermal annealing term T_2 and the resolution term due to fission spikes T_3 :

$$\frac{dg}{dt}=T_1-(T_2+T_3) \qquad (17)$$

Presence of dislocations in the matrix favours Xenon precipitation in trapping sites. Then T_1 can be formulated as follow :

$$T_1 = z_d.\rho_d.D_{Xe}.C_{Xe}^{hb} \tag{18}$$

where

z_d number of free sites next to the dislocation (3 to 6),

ρ_d dislocation density in fresh fuel before irradiation,

D_{xe} Xenon volumic diffusion coefficient in the matrix (m^2/s),

C_{Xe}^{hb} volumic concentration of intragranular gas atoms in the lattice ($atom/m^3$)

The second term limits the number of germs because of the partial temperature annealing of the defects on which atoms can be trapped. This term becomes very significative at high temperatures but is negligible in the rim where temperatures are lower.

$$T_2 = k_e.z_{nv}.D_v.g \tag{19}$$

k_e constant for defects thermal elimination rate (fitting factor)

z_{nv} volumic concentration for vacancy clusters in the matrix (m^{-3}) (10^{25} m^{-3})

D_v vacancies average diffusion coefficient (m^2/s)

g volumic concentration of gas bubbles ($bulles/m^3$)

The last term is related to the bubble average radius. Its expression is based on the TURNBULL theory which consider a complete resolution of the bubbles with a radius below the minimum value required to be stable. This resolution is activated by the fission spikes when the fission fragment interacts with a resident bubble. If b is the probability for a bubble to be destroyed, the third term is related to the fission density and to the number of bubbles :

$$T_3 = b.\dot{F}.g \tag{20}$$

With this three terms, the detailed expression to calculate the time evolution of the bubble concentration within the fuel is :

$$\frac{dg}{dt} = \underbrace{z_d.\rho_d.D_{Xe}.C_{Xe}^{hb}}_{A_1} - \underbrace{(k_e.z_{nv}.D_v + b.\dot{F})}_{B_1}.g \tag{21}$$

If Δt is the time step, the g concentration at instant t is then :

$$\boxed{g^t = g^{t-\Delta t}.\exp(-B_1.\Delta t) + \frac{A_1}{B_1}.\{1 - \exp(-B_1.\Delta t)\}} \tag{22}$$

3.2.4 - Détermination of the Xenon volume fraction in the restructured volume

The following expression contains a generation term, characteristic of the gas flow drained toward this fuel zone, reduced of a resolution term corresponding to the macroscopic destruction of the smallest gas bubbles.

$$\frac{dG_{rv}}{dt} = \underbrace{\left(S.D_{Xe}.\frac{C_{Xe}^{hb}}{d}\right)}_{A_2} - \underbrace{\left(b.\dot{F}\right)}_{B_2}.G_{rv} \qquad (23)$$

where

G_{rv} Xenon volumic concentration in the restructured zones (moles/m^3)

C_{Xe}^{hb} volumic concentration of intragranular gas atoms in the lattice (moles/m^3)

D_{xe} Xenon volumic diffusion coefficient in the matrix (m^2/s),

d average distance of resolution for gas atoms in the lattice (m)

b probability of resolution for the bubbles

$\dot{F}$ fission rate (fiss/cm^3/s)

then, the Xenon concentration at instant t is obtained by :

$$\boxed{G_{rv}^{t} = G_{rv}^{t-\Delta t}.\exp(-B_2.\Delta t) + \frac{A_2}{B_2}.\{1-\exp(-B_2.\Delta t)\}} \qquad (24)$$

remark : if t ---> ∞, G_{rv} ---> $\frac{A_2}{B_2} = \frac{S.D_{Xe}.C_{Xe}^{hb}}{d.b.\dot{F}}$

The mole fraction f present in the short cuts is then :

$$\boxed{f = \frac{S.D_{Xe}}{d.b.\dot{F}}} \qquad (25)$$

3.2.5 - Determination of the Xenon mole concentration in bubbles

As for the bubble concentration, the time evolution of the Xenon concentration in the bubbles can be written as the combination of three components : the bubble alimentation by the two diffusion processes described above (bulk diffusion and short cuts)(T_1), the gas contained in the bubbles created during the time step Δt (T_2) and a resolution term (T_3), macroscopic (TURNBULL) and microscopic (NELSON).

$$\frac{dC_{Xe}^{b}}{dt} = T_1 + T_2 - T_3 \qquad (26)$$

where C_{Xe}^{b} the Xenon atom concentration within the bubbles (moles/m^3)

For the formulation of the first term one can refer to OLANDER [23]. The retained expression is :

$$T_1 = 4\pi.R.D_{app}.(C_{Xe}^{tot} - C_{Xe}^{b}).g \qquad (27)$$

where

R average bubble radius (m)

D_{app} apparent Xénon diffusion coefficient (m^2/s)

C_{Xe}^{tot} total intragranular gas concentration (lattice+bubbles) (moles/ m^3)

C^b_{Xe} gas concentration in the bubbles (moles/ m^3)

g concentration of bubbles (bub/ m^3)

If N_0 is the minimum number of atoms for a bubble to be stable (a value of 2 is retained), and ($\Delta g.\Delta t$) the number of bubbles created during the time step Δt, the population of Xenon is increased of the following term :

$$T_2 = \frac{N_0}{\chi}\Delta g \Delta t = \frac{N_0}{\chi}(g^t - g^{t-\Delta t})\Delta t \qquad (28)$$

χ Avogadro number = 6,022045 10^{23}

The last term T_3 is the resolution term. Depending upon its size, a bubble can be totally or partly destroyed. In the first case, the fission fragment collides with a bubble and the gas atoms are spread in the surrounding matrix. As given above this term is :

$$T_3^t = b.\dot{F}.g \qquad (29)$$

This formulation is applied if $R \leq R_{bc}$ where R_{bc} is the maximum critical size of the bubble (R_{bc} fitted to 1.5 10^{-9} m). Above this size, the microscopic NELSON approach is more representative with the resolution of gas atoms in the bubble when a fission fragment collides with it. The bubble content can then decrease as collidings proceed, depending upon the alimentation term. The expression of the NELSON term is [23] :

$$T_3 = b_{re}.\eta_{re}.m \qquad (30)$$

where b_{re} is the probability per time unit for a gas atom in a bubble to get enough impact energy to reenter the matrix :

$$b_{re} = 2\mu_{ff}.\dot{F}.\ln\left(\frac{E_{ff}^{max}}{E^{min}}\right).\left(\frac{\pi.Z^4.e^4}{E_{ff}^{max}.E^{min}}\right) \qquad (31)$$

E_{ff}^{max} creation energy of the fission fragments (J)

E^{min} minimum energy for a Xenon atom for an effective resolution (J)

Z atomic number for Xenon = 54

e elementary electronic charge = 1.60219 10-19 Coulomb

μ_{ff}. fission fragments free path (m)

and η_{re} , the resolution yield:

$$\eta_{re} = 1 - \left\{1 - 15.10^{-10}.\left(\frac{1}{R} + \frac{1}{B}.\frac{kT}{2\gamma}\right)\right\}^3 \qquad (32)$$

k Boltzman constant = 1.3806624 10^{-23}

T gas temperature (K)

γ surface tension for the bubble (J/m^2)

R average bubble radius (m)

Finally, the evolution of the gas concentration in the bubble is ruled by the following equation :

$$\frac{dC_{Xe}^{b}}{dt} = 4\pi.R.D_{app}.(C_{Xe}^{tot} - C_{Xe}^{b}).g + N_0 \frac{\Delta g.\Delta t}{\chi} - T_3 \qquad (33)$$

if $R \leq R_{bc}$ $\quad T_3 = T_3^t$

if $R > R_{bc}$ $\quad T_3 = T_3^n$

The gas concentration in bubbles at instant t is (in moles/m^3) :

$$\boxed{C_{Xe}^{b} = \left(C_{Xe}^{b}\right)_{t-\Delta t}.\exp(-A_3.\Delta t) + \frac{B_3}{A_3}\left\{1 - \exp(-A_3.\Delta t)\right\}} \qquad (34)$$

with :

$$A_3 = 4\pi.R.D_{app}.g_{t-\Delta t} + T_3$$

$$B_3 = 4\pi.R.D_{app}.C_{Xe}^{tot} + N_0 \frac{\Delta g.\Delta t}{\chi}$$

3.2.6 - Average bubble radius

Solving the reduced Van Der Waals equation describing the thermodynamic state of the gases in the bubbles, one can evaluate the average bubble radius :

$$p.(V_{eff} - mB) = m.k.T \qquad (35)$$

or

$$(P_{ext} + \frac{(2\gamma + \alpha.G.b)}{R}).(\frac{4\pi.R^3}{3m} - B) = k.T \qquad (36)$$

where

P_{ext} is the hydrostatic pressure (Pa)

γ surface tension for the bubble (J/m^2)

α ratio coefficient

G shearing coefficient (Pa)

b lattice parameter (for UO_2, b = 5.475 10^{-10} m)

B the atomic volume of the Xenon atom = 85.10^{-30} m^3

m number of Xenon atoms per bubble

The tension $\frac{2\gamma}{R}$ at the bubble surface contributes to its stability. The second term $\alpha.\frac{G.b}{R}$ represents the distortion generated in the cristal lattice by the bubbles formation. The $1/\alpha$ is proportionnal to the number of vacancies flowing from the lattice towards the bubble. These vacancies participate to the bubble growing and a diminution of the internal

pressure. α must be proportionnal to $\frac{D_{Xe}}{D_{Xe}+D_v}$. Nevertheless, because we have no realistic data on the vacancies participation to the bubble stabilisation, α is taken presently equal to zero.

4. CONFRONTATION OF THE MODEL AGAINST OBSERVATIONS

The model predictions are presented for the major parameters in figures 5 to 9. First, figure 5 is a representation of the evolution of the fuel fraction restructured versus burnup Most of the restructuring is operating between 50 GWd/tU and 80 GWd/tU with a value of 80 % at 70 GWd/tU This is in accordance with the observations reported in reference [8] where a modification of the porosity is already observed for local burnup about 50 GWd/tU.

Figure 6 is a representation of the pore volumic concentration with a first singular point when restructuring starts and a second when the energy threshold is overpassed. The number of bubbles stabilize and their growing starts.

The average bubble radius (figure 7) evolves differently, depending on the local temperature, with a competition between resolution and bubble feeding. That explains why the 700 °C curve is above the 500 °C curve while the 800°C and 900°C curves are below. The average bubble radius is evaluated somewhere between 0.42 and 0.50 μm around 100 GWd/tU (0.84 and 1.00 μm diameter). These values are to be compared with the observations reported in reference [8], giving a pore distribution centered around 1.2 μm.

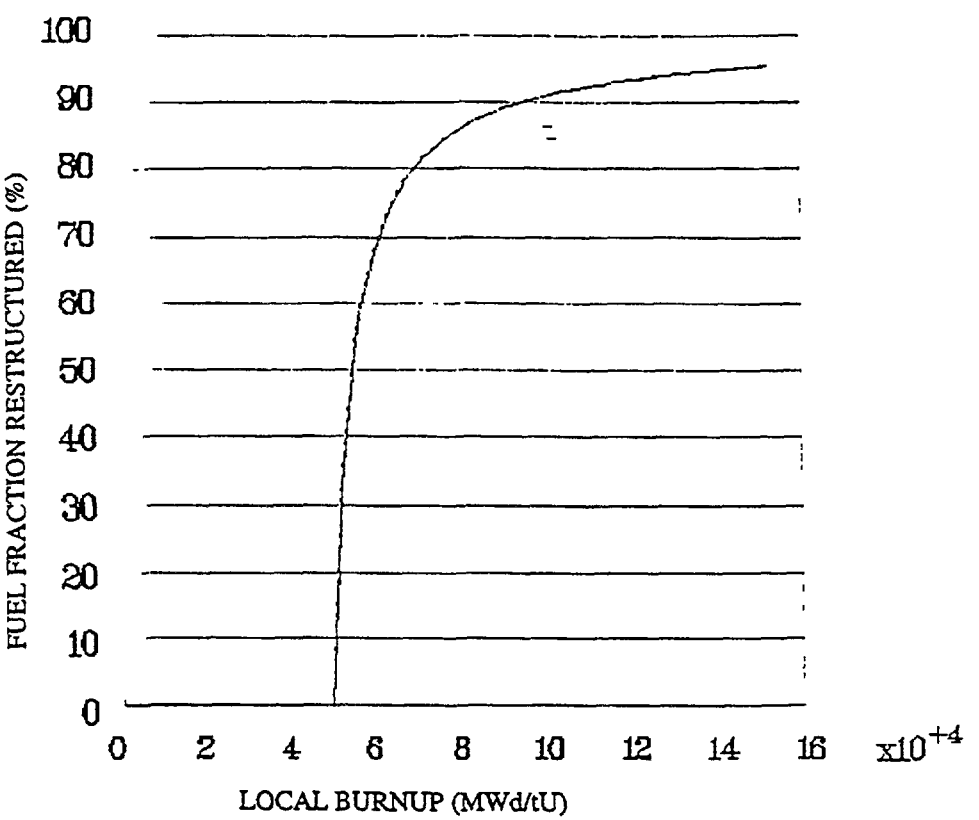

FIG. 5. Simulation of the fuel fraction restructured versus local Burnup

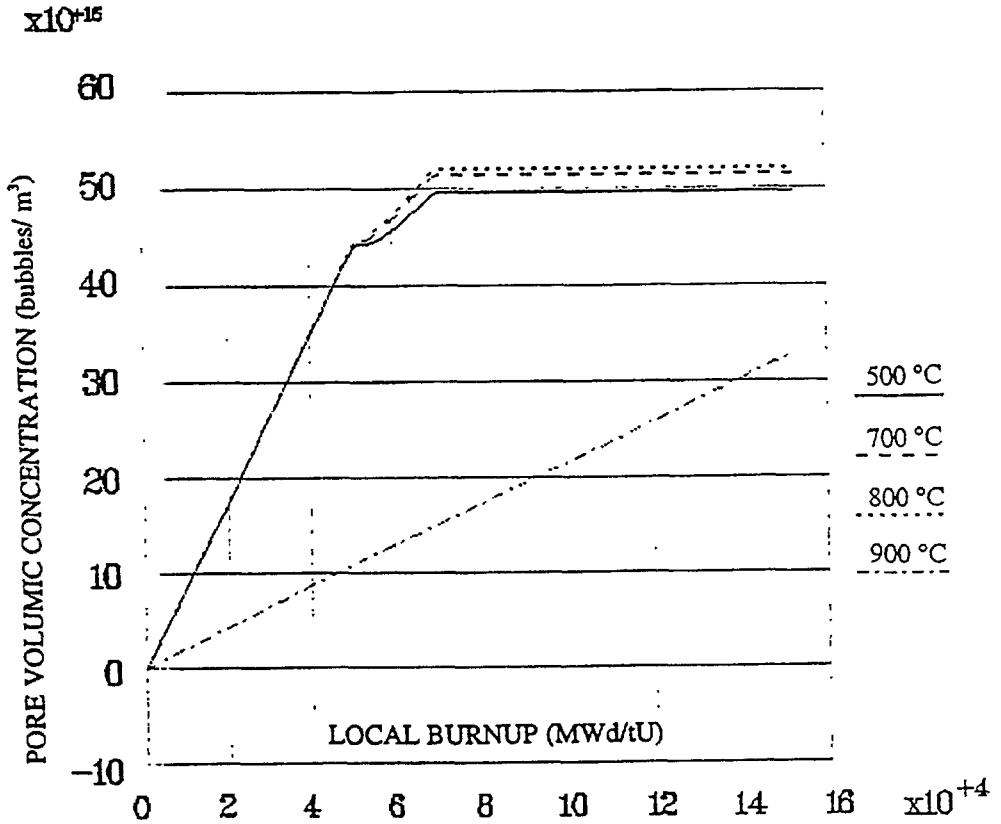

FIG. 6. Pore volumic concentration in the rim

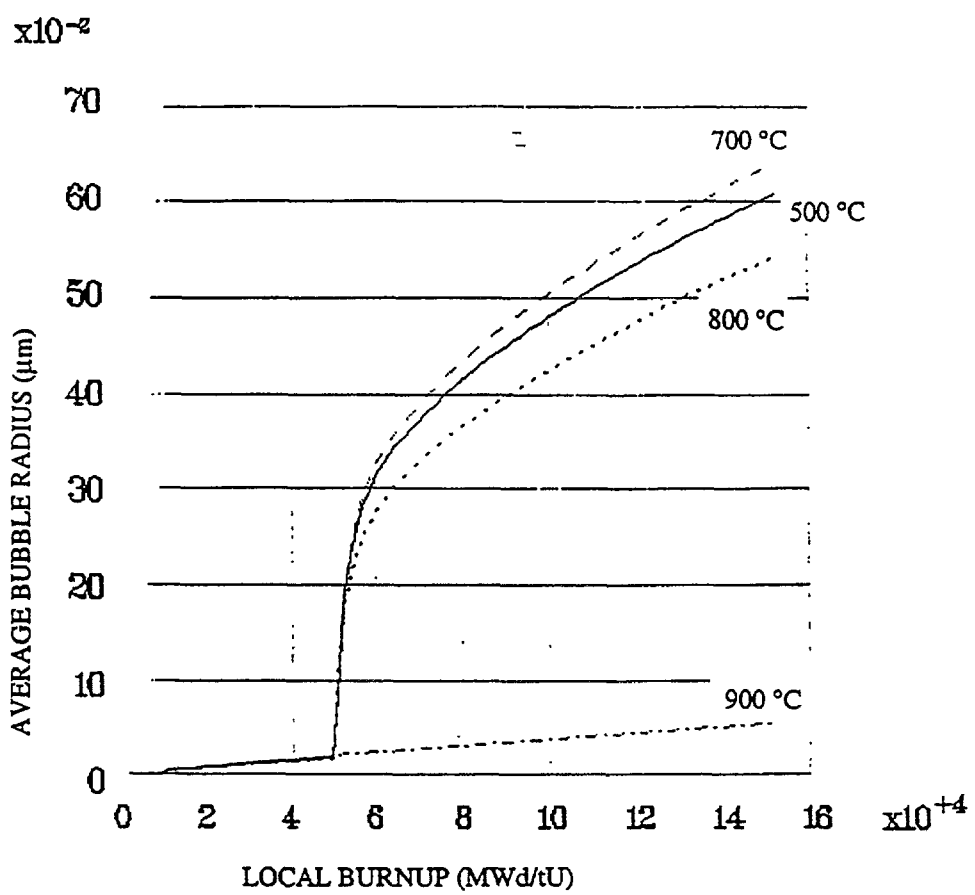

FIG. 7. Average bubble radius versus local burnup

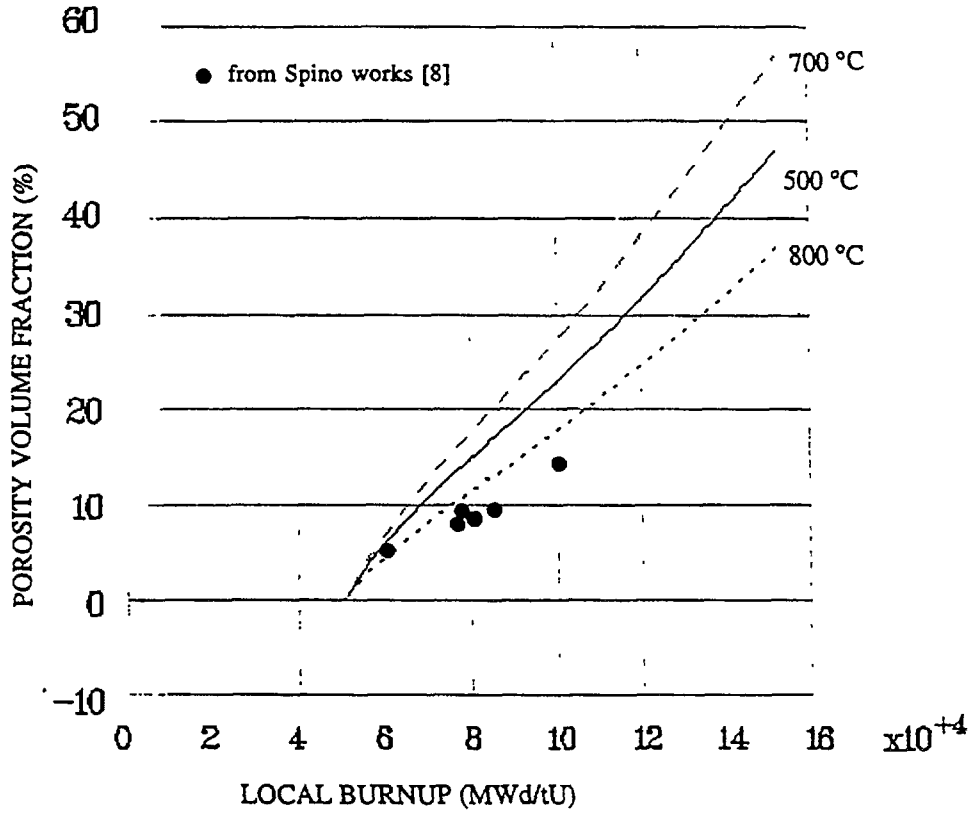

FIG. 8. Porosity volume fraction versus local burnup assuming no fission gas release

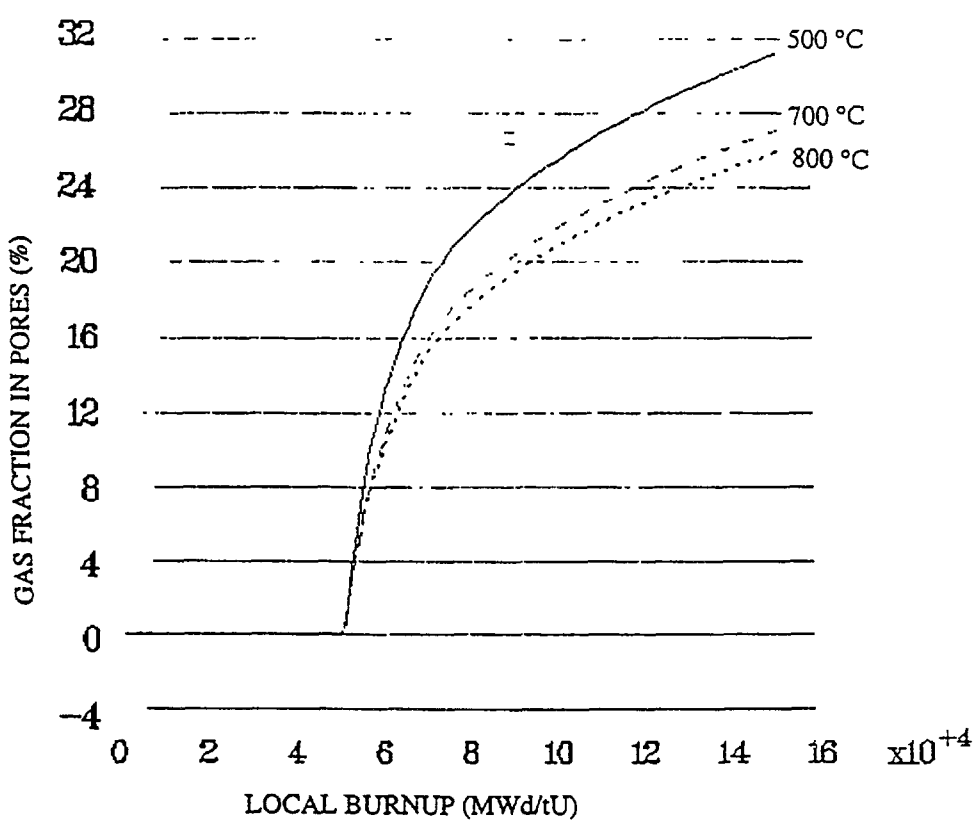

FIG. 9. Gas fraction in pores versus local Burnup

Another characteristic parameter is the porosity volume fraction. Various values are brought in the open literature. An accurate work has been conducted in TUI [8] giving an evolution of the pore volume fraction versus local burnup and for pellet average burnup ranging from 40.3 to 66.6 GWd/tU. The main conclusion was an apparent saturation of the porosity volume about 14 %. Figure 8 gives the prediction of the modelling for various temperatures. The values reported by SPINO for the 66.6 GWd/tU sample, for which the rim can be considered as almost formed, have been plot on the same graphic. The calculation gives an overestimation of the experimental data. Nevertheless, the modelling has been applied, assuming no fission gas release in the rim. Accounting for a local release, the porosity volume tend to decrease as shown on figure 10 and is more in accordance with the experimental values.

Figure 9 gives a the evolution of the fraction of gas in the pores. At 500 °C, a temperature representative of the pellet edge, the fraction of gas in the porosity is evaluated above 25 % at 100 GWd/tU. This amount, added to the gases released in the rim (about 15 to 18 % evaluated by our models) explains a lack of about 40 % of Xenon created in the pellet edge. This amount is compatible with the Xenon depletion observed on radial EPMA.

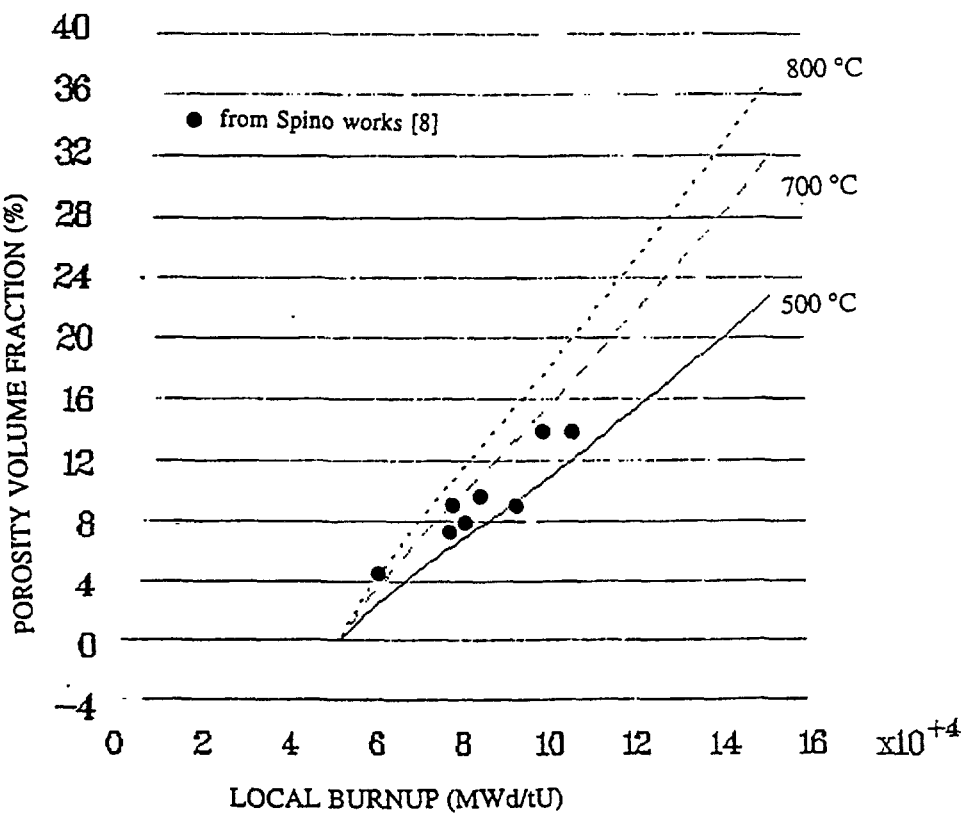

FIG. 10. Porosity volume fraction versus local burnup assuming an athermal fission gas release

5. CONCLUSIONS

The "rim effect" was identified fifteen years ago with the examination of the first rods irradiated over 45 GWd/tU (pellet average burnup) in test reactors as well as in power plants. Detailed PIE have shown a progressive subdivision of the original grains at the pellet edge, in

relation with a strong increase of the porosity. Despite the low temperatures in this region, cavities about 1 mm size are formed, surrounded by subgrains of 100 to 300 nanometers. Many observations have since been collected for a better understanding of the rim formation. Some programs are still undergoing such as the High Burnup Rim Project.

The fuel thermomechanical codes are obviously concerned and must be provided with models able to simulate the evolution of the materials properties. Many interpretations are already brought in the open literature. In this paper, a scenario has been retained for the rim buildup, based on a saturation process of the lattice by the irradiation defects at low temperature. In this approach, restructuring propagates around stabilized porosities able to trap gas atoms and vacancies, which diffusion is made easier by the local disorder of the matrix. Assumption is then made on the existence of short cuts, increasing the average Xenon diffusion rate at very short distances in the fuel zones in restructuring.

The formulation of a phenomenological modelling has been described. This model as been compared against experimental data. It allows to evaluate properly the pore volume fraction in the fuel, the mean size of this pores and the fission gas volume repartition within the bubbles and the fuel matrix.

The model presented herein was issued in the framework of a PhD, held on May 31st 1996 in the Marseille II University by Dr. Bruna HERMITTE [22].

REFERENCES

[1] BARON D., HOUDAILLE B, TROTABAS M., RAYBAUD A., Experience on Fission Gas Release in High Burnup Fuel Rods Operating in Power Plants, Fuel Rod IAEA TCM on Internal Chemistry and Fission Products Behaviour, KARLSRUHE, 11-15 November 1985.

[2] NOGITA K., UNE K., Radiation-induced Microstructural Change in High Burnup UO2 Fuel Pellets, Nuclear Instruments and Methods in Physics Research B 91 (1994) 301-306.

[3] NOGITA K., UNE K., Irradiation-induced Recrystallization in High Burnup UO2 Fuel, JNM 226 (1995) 302-310.

[4] UNE K., NOGITA K.,KASHIBE S., IMAMURA M., Microstructural Change and its Influence on Fission Gas Release in High Burnup Fuel, 188, (1992) pp 65-72.

[5] CUNNINGHAM M.E., FRESHLEY M., LANNING D.D., Development and Characteristics of the Rim Region in High Burnup UO2 Fuel Pellets, JNM,188 (1992) pp 80-89.

[6] BARNER J.O., CUNNINGHAM M.E., FRESHLEY M.D., LANNING D.D., Procedures International Topical Meeting on LWR Fuel Performance, Fuel for the 90's AVIGNON, France, Vol II(ANS/ENS,1991), pp 538.

[7] C BAGGER, M.MOGENSEN and C.T.WALKER, Temperature Measurements in High Burnup UO2 Nuclear Fuel : Implications for Thermal Conductivity, Grain Growth and Gas Release, JNM 211 (1994), pp 11-29.

[8] SPINO J., BARON D., Microstructure and Fracture Toughness Characterisation of Irradiated PWR Fuels in the Burnup Range 40-67 GWd/tU, Same IAEA TCM, TOKYO, Japan, 29 October to 1 November 1996;

[9] THOMAS L.E., BEYER C.E., CHARLOT L.A., Microstructural Analysis of LWR Fuels at High Burnup, 188, (1992) pp 80-89

[10] PATI S.R., GARDE A.M., CLINK L.J., Contribution of Pellet rim Porosity to low Temperature Fission Gas Release at extended Burnups, ANS Topical Meeting on LWR Fuel Performance, WILLIAMSBURG (Virginia), 1988, PP 204-215.
[11] WALKER C.T., TAMEYAMA T., KITAJIMA S., KONOSHITA M., Concerning the Microstructure Changes that occur at the Surface of UO2 Pellets on Irradiation to High Burnup, JNM 188 (1992) pp73-79.
[12] PIRON J.P., GEOFFROY G., MAUNIER C., BORDIN B., BARON D., Fuel Microstructure and Rim Effect at High Burnup, ANS Topical Meeting on LWR Fuel Performance, Palm Beach, April 1994.
[13] MANZEL R., EBERLE R., Fission Gas Release at High Burnup of the Pellet Rim, International ENS/ANS Topical Meeting on LWR Fuel Performance, AVIGNON, France, 21 au 24 Avril 1991.
[14] MATZKE Hj., On the Rim Effect in High Burnup UO2 LWR Fuels, JNM 189 (1992) pp 141-148.
[15] GUEDENEY P.,TROTABAS M., BOSCHIERO M., FORAT C., Fragema Fuel Rod Behaviour Characterization at High Burnup, International ENS/ANS Topical Meeting on LWR Fuel Performance, AVIGNON, France, 21 au 24 Avril 1991.
[16] NOGITA K., UNE K., Thermal Recovery of Radiation Defects and Microstructural Change in Irradiated Fuels, Journal of Nuclear Science and Technology, 30(9),pp900-910, September 1993.
[17] SPINO J., VENNIX K., COQUERELLE M., Detailed Characterisation of the Rim Microstructure in PWR Fuels in the Burnup range 40-67 GWd/tM, JNM (1996).
[18] HAWKINS R.J., ALCOCK C.B., A Study of Cation Diffusion in UO_{2+x} and ThO_2 using a Spectrometry, Journal of Nuclear Materials, 1968, vol 26, pp 112-122.
[19] TURNBULL J.A.,FRESHLEY M.D., LANNING D.D., The Diffusion Coefficients of Gaseous and Volatile Species during the Irradiation of UO_2, Journal of Nuclear Materials, 1982, vol 107, pp 168-184.
[20] REST J., HOFMAN G.L., Fundamental Aspects of Inert Gases in Solids, Eds S.E.Donelly and H.H.Evans, Plenum, New York, 1991, p 443.
[21] HARDING J.H.and MARTIN D.G., A Recommendation for the Thermal Conductivity of UO_2, Journal of Nuclear Materials, 1989, vol 166, pp 223-226.
[22] HERMITTE B., Etude et modélisation du rim dans le combustible des crayons REP, PhD held in Marseille II University on May 31st. 1996.
[23] OLANDER D.R., Fundamental Aspect of Reactor Fuel Elements, TID-26711-P1, Department of Nuclear Engineering, Berkeley, CA, 1976.

DISCUSSION

(Questions are given in italics)

Why is the energy accumulation E proportional to the "short cut" diffusion coefficient?*

In grain, the amount of local disturbance could be approximated to be proportional to the diffusion coefficient.

How can you explain a temperature drop of 200°C in the rim region? Porosity is not enough to explain such a degradation? It has been shown by Mr. Bakker that only 20-30 C can be explained by porosity buildup.

Our model does not consider measured porosity saturation at about 15% and thus might over-predict the effect of porosity. But based on the reported temperature drop of about 200°C by RISO, 20-30°C maximum temperature drop by porosity seems to be too small for rim.

DEVELOPMENT OF A THERMAL CONDUCTIVITY CORRELATION FOR THE PELLET RIM REGION AND ITS APPLICATION TO THE ANALYSIS OF BEHAVIOUR OF HIGH BURNUP FUEL

XA9847857

BYUNG-HO LEE, YANG-HYUN KOO, DONG-SEONG SOHN
Korea Atomic Energy Research Institute,
Taejon, Republic of Korea

Abstract

A thermal conductivity correlation has been proposed which can be applied to high burnup fuel by considering the degradation of thermal conductivity with burnup at pellet rim due to very high porosity. In addition, a correlation has been developed that can estimate the porosity of rim region as a function of rim burnup under the assumptions that all the produced fission gases are retained in the rim porosity and threshold pellet average burnup required for the formation of rim region is 40 MWD/kgU. Rim width is correlated to rim burnup using measured data.

For the RISO experimental data obtained at pellet average burnup of 43.5 MWD/kgU for three linear heat generation rates of 30, 35 and 40 kW/m, radial temperature distributions were calculated using the present correlation and compared with the measured ones. This comparison shows that the present correlation gives the best agreement with the measured data when it is combined with HALDEN's correlation for thermal conductivity which considers its degradation with burnup. another comparison with HALDEN's measured fuel centerline temperature as a function of burnup at 25 kW/m up to about 44 MWD/kgU also suggests that the present correlation yields the best agreement when it is combined with HALDEN's thermal conductivity.

1. Introduction

Rim region plays a significant role in heat flow as thermal barrier [1] which is characterized by the loss of optically definable grain structure and an increase in small intragranular porosity. Consequently rim effect has to be considered at high burnup fuel because high porous rim region induces an additional decrease in thermal conductivity.

In the present study, a thermal conductivity correlation considering both the thermal conductivity degradation with burnup and additional decrease in the rim region due to high porosity is developed to predict an accurate temperature distribution in a fuel rod.

2. Analysis method

2.1. Rim burnup and rim width

The rim which acts as thermal barrier develops in the periphery of pellet where local burnup is enhanced by plutonium production and fissioning in a low temperature [2]. To characterize the rim region, rim burnups are correlated from measured experimental results

[3,4]. As shown in Fig. 1, the rim burnup can be obtained from pellet-averaged burnup by least square method:

$$BU_{Rim} = 1.43 \cdot BU_{avg} \quad (1)$$

where BU_{Rim} is rim burnup and BU_{avg} average burnup of a pellet. A rim-to-average burnup ratio of 1.43 is consistent with the value measured in RISO project as well as with transport theory [5]. The threshold pellet average burnup for the formation of rim region is assumed to be 40 MWD/kgU.

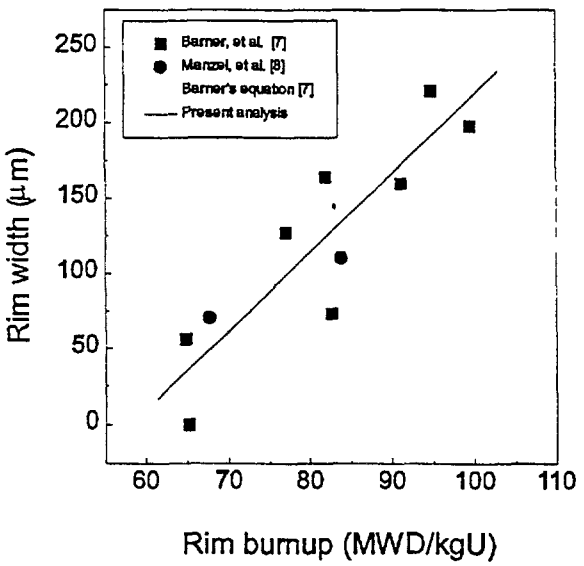

FIG. 1. Rim width as rim burnup

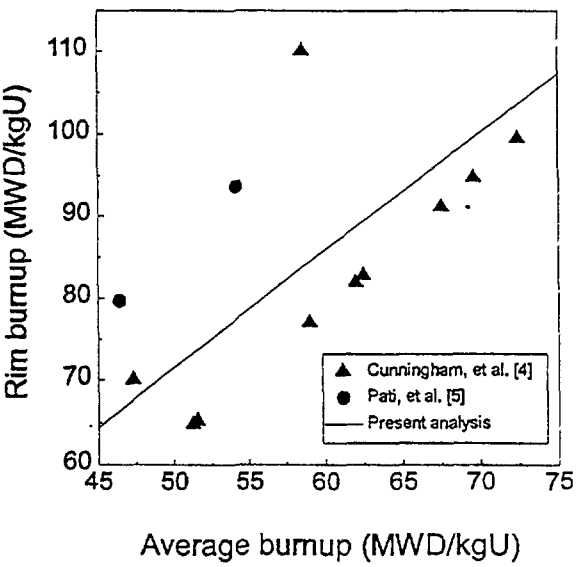

FIG. 2. Rim width as rim burnup

Another characteristic of rim region, rim width, is estimated by using the measured data [6,7]. EPMA data are chosen for the analysis due to larger fluctuation of optical microscopy data. Fig. 2 shows the fitted rim width as a function of rim burnup with experimental data. The least square method using linear relationship yields the following formula between rim width and rim burnup:

$$R_{Rim} = -305.8 + 5.24 \cdot BU_{Rim} \quad (2)$$

where R_{Rim} is the rim width in μm. Barner's relation [6] by using a parabolic dependence is also shown in Fig. 2. Compared with Barner's relation, the linear relationship of Eq. (2) can be considered more reasonable for PWR because the rim width could be larger than 200 μm at very high burnup.

2.2. Porosity in the rim region

In LWR fuel the pellet rim starts to become very porous at average burnup of 40~45 MWD/kgU. For the simplified analysis of porosity in the rim region it is assumed that 3 stable fission gas atoms (Xe, Kr) are generated from every 100 nuclear fissions. According to X-ray fluorescence analysis and X-ray mapping results [3], nearly all of the xenon atoms produced in the rim region do not escape to fuel outside but are retained in the matrix. Furthermore, as yet no microcracks have been detected in the structure and there is no evidence to suggest that the pores are interconnected. Therefore it is reasonable to assume that the produced xenon gas is retained in the newly formed pores [8].

Energy produced in the rim region, E_{Rim} is given by

$$E_{Rim} = M_{Rim} \cdot BU_{Rim} \quad (3)$$

where M_{Rim} is obtained from rim width. Then, the total fission gas produced in the pellet rim is expressed by

$$n_{Rim} = 0.895 \cdot E_{Rim} \quad (4)$$

where n_{Rim} is the produced total fission gas in mole.

Then the total fission gas volume under reactor operating condition is approximated by simple ideal gas law

$$V_{op} = \phi \cdot nR \cdot \left(\frac{T}{P}\right)_{op} \quad (5)$$

where ϕ is a fitting factor to fit the measured porosity in the rim region and subscripts *op* represents the properties at operating condition. The fitting factor, which covers the experimental data [4], was 0.4 as shown in Fig. 3.

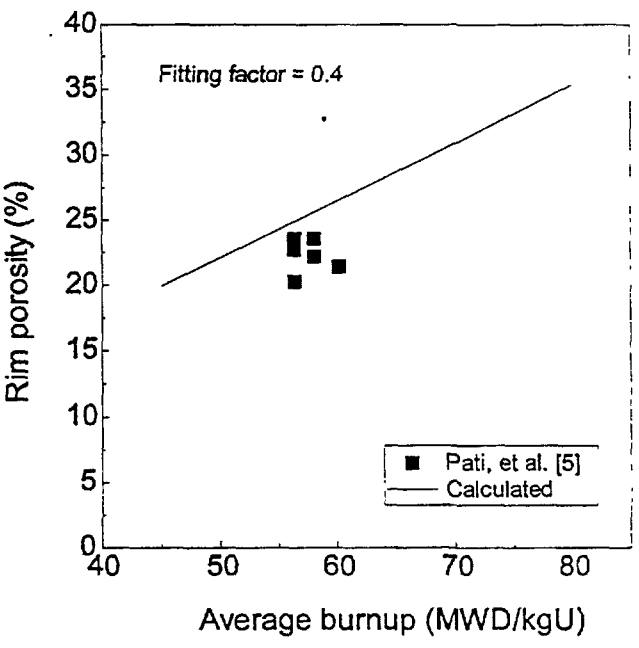

FIG. 3. Rim porosity

2.3. Thermal conductivity across the fuel pellet and in the rim region

Thermal conductivity during irradiation is degraded by the introduction of defects to the previously almost perfect UO_2 lattice. Furthermore, thermal conductivity steeply decreases across the rim with burnup due to the porous microstructure and higher local fissioning. Consequently the thermal conductivity of irradiated UO_2 fuel is dependent on porosity, stoichiometry and burnup as well as temperature [7]. Constants for three thermal

conductivities of MATPRO [10], SIMFUEL [7], and HALDEN [11] chosen for the present analysis are given in Table 1.

TABLE I. CONSTANTS FOR THERMAL CONDUCTIVITY AT 95% THEORETICAL DENSITY UO_2

	MATPRO [10]	SIMFUEL [9]
A	0.04670	0.053
β	0.0	0.0016
C	$2.294*10^{-4}$	$(2.2-0.0005*BU)*10^{-4}$
D	$1.0*10^{-2}$	0.0
E	$1.767*10^{-3}$	0.0

In the rim region, the thermal conductivity degradation is obtained under the assumption that the rim region consists of pores and fully dense material. The dependence of thermal conductivity on porosity is given as follows [12]:

$$k_{Rim} = k_0 \cdot \left\{ 1 - a \cdot P_{Rim}^{\frac{2}{3}} \cdot \left[1 - \frac{1}{1 + \frac{1}{a} \cdot P_{Rim}^{\frac{1}{3}} \cdot \left(\frac{k_0}{k_p} - 1 \right)} \right] \right\} \tag{6}$$

where k_{Rim} = thermal conductivity of the porous rim (W/m·K)

k_0 = thermal conductivity of the fully dense material (W/m·K)

$= k / \left[1 - (2.58 - 0.58 \times 10^{-3} T) P_j \right]$ [16]

k_p = thermal conductivity of the pore

P_{Rim} = porosity (volume fraction of the porous phase)

a = anisotropy factor (a=1 means isotropic pore distribution)

The obtained k_0 is shown in Fig. 4 as dash line. It is noted that the thermal conductivity of MATPRO is independent of burnup, while the others decrease with burnup.

For the analysis of the thermal conductivity of pores in the rim region, it is assumed that all the xenon gas produced in the rim region are retained in the porosity. Then the thermal conductivity of porosity in Eq. (6) can be replaced by thermal conductivity of xenon [12] expressed by

$$k_{Xe} = 0.72 \times 10^{-4} \cdot T^{0.79} \tag{7}$$

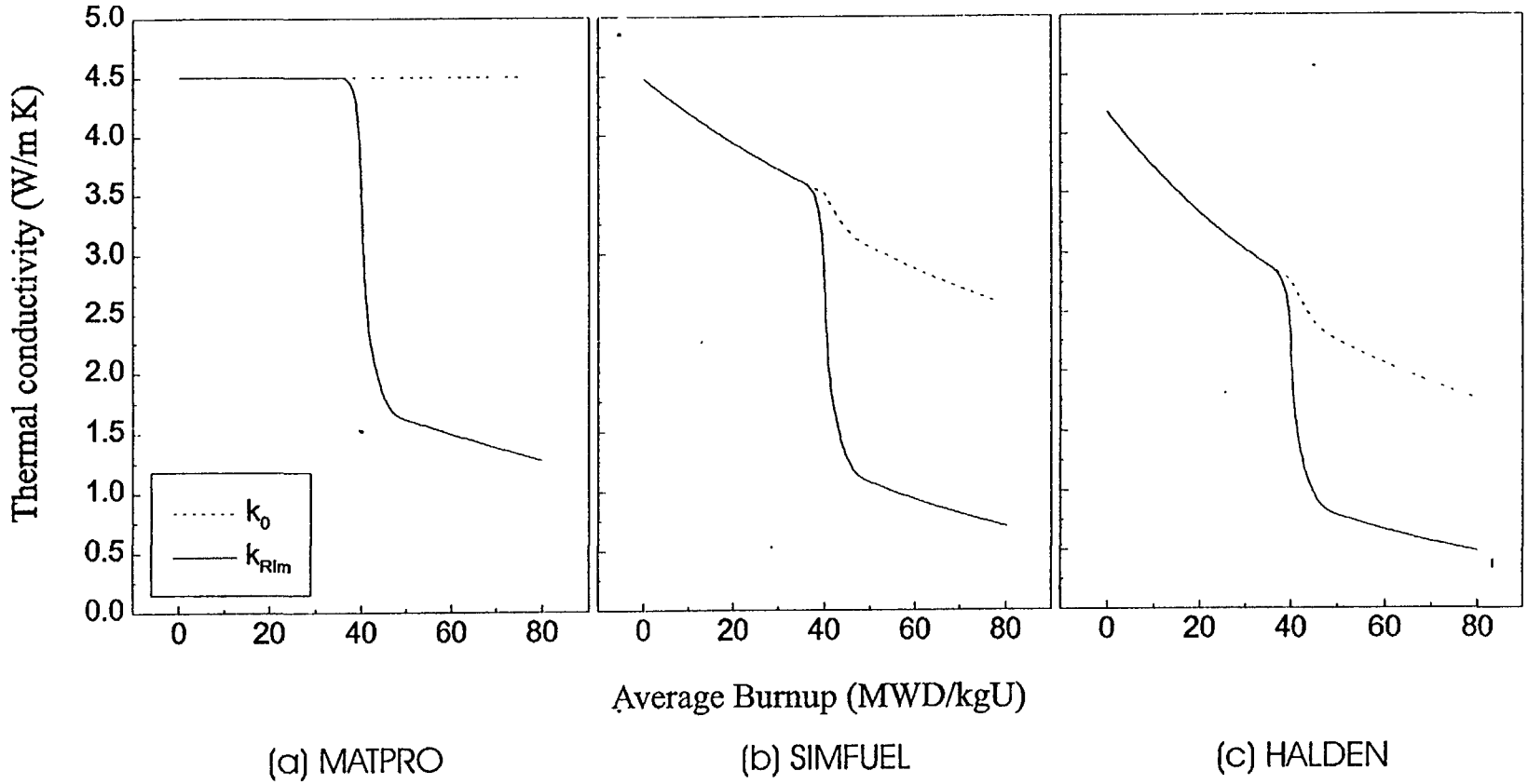

FIG. 4. Thermal conductivity in the rim

Under the assumption that all the pores are isotropically distributed, thermal conductivity of the rim is shown in Fig. 4 as solid line at 500°C. The thermal conductivity decreases abruptly around the pellet average burnup of 40 MWD/kgU. Fig. 4 shows that the thermal conductivity calculated by the HALDEN correlation is the lowest among three both in the rim and in the pellet interior.

2.4. Temperature distribution in a pellet containing rim region

To calculate the temperature distribution across fuel, a pellet is divided into several concentric rings of equal mass. Then the steady-state thermal conduction equation is solved for each ring. Taking the temperature of the outer surface of pellet as a basis, temperatures at the boundaries of each ring are determined starting from the pellet outside towards the inside up to the pellet center.

If the outer temperature of the jth ring, T_{j+1}, is known, the inner temperature, T_j, is calculated from the following equation [17] :

$$\int_{T_{j+1}}^{T_j} k_j(T, BU_j)dT = \frac{1}{4\pi H_j}\cdot\left(q_j - 2\cdot\frac{R_j^2\cdot Q_{j+1} - R_{j+1}^2\cdot Q_j}{R_{j+1}^2 - R_j^2}\cdot\ln\left(\frac{R_{j+1}}{R_j}\right)\right) \tag{8}$$

where BU_j = burnup of the jth ring

R_j = inner radius of the jth ring

R_{j+1} = outer radius of the jth ring

H_j = pellet height of the jth ring

Q_j = power released in a fractional pellet volume from R_1 to R_j

Q_{j+1} = power released in a fractional pellet volume from R_1 to R_{j+1}

Since radial power density across the pellet radius is a function of burnup, initial enrichment and fuel rod geometry, radial power depression should be considered to calculate the temperature distribution. If we denote q_j as the power of the jth ring, it is related to the average power of a pellet q_{avg} as follows :

$$q_j = g_j \cdot q_{avg} \tag{9}$$

where g_j is the power depression factor in the jth ring. This parameter is obtained from the FACTOR [13].

To calculate the temperature in the porous rim, Eqs. (6) and (8) are combined. First "old" temperature at the inner boundary of the rim region is assumed and from this we get the average temperature of the rim region. Using the thermal conductivity obtained at this average temperature, "new" temperature at the inner boundary of the rim region is calculated. This

process is repeated until the difference between the calculated (new) and assumed (old) temperature is substantially small. Once the inner temperature of the rim region is determined in this way, all the temperatures at the boundary of each ring are calculated by the same way. Finally, the centerline temperature of the pellet T_l is obtained from

$$\int_{T_2}^{T_1} k_1(T, BU_1)dT = \frac{q_1}{4\pi H_1} \tag{10}$$

3. Results and Discussion

Using Eqs. (6) and (8), radial and centerline temperature distributions are calculated and compared with the RISO and HALDEN experimental results, respectively.

Fig. 5 shows the comparison with the RISO data for the linear heat generation rates of 30, 35 and 40 kW/m at the pellet average burnup of 43.5 MWD/kgU. The radial temperature profile calculated using the MATPRO's correlation for thermal conductivity is compared with the RISO data in Fig. 5(a). This figure shows that the calculated temperatures are much lower than the measured ones across the pellet radius. This lower prediction can be explained from the fact that the MATPRO's correlation does not consider the effect of burnup on the degradation of thermal conductivity. Furthermore, temperature jump in the rim region, which is expected to occur at this burnup, is not observed in this case due to the following reason. As Eq. (6) displays, thermal conductivity developed in this study is composed of two terms; one for the degradation with burnup across pellet radius and the other for the degradation due to high porosity in the rim region. Therefore, the MATPRO's thermal conductivity, which does not consider the burnup effect, is large enough to offset the conductivity decrease in the rim region due to high porosity. This leads to the absence of the temperature jump in the rim region.

Fig. 5(b) shows the comparison when the thermal conductivity correlation from the SIMFUEL data is used. In contrast to Fig. 5(a), although the difference between the calculated and measured temperatures is slightly reduced, considerable discrepancy still exists. Of the factors that degrade the thermal conductivity of irradiated fuel, SIMFUEL has only precipitated and dissolved fission products and does not contain fission gas bubbles and volatile fission products [9]. Therefore, it is expected that the thermal conductivity derived from the SIMFUEL data would be larger than that for the irradiated fuel since there would be no degrading effects of the fission gas bubbles and volatile fission products on the thermal

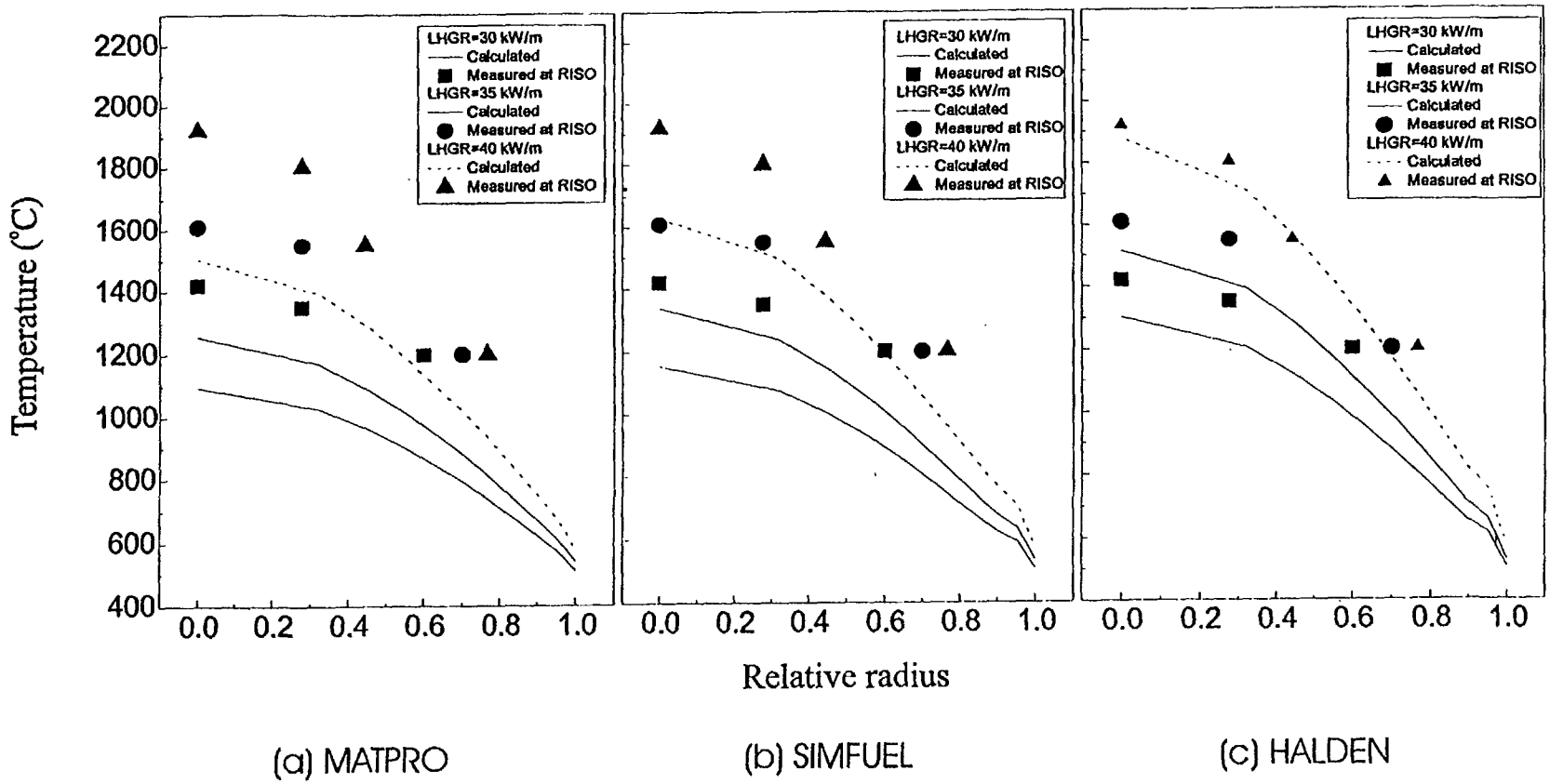

FIG. 5. Radial temperature distribution

conductivity, resulting in lower fuel temperature. In addition, a slight temperature jump in the rim is observed.

On the other hand, good agreement is obtained from the HALDEN's correlation in Fig. 5(c). This indicates that the assumption that all gas atoms produced in the rim region are retained in the porosity, which was used in deriving Eq. (6), is reasonable. However, for the linear heat generation rates of 30 and 35 kW/m, the calculated temperatures are about 100°C lower than the measured ones at the central parts of pellet. These differences may come from many uncertainties which were not considered in the present analysis due to the lack of relevant information. However, the temperature jump across the porous rim region is about 200°C and the surface temperature of fuel is nearly 600°C. Temperature jump at the pellet edge and the surface temperature obtained here are consistent with the RISO's experimental results [14].

Fig. 6 presents the comparison with HALDEN data measured at 25 kW/m as a function of burnup in a small diameter/gap rod operating at temperatures below 1000°C [15]. The calculated surface temperature of the pellet is also shown as a function of burnup. The measured centerline temperature increases linearly with burnup, whereas the calculated results show complicated trend. However, the substantial increase after 40 MWD/kgU results from the rim formation at the pellet edge; the porous rim acts as thermal barrier. In the early stage of irradiation, MATPRO and SIMFUEL correlations better predict the centerline temperature due to the intrinsic characteristics of thermal conductivity as mentioned before. On the other hand, at the late irradiation, the prediction combined with HALDEN is more consistent with experimental data. From this comparison, the centerline temperature can be more accurately predicted with HALDEN thermal conductivity for the high burnup fuel even though it needs more rigorous analysis for the HALDEN experimental condition.

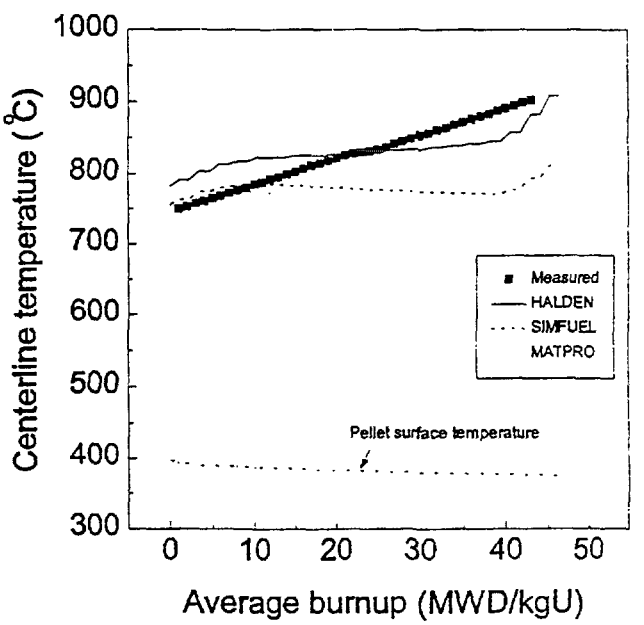

FIG. 6. Comparison with HALDEN data

4. Conclusion

Based on the MATPRO, SIMFUEL and HALDEN's correlation for thermal conductivity, a thermal conductivity correlation has been proposed that can be applied to highly porous pellet rim. In addition, a correlation has been developed that can estimate the porosity of rim region as a function of rim burnup under the assumptions that all the fission gases produced in the rim region are retained in the rim porosity and threshold pellet average burnup required for the formation of rim region is 40 MWD/kgU. Rim width is correlated to rim burnup using measured data.

Calculated radial temperature distributions were compared with the RISO experimental data. Best agreement was obtained when the thermal conductivity is combined with the HALDEN's correlation. On the other hand, both MATRPO and SIMFUEL conductivities give lower fuel temperatures. This comparison indicates that both the degradation of thermal conductivity with burnup and the temperature jump in the rim region due to high porosity should be taken into account in analyzing high burnup fuel.

Another comparison with the HALDEN's fuel centerline temperature measured as a function of burnup at 25 kW/m suggests that best agreement is made also when the present correlation is combined with the HALDEN's thermal conductivity, although the slopes of increase in fuel centerline temperature with burnup are different for the calculated and measured temperatures.

Through these two comparisons, it is concluded that a thermal conductivity correlation proposed in this paper can be used to calculate the temperature distribution in high burnup fuel by considering both the degradation of thermal conductivity with burnup across fuel pellet and additional degradation in pellet rim due to very high porosity.

References

1. J.O.Barner, et al., *International Topical Meeting on LWR Fuel Performance*, Avignon, France, April, (1991)21-24.
2. Hj. Matzke, *Journal of Nuclear Materials*, **189** (1992) 141.
3. M.E.Cunningham, et al., *Journal of Nuclear Materials*, **188** (1992) 19.
4. S.R.Pati, et al., *International Topical Meeting on LWR Fuel Performance*, Williamsburg, Virginia, April 17-20, 1982.

5. N.Kjaer-Pederson, Proceedings of a technical committee meeting, Ontario, Canada, April 28, p.111, 1992.
6. J.O.Barner, et al., *Nuclear Technology*, **102**, (1993) 210.
7. R.Manzel and R.Eberle, *International Topical Meeting on LWR Fuel Performance*, Avignon, France, April 21-24, 1991.
8. K.Lassmann, et al., *Journal of Nuclear Materials*, **226** (1995) 1.
9. P.G Lucuta, Hj. Hatzke, R.A. Verrall, *Journal of Nuclear Materials*, **217** (1994) 279.
10. MATPRO-VERSION 11 (Revision 2), NUREG/CR-0497, EG&G Idaho (1981).
11. Twenty Eighth NFIR Steering Committee Meeting, Halden, Norway (1995).
12. H. Kampf and G. Karsten, *Nuclear Application and Technology*, **9** (1970) 288.
13. Y.H.Koo, Siemens Technical Report B412/90/E84, 1990.
14. C.Bagger, M. Mogensen, and C.T.Walker, *Journal of Nuclear Materials*, **211** (1994) 11.
15. E.Kolstad and C.Vitanza, *Journal of Nuclear Materials*, **188** (1992) 104.
16. D.G.Martin, *Journal of Nuclear Materials*, **110** (1982) 73 .
17. D.S. Sohn, *Fuel Rod Design Manual*, Korea Atomic Energy Research Institute, 1988.

FUEL THERMAL BEHAVIOUR — THERMAL CONDUCTIVITY DEGRADATION OF GADOLINIA DOPED AND MOX FUEL

(Session 4)

THERMAL PROPERTIES AND IRRADIATION BEHAVIOUR OF Gd FUEL

Y. KOSAKA
Nuclear Development Corporation,
Ibaraki

S. DOI
Mitsubishi Heavy Industries, Ltd,
Kobe

K. YAMATE
Kansai Electric Power Company Inc.,
Osaka

Japan

Abstract

Thermal conductivity of UO_2 fuel doped with up to 10wt% Gadolinia has been measured to evaluate the effect of doping quantitatively. The thermal conductivity was evaluated through the measurements of thermal diffusivity and heat capacity by the laser flash technique. Thermal diffusivities of specimens with 0, 6 and 10 wt% Gadolinia was measured at temperatures up to about 1700K and the results show good agreement with recently reported values. Heat capacities of the specimens with 0 and 10 wt% Gd_2O_3 were measured at temperatures up to about 1100K. Our results were in good agreement with the curve of the Neumann-Kopp's law (additive law).

Following the thermal properties measurements, irradiation tests of the 10wt% Gd_2O_3 doped fuel were carried out in the Halden HBWR in order to measure the fuel centre-line temperature during irradiation. Fuel centre-line temperatures were estimated by our design code (FINE) which was implemented with a thermal conductivity model based on measured results. The predicted results showed appreciable agreement with the in-pile temperatures measured at power.

These systematic research programmes on the thermal behaviour of Gd fuel have led us to conclude that we have established a method to accurately predict the fuel temperature of Gd fuel during irradiation.

1. INTRODUCTION

Gadolinia doped UO_2 fuel (Gd fuel) has been developed for use in PWR plants in order to reduce the amount of burnable poison rod waste and to improve fuel management economics. To date 6wt% gadolinia doped fuel has been utilized in PWR plants. In order to achieve higher burnup and longer operation cycle times, higher gadolinia doped fuel, up to 10wt%, is required and several R&D programmes are being carried out.

It is well-known that the thermal conductivity of the UO_2 fuel is deteriorated by gadolinia doping. Such a deterioration induces an increase in fuel temperature during irradiation, which significantly affects the irradiation behaviour of a fuel rod.

In this study thermal properties of the Gd fuel were measured and followed by the irradiation test of measuring the in-pile fuel temperature. Consequently we confirmed the adequacy of our assessment on the thermal behaviour of the Gd fuel.

2. FUEL FABRICATION

Gadolinia and urania powders were blended mechanically and co-milled to achieve a homogeneous mixture. The resultant powder was sintered in a hydrogen atmosphere in excess of 1700°C in order to reach the specified pellet density. Ceramography of the fuel pellet showed sufficient homogeneity and gadolinia island sizes were evaluated to be less than about 30μm. Table I summarizes the main characteristics of the Gd fuel pellet. Theoretical densities of 0, 6 and 10wt% gadolinia doped UO_2 are 10.96, 10.76 and 10.63 g/cm^3 respectively.

TABLE I. MAIN CHARACTERISTICS OF THE GD FUELS

	UO_2	6wt%Gd_2O_3doped	10wt%Gd_2O_3doped
Gadolinia content, wt%	0	6.0	9.9
O/M ratio	2.00	2.01	2.01
Density, %TD	95.0	95.1	95.1
Grain size, μm	8-9	8-9	8-9
Impurities, ppm	<200	<300	<300

3. THERMAL PROPERTIES MEASUREMENTS

Thermal conductivity of Gd fuel has been measured by several investigators and systematic differences of measured values are reported [1-6]. Consequently we measured the thermal properties of the Gd fuel fabricated through the same process as fuel in commercial use.

Thermal conductivity (k) is expressed by the following simple equation:

$$k = \rho C p \alpha$$

where ρ : density
Cp : heat capacity
α : thermal diffusivity

In order to deduce thermal conductivity of the fuel material at high temperature, many investigators have used the laser flash technique because of its convenience. In this method temperature dependence data of the heat capacity are required.

There is discrepancy in reported values for the heat capacity [7-9], particularly at high Gd content. Accordingly we measured heat capacity of high Gd content fuel by the laser flash technique as well.

3.1 Experimental

a. Heat capacity

Heat capacity measurements by the laser flash technique were carried out up to about 1100K. Heat capacities in high temperature range have been generally measured by drop

calorimetry technique. In this method, enthalpy changes of the material are measured and heat capacities are deduced by differentiation of the enthalpy curve with respect to temperature. On the contrary, direct measurement of heat capacity has an advantage to detect thermal anomaly.

The laser flash technique is one such technique. This was developed by Takahashi et al. [10] for precise measurements of heat capacity.

Heat capacity is defined by the following equation:

$$Cp = \Delta Q \cdot m^{-1} \cdot \Delta T^{1}$$

where Cp : Heat capacity
ΔQ : Energy absorbed from a laser pulse
m : Mass of sample
ΔT : Temperature rise of the sample

Figure 1 shows a schematic layout of the laser flash apparatus. The technique for precise measurements has been described in detail in the literature [10] and only the main points will be briefly highlighted here. A laser pulse is directed at the front-surface of the sample and the temperature response of the back-surface is recorded and analysed. Figure 2 shows a typical temperature history at the back-surface.

Precise measurements of ΔQ and ΔT are necessary to obtain accurate results. Accordingly the temperature of the back-surface was measured by thermocouples and careful attention was paid to the thermal contact between the sample and thermocouples to obtain good reproducibilities. To minimize heat loss during measurement, the sample is placed in a holder with minimum thermal contacts and is held in atmosphere of less than 1.3×10^{-3}Pa. The sample holder also serves as a heat sink to reduce radiation heat losses. The absolute value of the heat capacity at room temperature was obtained from the literature [11]. The test samples were sliced from the 10wt% gadolinia fuel pellets to form disks approximately 2mm thick.

b. Thermal diffusivity

Thermal diffusivity measurements were also carried out up to about 1700K by the same apparatus but the temperature was measured by non-contact technique (infra-red detector) instead of thermocouples. In this measurement the time to reach the half of maximum temperature rise ($t_{1/2}$) is measured (also illustrated in figure 2). In the higher temperature region, heat losses are inevitable and experimental value of T_{max} can be lower than that in ideal conditions, which may induce significant error to the thermal diffusivity value.

Accordingly we applied the logarithmic correction method [13] of data reduction. This technique is independent of T_{max} and therefore is useful at high temperatures to reduce the heat loss affect. The measured samples were the same dimensions as those of heat capacity measurements and the gadolinia contents were 6 and 10wt%. A UO_2 sample (undoped) was also measured as the reference material.

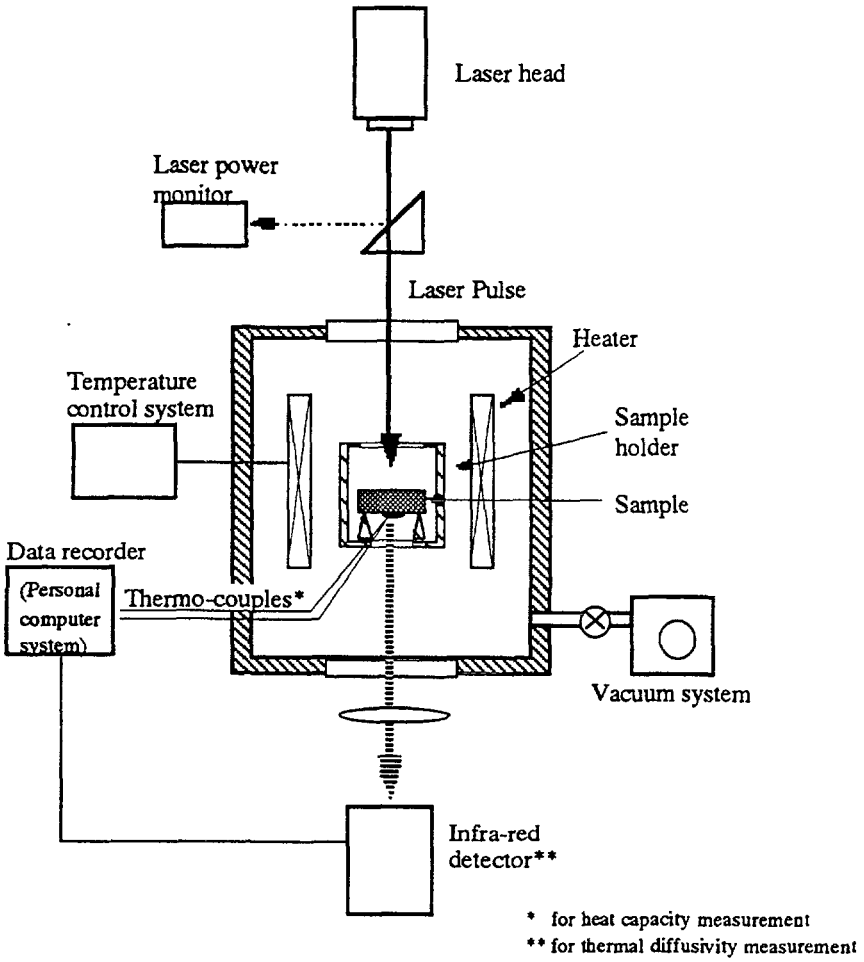

FIG. 1. Schematic of the experimental apparatus of laser flash technique

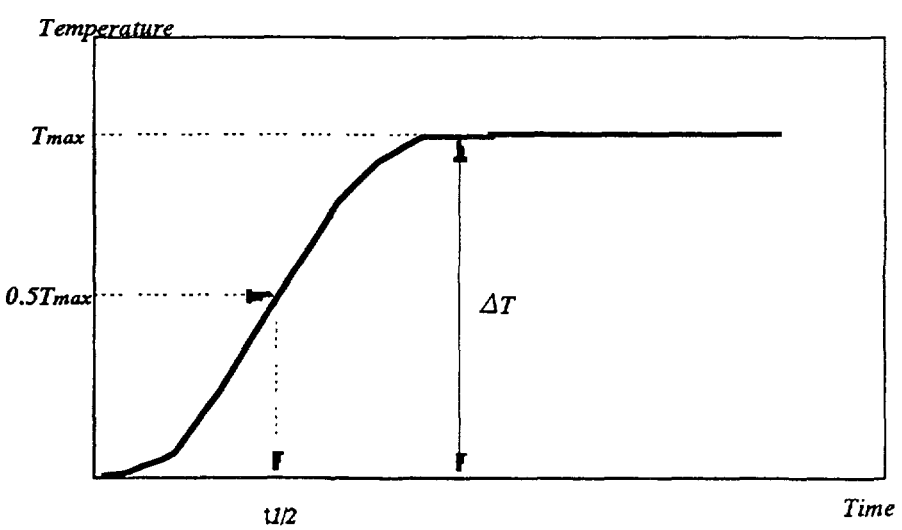

FIG. 2. Typical temperature history of sample back-surface in the laser flash technique measurement

3.2 Results and discussion

a. Heat capacity

The heat capacity of the reference UO_2 fuel was measured from room temperature up to about 1100K. The results are shown in figure 3 compared with values from the literature. The results show good reproducibility within $\pm 3\%$ in the measured temperature range. The present results are generally consistent with those reported by other investigators within the bounds of experimental uncertainty. These results reveal that our technique is reasonable for the UO_2 sample measurement up to about 1100K.

The heat capacity of the Gd fuel was also measured in a similar temperature range. The results are shown in figure 4 compared with values from the literature. In this figure, the additive law values are calculated by the weight averaged using the heat capacity values of pure UO_2 [11] and Gd_2O_3 [14]. The results show good reproducibility within the experimental uncertainty range of $\pm 3\%$. Stoichiometry (O/M ratio) changes were checked by measuring the sample weights before and after the heat capacity measurement and no change was detected within the experimental uncertainty of ± 0.003 (absolute value).

Our results are more consistent with those reported by Takahashi et al. [9] than those by Inaba et al.[7] in the measured temperature range. Thus our results are in agreement with the additive law (Neumann-Kopp's law) and showed no thermal anomaly in higher temperature region. Consequently, the additive law was applied to the heat capacity calculation of the Gd fuel.

b. Thermal diffusivity and thermal conductivity

The thermal diffusivities of the reference UO_2, 6wt% and 10wt% gadolinia doped fuel were measured from room temperature to about 1700K. The results are shown in figure 5

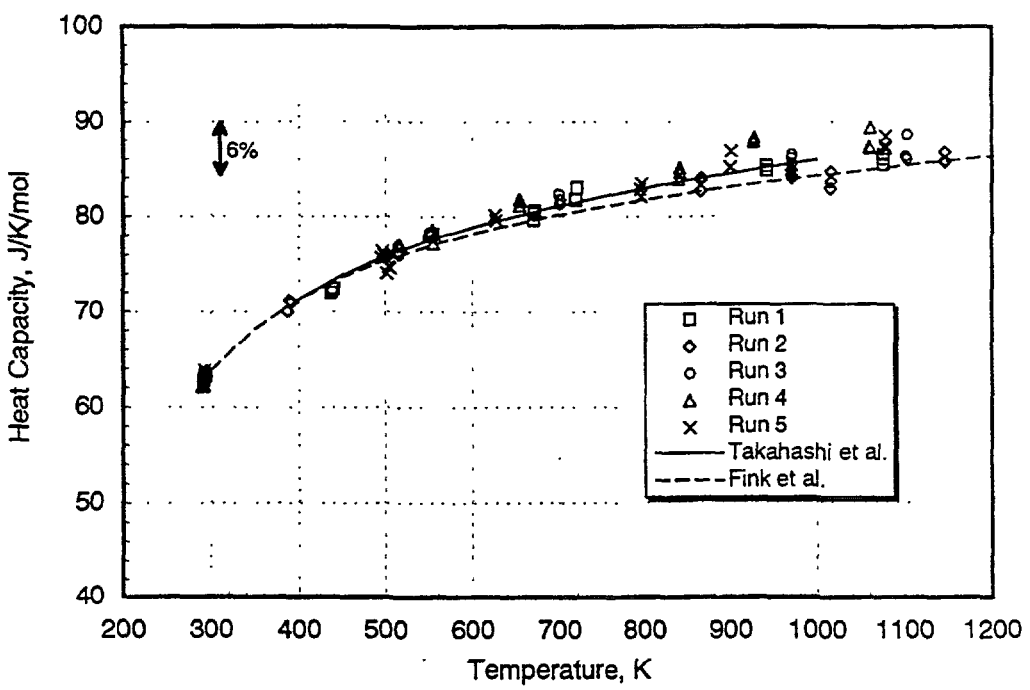

FIG. 3. Heat capacity of UO_2

compared with values from the literature. The observed values of the UO_2 fuel are consistent with those of the other investigators. From these results it is revealed that our measurement technique is accurate up to 1700K.

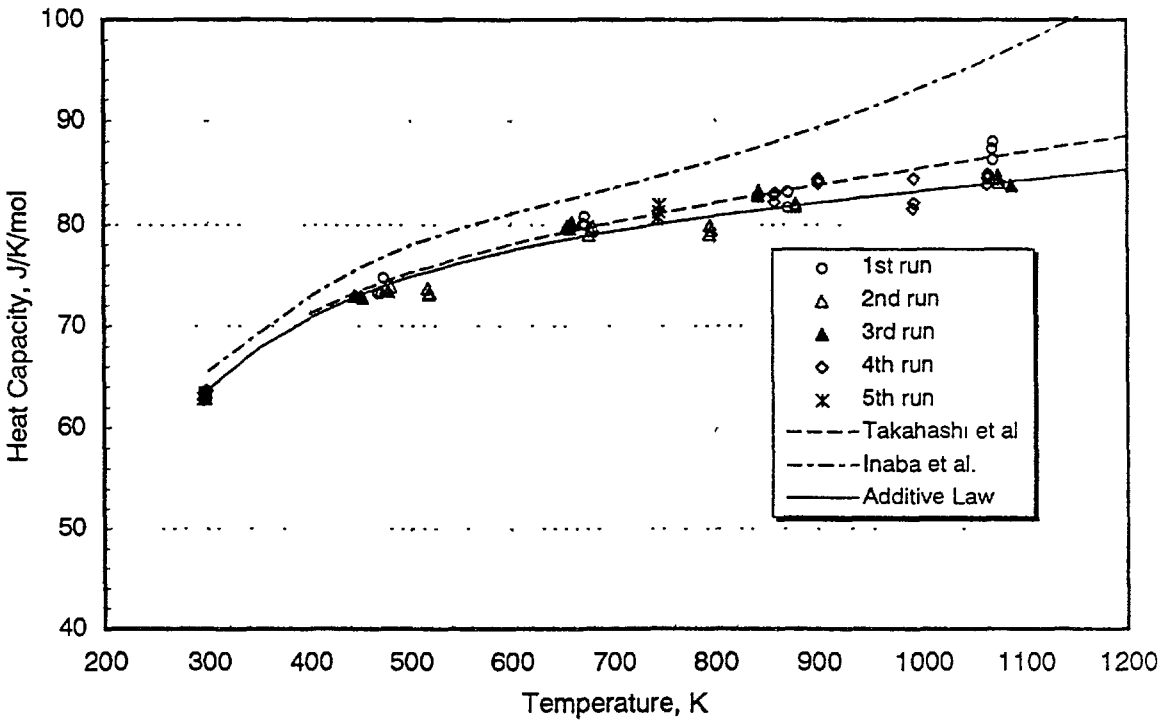

FIG. 4. Heat capacity of 10wt% Gd_2O_3 doped UO_2

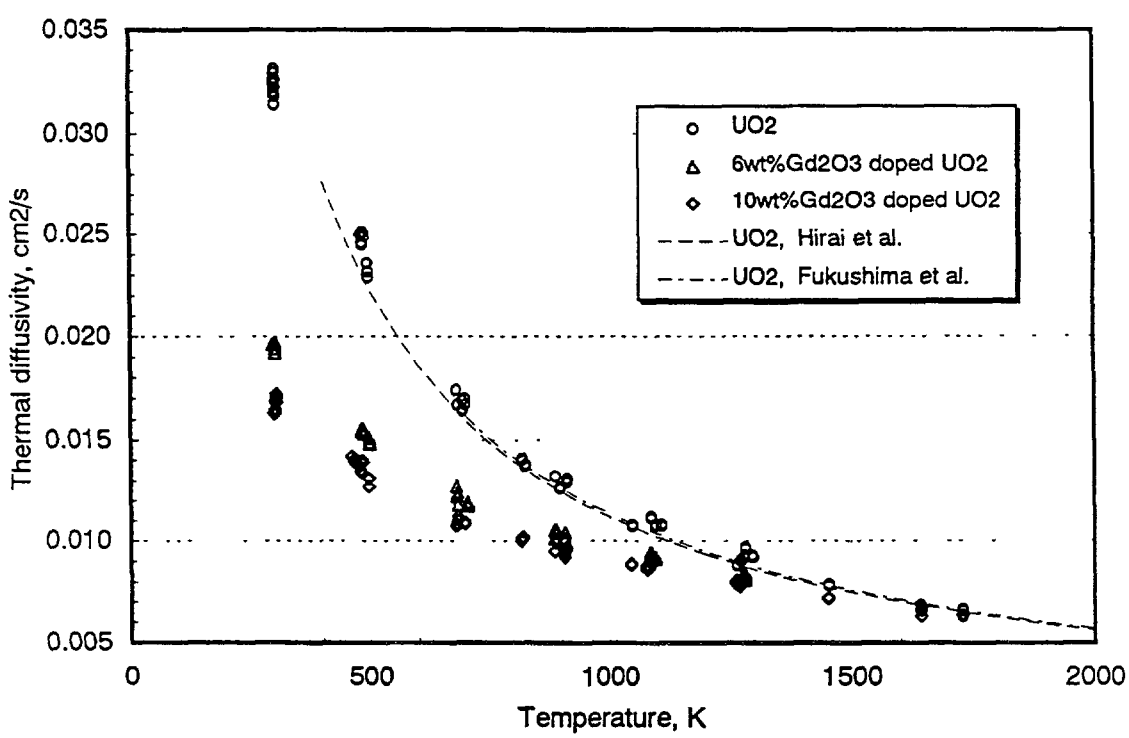

FIG. 5. Thermal diffusivity of (U,Gd)O_2

Calculated thermal conductivities using the measured thermal diffusivities were normalized to the density of 95% of theoretical density. The results are shown in Figure 6 compared with values from the literature. Our observed results show good agreement with those reported by Hirai et al.[1] but are higher than those reported by Fukushima et al.[3]. There is no clear evidence to explain the reason for this systematic difference, however, Hirai et al. [2] pointed out that the formation of micro cracks could deteriorate the thermal diffusivity.

Examination of sample microstructures before and after measurement showed no evidence of micro cracking. Furthermore O/M ratio measurements confirmed that the thermal diffusivity test had not brought about significant change. Accordingly we believe that our samples were free from such effects during measurements.

4. IRRADIATION TEST IN THE HALDEN HBWR

4.1 Experimental

A 10wt% gadolinia-urania short fuel rod was fabricated and instrumented with thermocouples to monitor fuel centre temperature. The thermocouples were inserted in the centre holes of both the Gd fuel and reference UO_2 pellets at the same axial elevation in the test rig. The dimensions of the test fuel pellets and the claddings are shown in Table II. The Gd fuel rod was installed in the centre of 3x3 rods configuration of the test rig as shown in Figure 7. The surrounding rods consisted of UO_2 reference fuel. The power balance between the Gd fuel and the UO_2 fuels during irradiation were well characterized by the WIMS code calculation and the power and the burnups of the test fuel rods were calculated based on the measured neutron flux signals from the neutron detectors which surrounded the test fuel rods.

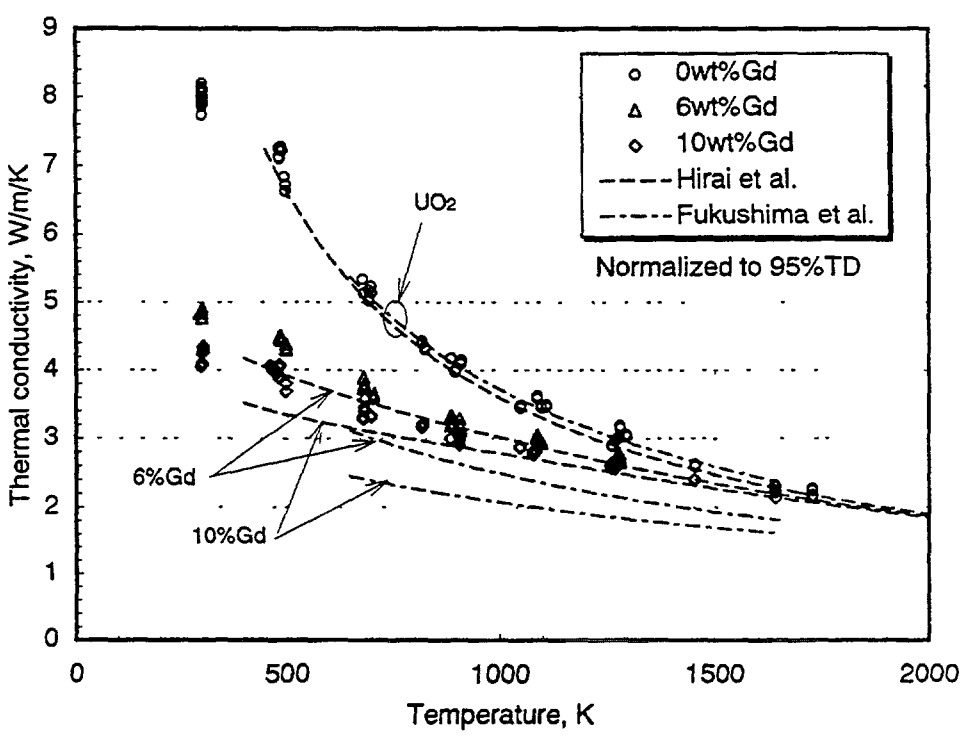

FIG. 6. Thermal conductivity of (U,Gd)O_2

TABLE II. MAIN DIMENSIONS AND CHARACTERISTICS OF THE IRRADIATION TEST FUELS

	UO_2	10wt%Gd_2O_3doped
Diameter, mm	8.19	8.19
Height, mm	11.3	13.5
Density, %TD	94.4	95.5
Gadolinia content, wt%	0	10.0
O/M ratio	2.00	2.00

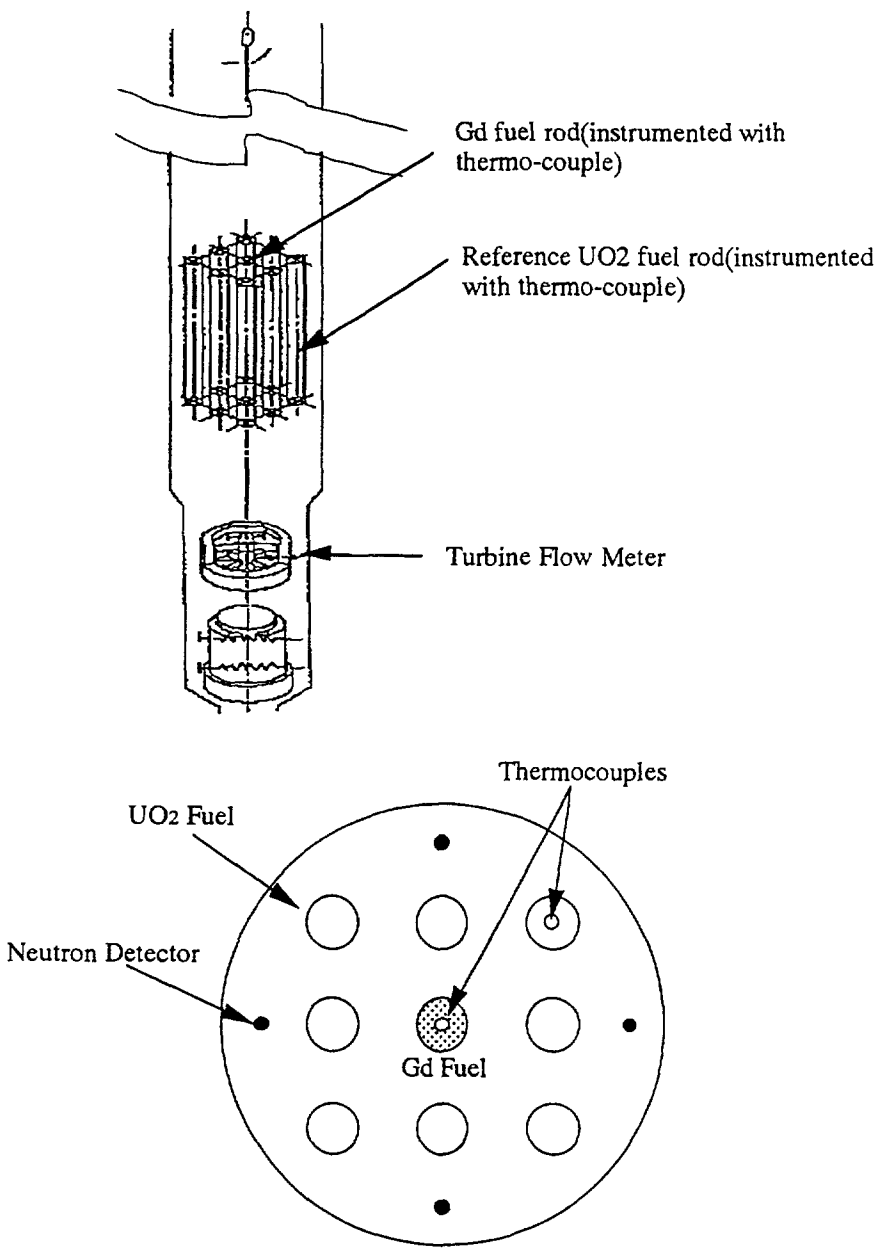

FIG. 7. Configuration of the irradiation test rig in the Halden HBWR (IFA-561)

4.2 Irradiation history

This test rig was irradiated for about two years with maximum power of about 20kW/m. The Gd fuel rod achieved a burnup of about 14GWd/t. Figure 8 illustrates the propensity of the Gd fuel temperature through the whole irradiation period and revealed that the Gd absorber was almost burned out at achieved burnup.

4.3 Results and discussion

In order to compare the in-pile measured temperature with the estimated fuel temperature using the measured thermal conductivity, the Mitsubishi fuel rod design code (FINE code [12]) was used. Originally the thermal conductivity of the Gd fuel in the FINE code was modelled based on the experimental results of Fukushima et al.[3].

Figure 9 shows the relationship between measured fuel temperatures and fuel power for both the Gd and UO_2 fuel rods. The temperature of the Gd fuel is significantly higher than that of the UO_2 fuel. This is attributed to a deterioration of thermal conductivity as a result of doping with gadolinium. Predictions of each test fuel by the FINE code are also shown in the same figure for comparison. The predicted temperature of the UO_2 fuel shows good agreement with the measured data. The predicted temperature of the Gd fuel, however, is considerably higher than the measured data. This result means that the FINE code prediction is conservative with respect to the behaviour of Gd fuel. This is advantageous from the view point of reactor safety design but it means that the safety margin with respect to the fuel operation temperature is unnecessarily decreased.

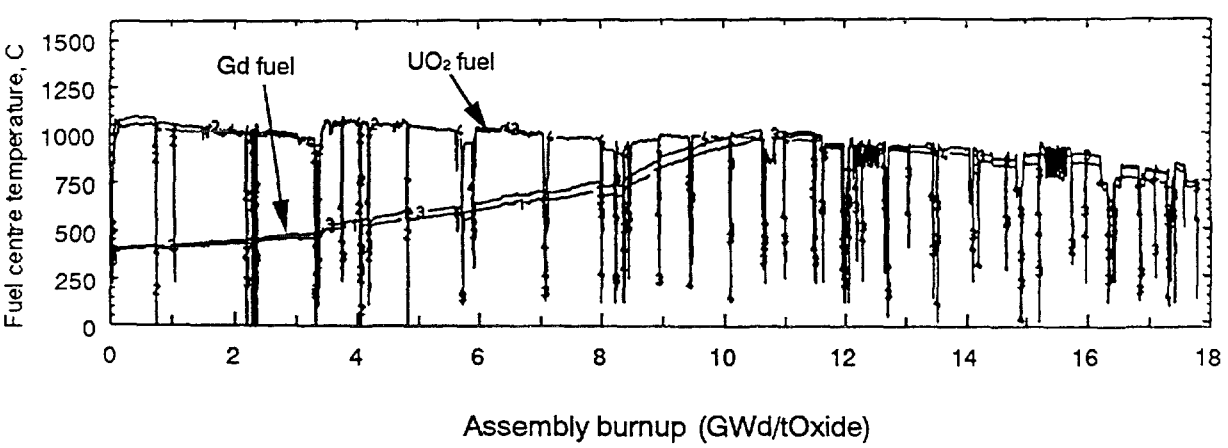

FIG. 8. Measured fuel temperature history during irradiation in Halden HBWR

This difference in the comparison of the Gd fuel, i.e. overestimation of the Gd fuel temperature implies that the thermal conductivity implemented in the FINE code is relatively conservative. In order to predict more precisely on the Gd fuel temperature, another analysis has been carried out in which a revised thermal conductivity model was implemented in the FINE code. As described previously, our measured thermal conductivity of the Gd fuel showed higher values than those of Fukushima et al., accordingly we modified the thermal conductivity model of the Gd fuel based on our measured results. The results of the evaluation are shown in figure 10 and the predicted values by revised model are improved and show a good agreement with the measured values.

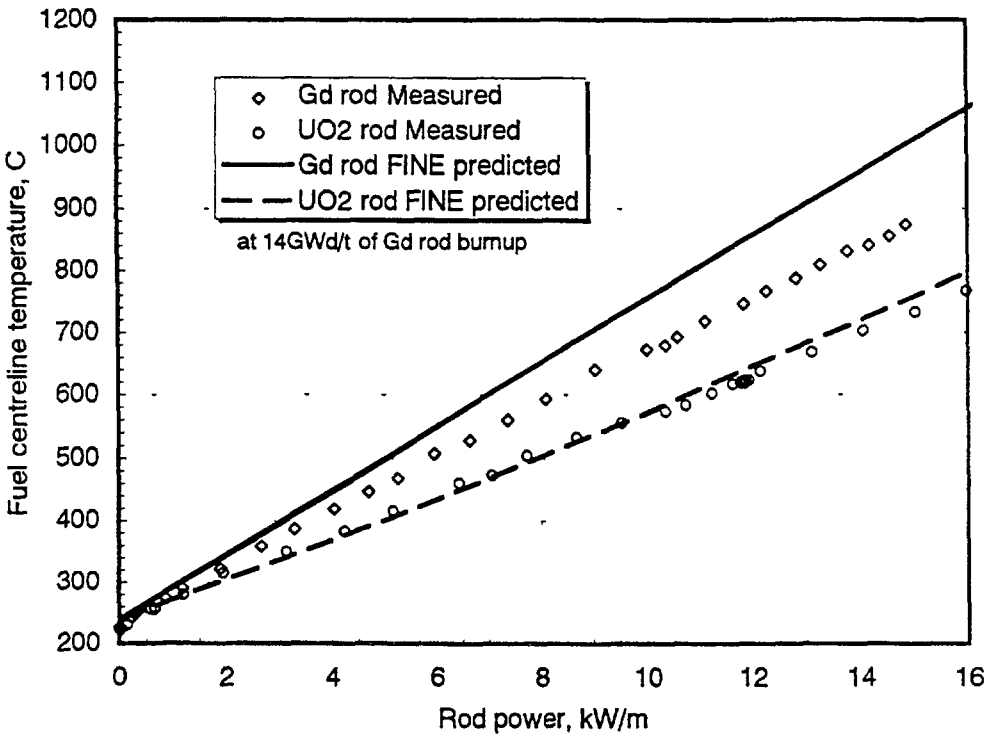

FIG. 9. Comparison of the measured fuel temperatures with the predictions

5. POWER TO MELT TESTING OF THE Gd FUEL

In order to check the adequacy of the fuel temperature evaluation for the Gd fuel, especially at high temperature close to melting temperature, a test rod of the Gd fuel (10wt%gadolinia) was subjected to power-to-melt testing[1]. The axial length of the melted region was measured after the power ramping and compared with the length predicted by the FINE code.

5.1 Test fuel rod configuration

The main design parameters of the Gd test fuel rod were identical to the standard 17x17 type of a PWR. The gadolinia content was 10 wt% and main characteristics were similar with those tabulated in Table I.

5.2 Irradiation history

A standard design test rod of the Gd fuel (17x17 PWR Type) has been base-irradiated up to a burnup of around 12GWd/t in the BR-3 reactor (Belgian PWR). After the base-irradiation the test rod was submitted to the power-to-melt testing in BR-2 (Belgian material test reactor). The maximum power of the ramping was 73kW/m for 60 seconds.

---

[1] The test was performed within the HBC International Programme (organized jointly SCK · CEN and Belgonucleaire, participants are AECL, KKG, PSI, ITU, SIEMENS/RBU, CEA/FRA, EdF, AEA, MHI, KEPCO, ABBATOM, SSPB, BWFC, EPRI and GE).

5.3 Results and discussion

After the power ramping test, the axial length of the fuel melted region was measured through the neutron radiography. In order to compare the melted region length, axial distributions of the test fuel temperature were evaluated by the FINE code. Figure 11 illustrates the results of the comparison between the measured and predicted axial length of melting region. The predicted results by the original thermal conductivity model show a

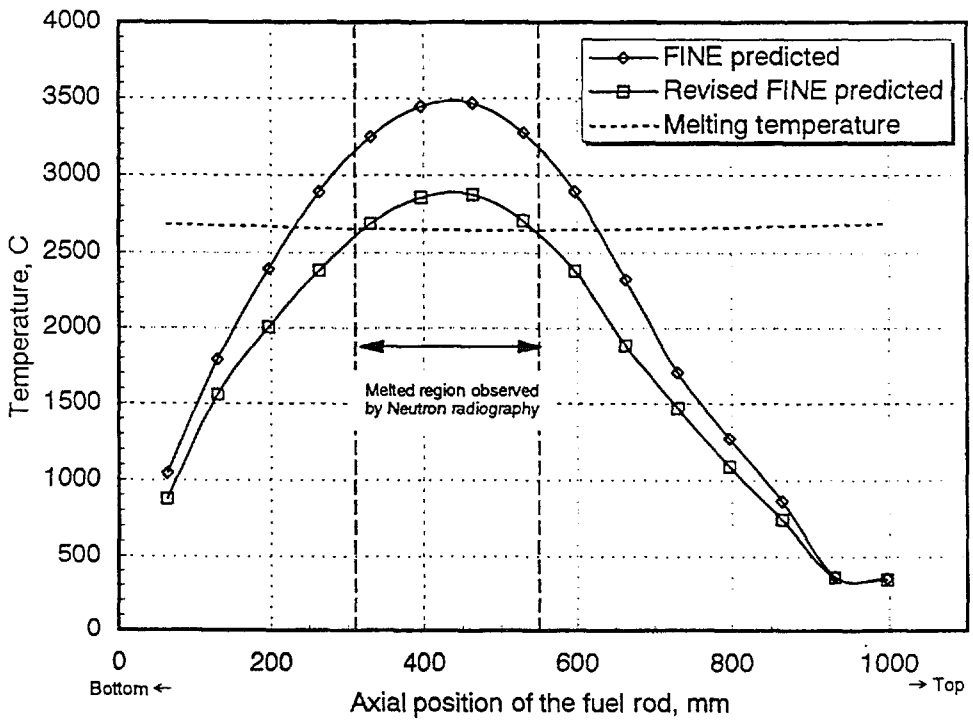

FIG. 10 Comparison of the measured fuel temperatures with the revised model predictions

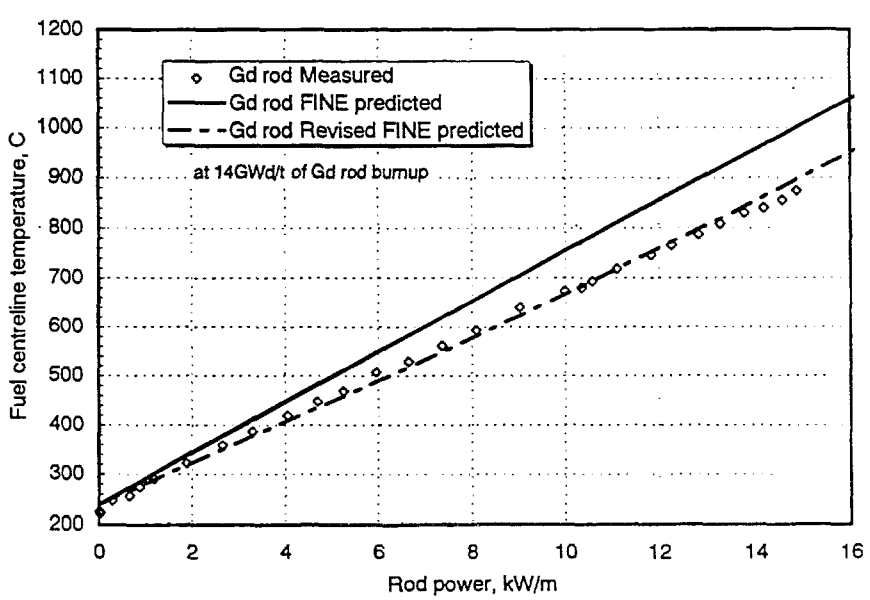

FIG. 11 Analysis of the high temperature behaviour of the Gd fuel

significantly larger melted region than was actually measured. This result also shows that the temperature prediction by this model is conservative. However the predicted results by the revised model indicate reasonable agreement with the measured length of the melted region.

6. CONCLUSIONS

Thermal conductivities of the Gd fuel were determined up to around 1700K through the thermal diffusivity and the heat capacity measurement by the laser flash technique. The measured thermal diffusivities show higher values than those reported previously and the measured heat capacities are consistent with those obtained by the additive law. The thermal conductivity model of the Gd fuel was implemented in the Mitsubishi fuel rod design code (FINE) based on the measured values and the predictions of the in-pile fuel temperature showed appreciable agreement with the measured data.

These systematic research programmes on the thermal behaviour of the Gd fuel have led us to conclude that we have established a method to accurately predict the fuel temperature of Gd fuel during irradiation.

REFERENCES

[1] HIRAI, M.,et al. J. Nucl. Sci.Technol.,28, 11(1991)995-1000
[2] HIRAI, M., J. Nucl. Mater.,173(1990)247-254
[3] FUKUSHIMA, S.,et al., J. Nucl. Mater.,105(1982)201-210
[4] THORNTON, T. A.,et al., Trans.Am.Nucl.Soc.,43(1986)348
[5] CHOTARD, A.,et al., "Out of pile physical properties and in pile thermal conductivity of $(U,Gd)O_2$ (Proc.TCM,Vienna,IAEA),IWGFPT-26(1987)
[6] PRESTON, S. D.,et al., High Temp. High Press.,21 (1989)287-295
[7] INABA, H.,et al., J. Nucl. Mater.,146(1987)341-348
[8] MILLS, K.C.,et al., Thermochimica Acta,139(1989)107-120
[9] TAKAHASHI, Y., et al., J. Nucl. Mater.,201(1993)108-114
[10] TAKAHASHI, Y., et al., J. Chem. Thermodynamics 11(1979)379-394
[11] FINK, J.K.,et al., J. Nucl. Mater.,102(1981)17-25
[12] SUZUKI, S. et al., "PWR Fuel Performance and Burnup Extension Program in Japan", IAEA Symposium, Stockholm, 1986.
[13] TAKAHASHI, Y., et al., "Usefulness of logarithmic method in laser-flash technique for thermal diffusivity measurement", Proc. 9th Japan Symp.Thermophysical Properties 1988,175-178
[14] TOULOUKIAN, Y. S.,et al., (Eds.):"Thermophysical Properties of Matter", Vol.5,TPRC Data Ser.,92 (1970), Plenum, New York.

DISCUSSION
(Questions are given in italics)

What is the width of the gap during fabrication of the rod which is irradiated in Halden? Is it necessary to know that the temperature drops in the gaps are the same for the Gd rod and the reference rod?

The densification and swelling model of Gd fuel in FINE code is well tuned and proved through the other PIE data, therefore, we think that gap conductance was well estimated.

Do you account for the effect of Gd in the power profile generation in the pellet? The effect is not negligible.

Yes. We have tuned the radial power distribution of Gd fuel by the PIE data in other research programme.

THERMAL CONDUCTIVITY MEASUREMENTS ON $(U,M)O_{2+X}$ PELLETS

M. AMAYA, M. HIRAI
Nippon Nuclear Fuel Development Company Ltd,
Ibaraki, Japan

XA9847859

Abstract

10wt% Gd_2O_3 doped UO_{2+x} samples with x between 0 and 0.15 and simulated soluble FP doped UO_{2+x} (equivalent to 30 and 60GWd/tU burnups) with x between 0 and 0.02 were prepared by an oxidation method. Sample thermal diffusivities were measured by using a laser flash method from 300 to 1400 K. Then, sample thermal conductivities were evaluated by multiplying the thermal diffusivities by the sample densities and the specific heat capacities derived from the literature. The thermal conductivities of $(U,M)O_{2+x}$ (M=Gd, simulated soluble FPs) decreased with increasing hyperstoichiometry and they were expressed as a function of each sample's hyperstoichiometry using the concentration of impurities such as Gd^{3+} and FP atoms and U^{5+} formed with the excess interstitial oxygen atoms.

Keywords
thermodynamic properties, thermal conductivity, thermal diffusivity, laser flash method, uranium oxides, gadolinium oxides, fission products, O/U ratios, O/M ratios, fuel pellets, nuclear fuels, temperature dependence, thermal conductivity equation.

1. INTRODUCTION

In the event of a fuel rod failure in a BWR, UO_2 fuel pellets react with high temperature and high pressure steam which enters the fuel rod and they are oxidized. The O/U ratio of the UO_2 pellets changes from 2 to about 2.1[1] in the initial leak stage. Thermal conductivity is one of the most important thermal properties to evaluate the temperature in the oxidized pellets, which may control the distribution of FPs in the pellets.

Thermal conductivities of unirradiated UO_{2+x}, pellets have been measured by several groups[2-6]. According to these published results, thermal conductivities of UO_{2+x} pellets are lower than those of UO_2 pellets, and the larger the deviation from the stoichiometry (x) is, the lower the thermal conductivity is. However, considerable disagreement between the published data was seen for O/U ratios above 2.05, and there were few thermal conductivity data for composition $O/U > 2.1$.

The authors have also measured the thermal conductivities of UO_{2+x} pellets [7] and 10wt%Gd_2O_3 doped UO_{2+x} pellets [8]. The thermal conductivities were expressed by using the deviation from the stoichiometry, x, applying Klemens' model based on quantum theory [9,10].

Recently, thermal conductivities of unirradiated hyperstoichiometric SIMFUEL were measured by Lucuta et al. [6]. From the comparison between their results for UO_{2+x} and our measured values [7], their results tend to be lower than our values above O/U = 2.05. Therefore, it is necessary to clear whether the thermal conductivities of hyperstoichiometric SIMFUEL have similar tendencies or not.

In this paper, thermal conductivities of $(U,M)O_{2+x}$ (M=Gd, simulated soluble FPs) pellets having various O/M ratios were measured from 300 to 1400 K and the thermal conductivities were expressed by using the deviation from the stoichiometry. The effects of pellet oxidation on the thermal conductivity were estimated in comparison with the unoxidized pellets.

2. EXPERIMENTAL

2.1 Sample preparation

$(U,M)O_{2+x}$ samples (M=Gd, simulated soluble FPs) were prepared by a method similar to that used to prepare UO_{2+x} samples in an earlier study [7]: disks about 1mm. thick were sliced from $(U,M)O_2$ pellets (M=Gd, simulated soluble FPs) which were sintered at 2023K for 4h in N_2-8%H_2 atmosphere. These disks were oxidized at 1273K for an appropriate time from 5h to 75h in an argon and steam mixture (P_{H2O} = 0.13 atm (323K in dew point)) or in pure argon. The preparative conditions are summarized in Tables I - II. The O/M ratios of the oxidized samples were calculated from the weight change before and after oxidation and compared with the results determined by a polarography method. The difference in results of deviation from the stoichiometry, x, between the two methods was about $\pm$ 2%.

TABLE I. SAMPLE PREPARATION CONDITIONS OF 10wt%GD_2O_3 DOPED UO_{2+X}

O/M ratio	Starting material	Preparation conditions
2.00	(green pellet)	sintered for 4h at 2023K in N_2-8%H_2-H_2O (dew point: room temperature)
2.06	$(U,Gd)O_2$ pellet	oxidized for 1h at 923K in Ar (Po_2<2 x 10^{-2}Pa) annealed for 2h at 1273K in vacuum (<1 x 10^{-4}Pa)
2.08	$(U,Gd)O_2$ pellet	oxidized for 10h at 1223K in Ar - 13%H_2O
2.11	$(U,Gd)O_2$ pellet	oxidized for 5h at 1273K in Ar-H_2O (dew point: room temperature)
2.15	$(U,Gd)O_2$ pellet	oxidized for 5h at 1273K in Ar-13%H_2O

TABLE II. SAMPLE PREPARATION CONDITIONS OF SIMULATED SOLUBLE FPs DOPED UO_{2+X} (EQUIVALENT BURNUP: 30 AND 60GWd/Tu)

O/M ratio	Starting material	Preparation conditions
2.00	(green pellet*)	sintered for 4h at 2023K in N_2-8%H_2-H_2O (dew point: room temperature)
2.02	(U,FPs*)O_2 pellet	oxidized for 15h at 1273K in Ar -13%H_2O

* Concentration of the additives(wt%)

Simulated burnup (GWd/tU)	SrO	Y_2O_3	ZrO_2	LaO_2	CeO_2	Nd_2O_3
30	0.090	0.050	0.403	0.118	0.407	0.397
60	0.142	0.080	0.717	0.227	0.750	0.809

Sample characteristics are shown in Tables III - IV. In Tables III - IV, the theoretical density of each sample was evaluated from its lattice constant. The phase identifications were carried out by X - ray diffractometry. Only diffraction peaks due to the UO_{2+x} fluorite structure were observed and no peaks for the M_4O_9 (M=U+Gd and U+FPs) type structure were seen for $(U,M)O_{2+x}$ samples.

2.2 Thermal conductivity measurements

Thermal conductivities of $(U,M)O_{2+x}$ (M=Gd, simulated soluble FPs) were measured by a laser flash method (LF/TCMFA8510SP4, Rigaku Co., Ltd.). The apparatus and the analysis method have been described elsewhere in detail [11]. The measurements were carried out three times at each temperature step in a vacuum of less than 2 x 10^{-4} Pa. The sample weights were measured before and after the thermal diffusivity measurements and the thermal diffusivity data were accepted only when the sample weights were unchanged. The temperature region with no change of sample weight was from room temperature to 1400K. The thermal diffusivity of each sample was calculated from its rear-surface temperature response by the "logarithmic method" [12].

Thermal conductivities of $(U,M)O_{2+x}$ samples (M=Gd, simulated soluble FPs) were estimated from the following equation:

$$\lambda_M = \alpha_M C_p \rho_M \quad (1)$$

TABLE III. SAMPLE CHARACTERISTICS OF 10wt%GD_2O_3 DOPED UO_{2+X}

O/M ratio	Thickness (mm)	Density (g cm^{-3})	Theoretical density (g cm^{-3})	Porosity (%)
2.00	1.505	10.32	10.64	3.0
2.06	1.058	10.39	10.72	3.08
2.08	1.519	10.38	10.74	3.36
2.11	1.505	10.43	10.78	3.25
2.15	1.502	10.40	10.84	4.08

TABLE IV. SAMPLE CHARACTERISTICS OF SIMULATED SOLUBLE FP DOPED UO_{2+X}

(a) Simulated burnup: 30GWd/tU

O/M ratio	Thickness (mm)	Density (g cm^{-3})	Theoretical density (g cm^{-3})	Porosity (%)
2.00	1.010	10.43	10.83	3.69
2.02	1.010	10.44	10.86	3.87

(b) Simulated burnup: 60GWd/tU

O/M ratio	Thickness (mm)	Density (g cm^{-3})	Theoretical density (g cm^{-3})	Porosity (%)
2.00	1.013	10.39	10.72	3.08
2.02	1.013	10.40	10.76	3.35

where λ_M is the thermal conductivity of the sample; α_M, the thermal diffusivity of the sample obtained from thermal diffusivity measurements; Cp, the specific heat capacity; and ρ_M, the density of the sample.

The specific heat capacities of $(U,M)O_{2+x}$ samples (M=Gd, simulated soluble FPs) samples were evaluated by an expression including the nonstoichiometry [13], because the difference between the molar heat capacities of (U,M)O O_{2+x} (M=Gd, simulated soluble FPs) calculated from Neumann - Kopp's law and that of UO O_{2+x}, was small, being about $\pm$ 3%.

3. RESULTS AND DISCUSSION

3.1 Thermal diffusivities of $(U,Gd)O_{2+x}$

The results of thermal diffusivity measurements on $(U,Gd)O_{2+x}$ (x = O - 0.15) are shown in Fig. 1(a). The thermal diffusivity calculated from ref. [11] is shown in the figure for comparison. The thermal diffusivities were in good agreement for each sample, irrespective of being a heating or cooling process.

3.2 Thermal diffusivities of (U, simulated soluble FP)O_{2+x}

The results of thermal diffusivity measurements on (U,simulated soluble FP)O_{2+x} (x = 0 - 0.02, equivalent burnup: 30 and 60GWd/tU) are shown in Figs. 1(b)-(c). The thermal diffusivities were in good agreement for each sample, irrespective of being a heating or cooling process, similar to Gd_2O_3 doped UO O_{2+x}.

3.3 Thermal conductivities of $(U,M)O_{2+x}$ (M=Gd, simulated soluble FPs)

Figs. 2(a)-(c) plot the thermal conductivities of $(U,M)O_{2+x}$ (M=Gd, simulated soluble FPs) pellets evaluated from Eq. (1). Thermal conductivity of each sample was corrected to that with 96.5% of the theoretical density (TD) by applying a modified Loeb's equation:

$$\lambda_{96.5} = \{(1 - 0\ 035\beta)/(1 - \beta P)\}\ \lambda_M \qquad (2)$$

where $\lambda_{96.5}$ is the thermal conductivity of the sample corrected to 96.5%TD; β a coefficient; P, the porosity of the sample; and λ_M the measured thermal conductivity of the sample. The value of β was assumed to be the same as for UO_2 [14]:

$$\beta = 2.6 - 5 \times 10^{-4}\ (T-273.15) \qquad (3)$$

where T is temperature in K.

As shown in Figs. 2(a)-(c), the thermal conductivities of $(U,M)O_{2+x}$ decreased as the deviation from the stoichiometric composition, x, increased. The break points of the thermal conductivities which were observed for UO_{2+x} due to the phase transition [7] were not observed for $(U,M)O_{2+x}$. Therefore, the M_4O_9 - MO_2 (M = U+Gd and U+FPs) mixture phase may not exist even at room temperature in (U, M)O_2. This fact was in agreement with the phase identification results by X-ray diffraction.

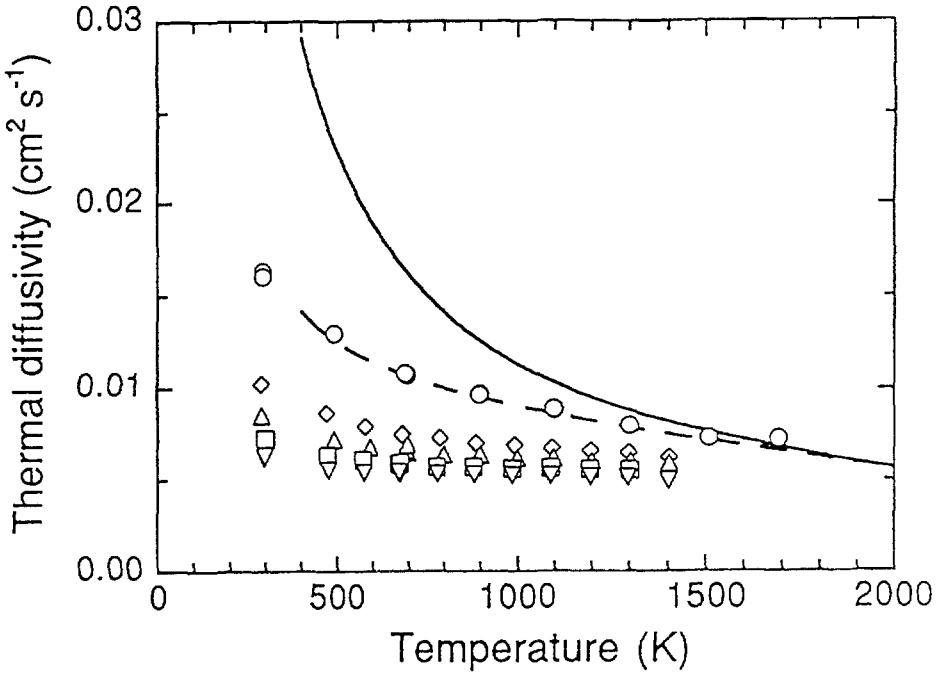

Fig. 1(a) Thermal diffusivities of 10wt%Gd_2O_3 doped UO_{2+x} pellets.
○: (U.Gd)$O_{2.00}$, ◇: (U,Gd)$O_{2.06}$, △: (U,Gd)$O_{2.08}$, □: (U,Gd)$O_{2.11}$, ▽: (U,Gd)$O_{2.15}$,
– – – : (U,Gd)O_2[11], — : UO_2[11].

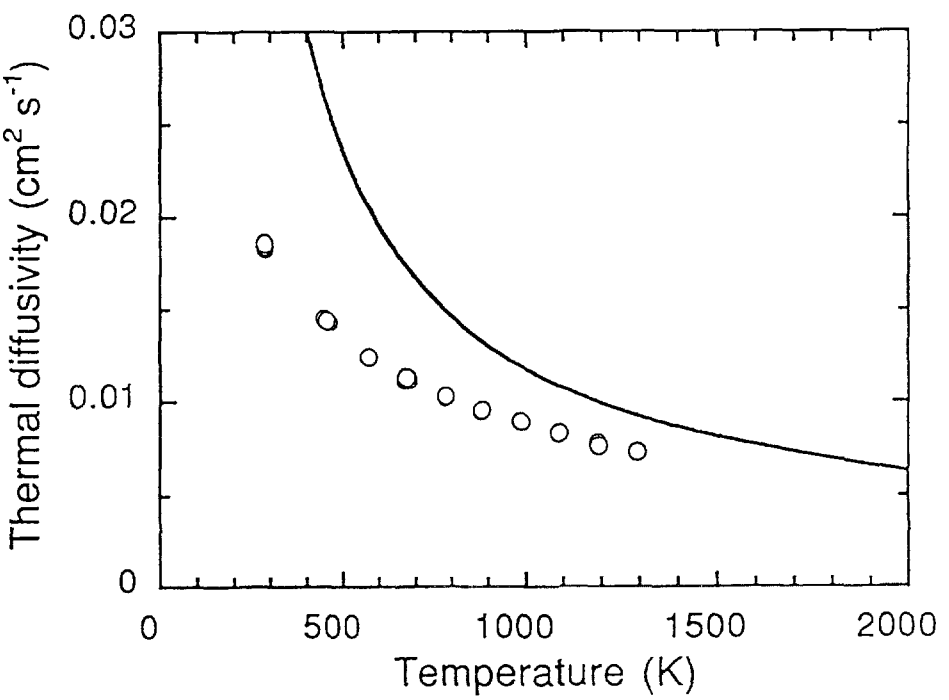

Fig. 1(b) Thermal diffusivities of simulated soluble FP doped UO_{2+x} pellets (equivalent burnup: 30GWd/tU).
○: (U,FP)$O_{2.02}$, —: UO_2[11].

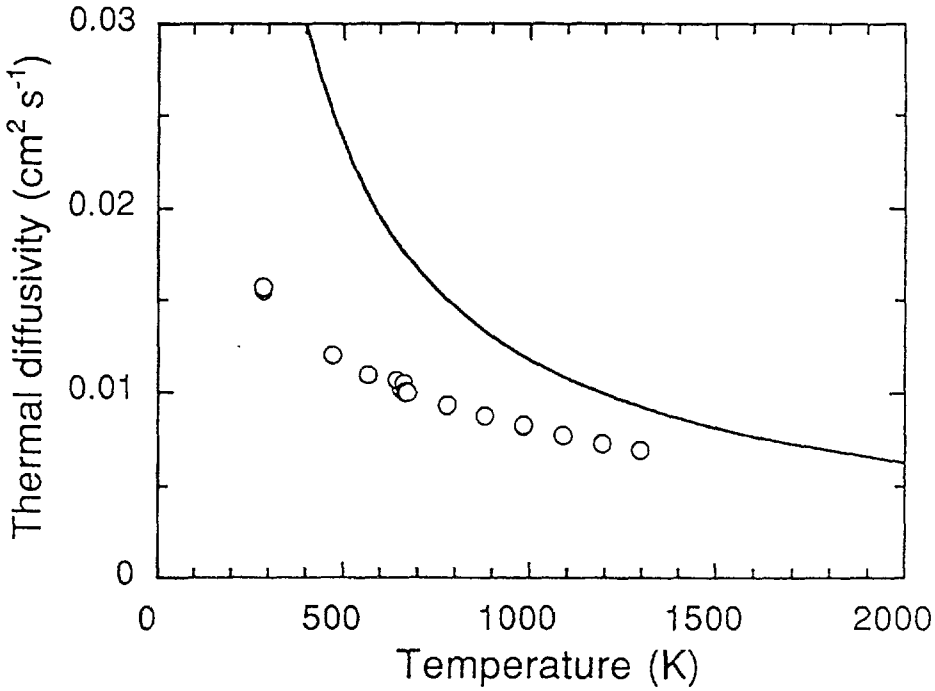

Fig. 1(c) Thermal diffusivities of simulated soluble FP doped UO_{2+x} pellets (equivalent burnup: 60GWd/tU).
○: $(U,FP)O_{2.02}$, —: UO_2[11].

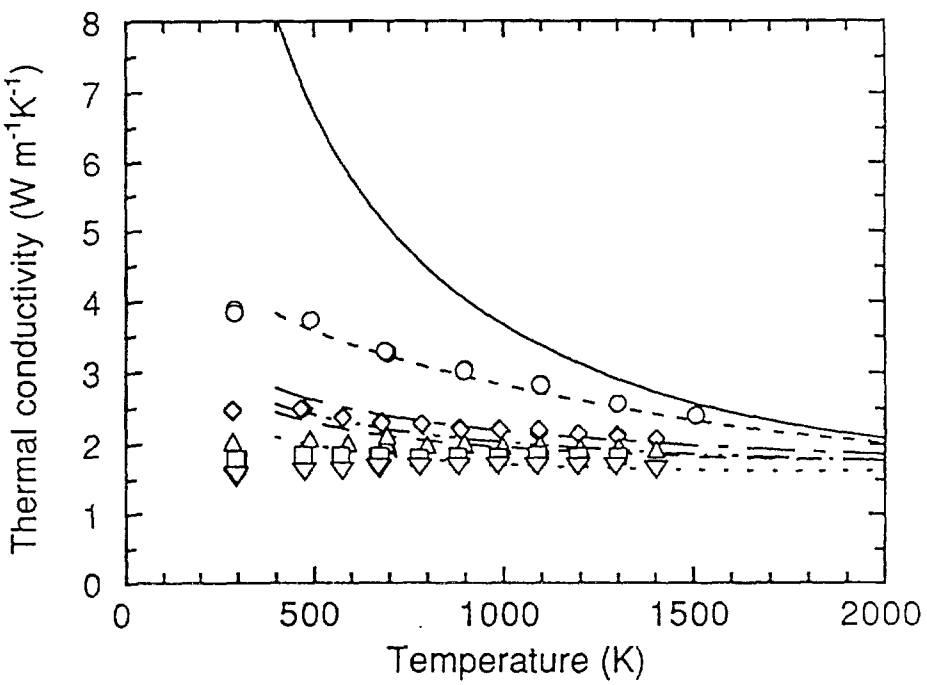

Fig. 2(a) Thermal conductivities of 10wt%Gd_2O_3 doped UO_{2+x} pellets.
○,◇,△,□,▽: measured values, —,---,—·—,—---—, — — —,···: calculated values from Eq.(10)
○: $(U.Gd)O_{2.00}$, ◇: $(U,Gd)O_{2.06}$, △: $(U,Gd)O_{2.08}$, □: $(U,Gd)O_{2.11}$, ▽: $(U,Gd)O_{2.15}$,
—: UO_2[15], ---: $(U,Gd)O_2$[15], —·—: $(U,Gd)O_{2.06}$, —---—: $(U,Gd)O_{2.08}$,
— — —: $(U,Gd)O_{2.11}$, ···: $(U,Gd)O_{2.15}$.

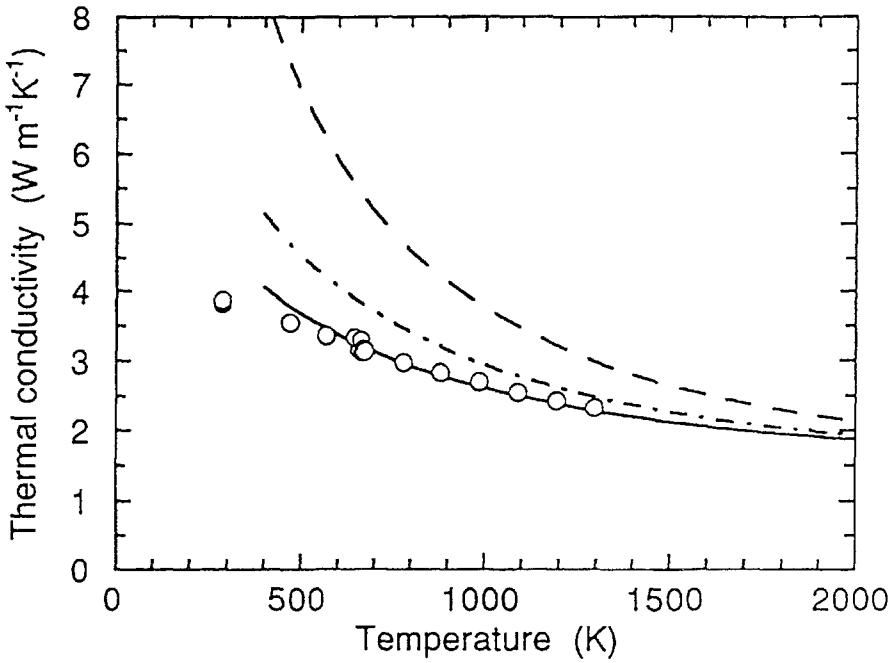

Fig. 2(b) Thermal conductivities of simulated soluble FP doped UO_{2+x} pellets (equivalent burnup: 30GWd/tU).
○: $(U,FP)O_{2.02}$, —·—: $(U,FP)O_2$[16], —: UO_2[15].

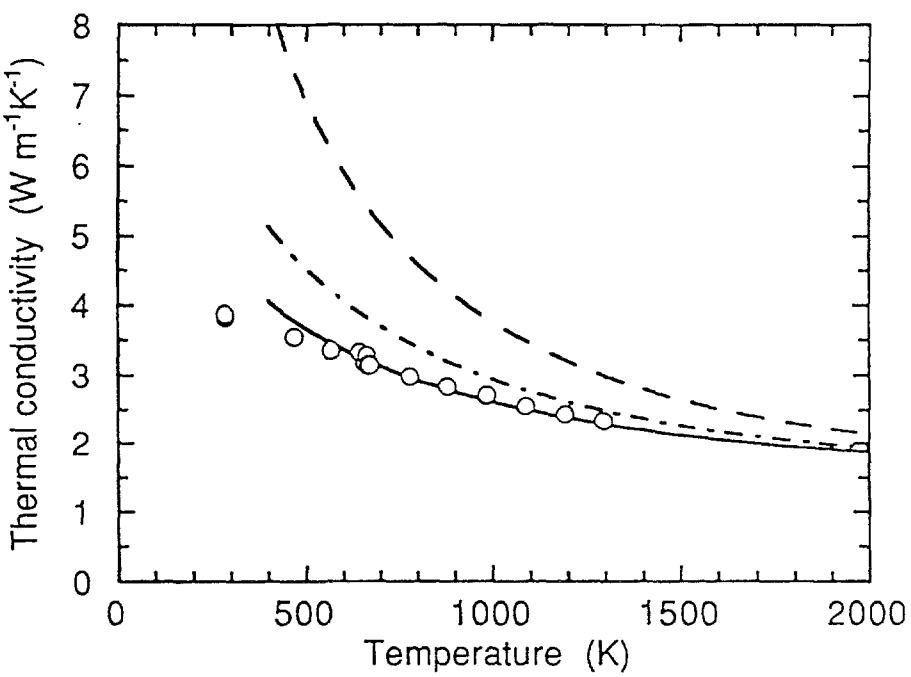

Fig. 2(c) Thermal conductivies of simulated soluble FP doped UO_{2+x} pellets (equivalent burnup: 60GWd/tU).
○: $(U,FP)O_{2.02}$, —·—: $(U,FP)O_2$[16], —: UO_2[15].

In general, phonon-phonon scattering (Umklapp process) and phonon-impurity (substitutional impurity) scattering are dominant mechanisms of heat resistance in ceramics above room temperature. Klemens [9,10] has proposed a heat conduction model in materials when phonon-phonon scattering and phonon-impurity scattering occur simultaneously. According to this model, the thermal conductivity of the crystal lattice in vibration λp is expressed as

$$\lambda_P = \lambda_0 \tan^{-1}(\theta)/\theta \quad (4)$$

$$\theta = S\sqrt{(\Gamma\lambda_0)} \quad (5)$$

where λ_0 is the thermal conductivity of impurity - free material; θ the phonon scattering parameter by the impurity; S, a coefficient; and Γ, a parameter expressed as

$$\Gamma = \sum_i y_i[(\Delta M_i/M)^2 + \xi(\Delta r_i/r)^2]. \quad (6)$$

Here y_i is the atomic partial ratio of the impurity; M, the mean mass; r, the mean ionic radius; ΔM_i, the mass difference between the impurity and matrix atoms; Δr_i, the ionic radius difference between the impurity and matrix atoms; and ξ, a coefficient.

In the $(U,M)O_{2+x}$ (M=Gd, simulated soluble FPs) crystal lattice, the excess oxygen atoms exist in interstitial positions and in order to maintain the electrical neutrality, U^{5+} ions must be present in the $(U,M)O_{2+x}$ crystal lattice.

From the thermal conductivity analyses of Gd_2O_3 [15] and/or simulated FP-doped UO_2 [16] and UO_{2+x} [7], the phonon scattering parameter, θ is nearly proportional to the square root of the concentrations of Gd^{3+}, and/or simulated FP and U^{5+} ions. Then, the following equation was assumed to hold:

$$\theta_i = [D_i\, y_i\, \lambda_0]^{1/2} \quad (7)$$

where θ_i is the phonon scattering parameter of impurity i (i = Gd^{3+}, simulated FP atoms and U^{5+}); D_i, a coefficient which expresses the effect of impurity i; and y_i, the atomic concentration of impurity i.

According to Klemens' theory [9, 10] based on the relaxation process of phonon scattering, the phonon scattering parameter, θ is proportional to the square root of the phonon scattering probability in the crystal lattice containing impurity. The phonon scattering probability by impurities in the $(U,M)O_2$ (M=Gd and/or simulated soluble FPs) crystal lattice is expressed as follows using the phonon mean free path:

$$(1/l_p) = (1/l_M) + (1/l_{O/U}) \quad (8)$$

where lp is the phonon scattering mean free path in $(U,Gd)O_{2+x}$; l_M is that in $(U,M)O_2$; and $l_{O/U}$ is that in UO_{2+x}. Therefore, the phonon scattering parameter θ is expressed as:

$$\theta^2 = \theta_M^2 + \theta_{O/U}^2 \quad (9)$$

where θ is the phonon scattering parameter of $(U,M)O_{2+x}$; θ_M is that of $(U,M)O_2$ and $\theta_{O/U}$ is that of $U\,O_{2+x}$. Fig. 3 compares the measured phonon scattering parameters evaluated from

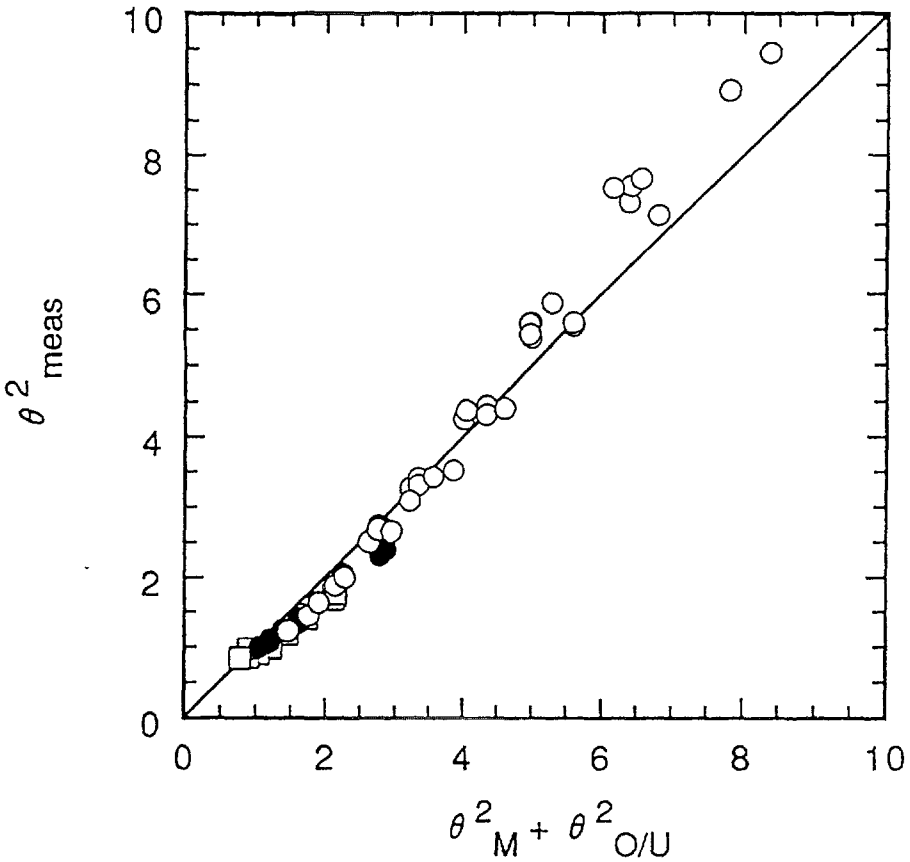

Fig. 3 Squared measured phonon scattering parameter, θ^2_{meas}, as a function of the calculated values using θ^2_M (M=Gd, simulated soluble FPs) and $\theta^2_{O/U}$ from Eq.(9).
○: $(U,Gd)O_{2+x}$, ●: $(U,FP)O_{2+x}$ (equivalent burnup: 30GWd/tU),
□: $(U,FP)O_{2+x}$ (equivalent burnup: 60GWd/tU), —: $\theta^2_{meas} = \theta^2_M + \theta^2_{O/U}$ (M=Gd, simulated soluble FPs).

the thermal conductivity and those calculated with Eq. (9) using our previous results of θ_M and $\theta_{O/U}$ [7,15,16]. The measured values showed fairly good agreement with the calculated values and the phonon scattering parameter could be expressed using the summation rule between the phonon scattering parameter of Gd^{3+} ions, soluble FP atoms and U^{5+} ions. The coefficients D_M (M=Gd, simulated soluble FPs) and $D_{O/U}$ were obtained in our previous studies [7,15,16]. Using these values, we formulated the thermal conductivity of $(U,M)O_{2+x}$ (M=Gd and/or simulated soluble FPs) for 96.5%TD as:

$$\lambda = \lambda_0 \{ \tan^{-1}(\theta)/\theta \} + CT^3 \quad (Wm^{-1}K^{-1}) \qquad (10)$$

where

λ_0 = $1/(A+BT)$
θ = $[D_{Gd}^2 y_{Gd}\lambda_0 + D_{FP}^2 y_{FP}\lambda_0 + D_{O/U}^2 (2x)\lambda_0]^{1/2}$
A = 3.24×10^{-2}
B = 2.51×10^{-4}
C = 5.95×10^{-11}
D_{Gd} = $D_{0,Gd} \exp(D_{1,Gd} T)$
D_{FP} = $D_{0,FP} \exp(D_{1,FP} T)$
$D_{O/U}$ = $D_{0,O/U} \exp(D_{1,O/U} T)$

$D_{0,Gd} = 3.24$
$D_{1,Gd} = -7.92 \times 10^{-4}$
$D_{0,FP} = 2.81$

$D_{1,FP} = -1.63 \times 10^{-4}$
$D_{0,O/U} = 3.67$
$D_{1,O/U} = -4.73 \times 10^{-4}$
x: deviation from stoichiometry

The values calculated by eq.(9) compared with measured ones in Fig. 3. Eq. (10) could express the thermal conductivity of $(U,M)O_2$ (M=Gd, simulated soluble FPs) fairly well in the temperature region above 700 K. Below 700K, the thermal conductivity calculated from Eq. (10) tended to be higher than the measured value. The difference between them could not be explained, but may be because of a Willis' (2: 1: 2) or (2 :2: 2) cluster which may exist in the $(U, M)O_{2+x}$, solid solution [17].

4. CONCLUSION

Thermal diffusivities of $(U,M)O_{2+x}$ (M=Gd, simulate soluble FPs) were measured by a laser-flash method from room temperature to 1400K. Thermal conductivities of $(U,M)O_{2+x}$ decreased as their hyperstoichiometry, x, increased. The concentration of U^{5+} ion formed by excess interstitial oxygen in relation to Klemens' equation led to the expression of λ, the thermal conductivity of $(U,M)O_{2+x}$ (M=Gd and/or simulated soluble FPs) pellets for 96.5%TD, as a function of their hyperstiochiometry x, impurity content y and temperature in K,

$$\lambda = \lambda_0 \{\tan^{-1}(\theta)/\theta\} + CT^3 \qquad (W\ m^{-1}\ K^{-1})$$

where

$\lambda_0 = 1/(A+BT)$
$\theta = [D_{Gd}^2 y_{Gd}\lambda_0 + D_{FP}^2 y_{FP}\lambda_0 + D_{O/U}^2(2x)\lambda_0]^{1/2}$
$D_{Gd} = D_{0,Gd} \exp(D_{1,Gd}\, T)$
$D_{FP} = D_{0,FP} \exp(D_{1,FP}\, T)$
$D_{O/U} = D_{0,O/U} \exp(D_{1,O/U}\, T)$
A, B, C, $D_{0,i}$ $D_{1,i}$ (i = Gd, FP, O/U): coefficient
y_M: atomic concentration of M (M = Gd, FP)

The values calculated by the above formula were in fairly good agreement with the measured values for 10wt% Gd_2O_3 doped UO_{2+x} ($0 \le x \le 0.15$) and simulated soluble FP doped UO_{2+x} ($0 \le x \le 0.02$, simulated burnup: 30 and 60GWd/tU).

ACKNOWLEDGEMENTS

The authors would like to express their gratitude to Dr. K. Une for valuable discussions. They also thank Mr. H. Masuda for sample preparation and Mr. Y. Okoshi for sample composition analysis.

REFERENCES

[1] UNE, K., IMAMURA, M., AMAYA, M., KOREI, Y., J. Nucl. Mater. 223 (1995) 40.
[2] ROSS, A.M., USAEC Reports, CRFD - 817, AECL - 1096 (1960).
[3] HOWARD, V.C., GULVIN, T.F., U.K.A.E.A IG Rpt., 51 (Rd/C) (1960).
[4] GOLDSMITH, L.A., DOUGLAS, J.A.M., J. Nucl. Mater. 47 (1973) 31.
[5] HOBSON, I.C., TAYLOR, R., AINSCOUGH, J.B., J. Phys. D (Appl. Phys.) 1003 (1974) 7.
[6] LUCUTA, P.G., MATZKE, Hj., VERALL, R.A., J. Nucl. Mater. 223 (1995) 51.
[7] AMAYA, M., KUBO,T., KOREI,Y., J. Nucl. Sci. Technol. 33 (1996) 636.
[8] AMAYA, M., HIRAI, M., KUBO, T., KOREI, Y., J. Nucl. Mater. 231 (1996) 29.
[9] KLEMENS, P.G., Proc. Phys. Soc. A68 (1955) 1113.
[10] KLEMENS, P.G., Phys. Rev. 119 (1960) 507.
[11] HIRAI, M., J. Nucl. Mater. 173 (1990) 247.
[12] TAKAHASHI, Y., YAMAMOTO, I., OHSATO, T., Netsu-Sokutei 15 (1988) 103.
[13] TREE-NUREG-CR-0497, HAGRMAN, D.L., REYMAN, G.A.(Eds.) (1979).
[14] BRANDT, R., NEUER, G., J. Non-Equilib. Thermodyn. 1 (1976) 3.
[15] HIRAI, M., ISHIMOTO, S., J. Nucl. Sci. Technol. 28 (1991) 995.
[16] ISHIMOTO, S., HIRAI, M., ITO, K., KOREI, Y., J. Nucl. Sci. Technol. 31 (1994) 796.
[17] WILLS, B.T.M., J. Phys. (Paris) 25 (1964) 431.

DISCUSSION

(Questions are given in italics)

What is the expected hyper-stoichiometry in fuel after ingress of steam?

We intend to estimate the fuel rod behavior after fuel rod failure in LWRs. The thermal conductivity degradation affects the fuel behavior largely.

CHEMICAL FORM OF FISSION PRODUCTS IN HIGH BURNUP FUELS

R.P.C. SCHRAM, R.J.M. KONINGS
Netherlands Energy Research Foundation,
Petten, Netherlands

XA9847860

Abstract

In order to make a proper assessment of candidate materials for advanced high-burnup fuels, thermochemical studies of fuel materials have been performed. Using data from the ECN thermochemical database (TBASE), which has been updated and extended for the present work, the suitability of various advanced fuel materials and inert matrices is studied. Detailed thermodynamic equilibrium calculations are performed for $Pu_{0.42}U_{0.58}O_2$ and $Pu_{0.40}U_{0.60}N$ for values of the burnup up to 200 MWd/kgHM. The formation of metallic phases, the pressure buildup and the stability of nitride or oxide phases is studied for each fuel type. The results for the chemical form of the solid fission products are given.

The chemical aspects of the use of the inert matrix spinel ($MgAl_2O_4$) in combination with oxide fuel will be discussed. Experimental research on the compatibility of various types of inert matrices (nitrides, spinel) is in progress at ECN.

1. INTRODUCTION

Fuels with burnup far beyond current values are presently considered for incineration of plutonium. This can be achieved by the use of MOX fuels in LWRs or LMRs, but also by the use of advanced fuels like nitride or inert matrix fuels, which seem more suited for LMRs. Development of such fuel concepts is presently underway, but extensive research is required to evaluate the fuel performance under such extreme conditions.

At high burnup, significant changes in the chemical composition of the fuel occur, since a large number of fission products is formed in the fuel matrix. Many of these fission products will dissolve in the fuel matrix, but some will be gases that collect in pores and some can precipitate in separate phases. It is important to know the chemical changes that occur at high burnup since such changes may affect the gas release and mechanical and thermal properties of the fuel.

Because information on the chemical composition at high burnup cannot be obtained easily from experiments (due to the long irradiation times), thermochemical calculations are an important tool to understand the chemical processes in nuclear fuels, as will be shown in the present paper. The thermochemical approach is used to evaluate the equilibrium composition of various fuel types as a function of burnup.

2. THERMOCHEMICAL DATABASE: ECN-TBASE

In order to predict the chemical state of high-burnup fuel, accurate thermochemical data are a necessity. In 1985, a project on the evaluation of physico-chemical properties of fission products and reactor materials was started at the Netherlands Energy Research Foundation ECN. This ongoing program has resulted in a thermochemical database which presently

contains data of about 800 compounds. A selection of 197 compounds was published previously [1]. Each compound is carefully assessed. The evaluated thermochemical properties are the enthalpy of formation and the entropy at room temperature and a set of coefficients of the enthalpy increments for each temperature range. For the condensed compounds, the transition enthalpies and crystallographic data are also stored. In addition, each compound has a short description about the assessment or the references. The thermodynamic database of ECN (TBASE) is available in electronic form. The database can be consulted by software (TBASE-consult) which can generate thermodynamic tables and graphs, evaluate chemical reactions calculate stability diagrams (Fig. 1). The Gibbs energy functions can be exported to Chemsage [2] datafiles for calculation of phase equilibria in, for example, high burnup fuels.

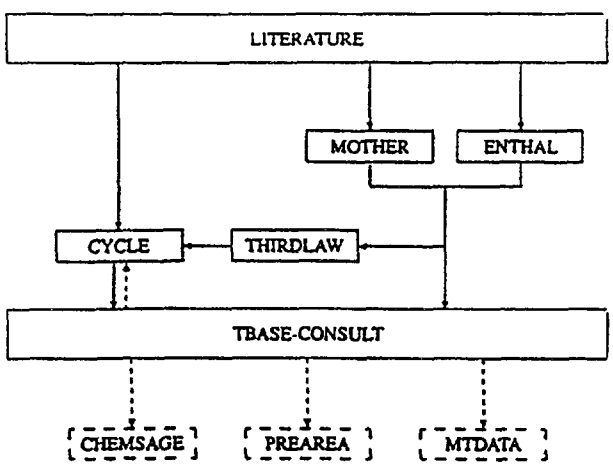

FIG. 1. Flow diagram of the ECN computer programmes used in the assessment of thermochemical properties.

Recently, the database has been updated with compounds relevant for actinide incineration studies. This includes data for inert matrices for both oxide and nitride fuels. The completion of the database with inert matrix data also requires data for the reaction products of these matrices with the fission products. Especially in high-burnup fuels the chemical reaction of the inert matrix with the fission products may affect the fuel integrity.

3. PHASE DESCRIPTION OF THE FUEL

Thermochemical calculations can predict the chemical behaviour of the fuel at high values of the burnup and may give a better understanding of the chemical processes in the fuel. The results of these calculations can be used as guidelines for the choice of fuel materials. In this section we will describe the input data files for the thermochemical calculations. Two data-input files for use with Chemsage were constructed; one is specific for oxide fuels, the other contains data for nitride fuels.

The predictive power of thermochemical calculations depends very much on the accuracy of the data and the completeness of the database that is used. Here we have chosen to take 30 elements into consideration. For the oxide fuel database these elements are: Ag, Al, Am, Ln, Ba, Ce, Cm, Cs, I, Kr, La, Mg, Mo, Nb, Nd, Np, O, Pd, Pr, Pu, Rb, Rh, Ru, Sr, Tc, Te, U, Xe, Y and Zr. Here the symbol Ln refers to lanthanide elements (=Pm, Sm,Eu,Gd,Tb,Dy,Ho,Er) that are treated as one representative lanthanide element. The elements Mg and Al are added to allow for the calculation of spinel matrices. All compounds that contain any of these elements are automatically selected within the ECN-Tbase and are exported to a Chemsage datafile. The compounds are grouped in different phases, so that phase separation phenomena during fission can be easily traced. The oxide fuel database is divided in five parts:

- GAS. This phase contains all gases. A total of 109 gases was considered.
- METAL. This phase represents the so-called five metal inclusions (Ru,Rh,Pd,Mo,Tc), the intermetallic compounds (U,Pu)(Ru,Rh,Pd)$_3$ and also metallic Ag and Te.
- OXIDE. This is the main oxide phase which contains 17 oxide compounds: actinide and lanthanide oxide (MO_2, M_2O_3) and solvents (BaO,MgO and SrO).
- GREY. This phase contains 9 perovskite compounds (Ba,Sr)(U,Pu,Zr)O_3 which form the so-called grey phase.
- Remaining condensed compounds(84) (e.g. CsI, Cs_2Te and spinel)

For the nitride fuel database the selected elements are: Ag, Am, Ln, Ba, C, Ce, Cm, Cs, I, Kr, La, Mo, N, Nb, Nd, Np, O, Pd, Pr, Pu, Rb, Rh, Ru, Sr, Tc, Te, U, Xe, Y and Zr. No OXIDE or GREY phase was defined here. The nitride datafile has the following structure:

- GAS. This phase contains all gases. A total of 116 gases was considered.
- METAL. This phase is identical to the METAL phase for the oxide datafile.
- NITRIDE. This phase contains all condensed nitride compounds (18). This includes the actinide and lanthanide mononitrides compounds (UN,PuN,LaN,CeN etc.) and U_2N_3, Mo_2N, Sr_3N_2 and Ba_3N_2.
- Remaining condensed compounds (119) (e.g. CsI and Cs_2Te)

All the mixture phases (GAS, METAL, NITRIDE,OXIDE and GREY) are assumed to be ideal mixtures phases. This is of course a very crude assumption which was made to get a quick insight in phase separation. In the future, it may however be necessary to add excess Gibbs energy terms for compounds with low solubility.

4. PHASE EQUILIBRIUM CALCULATIONS

The thermochemical calculations were performed for 1 cm^3 of oxide or nitride fuel. The temperature was fixed at 1500 K. The gas volume was assumed to consist of the porosity

of the fuel plus the available plenum volume in the pin per cm^3 of fuel. The calculations are performed as a function of the burnup. The nuclide inventory for $Pu_{0.42}U_{0.58}O_2$ and for $Pu_{0.40}U_{0.60}N$ was calculated for a fast reactor fuel inventory by use of coupled spectrum and burnup calculations [3].

4.1 Mixed oxide fuel

One of the most important parameters for oxide fuel is the oxygen potential. Since it is very hard to predict the oxygen potential in these large-scale thermodynamic calculations, the oxygen potential is fixed at a constant value of -300 kJ/mol. This is the approximate value of the oxygen potential of $Pu_{0.42}U_{0.58}O_2$ at 1500 K [4]. The actual oxygen potential may increase during fission, although a buffering reaction of the Mo/MoO_2 couple may limit the oxygen potential at a lower level: -325 kJ/mol.

The present composition is a reference oxide, other systems such as oxide fuel + inert matrices can be compared with the results of this system. The density of this oxide is 95.5%T.D. Evaluation of a typical fast reactor pin design shows that the free volume is 1.66 cm^3 per cm^3 of fuel pellet. It is assumed that the total available gas volume is the gas space in the solid (given by the porosity) plus the free volume. The gas volume for this system is therefore: $(1-0.955)*1cm^3 + 1.66cm = 1.71\ cm^3$. The gas pressure during fission is mainly determined by the noble gases; the gas phase consists for ≈ 90% of Xe and Kr. The pressure increases linearly with the burnup and reaches a maximum of 157 bar at 203 MWd/kgHM (Fig. 2(a)). The calculated pressures are the maximum pressures in the plenum in case all gases are released to the plenum, the actual pressures inside gas bubbles in the solid may be larger.

The phase behaviour of the fuel during fission is depicted in Fig. 2(b). At the lowest burnup the (fresh) fuel consists of one phase: the OXIDE phase. As the burnup increases, the concentration of the fission products increases and new compounds and phases are formed. One of the well-known phases is the METAL phase which represents the metallic inclusions that are found in irradiated fuel [5]. In addition to the METAL phase, oxide precipates were found to consist mainly of Cs_2MoO_4 and $BaMoO_4$. The GREY phase was not formed, presumably because the oxygen potential is too high.

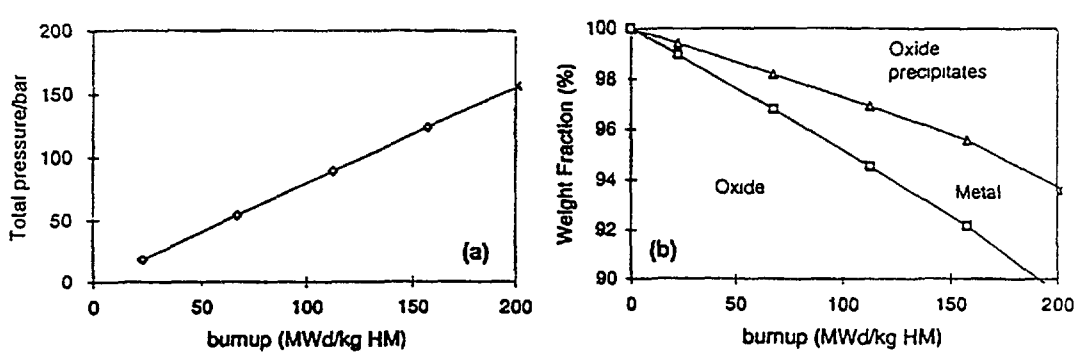

FIG. 2. Behaviour of the MOX fuel as a function of burnup at T=1500 K and oxygen potential of -33 kJ/mol.
(a) Pressure; (b) Weight percentage of the different solid phases.

As an example, the speciation of Mo and Cs in the solid phases was calculated. The mole fraction of these elements in different phases is plotted in Fig. 3(a) and (b). Molybdenum is found to occur both in the METAL phase and as molybdate in the oxide precipitates. All the iodine of the fuel is converted in CsI.

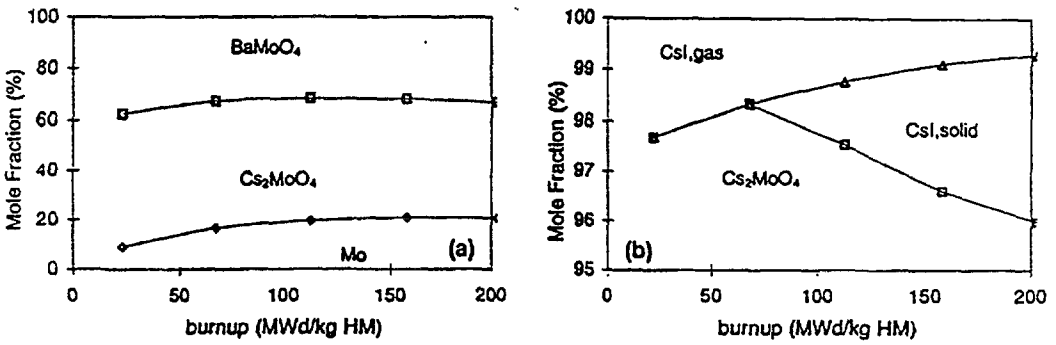

FIG. 3. *Speciation of (a) Mo and (b) Cs in oxide fuel at T = 1500 K and an oxygen potential of -300 kJ/mol.*

4.2 Nitride fuel

Here we will evaluate the behaviour of a mixed nitride fuel $Pu_{0.40}U_{0.60}N$. It is assumed that the fuel is free of oxygen. The density of the nitride fuel is 85 % T.D. The gas volume for this system is therefore: (1-0.85)* $1cm^3$ + $1.66cm^3$ = $1.81cm^3$. The development of the gas pressure as a function of the burnup is shown in Fig. 4(a). Again the gas atmosphere consists mainly of Xe and Kr. The gas pressure is deflected downwards at high burnup, which is related to the condensation of cesium. In contrast to the oxide fuel calculations, there are very few cesium compounds that can be formed in the nitride fuel. From the estimates in Ref. [6] it seems highly unlikely that cesium nitride (Cs_3N) will be formed.

The phase behaviour of the nitride fuel is shown in Fig. 4(b). As the burnup increases the amount of NITRIDE phase decreases and a METAL phase and "precipitates" in the form of Cs_2Te,Cs and CsI are formed. The METAL phase consists for more than 50 w% out of the very stable intermetallic compounds (U,Pu)(Ru,Rb,Pd)$_3$. The amount of METAL phase is slightly larger than the METAL phase of the oxide fuel. This is partly due to the high Mo content of the METAL phase, which is shown in Fig. 5(a). More than half of all the Mo can be found in the metallic phase, whereas for the oxide fuel (Fig.3(a)) only 20% of the Mo is metallic. At low values for the burnup more than 50% of the cesium is gaseous, the gas pressure of cesium increases to about 20 bars at 100 MWd/kgHM. At that burnup, the saturation pressure of cesium is reached and condensation of cesium metal starts. Part of the cesium reacts with Te and forms Cs_2Te.

The nitrogen pressure is shown in Fig. 6(a). The pressure remains below 0.1 bar and is controlled by the UN/U_2N_3 couple. As the burnup increases, the UN density decreases and U_2N_3 is formed (Fig. 6(b)). Uranium nitride (U_2N_3) plays an important role in the nitrogen balance, it takes up almost all nitrogen that is released during fission.

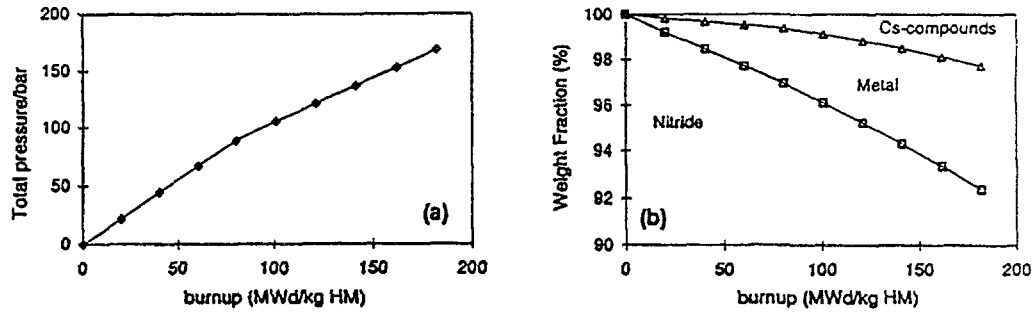

FIG. 4. *Behaviour of the nitride fuel as a function of burnup at T = 1500 K. (a) Pressure; (b) Weight percentage of the different solid phases.*

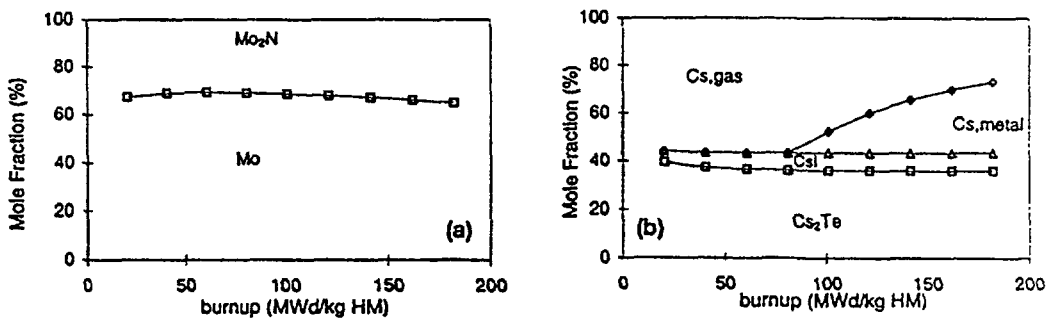

FIG. 5. *Speciation of (a) Mo and (b) Cs in nitride fuel at T = 1500 K.*

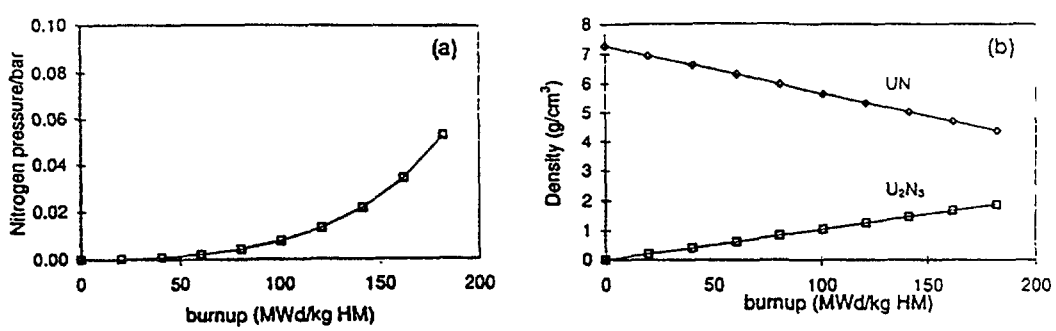

FIG. 6. *(a) Nitrogen pressure in the gas plenum and (b) Amount of UN/U_2N_3 in the solid at T = 1500 K.*

5. COMPATIBILITY OF SPINEL WITH OXIDE FUEL

Spinel ($MgAl_2O_4$) is one of the candidate materials for use as an inert matrix in oxide fuels. Apart from neutronic requirements (low activitation of Mg, Al and O) the inert matrix should have good chemical compatibility with the fuel and the fission products. Ideally, an inert matrix mixes in all proportions with the fuel and does not react with the fission products. Even at high burnup, when a large amount of fission products is dissolved in the fuel, the inert matrix should remain intact and chemical reactions may not affect the physical integrity of the fuel pellet.

One of the reactions with fission products that may occur in spinel-based fuel pellets is the reaction with the lanthanide elements:

$$MgAl_2O_4 + 2\,Ln + 1½O_2 \rightarrow 2LnAlO_3 + MgO$$

The lanthanide aluminates are stable compounds at normal operating conditions, so formation of these compounds may be expected. A calculation of the chemical state of spinel in a mixture of $PU_{0.42}U_{0.58}O_2$ + 60 vol% spinel was performed. All the lanthanide elements (Ln) were represented by lanthanum, and the lanthanide aluminates were represented by $LaAlO_3$. The thermochemical data of the lanthanide aluminates are given in Ref [7].

In Fig. 7 the speciation of Al in the different phases is shown. At 203 MWd/kgHM 95.5 w% of the initial amount of spinel is left. Aluminium is not only found in the spinel phase and as $LnAlO_3$ but also in Al_2O_3. This can be explained by the following reaction:

$$MgAl_2O_4 \rightarrow Al_2O_3 + MgO\ (OXIDE)$$

In this evaluation it was assumed that MgO dissolves in the OXIDE phase, which promotes this partial decomposition of spinel. Even when no lanthanide elements are present, spinel will decompose in Al_2O_3 and MgO. Lanthanum is found for more than 90% in the form of $LnAlO_3$, the rest is dissolved in the OXIDE phase as Ln_2O_3. The assumption that MgO forms an ideal mixture with the oxides is not completely correct. In fact, the evaluation of the MgO-PuO_2 phase diagram [8] shows that at 1500 K 0.6 mole% MgO can dissolve in PuO_2. According to [9] the solubility of MgO in UO_2 is approximately 35 mole% at 1600-1700°C. The calculated concentration in of MgO in the OXIDE phase (ideal mixing) is 4.8 mole% and does not depend on the burnup. Additional calculations showed that when MgO cannot dissolve in the OXIDE phase, no Al_2O_3 will be formed.

The compatibility of various inert matrices with fission products was examined at ECN. Interaction experiments were performed with spinel and lanthanide oxides. Lanthanide sesquioxide (Ln_2O_3, Ln=La,Nd and Eu) were mixed with spinel and heated at T=1473 K. The formation $LnAlO_3$ was confirmed by X-ray diffraction. This supports the thermochemical predictions for the formation of lanthanide aluminates. The question however is, if plutonium will form $PuAlO_3$ with spinel. $PuAlO_3$ was formed from PUO_2 and Al_2O_3 or $Al(OH)_3$ in

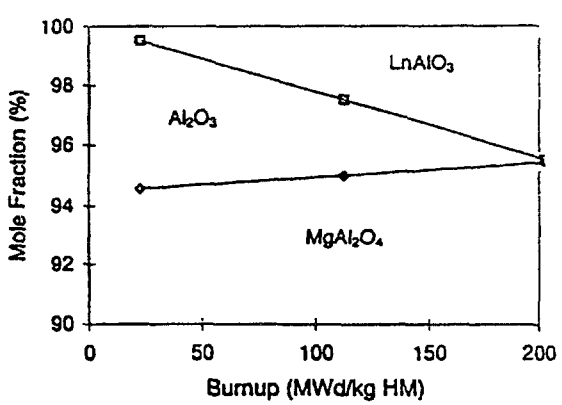

FIG. 7. Speciation of Al in spinel-based oxide fuel. The mole fraction Al is plotted as a function of the burnup at T = 1500 K.

strongly reducing environments (carbon powder or hydrogen atmosphere) [10]. Thermochemical data for $PuAlO_3$ are required to predict the compatibility of PuO_2 with spinel.

6. CONCLUSION

A thermochemical analysis of high burnup MOX and mixed nitride fuel was performed. For both the oxide and the nitride fuel it was found that a metal phase of about 4-5w% is formed at a burnup of 180 MWd/kgHM. The speciation of Mo showed that in oxide fuel molybdenum is predominantly present as cesium- or barium-molybdate, whereas in the nitride fuel it is mainly found in the metallic phase. The cesium pressure in the gas plenum of the nitride fuel reaches the saturation pressure at high burnup so that metallic cesium will be formed.

The chemical compatibility of spinel with oxide fuel was examined. It seems that the formation of lanthanide aluminates from spinel and the lanthanide elements is likely at normal thermodynamic conditions (T=1500 K, oxygen potential=-300 kJ/mol). At 203 MWd/kgHM about 4.5w% of the initial amount of spinel is decomposed. The solubility of MgO in the OXIDE phase seems to be important for the stability of spinel, already at low values of the burnup.

The presented thermochemical calculations are based on ideal mixture phases. More detailed models including excess parameters will be an item for future research.

Acknowledgement

The authors thank J. L. Kloosterman for providing the nuclide inventories of the oxide and nitride fuel.

References

[1] CORDFUNKE, E.H.P. and KONINGS, R.J.M., Thermochemical data for reactor materials and fission products. Elsevier Science Publishers, (1990).

[2] ERIKSSON, G. and HACK, K., ChemSage - A computer program for the calculation of complex chemical equilibria Metall.Trans. 21B (1989) 1013-1023.

[3] KLOOSTERMAN, J.L., KUIJPER, J.C., and DE LEEGE P.F.A., The octopus burnup and criticality code system. ECN-RX-96-032, ECN, (1996).

[4] BESMANN, T.M. and LINDEMER, T.B., Chemical thermodynamic representations of (PuO_{2-x}) and (U_{1-z},Pu_zO_w). J.Nuel.Mater. 130 (1985) 489-504.

[5] KLEYKAMP,H., The chemical state of the fission products in oxide fuels. J.Nucl.Mater 131 (1985) 221-246.

[6] ANDERSON, R.N. and PARLEE,N.A.D., Standard Free Energy of Nitride Formation from the Elements, an Estimation Technique. High.Temp.Sci. 2 (1970) 289-292.

[7] WU, P. and PELTON, A.D., Coupled thermodynamic-phase diagram assessment of the rare earth oxide-aluminium oxide binary systems. J.Alloys.and.Compounds 179 (1992) 259-287.

[8] ZHANG, H., HUNTELAAR, M.E., KONINGS, R.J.M., and CORDFUNKE, E.H.P., Melting behaviour of oxide systems for heterogeneous transmutation of actinides. Part I. The systems Pu-AI-O and Pu-Mg-O. ECN-I-96-046, ECN, (1996).

[9] BUDNIKOV, P.P., TRESVYATSKY, S.G., and KUSHAKOVSKY, V.I., Binary phase diagrams for UO_2-Al_2O_3, UO_2-BeO and UO_2- MgO. In Proceedings of the Second United Nations International Conference on the peaceful Uses of Atomic Energy, held in Geneva, 1 September-13 September 1958., volume 6, (1958) 124-131.

[10] RUSSELL, L E., HARRISON, J.D.L., and BRETT, N.H., Perovskite-type compounds based on plutonium. J.Nucl.Mater. 2(4) (1960) 310-320.

FISSION GAS RELEASE

(Session 5)

INFLUENCING AND OPTIMIZING FUEL PELLET PARAMETERS FOR ACHIEVEMENT OF EXTENDED BURNUP

A.V. MEDVEDEV, J.K. BIBILASHVILI,
O.V. MILOVANOV, S.M. BOGATYR
A.A. Bochvar All-Russia Research Institute of Inorganic Materials,
Moscow, Russian Federation

Abstract

Increase of burnup up to 50-60 MWd/ kgU with transition on 5 and 6 year fuel cycles makes an urgent problem of further fuel improvements.

In this connection the influence of fuel pellet characteristics on fuel rods behaviour at extended burnup is analysed. It is shown, that optimization of such structural parameters as the grain size, porosity can allow to improve performance of fuel rods and to reach high burnup. Data on stages of WWER-1000 pellet perfection, including the characteristic of perspective fuel are indicated. The executed researches of oxide fuel with the additives show profit of this direction in improvement of fuel rods reliability and burnup extension.

INTRODUCTION

The achieved level of design and technology has ensured now realization of fuel cycles in WWER reactors with average burnup 42- 45 MWd/kgU.

The primary coolant activity, inspection fuel integrity (IFI) and post-irradiation examination show their high performance and reliability. The loss-of-integrity intensity is as low as $(1\text{-}2)\cdot 10^{-5}$.

At the same time in Russia the working program on improvement of fuel cycles economy with burnup increase up to 50-60 MWd/kgU is carried out.

It dictates necessity of further perfection of fuel element design and technology in order to provide and increase of their serviceability and safety under extended burnup.

The important place in a complex of such work belongs to optimization of the fuel pellet characteristics.

1. CENTRAL HOLE SIZE IN FUEL PELLET

The fuel loading increase because of reduction of a central hole diameter in a fuel pellet is favorable for physics and economy of a reactor core. However it is accompanied by increase of fission gas release and reduction of free volume in a fuel rod.

Fig.1 shows the calculated fission gas release value in a fuel rod WWER-1000 depending on a central hole diameter in a range of 0.5 ...2.5 mm.

The influence of this pellet parameter is rather appreciable and it should be taken into account at development of fuel for increased burnup.

The growth of gas release is connected with increasing of temperature in central layers of a fuel pellet.

2. STRUCTURAL PARAMETERS OF FUEL PELLET

The fuel pellet structure influences complexly on a fuel rod performance and consequently its optimum parameters should be defined on the basis of the analysis of various processes inside a fuel rod. Here thermophysical as well as thermomechanical aspects of fuel rod behaviour are equally important.

The level of gas release is increased with burnup extension. As an example, gas release in WWER-440 fuel rods depending on average fuel rod burnup is submitted in Fig.2. Experimental data of post-irradiation examinations and also results of comparative calculations, executed on a code START-3, using in Russia for designing and licensing of power reactors fuel rods are shown there.

Such increase of gas release at transition to fuel cycles with extended burnup should be compensated at the expense of further improvement of fuel.

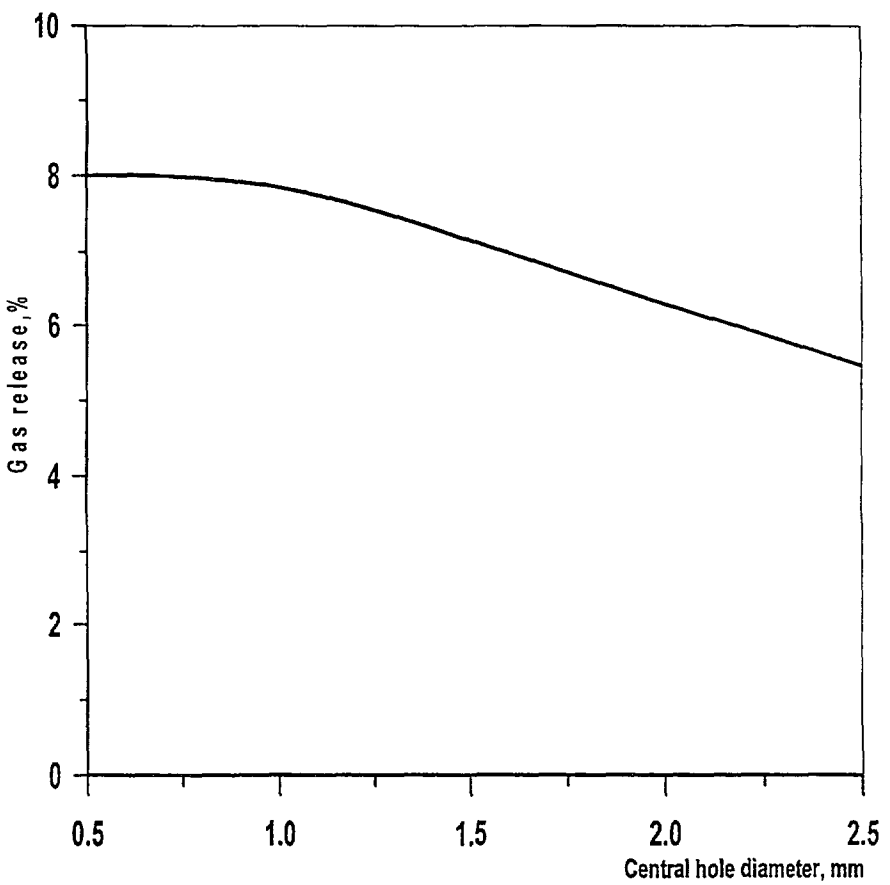

FIG. 1. Gas release v.s. central hole diameter

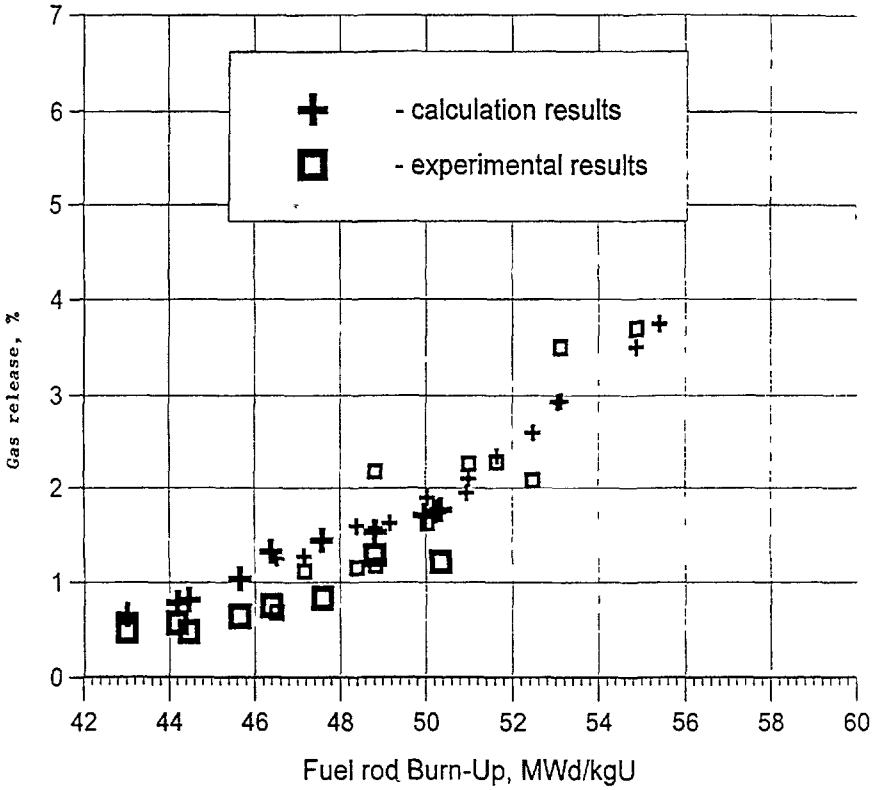

FIG. 2. Fission Gas Release from VVER-440 fuel at extended burnup

2.1. Open Porosity

The optimum pellet microstructure should provide a minimum open porosity. Open porosity is harmful for technology (adsorption of gases, moisture ...) and promotes increased gas release, as it is visible in Fig.3.

The requirements to this parameter become more and more rigid: from "unlimited" for early types of fuel, to < 1 % now and to < 0.5 % in the nearest future (Table 1).

2.2. Irradiation Densification

The irradiation densification can render essential adverse action on a fuel rod condition. First of all, one can result in occurrence of undesirable axial gaps in a fuel column. Secondly, the densification makes worse a heat-transfer between pellet and cladding (Fig.4), giving rise to the higher temperature of fuel and reserved energy (enthalpy), important characteristic of fuel rod behaviour in accident conditions. By means of fuel temperature the irradiation densification is able to effect on fission gas release (Fig.5).

For these reasons the densification is limited now by a value of 0.4 % linear and the further decrease up to < 0.25 % linear is supposed.

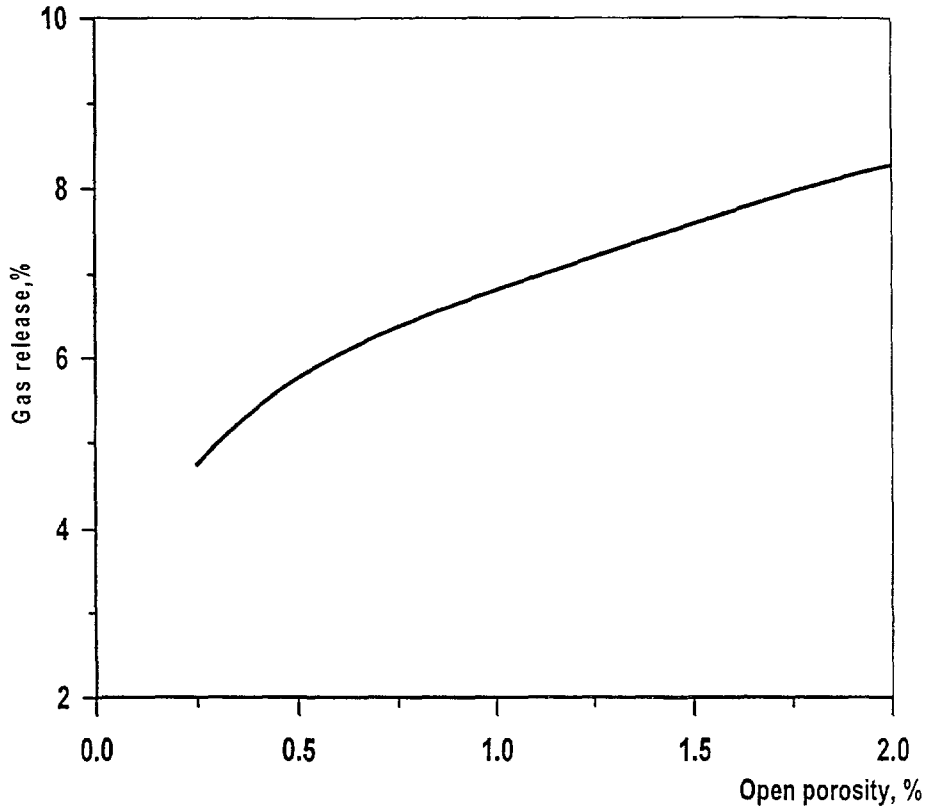

FIG. 3. Gas release v.s. open porosity

TABLE I. THE SPECIFICATION REQUIREMENTS FOR WWER-1000 FUEL PELLETS

Year	Density, g/cm3	The admission on a diameter, mm	The grain size, μm	Densification ability $\Delta D/D$, %	Open porosity, %	Hydrogen content, %
1982	10.3-10.8	0.05	Not lim.	Not lim.	Not lim.	0.0007 (moisture)
1983	10.4-10.8	0.05	Not lim. (6-8)	Not lim.	Not lim.	0.00009
1989	10.4-10.8	0.04	Not lim. (8-9)	0.4	Not lim.	0.00009
1995	10.4-10.7	0.03	10-20 (10-12)	0.4 (0.3)	$\leq$ 1	0.00006
Advanced fuel	10.4-10.6	0.025	20-25	0.25	$\leq$ 0.5	0.00006

Note: ( ) - practical data during manufacturing.

2.3. Grain Size

Grain size of a sintered pellet directly influences on fission gas release as it's shown in Fig.5.

At early stages of fuel production this parameter was not specially limited, however practically the grain size was rather small: 6...8μm (Tabl.1). The current fuel has a grain of 10...20 μm.

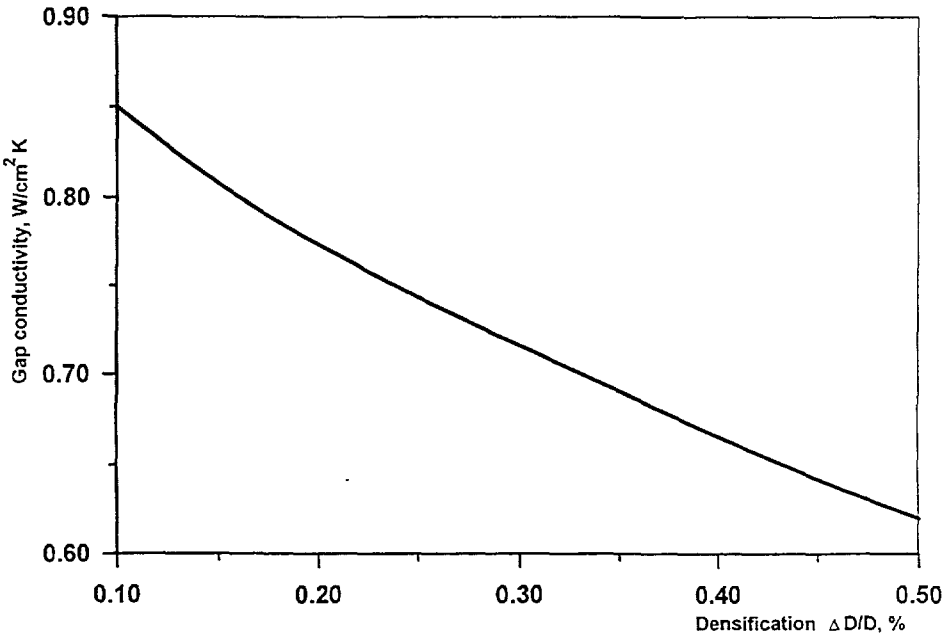

FIG. 4. Gap conductivity v.s. fuel pellet densification

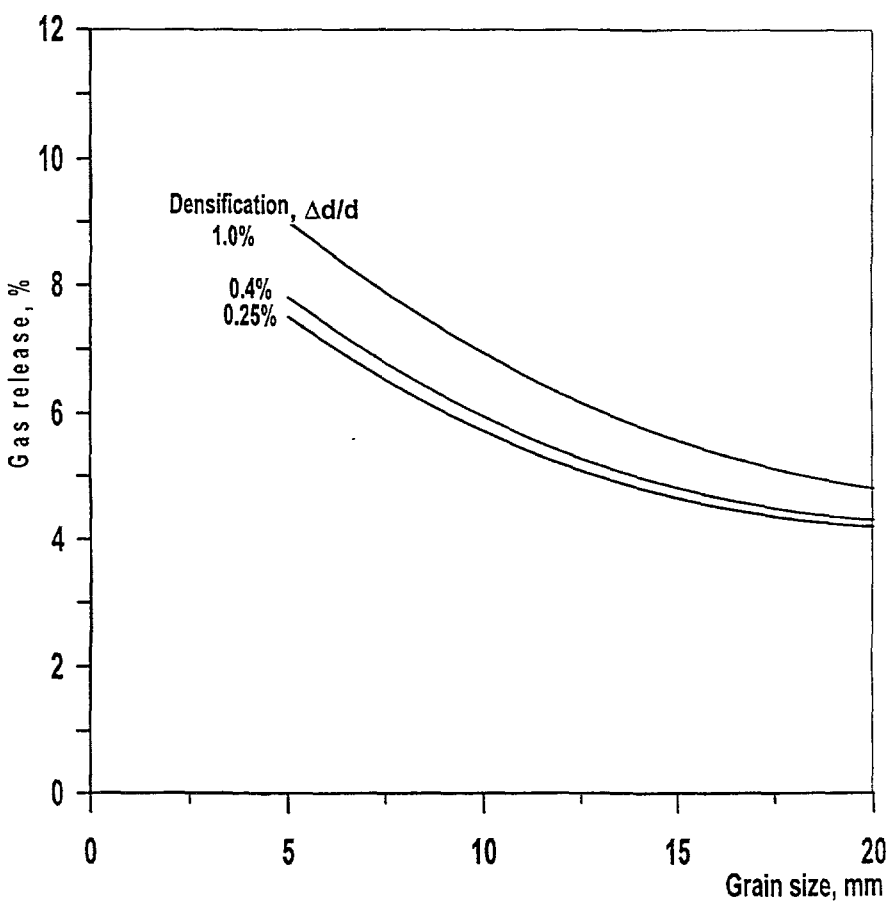

FIG. 5. Gas release v.s. grain size and fuel densification

Apparently the optimum size is of 20-25 μm. Besides technological problems the further increase of a grain results in loss of plasticity and creep of pellets, as the creep rate, for example, is inversely proportional to square of the grain size ($1/d^2$).

The separate consideration of the fuel pellet characteristics have shown a level of their influence on fuel rod behaviour. In Fig.6 with reference to 4 years fuel cycle their cumulative effect on calculated fission gas release in a fuel rod WWER-1000 is shown.

Here the"old" fuel means: grain size G = 6 μm, open porosity $P_o > 1\%$, densification $\Delta d/d > 0.4\%$;
the current fuel: G = 15 μm, $P_o = 1\%$, $\Delta d/d = 0.4\%$;
the advanced fuel: G = 20 μm, $P_o = 0.5\%$, $\Delta d/d = 0.25\%$.

The curves corresponds:

1- "old" fuel with a central hole diameter d_0=2.3 mm;
2- "old" fuel, d_0=1.5 mm;
3- current fuel, d_0=1.5 mm;
4- advanced fuel, d_0=1.5 mm.

The optimization of pellet structure results in effective reduction of gas release and is capable to ensure a high performance of fuel rods at extended burnups.

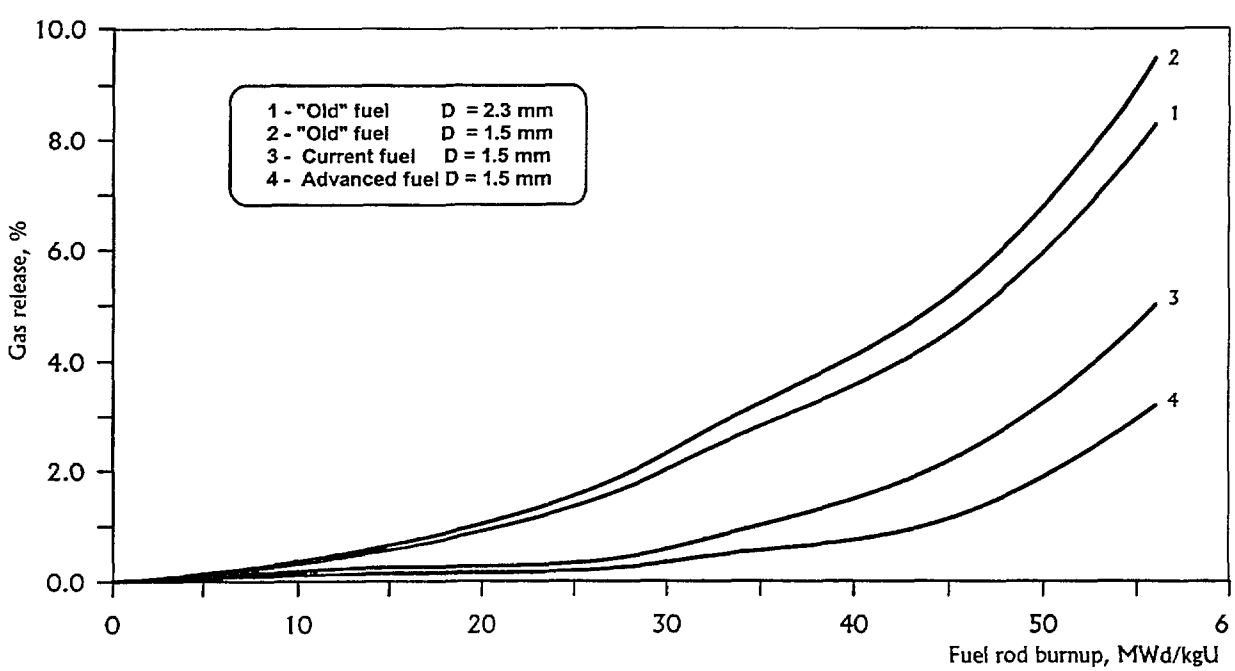

FIG. 6. Gas release v.s. burnup for different fuel pellet design parameters

In Table 1 stages of fuel pellets improvements, including perspective parameters are submitted.

3. OXIDE FUEL WITH ADDITIVES

In order to provide high serviceability of fuel rods the fuel pellets should have sufficient plasticity, creep rate (decrease PCI), and simultaneously low gas release (large grain structure).

These two opposite requirements cannot be easily realized in standard fuel. However this problem can be solved by introduction the special additives in a fuel. One of possible ways of ductility and creep rising of uranium dioxide is its doping by complex oxides, forming eutectics with low melting temperature on grain boundary. In this case there is possibility to receive also optimized pellet microstructure concerning gas release.

Such direction is under development now in Russia. Pellets with the additives demonstrate much lower (on 600°C) temperature of the brittle-ductile transition (below which fracture arises by brittle mode) and higher residual plasticity (Fig.7). The creep of such pellets also is rather higher than standard ones (Fig.8), including pellets with optimized microstructure.

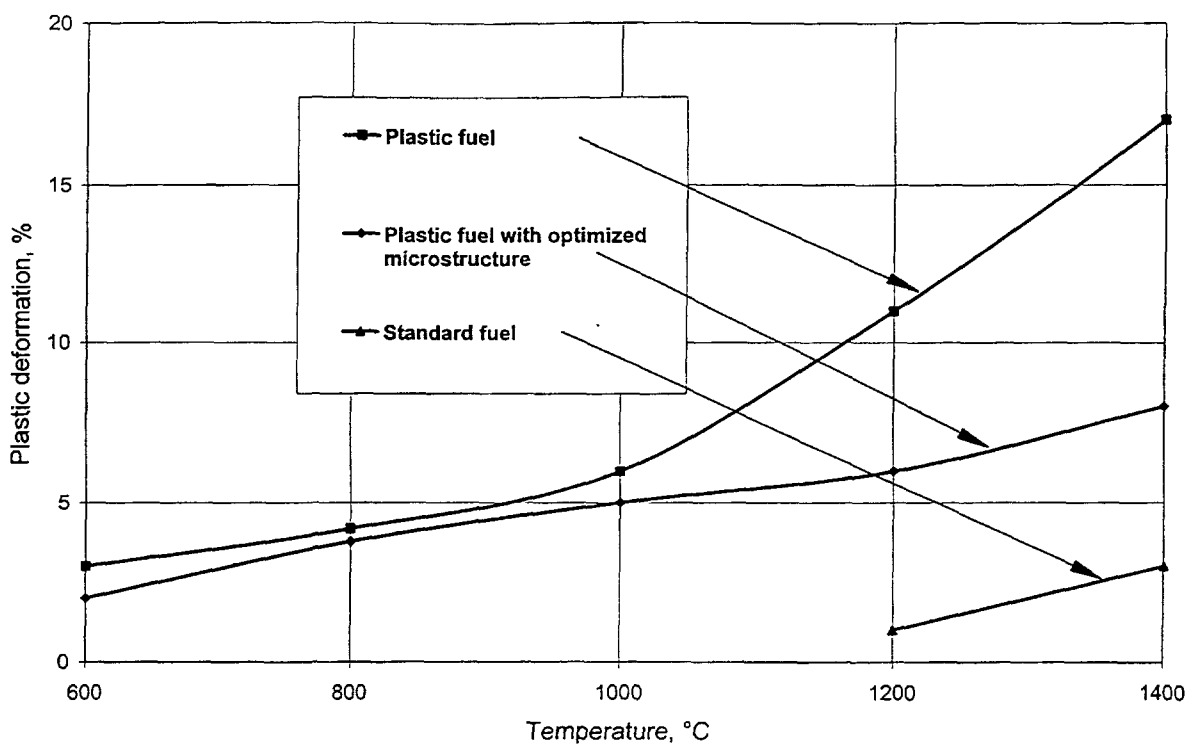

FIG. 7. Plastic fracture deformation of uranium dioxide fuel pellet

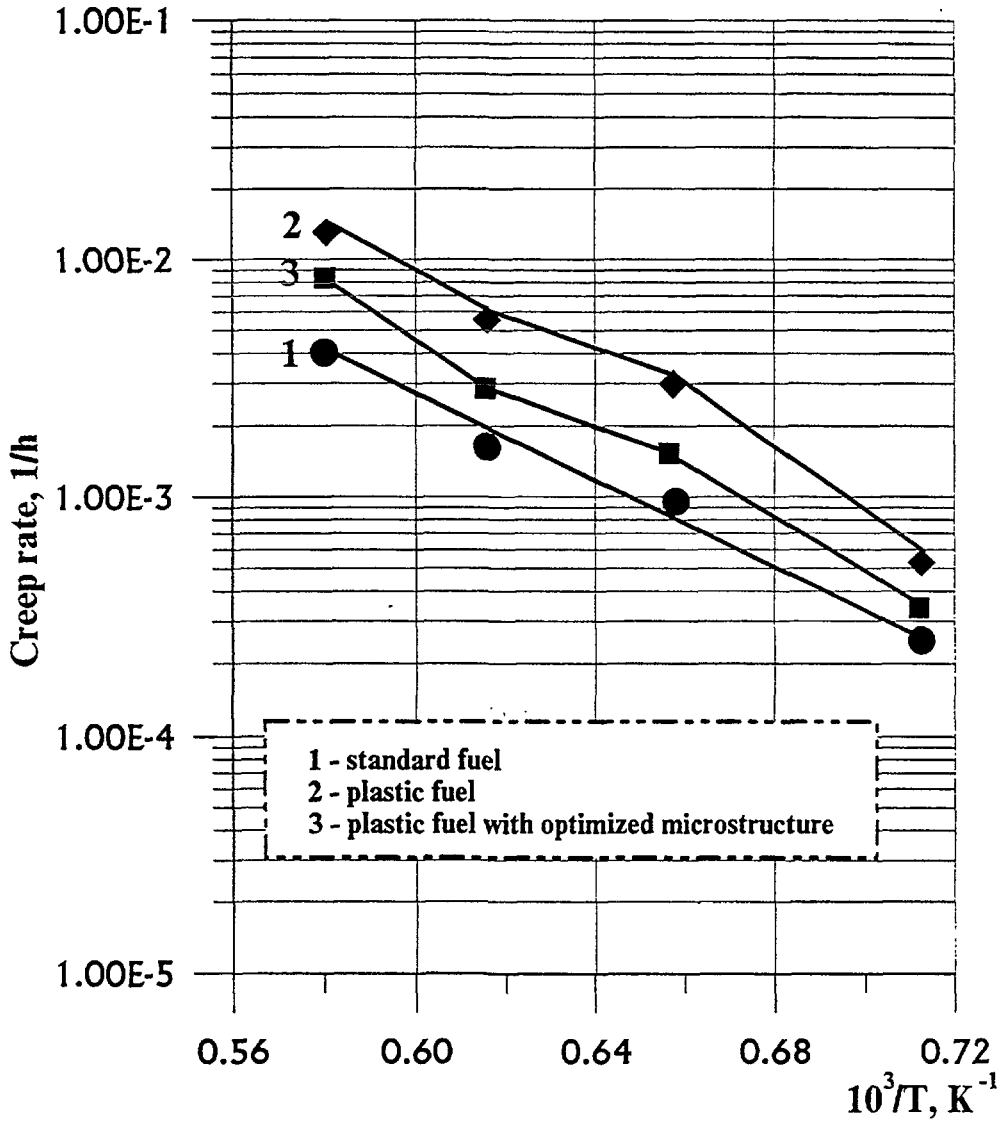

FIG. 8. Creep rate v.s. temperature for three types of fuel based on dioxide uranium

CONCLUSION

The conducted analysis confirms the importance of fuel improvements by means of pellet microstructure optimization for achievement of extended burnup. The fuel designed to the present time reliably provides serviceability of fuel rods in 4 years fuel cycle. Further improvement will allow to provide 5 and 6 years fuel cycles with burnup of 50-60 MWd/kgU.

The development and introduction of oxide fuel with additives can promote further progress in improvement of reliability of fuel rods and increase of burnup.

DISCUSSION

(Questions are given in italics)

Concerning Fig. 6, could you explain the power level of each fuel rod?

The various types of fuel were calculated under the same irradiation history. One corresponds to standard conditions of four years fuel cycle. The level of heat rating and its range during company correspond to assembly having maximum burnup in 4-years fuel cycle.

Could you give us some more information on plastic pellets? What is the reason for larger plastic deformation and higher creep rate?

Plasticity of fuel pellet is favorable for fuel rod behavior under transient conditions because of decreasing of pellet cracking. First of all, the pellet cracking promotes to FGR due to increase of free surface in pellet, temperature growth. Secondly, the fuel column with cracked pellets has more hard axial interaction with cladding that can stipulate high axial growth of fuel pin, particularly under load-following condition. Creep property appears to be useful so as to reduce PCI, essentially if pellets have center hole.

THE ROLE OF THE PELLET RIM ON FISSION GAS RELEASE AT EXTENDED BURNUP

R. MANZEL
Siemens AG,
Unternehmensbereich KWU,
Erlangen

M. COQUERELLE
CEC Institute for Transuranium Elements,
Karlsruhe

Germany

Abstract

In the past decade the discharge burnup of PWR fuel assemblies has steadily been increasing and in the meantime has reached maximum assembly average values of 55 MWd/kgU. Higher target burnups require higher fuel enrichments. Fuel rods with higher enrichment are operated at higher average power and hence higher fuel temperatures over a longer period of time. The fractional fission gas release of such fuel rods increases with burnup from about 7 % at 50 MWd/kgU to about 12 % at a rod average burnup of 75 MWd/kgU. The fission gas release characteristic is being discussed and correlated with fuel structural changes with emphasis on the pellet rim.

1. INTRODUCTION

Fission gas release is an important aspect in the analysis of the thermal and mechanical design of LWR fuel rods especially at extended burnup. With increasing discharge burnups more and more attention has to be paid to this aspect.

In order to reach the high burnups with complete reloads higher fuel enrichments than those being previously used for fuel reloads are necessary. As a consequence of the high enrichment fuel rods are operated at higher average power over a longer period of time and hence higher fuel temperatures. Fractional fission gas release values were found to be higher than previously observed and showed an increase with increasing burnup. This paper presents the results of the fission gas release measurements and evaluates the influence of fuel microstructural changes at the pellet rim on the fission gas release values measured.

2. FUEL ROD CHARACTERISTIC AND IRRADIATION HISTORY

The fuel rods were arranged in a 15x15 rod array. All fuel rods measured were precharacterized. Zirconium base alloys were used as cladding material and the UO_2 -fuel was produced by the AUC-process [1]. Characteristic fuel rod data are given below.

Fuel rod length	=	3842 mm
Fuel rod diameter	=	10.75 mm
Fuel/clad diametrical gap	=	180 to 195 μm
He fill gas pressure	=	22.5 bar

Fuel density	=	10.40 g/cm^3
Fuel grain size (liner intercept)	=	7 - 10 μm
Initial enrichment (U-235)	=	3.8 / 4.2 / 3.5* w/o
		* a few rods only

The fuel rods were operated for up to six consecutive cycles to maximum rod average burnups of 72 MWd/kgU. In order to achieve such high burnups a number of fuel rods were withdrawn from the fuel assemblies having reached their target burnups, and reinserted into fresh assemblies for further irradiation. Such procedures ascertained relatively high power levels even at high burnups.

Typical cycle average linear heat generation rates (LHGR) for the rods are given in the table below.

Cycle	Cycle Average LHGR W/cm	Cumulative Average Burnup MWd/kgU
1	270-310	15.0-30.0
2	230-270	29.5-30.0
3	210-230	41.5-44.0
4	180-200	51.5-54.0
5	170-180	60.0-64.0
6	160-170	71.0-72.0

After the second cycle and all following cycles fuel rods were withdrawn from the fuel assemblies and shipped to Hot Cell laboratories for post-irradiation examinations.

3. EXPERIMENTAL TECHNIQUES

Standard fuel rod puncturing techniques and mass spectrometric analysis were applied to determine the integral amount and the composition of fission gases released into the free rod volume.

Basis for a more detailed analysis of the fission gas release behaviour was the analysis by optical and electron scanning microscopy on polished and fractured cross sections. In order to quantify the radial distribution of fission gases (Xe), Cs, Pu, Nd in the fuel pellet a shielded electron microprobe was used. The radial distribution of xenon retained in single UO_2 grains was determined by point analysis at intervals between 50 μm and 150 μm along the radius. This gave the concentration of gas dissolved in the grains and of gas trapped in intragranular bubbles. The point analyses were made away from grain boundaries in order to avoid a contribution from gas contained in intergranular bubbles.

Scanning electron microscopy (SEM) has been used to relate the radial distribution of xenon to fuel restructuring.

4. RESULTS

The results of the standard puncturing and mass spectrometric analysis are plotted in fig. 1 in the form of fractional fission gas release as a function of rod average burnup.

As can be seen fractional fission gas release values are around 5 % at burnups of about 30 MWd/kgU and increase linearly to about 7 % at 50 MWd/kgU. Above that burnup the fractional release increases continuously to about 12 % at burnups of 72 to 75 MWd/kgU, in spite of decreasing rod power. Although the decreasing thermal conductivity of the fuel tends to keep fuel temperatures up there is a general tendency for decreasing fuel temperatures with increasing burnup. The increasing fractional fission gas release with burnup must therefore be attributed to other effects.

An electron probe microanalysis has been performed to determine the radial concentrations of xenon retained within individual UO_2 grains on fuel cross sections. Three different burnup levels of about 50 MWd/kgU, 70 MWd/kgU and 83 MWd/kgU have been examined. The radial concentration profiles measured are compared with the theoretically calculated concentrations of xenon generated (fig. 2). At all three burnup levels an equally low xenon concentration of about 0.2 w/o was measured in the center region of the pellets. With increasing relative radius r/r_0 the amount of xenon retained within the grains increases. This increase is not a continuous function of r/r_0 but shows steps with different slopes. These steps are associated with consecutive steps in power history, for instance due to reshuffling. They mark regions of fission gas release at certain time intervals of operation [3, 4].

At a relative radius r/r_0 of about 0.8 and up to a burnup of 70 MWd/kgU the xenon concentrations within the grains reach their theoretical values. At the burnup of 83 MWd/kgU the xenon concentration deviates from the generated xenon everywhere.

At the pellet periphery moving towards the fuel cladding (pellet rim), the xenon concentration decreases continuously at all three burnup levels analysed. The decrease in xenon concentration is associated with a specific fuel restructuring as described below and was first observed at a pellet burnup of about 45 MWd/kgU. This threshold value is a function of the initial U-235 enrichment and corresponds to a local burnup at the pellet rim of about 60 MWd/kgU. As shown in fig. 3 the width of the restructured fuel zone increases with increasing burnup. It should be noted that the values plotted in that figure were taken from optical micrographs and refer to the fully restructured zone.

Typical optical micrographs of that zone are presented in fig. 4 for two distinctly different burnups. The micrographs show a high density of pores (or bubbles) with diameters in the range of 0.5 to 2 μm. Measurements of the porosity in this zone yield values of 15 to 17%[5].

SEM examinations revealed that the restructured zone is characterized by subdivided equiaxed grains of $0.1 < \varnothing < 1\mu$m with intergranular fracture mode. Facetted bubbles of micron to submicron size are precipitated in this zone. They do most likely exist on new grain boundaries.

The extent of restructuring starting at the pellet rim seems to depend on burnup only, fission rate seems to be of minor influence.

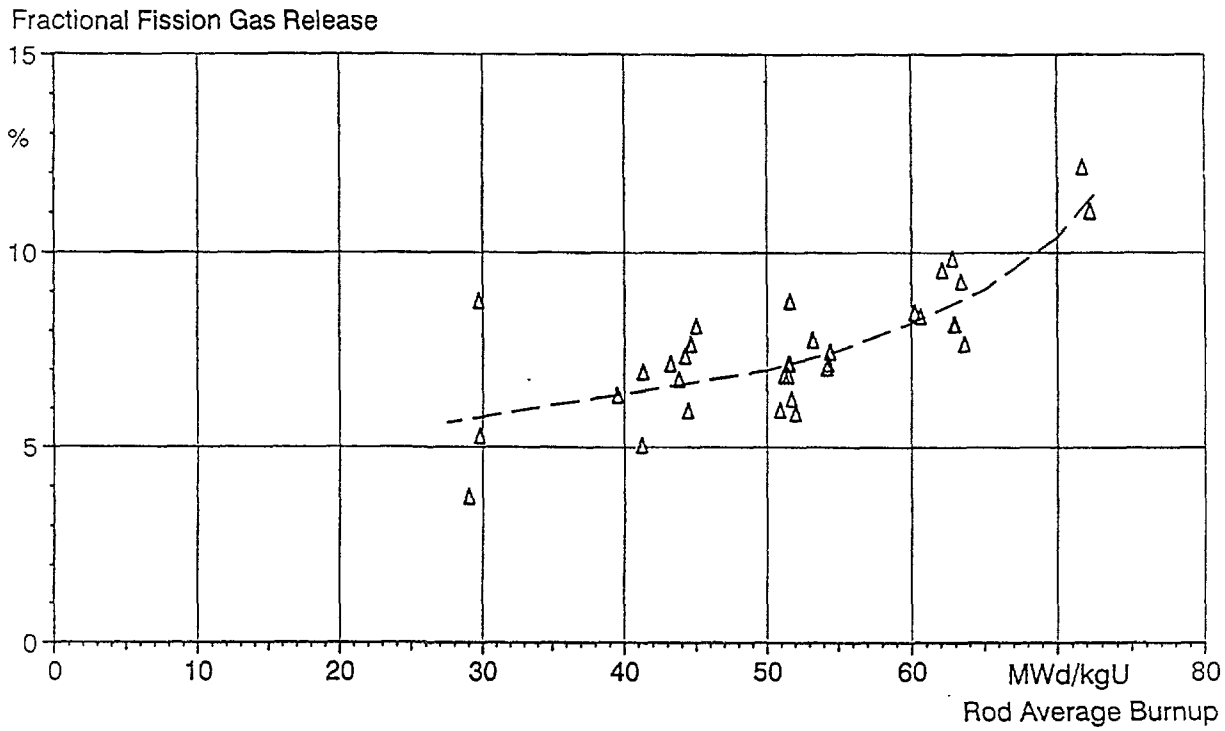

FIG. 1. *Fractional fission gas release of PWR fuel rods with enrichments of 3.5 w/o to 4.2 w/o as a function of rod burnup.*

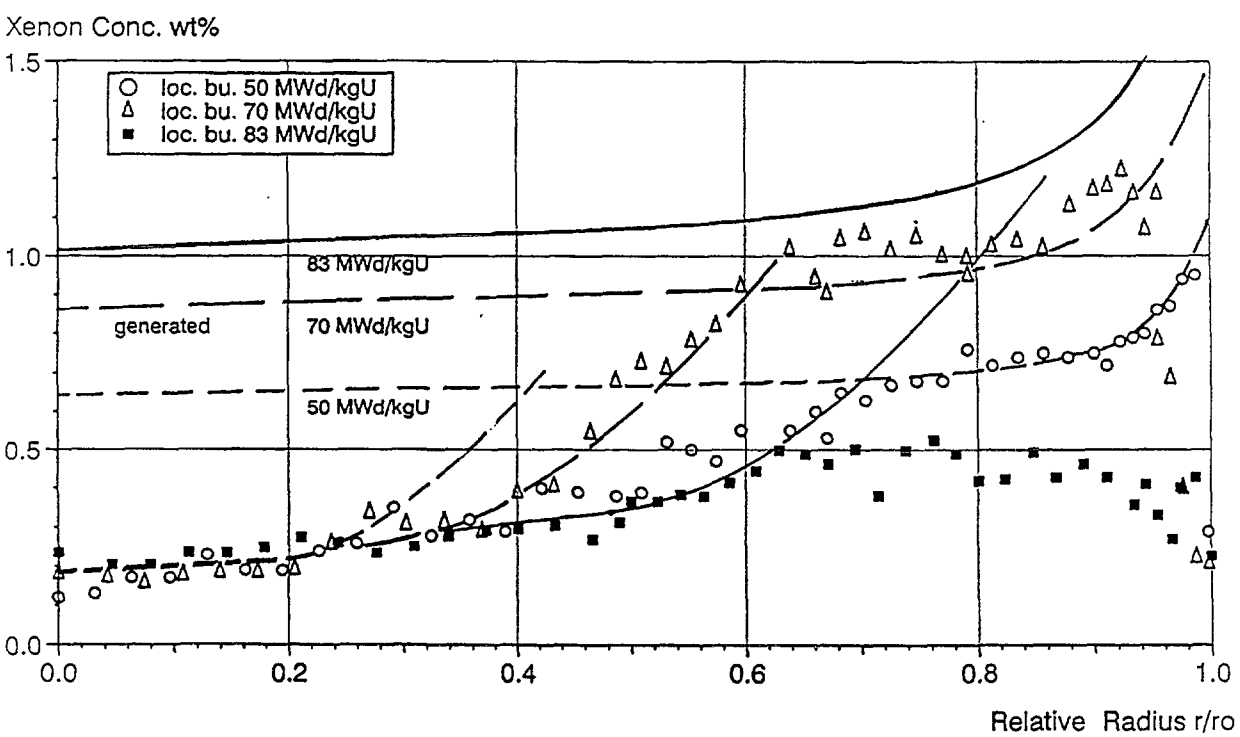

FIG. 2. *Radial xenon distribution in PWR fuel pellets as a function of relative radius, EPMA measurements of fuel matrix.*

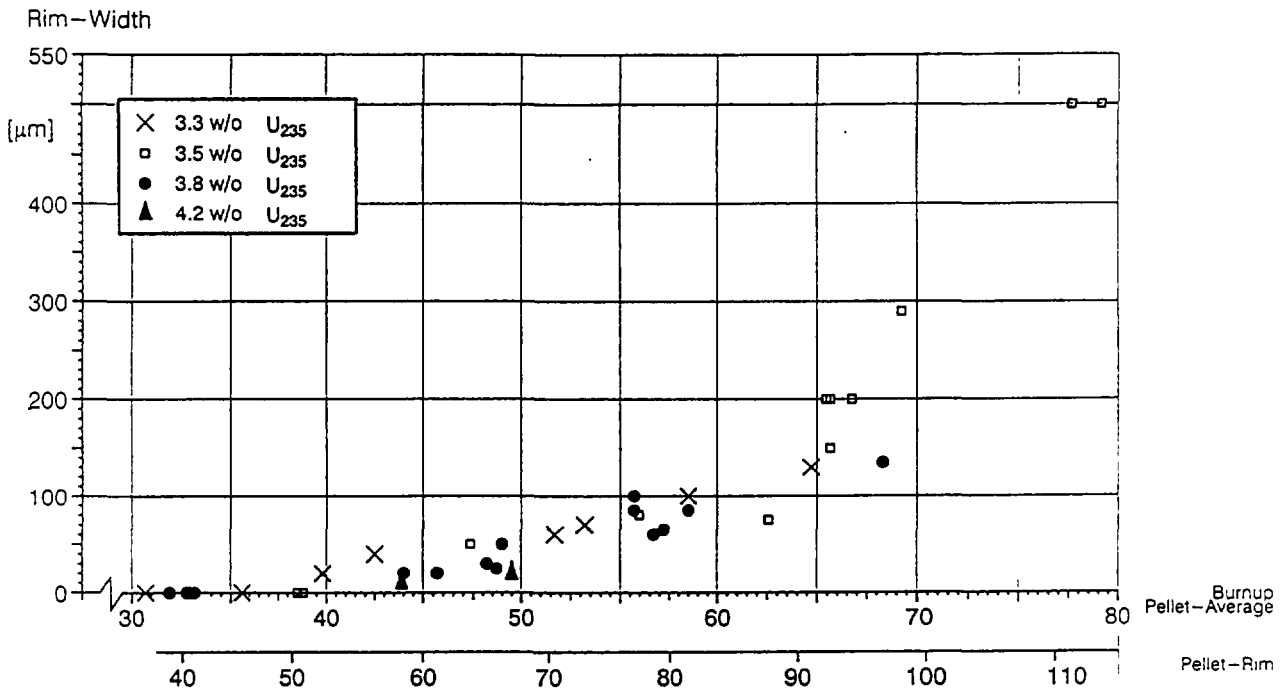

FIG. 3. *Development of the porous rim structure at the pellet periphery as a function of burnup for different initial enrichments.*

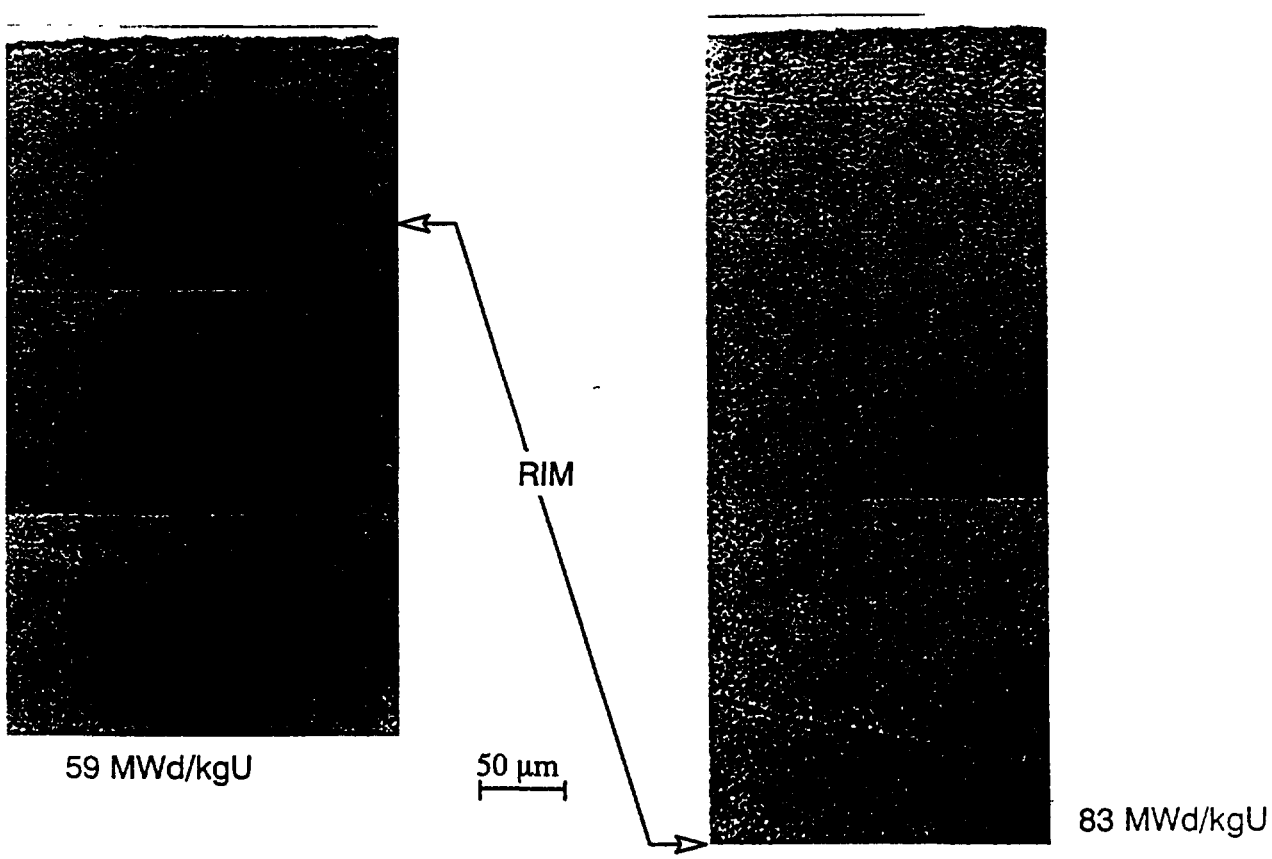

FIG. 4. *Fuel structure at the pellet rim after different burnups (optical microscopy, unetched).*

This is concluded from EPMA measurements performed on fuel pellets of identical burnups of 50 MWd/kgU but achieved at quite different powers and hence times of operation.

Temperatures at the pellet rim have always been below 500°C but fuel pullet center temperatures differed significantly from above 1300°C in the high power/high fission rate pellet to about 800°C in the low power/low fission rate pellet.

Fig. 5 compares the radial xenon concentration profiles of the two pellets. In the center region of the high power/high fission rate pellet a depletion of xenon and a low xenon concentration was measured whereas in the low power/low fission rate pellet no release has occurred and the measured values correspond to the amounts of xenon generated. In the region of r/r_0 0.7 to 0.95 an identical xenon concentration was measured in the high power/high fission rate and in the low power/low fission rate pellets. The absolute values correspond to the theoretically calculated concentrations of xenon generated. Moving from a relative radius of 0.95 towards the pellet periphery $r/r_0 = 1$ a decreasing xenon concentration was found in both the high power/high fission rate pellet and the low power/low fission rate pellet.

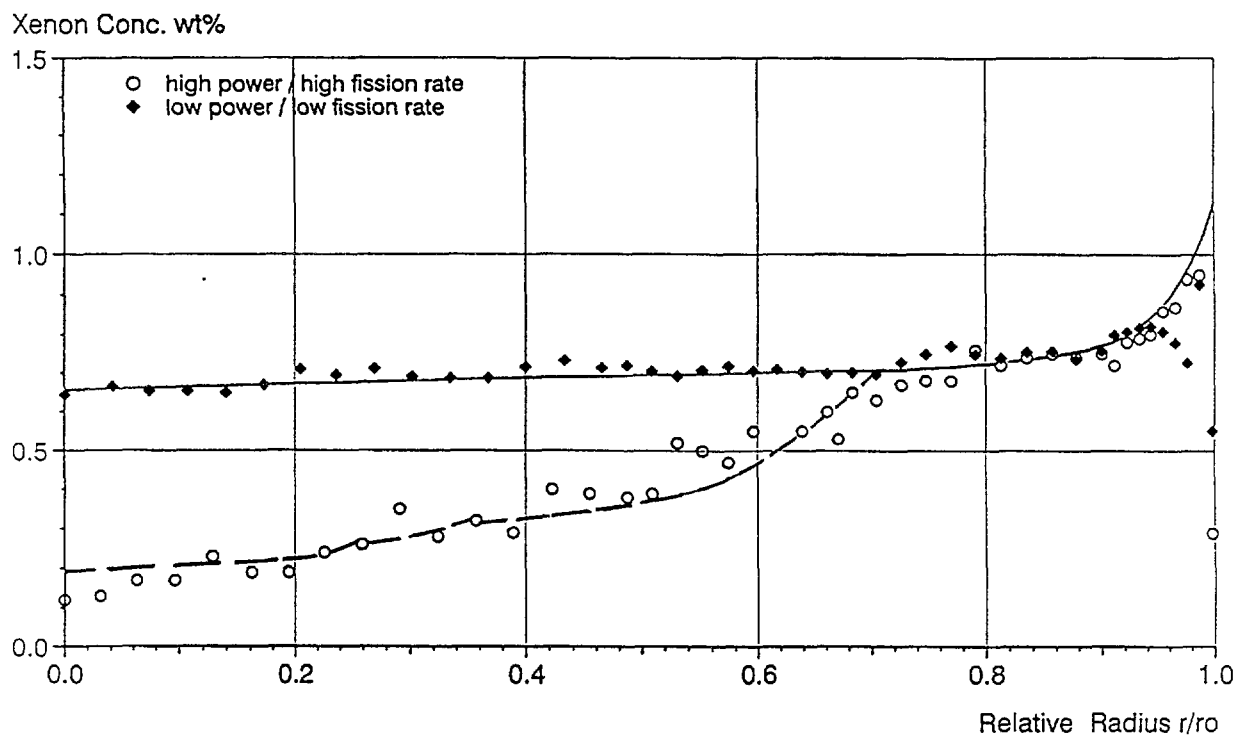

FIG. 5. Radial xenon distribution in PWR fuel pellets as a function of relative radius, EPMA measurements of fuel matrix, pellet burnups 50 MWd/kgU.

5. DISCUSSION

PWR fuel rods with the appropriate high enrichment to reach the high burnup target are operating at high fuel temperatures for a long period of time. As a consequence thermally activated diffusion processes [6] lead to significantly higher fission gas release than those measured and published earlier for lower enriched rods [2,3].

EPMA has shown that the release of fission gases occurs from the center of the pellets. The release is governed by two factors: the diffusion of xenon as atoms or bubbles to grain boundaries and the formation of interconnected intergranular porosity (tunnels) by a coalescence process. Once such a tunnel system has developed, usually during the first and second operational cycle, it remains open thus providing paths for a continuous gas release from the pellet center. For the fuel rods examined here the equilibrium between generated and released xenon in the center region was about 0.2 wt %.

From the intermediate pellet regions fission gas release is burnup dependent. With increasing irradiation time the pellet region where fission gases are released from is increasing and moved radially further outward. With steadily increasing burnup more and more pellet regions at lower temperature become saturated with fission gases [7]. If during operation the saturation temperature is exceeded fission gas release will start from these zones, leading to an increase in the fractional fission gas release with burnup.

These release mechanisms are now well established and up to the burnups reached so far give the essential contribution to fission gas release. Fission gas release calculations have been performed based on the EMPA profiles obtained from the high power and low power positions of a fuel rod. The results do clearly indicate that the gas release from the center regions of the pellets is sufficient to account for the amount of fission gas released into the rod free volume.

The xenon depletion of the UO_2 -matrix at the pellet periphery operated at temperatures below 500°C is a result at the restructuring in this zone. The restructuring is an athermal process directly related to the accumulation of radiation damage [8]. The released xenon is most probable contained in the large number of bubbles there.

Micro-coring had already indicated that the xenon released from the UO_2 -matrix is still confined in the porous rim structure [3]. EPMA has confirmed a high xenon concentration in bubbles just below the specimen surface. Also from X-ray fluorescence measurements it has been concluded that a significant fraction of the xenon produced was retained in that zone [9].

At a pellet burnup of 83 MWd/kgU xenon depleted and restructured areas extend as far as $r/r_0 = 0.65$ into the pellet [10]. The existence of such areas is an indication that fuel temperatures must have been fairly low at the end of operation.

6. CONCLUSION

The fractional fission gas release of higher enriched PWR fuel rods increases with burnup from about 7 % at a burnup of 50 MWd/kgU to about 12 % at a rod average burnup of 75 MWd/kgU.

Fission gas release in general occurs from the center region of the pellet. The diameter of that region and the amount of fission gases released is determined by the local temperature. However, the microstructural features clearly indicate that the diameter of that region is also dependent on burnup. With increasing burnup more and more pellet regions at lower temperature become saturated with fission gases. Exceeding the saturation temperature in the

course of burnup will result in an additional release of fission gases even at decreasing power as the burnup increases.

At the pellet periphery significant restructuring occurs. The threshold burnup for this restructuring was determined to be about 60 MWd/kgU. With increasing burnup above this threshold, restructuring progresses further into the fuel pellet. The initial grain structure in the restructured zones has disappeared and has been substituted by a subgrain structure with a high density of fine bubbles precipitated on subgrain boundaries (rim structure). Fission gases have partly been released from the UO_2 -matrix of that region but seem still to be confined in the small bubbles, and hence do not yet significantly contribute to the overall fission gas release

REFERENCES

[1] AßMANN H. AND DORR,W. "Microstructure and density of UO_2 pellets for Light Water Reactors as related to powder properties"; Ceramic Powders, edited by P. Vincenzini, Elsevier Scientific Publishing Comp., Amsterdam 1983, p. 707-718

[2] MANZEL,R. SONTHEIMER F. and STEHLE, H., "Fission gas release of PWR fuel under steady and transient conditions up to high burnup", Proceedings of the ANS Topical Meeting on Light Water Reactor Fuel Performance, Orlando, Florida, April 21-24, (1985).

[3] MANZEL R. and EBERLE, R.,"Fission gas release at high burnup and the influence of the pellet rim", Proceedings of the ANS Topical Meeting on Light Water Reactor Fuel Performance, Avignon, France, April 21-24, (1991).

[4] MANZEL, R. COQUERELLE M. and BILLAUX, M. R., "Fuel rod behaviour at extended burnup", Proceedings of the ANS Topical Meeting on Light Water Reactor Fuel Performance, West Palm Beach, Florida, April 17-21, (1994)

[5] SPINO, J. VENNIX K. and COQUERELLE, M.,"Detailed characterization of the rim microstructure in LWR fuels in the burnup range 40 - 67 MWd/kgU", J. Nucl. Mat. 231, No 3, pp. 179-190, (1996)

[6] TURNBULL J. A. et. al.,The diffusion coefficients of gaseous volatile species during the irradiation of uranium dioxide", J. Nucl. Mat. 107, pp. 168-184, (1982).

[7] ZIMMERMANN, H. "Untersuchungen zum Schwellen und Spaltverhalten in oxidischem Kernbrennstoff unter Neutronenbestrahlung", KFK-Report 2467, (1977).

[8] NOGITA K. and UNE, K., "Irradiation - induced recrystallization in high burnup UO_2 fuel", J. Nucl. Mat. 226, pp. 302-310, (1995)

[9] BARNER J.O. et. al."Relationship between microstructure and fission gas release in high burnup UO_2 fuel with emphasis on the rim region", Proceedings of the ANS Topical Meeting on Light Water Reactor Fuel Performance, Avignon, France, April 21-24, (1991).

[10] MANZEL R. and COQUERELLE M.,"Fission gas release at extended burnup", Enlarged Halden Programme Group Meeting, Loen, Norway, May 19-24, (1996)

DISCUSSION

(Questions are given in italics)

The FGR as a function of burnup suggested in Fig.1 indicate 4% FGR at burnup near to 0 MWd/kgU. How can this be explained?

1) Final fission gas release data have been obtained after operational cycles (30MWd/kgU burnup). It is not justified to extrapolate this to zero burnup, and the authors did not attempt that FGR at zero burnup will certainly not be 4%.

   First cycle average LHGR of 310 W/cm is typical for high burnup fuel assemblies irradiated in a lower target burnup core. Once the core will be at equilibrium in high burnup regime, such high LHGRs will not occur in the future; the power in the fresh fuel assemblies will be depressed by burnable absorbers, since the tendency is for longer reactor cycles, to make better use of the reactors.

2) Many utilities adopted low leakage loading schemes that result in comparable high power in the first and second cycles.

Comment:

Conclusion FGR is mainly related to a data base containing only high temperature fuel rods. Another study based on low power operation conditions shows that 2% release at 70000MWd/tU is due to a thermal mechanism that means a FGR of 15% in the rim.

In Fig.2 of your paper the measured retained gas is always below 50% of the inventory. Does it mean the fission gas release was about 50% at 83MWd/kg?

In the center of the pellet fission gas release was between 60 and 75%($r/r0<0.25$). In the regions between 0.25 and 0.8($r/r0$) a large quantity of gas is being released from the matrix (grains) but retained at grain boundary and grain edge. Only smaller quantities are being released into the free volume leading to the integral release as shown in Fig.1. In the rim region ($r/r0>0.8$) the fission gases are still confined in the bubble there.

IRRADIATION OF UO_{2+X} FUELS IN THE TANOX DEVICE

Ph. DEHAUDT, L. CAILLOT, G. DELETTE,
G. EMINET, A. MOCELLIN
CEA Centre d'Etudes de Grenoble
Grenoble, France

Abstract

The TANOX analytical irradiation device is presented and the first results concerning stoichiometric and hyperstoichiometric uranium dioxide fuels with two different grain sizes are given.

The TANOX device is designed to obtain rapidly significant burnups in fuels at relatively low temperatures. It is placed at the periphery of the SILOE reactor and translated to adjust the irradiation power. The continuous measure of the centre-line temperature allows to control the experiment and to evaluate the thermal behaviour of the rods. A TANOX fuel rod has a length of 100 mm with 20 fuel pellets in a stainless steel cladding and is inserted in a thick aluminium alloy overcladding which is cooled by the primary water circuit reactor. These conditions of small size pellets and improved thermal exchanges have been designed to dissipate the heat power due to fission densities three to five times higher than in a PWR.

The first analytical irradiation was devoted to the study of $UO_{2.00}$, $UO_{2.01}$ and $UO_{2.02}$ fuels with standard and large grain sizes obtained by annealing. A burnup of about 9000 $MWd.t_U^{-1}$ was reached in these fuels. The thermal analysis shows a degraded conductivity for the $UO_{2.02}$ fuel rod due to the hyperstoichiometry. The released fractions of ^{85}Kr during irradiation are negligible as expected (lower than 0,1%). Some of the pellets were heat treated at 1700°C for 5 hours. The gas release was analysed after 30 minutes and at the end of the treatment. The main results are as follows: the fission gas release (FGR) of the standard UO_2 varies from one sample to another; the FGR of the hyperstoichiometric fuels is of the same order of magnitude than that of the stoichiometric UO_2 fuel of normal grain sizes; the grain size increase has no effect on FGR for $UO_{2.00}$ but considerably decreases the FGR for $UO_{2.01}$ and $UO_{2.02}$ fuels. These heat treated samples are also observed to characterize the inter- and intragranular fission gas bubbles.

1. INTRODUCTION

The purpose of this article is to present the TANOX irradiation device and the first analytical study performed on stoichiometric and hyperstoichiometric UO_2 fuels.

The TANOX device has been specifically designed for work on innovative fuels to test a lot of samples. It is a facility for characterising and selecting potentially advantageous microstructures. In view of the fact that these new microstructures are required, among other things, to withstand high burnups (>60000 MWd/tU) with optimum fission product retention, a second device allows to check the behaviour of the most promising microstructures under high burnup conditions. In both cases, the fission densities are higher than in a PWR whereas the fuel temperature is of the same order of magnitude or even lower: significant burnups are rapidly obtained. The release of gaseous and volatile fission products is provoked by post-irradiation heat treatment. Numerous fuels have been irradiated in TANOX within the context of various research programmes, each of which is aimed at enhancing a particular aspect of fuel performance [1].

The UO_{2+x} fuels study is justified by the fact that irradiation tends to increase the O/U ratio. It is also necessary to know their thermal behaviour and their capacity for retaining fission gas.

2. DESCRIPTION OF THE TANOX DEVICE

2.1. TANOX fuel rod

The 100 mm long fissile column contains 20 pellets of 5 mm height and 4.9 mm outside diameter. The 10 pellets in the top half of the stack always have an annular shape (diameter of central hole 1.3 mm) allowing the introduction of a Cr-Al centre-line thermocouple. The cladding is made of stainless steel with possibly a platinum internal coating, if necessary (case of the study presented in § 3 below) in order to maintain the hyperstoichiometry of the fuel. The fuel rod equipped with its thermocouple (Fig. 1) is placed in an overcladding made of aluminium alloy which isolates it from the primary coolant of the reactor and allows a significant increase in fission densities in the fuel (3 to 5 times greater than those of a PWR). The fuel/cladding and cladding/overcladding gas gaps, filled with pressurised helium (2 and 3 bars respectively) are reduced to 20μm and 10μm at the diameter respectively in order to dissipate the heat generated in the fuel by improving heat transfers (Fig. 2).

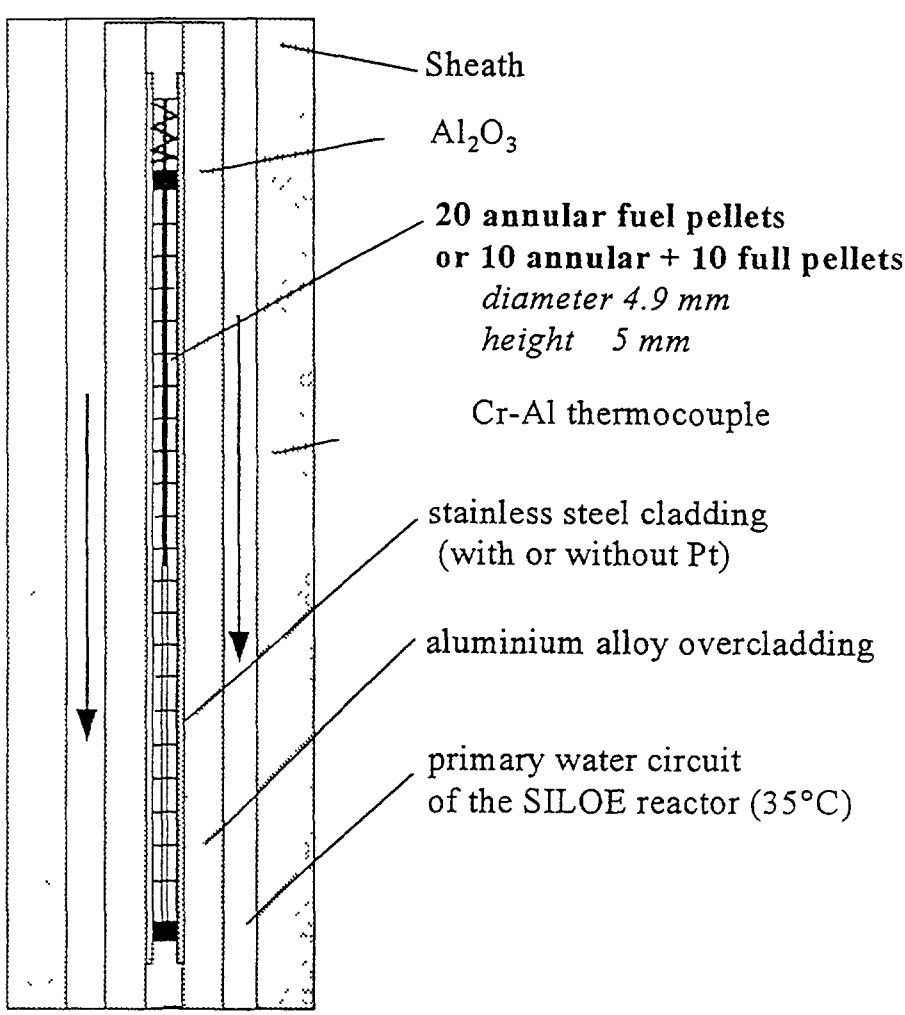

FIG. 1. Presentation of a TANOX rod

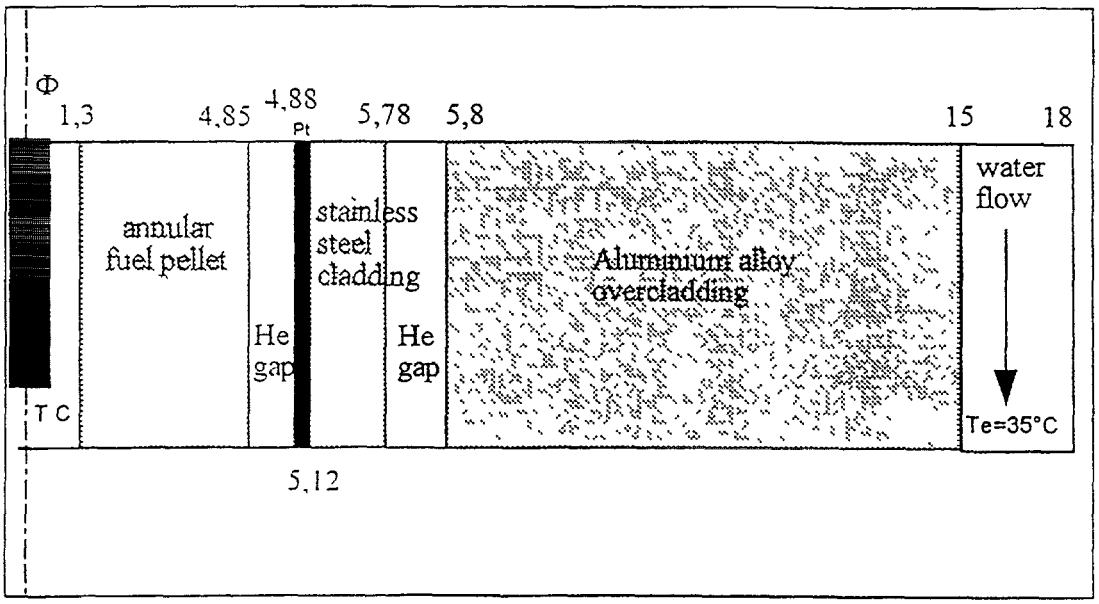

FIG. 2. Geometry of a TANOX location

2.2. TANOX Device

The TANOX device can be used to irradiate up to 6 fuel rods simultaneously (Fig. 3). The overcladdings are fixed in a sample chamber which provides a means of flexible device management: overall rotation and permutation to homogenize the burnups, loading and unloading of overcladdings. The entire assembly is placed in a sheath which channels the heat carrying fluid, water at 35°C in contact with the external surface of the overcladding, and is equipped with collectrons to measure the neutron flux. This sheath is fixed to a displacement system which allows the device to be moved with respect to the reactor core so as to adjust the irradiation power to the required level. Experimental control is based on the continuous measurement of fuel rod centre-line temperatures by thermocouples.

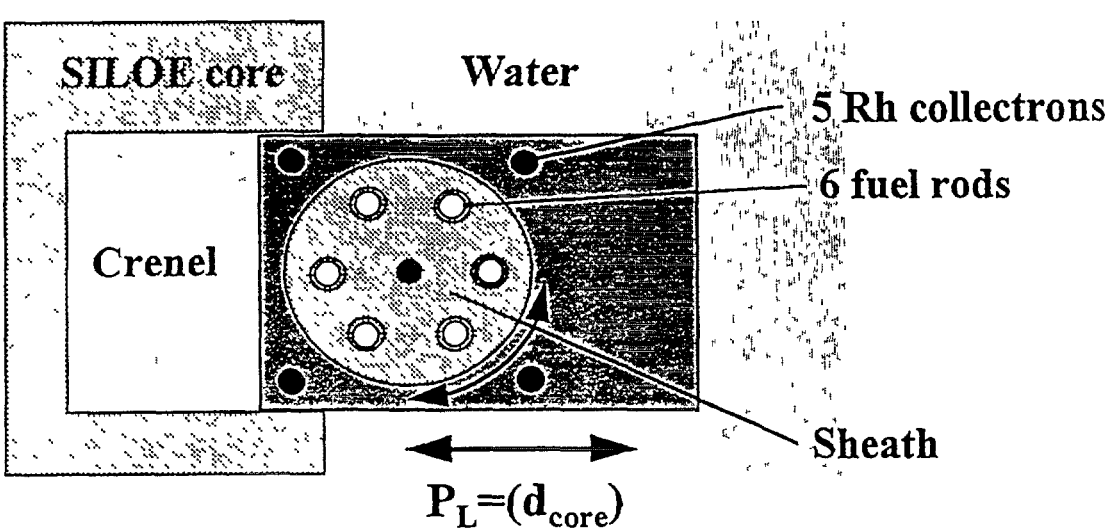

FIG. 3. Schematic view of the TANOX device (above view)

2.3. Irradiation conditions

Two irradiation modes in TANOX were defined and used:

- in the so-called TANOX 1 conditions, which prevailed for the first experiment (§ 3), the annular pellet temperature does not exceed 700°C and the desired burnup is of the order of 10 GWd/t_U (PWR equivalent value);
- in the so-called TANOX 2 conditions, the core temperature of the fuel may reach 1100°C (in annular pellets), a value which is close to that occurring in a PWR under nominal operation, and the burnups aimed for are greater than or equal to 20 GWd/tU.

In both cases, fission products accumulate in the UO_2 matrix without activating the thermal release mechanisms, or just weakly activating them in the second case. Subsequent annealing treatments are performed in order to quantify the fission gas release in well-defined temperature and time conditions.

Irradiation at representative and controlled temperature gives valuable information on the thermal response of fuel rods and the thermal conductivity of the fuels studied. For this thermal analysis, the fissile power is readjusted at the end of the irradiation cycle on the basis of a quantitative measurement of certain fission products by means of γ spectrometry.

3. IRRADIATION OF UO_{2+x} FUELS

3.1. Characteristics of fresh and irradiated fuel

Within the context of the UO_2 advanced microstructure programme, the independent and combined effects of grain size and hyperstoichiometry were studied by means of specific fuel preparations. Six batches of fuel were used with two grain sizes, about 10 et 50μm, and three stoichiometries with O/U ratios of 2.00, 2.01 and 2.02 (Tab. I). Grain growth is achieved by annealing at 1800°C for 100 hours and hyperstoichiometry by controlled oxidation. The microstructures obtained, observed on a polished section under optical microscopy, show the presence of U_4O_9 precipitates in needle form in the $UO_{2.01}$ and $UO_{2.02}$ fuels (Fig. 4).

TABLE I. CHARACTERISTICS OF THE STUDIED FUELS

Fuel	Grain size	Burn-up (MWj/t_U)	^{85}Kr release fraction during irradiation
$UO_{2.00}$	standard : 13 µm	9090	0.0007
	large* : 50 µm		
$UO_{2.01}$	standard : 14 µm	9180	0.00075
	large* : 50 µm		
$UO_{2.02}$	standard : 13 µm	8756	0.00088
	large* : 50 µm		

* high grain size are obtained by annealing

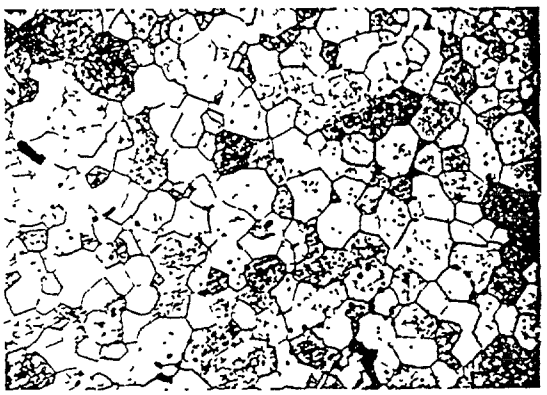

$UO_{2\,00}$
Standard grain size

$UO_{2\,00}$
Large grain size

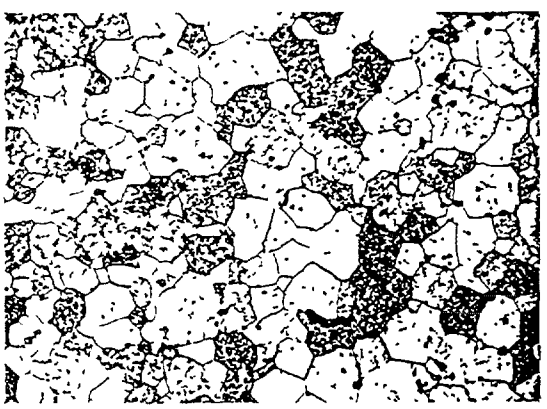

$UO_{2\,01}$
Standard grain size

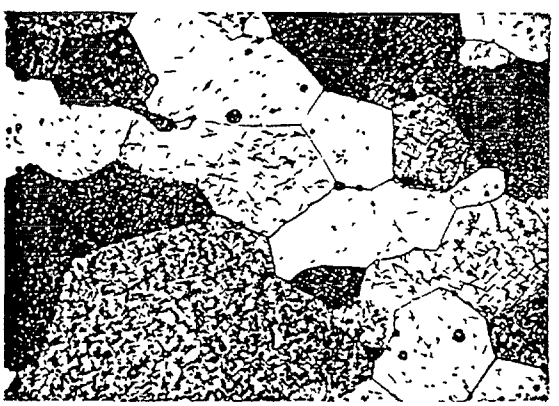

$UO_{2\,01}$
Large grain size

$UO_{2\,02}$
Standard grain size

$UO_{2\,02}$
Large grain size

30 µm

FIG. 4. Microstructure of the UO_{2+x} fuels before irradiation (with chemical etching)

The irradiation cycle in the TANOX device covered a period corresponding to four operating cycles of the SILOE experimental reactor for a total duration of 78 days equivalent full power. The burnup reached by the three rods considered is 9000 MWd/t_U on average (Tab. I) under TANOX 1 conditions. At the end of irradiation, the cladding was drilled to check that no fission gas release had occurred: the fraction of ^{85}Kr released and measured is strictly less than 10^{-3} which is negligible compared to the accuracy of the measurement (Tab. I). The microstructural state of the UO_{2+x} fuel observed by optical microscopy would not appear to be modified to any great extent by the irradiation process, only the U_4O_9 precipitates are no longer visible in the $UO_{2.01}$ and $UO_{2.02}$ whether before or after etching (Fig. 5).

3.2. Thermal analysis

The thermal analysis was performed on the basis of the experimental values of centre-line temperature Tc and corresponding fissile power Pf. These Tc(Pf) relationships include all the elements of the relatively complex thermal chain (Fig. 2). For example, the fuel contribution to the overall thermal response is not always predominant. The simplified modelling process that has been developed to analyse the experimental results obtained takes into account all these parameters and quantifies their relative importance. It consists in integrating the static heat equation by considering the hot geometry of the device and the temperature dependent change in thermal properties, expansion and conductivity. The calculation of the fuel thermal conductivity integral makes allowance for power flux depletion, a function of ^{235}U enrichment, and the deterioration due to porosity and hyperstoichiometry [2-3]. It has to be noticed that the single UO_{2+x} ($x \leq 0.02$) compound exists at the irradiation temperatures ($\geq 400°C$). The U_4O_9 compound forms at lower temperatures.

Figure 6 gives the experimental points and the laws calculated in the (Tc, Pf) plane for the 3 fuel rods. It is worth noting that:

- rods $UO_{2.00}$ and $UO_{2.01}$ exhibit similar behaviour (~580°C at 170 W/cm) whereas rod $UO_{2.02}$ is hotter (+90°C at 170 W/cm);
- the deterioration in thermal conductivity of fuel rod $UO_{2.02}$ could well be due to the hyperstoichiometry of the fuel because the calculation result coincides with the measurements when taking Martin's degraded conductivity law [3];
- using this same law, the calculated centre-line temperature of fuel rod $UO_{2.01}$ is overestimated by 8%: either the $UO_{2.01}$ does not have a deteriorated thermal conductivity, or the power is not precisely known.

4. FISSION GAS RELEASE

The annealing operations are performed on the individual irradiated pellets to provoke fission gas release. These operations are carried out under vacuum at 1700°C, last 5 hours and include the collection of two gas samples, one after 30 minutes and the other at the end of heat treatment. A distinction is made between the gas already existing in the grain boundaries, which escapes at the very beginning of heat treatment (burst release), and the gas which comes from inside the grains and which diffuses before escaping from the pellet (volume release). The collected gases are analysed by gamma spectrometry in order to count the number of ^{85}Kr atoms. This number of atoms divided by the number of ^{85}Kr atoms present in the pellet on the date of heat treatment gives the fraction of ^{85}Kr gas released. The mean values obtained for

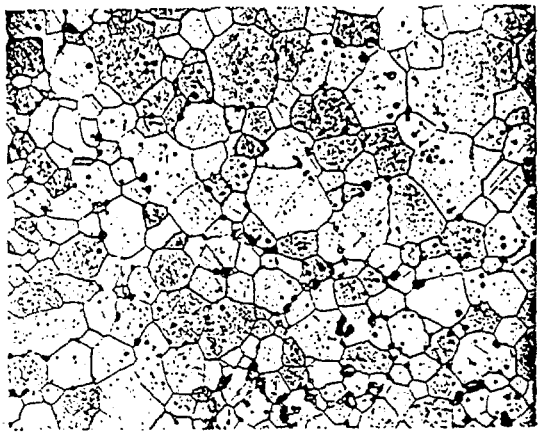

$UO_{2.00}$
Standard grain size

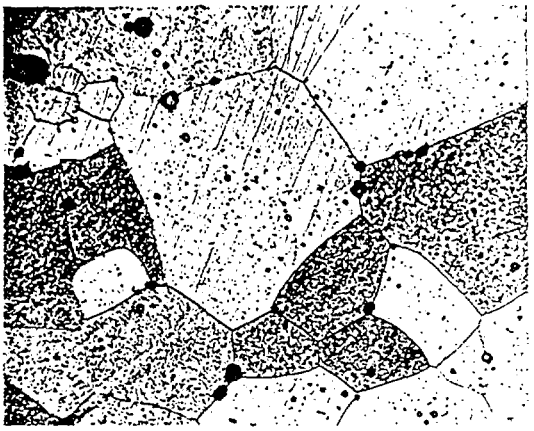

$UO_{2.00}$
Large grain size

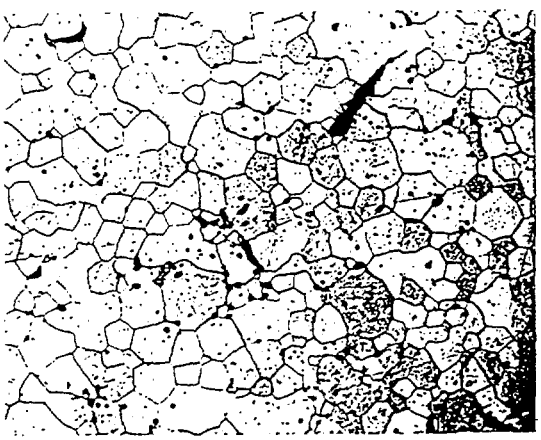

$UO_{2.01}$
Standard grain size

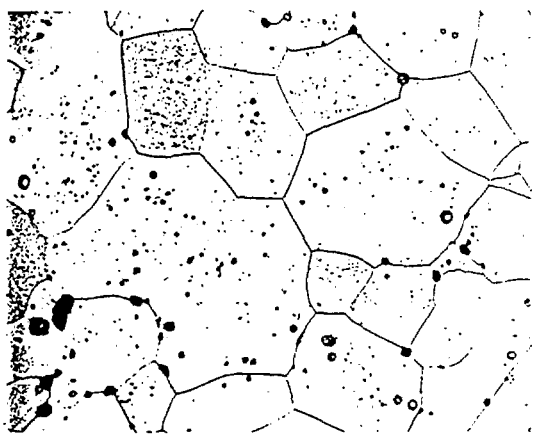

$UO_{2.01}$
Large grain size

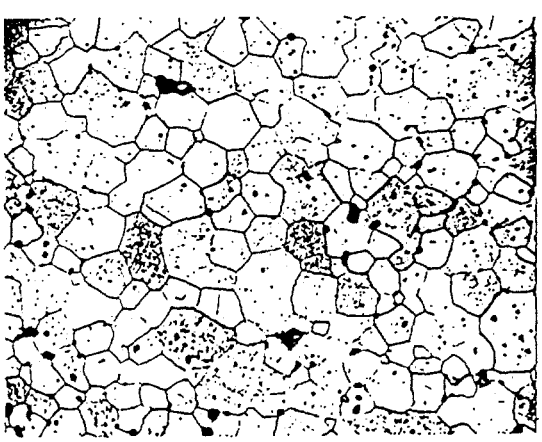

$UO_{2.02}$
Standard grain size

$UO_{2.02}$
Large grain size

FIG. 5. Microstructure of the UO2+x fuels after irradiation (with chemical etching)

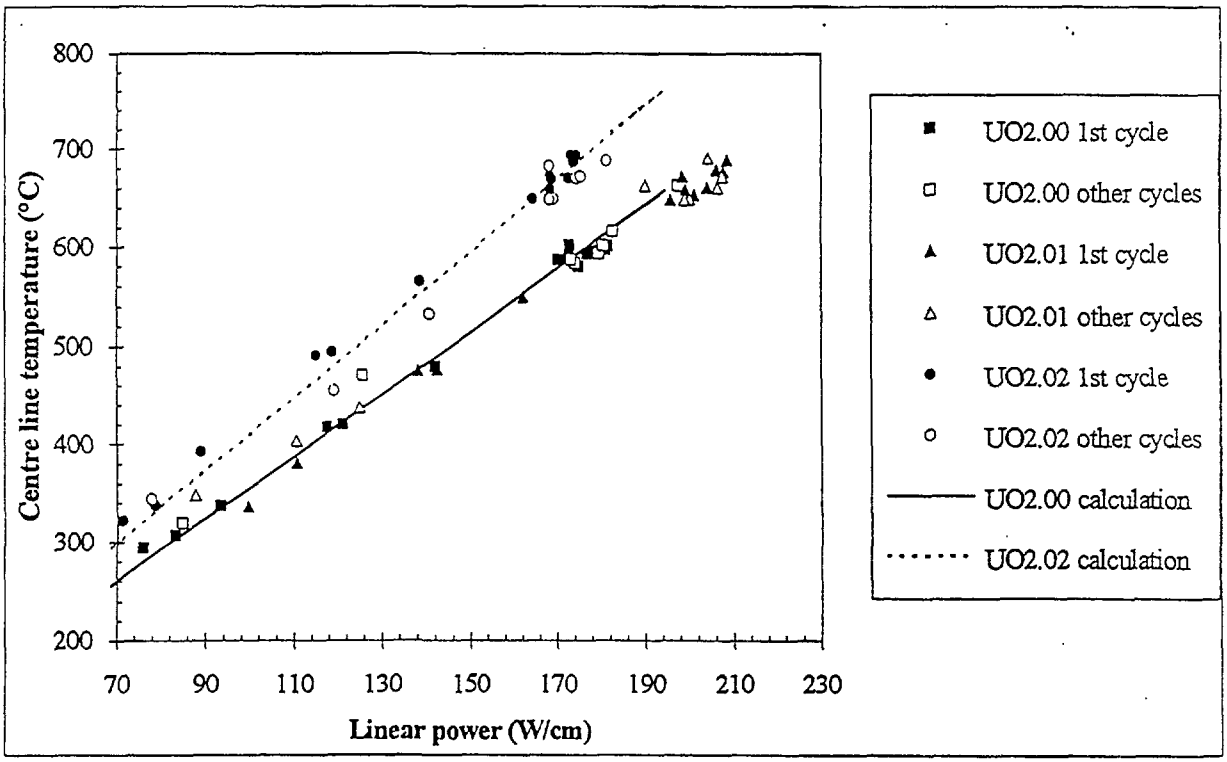

FIG. 6. Centre line temperature versus linear power diagram

the six batches of fuel used are listed in Table II. All results are reproducible except for the UO_2 reference fuel giving variable release values from one treatment cycle to another.

The one remarkable fact, made all the more remarkable because it was unexpected, is that the hyperstoichiometric fuels have gas releases comparable to those of $UO_{2.00}$ in the case of standard grains and much lower releases in the case of large grains. The difference already exists at the burst release stage which means that the gas accumulation at grain boundaries of

TABLE II. MEAN VALUES OF ^{85}Kr RELEASE FRACTIONS DURING ANNEALING TESTS AT 1700°C

	Mean values of ^{85}Kr release fractions	
	1700°C - 30 min	1700°C - 5 h
$UO_{2.00}$; grain size13 µm	0.10*	0.30**
$UO_{2.00}$; grain size50 µm	0.13	0.29
$UO_{2.01}$; grain size14 µm	0.13	0.39
$UO_{2.01}$; grain size50 µm	0.02	0.03
$UO_{2.02}$; grain size13 µm	0.10	0.24
$UO_{2.02}$; grain size50 µm	0.07	0.08

* The values vary from 0.02 to 0.26

** The values vary from 0.13 to 0.45

UO_{2+x} does not increase during irradiation in unthermal conditions (T ≤ 700°C). The burst release is almost the only gas release type for $UO_{2.01}$ and $UO_{2.02}$. The gas release decrease due to grain size increase is not checked for the $UO_{2.00}$ standard fuel.

The irradiated fuels are once more observed by optical microscopy after heat treatment (Fig. 7). The fission gas bubbles inside the grains and at grain boundaries are clearly visible.

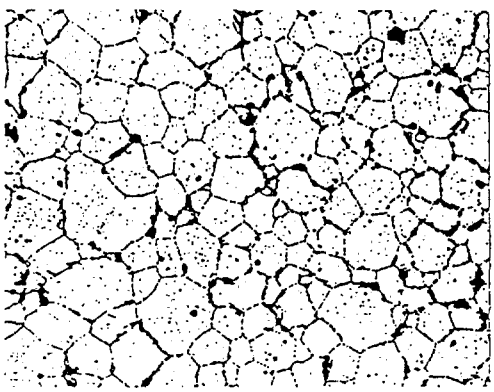

$UO_{2.00}$
Standard grain size
Annealing : 1700°C - 5h

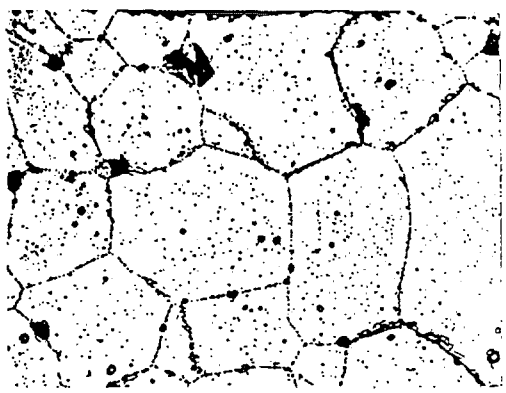

$UO_{2.00}$
Large grain size
Annealing : 1700°C - 5h

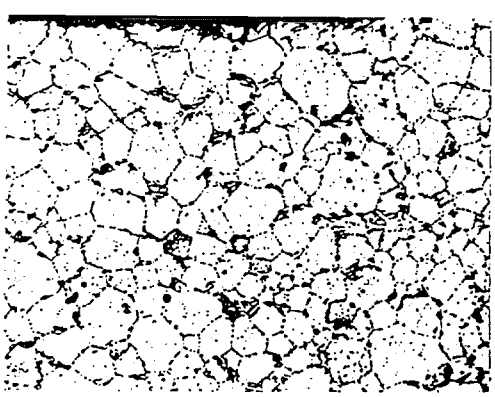

$UO_{2.01}$
Standard grain size
Annealing : 1700°C - 30 min

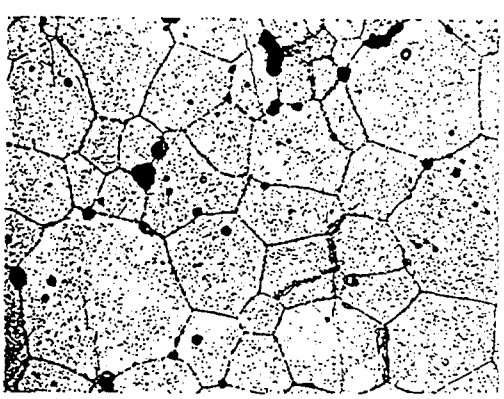

$UO_{2.01}$
Large grain size
Annealing : 1700°C - 5h

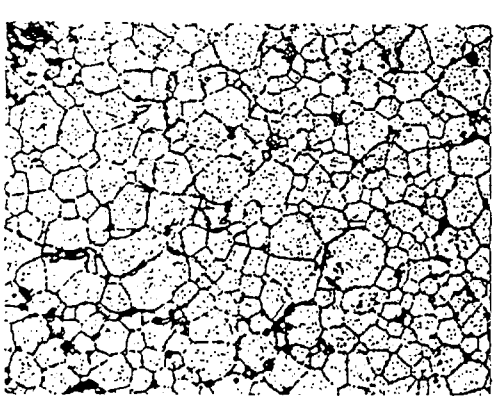

$UO_{2.02}$
Standard grain size
Annealing : 1700°C - 5h

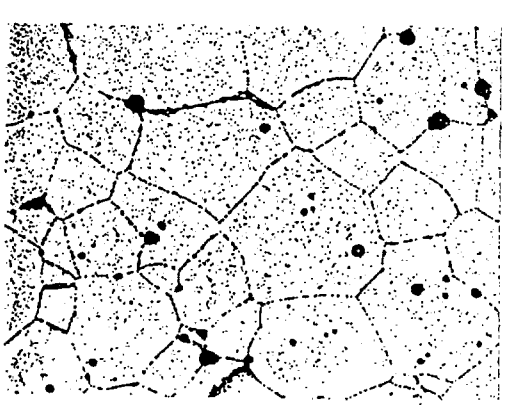

$UO_{2.02}$
Large grain size
Annealing : 1700°C - 5h

FIG. 7. Microstructure of the UO_{2+x} fuels after irradiation and annealing (without chemical etching)

The intergranular bubbles may coalesce, forming labyrinths on grain boundary planes and channels at triple boundaries (Fig. 8). Gas release appears to be closely related to the existence or not of this interconnection. It is difficult to associate a bubble configuration and

Annealing at 1700°C
for 30 minutes

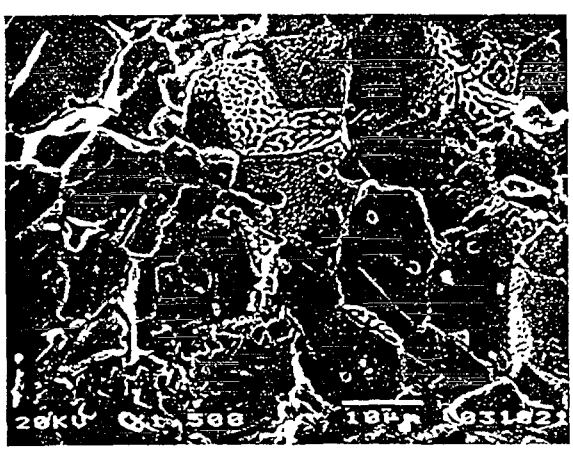

Annealing at 1700°C
for 3 hours

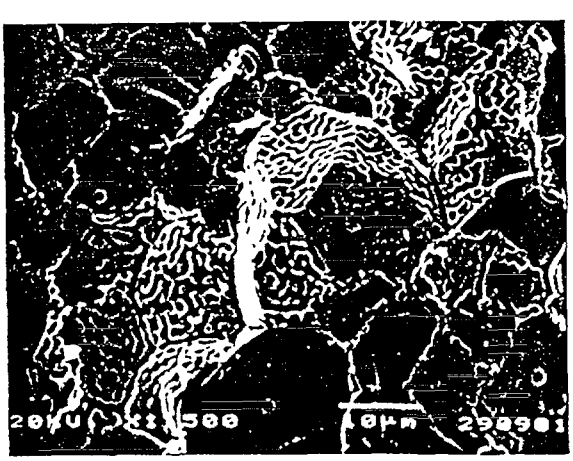

Annealing at 1700°C
for 5 hours

FIG. 8. *Scanning Electron Microscopy observation of the standard $UO_{2.00}$ fuel after irradiation and annealing*

density with a release rate. However, in the light of the observations made, the following correlations can be established (cf Fig. 7):

- when the release rate is low, fine dense intragranular bubbles and relatively discrete intergranular bubbles are observed;
- when the release rate is high, the intragranular bubbles are bigger and less numerous and the intergranular bubbles are quite widely connected.

The preliminary conclusions drawn from the results include the following:

- the intragranular storage of gas is potentially greater for large grains but appears to depend on the existence of preferential gas bubble nucleation sites which would be crystal lattice defects or the solubility decrease in the case of hyperstoichiometry;
- after burst release, fission gas release is related to the proportion of connected intergranular bubbles which may be reduced because of a lower intergranular area when the grain size increases or because of resintering promoted by the hyperstoichiometry (increase in uranium diffusion coefficients).

5. CONCLUSION

The originality of the TANOX irradiation device lies in considerably reduced irradiation times thanks to the fission densities which are 3 to 5 times greater than those obtained in a conventional PWR. This is possible with the presence of an overcladding between the small-size fuel rod cladding (6 mm diameter, 170 mm high) and the primary cooling water circuit of the reactor.

The first research fuels irradiated in TANOX have illustrated the role played by hyperstoichiometry and grain size on UO_2 thermal conductivity and on the post-irradiation release of krypton 85. Our thermal analysis shows a significantly deteriorated conductivity for $UO_{2.02}$ compared to $UO_{2.00}$ as a result of the hyperstoichiometry. Fission gas release is provoked by annealing at 1700°C. The six fuel batches studies are divided into two categories:

- standard UO_2 (small and large grains) and small-grained UO_{2+x} release ^{85}Kr fractions greater than 0.2 and the release takes place throughout the duration of the heat treatment process;
- large-grained UO_{2+x} release ^{85}Kr fractions less than 0.1 and the release takes place mainly at the start of heat treatment (burst release).

Consequently, under the specific post-irradiation heat treatment conditions considered, a very clear reduction in fission gas release is observed with hyperstoichiometric UO_2 fuels with large grains. This reduced release is linked to the presence of numerous fine intragranular bubbles and intergranular bubbles with few connections.

REFERENCES

[1] DEHAUDT, Ph., LEMAIGNAN, C., CAILLOT, L., MOCELLIN, A., EMINET, G., New UO_2 fuel studies, TCM IAEA Tokyo, these Proceedings.

[2] STORA, J.P., Thermal conductivity of two-phase solid bodies, Nucl. Technol., 17 (1973) 225-233.
[3] MARTIN, D.G., A re-appraisal of the thermal conductivity of UO_2 and mixed (U, Pu) oxide fuels, J. Nucl. Mater. 110 (1982) 73-94.

DISCUSSION

(Questions are given in italics)

The result reported on UO_2+X fuel are somewhat consistent with ramp test results reported at Halden Bolkesjo meeting in 1994. The absence of U_4O_9 precipitates in the micro structure was also noted. Could you speculate on a reason for this?

We think that nucleation of U_4O_9 needles can not occur in the presence of fission products. Excess of oxygen should be useful for the formation and the stability of a solid solution between UO_2 and some fission product. The same controlled oxidation was performed on an unirradiated pellet containing impurities: no U_4O_9 needles appeared.

BNFL ASSESSMENT OF METHODS OF ATTAINING HIGH BURNUP MOX FUEL

C. BROWN
BNFL International Group,
British Nuclear Fuels Plc,
Sellafield, Seascale, Cumbria

K.W. HESKETH, I.D. PALMER
LWR Business Unit,
British Nuclear Fuels Plc,
Springfields

United Kingdom

Abstract

It is clear that in order to maintain competitiveness with UO_2 fuel, the burnups achievable in MOX fuel must be enhanced beyond the levels attainable today. There are two aspects which require attention when studying methods of increased burnups - cladding integrity and fuel performance.

Current irradiation experience indicates that one of the main performance issues for MOX fuel is fission gas retention. MOX, with its lower thermal conductivity, runs at higher temperatures than UO_2 fuel; this can result in enhanced fission gas release. This paper explores methods of effectively reducing gas release and thereby improving MOX burnup potential.

1. INTRODUCTION

In opting to displace a fraction of its UO_2 fuel requirements with MOX fuel, an utility would expect the MOX fuel to attain the same discharge burnups as its UO_2 fuel. If the MOX fuel were to be discharged at a lower burnup, this would imply an increased fuel procurement requirement and hence increased fuel cycle costs. Thus, the very minimum requirement for MOX burnup is that it should at least match that of the coresident UO_2 fuel. There are, however, significant differences in the underlying economic drivers.

For normal UO_2 fuel, the fuel cycle economics generally improves with increasing burnups, but has a tendency to level out or even deteriorate a little beyond 55 GWd/t. This levelling results from a balance between the increasing uranium ore and enrichment costs needed to attain high burnups and the extra electrical generation from each fuel assembly during its lifetime; the two effects are roughly compensating at burnups of 55 GWd/t or more. Therefore, for UO_2 fuel, there is little incentive from the point of view of fuel cycle economics to increase burnups much beyond these levels, although there may be other important drivers, such as minimising spent fuel quantities that may influence an utility's decision to push for higher burnups.

The burnup dependence of the fuel cycle economics is quite different for the MOX component of a core, because fuel fabrication is the main cost component and it does not vary significantly with burnup. Thus the total cost of a MOX fuel assembly is essentially constant with burnup, whereas the electricity it generates increases proportionally with burnup. Simplistically, the fuel cycle cost of the MOX component is therefore inversely proportional

to burnup, which gives an incentive to increase burnups beyond that where the UO_2 levels out. In practice, discounting effects somewhat offset the improvement with burnup (since the electricity is generated over an extended period of time its discounted value is lower than it would be if it was generated instantaneously), but there still remains a significant benefit to be gained.

This paper briefly reviews some of the technical issues and possible solutions associated with extending MOX discharge burnups. While the focus is on fuel technology, it is recognised that any developments in this area must be matched by equivalent developments in cladding performance, particularly with regard to corrosion resistance; a detailed discussion of this area however lies beyond the scope of this paper.

2. FACTORS INHIBITING HIGH BURNUP

For all fuel types, including conventional UO_2 fuels, a number of technical factors combine to inhibit the trend toward the target of higher discharge burnup. Principal amongst these are (a) thermal performance, (b) accelerating fission gas release, and (c) increasing cladding waterside corrosion. For a given discharge burnup, all are somewhat more limiting for MOX than UO_2 because of differences in power histories.

MOX tends to have a flatter reactivity variation with burnup than UO_2 because of the lower burnout rates of the fissile nuclides in the lower thermal flux and because of the effect of Pu-240 acting as a fertile material by being converted to Pu-241 by neutron captures. An important effect of the different reactivity characteristics is that MOX assemblies, all other things equal, tend to run at a higher rating than equivalent UO_2 assemblies late in their lives. Both clad corrosion and fission gas release are affected particularly by high ratings late in life and this may lead to the MOX fuel being more limited in both respects at any given burnup.

With MOX, various inherent characteristics of the fuel tend to enhance the factors which inhibit high burnup. For example, the lower thermal conductivity, smaller grain sizes and higher late-in-life powers associated with MOX fuel all exaggerate the problems of fission gas release, clad corrosion and reduced thermal margins. The challenge for the fuel vendor is the development of advanced MOX fuels capable of overcoming these difficulties and achieving the levels of burnup which optimise fuel cycle economics.

3. THERMAL PERFORMANCE

As burnup progresses both the thermal conductivity and melting point of fuel are reduced. Although the rate of degradation is not significantly different with MOX fuel compared with UO_2 fuel, the initial level is in each case lower. Fission gas release can also become significant at high burnup, leading to a reduction of fuel-clad gap conductance. For the reasons discussed below, gas release tends to be more pronounced in MOX fuels, enhancing this reduction. The combined effect of these factors on the high burnup thermal performance of MOX fuel is two-fold. Firstly, steady state temperature levels are increased, particularly since the late-in-life rating level in MOX assemblies can be high. These higher temperatures can lead to further fission gas release and swelling. Secondly, the margin to fuel melting under fault and accident conditions is decreased.

In targeting possible solutions to the problem of high temperatures, two basic strategies can be considered:

- Changes in fuel rod design
- Changes affecting fuel physical properties

The former category includes the use of smaller diameter rods and also the use of annular pellets. Both of these options are already available with existing technology and to some extent are already partially proven. Both could be brought into use with relative ease, although each would result in some degree of fabrication cost penalty. The advantage of hollow fuel is also doubtful under circumstances where gas diffusion can be sufficiently rapid to induce swelling of the unrestrained central portions of the annular pellet.

In the latter category come developments which could lead to an improvement of fuel thermal conductivity. (Other developments aimed specifically at improving fission gas retention also provide an indirect benefit, but these are discussed separately below.) One way to increase the thermal conductivity of fuel is to reduce its porosity content; two options are available for this. The population of fine (sub-micron and micron sized pores) is determined by sintering conditions. Various techniques are available, including longer sintering times, modified sintering atmospheres, and the use of active powders and dopants, which could reduce or largely eliminate the residual fine porosity. The benefits of this, however, are unlikely to be significant, since this population of pores is in any case quickly eliminated by irradiation.

A potentially more fruitful approach to producing high density fuel is via the elimination of the more stable larger pore population. In many fuel manufacturing routes the characteristics of the large pore population are controlled by the use of pore forming agents, in BNFL's case this being CONPOR. Complete elimination of the pore former can be used to produce fuels up to 98% dense. UO_2 fuel of this density has been irradiated without problems for many years in the UK's gas-cooled reactors, although use in MOX fuel and at high burnup remains untested. Moreover, the role of the large pores in accommodating fuel swelling and creep during normal and off normal operation, while not fully understood and quantified, may be significant. The complete elimination of the large pore population may therefore be too radical a step, and more value may come from research into adaptation of pore forming agents to produce fuels with a higher density but which still demonstrate satisfactory swelling accommodation.

The other major option for increasing the thermal conductivity of fuel is via the introduction of a second, higher conductivity, material. This could be an oxide, for example some recent UO_2 experiments have studied beryllium oxide (BeO)[1]. This has the highest conductivity of any oxide, a high melting point, and low neutron absorption, although its toxicity presents handling difficulties. By sintering above the eutectic temperature of UO_2 -BeO, BeO can be precipitated almost continuously along the grain boundaries, yielding conductivity improvements of the order of 25%. The other candidate for a high conductivity second material is a metal, in other words producing a cermet fuel. Cermets have been studied extensively in the past, with molybdenum generally considered to be the most promising metal. Recent work with UO_2 has shown that it is possible to fabricate pellets in which high density fuel agglomerates are enclosed within a continuous, interconnected metal matrix using as little as 5% molybdenum content.

The in-reactor performance of such advanced fuels is largely untested. The impact on MOX fuel manufacturing routes is also unclear. Nevertheless, should significant improvement of fuel thermal conductivity be deemed imperative for the accomplishment of high MOX fuel burnups, then some promising development paths would appear to be available.

Further, more radical development possibilities could combine both pellet design changes and materials property changes. In particular, the use of duplex pellets would seem to offer potential advantages, although again with some likely cost penalty. Duplex fuel designs have been used in a number of trial irradiations in the past, but have been limited to studies of the effects of dual enrichments. In principle, the two pellet regions could be designed not only with different enrichments, but also with different microstructural characteristics. The optimum microstructure for fuel positioned in the hotter central regions of a pellet are not the same as those for fuel near the pellet periphery. This additional degree of freedom therefore offers scope for development of fuels with improved thermal performance, as well as other advantageous, characteristics.

4. FISSION GAS RELEASE

Fission product release, and associated gas bubble swelling, is potentially burnup limiting in all fuel types. With MOX fuel, the inherently lower thermal conductivity, higher late-in-life powers, generally smaller grain sizes and, possibly, inhomogeneity of the pellet structure would all point to higher gas release levels compared with standard fuel. Mitigating the effects of these four factors is therefore important to the achievement of high MOX burnup. The first two of these factors have already been discussed elsewhere in this paper, the latter two are considered below. While the focus here is on potential solutions to the underlying problems, it is clear that other more straightforward design changes, such as introducing larger or cooler plenum volumes, or using annular fuel, can also alleviate the problems of gas release and might also have a role to play in any high burnup MOX fuel design.

The present generation of MOX fuels have mean grain sizes that are typically a factor of two to three times smaller than present UO_2 fuels. Although, to first order, grain size has no effect on pre-interlinkage gas release rates, nor on the incubation burnup necessary to achieve interlinkage, there is a strong inverse correlation between gas release and grain size in the post-interlinkage, thermal release regime that is most significant, and potentially life limiting, at high burnup. Increasing fuel grain size is therefore a key to unlocking the high burnup potential of MOX fuel.

High furnace temperature and/or long sintering times are the most orthodox means to fabricate large grained material. However, very high temperatures and/or very long times are likely to be required to achieve significant improvements in the grain size of MOX fuel. Alternative sintering techniques are therefore likely to be necessary. One such approach is the use of sintering atmospheres with higher oxygen potential produced using either CO_2 or water vapour in hydrogen. A second approach involves the use of active powders. This technology has been studied in the context of high burnup UO_2 fuels [2], but application to mixed oxides may be less successful due to differences between the UO_2 and PuO_2 powders. A third approach involves seeding. Seed crystals of UO_2 (from recycled sintered scrap material), introduced at the powder blending stage, grow preferentially during sintering, leading to a

large grained material. A separate BNFL paper at this meeting describes the technique in more detail [3]. All of these approaches may offer some potential for achieving large grain size MOX fuel.

The use of dopants is an alternative approach to producing large grained material. Many dopants, including niobia, chromia, titania and magnesia, have been shown to readily produce large grain UO_2 fuels. However, the irradiation experience shows that the benefits of large grains are at least partially offset by the associated increase in fission product diffusion rates, resulting in only modest benefits in gas retention. Work on UO_2 with this class of dopants is still being pursued, e.g. [4], although within BNFL [5] the focus is on achieving improved PCI resistance (which is less of an issue with MOX fuel) rather than fission gas retention. A small amount of work has been published on doped MOX fuels, but this remains a fruitful area of research.

A second class of fuel dopants are those which form a liquid phase during sintering, leading to enhanced grain boundary diffusion. Such dopants are capable of producing large grain fuel but without the drawback of enhanced matrix diffusivity. A recent study has confirmed the satisfactory performance of alumino-silicate doped UO_2 in irradiation trials to 60 MWd/kgHM burnup. Application of this technology to MOX fuel may be worth pursuing.

It is well established that mixed oxide fuels with poor plutonium homogeneity lead to a marked enhancement of fission gas release for a broad range of irradiation conditions. On the other hand more uniform dispersal of the plutonium in solid solution can lead to a small reduction of thermal conductivity. BNFL's Short Binderless Route (SBR) produces a MOX fuel microstructure which meets the optimum for current fuel duties. BNFL is involved in the development of fuels targeted at higher burnup duties where fission product retention is paramount. Adaptation of the SBR to meet these requirements is considered to be relatively straightforward.

5. OTHER CONSIDERATIONS

Fuel Cladding

Current cladding technology is only demonstrated for burnups up to approximately 60 GWd/t. For higher burnups new cladding types will be required, irrespective of whether the fuel is UO_2 or MOX. The difference in fission gas release, although significant, is modest enough that relatively small changes in fuel design (such as a larger plenum volume or optimised grain size) are sufficient to accommodate it.

Power Histories

One possible approach to improving the high burnup potential of MOX fuel involves optimisation of core design schemes to give lower ratings in MOX assemblies late during their lifetime, while compensating early in life with higher ratings. What is important here is not so much the average rating that a MOX assembly is subjected to, but that of the peak rating locations. This is because the fission gas release is nonlinearly dependent on rating and the peak locations therefore make the biggest contribution to the overall plenum inventory. There is the possibility of optimising fuel shuffling patterns with respect to power histories, using

automated loading pattern search methods. Although the field of loading pattern optimisation is a very active research area at the moment, little work has been carried out to optimise in this respect; normally loading patterns are optimised with respect to single parameters such as reactivity coefficients, cycle length or feed enrichment. Optimising on power histories is a more difficult task, but one which is now within reach of the latest optimisation codes.

The use of burnable poisons has a limited role to play in achieving high MOX burnups. They are essential to hold down the excess reactivity early in life of the fuel, however they have little role beyond the first cycle of irradiation, as they are designed to be completely burnt out by then. Nevertheless, without burnable poisons, high burnup fuel management schemes would be impractical to achieve.

6. CONCLUSIONS

It is believed that BNFL's SBR MOX has the capability of exceeding the current burnup constraints on MOX fuels; however, the current generation of fuels have not been optimised for very high burnup operation, > 60 GWd/t. Assuming fuel developments can be matched by appropriate advances in cladding technology, a number of avenues are available which can be pursued in the quest for higher burnup, many of which may, in principle, be easily incorporated in the SBR. These range from straightforward design changes to more radical developments:

- Smaller diameter rods, larger and cooler plenum volumes and annular pellets;
- Core design optimisation with respect to power histories
- Fuel microstructures specifically optimised for high burnup duty with respect to plutonium homogeneity and pore and grain size distributions
- Use of dopants
- Use of duplex pellet designs
- Use of oxide or metal additives to increase thermal conductivity.

REFERENCES

[1] ISHIMOTO S., KUBO T., HIRAI M., and ITO K., Effective Thermal Conductivity of UO_2 -BeO Enlarged Halden Programme Group Meeting, November 1994.

[2] HARADA Y., DOI S., ABETA S.,and YAMATE K.,Behaviour of Large Grain UO_2 Pellet by New ADU Powder, IAEA Windermere, September 1994.

[3] WOOD G A., and PERKINS C P., Grain Size Distribution in Seeded Large Grain Size UO_2 IAEA Tokyo, November 1996.

[4] KUBO T.,et al., Fission Gas Behaviour in Advanced UO_2 with Controlled Microstructures ANS West Palm Beach, April 1994.

[5] HOWL D A , PALMER I D, TOPLISS I R., Niobia-Doped Fuel as a PCI Remedy ANS West Palm Beach, April 1994.

[6] YUDA R., et al., Effects of Pellet Microstructure on Irradiation Behaviour Enlarged Halden Programme Group Meeting, May 1996.

DISCUSSION

(Questions are given in italics)

Why look at BeO in a CERCER fuel? It is toxic, it reacts with water, it lowers the melting point of the fuel and it produces helium

BeO is quoted as an example of a material with high thermal conductivity It is recognized that there are many disadvantages associated with its use. Perhaps Mr Konings can suggest a better alternative

Before undertaking a new programme on FGR for MOX, don't you think the first thing to know is the reality of the increased temperature (therefore, FGR) in high burnup MOX fuel For that irradiation of MOX fuel up to high burnup should be undertaken in loops?

Yes, I agree and BNFL has undertaken such a programme

FISSION GAS RELEASE AND PELLET MICROSTRUCTURE CHANGE OF HIGH BURNUP BWR FUEL

N. ITAGAKI, K. OHIRA, K. TSUDA
Nuclear Fuel Industries Ltd,
Ibaraki, Japan

G. FISCHER
Siemens AG,
Unternehmensbereich KWU,
Erlangen, Germany

T. OTA
Tokyo Electric Power Company,
Tokyo, Japan

Abstract

UO_2 fuel, with and without Gadolinium, irradiated for three, five, and six irradiation cycles up to about 60 GWd/t pellet burnup in a commercial BWR were studied. The fission gas release and the rim effect were investigated by the puncture test and gas analysis method, OM (optical microscope), SEM (scanning electron microscope), and EPMA (electron probe microanalyzer).

The fission gas release rate of the fuel rods irradiated up to six cycles was below a few percent; there was no tendency for the fission gas release to increase abruptly with burnup. On the other hand, microstructure changes were revealed by OM and SEM examination at the rim position with burnup increase. Fission gas was found depleted at both the rim position and the pellet center region using EPMA. There was no correlation between the fission gas release measured by the puncture test and the fission gas depletion at the rim position using EPMA. However, the depletion of fission gas in the center region had good correlation with the fission gas release rate determined by the puncture test. In addition, because the burnup is very large at the rim position of high burnup fuel and also due to the fission rate of the produced Pu, the Xe/Kr ratio at the rim position of high burnup fuel is close to the value of the fission yield of Pu. The Xe/Kr ratio determined by the gas analysis after the puncture test was equivalent to the fuel average but not to the pellet rim position.

From the results, it was concluded that fission gas at the rim position was released from the UO_2 matrix in high burnup, however, most of this released fission gas was held in the porous structure and not released from the pellet to the free volume.

1. INTRODUCTION

To reduce fuel cycle costs and the amount of spent fuel produced, higher burnup fuel has been developed. In Japan, 9×9 type fuel has just been loaded in a BWR. This new fuel will be standard reload fuel for most Japanese BWRs replacing 8×8 type fuel within a few years. The new fuel is licensed for 55 GWd/t maximum assembly burnup; the average discharge burnup is scheduled to be about 45GWd/t.

The mechanical integrity must be maintained for this high burnup fuel. One factor that limits burnup is fission gas release. With the development of the microstructure change at the rim position of high burnup fuel, called the "rim effect," and the depletion of fission gas at the rim position detected by EPMA, there was concern that fission gas release from the rim position might be accelerated with burnup increase [1]. Recent reports, however, state that

fission gas at the rim position released from a pellet having high burnup could be negligible. These reports are based on the results of analysis by a special method using X-ray fluorescence spectrometry [2] and a micro coring technique [3].

In this study, the fission gas release behavior was investigated for high burnup fuel. The influence of the rim effect on fission gas release in high burnup fuel was estimated by the puncture test and the gas analysis method, SEM, and EPMA on UO_2 fuel with and without Gd.

2. EXPERIMENT

This experiment examined fuel rods from the 9×9 assemblies made by Siemens KWU that were irradiated for three, five, and six cycles in a German commercial BWR. The rods were examined by the puncture test and gas analysis. Then OM (optical microscope), SEM (scanning electron microscope), and EPMA (electron probe microanalyzer) techniques were used to determine the influence of the rim effect on the fission gas release of the UO_2 fuel with and without Gd.

The dimensions and irradiation data including the pellet edge burnup at the axial peak position of the experimental samples are summarized in the following table. Absorption of epithermal neutrons results in the high Pu accumulation which results in very high burnup at the pellet rim position. Such very high burnup at the pellet rim position is the cause of the pellet microstructure change at the rim position. The pellet edge burnup was calculated with the pellet average burnup, the enrichment and the fuel diameter in a 40% void BWR condition by the simplified method derived from Kameyama [4]. The relation between pellet average burnup and pellet edge burnup is shown in Fig. 1.

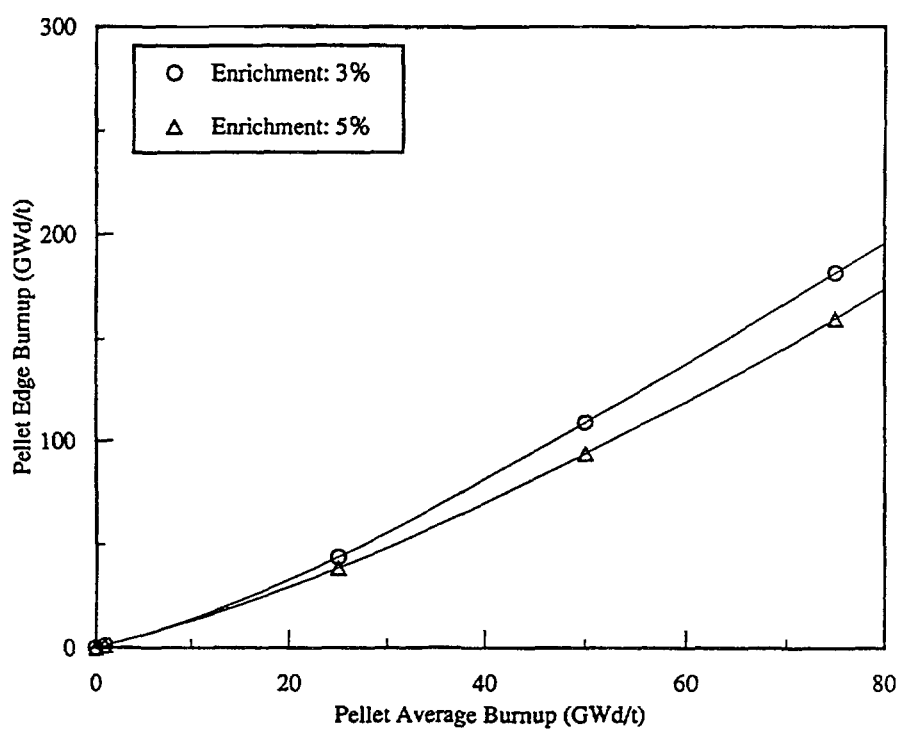

FIG. 1. Relation between pellet burnup and pellet edge burnup [4].

Rod No.	No.1	No.2	No.3	No.4	No.5	No.6	No.7	No.8	No.9
Fuel rod diameter (mm)	10.75	10.75	10.75	10.75	10.75	10.75	10.75	10.75	10.75
Pellet diameter (mm)	9.1	9.1	9.1	9.1	9.1	9.1	9.1	9.1	9.1
He fill gas pressure (MPa)	0.65	0.65	0.65	0.65	0.65	0.65	0.65	0.65	0.65
Enrichment (%)	4.0	4.0-	3.0	4.0	4.0	3.0	4.0	4.0	3.0
Gd203 content(%)	--	--	3.0	--	--	3.0	--	--	3.0
Irradiation cycles	3	3	3	5	5	5	6	6	6
Fuel rod burnup (GWd/t)	35	34	32	50	52	45	50	55	49
Pellet burnup (GWd/t)*	39	38	36	56	58	50	55	61	55
Pellet edge burnup (GWd/t)*	71	69	71	118	123	110	118	137	121

* axial burnup peak position

3. PIE RESULTS

3.1 Fission gas release

Results of the fission gas release rate measurements are shown in relation to fuel rod average burnup in Fig. 2. The results of previous work [5,6] are also shown. For the fuel rods irradiated up to six cycles, the fission gas release was below a few percent. The release rates were significantly lower than obtained with the previous work. Further, there was no tendency of the fission gas release to increase abruptly with burnup increase in the high burnup region. The dependence of the fission gas release on the fuel rod power is shown in Fig. 3. The results of previous work [5] are also shown. In the similar power region, around 300 W/cm, the fission gas release rate of the fuel in this study is lower than in the previous work. It is well known that fission gas released to the free volume degrades the thermal gap conductance between the cladding tube and the pellet surface. The degradation of gap conductance increases the pellet temperature, which then accelerates the release of fission gas. This phenomenon is called thermal feedback. The thermal feedback is very pronounced in fuel having low helium prepressure. The reason for the minimal fission gas release from the fuel in this study can be attributed to the higher He prepressure compared with the unpressurized fuel used in the previous work.

3.2 Microstructure

At the rim position of the high burnup pellet, the microstructure changed to very fine grain, porous structure. This is referred to as the rim effect. In this study, pellet

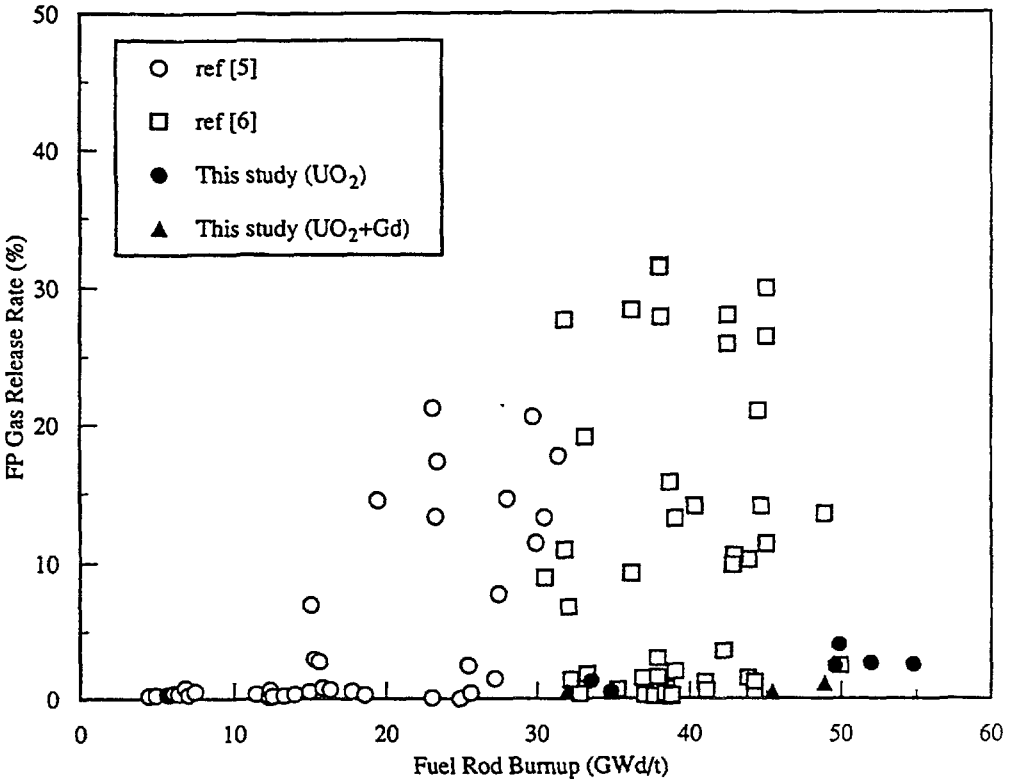

FIG. 2. Dependence of FP gas release rate on fuel rod burnup.

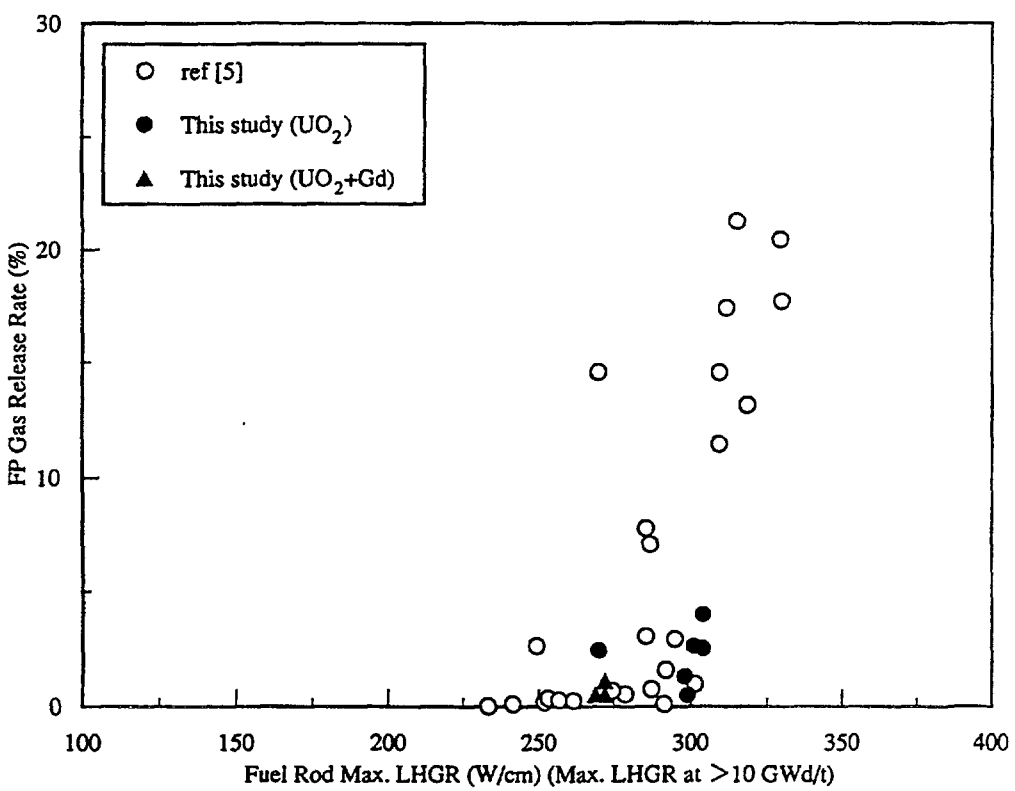

FIG. 3. Dependence of FP gas release rate on max. LHGR.

microstructures were observed by OM and SEM. Photos of the microstructures are shown together with macrographs in Photo 1 for UO_2 pellets with and without Gd. The microstructure changes were observed after three irradiation cycles although initially they were not conspicuous. After five and six cycles, the microstructure at the rim position became very porous and the grain boundary became indistinct and finally disappeared. The structure then exhibited the typical appearance of the rim effect. The relation between the pellet edge burnup and the rim width of the microstructure change determined by OM is shown with previously reported data [2] in Fig. 4. The rim width in this study lay within that of the previous work; the rim effect began beyond a burnup of about 50 GWd/t at the pellet edges. From the SEM images, the porosity at the rim position was also estimated, as shown in Fig. 5, The porosity increased with burnup. From both Fig. 4 and Fig. 5., it seemed that the rim effect was pronounced in the Gd bearing UO_2 pellets.

3.3 EPMA

The Xe depletion at the rim position of high burnup fuel was reported in the results of EPMA analysis in previous work [1, 2]. The results in this study are shown in Photo 1 with the SEM images. The fission gas content was found depleted at both the rim position and the pellet center region in the UO_2 pellet that did not contain Gd. Xe depletion in the UO_2 +Gd pellets was also found at the rim position, but less there was depletion in the center region.

From the results of EPMA, we estimated the Xe depletion rate at the rim, i.e. Xe release rate from the UO_2 matrix at the rim region. This was defined in a previous study [2] as shown in Fig. 6. The burnup dependence of the Xe depletion rate is shown in Fig. 7. These data are comparable with the previous study and the tendency was expressed well by the Barner equation. We estimated the hypothetical fission gas release rate from the rim position, that is, the rate of the Xe depletion at the rim to the total Xe amount generated in a pellet, as shown in Fig. 8. The hypothetical fission gas release rate from the rim was not negligible, being equivalent to nearly ten percent in some fuel irradiated for six cycles.

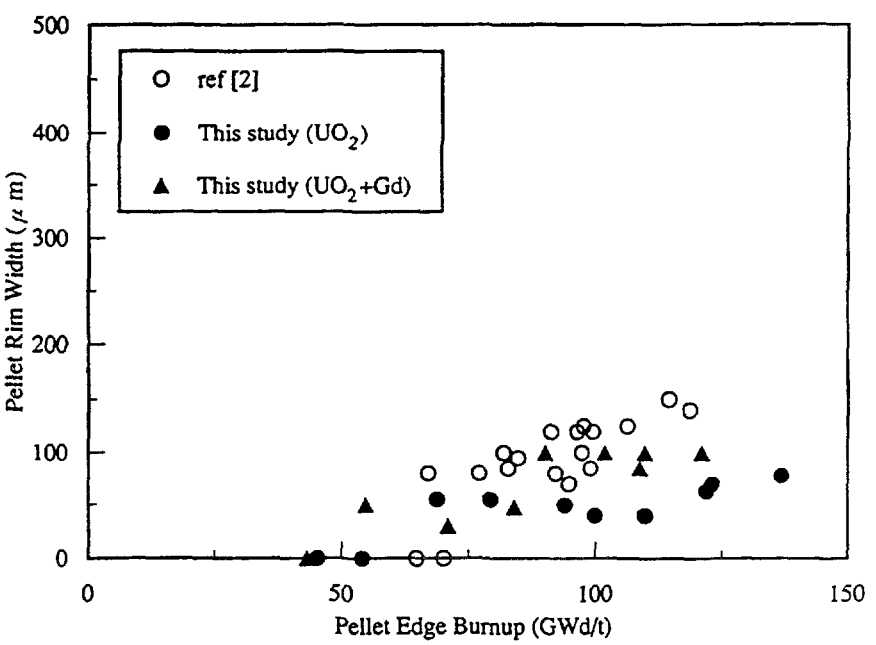

FIG. 4. Dependence of pellet rim width on pellet edge burnup (metallographic examination)

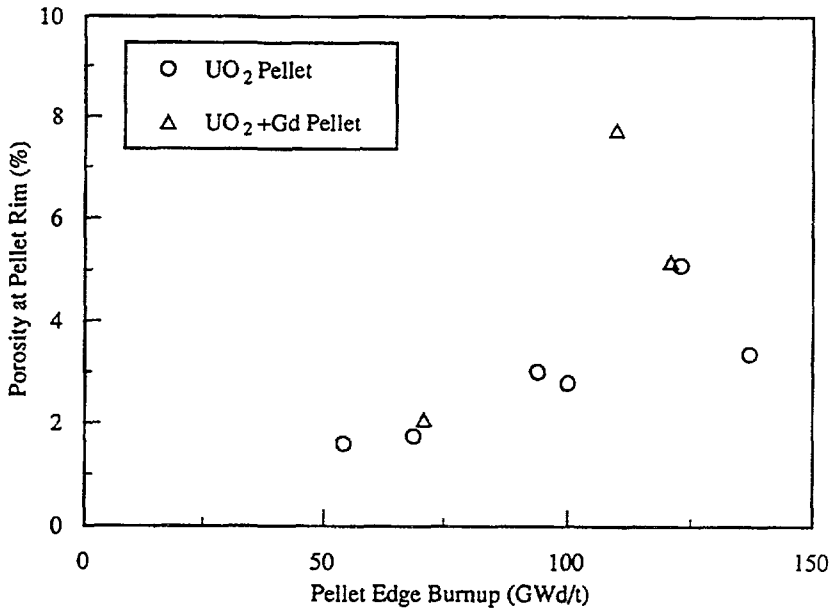

FIG. 5. Dependence of porosity at rim on pellet edge burnup (SEM examination, pore diameter: ~3μm)

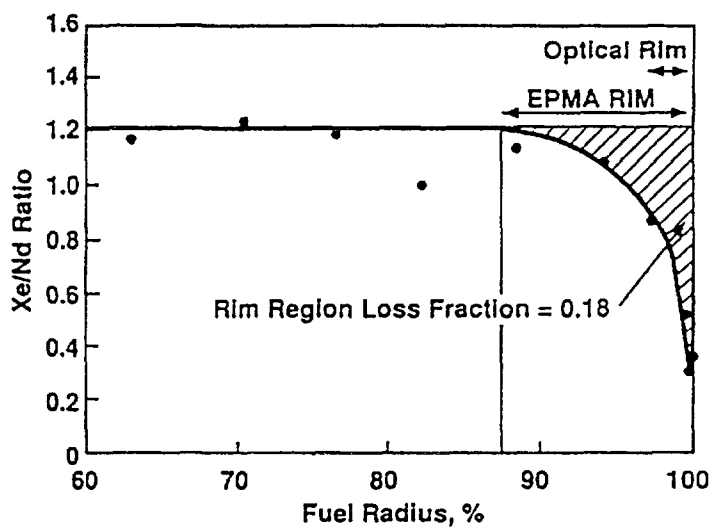

FIG. 6. Example of analysing EPMA data for Xe depletion at rim [2].

4. DISCUSSION

The hypothetical fission gas release from the rim region can not be ignored for the high burnup fuel.

From the results of this study, we estimated the influence of the rim effect to the actual fission gas release as follows.

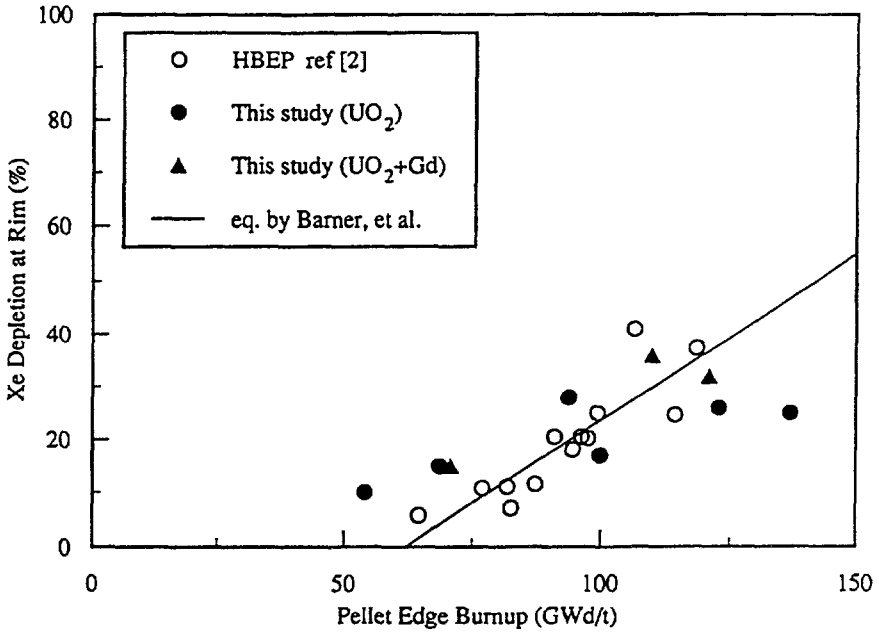

FIG. 7. Dependence of Xe depletion at rim on pellet edge burnup (EPMA examination)

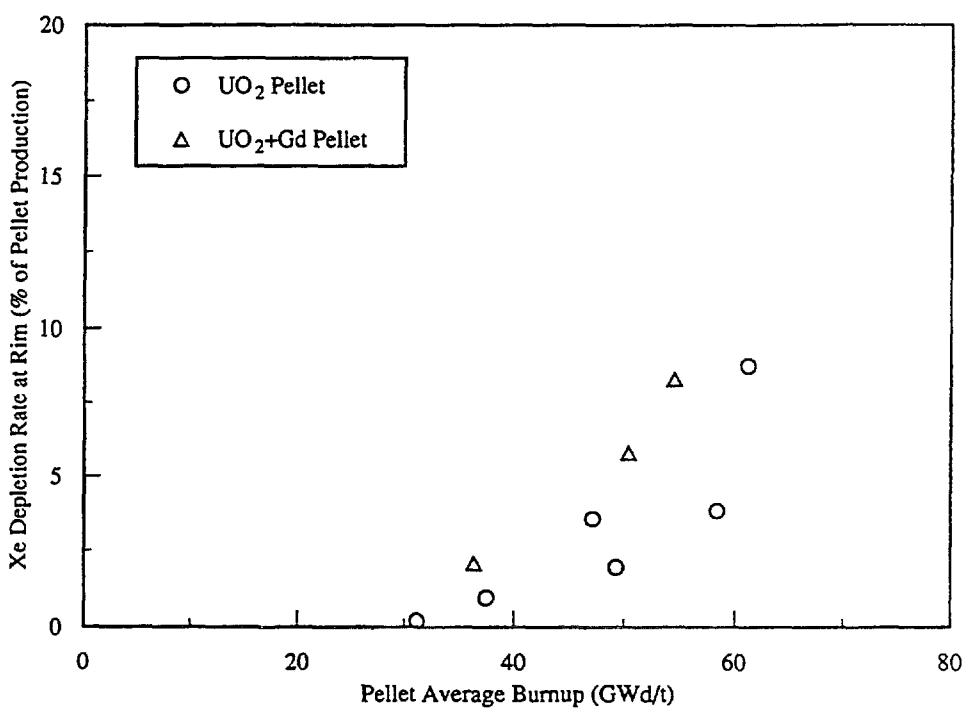

FIG. 8. Hypothetical fission gas release rate from rim (Xe depletion rate at rim (% of pellet production)).

(1) Fission gas release rate and Xe depletion

To investigate which region is the major source of fission gas release into the free volume, we examined the correlation between the actual fission gas release estimated by the puncture test and both the depletion of fission gas content at the rim position and in the center

region by EPMA. As shown in Fig. 9, there was no correlation between the fission gas release rate and the Xe depletion at the rim position. Specifically, the Gd bearing fuel showed a small fission gas release, less than one percent, though a large Xe depletion was shown after 5 and 6 cycles irradiation. However, the Xe depletion in the center region had good correlation with the fission gas release rate determined by the puncture test, as shown in Fig. 10. From the results, it seems that the fission gas was released to the free volume from the pellet center region but not from the rim position.

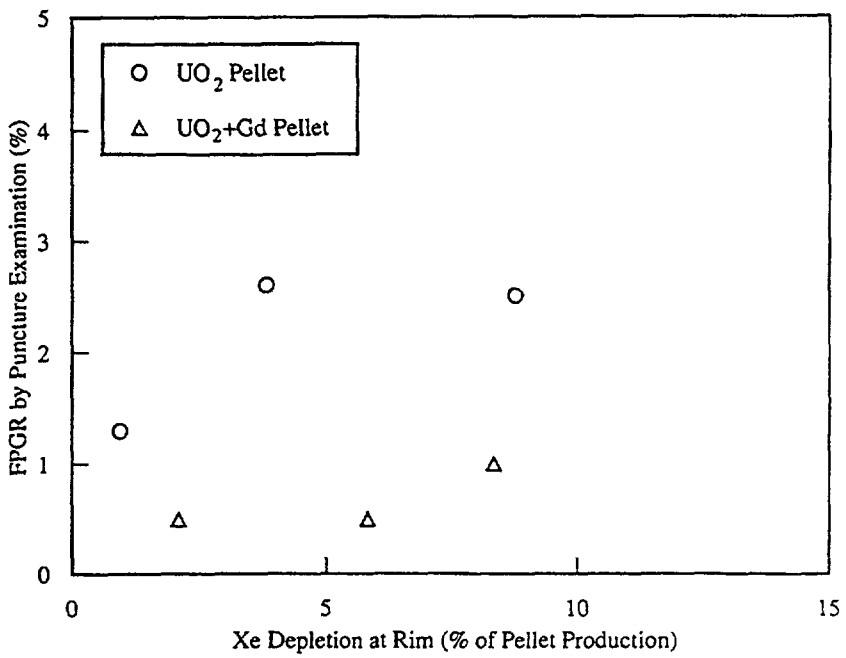

FIG. 9. *Relation between Xe depletion (EPMA) and FP gas release rate (puncture examination) at pellet rim.*

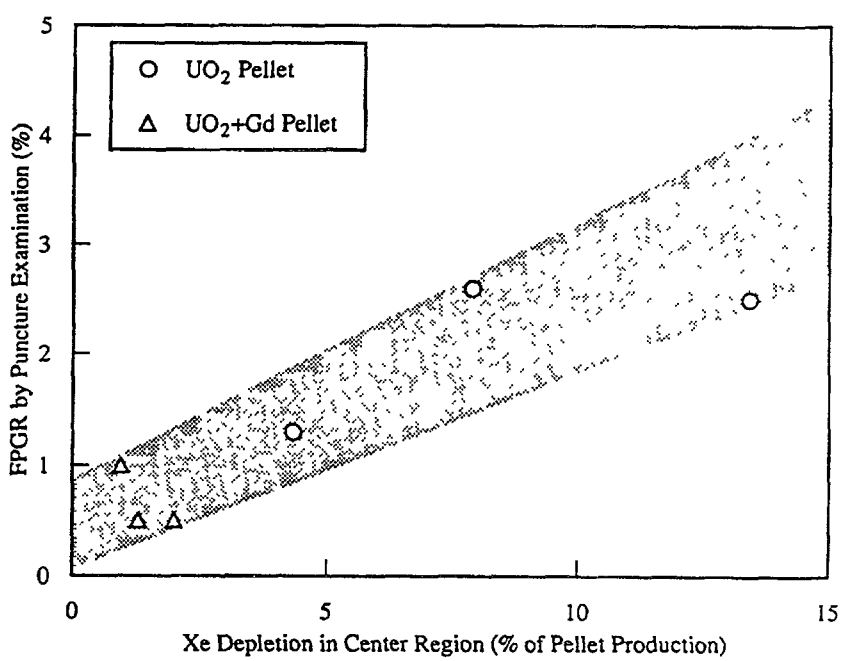

FIG. 10. *Relation between Xe depletion (EPMA) and FP gas release rate (puncture examination) in pellet center region.*

(2) Xe/Kr ratio

Generally, the contribution of Pu to the fission becomes larger than that of U-235 with burnup increase. Because of the Xe/Kr ratio of the fission yield of Pu is more than twice that of U-235, the Xe/Kr ratio increases with burnup increase. In particular, the accumulation of Pu at the pellet edge is very large. Also, the pellet edge burnup is more than twice that of the pellet average. Thus, the Xe/Kr ratio at the rim position of high burnup fuel is closed to the ratio determined by the fission yield of Pu rather than the pellet average. The Xe/Kr ratio derived from the gas analysis after the puncture test is shown in Fig. 11. The Xe/Kr ratio of the fuel average calculated by the ORIGEN-2 code is also shown along with the Xe/Kr ratio at pellet edge determined by the pellet edge burnup. In the figure, however, the Xe/Kr ratio from the puncture test was equivalent to the average value in fuel and not equivalent to the ratio at the rim position of high burnup fuel. These results suggest that the rim position was not the dominant source of the fission gas release into the free volume.

(3) Porosity observed by SEM and Xe depletion by EPMA

One significant characterization of the rim effect is the very porous microstructure at the rim. The relation between the porosity and the Xe depletion at the rim position, shown in Fig. 12, has good correlation. The relation between the porosity and the Xe depletion in the center region, shown in Fig. 13, has no correlation. These figures suggest that the Xe in the center region was released from the pores to the free volume without accumulation in the pores, while the Xe at the rim position migrated from the UO_2 matrix into the pores. The Xe accumulated in the pores and was not released to the free volume. This idea is not inconsistent with the results of EPMA at the rim position, since EPMA cannot detect Xe in the pores because the detection depth is very small, as mentioned in previous work [2].

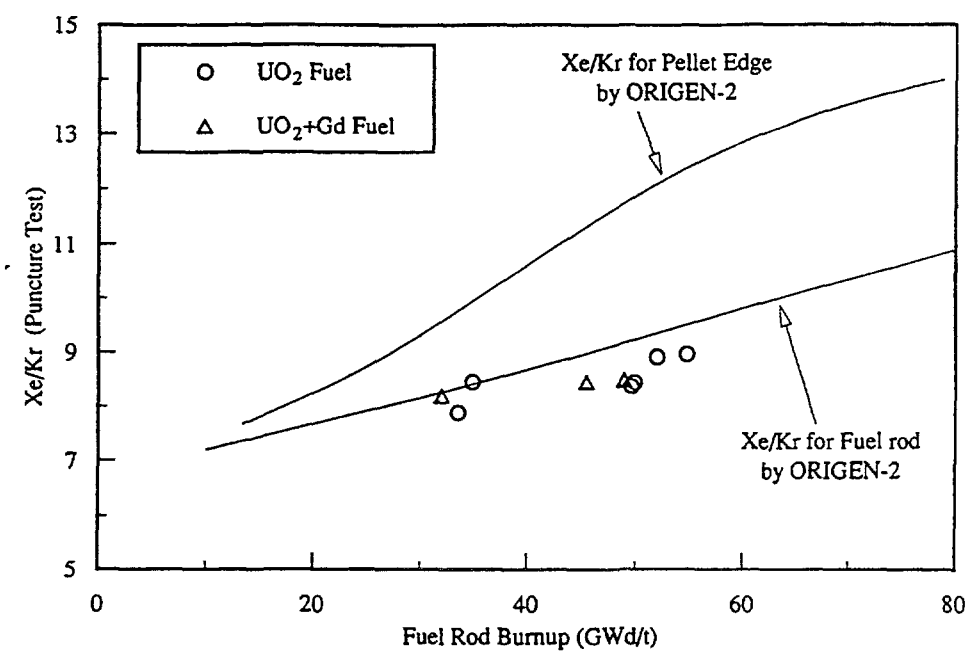

FIG. 11. Dependence of Xe/Kr on fuel rod burnup.

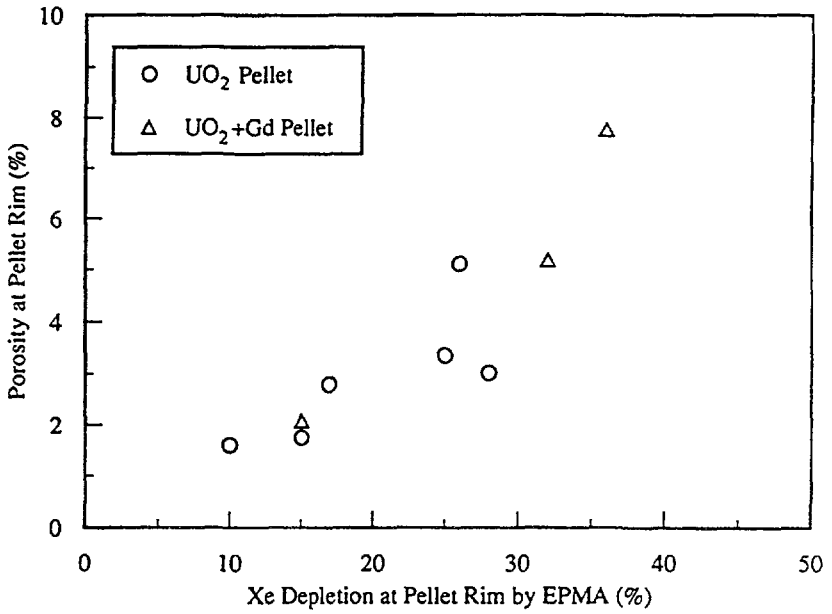

FIG. 12. Relation between porosity and Xe depletion by EPMA at rim (pore diameter: ~3μm)

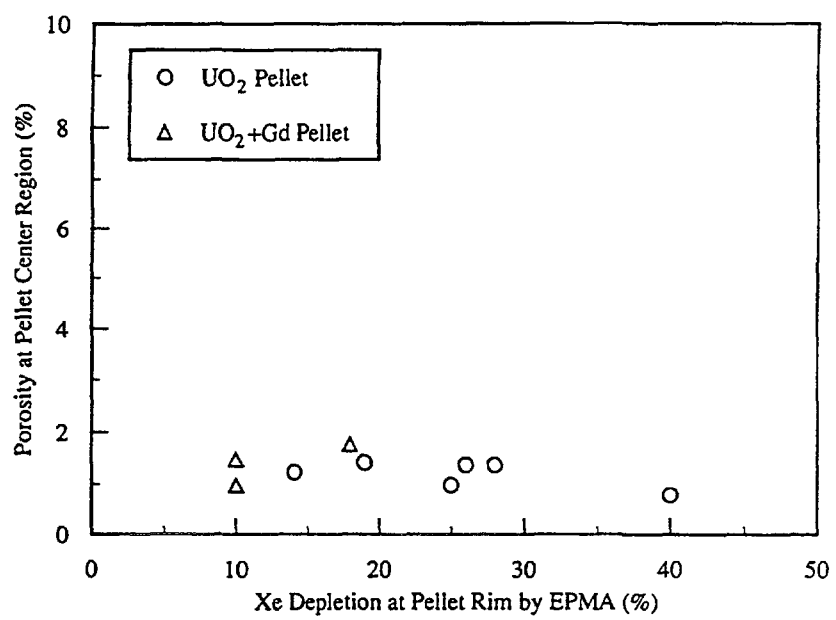

FIG. 13. Relation between porosity and Xe depletion by EPMA at center region (pore diameter: ~3μm)

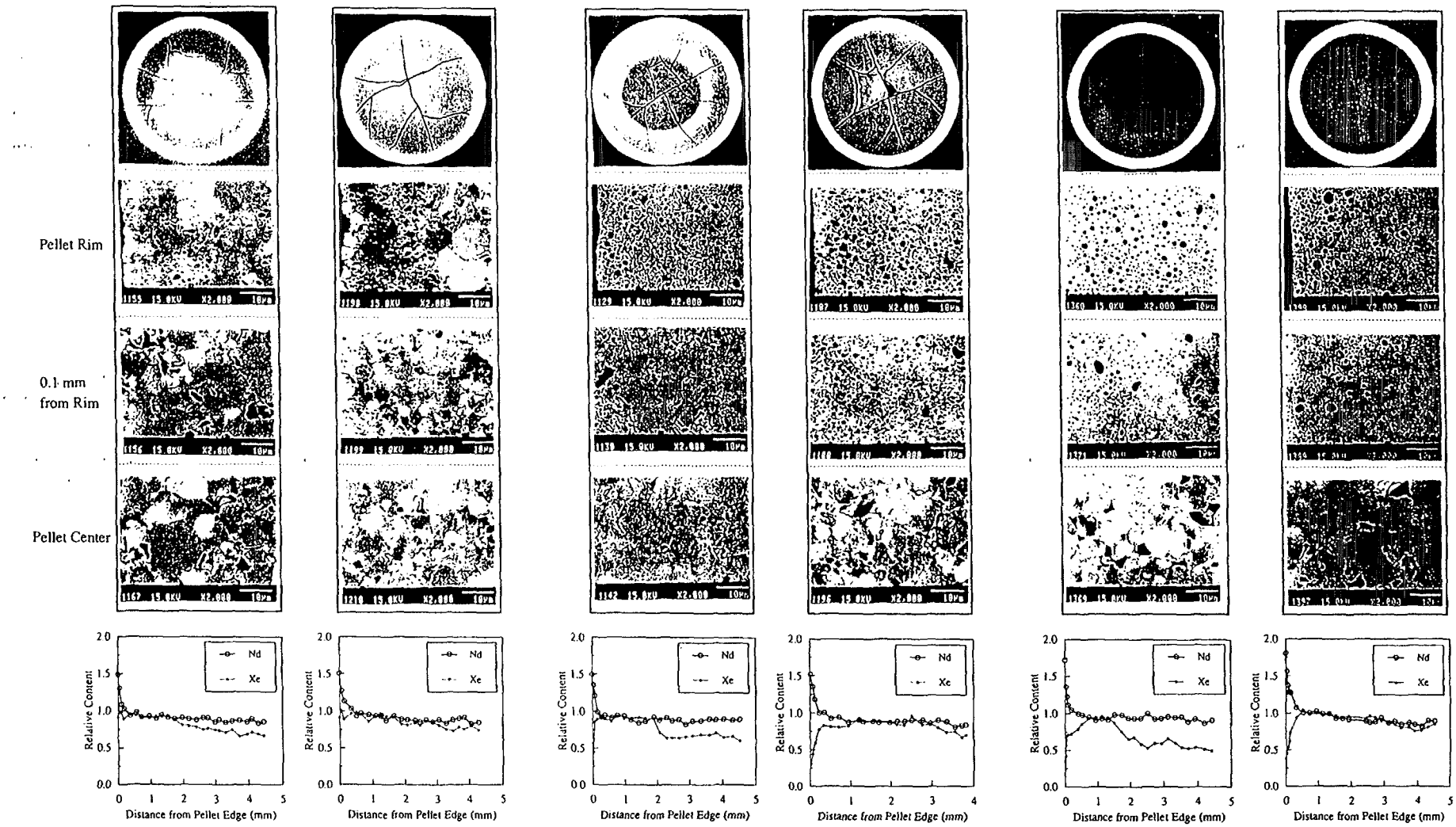

PHOTO 1. Pellet microstructure and EPMA results

5. CONCLUSIONS

(1) Fission gas release

The fission gas release rate was below a few percent for the fuel irradiated up to six cycles. For the fuels, there was no tendency of the fission gas release to increase abruptly with burnup. One reason for the low fission gas release rate of the fuel in this study is deemed to be the high He prepressure which prevent from degradation of thermal gap conductance by thermal feedback.

(2) Microstructure change

The microstructure change or rim effect developed with burnup increase. The dependence of the rim effect on burnup was comparable with the results of previous work. It seemed that the rim effect was pronounced in the Gd bearing UO_2 pellets.

(3) Fission gas release and Xe depletion

There was no correlation between the fission gas release and the Xe depletion at the rim position. However, the fission gas release rate showed good correlation with the Xe depletion in the pellet center region.

(4) Xe/Kr ratio

Xe/Kr ratio of the fission gas released into the free volume was equivalent to the average value in a fuel rod and not equivalent to the value at the rim position, even in the high burnup fuel.

(5) Porous structure and Xe depletion

Pore fraction at the rim position had good correlation with the Xe depletion ratio.

(6) Influence of rim effect on fission gas release

The fission gas release from the rim position can be neglected even in the high burnup fuel. The fission gas at the rim position is believed to migrate from the UO_2 matrix into the pores. The fission gas accumulates in the pores and is not released to the free volume.

ACKNOWLEDGEMENTS

This work was supported by Japanese electric power companies, that is, Tokyo Electric Power Company, Tohoku Electric Power Company, Chubu Electric Power Company, Hokuriku Electric Power Company, Chugoku Electric Power Company, Japan Atomic Power Company. The authors are indebted to Mr. M. Gartner and Mr. R. Manzel of Siemens KWU in Erlangen, Germany, Dr. H. G. Morgan and Mr. N. Leech of AEA Technology in Windscale, the United Kingdom. The authors acknowledge all the people who supported and encouraged this work.

REFERENCES

[1] SATYA R. PATI, et al., "Contribution of Pellet Rim Porosity to low-temperature fission Gas Release at Extended Burnup," ANS, Williamsburg, Virginia,1988.

[2] BARNER, J.O. et al., "Relationship between Microstructure and Fission Gas Release in High Burnup UO_2 Fuel with Emphasis on the Rim Region," ANS & ENS, Avignon France,1991.

[3] MANZEL R. and EBERLE R. , "Fission Gas Release at High Burnup and The Influence of The Pellet RIM," ANS & ENS, Avignon France,1991.

[4] Kameyama,T. et al., "Analysis of rim effect in high burnup LWR fuel, "Central Research Institute of Electric Power Industry, Komae Research Laboratory Rep.No. T89024, 1989.

[5] Mishima,Y. et al., "Proving Test on the Reliability for 8X8 Fuel Assemblies in Japan," IAEA International Symposium on Improvements in Water Reactor Fuel Technology and Utilization, Stockholm Sweden,1986.

[6] US DOE "BWR Fuel Bundle Extended Burnup Program," DOE/ET/34031 - 18, 1984

DISCUSSION

(Questions are given in italics)

With reference to figure 11: data points are found under the lower line probably due to the explanation that enrichment of experimental rods are a little higher than those calculated. My comment is a support to the suggested explanation?

Lower line is calculated with 4% enrichment, being equivalent to UO_2 rod. If we calculate $Ge+UO_2$ fuel which has 3% enrichment, the line will be slightly much higher. The reason that data points is lower than the line is elsewhere but not enrichment in calculation.

STATE OF THE TECHNOLOGY REVIEW

J. SPINO
CEC Institute for Transuranium Elements,
Karlsruhe, Germany

Abstract

This paper presents a review of different behaviours of fuel elements in relation to fission gases. The influence of the fission gas level and its location regarding different fuel structures is commented. The gas release process at high burnup is described and some topics that need to be further investigated are suggested.

The behaviour of the fission gases in water reactor fuels has been a matter of concern since more than 30 years, and even today questions arise especially when burnups above 4-5 irradiation cycles are envisaged. In that case, more pronounced effects on fuel behaviour are expected, either if these gases are released to the rod free-volume, or if they remain trapped in the fuel matrix. In the first case, besides the drop of the gap-conductance due to the low thermal conductivities of Xe and Kr, an excessive pressure build-up can occur at high release rates, leading to undesired cladding lift-off and gap reopening effects at end of life. On the other hand, occluded gases in the fuel voids induce matrix swelling, enhancing the pellet-cladding mechanical interactions and the risks of cladding failures by stress corrosion cracking. Given the above set of interrelated effects, the design challenge is to achieve the highest possible retention of the fission gases in the fuel matrix, compatible with the lowest fuel swelling and the lowest probability of cladding failures.

In different international meetings on water reactor fuels performance during the last years it has been shown that up to burnups of around 40 GWd/tHM and under normal reactor operation conditions, the integral fission gas release for PWR fuels can be maintained under the acceptable level of about 1 % of the inventory [1-2]. In this respect, it is interesting to note that with the introduction of improved fuel element designs and with appropriated operational measures, both allowing a more homogeneous power distribution in the fuel rods, a reduced integral gas release can be achieved not only under steady state operation [1-2], but also under load following conditions [2]. In the burnup range described (i. e. < 40 GWd/tHM), if temperature effects are moderate, the integral gas release can be almost entirely described by athermal processes, namely knock-out and recoil, showing a slight dependence with burnup and the specific area of the fuel [2-3].

Differently to the above, on surpassing burnups of about 40 GWd/tHM a steady increase of the gas release rate towards values of several percents at about 70 GWd/tHM has been reported by different fuel vendors and utilities [1-5]. In this burnup range, also the onset and growth of the so-called 'rim structure', i.e. the porous and submicron grained structure formed at the pellet edge due to the fissioning of converted Pu^{239}, has been observed [3-6]. In this region, almost the totality of Xe is depleted from the fuel matrix and contained in pressurized pores [6-7]. In some appreciations, venting of these pores through cold creep and microcracking has been postulated as a possible cause for the overall release enhancement at high burnups [8-9]. However, analysis of the gas retained at different radial positions demonstrated that the majority of the gas which is released at these burnups stems from the central regions of the pellets [10]. Accordingly, the widest consensus today is that under normal irradiation conditions the depleted gas at the fuel periphery would remain trapped in the pores, being the main contribution of the rim zone to elevate the central fuel temperatures due to the additional thermal barrier created in the gap [4-6,10-12]. The thermomechanical behaviour of this zone under severe transient conditions (i.e. RIA) is still not completely understood.

An apparent change of the gas release processes at high burnups becomes evident from the plot of the centerline temperatures for 1 % integral release versus the peak pellet burnup, when it is compared with the well established Vitanza or Halden threshold [10,13,14]. The Vitanza threshold, denoting the fuel centerline temperatures at which saturation of grain boundaries is achieved, shows an asymptotic trend to temperatures of 1000-1100 °C at burnups above 30 GWd/tHM [13]. On the contrary, the derived values for high burnup fuels indicate continuous decrease of these temperatures up to values of about 600 °C at 55 GWd/tHM [10,13]. This trend splitting may be due to two reasons, namely to an enhanced intragranular diffusion at high burnups promoting saturation of the grain boundaries at lower temperatures, or to the underestimation of the centerline temperatures due to overvaluation of the fuel thermal conductivity [13]. Due to the experimental evidences of a high temperature regime even after the 4th cycle, the second explanation appears to be the most plausible one [13]. In that case, doing the proper corrections to the thermal conductivity, the Vitanza threshold appears to be still applicable at extended burnups.

Considering the mitigation of gas release through fuel material improvement, practically the unique measure explored up to now has been the grain size enlargement. Larger grain sizes would retard gas atom diffusion to the grain boundaries, and would show also smaller swelling [15]. Various types of large grained fuels have been tested in-pile, namely undoped urania [16], UO_2 doped with metal oxides (NbO_5,TiO_2,Cr_2O_3 La_2O_3) [16-18] and UO_2 doped with Al and Ti-silicates [16]. Under steady state operation, both gas release and swelling were improved in all cases. However, under simulated power transient conditions after a burnup of ~25 GWd/tHM, only undoped and silicate doped large grained fuels showed better behaviour than standard UO_2. Contrarily, the Nb_2O_5 and TiO_2 doped fuels showed a high gas release under transient heating [16]. Since doping of large grained UO_2 is necessary to counteract its otherwise worse creep and PCI behaviour, the above results suggest a more preferable use of silicates as plasticizers (grain boundary sliding) than of dissolved niobia and titania. However, in-reactor ramp testing of silicate doped fuels is needed to prove their actual effectiveness as PCI remedy, as it was the case of niobia, in spite of the experienced large bubble swelling and increased cladding ridging [19].

Less explored up to now has been the possibility of increasing the matrix gas retention by pinning of gas bubbles at finely dispersed precipitates. Hindering the bubble growth through anchorage at preferential sites may result not only in less swelling [20], but also in a better thermal conductivity through a smaller amount of large matrix voids [21]. Avoidance of fuel hyperstoichiometry is also a point which must be attended at high burnups in order to impede gas release enhancement [22] and thermal conductivity deterioration [21]. From the point of view of pellet design, use of the alternative anular pellets, diminishing gas release and PCI effects [23-24], might be considered.

Utilization of gadolinia as burnable neutron absorber is at present a standard design feature in PWRs and BWRs to achieve more flexible core management [25]. Up to 10 wt. % Gd_2O_3 in UO_2 fuels has been normally used, with no detrimental effects in the fission gas release and swelling behaviour being reported [26]. However, due to the lower thermal conductivity of the gadolinia bearing fuels, higher operation temperatures and subsequently larger gas release of these rods are expected [16].

Burning of Pu as mixed oxide (MOX) fuel in water reactors is today an alternative not only for spent fuel recycling but also for the dispositioning of weapons fissile material. MOX fuels behave similarly to UO_2 fuels [27-30], with even superior resistance to PCI failures [29], but with the drawback of an apparently higher gas release [28]. However, this is due to the higher power rating of the MOX fuels, since when plotted as function of the linear power the integral gas release of MOX is similar to that of UO_2 [28,30]. Since in heterogeneous MOX fuels most of the fission gases are produced within the dispersed Pu-rich agglomerates, gas release to the rod free volume may occur only if enough channels (grain boundary porosity) are available in the matrix [31]. With increasing

burnup the amount of Xe migrated into the matrix increases significantly, being released after a certain time according to thermally activated processes [32]. In this sense, it is noteworthy that the onset of gas release for solid and hollow MOX fuels has been appropriately predicted by application of the Vitanza threshold for UO_2 [30].

From the above exposed it appears that the fission gas release behaviour is in general terms well understood and controlled up to average burnups of about 40 GWd/tM, whereas for extending burnups beyond this level some further investigations seem to be needed in topics like

- Diffusion coefficient of Xe in heavily irradiated UO_2 matrix with large amounts of lattice defects and high fission products concentrations (precipitated and dissolved);
- Elucidation of the true capability of the rim zone to retain fission gases within its closed porosity. Thermal-mechanical stability of the rim structure under rapid power transients (RIA);
- Intragranular fission gas retention at preferential anchorage sites (i.e. finely dispersed precipitates);
- Gas retention enhancement vs. worsening of mechanical properties in large grained fuels. Matrix dissolved vs. grain boundary segregated plasticizers;
- Heterogeneous vs. homogeneous Pu-distribution in MOX fuels.

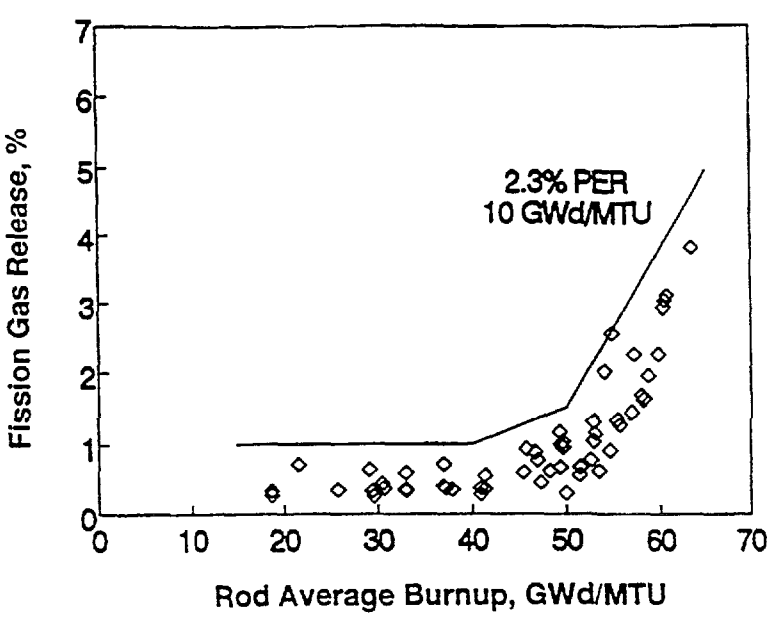

FIG. 1. PWR fission gas release as function of the rod average burnup (Ref. 2).

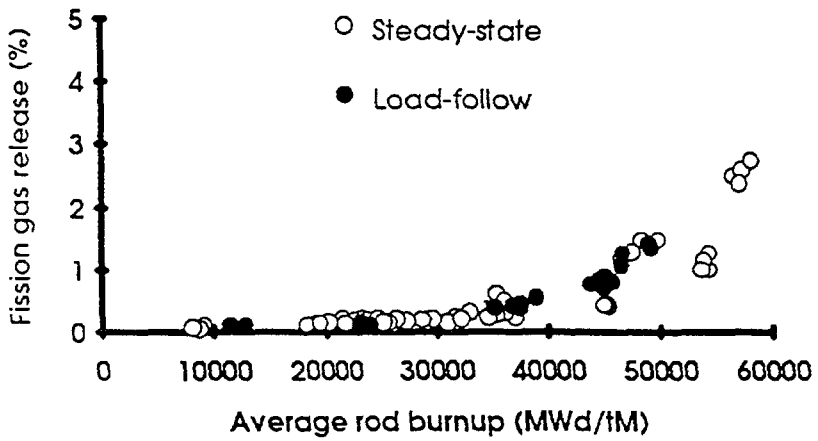

FIG. 2. Integral fission gas release from PWR rods under steady state and load following conditions (Ref. 1).

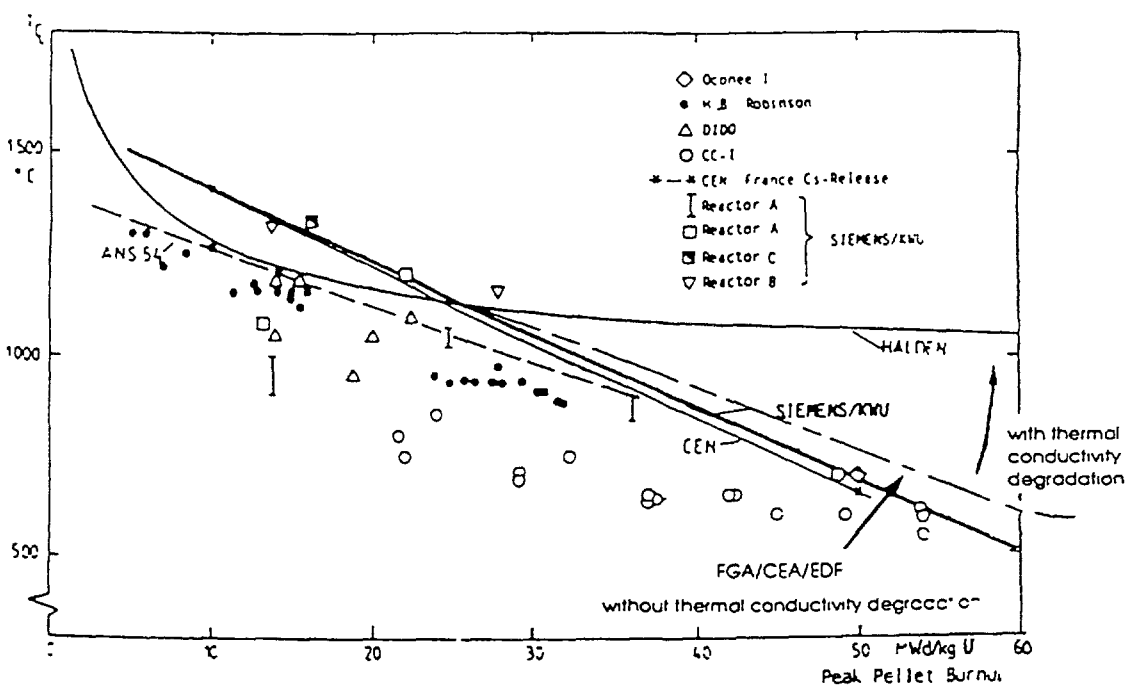

FIG. 3. Threshold temperature for 1% integral gas release as function of the peak pellet burnup (Refs. 5 and 13).

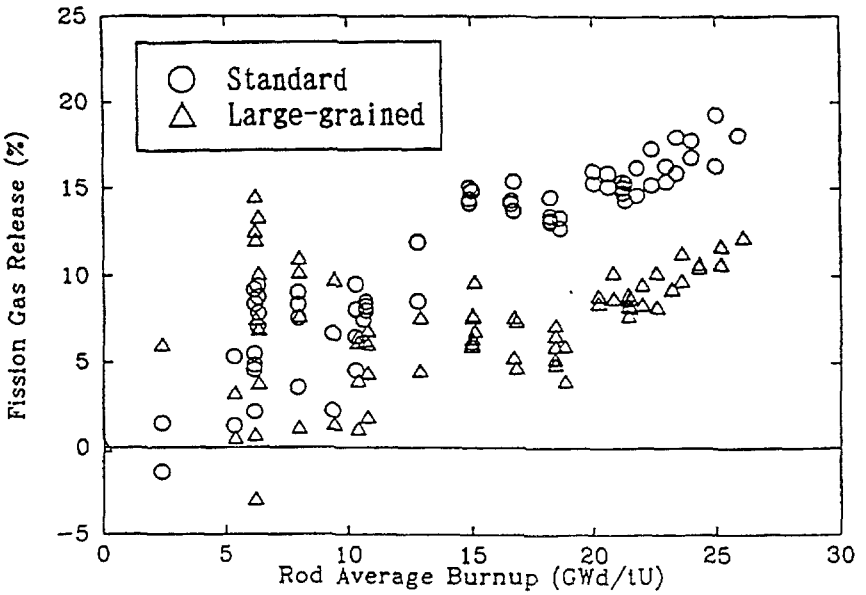

FIG. 4. Fission gas release of standard and non-additive large grained UO_2 fuels, (BWR, type 9x9) Ref. 16).

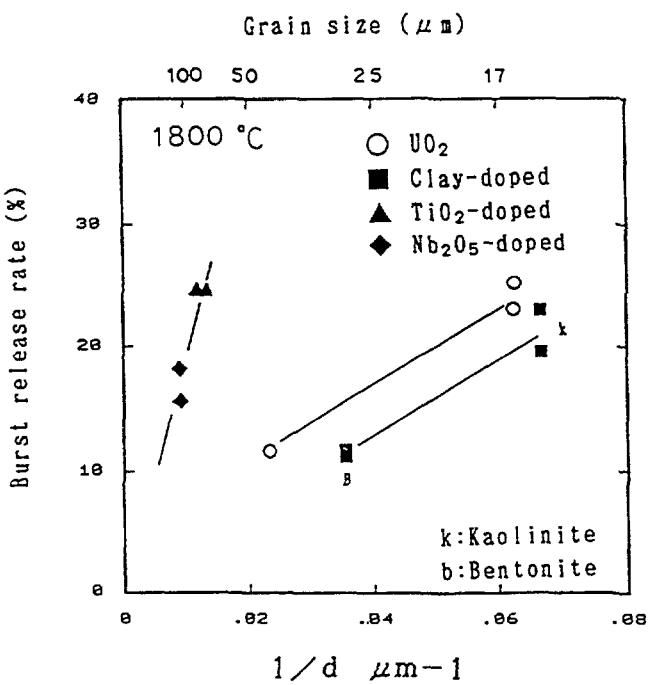

FIG. 5. Burst release rate vs. grain size in post-irradiation annealing for doped and updoped UO_2 fuels (Ref. 16).

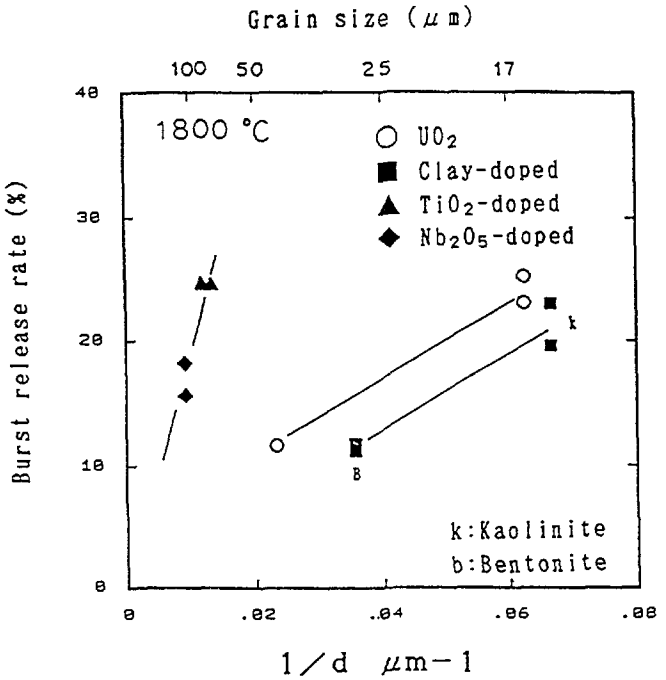

FIG. 6. Bubble swelling vs. grain size in post-irradiation annealing for doped and undoped UO_2 fuels. (Ref. 16)

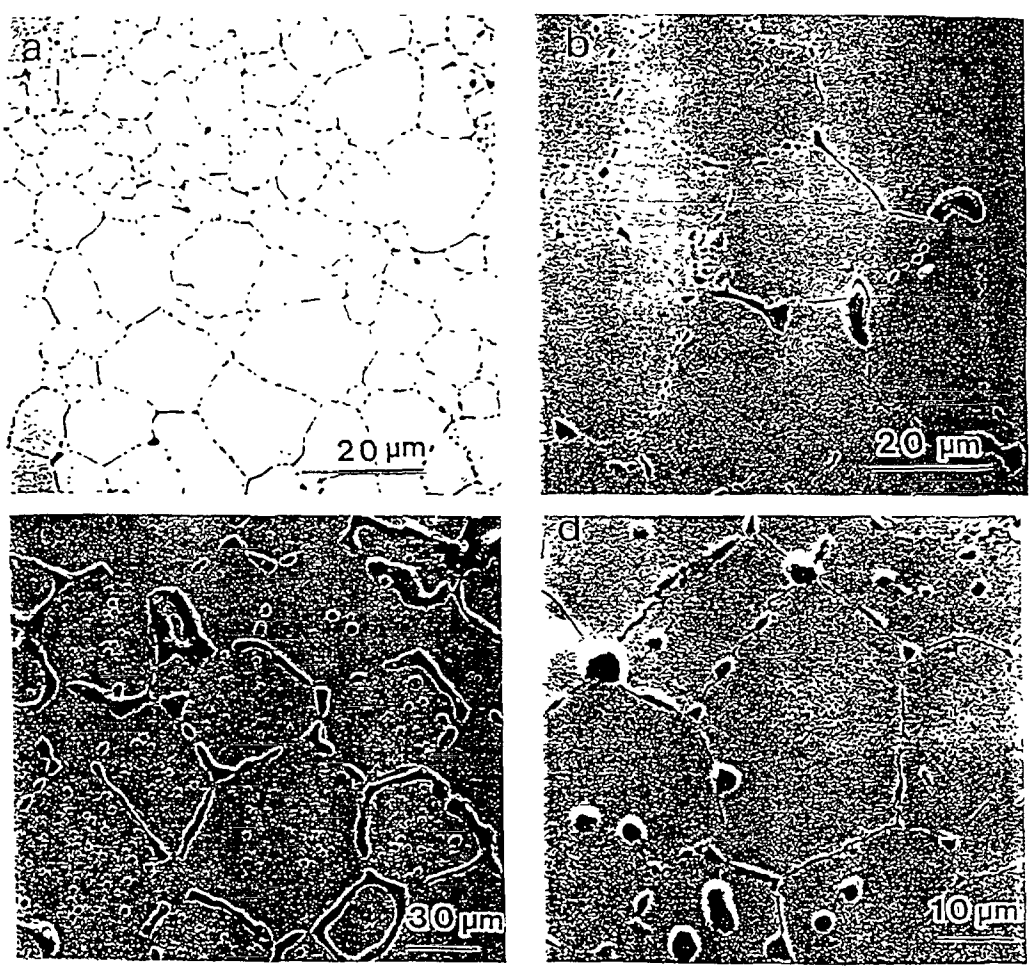

FIG. 7. SEM micrographs of post-irradiation annealed fuel samples.
(a) Standard UO_2 *(b) Undoped large grained UO_2*
(c) TiO2- doped UO_2 *(d) Bentonite-dopedm UO_2*

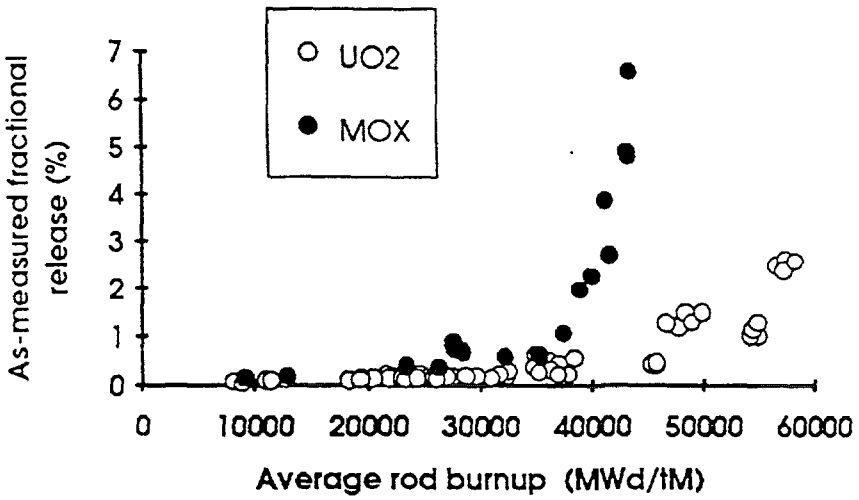

FIG. 8. Fission gas release of PWR - MOX and UO_2 fuels as function of the rod average burnup (Ref. 32).

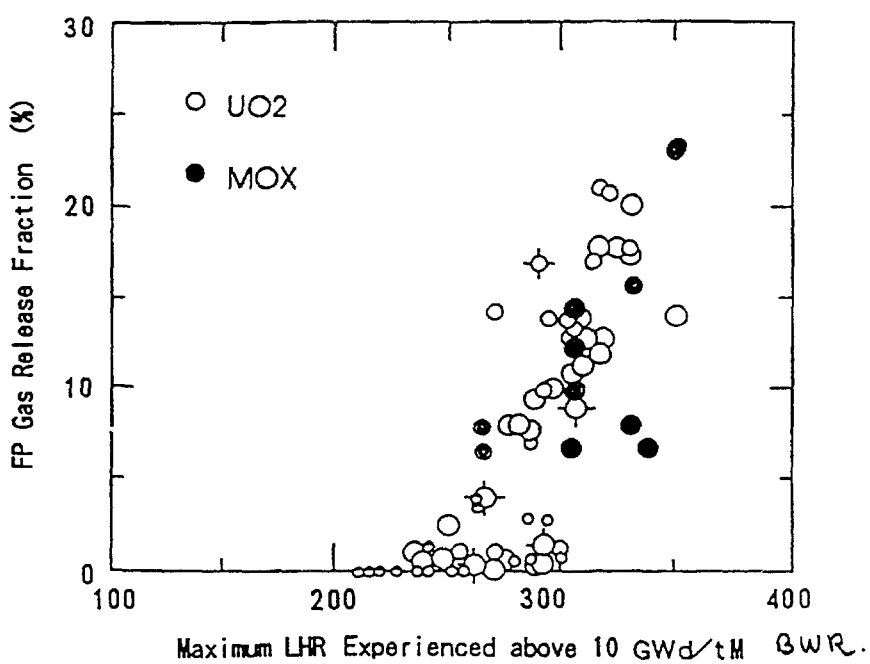

FIG. 9. Fission gas release of PWR - MOX and UO_2 fuels as function of the linear hear rate (LHR) Ref. 30).

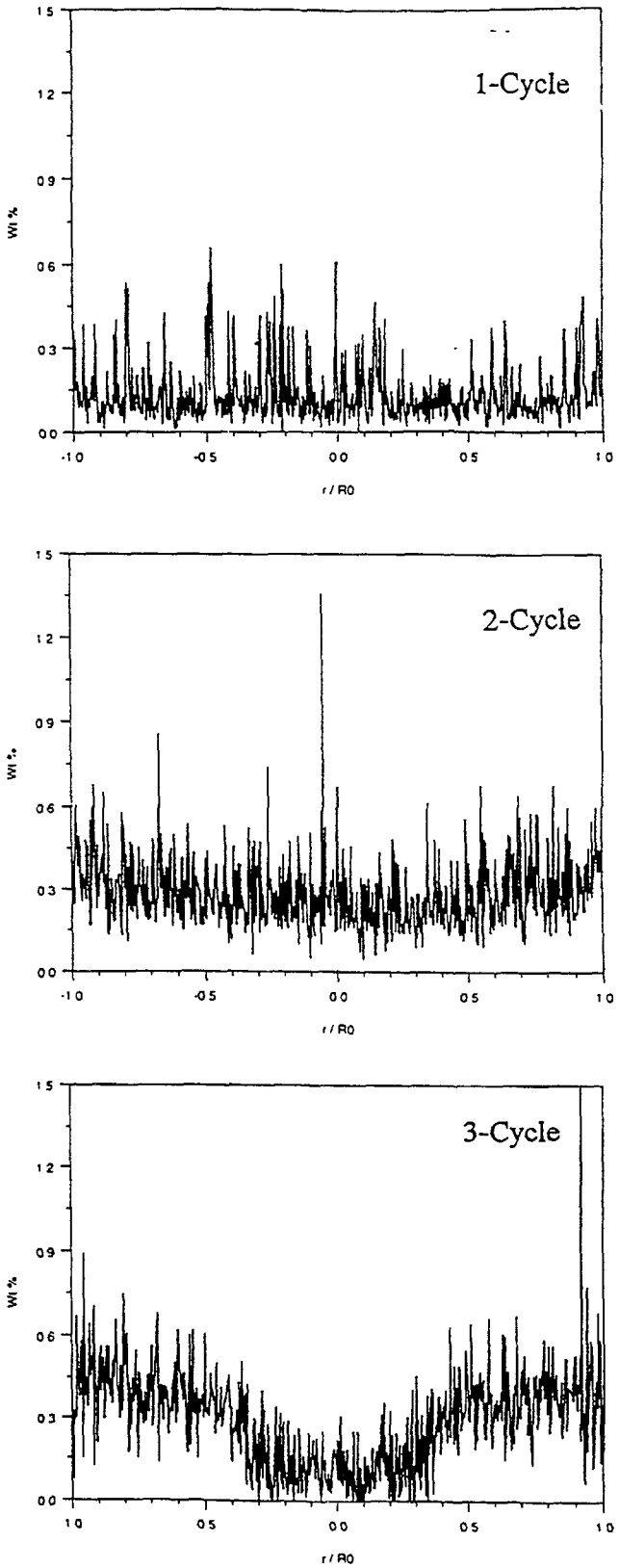

FIG. 10. EMPA diamteral scan of Xe in the UO_2 matrix of MOX fuels after the first, second and third irradiation cycles (Ref. 32).

REFERENCES

[1] MOREL, M., MELIN, P. and DUPONT,A. "Updated status of in reactor experience of Fragema fuel products", Int.Topical Meeting on Light Water Reactor Fuel Performance, West Palm Beach, Florida, April 17-21, 1994, p. 15.

[2] VESTERLUND, G. and CORSETTI, L.V., "Recent ABB fuel design and performance experience", ibid p. 62.

[3] PATI, S.R. et al., "Contribution of the pellet rim porosity to low temperature fission gas release at extended burnup", ANS Topical Meeting on LWR Fuel Performance, Williamsburg, VA, April 17-20, 1988, p. 90.

[4] BARNER, J.O. et al., "Relationship between microstructure and fission gas release in high burnup UO_2 fuel with emphasis on the rim region", Int.Topical Meeting on LWR Fuel Performance, Avignon, France, April 21-24, 1991, p.538.

[5] MANZEL, R. and EBERLE, R., "Fission gas release at high burnup and the influence of the pellet rim", ibid p.528.

[6] WALKER, C.T. and COQUERELLE, M., "Correlation between microstructure and fission gas release in high burnup UO_2 and MOX fuels", ibid p. 506.

[7] CUNNINGHAM, M.E., FRESHLEY, M.D. and LANNING, D.D., "Development and characteristics of the rim region in high burnup UO_2 fuel pellets", J.Nucl.Mater. 188 (1992) p. 19.

[8] SHANN, S.H., "Proc. of Technical Committee Meeting on Fission Gas Release and Fuel Rod Chemistry Related to Extended Burnup", Penbroke, Ontario, Canada, 28 April-1 May 1992. IAEA-TECDOC-697, p. 231.

[9] BILLAUX, M.R., VAN SWAM, L.F. and SHANN, S.H., "Effect of grain size on the fission gas release from the rim of high burnup fuel pellets Int.Topical Meeting on Light Water Reactor Fuel Performance", West Palm Beach, Florida, April 17-21, 1994, p. 242.

[10] MANZEL, R., COQUERELLE, M. and BILLAUX, M.R., "Fuel rod behaviour at extended burnup", Ibid p. 335.

[11] BAGGERAND, C., MOGENSEN, M., "Experimental assessment of a temperature threshold for thermally induced fission gas release in transient tested water reactor fuel with extended burnup", Proc. of Technical Committee Meeting on Fission Gas Release and Fuel Rod Chemistry Related to Extended Burnup, Penbroke, Ontario, Canada, 28 April-1 May 1992, IAEA-TECDOC-697, p. 38.

[12] KJAER-PEDERSEN, N., "Rim effect observations from the third Riso fission gas project", ibid p. 111.

[13] FORAT, C. et al., "Fission gas release enhancement at extended burnup. Experimental evidence from French PWR irradiation", ibid p. 68.

[14] VITANZA, C. et al., "Fission gas release from in-pile measurements", Halden Project Report, HPR 221.10, 1978.

[15] HARGREAVES, R. and COLLINS, D.A., "A quantitative model for fission gas release and swelling in irradiated uranium dioxide", J.Br.Nucl.Energy Soc.,1976,15,0ct.,N°4, p. 311.

[16] KUBO, T. et al., "Fission gas behaviour in advanced UO2 with controlled microstructures", Int.Topical Meeting on Light Water Reactor Fuel Performance, West Palm Beach, Florida, April 17-21, 1994, p. 650.

[17] KILLEEN, J.C., "The effect of additives on the irradiation behaviour of UO_2", J.Nucl.Mater.58 (1975) p. 39.

[18] KILLEEN, J.C., "Fission gas release and swelling in UO_2 doped with Cr_2O_3", J.Nucl.Mater. 88 (1980) p. 177.

[19] HOWL, D.A., PALMER, I.D. and TOPLISS, I., "Niobia doped fuel as PCI remedy", Int.Topical Meeting on Light Water Reactor Fuel Performance, West Palm Beach, Florida, April 17-21, 1994, p. 694.

[20] OLANDER, D.R., "Fundamental Aspects of Nuclear Reactor Fuel Elements", Technical Information Center, Energy Res. and Development Administration, TID-26711-P1, 1976, p.249.

[21] LUCUTA, P.G., MATZKE, Hj. and HASTINGS, I.J., "A pragmatic approach to modeling thermal conductivity of irradiated UO_2 fuel: Review and Recommendations", J.Nucl.Mater. (1996), in press.

[22] MATZKE, Hj., "Gas release mechanisms in UO_2 - A critical review Radiation Effects", 1980, Vol. 53, p. 219.

[23] HOWL, D.A. and TOPLISS, I.T., "The effect of fuel pellet variants on fission gas release following power ramps", Proc. of Technical Committee Meeting on Fission Gas Release and Fuel Rod Chemistry Related to Extended Burnup, Penbroke, Ontario, Canada, 28 April-l May 1992, IAEA-TECDOC-697, p. 75.

[24] OHARA, H. et al., "Fuel behaviour during power ramp tests", Int.Topical Meeting on Light Water Reactor Fuel Performance, West Palm Beach, Florida, April 17-21, 1994, p. 674.

[25] HILL, L.C. and HARTLEY, K.D., Siemens Power Corporation-Nuclear Division: Gadolinia Fuel Experience, Ibid p. 133.

[26] SUZUKI, S., MURAKAMI, K. and TAKAHASHI, T., "Burnup extension and improved reliability", Ibid p. 352.

[27] GOLL, W., FUCHS, H.P., MANZEL, R. and SCHLEMER, F., "Irradiation behaviour of UO_2/PuO_2 fuel in Light Water Reactors", Nuclear Technology, 102, 29 (1993).

[28] HASS, D., "MOX fuel fabrication experience at Belgonucleaire", IAEA- Technical Committee Meeting on Recycling of Plutonium and Uranium in Water Reactor Fuel, Newby Bridge, Windermere, UK, 3-7 July 1995.

[29] MORGAN, J.N. and KREBS, W.D., "Siemens' experience with large scale mixed oxide fuel assembly insertion in light water reactors", Int.Topical Meeting on Light Water Reactor Fuel Performance, West Palm Beach, Florida April 17-21, 1994, p. 711.

[30] KAMIMURA, K., "FP gas release behaviour of high burnup MOX fuels for thermal reactors", Proc. of Technical Committee Meeting on Fission Gas Release and Fuel Rod Chemistry Related to Extended Burnup, Penbroke, Ontario, Canada, 28 April-1 May 1992, IAEA-TECDOC-697, p 82.

[31] WALKER, C.T., GOLL, W. and MATSUMURA, T., "Effect of inhomogeneity on the level of fission gas and cesium release from OCOM MOX fuel during irradiation", J.Nucl.Mater. 228 (1996) p. 8.

[32] BLANPAIN, P., THIBAULT, X. and TROTABAS, M., "MOX experience in French power reactors", Int.Topical Meeting on Light Water Reactor Fuel Performance, West Palm Beach, Florida, April 17-21, 1994, p. 718.

PELLET–CLAD MECHANICAL INTERACTION

(Session 6)

EXAMINATION OF VVER-440 FUEL MICROSTRUCTURE AND COMPOSITION IN A BURNUP INTERVAL OF 42–63 MWd/kgU

A. SMIRNOV, A. PETUHOV, B. KANASHOV
Research Institute of Atomic Reactors,
Dimitrovgrad, Russian Federation

XA9847867

Abstract

The report considers the VVER-440 fuel state at a burnup of >46 MWd/kgU. Based on two FAs fuel operated during 4 and 5 fuel cycles the effects being not earlier observed in the VVER-440 FE behaviour are considered:

- rim-layer on the periphery of the fuel column with the increased porosity and Pu concentration is formed ;
- radial cracks on the fuel pellet periphery are closed, the pellets are linked along their ends, the fuel-cladding gap in the FE central part is disappeared;
- fuel column-cladding physical and chemical interactions are absent.

The macro- and microstructures of the fuel columns are presented. The particular attention is paid to rim-layer characteristics: porosity, grain size, microhardness, Pu, Xe composition.

The necessity to take into account the given parameters at foreseeing the fuel behaviour is emphasised. There was made a conclusion of high VVER-440 FE efficiency at high burnups under standard operation conditions.

Introduction

As the result of the examination of VVER-440 FAs 1422198 and 1422222 which were under operation at Kola NPP Unit up to an average burnup of 46.2 and 48.2 MWd/kgU respectively, the following peculiarities of FE state were pointed out:

- the pellet-cladding gap absence for the most part of the FE cladding;
- extension of the average cladding diameter in the central part of the fuel column relative to its minimal value corresponding to a burnup of 30-35 MWd/kgU;
- the rise of the pellet-cladding interaction in the form of the diameter local increase on the outer cladding surface. The step is multiple to the pellet height and the maximal amplitude is up to 50 μm at a maximal burnup of 63 MWd/kgU;
- redial crack closing on the pellet periphery;
- increase of fuel fission gas release in the range from 0.5-0.7 to 6%.

To clear up the reasons for rising the above mentioned peculiarities extra destructive examination was carried out using metallography, electron microscopy, diffractometry and EPMA.

The results of these examinations are considered in the present report.

1. Initial data and operation history of FAs 198 and 222

Working FAs 14422198 and 14422222 (further FA s198 and 222) were manufactured by JSC MSZ in May, 1986 (Table 1). Zr-1%Nb alloy was used as material for FE claddings and end components. FEs were filled by He under pressure of 0.5 MPa. FE sealing was performed by 3 electron-beam and 1 helium-arc welds. Pellets with central hole made of sintered uranium dioxide enriched by ^{235}U up to 4.4% were used as fuel. Fuel column was fixed by steel bushing with split. Headpiece, tailpiece and spacer grids (SG) are manufactured of stainless steel.

FA s 198 and 222 operated in Kola NPP Unit 3 during 5-8 and 5-9 fuel cycles respectively (Table 2).

Coolant temperature at reactor inlet and coolant heating did not exceed 265 and 30°C. Pressure in circuit 1 was 12.5 MPa. Coolant characteristics corresponded to branch standards of 95.10165-85.

Effective time of FAs 198 and 222 operation was 1259.8 and 1564.9 eff.days respectively.

TABLE I. BRIEF CHARACTERISTIC OF FEs AND FAs 198 AND 222

Parameter	Value
Fuel assembly:	
Dimensions of shroud tube, mm:	
length	3217
inside across flats dimension	144.2
Shroud tube list thickness, mm	2.0
Fuel elements	
FE length, mm	2557
Cladding material	Zr-1%Nb
Outer diameter of cladding, mm	9.1
Inner diameter of cladding, mm	7.72
Fuel material	sintered UO_2
Fuel pellet:	
outer diameter, mm	7.60
hole diameter, mm	1.2
height, mm	8-14
Fuel column length, mm	2420
Fuel column mass, g	1087
FE space volume, cm^3	16.7-17.2
Helium content in fuel gas, %	not less than 90.0

Calculated according to code BIPR-7 average fuel burnup in FAs 198 and 222 was 46.2 and 48.2 MWd/kgU.

During 5-8 fuel cycles reactor stopped 15 times at EP-1 system signals. During fuel cycle 9 there were no reactor scrams.

Cladding leak testing carried out in the unit showed no leaking FEs in both FAs.

TABLE II. OPERATION CONDITIONS OF FAs 198 AND 222

	198	222
Operation location	Kola NPP-3	Kola NPP-3
Date of loading into the core	24.09.86	24.09.86
Date of unloading out of the core	02.11.90	15.10.91
Life time, fuel cycles	4	5
Life time, eff.d.	1259.8	1564.9
Average fuel burnup, MWd/kgU	46.2	48.2
Maximal linear heating, W/cm	319	264
Number of actions of Reactor Protection System	15	15

2. FE selection for examination and their characteristics

Two FEs of FA 198 and three FEs of FA 222 were chosen for examination. They differ in burnup and fuel gas release. FE characteristics in detail, a scheme of sample cutting out for the examination and methods are given in table 3.

TABLE III. FE CHARACTERISTICS, SCHEME OF SAMPLE CUTTING OUT FOR EXAMINATION AND METHODS

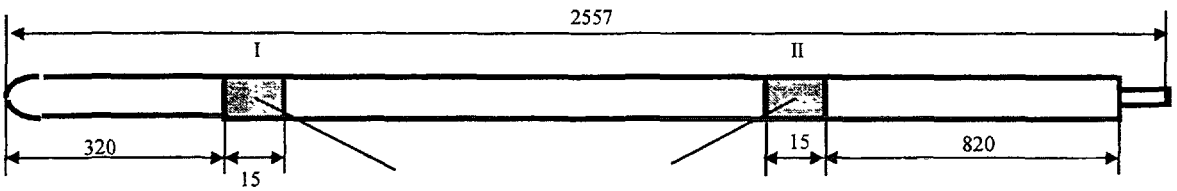

Fragments of sample cutting out

FA №	FE №	FE average burnup, MWd/kgU	Gas release, %	1st fragment section average burnup, MWd/kgU	Examination methods	2d fragment section average burnup, MWd/kgU	Examination methods
198	57	47.3	2.37	-	-	54.4	metallography
	76	44.3	0.64	-	-	50.80	metallography
222	59	48.7	2.29	45.0	metallography, diffractometry	56.1	metallography, diffractometry
	62	45.8	0.78	41.9	metallography	52.0	metallography
	69	55.2	3.52	53.7	metallography, EPMA	63.0	metallography, fractography, elect.microscopy

3. Basic examination results

3.1. Fuel macro- and microstructure

Macro- and microstructure of the fuel column, cladding and column-cladding gap state (fuel element of FA 198, a burnup of 50.8 MWd/kgU and the fuel element of FA 222, a burnup of 56.1 MWd/kgU) are given in figs.1,2. The corresponding FE structures for FA 13626135 worked during three fuel cycles (a burnup of 35.1 MWd/kgU) are given here for comparison. As one can see in the macrostructure of the FE cross and longitudinal sections (fig.1a,b) radial cracks and pellet gaps in FE of a burnup of 35.1 MWd/kgU go up to the cladding; at that the fuel column is divided into pellets along the height and into radial segments along the FE radius. In contrast to the fuel column state after three fuel cycles, in FEs after four and five fuel cycles (a burnup of 50.8 and 56.1 MWd/kgU) radial cracks and pellet gaps don't go up to the cladding closing on the fuel column periphery. The larger length of the column is a set of the linked pellets and fragments.

There is a considerable distribution in the pellet-cladding gap state (fig.2b). A diameter gap of ~ 50 μm is observed at a burnup of 35.1 MWd/kgU while it is absent at a burnup of 50.8 and 56.1 MWd/kgU and the fuel column is in close contact with the cladding.

The considerable differences of the fuel structure in the middle part of the pellet in the burnup interval under analysis are not discovered. The physical and chemical pellet-cladding interaction is not observed either except an oxide film 12-17 μm in depth.

The fuel grain parameters in the central part of the column at an average section burnup of 63.0 MWd/kgU were found by the method of quantitative metallography. One can see that an average grain dimension is 6.8 μm and it doesn't differ from the initial grain value (6-8 μm). It testifies to the fact that maximal fuel temperature wasn't more than 1500°C. Grain unequiaxity (D_{min}/D_{max}) is 0.64 and the tendency of the larger grain axis orientation along the fuel pellet radius is clearly observed.

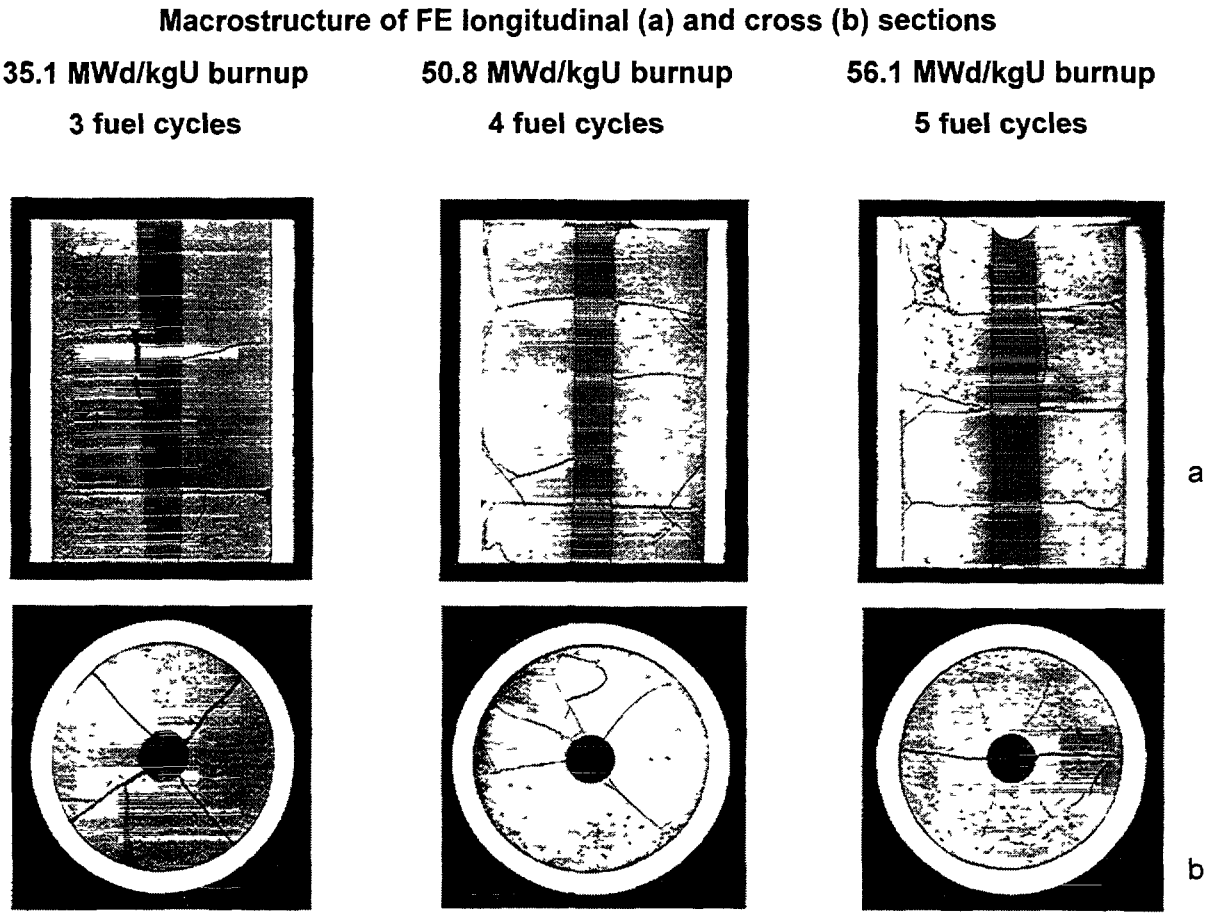

FIG. 1. Macrostructure of FE longitudinal (a) and cross (b) sections.

3.2. Fuel column rim-layer structure

One of the basic fuel column characteristics is porosity. Its value and morphology determine swelling and gas release. Porosity value affects fuel column thermal conductivity.

Porosity parameters and its behavior along the pellet radius at a burnup of 53.7 MWd/kgU are given in fig.3. Thus, increased porosity is observed in the pellet surface annular layer (rim-layer) as compared with the other part of the pellet, at that, pellet rim-layer value and its porosity increase with burnup rise.

To compare the rim-layer porosity (~40 μm from the pellet edge) with the porosity in the central part of the pellet porosity parameters of the area at a fuel burnup of 56.1 MWd/kgU are given in fig 4. An average pore dimension of the rim-layer is two times larger than the corresponding parameter in the centre of the pellet. Rim-layer pores begin making continuous chains linking with each other. This process may affect gas release greatly, because the open porosity is generated and the fission gases (Xe, Kr) has the possibility to release under to FE cladding.

The destructive examination of uranium dioxide fracture (fig 5) shows that pellet distribution occurs along the grain boundaries by the mechanism of intergranular brittle fracture. The pores are concentrated on the grain boundaries and, obviously, cause the destruction of uranium dioxide and appearance of the microcracks. One can see in the given fractograms, the structure of fracture on the grain boundaries is available along all the column radius except the outer layer where the grain boundary structure is absent. Besides, on the column periphery the grains become smaller and in the layer 20-100 μm in depth they are not observed. The structure of "cauliflower" type is formed here. It has significant porosity, which reaches ~20% and it is 5-6 times larger than the pore concentration in the central part of the pellet.

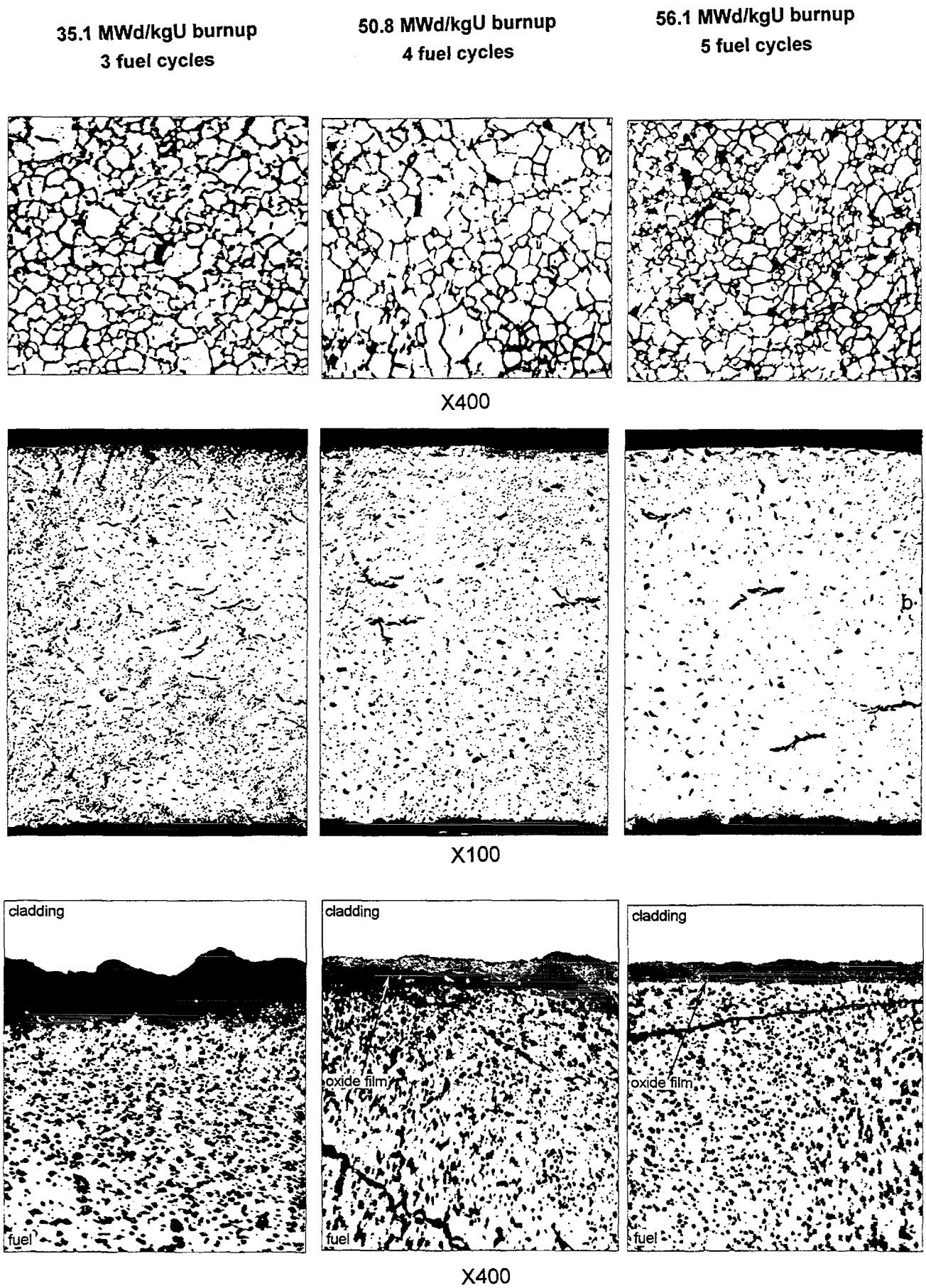

FIG. 2. Structure of fuel (a), cladding (b) and gap state (c) of fuel elements.

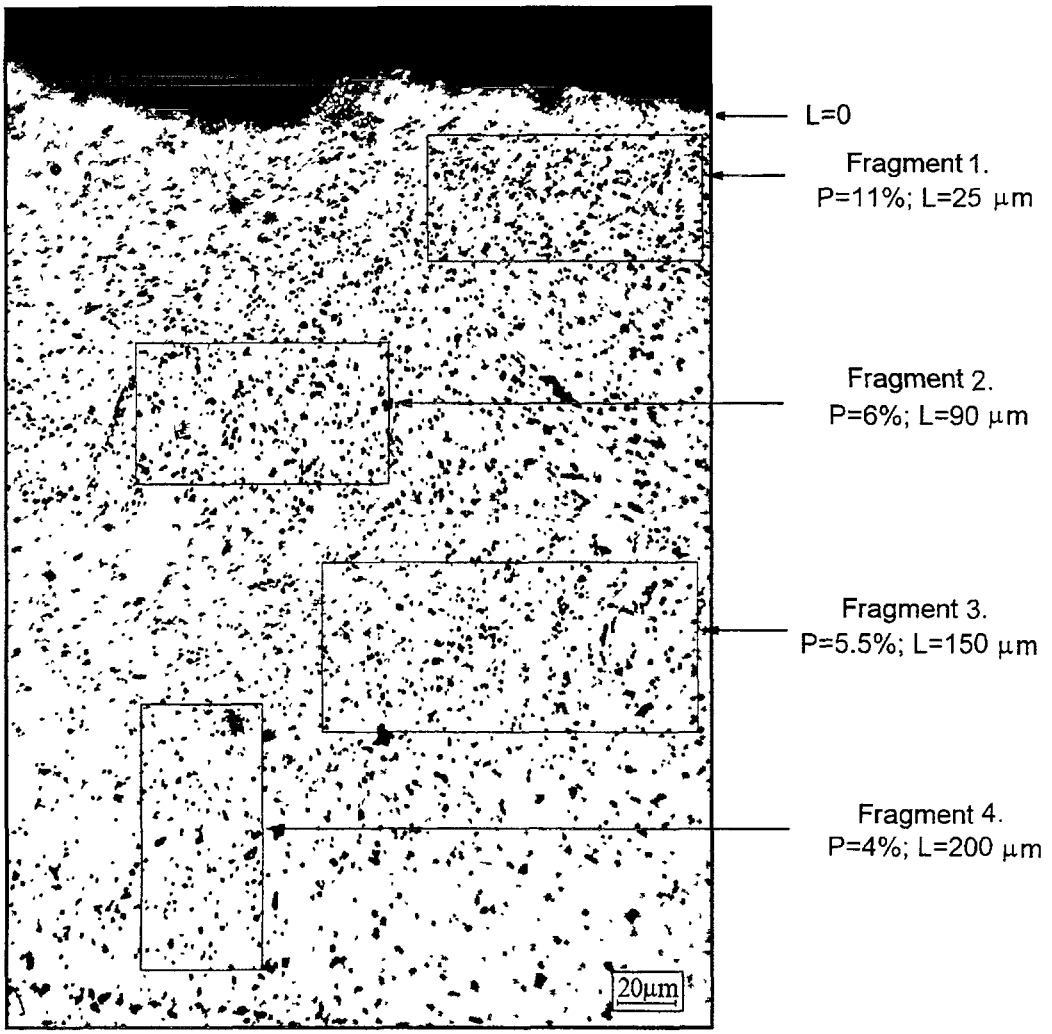

FIG. 3. Porosity distribution analysis along fuel pellet radius for FE 69 (53.7 MWd/kgU average burnup for FE section).

The typical microtracks and the values of the microhardness by Vickers (15 measurements) at the different distances from the fuel pellet edge are given in fig.6. One can see from the given results that the uranium dioxide hardness in the rim-layer (HV=657-673 kg/mm^2) is approximately 100 times less than the hardness in the central part of the pellet (HV=724-752 kg/mm^2).

Rim-layer, L=37 μm
(pore area = 23%)

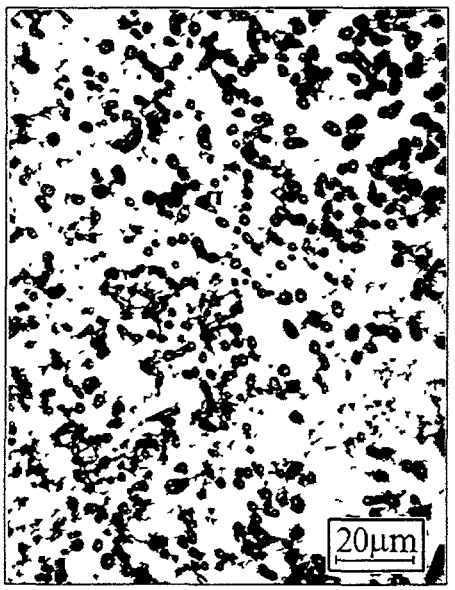

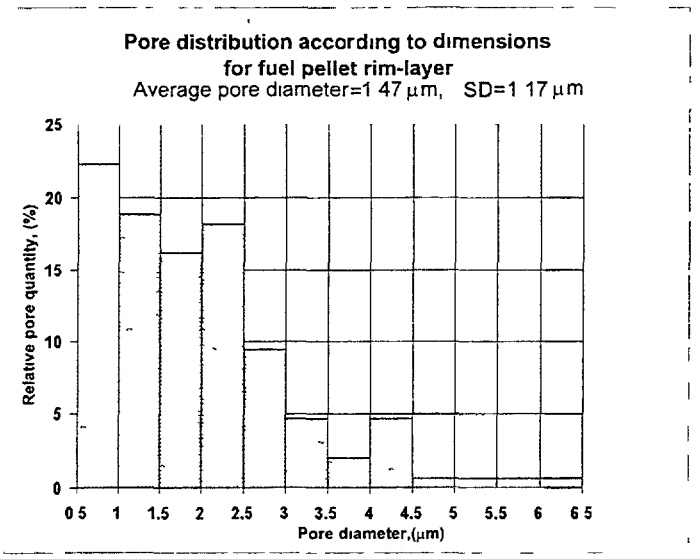

Fuel pellet centre L=3 mm
(pore area = 5.5%)

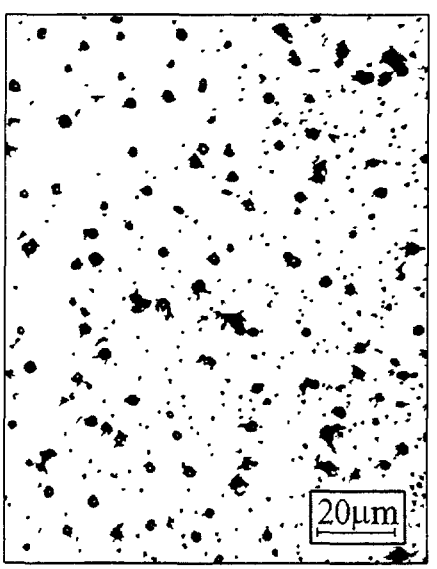

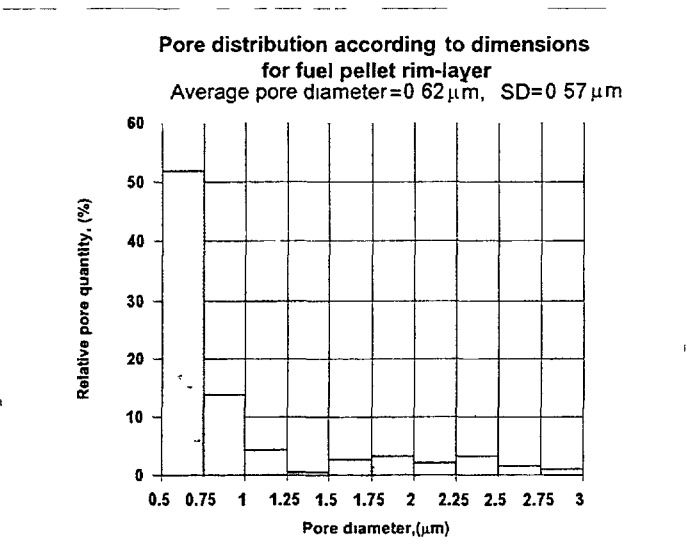

FIG. 4. Fuel pellet porosity parameters for FE 59 (56.1 MWd/kgU average burnup for FE section).

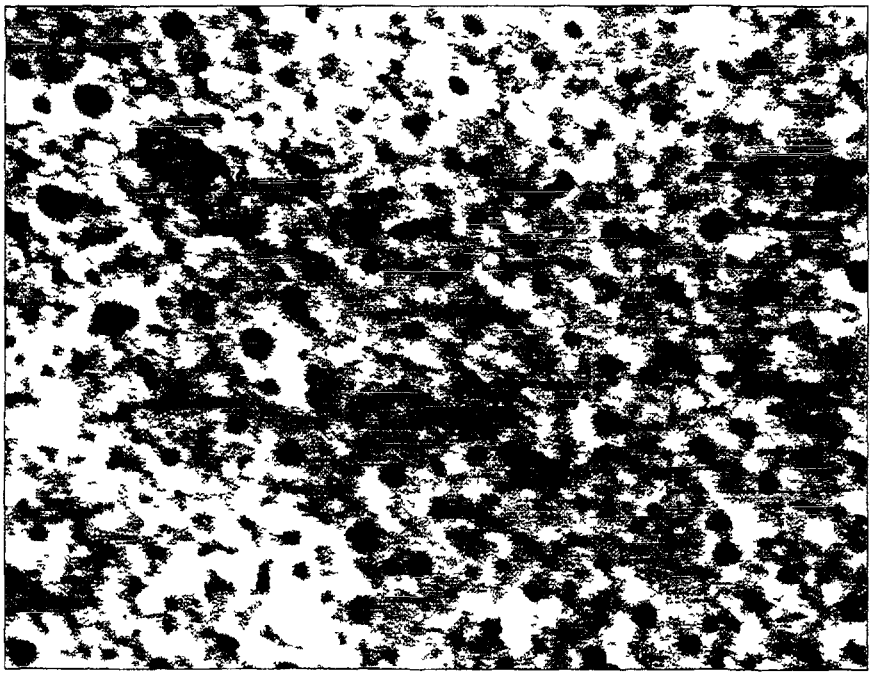

Fig 5a. R/R_o =0.998, x4530

FIG. 5a. Fuel structure fractograms along fuel column radius for FE 69 (63.0 MWd/kgU average burnup for FE section) R/R_o = 0.998, x 4530.

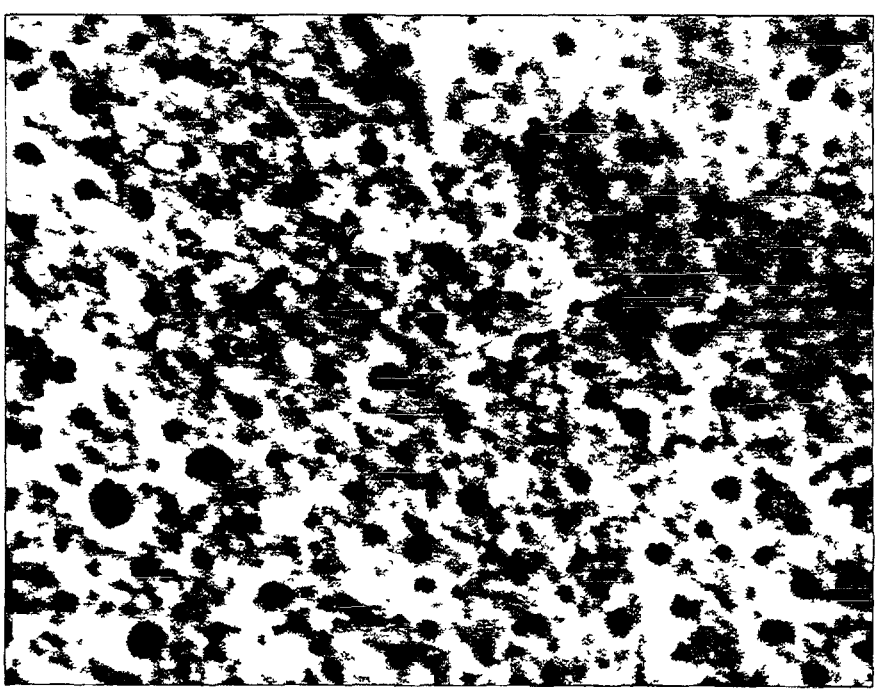

Fig 5b R/R_o =0.995, x4530

FIG. 5b. Fuel structure fractograms along fuel column radius for FE 69 (63.0 MWd/kgU average burnup for FE section) R/R_o = 0.995, x 4530.

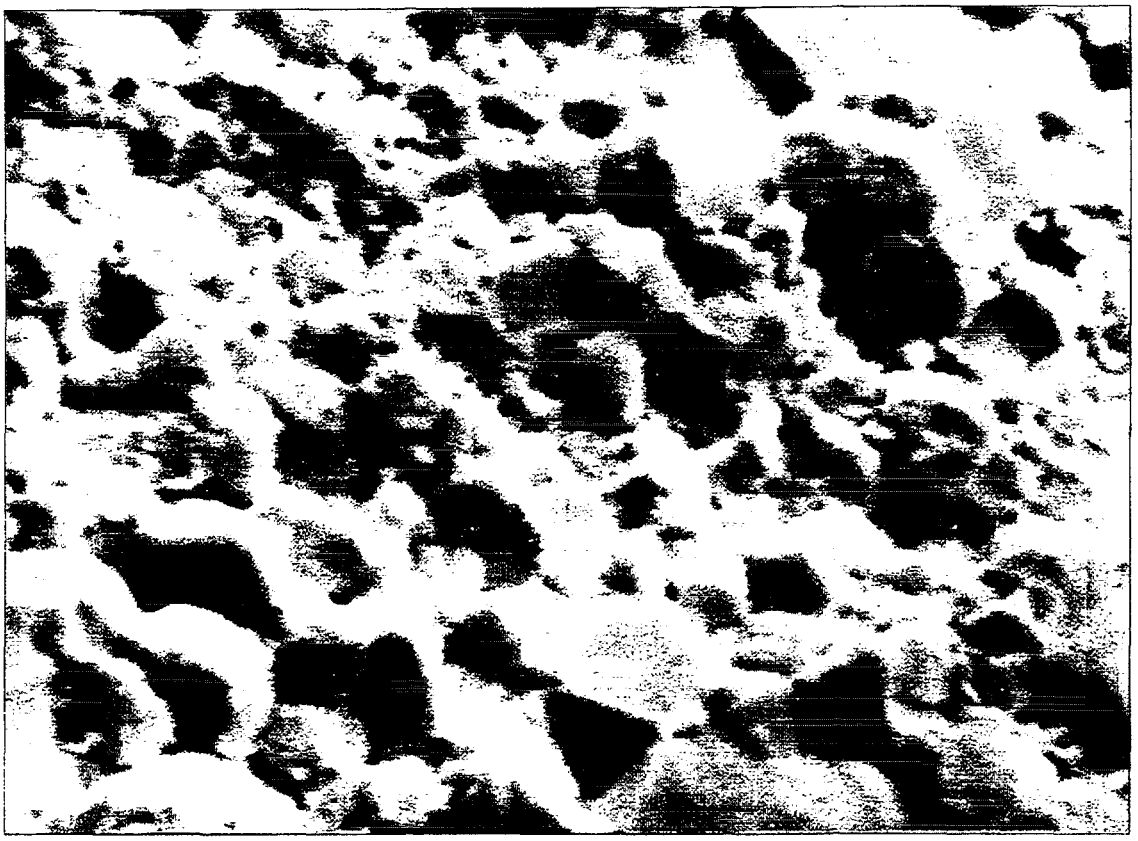

Fig.5c. R/R_o =0.900, x4530

FIG. 5c. Fuel structure fractograms along fuel column radius for FE 69 (63.0 MWd/kgU average burnup for FE section) R/R_o = 0.900, x 4530.

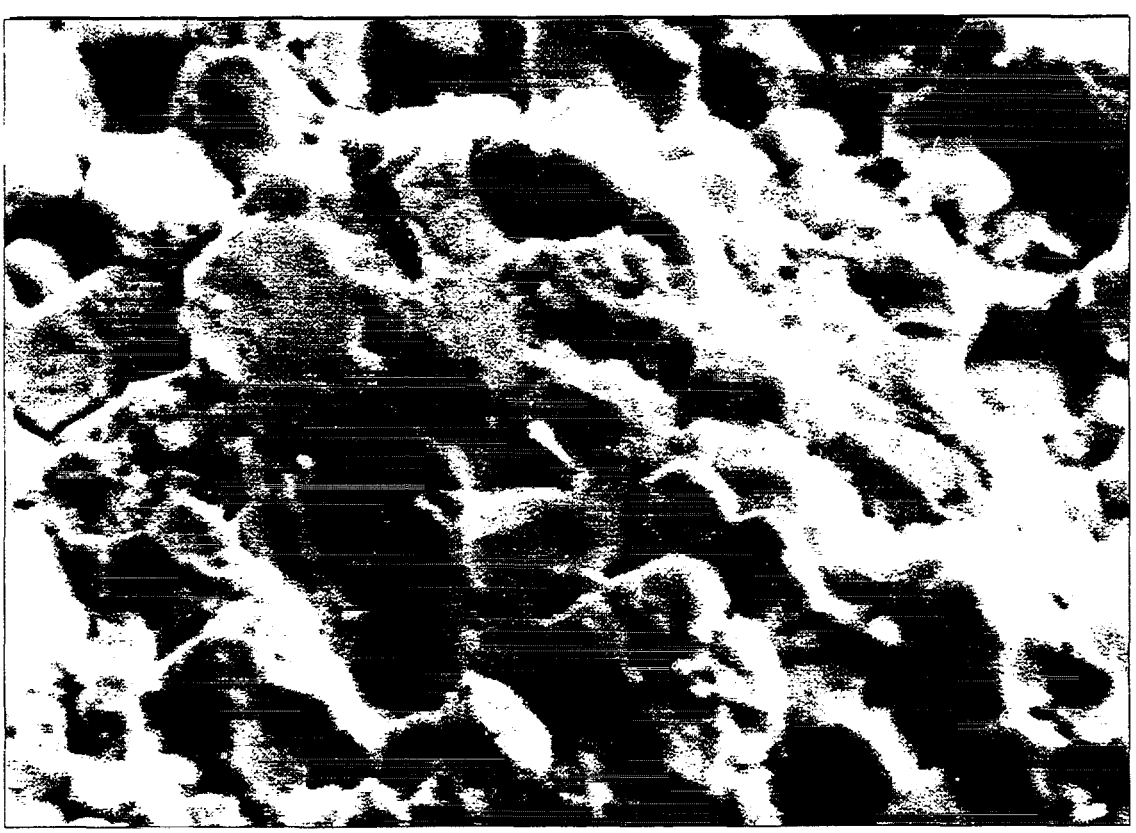

Fig.5d. R/R_o =0.680, x4530

FIG. 5d. Fuel structure fractograms along fuel column radius for FE 69 (63.0 MWd/kgU average burnup for FE section) R/R_o = 0.680, x 4530.

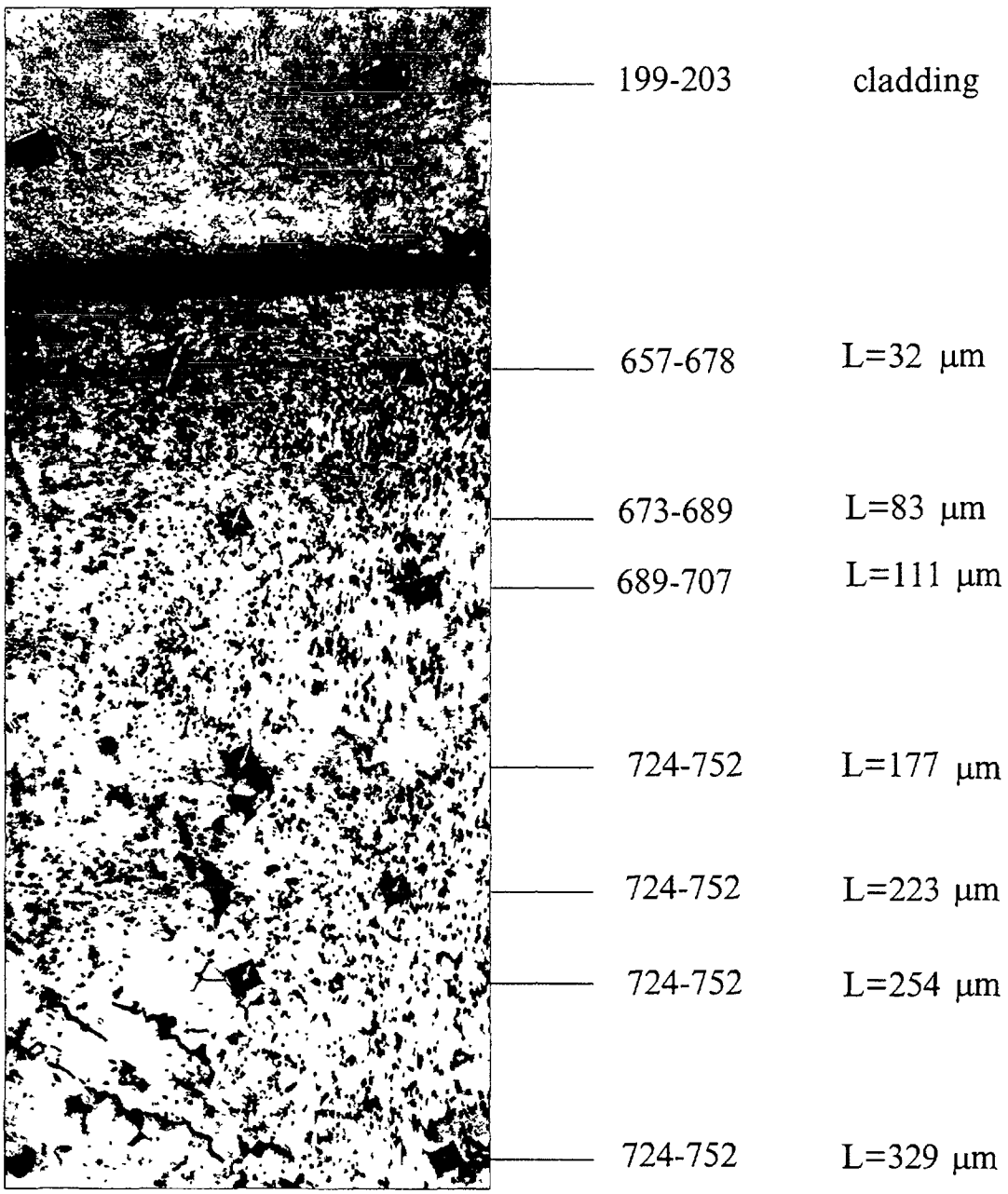

FIG. 6. Results of microhardness (kg/mm^2) measurements for fuel sample from FE 59 with an average burnup in FE in cross section of 56.1 MWd/kgU.

3.3. Content variation of plutonium and fission product along the radius of fuel column

The sample overview for EPMA and the scheme of segment location there are given in fig.7.

The distributions of plutonium, uranium, cesium and xenon along the pellet radius (scanning route "d") are given in figs.8,9. One can see in fig.10a that the distribution of the plutonium concentration along the pellet radius is irregular. In the range of 100-250 μm plutonium mass fraction is 1.5% and in the annular layer (D≤100 μm) plutonium mass fraction increases from 1.5 to 4.2% in the direction to the pellet surface. The distribution of the plutonium concentration being compared with the pellet microstructure along the pellet radius (fig.8a,b) brings to the conclusion that a correlation between plutonium mass fraction and pellet porosity is observed Xenon distribution (fig.9) is irregular along the pellet radius as well Intensity of the xenon peak in the annular layer (D≤100 μm) is roughly 1.5-2 times less then peak intensity in its central part Local decrease of xenon intensity peak distribution in some points is determined by fallout of some uranium dioxide grains Distribution of other elements under analysis is roughly regular while there is a tendency of insignificant rise of cesium and neodymium concentration in the direction to the pellet surface and decrease of uranium concentration.

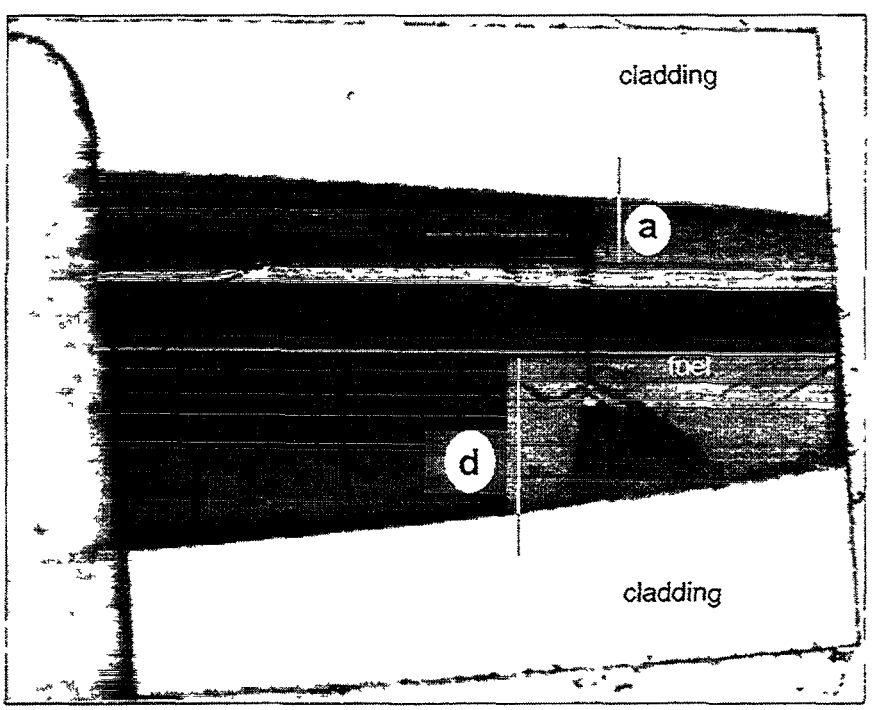

FIG 7. Sample overview for FE 69 with 53.7 Mwd/kgU average burnup for FE section and location or routes under examination, X10.

3.4. Pellet-cladding interaction

As it is well-known thermal and mechanical pellet-cladding interaction is determinated by different temperatures of fuel and cladding, as well as considerably less coefficient of zirconium thermal expansion as compared with uranium dioxide one. External factors which determine pellet-cladding interaction are deformation caused by creep of the cladding under the influence of coolant pressure and fuel column swelling.

If the pellet-cladding gap is available due to the deformation caused by cladding creep under the influence of coolant pressure, the fuel element diameter decreases. After pellet-cladding contact at a burnup of 35-45 MWd/kgU the stage of mechanical pellet-cladding interaction appears. As one can see in the FE cross section macrostructure (fig.1) the fuel column is divided into 5-6 segments by regular cracks at a burnup of 35 MWd/kgU. During the volume changes of the fuel column, radial cracks accommodate them and even in a case of the gap absence mechanical pellet-cladding interaction is not observed. At a burnup of > 45 MWd/kgU mechanical interaction features appear in the form of cladding diameter increase relatively to its minimal value at a burnup of 30-40 MWd/kgU.

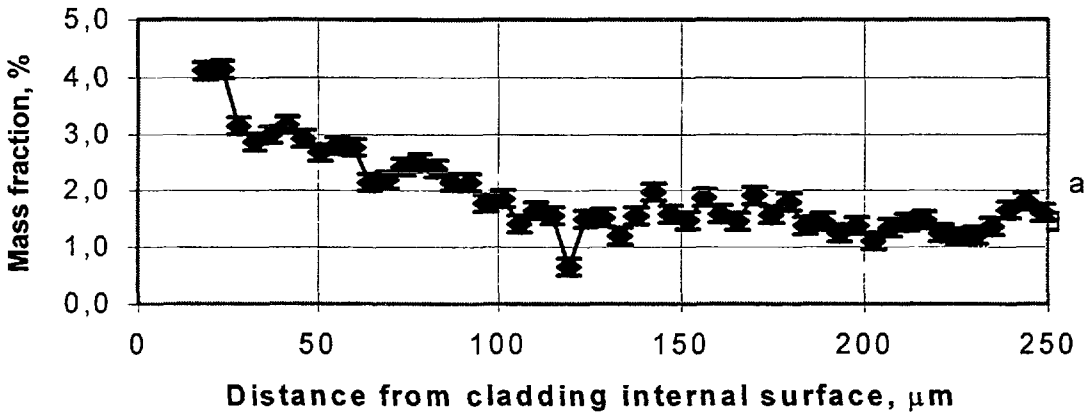

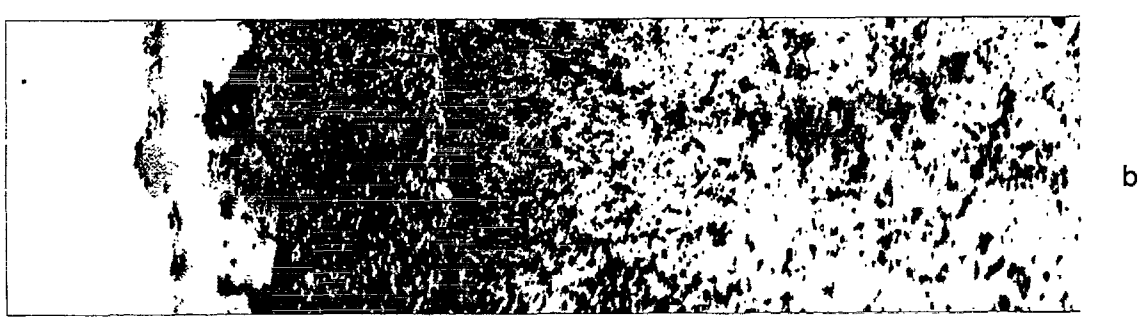

FIG. 8. Plutonium distribution along pellet radius (a) (route "d", systematic error ± 0.5) and microstructure along fuel column radius, X 400 (b)

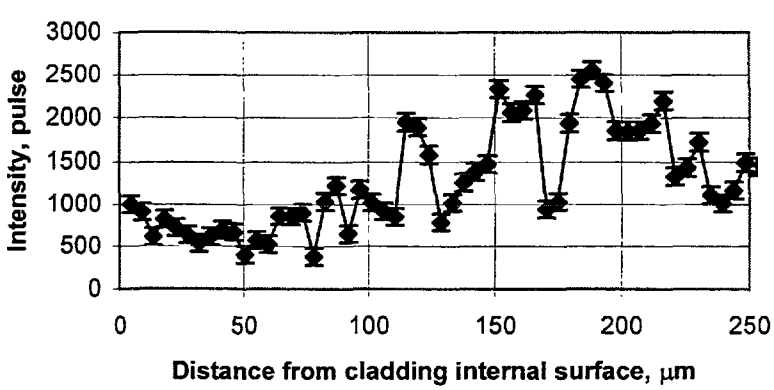

FIG. 9. Xenon distribution along pellet radius (route "d")

It is associated with the changes in the macro- and microstructure of the fuel column As one can see in the microstructure of the fuel column with a burnup of > 48 MWd/kgU the radial cracks close on the periphery and the column in the central fuel part consists of the linking pellets and their segments. Radial cracks closing occurs due to fuel swelling on the column periphery as a result of increased porosity rim-layer creation Hence, mechanical pellet-cladding interaction may be determined by the fuel column rim-layer creation along with other factors.

The distribution of U, Pu, Zr in the intermediate pellet-cladding area is presented in fig 10

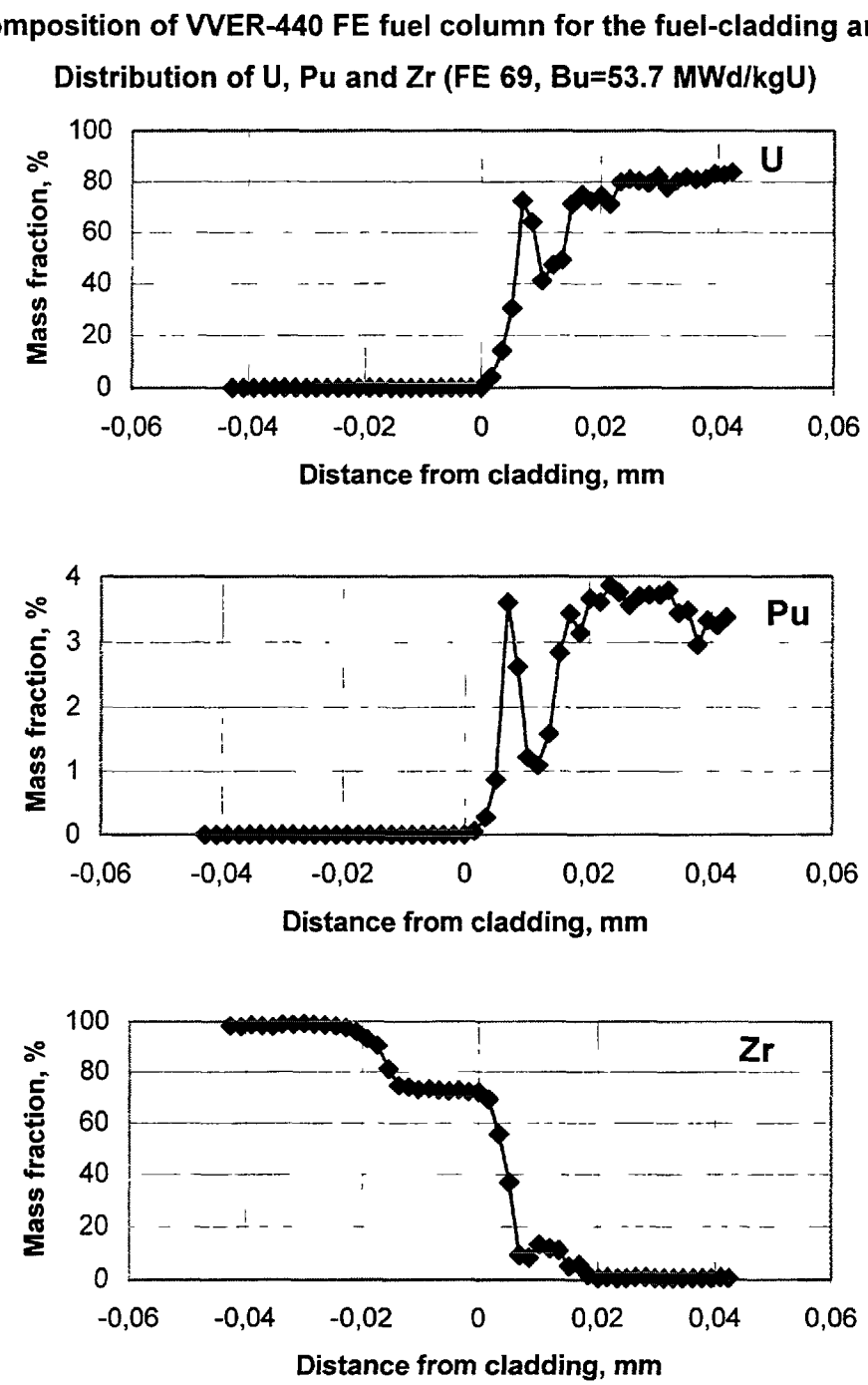

FIG. 10. Composition of VVER-440 FE fuel column for the fuel-cladding area Distribution of U, Pu and Zr (FE 69, Bu=53.7 MWd/kgU)

Conclusion

The results obtained during postirradiation examination of two FAs for VVER-440 which were under steady-state operation for 4 and 5 fuel cycles in Kola NPP Unit 3 along with analysis of the results of the VVER - 440 FA examined beforehand show that capacity of VVER-440 FAs and FEs remains the same during operation up to the maximum fuel burnup of 63 MWd/kgU.

None of the parameters limited fuel life, i.e. FE dimension stability, cladding corrosion and hydrogenation, degradation of the cladding mechanical properties, fuel swelling, maximal fuel temperatures and fission gas release, reaches the critical value in the burnup range under analysis.

Based on the analysis of the common mechanism for fuel behavior at a burnup of > 40 MWd/kgU it can be pointed out that gas release and thermal-mechanical state of the cladding are changed greatly relatively to the state at a burnup of 25-40 MWd/kgU, namely:

- pellets are in close contact with the cladding along the considerable part of the FE working length;
- average cladding diameter increases relatively to its minimal value at a burnup of 35-40 MWd/kgU;
- the fuel column rim-layer with increased porosity is created and that results in sharp increase of gas release and thermal-mechanical pellet-cladding interaction starts;
- increased plutonium concentration is observed in the fuel column rim-layer;
- under the influence of fuel swelling the cladding stresses gets the opposite sign and the cladding is in tension.

All these peculiarities of fuel behavior at a burnup of > 40 MWd/kgU should be taken into account in simulating codes estimated and predicted high burnup fuel behavior.

DISCUSSION

(Questions are given in italics)

Pores in rim layer linking each other. It is a consequence of high burnup. It is not a consequence of the procedure of the sample preparation.

Power ramps invariability show that hollow pellets give milder deformations than solid pellets. Temperature data, which are always made in hollow pellets, never exhibit irregular overheating.

POST IRRADIATION EXAMINATION EXPERIENCE OF HOLLOW PELLETS FOR PWRs

H. UCHIDA
Nuclear Power Engineering Corporation,
Tokyo

S. UEHARA, A. OE, S. MATSUMOTO
Nuclear Fuel Industries Ltd,
Ibaraki

Japan

Abstract

In order to increase the flexibility of the reactor operation mode, a high performance fuel has been investigated in Japan. Hollow fuel pellets are adopted as a design improvement for the mitigation of pellet cladding interaction (PCI) by decreasing the fuel pellet temperature during irradiation.

The high performance 17×17 B type PWR fuel was supplied by Nuclear Fuel Industries, Ltd.(NFI) and achieved a burnup of 34.3GWd/t after 2 cycles of irradiation under normal operating conditions in Ohi Unit 2 of the Kansai Electric Power Co. Inc.(Kansai). The irradiation test program of the high performance fuel was conducted by Nuclear Power Engineering Corporation (NUPEC) under the sponsorship of the Ministry of International Trade and Industry (MITI) from 1981 to 1993.

After the completion of irradiation, the high performance fuel assembly was transported to the hot-cell facility at Japan Atomic Energy Research Institute (JAERI) in Tokai-mura. Nondestructive and destructive examinations were performed on the standard fuel rods and the improved fuel rods.

In order to evaluate the ridging deformation, the cladding outer diameter profile of these fuel rods was measured. Ridging deformation of the hollow fuel pellets was smaller than that in the standard fuel pellets. Gamma scanning was performed by measuring the total γ-ray intensity and specific nuclides' intensity. The axial distribution of the γ-ray intensity was fairly flat within the measured active region of each fuel rod. The puncture test was performed for the evaluation of fission gas release (FGR) and fuel rod internal pressure. The FGR of fuel pellets showed no significant difference between the two types of fuel pellets, whereas the internal pressure increase in the hollow pellet fuel rods was slightly lower than that of the standard fuel rods. This is due to the greater free volume in the hollow pellet fuel rods as fabricated.

The density change and microstructure of the hollow fuel pellets after irradiation were compared with the standard fuel pellets. There was no significant difference between these fuel pellets based on these test results.

From these PIE results of the hollow fuel pellets and standard fuel pellets, the integrity of the hollow fuel pellets was demonstrated in the PWR fuel rod under normal operating conditions, and the improved fuel rods showed better performance with respect to internal pressure and PCI.

1. INTRODUCTION

In order to increase the flexibility of the reactor operation mode in Japanese PWRs, a high performance fuel, which has a higher resistance for pellet cladding interaction (PCI) has been investigated. The design improvement for the high performance fuel has been investigated using a fuel cladding tube and fuel pellet. Zirconium liner tubes and hollow fuel pellets were selected as the improved design respectively. The zirconium liner tube has a sponge zirconium liner which is softer than zircaloy-4 inside the cladding tube in order to mitigate PCI. The hollow pellet has the effect of PCI mitigation by decreasing the fuel pellet temperature during irradiation.

Two 17×17 B-type fuel assemblies designated N02J1R and N02J2R which contain these improved designs were supplied by Nuclear Fuel Industries, Ltd.(NFI) as high performance fuels. They were irradiated for 2 or 3 cycles in Ohi Unit 2 of the Kansai Electric Power Co. Inc. (Kansai) and they achieved a burnup of 34.3GWd/t or 37.7GWd/t, respectively, under normal operating conditions. The irradiation test program of the high performance fuel was conducted by Nuclear Power Engineering Corporation (NUPEC) under the sponsorship of the Ministry of International Trade and Industry (MITI) from 1981 to 1993. One of the high performance fuel assemblies, N02J2R, was transported to the hot-cell facility of Japan Atomic Energy Research Institute (JAERI) in Tokai-mura. Nondestructive and destructive examinations were performed on the standard fuel rods and the improved fuel rods. This paper summarizes the results of the post irradiation examination (PIE) of the hollow fuel pellets.

2. DESCRIPTION OF TEST FUEL ASSEMBLY

The main description of the test fuel assembly is shown in Table I. The specification of the test assembly is the same as NFI's standard 17×17 B-type fuel except that the zirconium liner cladding tubes and hollow fuel pellets are assembled in part of the fuel rods.

The hollow pellets have an outer diameter of 8.1 mm, an inner diameter of 2.6 mm and a height of 9 mm, respectively. Both the hollow pellets and standard pellets have dishes and chamfers on both ends. The volume share of the hollow in a fuel pellet is approximately 10%, which leads to greater free volume in a fuel rod than the standard fuel.

The location of the hollow pellet fuel rods in the test fuel assembly is shown in Figure 1. Four hollow pellet fuel rods were assembled in the test fuel assembly.

3. IRRADIATION HISTORY OF TEST FUEL ASSEMBLY

The irradiation history of the N02J2R test fuel assembly is summarized in Table II. The test assembly experienced a slightly higher linear heat rate than the core average value in Ohi unit 2. The hollow pellet fuel rods burnt at almost the same linear heat rate as the core average value and achieved 34-35 GWd/t which is the same level of burnup as the average value of the test fuel assembly.

TABLE I. MAIN DESIGN PARAMETER OF HIGH PERFORMANCE FUEL

Fuel Assembly	Total Length	4 m			
	Cross Section	214 mm x 214 mm			
	Number of Spacer Grids	9			
	Array of Fuel Rods	17 x 17			
	Number of Fuel Rods	264			
	Number of RCC Guide Thimbles	24			
	Number of Instrumental Sheath	1			
Type of Fuel Rod		B1 type	B3 type	B2 type	Standard
Cladding tube	Material	Zircaloy-4 with Zirconium Liner (Stress Relieved)		Zircaloy-4 (Stress Relieved)	
	Outer Diameter	9.5 mm			
	Wall Thickness	0.64 mm including Zr liner		0.64 mm	
Fuel Pellet	Material	UO_2			
	Outer Diameter	8.1 mm			
	Inner Diameter	None	2.6 mm		None
	Height	9 mm			
	Density	95 % T.D.			
	^{235}U Enrichment	3.4 wt %			
Fuel Rod	Total Length	3.9 m			
	Fuel Column Length	3.6 m			
	Filling Gas	Helium			

4. RESULTS OF PIE

The N02J2R test fuel assembly was transported from the Ohi reactor site to the hot laboratory of JAERI in Tokai-mura as a complete fuel assembly. After the completion of the non-destructive test (NDT) of the fuel assembly, twenty fuel rods were extracted from the test fuel assembly for further examination. Table III summarizes the PIE item which was performed on the test fuel rods. Four hollow pellet fuel rods were non-destructively examined and one of them was also destructively examined.

(1) NDT of fuel rods

The entire length of the hollow pellet fuel rods was visually examined and no anomaly was found. The eddy current test demonstrated that these fuel rods had not failed.

The outer diameter axial profile of these fuel rods was measured in four or twelve circumferential directions. The typical outer diameter profile of a hollow pellet fuel rod is shown in Figure 2 and compared with a standard fuel rod. Ridging deformation of the hollow

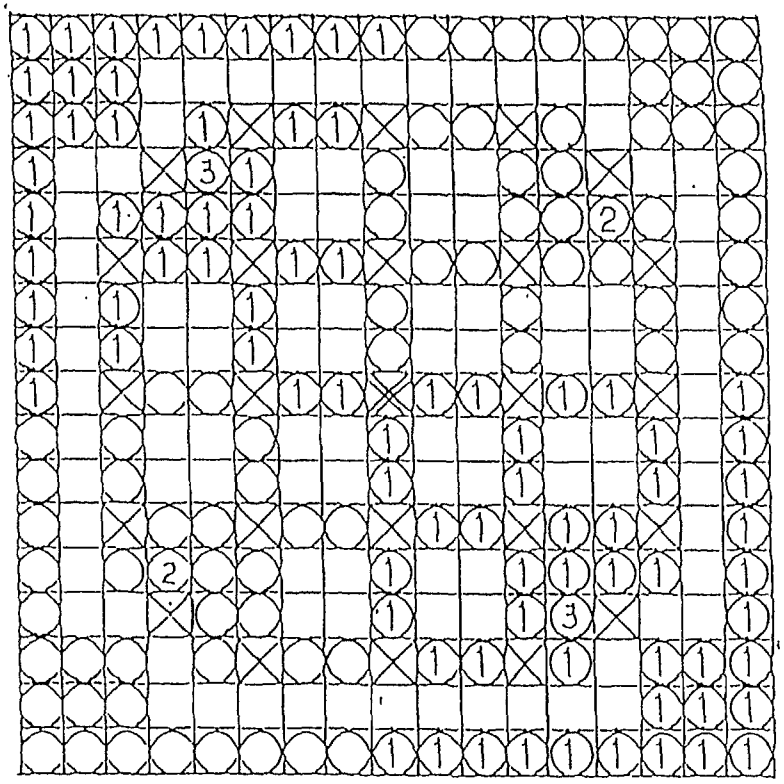

①	B1 type Fuel Rod (Zr liner cladding + Solid Pellet)	□	Standard Fuel Rod (Non - Characterized)
②	B2 type Fuel Rod (Zircaloy-4 cladding + Hollow Pellet)	⊠	RCC Guide Thimble
③	B3 type Fuel Rod (Zr liner cladding + Hollow Pellet)	▩	Instrument Sheath
○	Standard Fuel Rod (Zircaloy-4 cladding + Solid Pellet), Characterized		

FIG. 1. Fuel rod location in the high performance fuel assembly.

TABLE II. IRRADIATION CONDITIONS OF TEST FUEL ASSEMBLY (NO2J2R)

Item	First Cycle	Second Cycle
Thermal Power of Fuel Assembly (MWt)	19.2	19.0
Average Linear Heat Rate of Fuel Rod (W/cm)	199	197
Achieved Burnup (MWd/t)	17.7	34.3
EFPH (h)	9,800	9,300

TABLE III. PIE ITEMS FOR FUEL ROD (NO2J2R)

	PIE Items
Non-Destructive Test	Visual Examination of Fuel Rod
	Fuel Rod Profilometry and Length Measurement
	Eddy Current Test of Fuel Rod
	Oxide Thickness Measurement of Fuel Rod
	X-ray Radiography of Fuel Rod
	Axial Gamma Scanning of Fuel Rod
	Pellet-Cladding Gap Measurement of Fuel Rod
	Puncture and Gas Analysis
Destructive Test	Ceramo/Metallo-graphy of Fuel Rod Cross Section
	EPMA of Fuel Pellet
	Radial Gamma Scanning of Fuel Pellet
	Chemical Burnup Analysis of Fuel Pellet
	Density Measurement of Fuel Pellet
	Residual Gas Analysis of Fuel Pellet
	Macrograph of Cladding Outer and Inner Surface
	Hydrogen Analysis of Cladding Tube
	EPMA of Cladding Tube
	^{54}Mn Analysis of Cladding Tube
	Hardness Measurement of Cladding Tube
	Axial Tensile Test of Cladding Tube
	Burst Test of Cladding Tube
	SCC Test of Cladding Tube

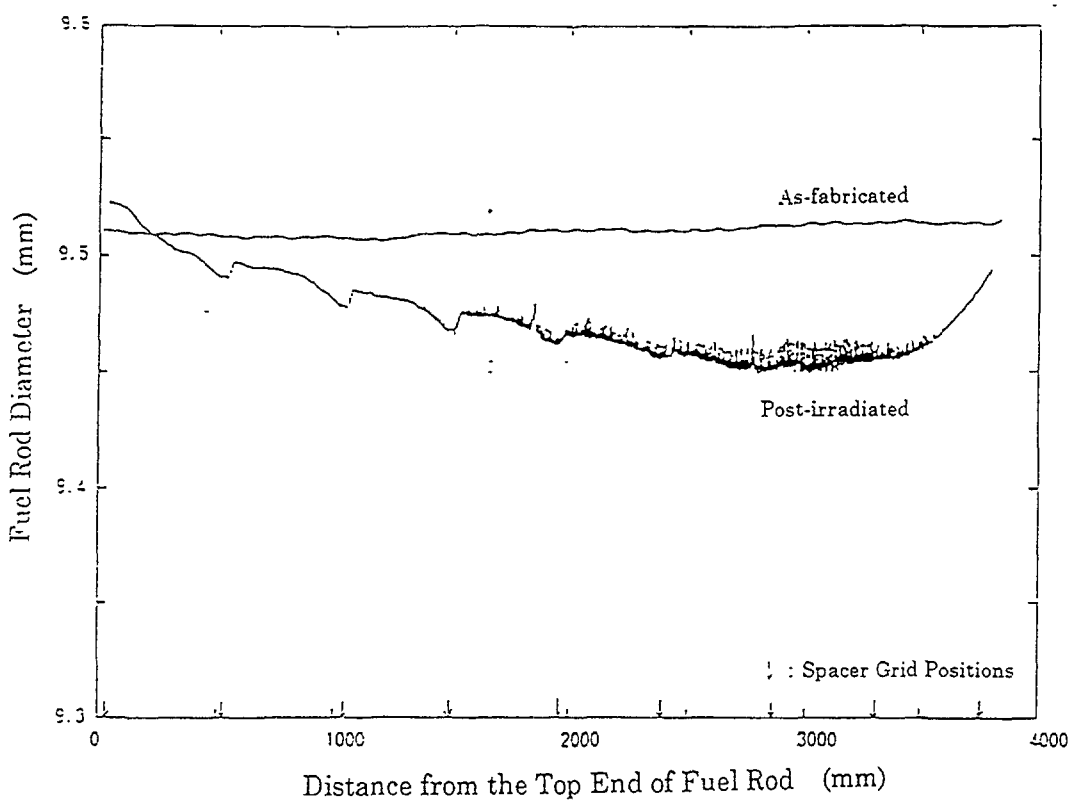

FIG. 2a. Fuel rod diameter (No. 1 Fuel Rod, Standard type)

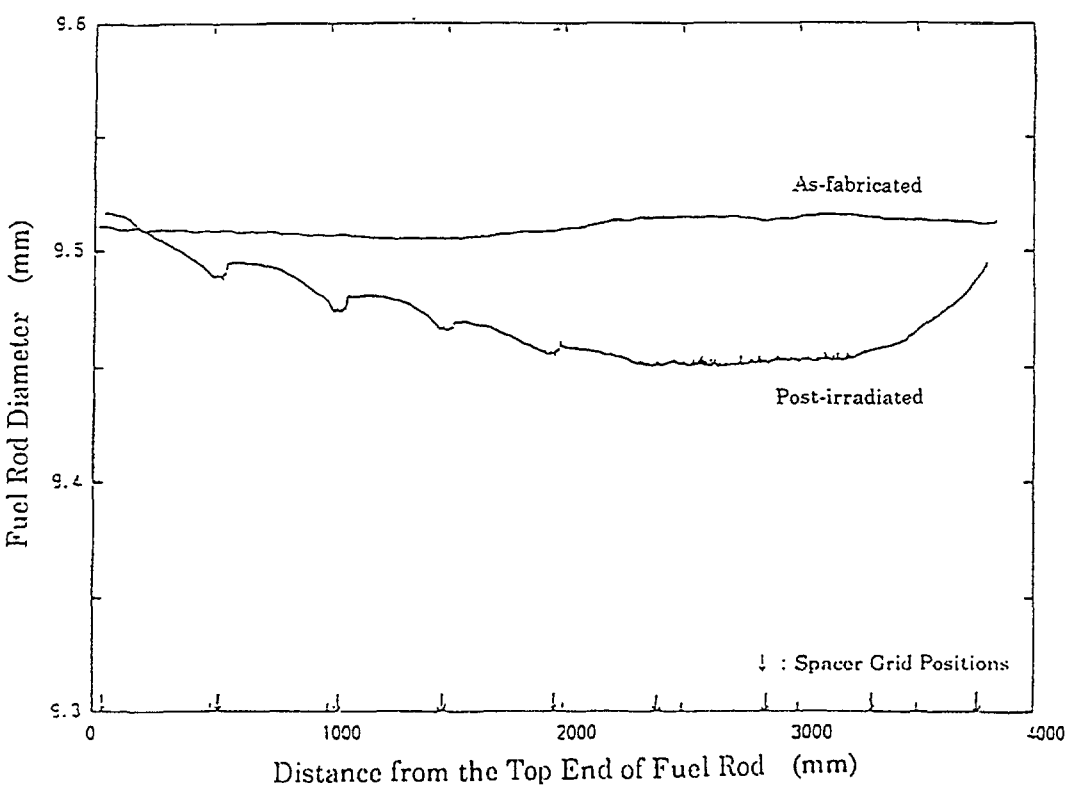

FIG. 2b. Fuel rod diameter (No. 17 Fuel Rod, B type)

pellet fuel rods was smaller than that of the standard fuel rods. One reason for this smaller ridging is that the thermal deformation of the hollow fuel pellets was smaller than that of the standard fuel pellets due to the lower temperature of the fuel pellets. Another is that the hollow fuel pellets have smaller chamfers than the standard fuel pellets, which caused less stress on the cladding tubes.

The total length of the fuel rods was measured but there were no significant differences between the hollow pellet fuel rods and standard fuel rods. The growth of these fuel rods is shown in Figure 3. This figure shows that the growth of these fuel rods was within the range of previously obtained results. This means that the major factor on fuel rod growth is not PCI but irradiation growth, which did not show any difference in PCI between these two types of fuel pellets.

Gamma scanning was performed by measuring the total γ-ray intensity and specific nuclides' intensity. The axial distribution of the γ-ray intensity was fairly flat within the measured active region of each fuel rod. This means that the axial burnup distribution of these fuel rods was fairly flat. The active length of the fuel rods was determined by total γ-ray scanning. The active length of the hollow pellet fuel rods was similar to that of the standard fuel rods. This result has a good correlation with the fuel pellet density measurements which will be mentioned later. The fuel column length of these fuel rods was also measured by X-ray radiography. These results have a good correlation with the gamma scanning. The entire length of the fuel column was examined by X-ray radiography. There were small gaps between the pellets and local circumferential cracks in some fuel pellets but no harmful defects in the fuel pellets were found.

The puncture test was performed for the evaluation of fission gas release rate (FGR) and fuel rod internal pressure. The FGR of the fuel pellets was less than 0.5 % and there were no significant differences between the two types of the fuel pellets. However, the internal pressure increase of the hollow pellet fuel rods was slightly lower than the standard fuel rods due to the greater free volume in the fuel rods as fabricated. These results indicate that the main fission gas release was caused by a recoil and knock-out mechanism due to the mild irradiation history and the effect of lower center temperature of the hollow pellets that did not have a significant effect on decreasing FGR.

(2) Destructive test of fuel pellets

After the completion of the NDT of the fuel rods, four fuel rods including one hollow pellet fuel rod was cut into test pieces in order to perform a destructive examination of the fuel pellets and cladding tubes.

The samples for fuel pellet ceramography were cut from the region of maximum burnup. A macrograph of a hollow fuel pellet is shown in Figure 4 and compared with the standard fuel pellet. It can be seen that the hollow of the fuel pellet after irradiation had almost the same configuration as fabricated. The main crack of the hollow fuel pellet was radial in a direction from the hollow to the outer surface of the fuel pellet, which means that no harmful thermal disturbance was caused by such cracks. The microstructure of the hollow fuel pellet was observed as shown in Figure 5. The micrograph of a standard fuel pellet is also shown for comparison. There was no significant difference in the microstructure such as porosity distribution and grain size between the hollow fuel pellets and standard fuel pellets.

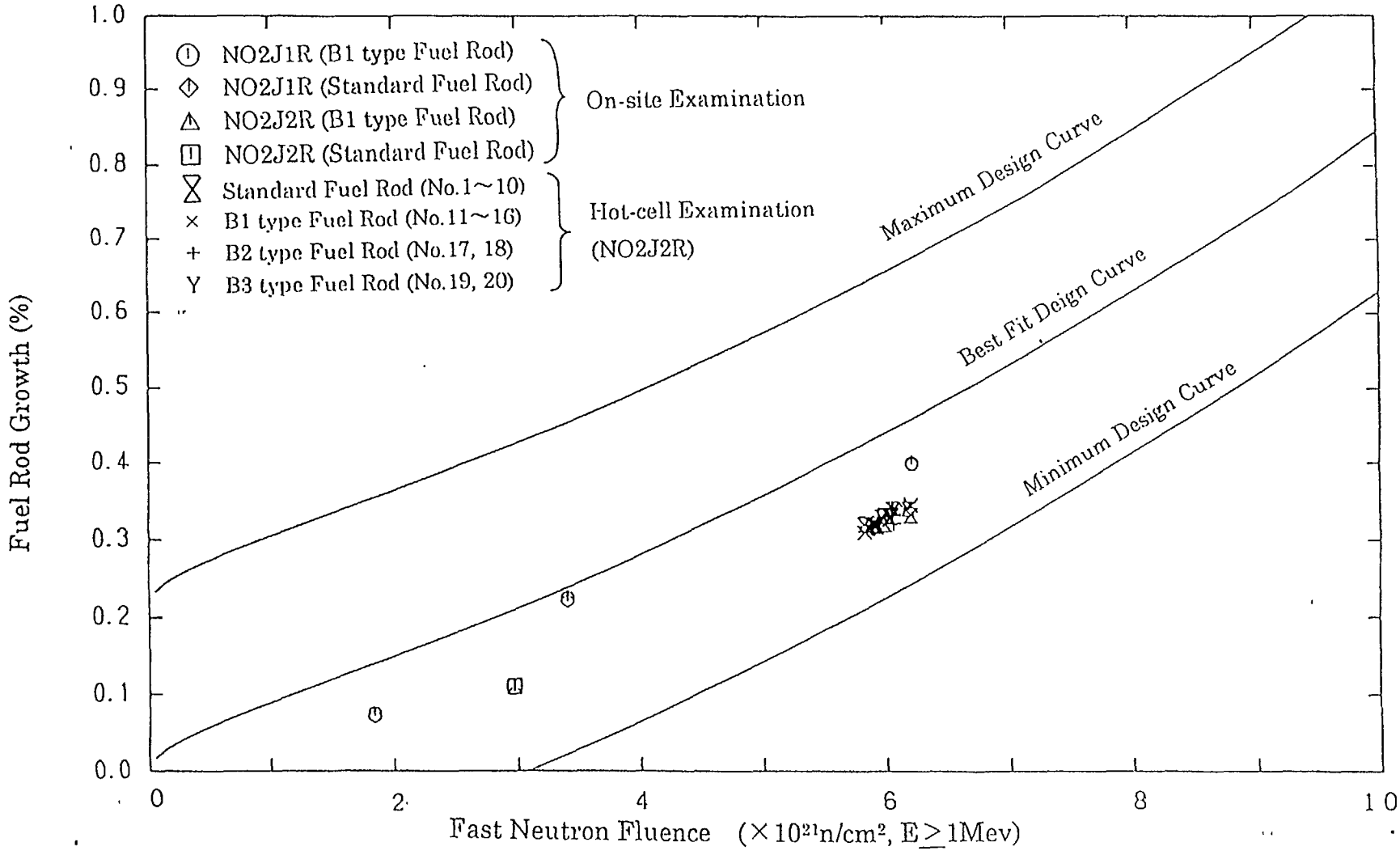

FIG. 3. Relation between fuel rod growth and fast neutron fluence

No.1 Fuel Rod (Solid Pellet)

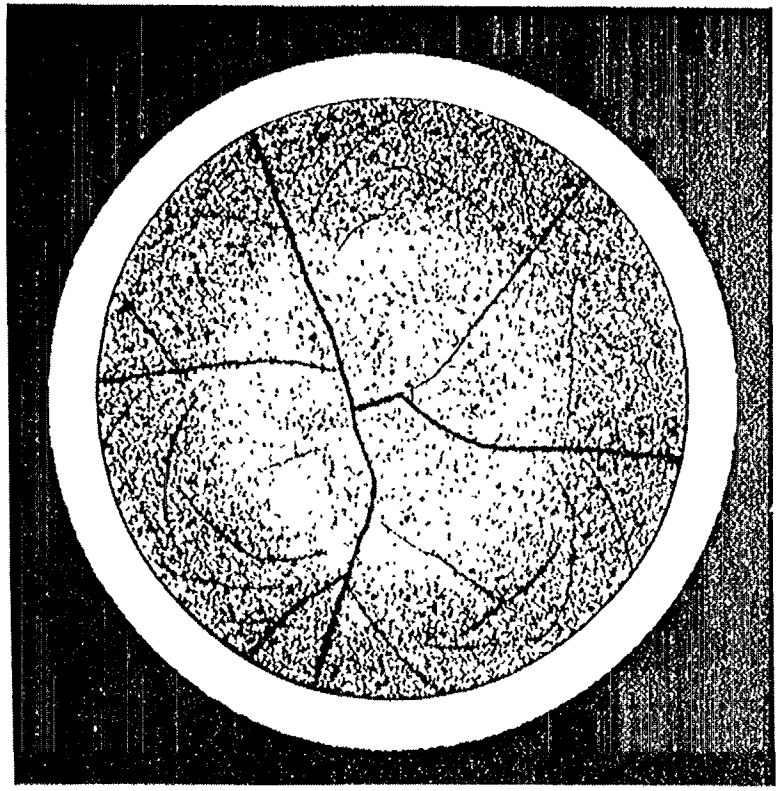

No 17 Fuel Rod (Hollow Pellet)

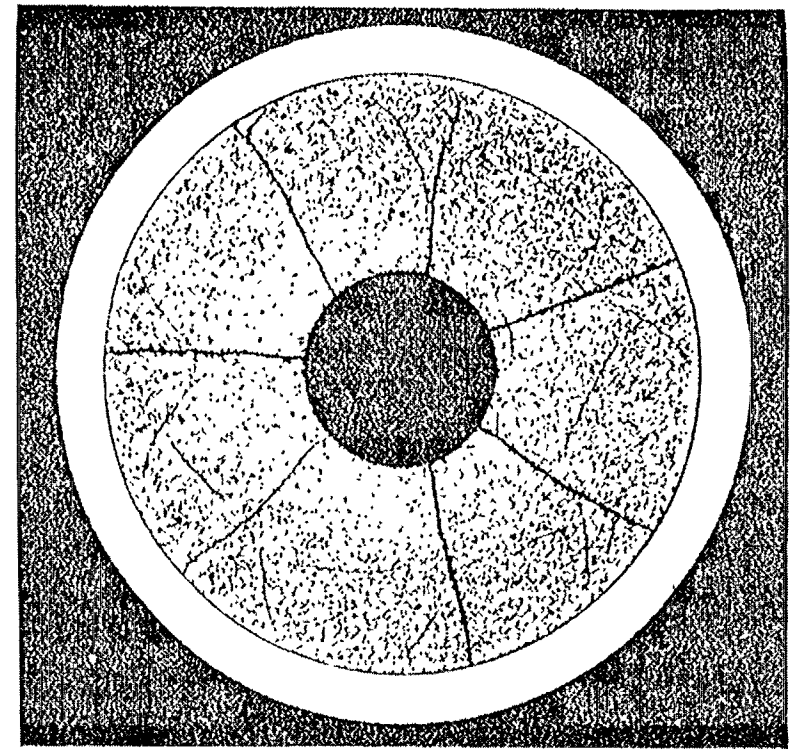

FIG. 4. Cross section of fuel rod (No. 1 Fuel Rod and No. 17 Fuel Rod)

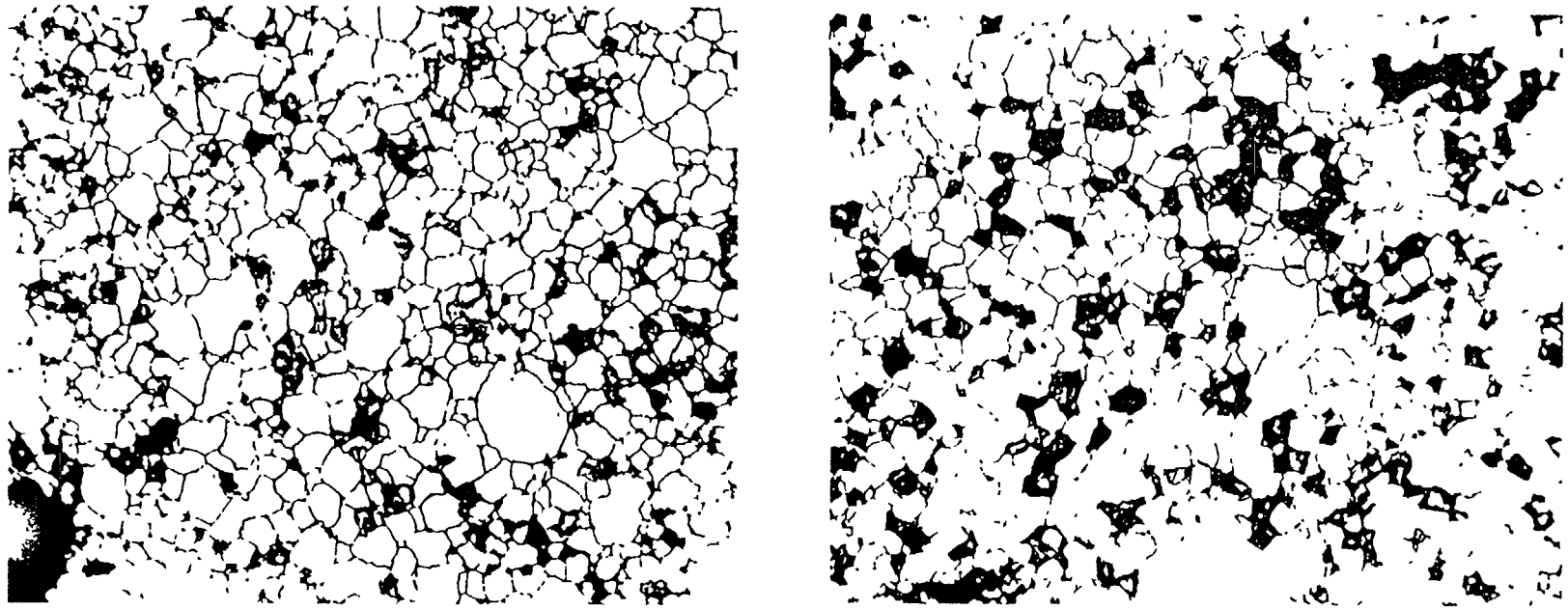

FIG. 5. Microstructure of fuel pellets

The inner surface of the cladding tubes was observed in order to investigate the PCI phenomena. The local color change and some attachment of fuel pellet fragments were observed at the interface between the fuel pellets. These local color change and pellet fragment attachment of the hollow fuel pellets were relatively less than the standard fuel pellets. In order to observe the incipient stress corrosion cracking on the inner surface of the cladding tubes, half cylindrical cladding samples were circumferentially expanded by pressing the outer surface of the sample causing fracture on a flat table. However, no incipient cracking was found.

In order to investigate the PCI phenomena, the cross section of the cladding inner surface and fuel pellet rim region were observed using a scanning electron microscopy (SEM) and the element analysis was performed by electron probe micro-analysis (EPMA). Local zirconium oxide was found on the inner surface of the cladding tube and fission products such as Xenon were detected in the oxide as a result of the EPMA analysis. The inner surface oxide of the cladding of the hollow pellet fuel rod was less than that of the standard fuel rod. This means that the PCI of-the hollow fuel pellet was less than that of the standard fuel pellet.

The density changes in the hollow fuel pellets after irradiation were compared with the standard fuel pellet and previous results as shown in Figure 6. The density change in the hollow fuel pellets was confirmed to be within the scattering of the previously obtained data.

Radial γ scanning of the fuel pellets was performed in order to investigate the radial burnup distribution and fission product distribution. Figure 7 shows the total γ-ray intensity of the hollow fuel pellet and standard fuel pellet. The distribution of the total γ-ray correlated well with the calculated burnup distribution. The effect of the hollow fuel pellet on the nuclear physics was confirmed not to be specific.

Residual fission gas in the fuel pellets was determined by the hot extraction method for the hollow fuel pellets and standard fuel pellets. The measured fission gas volume was almost the same as the calculated total fission gas volume which was generated during irradiation for both types of fuel pellets. This result showed that local FGR from the fuel pellets was not very remarkable.

5. CONCLUSIONS

From these PIE results of the hollow fuel pellets and standard fuel pellets, the integrity of the hollow fuel pellets was demonstrated in the PWR fuel rod under normal operating conditions. The free volume increase in the hollow fuel pellet had an advantage for internal pressure, however, the FGR of the hollow fuel pellets was almost at the same level as that of the standard fuel pellets. Generally speaking, the hollow fuel pellet has a better PCI performance than the standard fuel pellet, but no quantitative effect could be confirmed due to the relatively mild irradiation history under normal operation. On the other hand, the hollow fuel pellet has the disadvantage of less fissile material in a fuel rod from the viewpoint of fuel cycle economy. So, the adoption of hollow fuel pellets will be investigated considering the necessity of the design margin for PCI and the fuel cycle economy.

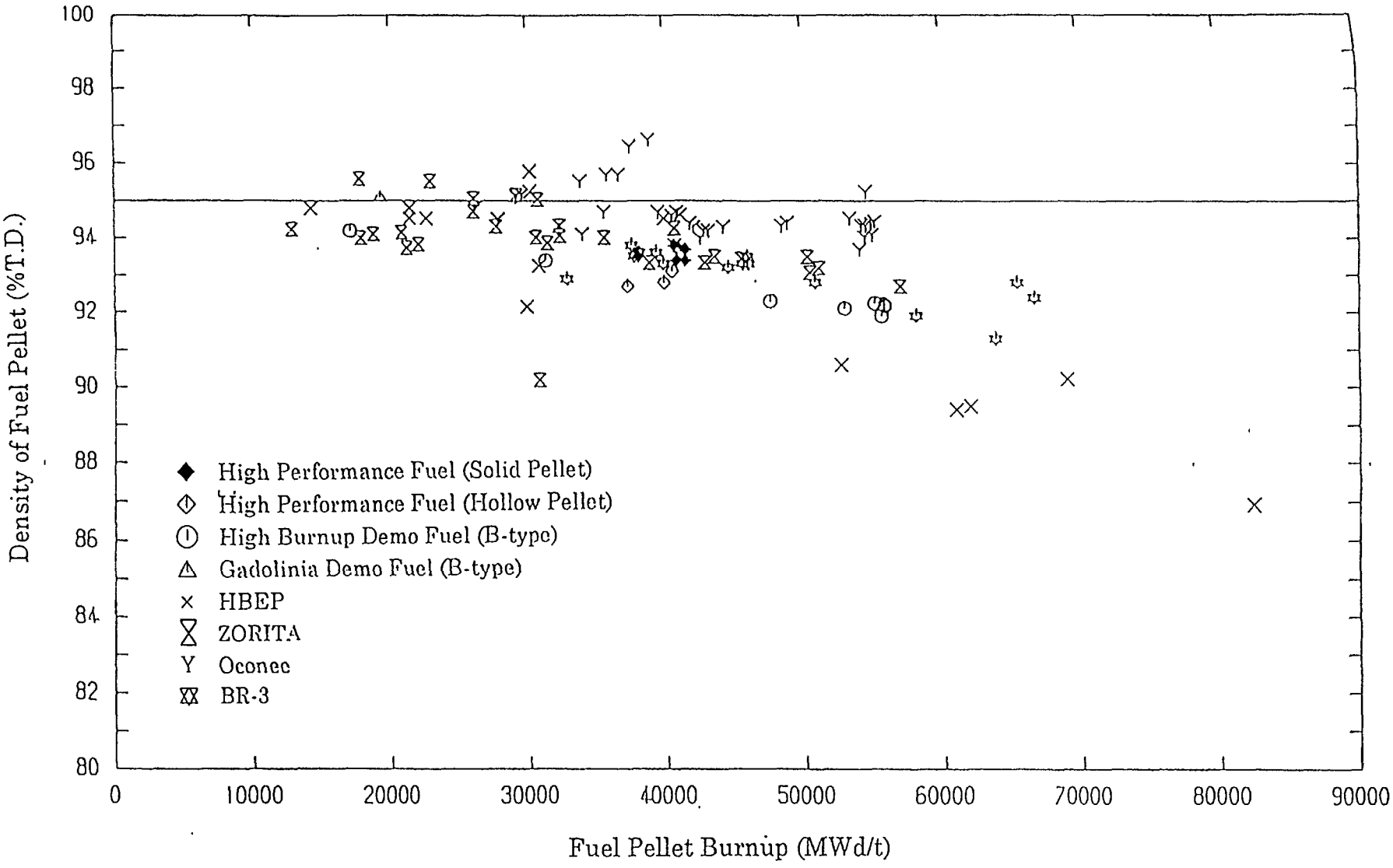

FIG. 6. Density change of fuel pellet

FIG. 7. Radial γ scanning of fuel pellet

ACKNOWLEDGEMENTS

The authors wish to express their great thanks to Prof. T. Okubo, Sophia Univ., and all the managers, staff and engineers in each research institute and PWR utility involved in this program. We also wish to thank the people in JAERI who helped to perform the PIE studies for this program.

DISCUSSION

(Questions are given in italics)

Have you information on the problems encountered with hollow pellets within the HBC programme? Grain de-cohesion during power increase on a 45GWd/tU fuel rod led to a fuel center line temperature of 2000°C instead of 1500°C expected. This was explained in the presentation I made at the last IAEA meeting in 1994.

Hollow pellet BWR fuel ramp tested in the 1970's had a tendency for de-cohesion of the grain boundaries around the unrestrained bore of the fuel. Consequently, the bore lost its integrity and it was even possible to get melting due to the thermal impedance of the grain separations.

STRUCTURAL CHANGES IN THE VVER-1000 OXIDE FUEL AFTER IRRADIATION

V.N. GOLOVANOV, V.I. KUZMIN, A.V. SMIRNOV
Research Institute of Atomic Reactors,
Dimitrovgrad, Russian Federation

Abstract

The investigation results of the structure of oxide fuel irradiated in the RIAR research reactors and VVER-1000 up to burnup 45 MWd/kgU are presented. Peculiarities of the fuel-cladding interaction are considered. Change of the irradiated fuel structure after overheatings is shown. Conclusions of the possibility of burnup increase are made.

INTRODUCTION

Increase of fuel burnup is one of the considerable ways of enhancing economical efficiency of the VVER fuel cycle.

In this connection wide investigations of change of the main characteristics of oxide fuel influencing the fuel elements serviceability are conducted to substantiate safe and reliable operation of reactors in Russia.

The investigation results of change of the VVER-1000 standard fuel structure and swelling at high burnup are presented in this report. Some peculiarities of mechanical fuel pellets-claddings interaction are considered.

MAIN CHARACTERISTICS OF LOADED FUEL PELLETS

Fuel pellets in the VVER fuel elements have a cylindrical shape with a central hole. The outer diameter of pellets is equal to 7.55 mm, the inner one for the VVER-440 fuel elements is 1.4 mm, and for the VVER-1000 fuel elements - 2.4 mm. The pellets height makes up 9-12 mm. The initial density is within 10.4 - 10.8 g/cm^3. The average grain size is equal to 10-30 mm.

FUEL OPERATING CONDITIONS

The main operating parameters of the VVER 440 and VVER-1000 fuel elements and fuel are close (Table l).

The linear power and temperature of fuel change in the course of operation. Maximal values are usually achieved at the initial stage and then are decreased: linear power up to 70-90 W/cm, the temperature in the fuel centre up to 800-1000°C.

TABLE I. OPERATING PARAMETERS OF THE VVER INVESTIGATED FUEL ELEMENTS AND FUEL

Parameter	Parameter value	
	VVER-440	VVER-1000
Inlet coolant temperature, °C	270	290
Outlet coolant temperature, °C	300	320
Coolant pressure, MPa	12.2	15.7
Maximal linear power, W/cm	260	320
Maximal temperature in pellets centre, °C	1300	1450
Duration of power operation, hour	21000	21000
Maximal burnup in pellet section MWd/kgU	64	55

INVESTIGATION TECHNIQUES

The full investigation cycle of fuel irradiated at NPP is conducted in the hot laboratory of SSC RF RIAR using the following techniques:

- optical metallography with quantitative analysis of image;
- scanning electron microscope;
- secondary-ion microanalyzer.

For detailed structural investigations use is made of the most important fuel elements sections separated due to the detailed non-destructive investigation results.

PELLETS CRACKING, DIAMETRAL GAP CHANGE AND MECHANICAL PELLETS-CLADDING INTERACTION

At the beginning of operation under the influence of thermomechanical stresses the pellets are cracked in the radial and cross directions (Fig. 1). The fragments size 2-4 mm and limited diametral gap 0.19-0.3 mm provide stability of the total configuration of pellets and fuel column as a whole. So pellets fragments do not move to the central cavity.

While the burnup increases, the diametral gap between pellets and cladding decreases due to fuel swelling and cladding creep strain under the coolant pressure (Fig.2),and a close contact under operating conditions occurs at burnup 35 MW d/kgU.

It is most probably that at first the contact appears in the area of pellets faces, where their diameter is maximal and then the contact area gradually penetrates to the whole pellets surface. After the contact is achieved, pellets are swelled over the whole surface under

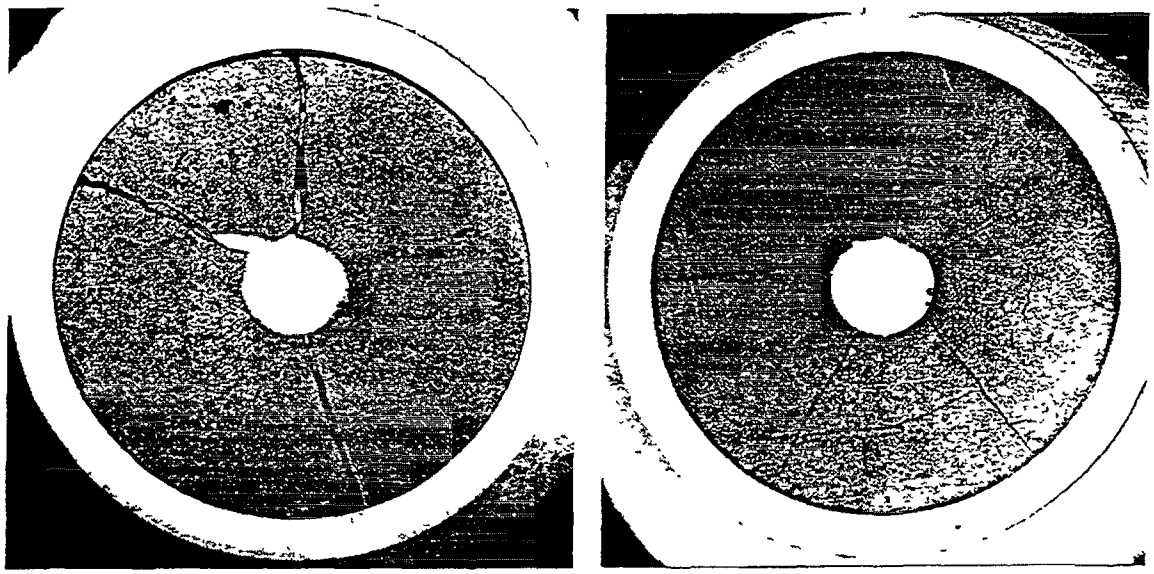

a b

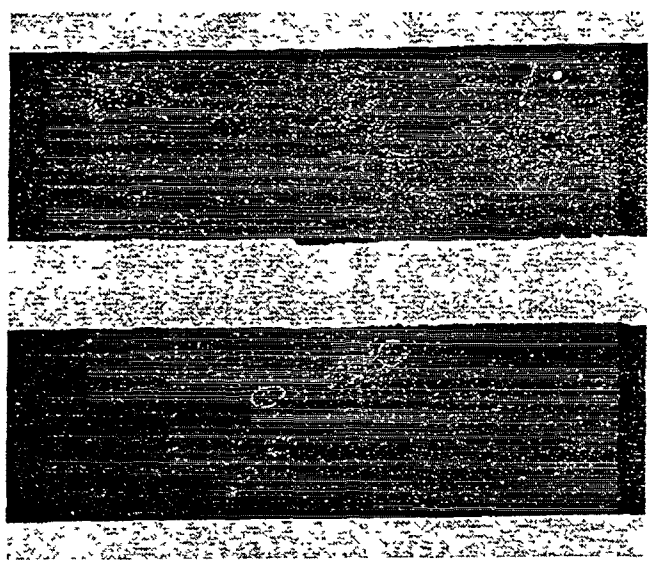

c

FIG. 1. Gaps between pellet fragments at burnup 30 (a) and 63 MW d/kgU (b,c).

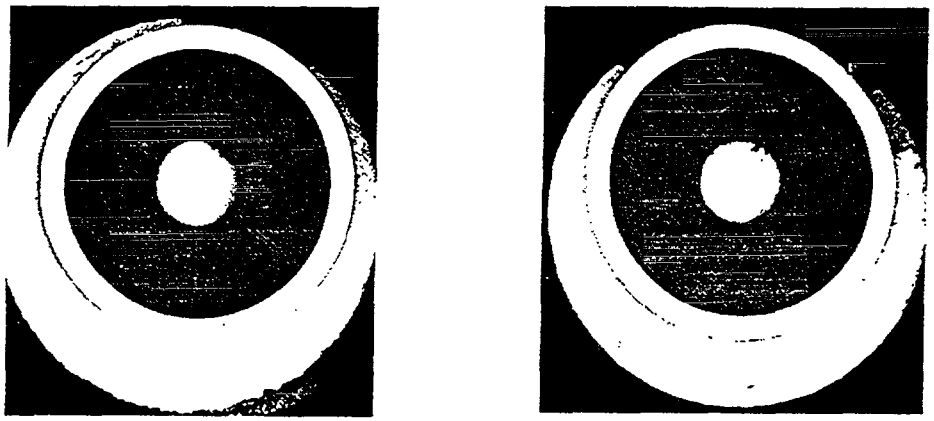

d e

FIG. 1 contd. *Gaps between pellet fragment at burnup in the VVER -1000 reactor 33 MW d/kgU (d) and 45.3 MW d/kgU (e).*

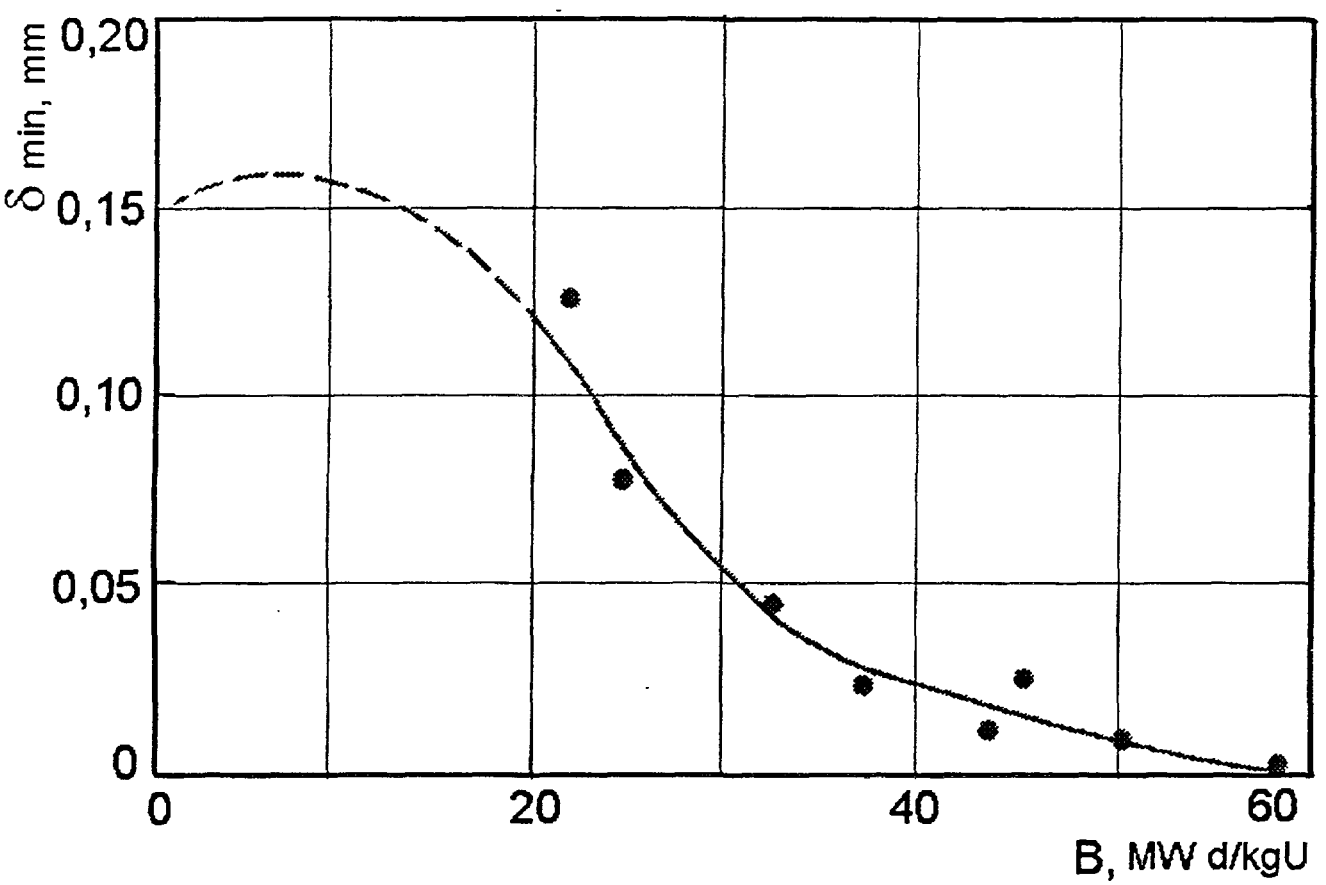

FIG. 2. *Change of the diametral gap versus burnup.*

conditions of its containing by the cladding. This circumstance leads to the fact that swelling compensation occurs at the expense of the cracks width. This process is accelerated because of intensive formation of porosity in the outer layer of fuel pellets. As the result of this at burnup 55 64 MWd/kgU full filling of radial and cross cracks on the periphery of fuel pellets occurred (Fig. 1b,c).

The diameter of the pellets central hole in this case practically did not change as compared to the initial value. As the result of such a change of sizes and mechanical fragments interaction, there appeared a continuous, rigid arch-type pellets outer layer, the swelling of which with further increase of burnup cannot only retard the speed of the cladding diameter decrease, but also can change the strain sign, i.e. cause the reverse diameter increase. The direction and speed of the diameter change will be determined by the ratio of the coolant pressure compression stresses and swelling fuel pressure tensile stresses in the cladding.

In conclusion of this section we shall note that in spite of the gained rigid fuel-cladding contact at burnup more than 50 MW d/kgU there was not a single case or even any signs of corrosion cracking of claddings under stress.

FUEL SWELLING

Swelling of the VVER fuel stipulated by fission products accumulation has the incubation period stipulated by radiation after-sintering. Duration of this period corresponds to burnup 15-20 MW d/kg U (Fig.3). At higher burnup the volume increase is in proportion to burnup. Specific swelling in the burnup range 20-65 MW d/kg U is equal to average 0.9%/MW d/kg U.

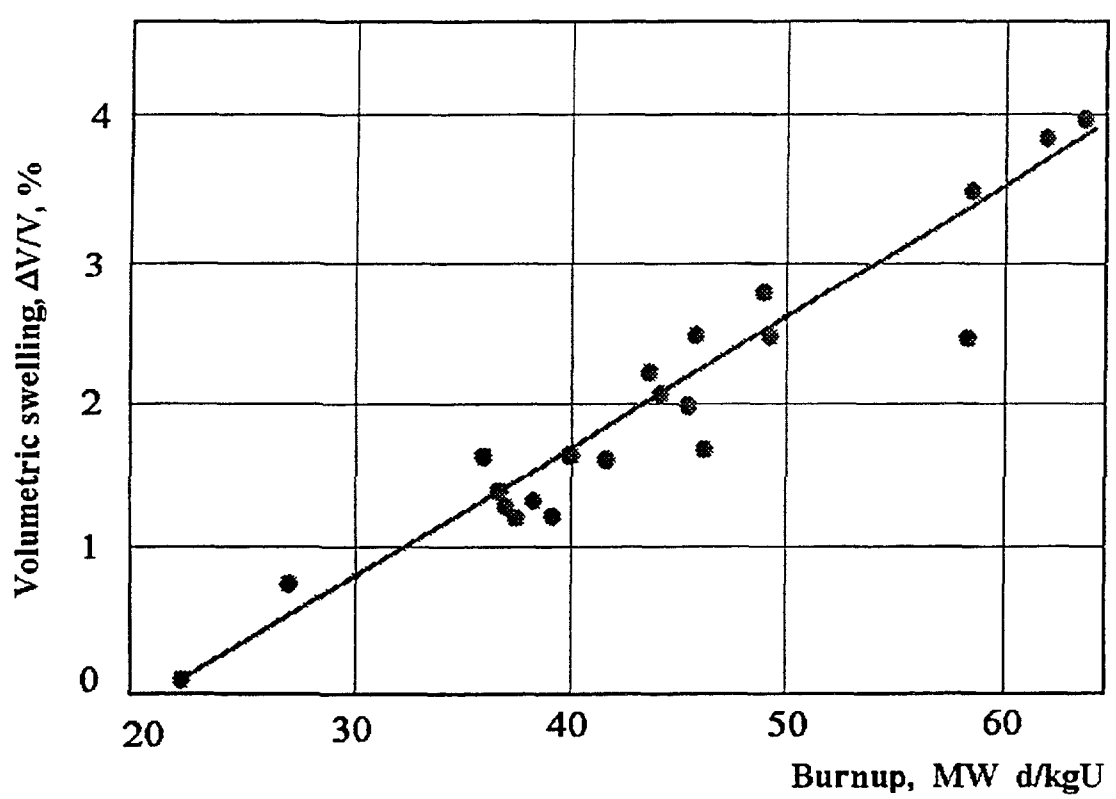

FIG. 3. Swelling of the VVER-1000 fuel versus burnup.

STRUCTURE CHANGE

Structural changes of the VVER fuel are stipulated by a relatively low temperature. Within the whole operating period the maximal linear power in the investigated fuel elements did not exceed 320 W/cm. Respectively, the maximal temperature in the fuel centre was lower than the temperature of equiaxial grains growth. Therefore, the grain size even in the hottest part of pellets did not increase and made up 10-30 mm. The most noticeable changes of structure took place in the outer radius fuel layer, 30-100 mm, at burnup more than 40 MW d/kgU. Due to over saturation with gaseous and solid fission products because of their low solubility in U dioxide there were formed gas-filled voids (Fig.4), up to 2 mm in size. Increase of the blocks interface facilitates and speeds up diffusion of Kr and Xe atoms, which leads to increased gas release from this layer.

Distributions of Zr as well as Xe and Nd fission products in the layer of interaction between the VVER-1000 fuel spent up to burnup 45 MW d/kg U and the cladding were obtained by the X-ray microanalysis method (Fig.5-7). The layer thickness on the analysis section made up 8 mm. Presence of Xe and Nd in the layer is stipulated by recoil nuclei. Certain contribution is also possible by diffusion with close contact.

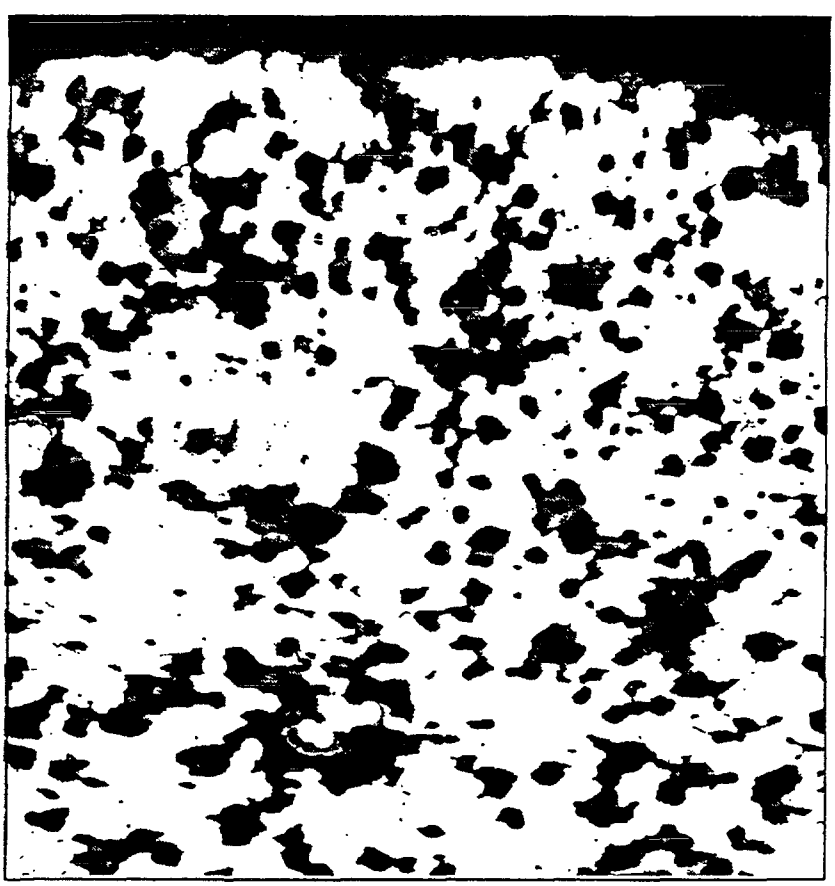

FIG. 4. *Voids in the VVER-1000 fuel rim-layer. Average pellet section burnup 45 MW d/kgU.*

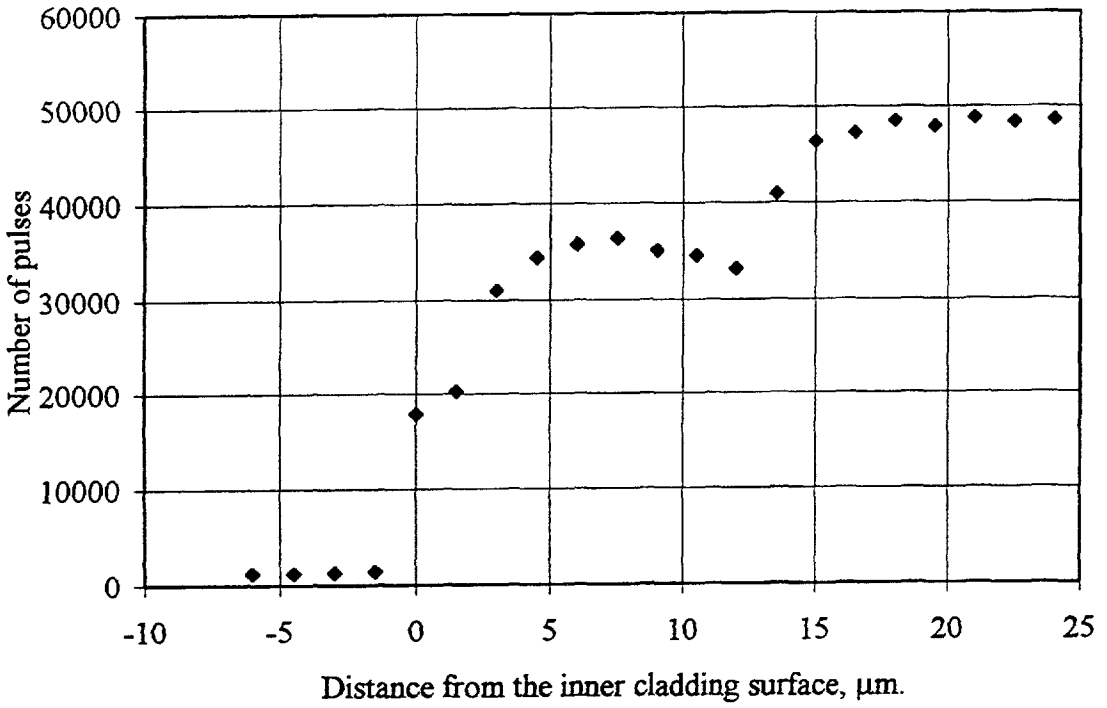

FIG. 5. *Distribution of Zr in the cladding near inner surface.*

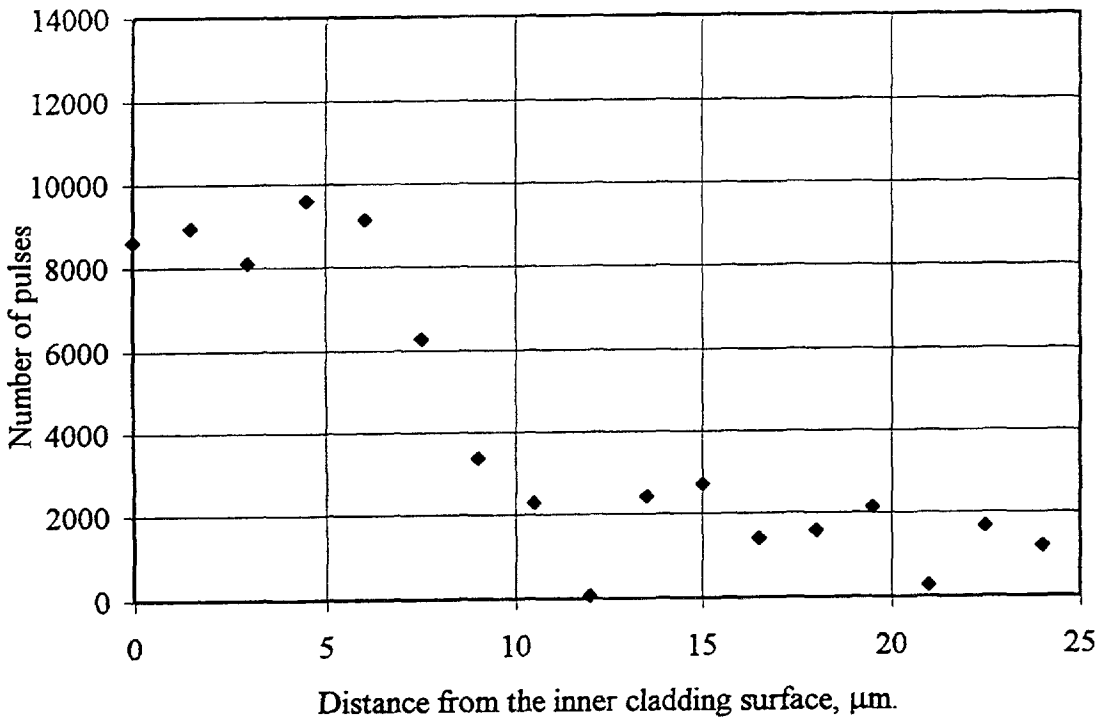

FIG. 6. *Distribution of Xe in the cladding near inner surface.*

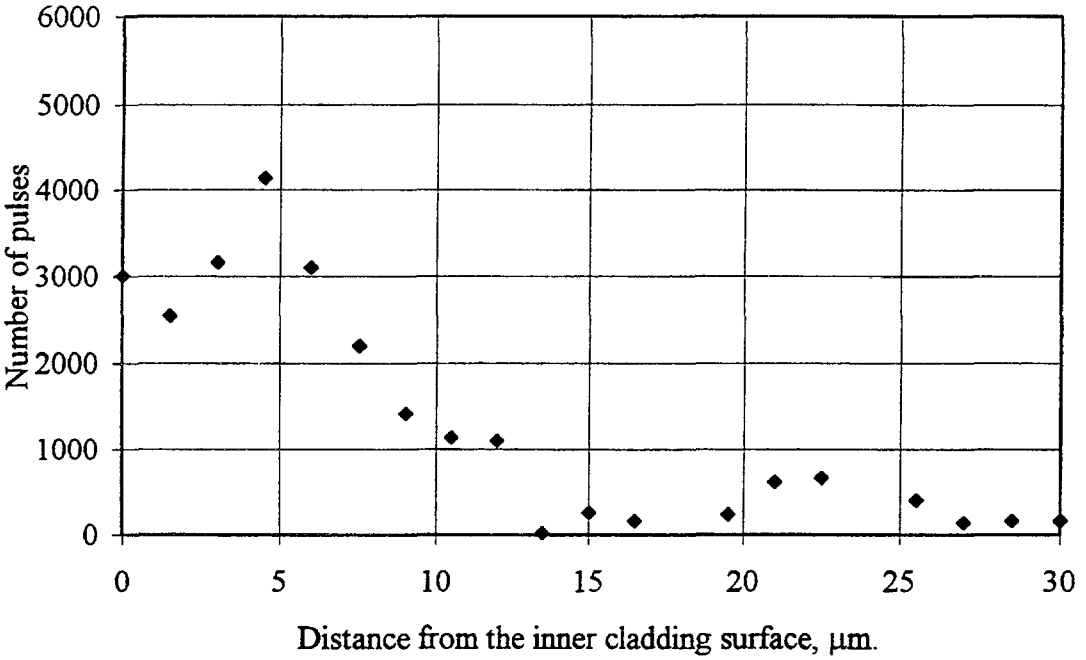

FIG. 7. Distribution of Nd near the inner cladding surface.

HEATING OF THE VVER-1000 IRRADIATED FUEL

A possible variant of the VVER-1000 fuel modernization is increase of UO_2 grain. Decrease of gas release from such fuel allows increase of burnup fraction under normal operating conditions, which is an important positive effect. However, at large burnups in the fuel with small gas release the increase of accumulated gaseous fission products is inevitable. Some signs of "explosive" gas release were detected with overheatings of the VVER-1000 fuel elements pieces (Fig.8). In these fuel elements use was made of UO_2 with the standard grain size. Burnup was 45 MW d/kgU.

Thus, some results of overheating fuel elements containing UO_2 fuel evidences of the necessity of careful approach to the proposed modernizations of the VVER-1000 fuel and fuel elements, aimed at increase of burnup and reliability of these fuel elements under normal operating conditions. Efficiency of the proposed modernizations should be experimentally checked not only in standard operating regimes but also under emergency conditions, in particular, during overheatings of irradiated fuel elements.

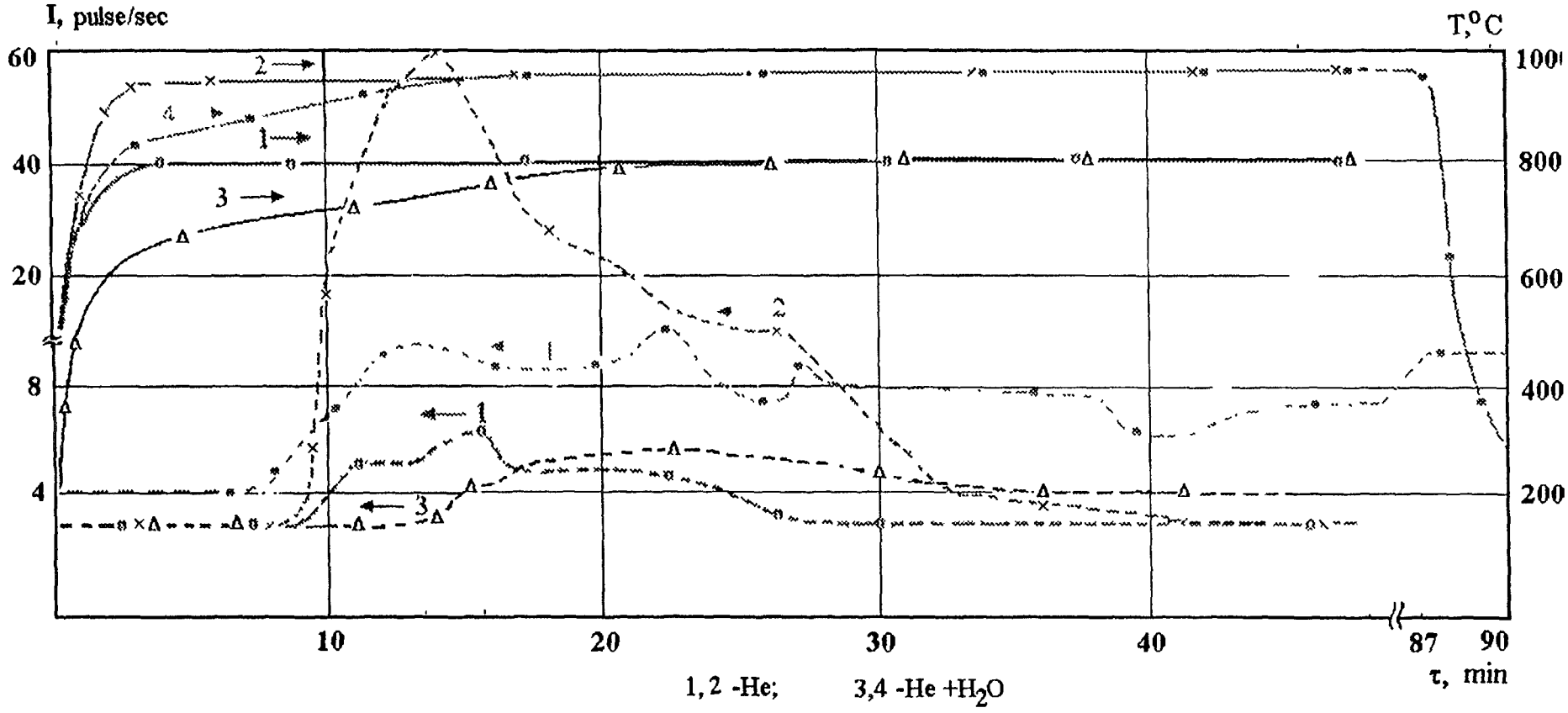

FIG. 8. *Change of temperature and ^{85}Kr yield during overheatings of the VVER-1000 irradiated fuel element pieces (fuel assembly N 0329).*

CONCLUSION

The large scope of material science investigation results of the VVER-1000 reactors fuel performed at RIAR and presented in the report shows the following:

- fuel elements with pellet fuel have high reliability indices up to large burnups. The main parameters determining serviceability of fuel element on the part of fuel do not achieve critical values.

- structural changes in the VVER-1000 and VVER-440 pellet fuel with burnup increase coincide in the main indices:
  - close contact of the fuel and cladding appears;
  - rim-layer with increased porosity is formed.

- while modernizing the pellet fuel it is necessary to estimate its properties after tests in different regimes including those having deviation from the standard operating conditions of fuel elements.

DISCUSSION

(Questions are given in italics)

Did you perform ramp test on the fuel rods at 20GWd/t with large gap presented in your paper?

Fuel pellets of WWER-1000 have central hole, which compensates stresses in the process of ramp testing.

Fig. 2 gives the gap accumulation to burnup. The gap is filled at 60MWd/kg. I believe this value is very high because I had in mind that the minimum (earliest) creep down for WWER-1000 was at about 40 or 45 MWd/t. Can you comment?

The main reason of decreasing gap after burnup of 50MWd/kgU is decreasing width of cracks, which was formed in the first stage of irradiation in the pellets.

You indicated average grain size of 10 to 30μm for WWER-440 and WWER-1000. It is not in line with the fractograms presented by A. Smirnov, indicating grain size 5μm. Could you clarify?

From your Fig.3 it can be deduced that densification is 2.0v/o. It is high for low fine porosity and 10–30 mm grain size fuel. Could you comment?

Grain size of fuel pellets of WWER-1000 is 10-12 mm. I use statistical information about grain size of 10-30 mm influenced by the gap between fuel pellet and clad.

CHEMICAL STABILITY AND PHYSICAL PROPERTIES OF CAESIUM URANATES

J.P. BERTON
Electricité de France,
Septen, France

D. BARON
Direction des études et recherches,
Electricité de France,
Moret-sur-Long, France

M. COQUERELLE
EC Institute for Transuranium Elements,
Karlsruhe, Germany

Abstract

Caesium is one of the most abundant fission products in PWR nuclear fuel or in fast reactor fuel as well. A work program has been started at the TUI Karlsruhe, in collaboration with EDF Etudes et Recherches, to determine the thermal stability and conductivity, the mechanical properties and the thermal expansion coefficient of Cs_2UO_4.

The Caesium mono-uranate was obtained by a chemical reaction between Cs_2O_3 and U_3O_8 powders mixed together, pressed and heated at 670°C for 24 hours. The compound was found stable up to 830°C.

Mechanical compressive hardening tests allowed to evaluate the elastic modulus versus temperature in the range 200 to 800°C. Furthermore the viscous behaviour of the compound above 400°C was confirmed.

The thermal expansion coefficient of Cs_2UO_4 was found somewhat 40% higher than the thermal expansion coefficient of UO_2. The thermal conductivity is about 1.5 to 1.8 W/m/K for temperatures ranging from 100 to 700°C, a value very similar to the UO_2 fuel thermal conductivity at high burnup in the same temperature range.

1. INTRODUCTION

Caesium is one of the most abundant fission product in PWR nuclear fuel or in fast reactor fuel as well. Under reactor operating conditions, depending on the local temperature, it can migrate by vapour transfer or thermal diffusion processes towards the fuel pellet periphery and react with uranium dioxide or with the zirconium dioxide layer on the cladding inner face. The nominal composition of the compounds formed depends on the value of the oxygen potential in the "rim" region. Analysis of the pellet edge in spent fuels indicated after particularly high local power history, the presence of caesium in high concentration and probably in form of compounds of the (Cs-U-O) and (Cs-Zr-O) systems. The Cs_2UO_4 is one of the most stable phase of the various caesium uranates, under the local conditions existing in PWR fuel rods. It has also been found a new phase type $Cs_2UO_{3.56}$. When thermal conditions are met, caesium phases appear as dots in the fuel-clad gap at 45 GWd/tU (pellet average).

Over 50 GWD/tU, a continuous layer is observed, able to penetrate radial fuel cracks. The presence of these compounds in such position must change drastically the conditions of the Pellet Cladding Mechanical Interaction (PCMI). Moreover, it has been suggested that formation of low densities caesium uranates contributes to swelling processes and consequently to the deformation and cracking of fuel cladding.

Therefore these results justify the numerous investigations undertaken to study the Cs-U-O system, the thermodynamics, the thermal stability of various caesium uranates and their physical and mechanical properties. The thermo-chemical data published so far are not sufficient to interpret the behaviour of caesium and its influence on the performance of the nuclear fuel rod. They are generally not sufficient to solve the problem of the interaction between, caesium and the fuel components. A work program has been therefore started at the TUI Karlsruhe, in collaboration with EDF Etudes et Recherches, to determine the thermal stability and conductivity, the mechanical properties and the thermal expansion coefficient of Cs_2UO_4.

2. EXPERIMENTS

2.1 Preparation of the Cs_2UO_4 compound

Various methods of preparation of the mono-uranate Cs_2UO_4 are reported in the literature [1-7]. The reaction in air:

$$3\ Cs_2O_3 + U_3O_8 + 0{,}5\ O_2 \text{----}> 3\ Cs_2UO_4 + CO_2$$

was chosen because the starting materials are stable in dry atmosphere and their low density favours the preparation of homogeneous mixtures and then the efficiency of the reaction. Stoichiometric amounts of Cs_2O_3 and U_3O_8 powder were mixed in a mill, pressed in form of cylindrical pellets and heated at 670°C during 24 hours in air. The lattice parameter of the intermediate and final products were analysed by X-ray techniques in order to identify the compounds formed (see Table I). These products are hygroscopic and were handled in a glove box under flowing dry nitrogen atmosphere.

TABLE I. ESTIMATION IN % OF MASS OF THE INTERMEDIATE PHASES IN PRESENCE DURING THE SYNTHESIS OF CAESIUM MONO-URANATE MEASURED WITH A DIFFRACTOMETER

Reaction temperature, °C	Atmosphere	Cs_2UO_4 (%)	a-$Cs_2U_2O_7$ (%)	ß-$Cs_2U_2O_7$ (%)
500	Hélium	~30	~30	~30
600	Hélium	~50	~20	~20
700	Hélium	< 80	< 5	> 5
500	Air	< 100	> 5	> 5
700	Air	**~100**	-	-

2.2 Characterisation of the Cs_2UO_4 compound

The final reaction product Cs_2UO_4 obtained in pure state was in form of orange coloured, swelled and friable pellets. These have been milled and the powder obtained was used to experiment the thermal stability of the compound and then for compacting operations. Cylindrical pellets with density ranging between 75 and 90% of the theoretical density were prepared by pressing Cs_2UO_4 powder at room temperature. Density around 97% have been obtained by hot pressing techniques, using a tungsten carbide die and a pressure of 6 ton/cm^2 at 730°C. The caesium uranate samples were investigated with different techniques to determine the major physical and chemical characteristics of such material and the results compared against other compounds. Then the techniques engaged were :

- scanning electron microscopy to investigate fracture surfaces and to obtain topographic information about grains, grain boundaries, porosity, cracks, etc...

- X-ray of finely ground powder in quartz capillaries placed in a Debye-Sherrer chamber using the CuKα rays (0.1504 and 0.15443 nm) to identify the reaction products (figure 1),

- dilatometry in a temperature range 20-700°C. The thermal expansion of pellets 10,5 mm in length, was determined using a differential dilatometer. Reference materials were Platinum (Pt), Copper (Cu), Uranium dioxide (UO_2) and alumina (Al_2O_3). The sample heatings were carried out under Argon atmosphere at a rate of 3°C/mn,

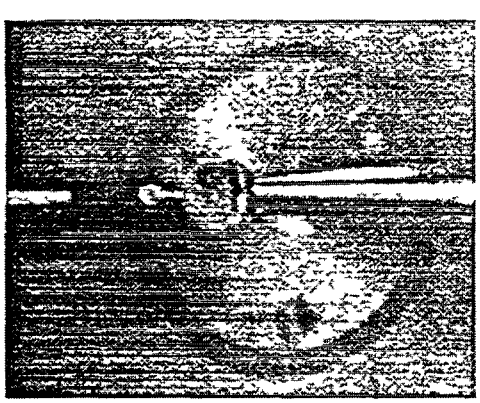

1A - Debye Sherrer chamber

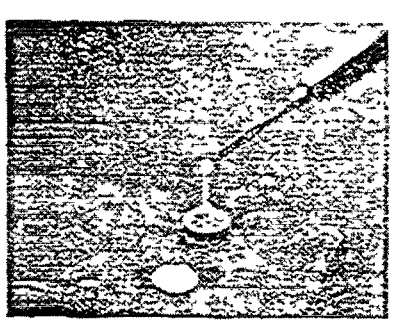

1B- Capillary

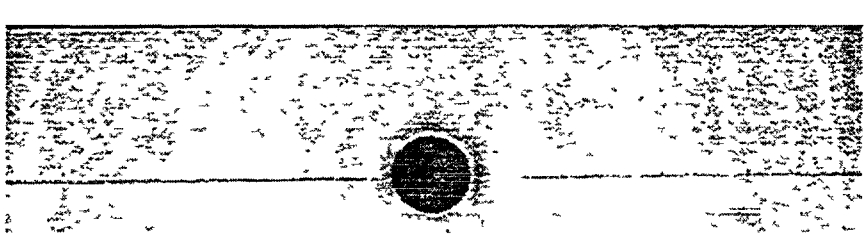

1C - X-Ray film with Cs_2UO_4 rays

FIG. 1 Disposition for X-RAY diffraction Analysis

- thermogravimetry. About half a gram of Cs_2UO_4 powder was introduced in a thermobalance and heated up to 900°C under Argon and air atmosphere. This was done to determine the thermal stability of Cs_2UO_4. Weight changes were automatically recorded as a function of time and temperature,

- compression tests. These were carried out by using a mechanical testing machine operating at constant load or constant deformation rate and having the following main characteristics:

  minimum pressure = 10 Newton

  minimum move = 2 μm

  deformation rate investigated = 5 to 100 μm/mn

  temperature range = 20-1800°C

  The measurements were carried out under vacuum. The specimen in form of cylindrical pellets were placed between two silicium carbide pistons and heated to desired temperature (figure 2). Then, the displacement of one of the piston was applied at a programmed rate. The compression force was recorded. Measurements ended with rupture of the specimens.

- Thermal conductivity. The apparatus was delivered by ANTER (American company) and allowed a direct measurement of the thermal conductivity in the temperature range 20 to 800°C, by using a comparative method. Briefly, the Cs_2UO_4 specimens were placed between two pellets with the same diameter and known conductivity. This set-up was introduced in a special furnace and a light compression was applied to the specimen. The heat losses were minimised by a system of three concentric heating

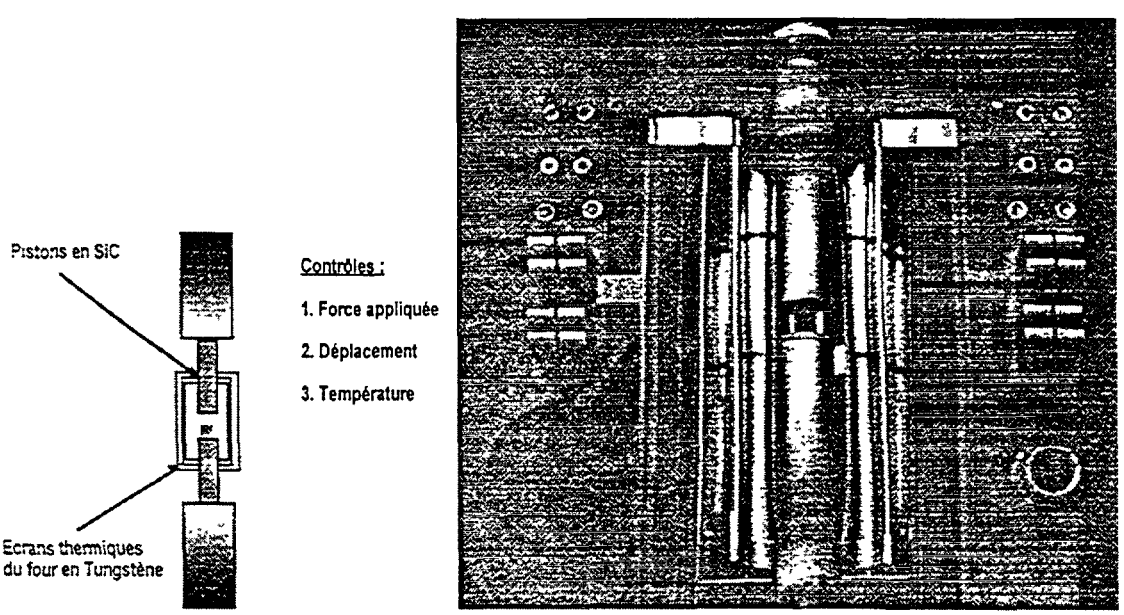

FIG. 2 Design of the Mechanical testing apparatus

resistances. An axial heat flow was generated into the pellets and temperature gradients in the reference and the pellets were measured with thermo-elements. The thermal conductivity was simply calculated from the conduction equation of FOURRIER-BIOT [8] et [9] :

$$K = \frac{-\Phi.\Delta x}{A.\Delta T}$$

K is the thermal conductivity at the average sample temperature (W/K.m)
Φ, the power (W)
A, the sample cross section surface (m^2)
Δx, the distance between the two thermocouples.

3. RESULTS AND DISCUSSIONS

3.1 Thermal stability

Cs_2UO_4 in form of powder was heated in a thermobalance in air, pure Helium and Helium containing 100 ppm Oxygen to simulate various Oxygen potentials. The results exhibit a notable weight change starting around 850°C. X-ray diffraction analysis, carried out afterwards in glove box under dry nitrogen atmosphere, revealed that the powder heated at 850°C contained $Cs_2U_2O_7$, i.e.a compound formed by the reaction:

$$2\ Cs_2UO_4 \text{ ----> } Cs_2U_2O_7 + Cs_2O$$

Moreover, it has been found that the powder after the heat treatment at 850°C was cemented to form a conglomerate. Assuming that the weight variation recorded was essentially caused by the evaporation of Cs_2O, one could estimate the dissociation rate of Cs_2UO_4 by measuring the weight decrease (figure 4) as a function of time and temperature. The evaporation of Cs_2O has been tested and the results indicated that a detectable evaporation of Cs_2O started below 800°C, a temperature over the melting point.

Combining the evaporation rate of Cs_2O, the formation of a compound and the detection of $Cs_2U_2O_7$ above 800°C, one can in first approximation use the evaporation rate of Cs_2O to determine the kinetic of decomposition of Cs_2O_4. The results reported in the literature [2], [4], [5], [7] show some discrepancy certainly depending on experimental procedures caused by use of powders with different properties or/and the handling under different atmospheres.

Additional experiments carried out in dry atmosphere clearly showed that Cs_2O evaporation is discernable as low as 500°C. This is in agreement with the Cs_2O partial pressure calculated by [5] in equilibrium with caesium uranate.

The Cs_2UO_4 decomposition temperature presently found, located more accurately between 800 to 830°C, is somewhat lower than that reported by D. K. BOSE [2], > 950 °C, or S. R. DHARWADKAR [3], about 950°C. Our results are nevertheless more consistent with these works than with those of Cordfunke [4] who reported a decomposition starting around 650 °C. In this case, the experiments were not carried out in dry atmosphere and were perhaps influenced by the presence of water vapour which favoured the decomposition of Cs_2UO_4 into $Cs_2U_2O_7$ + CsOH around 600°C.

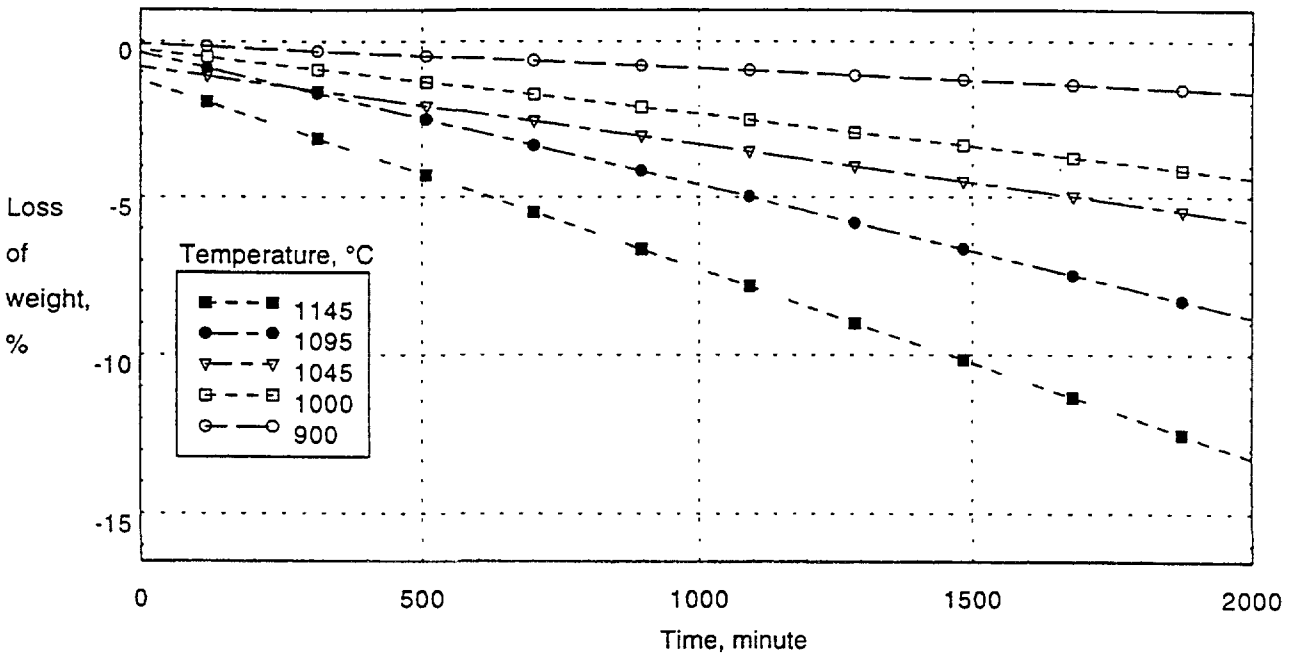

FIG. 3 Decrease of weight versus time and temperature.

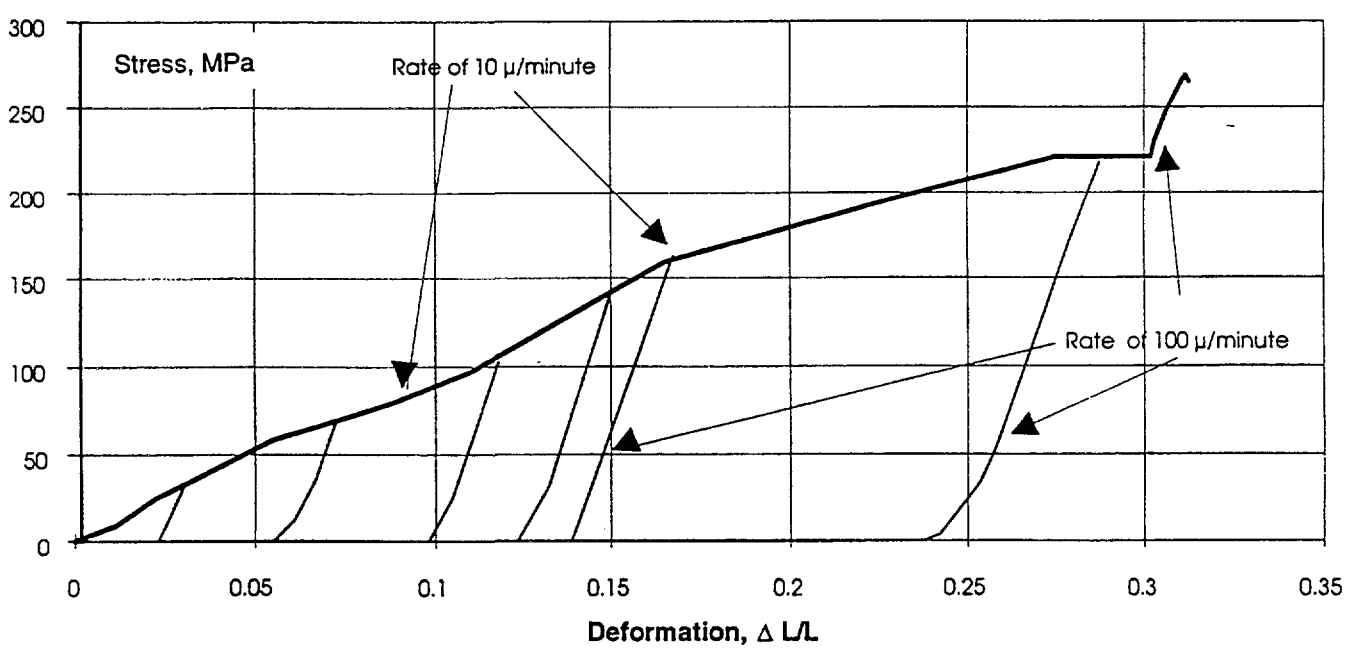

FIG. 4 Stress - deformation curve et 700°C with load and unload cycle

Weight decrease was analysed on periods up to 35 hours. Figure 3 shows the weight decrease rate of the Cs_2UO_4 samples for several temperatures level.

3.2 Mechanical properties under compression

Hardening compressive tests were carried out using pellets (6 mm in diameter and 2 to 3 mm in height) with density ranging between 87 and 97% of the Cs_2UO_4 theoretical density. Having no extensometer available on the testing machine, the sample deformation is deduced from the cross member displacement after a correction accounting for the apparatus deformation.

The caesium uranate is expected to have a visco-plastic mechanical behaviour. Therefore, two series of tests have been conducted to verify this hypothesis. The first test procedure consists in the application of a monotonous constant displacement rate of 10 μm/min and the second a load cycling, loadings and unloadings, with different displacement rate (up to 100 μm/min) (figure 4). This aimed to demonstrate the influence of the load rate on the sample deformation and exhibit the viscous component.

Below 400°C, no notable influence was observed. This confirms a pure elastic behaviour of the caesium uranate samples in this temperature range. On the other hand, above 400°C, the records clearly show a modification of the apparent elastic modulus, characteristic of a viscous deformation component. Cs_2UO_4 exhibits therefore a strong trend for visco-plastic deformation at temperatures comparable to those existing in nuclear fuel pellets (> 400°C).

The compressive elastic modulus has been determined and plotted against the testing temperature for the density group samples which porosity was around 10% D.T. The temperature range is 200 to 800 °C. A polynomial approximation is proposed as follows:

$$E(T,10\%DT) = 28{,}8 - 7{,}5.10^{-2}.T + 7{,}2.10^{-5}.T^2$$

where E is in GPa and T in °C. Nevertheless, this must be considered as an indicative formulation. More tests would be required to confirm this correlation. The compressive test is indeed complex to interpret and the quality of the samples could be improved by improving the fabrication process. The data scattering observed on the data base is partly due to the unknown initial micro-damages in the tested specimens, the discrepancy in the densities obtained and the weight of the damage propagation in the permanent deformation measured during the mechanical tests.

The elastic modulus have also been determined at 400°C for all the range of densities available. A porosity correction have then been determined from this data group as follows:

$$\frac{E(400°C,por)}{E(400°C,por=0} = 1.00 - 1{,}56.por$$

where por is the volume porosity fraction. Assuming that this porosity correction is available for the temperature range 200 to 800 °C, it comes :

$$E(T,por) = (34{,}1 - 8{,}9.10^{-2}.T + 8{,}5.10^{-5}.T^2).(1.00 - 1{,}56.por)$$

The second step in mechanical testing was the characterisation of the Cs_2UO_4 creep behaviour. Compressive tests at constant load, ranging from 21 MPa to 88 MPa, were performed on the same kind of samples. Once again, due to the various quality of the sample and the discrepancy in specimen initial densities, the data obtained are to be interpreted carefully. The secondary creep rate was found similar at 4% and 5% deformation. Figure 6 gives an overview of the results obtained versus the reverse of the temperature at which test was performed. From these data, a Norton law has been fitted as follows:

$$\dot{\varepsilon} = \sigma^{2,57} \exp\left[-\frac{89000}{kT}\right]$$

where $\dot{\varepsilon}$ is the secondary creep rate (h^{-1}), T is the test temperature (K), σ is the stress applied (Mpa).

3.3 Thermal expansion

Table 2 shows the values of the thermal expansion of Cs_2UO_4 determined using various reference materials. The expansion curves reported in the literature for the reference materials are also plotted for comparison on the figure 7. The results show that the thermal expansion values of the Cs_2UO_4 were in between the UO_2 and Cu values. The most important aspect to remind is that the Caesium uranate samples have a thermal expansion about 40 % higher than the UO_2 fuel which must have consequences on the fuel pellet behaviour.

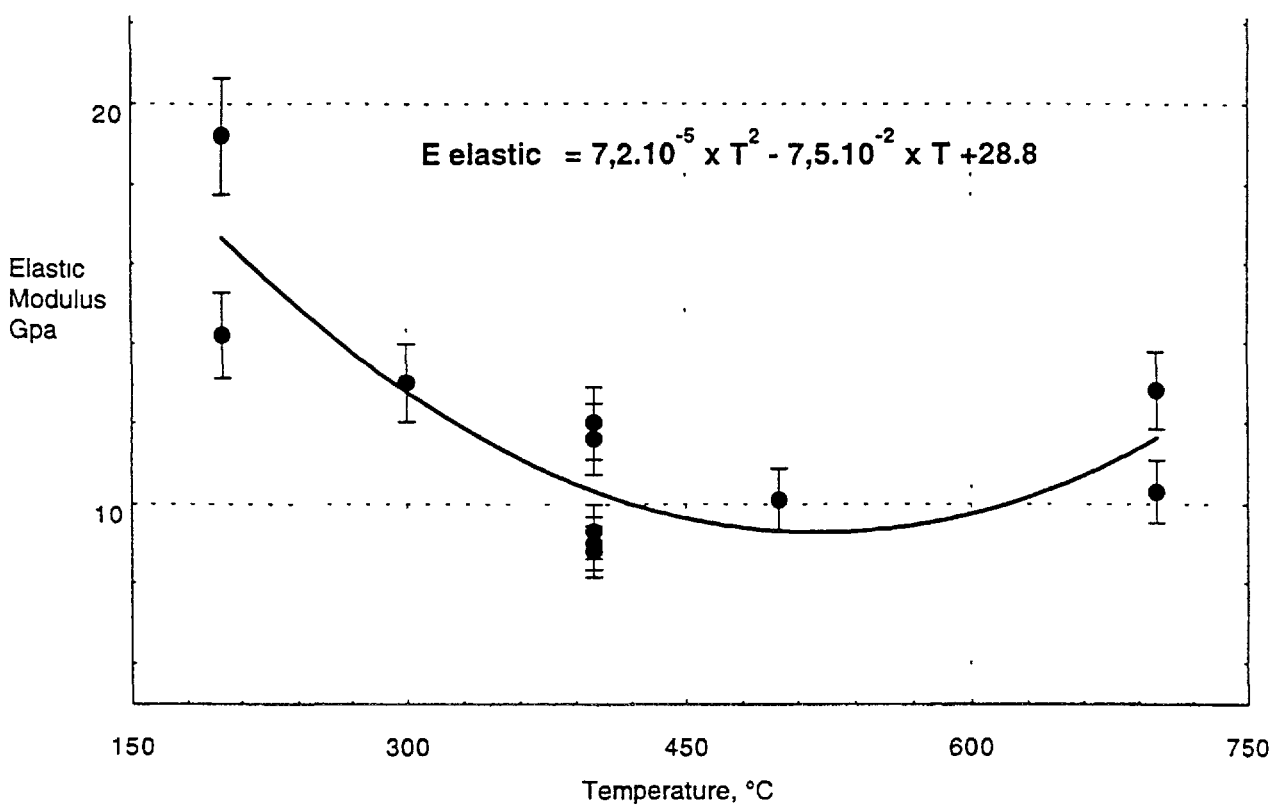

FIG. 5 Elastic modulus versus temperature

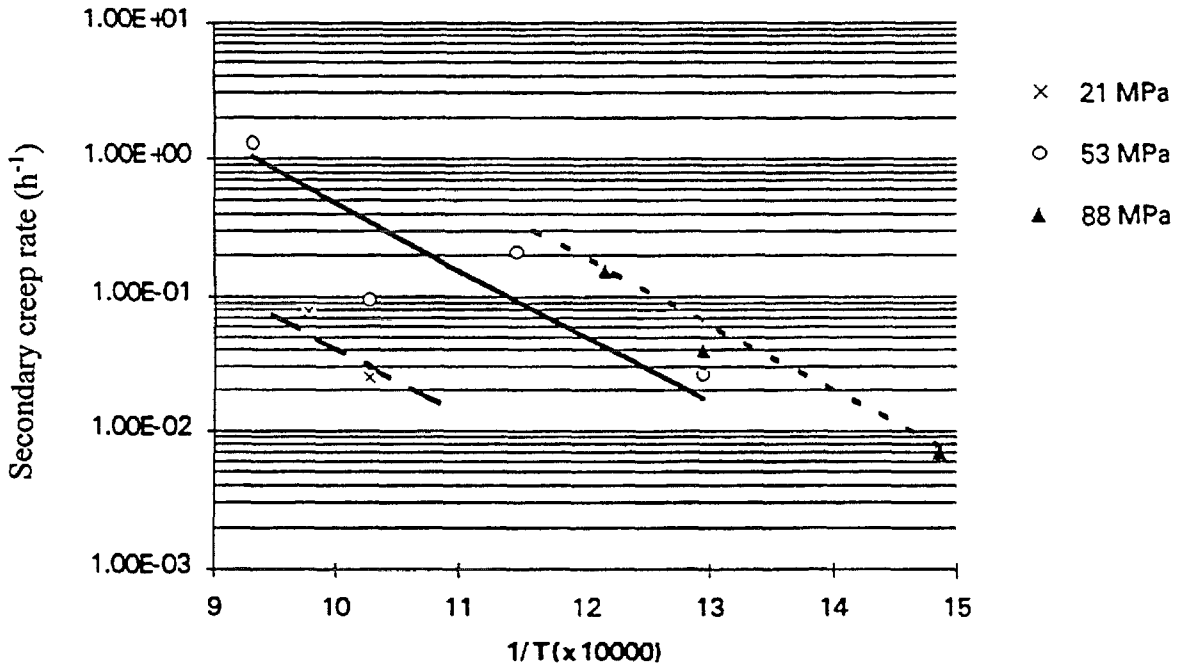

FIG. 6 Secondary creep rate measured at 5 % deformation

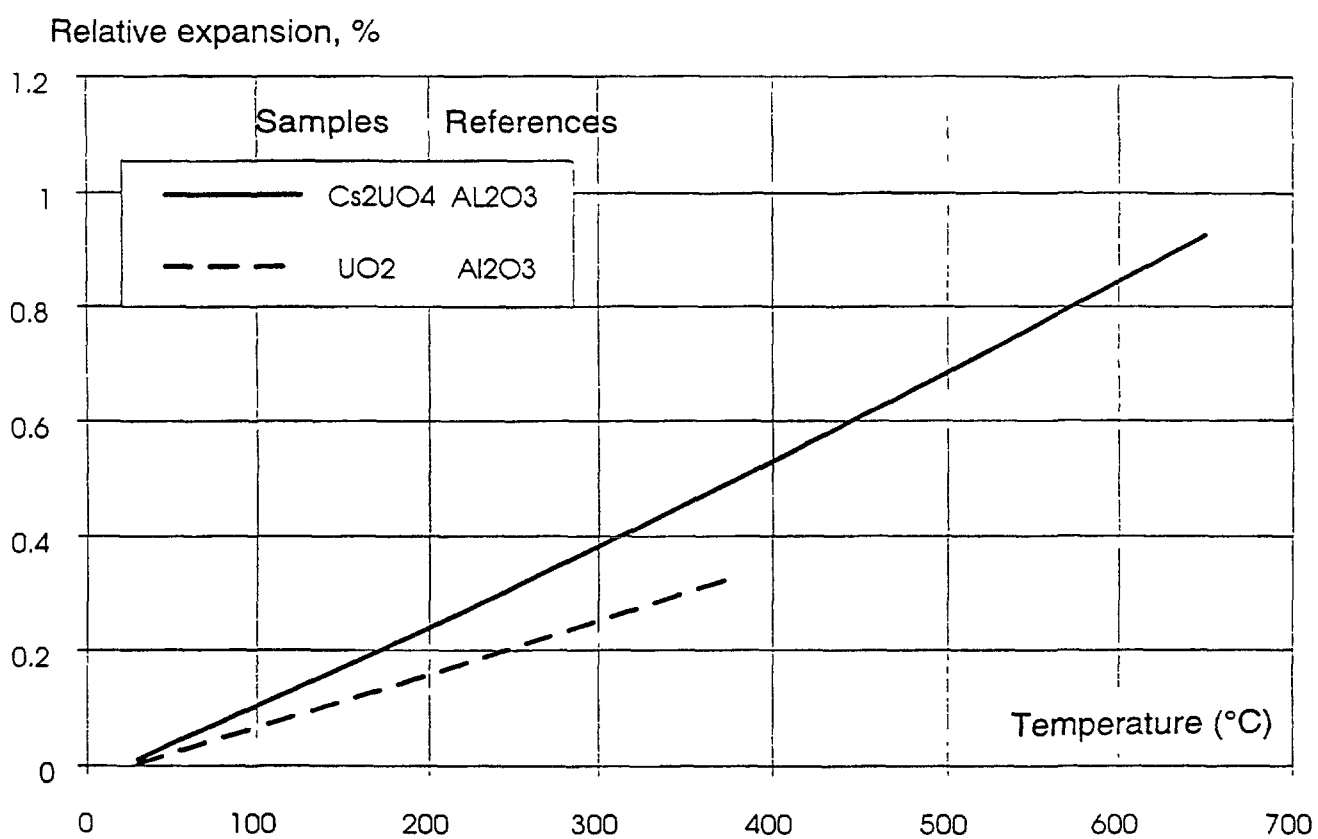

FIG. 7 Relative expansion versus temperature for different materials.

Obviously, for modelling purposes, a formulation can be drawn from these experiments. The correlation proposed is as follows:

$$\left(\frac{\Delta l}{l}\right)_{Cs2UO4} = 3.0.10^{-7}.T^2 - 0{,}0253$$

where T is the temperature in °C and $\left(\frac{\Delta l}{l}\right)$ the relative Cs_2UO_4 sample thermal expansion for temperature ranging from 20 to 700 °C.

TABLE II. EXPANSION COEFFICIENTS OF Cs_2UO_4,UO_2, Al_2O_3 AND Cu

Materials	Cs_2UO_4	Cs_2UO_4	Al_2O_3*	UO_2*	UO_2	Cu*
References	Cu	Al_2O_3	-	-	Al_2O_3	-
Temperature (°C)	Expansion coefficient (10^{-6}/°)					
300	14,2	14,1	6,89	8,07	9,14	18,7
400	14,4	14,3	7,13	8,28	9,34	19,35
500	14,5	14,6	7,34	8,47	9,49	20,1
600	14,6	14,9	7,53	8,66	9,62	20,97
700	14,7	15,1	7,71	8,84	9,75	22,06

* *reference materials.*

3.4. Thermal conductivity

The thermal conductivity of caesium mono-uranate was measured in comparison with UO_2 and ZrO_2 samples. The figure 8 shows the principal results of these measurements.

Three samples of caesium mono-uranate with different relative densities (75% DT, 91% DT and 95% DT) have been measured. This gave us the opportunity to determine the best model able to define the influence of the porosity on the thermal conductivity of Caesium mono-uranate. Several correlations have been tested. The relations described by Schulz & al, Maxwell and Eucken [10-11] have been shown to be the most accurate formulation to account for the effect of the porosity on the thermal conductivity of the Caesium mono-uranate. These relations are :

$$K(T,por) = K(T,por = 0).\frac{2.(1.0-por}{2.0-por} \quad (1)$$

and

$$K(T,por) = K(T,por = 0).(1.0-por)^{\frac{3}{2}} \quad (2)$$

where por is the volume porosity fraction (-). The figure 9 shows then the thermal conductivity measured on caesium uranate samples, corrected to 100 % DT with the two formulations (1 and 2) and the polynomial approximation found from this plot is:

$$K(T,por = 0) = 8.89.10^{-7}.T^2 - 1.13.10^{-4}.T + 1.56$$

with

T: Temperature, °C
K: Thermal conductivity, $W.m^{-1}.K^{-1}$

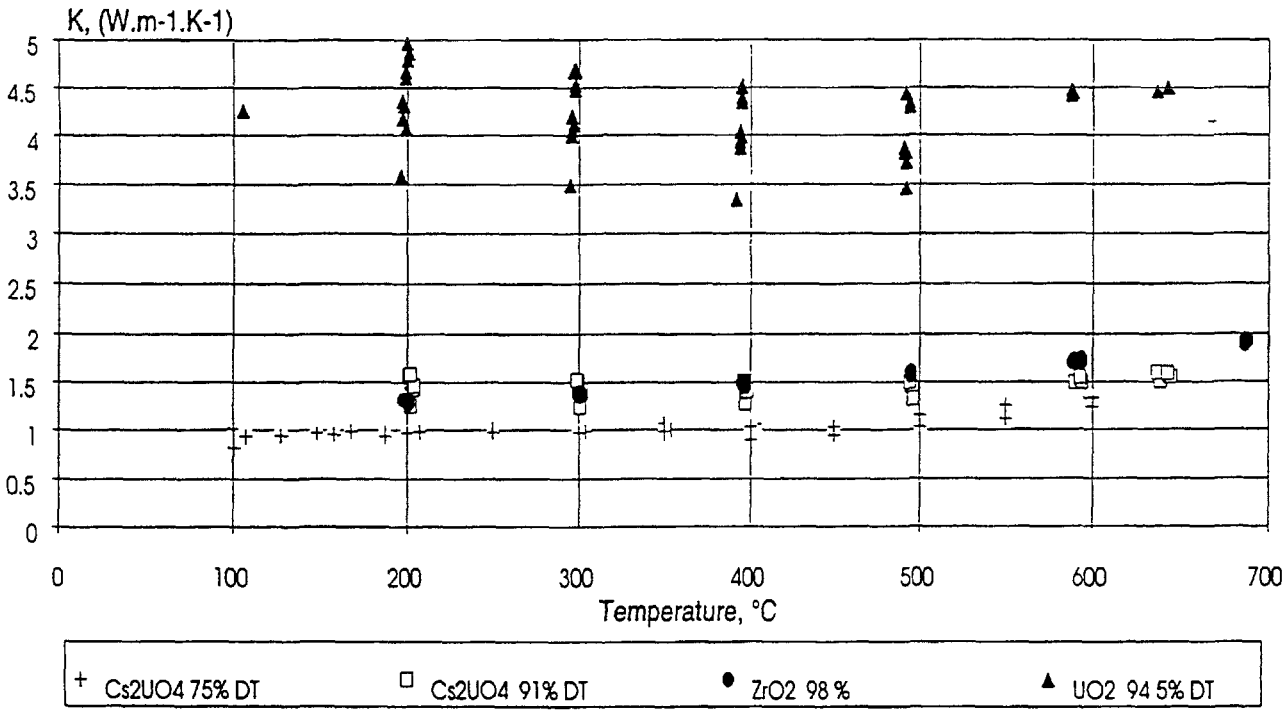

FIG. 8 Thermal conductivity of caesium mono-uranate, UO2 and ZrO2 samples.

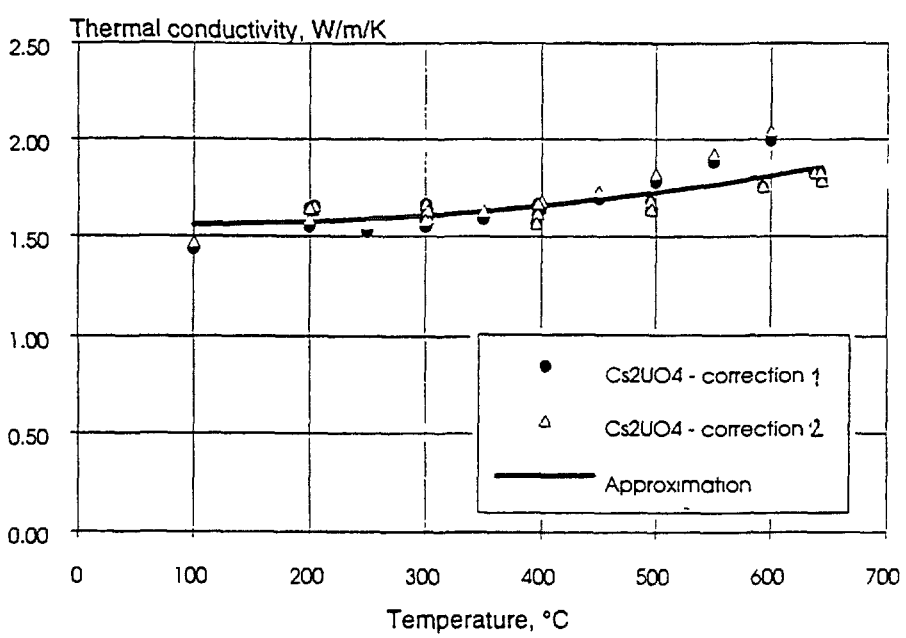

FIG. 9 Thermal conductivity of caesium mono-uranate corrected (100% DT).

4. CONCLUSIONS

The Caesium mono-uranate was obtained through a chemical reaction between Cs_2O_3 and U_3O_8 powders mixed together, pressed and heated at 670°C for 24 hours.

$$3\ Cs_2O_3 + U_3O_8 + 0{,}5\ O_2 \text{ ----> } 3\ Cs_2UO_4 + CO_2$$

The method allows a complete reaction, confirmed by a Debye Scherer X-ray analysis. The compound obtained was found chemically stable for temperatures below 800°C. The transformation threshold under neutral atmosphere is evaluated between 800 and 830°C. The decomposition schemes was found as follows:

$$2\ Cs_2UO_4 \text{ ----> } Cs_2U_2O_7 + Cs_2O$$

with a Cs_2O evaporation. That means that the compounds observed in a fuel rod at high burnup in the gap is a combination of several uranates in which Cs_2UO_4 and $Cs_2U_2O_7$ are the more likely.

From the powder obtained, samples were prepared, first by cold pressing then, improving the method, by hot pressing, and their properties were characterized. Mechanical compressive hardening tests allowed to evaluate the elastic modulus versus temperature in the range 200 to 800 °C. Furthermore the viscous character of the compound above 400°C was confirmed.

The thermal expansion coefficient of Cs_2UO_4 was found somewhat 40 % higher than the thermal expansion coefficient of UO_2. The thermal conductivity is about 1.5 to 1.8 W/m/K for temperatures ranging from 100 to 700°C, a value very similar to the UO_2 fuel thermal conductivity at high burnup in the same temperature range.

Coming back to the visco-plastic properties of the caesium mono-uranate one can expect that the presence of such a compound in the gap at high burnup, mainly at cracks lips tend to uniform the azimuthal stress distribution on the cladding. This is a benefit for PCMI during power ramps. Furthermore, if this type of compound is present at grain boundaries in the rim region, it can explain the propensity of this region to dissipate the energy in a micro-harness test (observed by SPINO et al [12]) better than in the center of the pellet.

ACKNOWLEDGEMENTS

The authors address thanks to Carlo SARI who participated actively in this project and gave much advice to the person in charge of the experiments. He is now retired. Thanks are also addressed to J.C.SPIRLET for the help brought in the sample manufacturing, J.F.BABELOT for the use of the facilities in his laboratory and R.FORST for the help on the rehabilitation of the mechanical testing machine.

REFERENCES

[1] CORDFUNKE E.H.P., OUWELTJES W. and PRINS G. Standard enthalpies of formation of uranium compounds Cs_2UO_4. Journal of Chemical Themodynamics,1986, Vol. 18, p.503-509.

[2] BOSE D.K., SUNDARESAN M., TANGRI R.P., KALYANARAMAN R., Some thermochemical studies of caesium uranate, molybdate and chromate. Journal of Nuclear Materials, 1985, Vol. 130, p.122-125.
[3] DHARWADKAR S.R., SHYAMALA M., CHATTOPADHYAY G. and CHANDRASEKHARAIAH M.S., Thermal stability of Cs_2UO_4 phase at high temperature. Transactions of the Indian Institute of Metals, 1983, Vol. 36, p.295-297.
[4] CORDFUNKE E.H.P , VAN EGMOND A.B. and VAN VOORST G. Investigations on caesium uranates-I: Characterization of the phases in the Cs-U-O system. Journal of Inorganic Nuclear Chemistry, 1975, Vol 37, p.1433-1436.
[5] O'HARE P.A.G.; HOEKSTRA H.R.Thermochemistry of uranium compounds : Standard enthalpy of formation of caesium diuranate. Thermodynamics of formation of caesium and rubidium uranates at elevated temperatures. Journal of Chemical Themodynamics, 1975, Vol. 7, p.831-838.
[6] FEE D.C and JOHNSON C.E. Phase equilibria in the Cs-U-O system in the temperature range from 873 to 1273 K. Journal of Inorganic Nuclear Chemistry, 1978, Vol. 40, p.1375-1381.
[7] LORENZELLI R., LE DUDAL R., ATABECK R. Etude hors-pile des réactions de UO2, PuO2 et (U,Pu)O2 avec le césium. CEA, IAEA-SM-236/87, p.539-563.
[8] BIOT J.B.Traité de Physique, Vol. 4, Paris 669, 1816.
[9] FOURIER J.B.J. The analytical theory of heat. Gautier-Villars, Paris, 1822; Traduction anglaise par Freeman, A., Cambridge University Press, 466 pages., 1878 ; Nouvelle Publication, Dover Publications, New York, 1955.
[10] SCHULZ B. Thermal conductivity of porous and highly porous materials. High Temp.-High Pressures, 1981, Vol. 13, p.649-660.
[11] EUCKEN A., VDI-Forschungsheft 353 (1932) p.6.
[12] SPINO J., VENNIX K., COQUERELLE M., Detailed characterisation of the rim microstructure in PWR fuels in the burnup range 40-67 GWd/tM, *Journal.of Nucl. Mater.*, vol 231, pp 179-190, 1996.

DISCUSSION

(Questions are given in italics)

Do you think that the Cesium Uranate properties may be useful for thermochemical codes?

Not directly but it gives indications on the way stress concentration at crack tips can evolve at high burnup when this kind of compounds are formed. Furthermore, the creep properties lead to conclude that if these compounds are present in subgrain boundaries it favors grain sliding.

Comment:

Cesium silicate and cesium nitronate have been studied, prepared and characterized at ECN.

Congratulations on performing an interesting and useful characterization on a compound that is often talked about, but is not well understood. Do you plan to measure stability of Cs alumina-silicates, proposed for Cs retention?

Cesium silicate and cesium nitronate have been studied, prepared and characterized at ECN.

THE FORMATION PROCESS OF THE PELLET–CLADDING BONDING LAYER IN HIGH BURNUP BWR FUELS

XA9847871

K. NOGITA, K. UNE
Nippon Nuclear Fuel Development Co., Ltd,
Ibaraki, Japan

Abstract

The bonding formation process was studied by EPMA analysis, XRD measurements, and SEM/TEM observations for the oxide layer on a cladding inner surface and the pellet-cladding bonding layer in irradiated fuel rods. Specimens were prepared from fuels which had been irradiated to the pellet average burnups of 15, 27, 42 and 49 GWd/t in BWRs. In the lower burnup specimens of 15 and 27 GWd/t, no bonding layer was found, while the higher burnup specimens of 42 and 49 GWd/t had a typical bonding layer about 10 to 20 μm thick. A bonding layer which consisted of two regions was found in the latter fuels. One region of the inner surface of the Zr liner cladding was made up mainly of ZrO_2 with a small amount of dissolved UO_2. The structure of this ZrO_2 consisted of cubic polycrystals a few nanometers in size, while no monoclinic crystals were found. The other region, near the pellet surface, had both a cubic solid solution of $(U,Zr)O_2$ and amorphous phase in which the concentrations of UO_2 and ZrO_2 changed continuously. Even in the lower burnup specimens having no bonding layer, cubic ZrO_2 phase was identified in the cladding inner oxide layer. The XRD measurements were consistent with the TEM results of the absence of the monoclinic ZrO_2 phase. Phase transformation and amorphization were attributed to fission damage, since such phenomena have never been observed in the cladding outer surface. Phase transformation from monoclinic to cubic ZrO_2 and amorphization by irradiation damage of fission products were discussed in connection with the formation mechanism and conditions of the bonding layer.

1. INTRODUCTION

Maximum fuel discharge burnup of light water reactors (LWRs) in Japan has been extended for the purpose of reducing the amount of spent fuels and improving the fuel cycle cost [1]. When increasing burnups, the pellet-cladding gap in fuel rods of LWRs tends to close up due to pellet swelling and cladding creep-down, until eventually a bonding layer is formed between the pellet and the cladding at high burnups [2]. This bonding can have detrimental effects on fuel rod behavior under irradiation, i.e. preventing the axial mixing of fission gases in a fuel rod and inducing a severe pellet-cladding mechanical interactions. In spite of the significance of bonding formation at high burnups, systematic studies on the formation process, based on detailed analyses of this region, are still lacking. Furthermore, only TEM results for a high burnup specimen of 49 GWd/t irradiated in a boiling water reactor (BWR) have been previously reported by us [3], leaving the burnup dependence on microstructural change, which must give valuable information for the mechanism of bonding layer formation, unstudied. In the light of this, we have examined the cladding inner surface and pellet-cladding bonding layer on high burnup fuels irradiated to a wide range of burnups (15-49 GWd/t) in BWRs. Bonding process details were elucidated using scanning electron microscopy (SEM), electron probe microanalyzer (EPMA), X-ray diffractometry (XRD), and transmission electron microscopy (TEM).

2. EXPERIMENTAL PROCEDURE

2.1 Fuel samples

The fuel specimens examined were taken from fuel rods base-irradiated in commercial BWRs. The pellet average burnups were 15, 27, 42 and 49 GWd/t. Owing to the neutronic rim effect, locally enhanced burnups at the pellet outer edge were about 30, 50, 80 and 100 GWd/t, which were derived from the Ce and Nd concentration profiles obtained by EPMA.

2.2 Examinations

Elemental analyses of U, Zr and fission product of Cs were carried out using a shielded EPMA. The measurement conditions were as follows: acceleration voltage, 20 kV; specimen current, 200 nA; beam diameter, 30,μm.

The XRD measurements were conducted by means of a shielded diffractometer with Ni-filtered Cu K_α radiation. The accelerating voltage and current were 40 kV and 30 mA, respectively. The diameter of the X-ray beam was 1.0 mm. Characterization of ZrO_2 crystal structure was obtained from diffraction lines between 20° and 60° in 2θ.

The samples for TEM were prepared by an ion milling technique. Small cubic pieces of cladding (including pellet in the case of bonding samples of 42 and 49 GWd/t burnups), about 1 mm on each side, were cut from each fuel using a cross cutter. The TEM specimens were embedded in inorganic cement within a 3 mm-diameter stainless steel washer and ground to a thickness of about 100 μm. Then, a dimple was made on the inner surface of the cladding using a dimple grinder. The thinning process was completed by ion micromilling with 5 keV argon ions. Microstructural observations were done by a 200 kV TEM. In addition to observation of the bright-field images, crystallographic information and composition analysis of constituent atoms in the oxide and bonding layer were scrutinized by selected area electron diffraction (SAD) patterns and an energy dispersive X-ray analyzer (EDX).

3. RESULTS

In the lower burnup specimens below 30 GWd/t, the bonding layer was not clearly observed by optical micrography, while the higher burnup specimens of 42 and 49 GWd/t had a typical bonding layer about 10-20μm thick. SEM images and characteristic X-ray images obtained by EPMA for the inner surface of Zr cladding of 27 GWd/t specimen and the bonding layer of the 42 GWd/t specimen are shown in Figs.1 and 2, respectively. The U concentration of the 27 GWd/t specimen is slightly higher on the surface of ZrO_2 film, which formed on the inner surface of the Zr cladding (Fig. 1). This small amount of uranium is expected to be transported from a slightly hyper-stoichiometric UO_{2+x} pellet via UO_3 gas species during an early stage of irradiation [14]. In Fig. 2, the bonding layer has slightly different contrast from the cladding and the UO_2 pellet appears to bond chemically to the cladding. The X-ray images of Zr, U and Cs reveal that (i) a ZrO_2 phase about 10 μm thick forms on the cladding inner surface; (ii) the subsequent mixture phase, composed of ZrO_2 and UO_2 and about 5 μm thick, is observed; and (iii) there is no significant enrichment of Cs in the bonding layer, while a slightly higher Cs concentration is observed in the UO_2 pellet. The third point suggests that

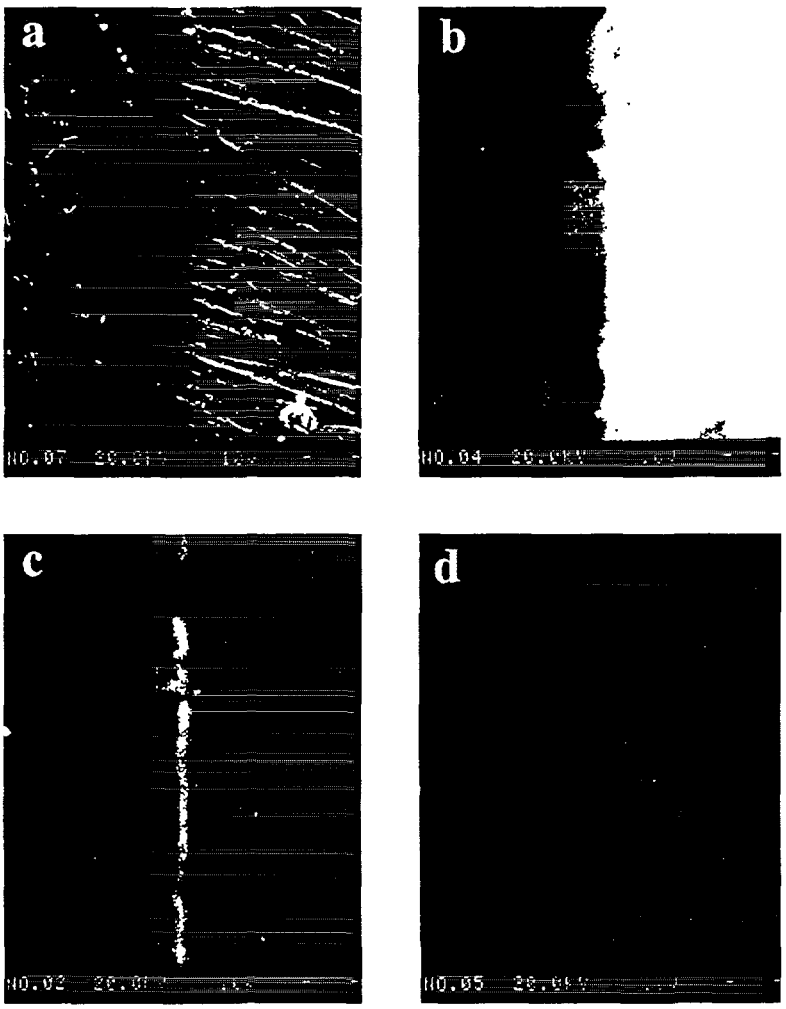

FIG. 1. An SEM image and characteristic X-ray images for inner surface of Zr cladding of 27 Gwd/t specimen: (a) SEM image; (b) Zr; (c) U; and (d) Cs

Cs transported from the pellet hot region does not play an important role in the formation of the bonding layer.

Figures 3a and 3b show XRD patterns of ZrO_2 of 15 and 27 GWd/t specimens, respectively. From the X-ray measurement conditions, effective thickness for the 90% X-ray reflection of ZrO_2 in 2θ (= 20-60°) is about 3.4-9.7μm. Therefore, these XRD patterns also indicate the presence of UO_2 at the surface of the ZrO_2 film and Zr cladding. The peaks of ZrO_2 in Figs. 3a and 3b distinctly demonstrate the cubic type ZrO_2 phase ((111) peak around 30.5° and (220) peak around 50.6°), but not the monoclinic phase. This result indicates that even in the lower burnup specimen having no bonding layer, the cubic ZrO_2 phase forms instead of monoclinic ZrO_2. The cubic ZrO_2 has also been identified at the oxide layer of a cladding inner surface (no bonding layer formed) by Ohuchi and Sakurai [4] in a sample, which was irradiated at the average fuel burnup of 28 GWd/t.

The bright-field TEM image and corresponding SAD patterns of the ZrO_2/Zr interface region of the 27 GWd/t specimen are shown in Fig. 4. The SAD pattern of A demonstrates the single crystal structure of hexagonal Zr metal. The oxide layer of B shows a cubic type ZrO_2 patterns. From the geometry of the SAD pattern, the radial distance, R, of the reflection

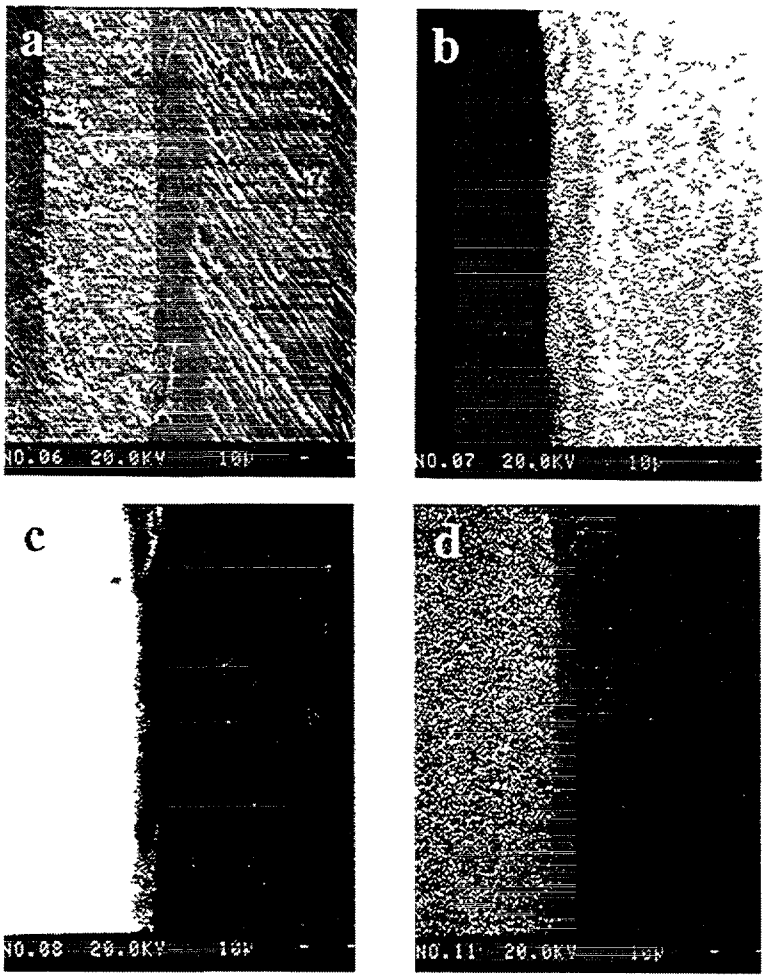

FIG. 2. *An SEM image and characteristic X-ray images for bonding layer of 42 Gwd/t specimen: (a) SEM image; (b) Zr; (c) U; and (d) Cs*

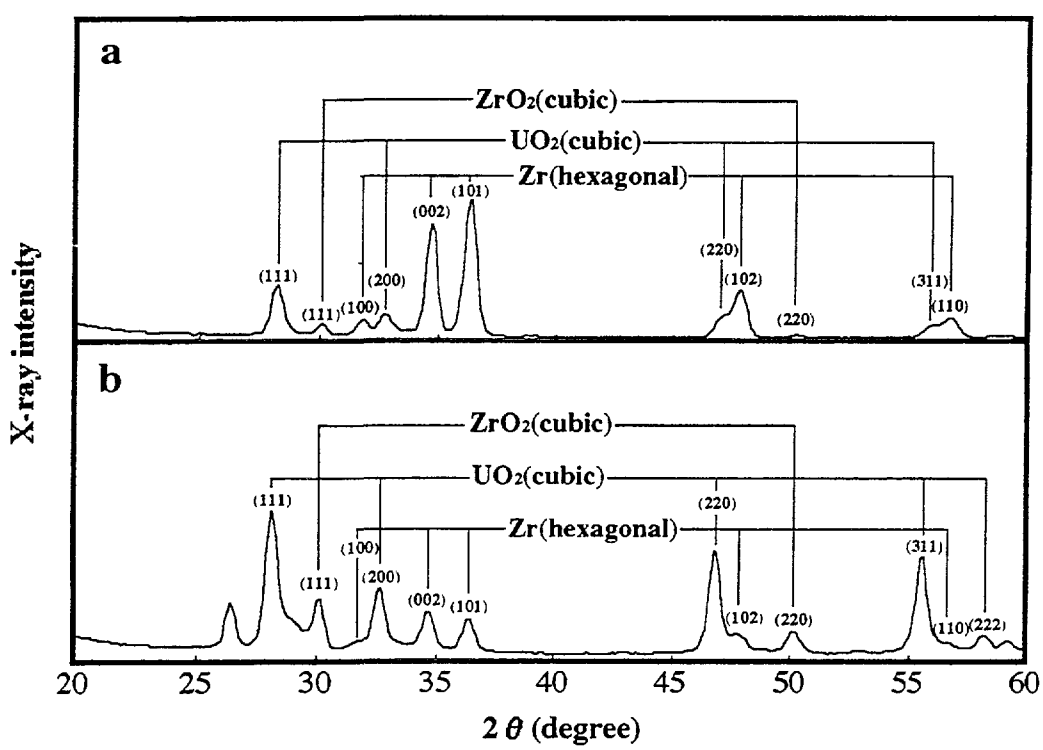

FIG. 3. *X-ray reflection patterns of inner surface of Zr cladding (a) 15 Gwd/t (b) 27 Gwd/t*

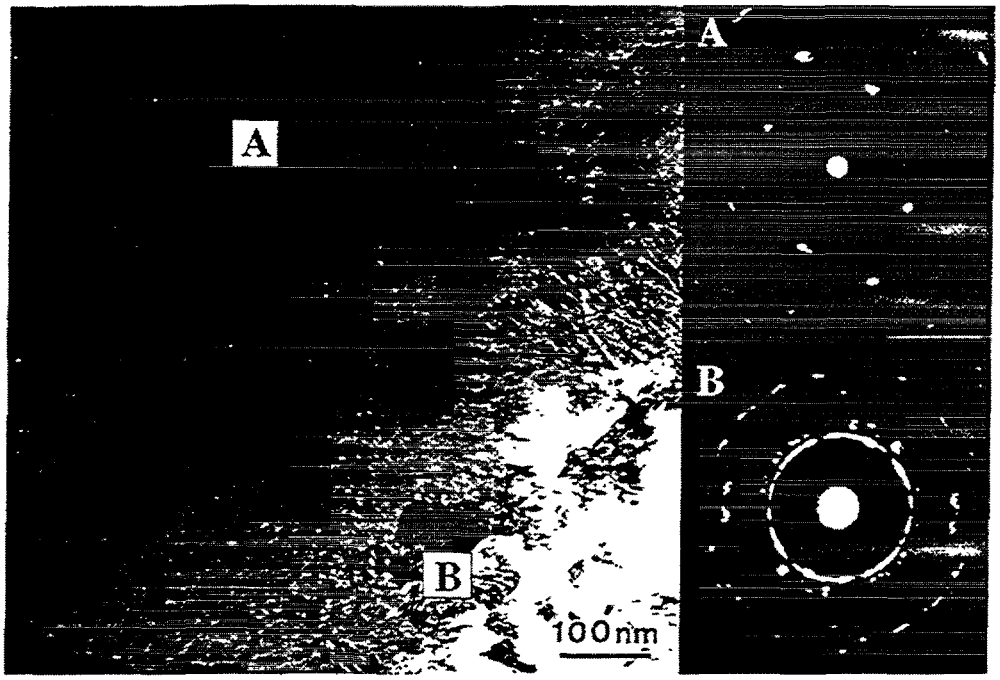

FIG. 4. The bright-field TEM image and SAD patterns of the ZrO_2/Zr interface region of 27 Gwd/t specimen: (A) single crystal structure of hexagonal Zr metal; (B) cubic ZrO_2/Zr structure

from the center of the pattern is expressed as R=L λ/d, where L is the camera constant, λ is the relativistic wavelength and d is the d-spacing of that reflection [5]. The radial distance, R, of the cubic ring B is in good agreement with the distance of cubic ZrO_2, but not that of UO_2. It is of note-that the crystal structure of ZrO_2 in this region consists of cubic polycrystals with a size of a few nanometers, while there is no monoclinic crystal form, which is the stable phase of ZrO_2 at temperatures below 1170 °C. This result is in good agreement with XRD results of 15 and 27 GWd/t specimens.

Figures 5 and 6 give TEM images and corresponding SAD patterns of the ZrO_2/Zr interface region and near the UO_2 pellet edge region of the 42 GWd/t specimen, respectively. In one region near the inner surface of the Zr liner cladding (Fig. 5), the ZrO_2 oxide film consists of cubic polycrystals, a few nanometer in size, but no monoclinic crystals. In a second region near the UO_2 pellet surface (Fig. 6), both a cubic solid solution $(U,Zr)O_2$ with the fluorite structure and an amorphous phase exist. The TEM image and SAD patterns of Fig. 6 indicate small grains of several nanometers in size, and mixing of cubic Debye-rings (such as (111), (200) and (220)) and an amorphous ring. From the reported phase diagram of the UO_2 -ZrO_2 system [6], a 100 % UO_2 system is cubic up to its melting temperature (2850 °C) with the lattice parameter of 0.547 nm. A 100 % ZrO_2 system, on the other hand, is monoclinic to 1170°C, tetragonal to 2300°C, then cubic to the melting temperature (2710°C) with the lattice parameter of 0.509 nm. According to the reported phase diagram, this second region near the UO_2 pellet surface with an irradiation temperature of 400°C is expected to be composed of cubic UO_2 and monoclinic ZrO_2. In the present case, having the lattice parameters of the cubic phases of UO_2 and ZrO_2 , d-spacings can be calculated, therefore, the ratio of (R_{UO2} /R_{ZrO2}) is 0.93, where R_{UO2} is the distance in UO_2 and R_{ZrO2} is that in ZrO_2. However, R of the Fig. 6 SAD pattern indicates a distance between those of RUO_2 and $RZrO_2$. This result suggests the presence of a cubic solid solution of UO_2 and ZrO_2, i.e. $(U,Zr)O_2$ phase.

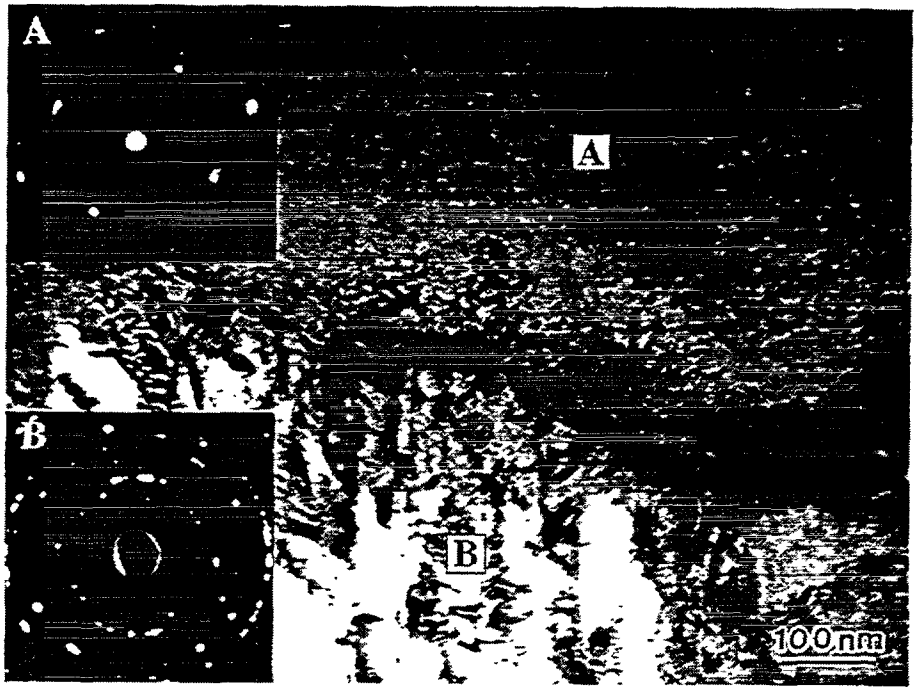

FIG. 5. *The bright-field TEM image and SAD patterns of the ZrO_2/Zr interface region of 42 Gwd/t specimen: (A) single crystal structure of hexagonal Zr metal; (B) cubic ZrO_2/Zr structure*

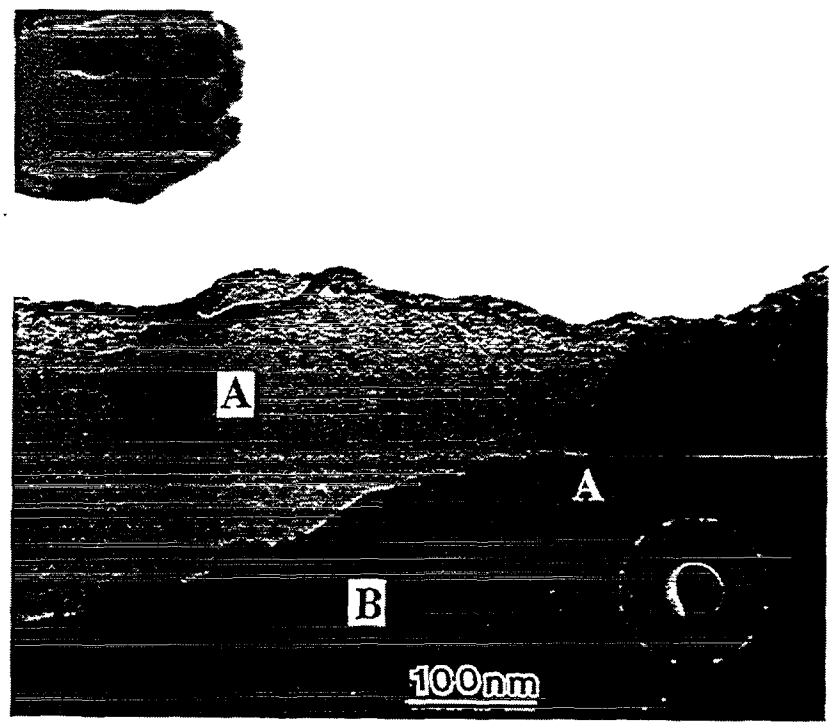

FIG. 6. *The bright-field TEM image and SAD pattern near the UO_2 pellet edge region of 42 Gwd/t specimen: (A) cubic solid solution $(U,Zr)O_2$ and amorphous phase; (B) UO_2 pellet*

Profiles of UO_2 or ZrO_2 concentration vs. distance from UO_2 fuel pellet outer edge and Zr liner cladding surface of 49 GWd/t specimen, obtained by EDX, are shown in Fig. 7. Results of these point analyses indicate that concentrations of Cs or other fission product (FP) elements are less than 1 at%. The concentration of ZrO_2 is more than 85% in the region about 12-13 μm from the Zr cladding surface, except for the region of the ZrO_2/Zr interface. On the other hand, the concentration of UO_2 is the highest at the UO_2 pellet edge, then gradually decreases to less than 15% at about 7μm from the edge. The reason for the higher UO_2 concentration at the ZrO_2/Zr interface is not clear, though, one possible explanation may be adhesion of evaporated UO_2 on the Zr surface at the beginning of the irradiation. The profiles indicate that the region from the cladding surface to 12-13 μm is mainly composed of ZrO_2 and the region from the pellet edge to 7 μm is composed of a mixture of UO_2 and ZrO_2. The corresponding TEM images and SAD patterns have been reported by us [3]. A mixture of cubic polycrystals with a few nanometer size and amorphous phase in the ZrO_2/Zr interface region, and a mixture of cubic solid solution of $(U,Zr)O_2$ and amorphous phase in the UO_2 pellet edge region were observed. These results are in good agreement with present results of 42 GWd/t burnup specimen. Namely, ZrO_2 forms on the cladding internal surface at the beginning of the irradiation, then the interdiffusion of U and Zr takes place with strong contact of UO_2 and ZrO_2 due to pellet swelling and cladding creep-down at high burnups.

4. DISCUSSION

4.1 Irradiation-induced phase transformation and amorphization

Phase transformation from monoclinic to cubic ZrO_2 can generally be attributed to the stress-induced phase transformation, formation of stabilized zirconia, and fission-induced phase transformation. The discussion below considers the possibilities that these three relate to the irradiation conditions of this bonding layer.

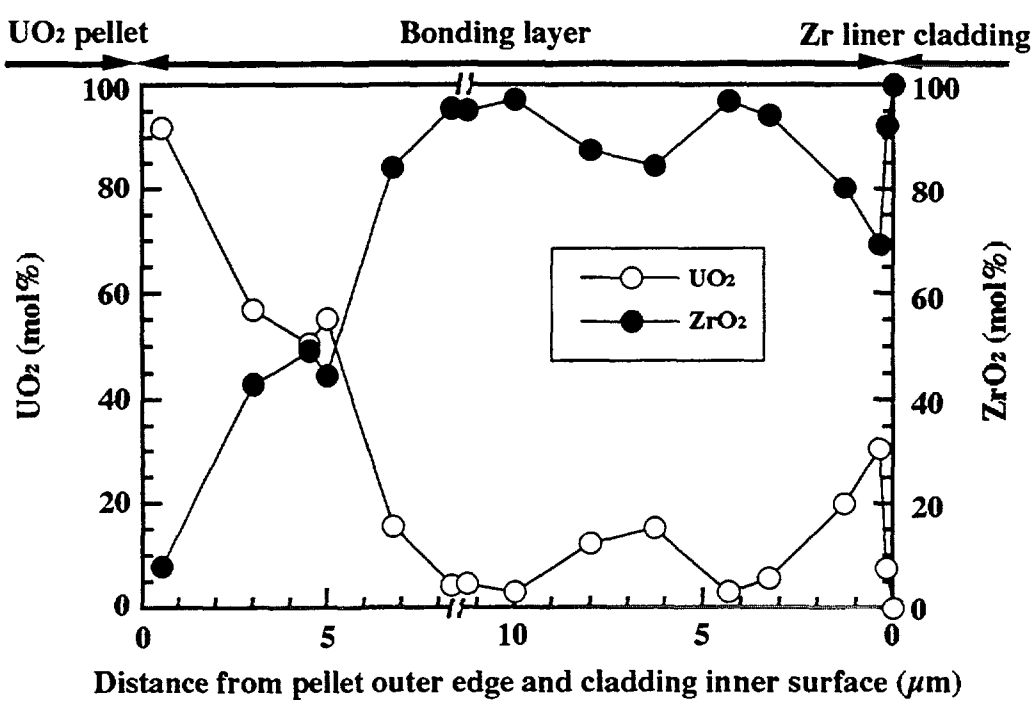

FIG. 7. Profiles of UO_2 or ZrO_2 concentration vs distance from UO_2 fuel pellet edge and Zr cladding inner surface of 49 Gwd/t specimen [3].

It is widely known that a monoclinic to tetragonal or cubic phase transformation takes place with stresses of about 3 GPa at around 400°C [7]. Stress at the bonding layer is expected to be caused by the following two factors. First of all, hoop stress (tensile stress) on the cladding inner surface, which is brought about by the pellet-cladding interaction (PCI) of the bonding layer, was calculated by a finite element method (FEM) program [8,9]. In the case of the linear heat rate of 280 W/cm, maximal hoop stress is estimated to be about 100-200 MPa. On the other hand, compressive stress of the radial direction is expected to be only 20-40 MPa. Therefore, the hypothesis of a phase transformation caused by PCI is unreasonable. Secondly, the stress at the interface of the ZrO_2 and Zr, which is attributable to the difference in volume between the oxide and the metal, brings about the phase transformation. According to TEM observations [5,10], and X-ray diffraction and Raman spectroscopy measurements [10,11] of Zry cladding outer surface (water cooling side), the oxide scales contain three phases, the monoclinic structure accompanied by some amounts of tetragonal and cubic forms. The order of magnitude of the mean compressive stress in the scales is expected to be higher than that of the critical level of about 3 GPa [11], though, due to the stress relaxation, the tetragonal and/or cubic phase is formed up to at most 1μm from the oxide-metal interface. Therefore, the phase transformation being caused by the stress at the interface of ZrO_2 and Zr is also unreasonable, since the whole oxide and bonding layer, about 10-20μm, is composed of cubic or amorphous phase.

Commercially used stabilized zirconia (cubic phase) is produced by adding the elements Y, Ca or Mg, which have lower valences than the +4 of Zr. As a rule, the amount of additional elements is about 8-10 mol% for the phase transformation from monoclinic to 100% cubic at around 400°C [12]. In the case of the oxide and bonding layer, concentrations of Cs or other FP elements, which have lower valences than Zr, could not detected by EPMA measurements. These results indicate that the possibility of formation of stabilized zirconia is low. Reported EPMA data [2], however, provided unequivocal evidence of a Cs-concentrated area in the bonding layer. Therefore, the role of Cs or FP elements in the bonding layer is still not clear and further study on their behavior is needed.

Fission-induced phase transformation of ZrO_2 is not a new phenomenon, being evident from early X-ray diffraction measurements by Wittels and Sherrill [13] and Wittels et al.[14]. ZrO_2 samples with known concentrations of fissionable impurities (U, Pu and Th) were subjected to thermal neutron dosages at irradiation levels capable of producing a partial transformation from the monoclinic to the cubic structure. The results indicated that fission fragment irradiations in the range of 10^{15}-10^{16} fissions/cm^3 ($4x10^{-5}$-$4x10^{-4}$ GWd/t) produced a monoclinic to cubic phase change in ZrO_2, though fast neutrons solely, cannot induce the phase transition.

From the results of the calculation using the Trim code [15], two widely different phenomena are thought to be taking place along the fission track (10 μm) in the ZrO_2 crystal. First, at the beginning of the fission fragment range (0-5 μm), energy is lost by electron excitation. In the electronic energy loss process, two mechanisms, the thermal spike model [16] and the Coulomb explosion spike model [17,18], have been proposed in order to explain how the energy lost in electronic excitation can induce atomic displacements. The thermal spike-model considers that the kinetic energy acquired by the excited electrons is transferred to the lattice by an electron-phonon interaction and it leads locally to an increase of the lattice temperature, with a possible melting followed by a rapid quenching. Assuming the thermal diffusion coefficient of ZrO_2 is $5x10^{-3}$ cm ^{2}/s at 400°C [19], which corresponds to the irradiation temperature of the bonding layer, transferred energy to the center of fission track

can be converted to a temperature increase of about 1.5×10^{4}°C in 10^{-12} s and 5×10^{3}°C in 10^{-11} s after collisions. This rapid quench can form a large number of interstitials and maintain the cubic phase of ZrO_2. The Coulomb explosion spike model, on the other hand, considers that the potential energy of the ionized atoms is directly converted into atomic motion due to repulsive Coulomb interactions. Secondly, near the end of the range (5-10μm), energy is lost by nuclear stopping and very high concentrations of interstitials may be produced by elastic collisions [20]. In either case, the electronic energy loss process and/or the nuclear energy loss process, the pressure-exerted by the interstitials would cause a collapse to a denser material, i.e. the more symmetrical structure of cubic ZrO_2 [14]. Fig. 8 summarizes the results of the burnup (fission dose) dependence of the transformed percentage from the monoclinic phase to the cubic one [13,14]. In this figure, burnup for the present results was estimated by taking a rough correlation of the pellet edge burnup. The value indicates that the fission dose of the bonding layer is sufficient to change phase. Therefore, the fission induced phase transformation from monoclinic to cubic is the most reasonable among the above causes.

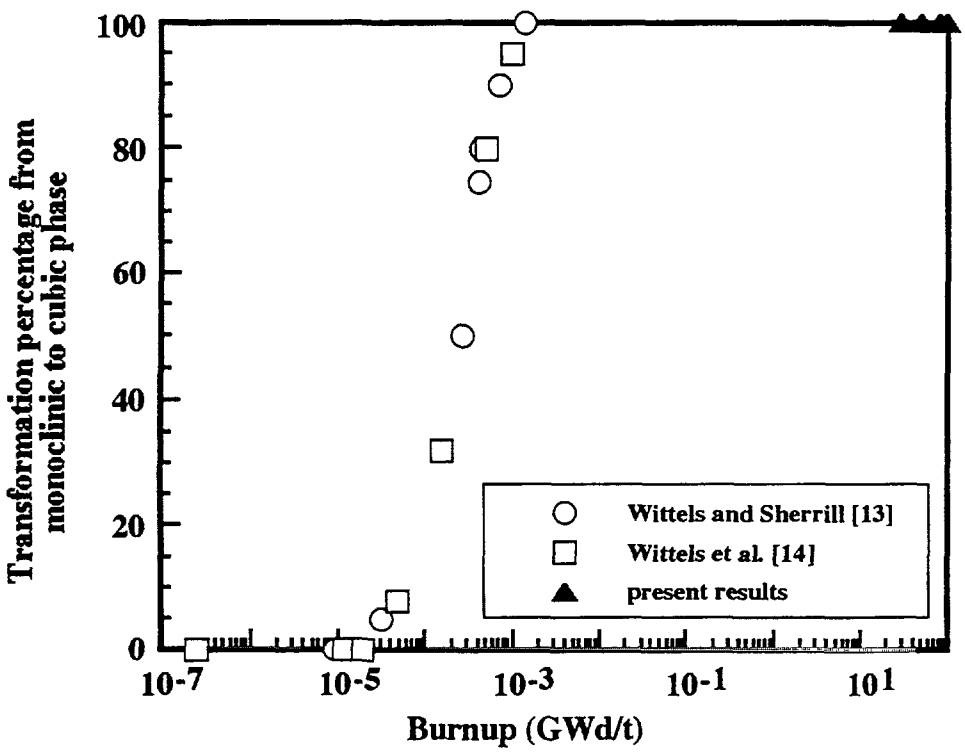

FIG. 8. *Burnup dependence of transformation percentage from monoclinic to cubic phase.*

From reviews describing radiation damage in insulators [21-23], irradiation-induced amorphization can be summarized as a function of structural topology (e.g., degree of complexity), melting point (e.g., bond strength), and bond type (e.g., degree of ionicity) to the critical amorphization dose. The crystal structure for the occurrence of amorphization in insulators indicates that single UO_2 and ZrO_2 are structurally stable to a high burnup in fission or at a high dose of ions. From the results of irradiated UO_2 pellets observations [24,25], the amorphous phase was not recognized, but the recrystallized structure of about 200 nm in size was seen, which was induced by the accumulation of radiation damage, in high burnup UO_2 fuels irradiated to 83-100 GWd/t ($2.1\text{-}2.5 \times 10^{19}$ fissions/cm^3). The bonding layer in the present study, on the other hand, shows the presence of the amorphous phase. The causes for

amorphization are not clear at present, though, one aspect has been reported by Joslin et al.[26]. Bombardment of the ZrO_2/Al_2O_3 interface region by 160 or 340 keV Cr+ and 475 keV Kr+ to a fluence of $4x10^{16}$ ions/cm^2 at room temperature could result in the formation of an amorphous, but single ZrO_2 and Al_2O_3 region. They concluded that the solid solution of ZrO_2 and Al_2O_3 brought about by ion mixing and irradiation-produced defects was necessary to produce the amorphous phase.

4.2 Formation mechanism and conditions of bonding layer

The derived formation mechanism of the bonding layer is summarized in Fig. 9. A key process for the formation of the bonding layer is the phase transformation of ZrO_2 oxide film from monoclinic to cubic phase. As discussed in section 4.1, usually the monoclinic ZrO_2 phase is stable at temperatures below 1170°C, even under in-pile neutron irradiation. In fact, ZrO_2 film formed on the outside surface of the cladding has been reported to have monoclinic and tetragonal structures [27]. The phase change of ZrO_2 identified in our examinations is attributed to fission damage. There are indications that fission products in the cladding, which were implanted by recoil, have been analyzed by a radiochemical technique [28,29]. Fig. 1 of the 15 GWd/t specimen shows, and Ohuchi and Sakurai [4] have reported, that small amounts of uranium are transported to the cladding inner surface from slightly hyper-stoichiometric UO_{2+x} pellets via UO_3 gas species during an early stage of irradiation. Therefore, monoclinic ZrO_2 film would be easily changed to the cubic phase even in low burnup fuels. The formation of a substitutional solid solution progresses during irradiation due to a strong contact between cubic UO_2 and ZrO_2 at higher burnups, which induces subsequent mutual diffusion of U and Zr.

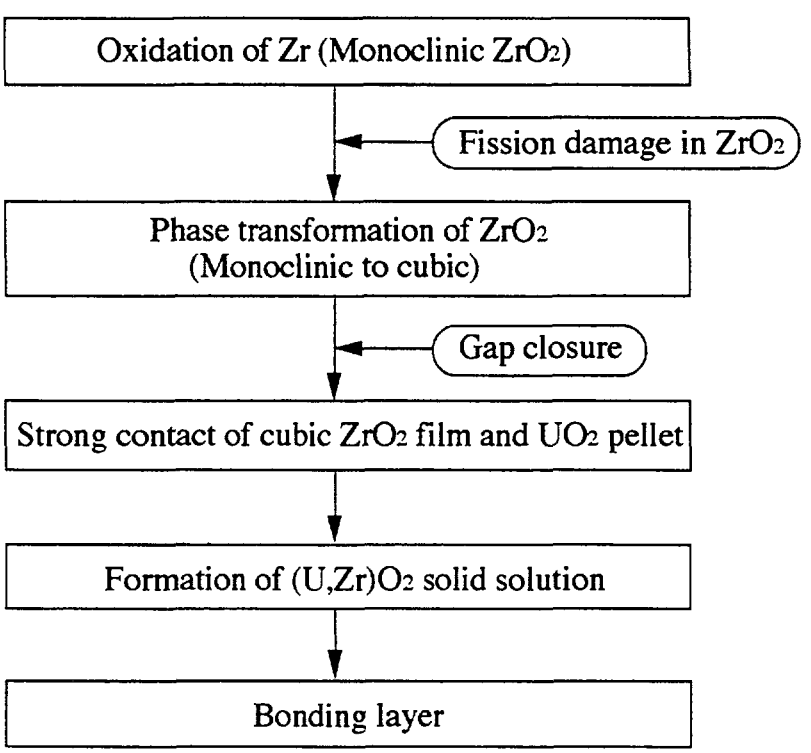

FIG. 9. Formation mechanism of the bonding layer.

For formation of the bonding layer, a strong contact between the cubic ZrO_2 film and cubic UO_2 pellet is essential. The pellet-cladding gap tends to dose due to pellet swelling and cladding creep down when increasing burnup. In both PWR [30] and BWR [31] fuel rods, residual gaps measured by a compression technique became narrower with higher burnups. Hence, the linear heat generation rates necessary to establish the strong contact can be calculated from the previously reported residual gap versus burnup data of LWR fuel rods, using a pellet thermal deformation model. The results are represented in terms of fuel burnup and average power in the last irradiation cycle in Fig. 10, in which the solid line gives the conditions for the hard contact. The data marked by an asterisk come from our detailed PEs for BWR fuels, and the others are based on ceramography for our and previously reported fuels irradiated in LWR conditions [4,30,32]. Full bonding is observed at high burnups above 50-60 GWd/t even at low powers around 150 W/cm. The predicted conditions for bonding formation in Fig. 10 are in good accordance with the PIE data.

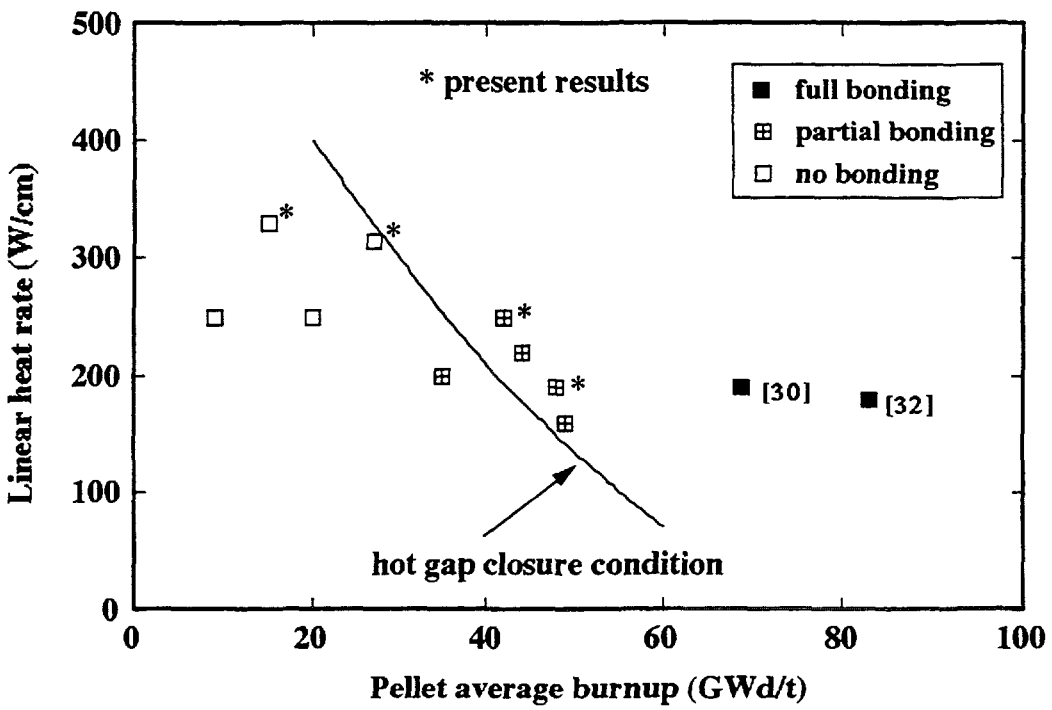

FIG. 10. Formation conditions of bonding layer

5. CONCLUSION

From the systematic examinations for cladding inner surface and pellet-cladding bonding layer of BWR fuels with 15, 27, 42 and 49 GWd/t burnups, by using SEM, EPMA, XRD and TEM, the formation mechanism of the bonding layer was clarified. Two regions were observed in the bonding layer (thickness: 10-20μm) of the high burnup specimens of 42 and 49 Gwd/t. In one region near the inner surface of the Zr liner cladding, a ZrO_2 layer consisting of cubic polycrystals was found, but no monoclinic crystals. In a second region near the UO_2 pellet surface, both a cubic solid solution of $(U,Zr)O_2$ and an amorphous phase existed, in which the concentrations of UO_2 and ZrO_2 changed continuously. The formation

of a substitutional solid solution progressed during irradiation due to a strong contact between cubic UO_2 and ZrO_2. Even in the lower burnup specimens having no bonding layer, the cubic ZrO_2 phase was also identified in the cladding inner oxide layer. The phase transformation from monoclinic to cubic ZrO_2 was attributed to fission damage.

References

[1] MUTO, S., YASUDA, T., HAYASHI, Y., KOYAMA, T., KOIZURNI, S., Proc. Int. Topical Meeting on LWR Fuel Performance, West Palm Beach, Florida (1994) p. 71.

[2] OISHI, M., Proc. IAEA Technical Committee Meeting on Fuel Performance at High Burnup for Water Reactors, Studsvik, Sweden (1990) p. 46.

[3] NOGITA, K, UNE, K, KOREI, Y. Nucl. Inst. Meth. B116 (1996) 521.

[4] OHUCHI, A., SAKURAI, H.: Proc. Int. Topical Meeting on LWR Fuel Performance, Williamsburg (1988) p. 180.

[5] PLOC, R. A., J. Nucl. Mater. 99 (1981) 124.

[6] ROMBERGER, K. A., BASE JR, C. F., STONE, H. H., J. Nucl. Chem. 29 (1967) 1619.

[7] ARASHI, H., ISHIGAME, M., Phys. Stat. Sol. (a) 71 (1982) 313.

[8] NERMAN, H., Nucl. Eng. Des.56 (1980) 289.

[9] NOBERGE, B. N., KING, J. S., WAS, G. S., ADAMSON, R. B., J. Nucl. Mater. 131 (1985) 126.

[10] BLANK, H., BART, G., THIELE, H., J. Nucl. Mater. 188 (1992) 273.

[11] GARZAROLLI, F., SEIDEL, H., TRICOT, R, GROS, J. P., Zirconium in the Nuclear Industry: 9th International Symp., ASTM STP 1132, C. M. Eucken and A. M. Garde, Eds., American Society for Testing and Materials, Philadelphia (1991) p. 395.

[12] YOSHIMURA, M., Am. Ceram. Soc. Bull., 67 (1988) 1950.

[13] WITTELS, M. C., SHERRILL, F. A., Phys. Rev. (Letters), 3 (1959) 176.

[14] WITTELS, M. C., STIEGLER, J. O., SHERRILL, F. A., Reactor Science and Technol. 16 (1962) 237.

[15] ZIEGLER, F. F., BIERSAK, J. P., LITTMARK, U. L, The Stopping and Range of Ions in solid (Pergamon, New York, 1985).

[16] TOULEMONDE, M., DUFOUR, C., PAUMIER, E., Phys. Rev. B46 (1992) 14362.

[17] DANLOP, A., LESUEUR, D., BARBU, A., J. Nucl. Mater. 205 (1993) 426.

[18] LESUEUR, D., DANLOP, A., Shim 92, Radiat. Eff. Def. Solids, 126 (1993) 163.

[19] RUDKIN, R. L., PARKER, W. J., JENKINS,R. J., "Thermal Diffusivity Measurements on Metals and Ceramics at High Temperatures", US Air Force Rept. ASD-TDR-62-24, 1-20, 1963.

[20] CARTER, G., ARMOUR, D. G., DONNELLY, S. E., WEBB, R., Radiat. Eff., 36 (1978) 1.

[21] EWING, R. C., Nucl. Instr. Meth. B91 (1994) 22.

[22] KELLY; R., Nucl. Instr. Meth. 182/183 (1981) 351.

[23] MATZKE, Hj. Radiat. Eff. 64 (1982) 3.

[24] NOGITA, K., UNE, K., Nucl. Instr. Meth. B91 (1994) 301.

[25] NOGITA, K., UNE, K., J. Nucl. Mater. 266 (1995) 302.

[26] JOSLIN, D. L, McHARGUE, C. J., WHITE, C. W., EVANS, N. D., Nucl. Instr. Meth. B91 (1994) 562.

[27] ILTIS, X., LEFEBVRE, F., LEMAIGNAN, C., J. Nucl. Mater. 224 (1995) 109.
[28] HIRABAYASHI, T., J. Nucl. Mater. 174 (1990) 45.
[29] VEHLOW, J., The Third Int. Conf. on Nuclear Fuel Reprocessing and Waste Management, Sendai, Japan, April (1991).
[30] MANZEL, R., COQUERELLE, M., BILLAUX, M. R., Proc. Int. Topical Meeting LWR Fuel Performance, West Palm Beach, Florida (1994) p. 335.
[31] SCHRIRE, D., SONTHEIMER, F., LYSELL, G., Proc. Int. Topical Meeting LWR Fuel Performance, West Palm Beach, Florida (1994) p. 212.
[32] BARNER, J. O., CUNNINGHAM, M. E., FRESHLEY, M. D., LANG, D. D., DOE/NE/34046-1 [HBEP-61 (3P27)], Battelle Pacific Northwest Laboratories (1990).

DISCUSSION

(Questions are given in italics)

What is the difference of oxide layer between cladding outer (water side) region and inner surface?

Bonding and phase transformation of ZrO_2 are caused by fission damage, so in the case of cladding outer region where there is no fission damage, only neutron damage, which is not important to change phase.

In Fig.10, formation condition of bonding layer depends on initial gap and/or BWR or PWR conditions, so this hot gap closure condition is not so correct?

I agree, this closure condition was obtained by Dr. Manzel's data of PWR fuel. Condition of BWR must shift toward higher burnup.

Tell me more details on UO_3 gas transport to Zr cladding surface at the early stage of the irradiation.

Because of the difference of O_2 potential, U is transported from a slightly hyper-stoichiometric UO_2.003-4 pellet via UO_3 gas species during an early stage of irradiation. This UO_3 changes to UO_2 because of Zr oxidation to ZrO_2.

The power of your fuel is low, so there are no Cs or Cs compound at the pellet-cladding gap?

I agree, but even low power and lacking of Cs, bonding layer had formed, so I think Cs does not play an important role in the formation of bonding layer.

Any differences for the bonding layer formation between Zr liner cladding and Zry-2 cladding?

I don't think there are any differences, because according to my formation mechanism of bonding layer, only strong contact of UO_2 and ZrO_2 and fission damage are the key.

DEVELOPMENT OF A MICROINDENTATION TECHNIQUE TO DETERMINE THE FUEL MECHANICAL BEHAVIOUR AT HIGH BURNUP

D. BARON, S. LECLERCQ
Direction des études et recherches,
Electricité de France,
Moret-sur-Long, France

J. SPINO
EC Institute for Transuranium Elements,
Karlsruhe, Germany

S. TAHERI
Direction des études et recherches,
Electricité de France,
Clamart, France

Abstract

One of the major problems that face the conceptors and users of nuclear power plants is the demonstration of the cladding integrity (the Zircaloy clad that contains the fuel pellets), particularly in class I and II operating conditions. A long term collaboration between EDF and the Applied Mechanics Laboratory (LMA) of Besancon (France) has existed for several years, and a unified modelling of the cladding has been developed in this frame. But a good understanding of the cladding response is not of total use if the mechanical solicitation applied to this clad by the fuel pellet is not completely known.

The potential evolution and the non-homogeneity of the fuel stiffness was recently demonstrated by Spino (TUI) on Vickers micro-hardness tests at room temperature. Thus, in order to get furthermore data, TUI and EDF decided to build a specific microindentation device able to perform the tests needed by the modellers.

After a brief recall of what the effects of irradiation are on the fuel pellet mechanical behaviour, this paper presents the microindentation device to be built, as well as the principles that underline its use. Finally, the way the experimental results will be used to determine the mechanical behaviour of the fuel pellet under irradiation is pointed out.

1. INTRODUCTION

One of the major problems that face the conceptors and users of nuclear power plants is the demonstration of the cladding integrity (the Zircaloy clad that contains the fuel pellets), particularly in class I and II operating conditions. The several phenomena that are responsible for the damage of the cladding during the fuel life are respectively the corrosion of the Zircaloy cladding, the irradiation effects that degrade the physical properties of the material, and the mechanical aspects. Thus, in parallel with the studies carried out in the frame of corrosion or irradiation, a good knowledge of the mechanical behaviour of the cladding must be developed. For instance, a long term collaboration between EDF and the Applied Mechanics Laboratory (LMA) of Besancon (France) has existed for several years, and a unified modelling of the cladding has been developed in this frame [1]. But a good understanding of the cladding response is not of total use if the mechanical solicitation applied to this clad is not completely known.

These mechanical solicitations are essentially internal pressure, external pressure and the mechanical action of the fuel pellet on the cladding in case of Pellet-Cladding Mechanical Interaction (PCMI). Thus it seems clear that stress concentrations (which are effective essentially in front of the crack lips) can be generated by the pellet upon the cladding, leading to a possibility of failure by corrosion under stress. One of the missions of EDF is to prove that such eventuality is negligible. Thus one easily understands the need of improvement concerning the phenomena that are responsible for the mechanical response of the fuel pellet, from the viewpoint of base irradiation as well as for power transient.

Many national and international programs have provided a great number of ramp tests in order to define the risk of failure against power change. The data base obtained exhibits an improvement of the fuel rod PCMI behaviour over an average burnup of 40 Gwd/tU. In order to properly simulate the fuel rod thermomechanical behaviour, the codes have to be provided with correct local material properties. It is obvious that the material properties are modified by irradiation. As burnup increases, the fuel is submitted to physical and chemical evolutions depending mainly on the local thermal conditions during irradiation. Unfortunately, few data exist today on spent fuel mechanical properties and the modellers must be satisfied with using non irradiated data.

The potential evolution and the non-homogeneity of the fuel stiffness was recently demonstrated by Spino et al [2] on Vickers micro-hardness tests at room temperature. Thus, in order to get further data, TUI and EDF decided to build a specific microindentation device able to perform the tests needed by the modellers.

The present paper is set out as follows: first, a brief recall of what the effects of irradiation are on the fuel pellet mechanical behaviour (the formation of the rim, which constitutes a good example of these effects, will be described briefly). Then, the microindentation device will be presented, as well as the principles that underline its use. Finally, the way the experimental results will be used to determine the mechanical behaviour of the fuel pellet under irradiation will be pointed out.

2. THE EFFECT OF IRRADIATION ON FUEL MECHANICAL PROPERTIES

2.1 The pellet bulk

It has just been mentioned that the mechanical properties of the fuel pellet are known, at present, only in the case of non-irradiated material.

Two major reasons can be laid down to explain this matter of fact .

- First, the performance of tests on irradiated materials is much more complicated than those on virgin materials, in particular for high temperatures. The mechanical properties tend to evolve differently in each point of the specimen as regards the local burnup and the local temperature history;
- Second, the way the specimen tends to fracture even at the beginning of the fuel's life prevents the performance of any "classical" mechanical behaviour (tensile tests, compression tests, ... on the specimen at the macro scale).

This is quite problematic as far as the mechanical properties evolution of the fuel pellet have to be properly known to be able to perform an accurate prediction of the fuel rod behaviour above three cycles. Thus it seems necessary to develop new investigation methods that are compatible with the physical state of the pellet.

The so-called rim (in fact the periphery of the fuel pellet) represents the state of the fuel where the mechanical properties are the most modified by irradiation. Thus, it constitutes a good basis to explore the dependance of the fuel pellet behaviour on irradiation.

2.2 The rim (figure 1)

There exist two stages for the rim formation. The first one can be observed with an optical microscope. It is characterized by the appearance of a very small porosity of the order of the micrometer. This porosity is intra and inter-granular and exists over quite a short distance (100 micrometers) in the periphery of the fuel pellet. The increase of the local burnup induces the disappearance of the initial granular texture and a restructuring of the lattice around the porosity. The new grains that are thus formed are very small (not exceeding 0,1 micrometer). Several works developed by EDF [3] have lead to a better understanding of the rim formation in particular concerning the evolution of the porosity.

The mechanisms that lead to the rim formation differ according to the different authors [4]. Generally one can consider three hypotheses. The first one is due to Matzke (TUI Karlsruhe) who points out the major role of the fission gases in the porosity increase. The second one, developed by Une (NFD), proposes the lattice internal energy evolution as responsible for the rim formation, thanks to the accumulation of stacking faults and fission products. The last possible explanation is the phase change in Uranium oxide.

The HBRP program will be able to allow a better understanding of the conditions of the rim formation and a good characterization of the physico-chemical material properties. Nevertheless, traditional mechanical tests are not of easy use on the sample pellets (5 mm diameter, 1 mm thickness), so in such a case new techniques such as microindentation may be of great interest.

3. THE MICROINDENTATION TECHNIQUE

3.1 The principle

This technique constitutes a key point in the future determination of the irradiation effects. Indeed, it will allow one to clearly identify the behaviour of a pellet with important loading history. The classical techniques failing in the frame of the mechanical tests, this method seems to be the best one to supply them.

The main idea is to perform mechanical tests on the fractured pellet, with the help of a microindenter, while all the parameters involved in the loading process are controlled. Thus, it must be possible to develop loading-unloading mechanical tests at constant rate (rational curve), creep tests (constant stress) as well as relaxation tests (constant strain). Thanks to this, and if one considers that the mechanical behaviour may present a certain homogeneity at a constant radius (but not along the whole radius !), one can obtain indentation curves and

micrographs of the imprint that may help the modeller to determine the macroscopic response of the material, at a given mechanical loading and different temperature levels.

Nevertheless, the experimental results that are available do not fully correspond to those obtained from classical mechanical tests. In particular, the shape of (σ, ε) curves is slightly different. This is due to the fact that the stress state induced by the microindenter is highly non-homogeneous. Thus one cannot *a priori* identify classical constitutive equations (in the sense of thermodynamics of irreversible processes [5, 6]), and it is necessary to develop an original identification method devoted to this type of tests. The most interesting idea, and the easiest to develop, consists in using the inverse problems theory in correlation with a finite element method to identify the parameters of an elastoviscoplastic model which would have been chosen *a priori*. In other words, it is planned to develop a "numerical indenter", which could be able to help the modeller to understand the experimental results, as well as to justify the choices made for the evolutions of the constitutive equations as regards the parameters involved in the irradiation process (in particular the local burnup and the porosity).

Moreover, one has to note that microindentation tests shall be coupled with acoustic microscopy ones, in order to easily get, with a good accuracy, the elastic material parameters (which are directly linked to the Rayleigh waves). Indeed, the knowledge of these parameters shall slightly lighten the inverse identification calculations, which will only focus on the non-elastic behaviour. The microacoustic technique will also be used to analyse local porosity spectrum, combining micro-echography at 15GHz with an image analysis device.

3.2 The project

As was already mentioned, the microindentation device shall be able to perform tests at constant strain rate (rational curve), at constant stress (creep tests), as well as constant strain (relaxation tests). A closed box allows the control of the atmosphere and prevents from an oxygen potential evolution during the test. The specimen support is controlled by a thermocouple and the local contact temperature between specimen and microindenter by an infra-red detector. The control of the indenter displacement is performed in such a way that bends and gaps will not influence the measurements. The load control is performed by a high precision load cell. A microscope next to the installation will allow the residual imprints characterization after the test.

A high accuracy translation system between the microscope and the microindenter is needed in order to target properly the indentation location before the test and find the correct imprint under the microscope after the test. Furthermore, the heating system must be part of the sample support for the same reason, to avoid a change in the sample geometry between the mechanical test and the imprint observation.

This microindentation device is developed in the frame of a long term cooperative program between Electricite de France and the Institute for Transuranium Elements. The end of building of the machine and the first tests are foreseen for mid 1997.

4. INTERPRETATION

The aim of the present part of the paper is to propose a brief overview of the possible constitutive equations that could be established thanks to the microindentation technique.

4.1 The viscoplastic material properties

Even if the Uranium dioxide is still a brittle ceramics at room temperature, the several phenomena that are involved in the irradiation process make it impossible to neglect the viscoplasticity of the fuel pellet at high temperature (T > 1300°C). Moreover, one can say that these aspects are of major importance during power ramps. Thus, it is important to develop models that are able to take into account this aspect.

One can identify two types of loading conditions during the fuel's life:

- The "base" conditions, during long time periods, where creep material properties are activated (see for instance [7]).

- The "power ramp" conditions, where phenomena are activated during quite short time periods. In these conditions, the mechanisms involved in the material mechanical behaviour are different. Processes such as hardening (or softening), as well as relaxation are concerned.

4.2 A need of more phenomenological simulation

It is clear that the phenomena described above must be taken into account in the constitutive equations derived from the experimental procedure. As a matter of fact, the behaviour laws available at the present time are only creep laws [7], which do not account for hardening processes.

Thus, the microindentation technique may help one to derive constitutive equations compatible with all aspects of the mechanical behaviour. In the frame of thermodynamics of irreversible processes, equations based on the local state postulate [8], assuming the existence of internal variables able to describe the macroscopic response of the material shall be established.

At the present time, the easiest way to proceed seems to choose a law of the type "hardening multiplicative viscosity", which form reads,

$$\underline{\dot{\varepsilon}}_{vp} = \frac{3}{2}\dot{p}\frac{dev(\underline{\sigma})}{\bar{\sigma}}$$

where

$\underline{\dot{\varepsilon}}_{vp}$ viscoplastic strain rate tensor

$\underline{\sigma}$ stress tensor

$\bar{\sigma}$ Von Mises equivalent stress

p cumulative viscoplastic strain formulated as follows:

$$\dot{p} = \left(\frac{1}{K}\frac{\bar{\sigma}}{p^{\frac{1}{m}}}\right)^{n}$$

K, m and n are constants derived thanks to the inverse method.

This kind of equation presents the great advantage to be representative of monotonous, creep and relaxation tests. Only isotropic hardening (dilatation of the viscoplastic potential) is taken into account by this law. In case such hardening would not be sufficient to simulate the experimental curves, it would also be possible to identify a "hardening-additive viscosity" rule, in which the choice of a kinematic hardening (translation of the viscoplastic potential) is possible. For instance, it has been shown that the simulation of the unloading behaviour may be different, depending on the use of a kinematic or an isotropic hardening approach [9].

For both types of equations, the irradiation effects are taken into account through the dependence of the plastic parameters (K, m, n) on internal variables such as the porosity or the local burnup. The microindentation tests will give several information to establish the correspondence between parameters and internal variables.

FIG. 1a *Fuel fractography at high burnup: the pellet center*

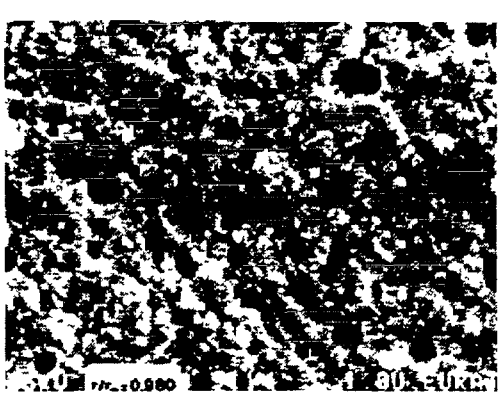

FIG. 1b *Fuel fractography at high burnup: the pellet rim exhibiting a high porosity level with a complete restructuring*

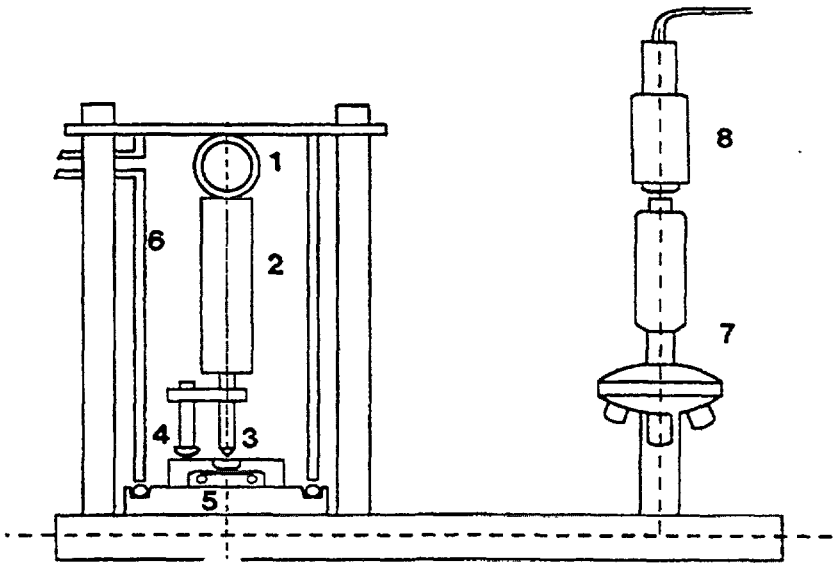

1	Load cell	5	H.T.sample holder and x-y table
2	Piezoelectric transducer	6	Vacuum chamber
3	Indenter	7	Microscope (x 1000)
4	Displacement sensor (LVDT)	8	Video-camera

FIG. 2 Microindentation device for high temperature application

5. CONCLUSIONS

The goal of the present paper was to present a new investigation method to derive the constitutive equations of the fuel at high burnup.

It has been shown that the classical experimental methods fail in this frame, because the fuel pellet tends to fracture even at the beginning of its life. Moreover, experimental results have shown that the fuel behaviour was not homogeneous along a given radius of the pellet, and the rim effect constitutes a good example of this.

So the development of a new experimental method, able to be efficient even on fractured samples, and also able to take into account the non-homogeneity of the material, was essential in order to derive models for the thermomechanical codes. The microindentation technique is one of these new methods, as well as the acoustic microscopy.

A microindentation device has been designed, and is at present time about to be built. It shall give information concerning the viscoplastic behaviour of the fuel pellet. A "numerical indenter" is also developed, in order to perform an accurate interpretation of the experimental tests. This will allow to derive models that are written in the sense of thermodynamics of irreversible processes, giving a broader range of applications than the conventional creep laws classically used.

REFERENCES

[1] DELOBELLE P., ROBINET P., GEYER Ph., BOUFFIOUX P., LE PICHON I., A unified model to describe the anisotropic viscoplastic behavior of Zircaloy-4 cladding tubes, 11th Symposium "Zirconium in the nuclear industry" ASTMSTP, Garmish-Partenkirchen, September 11-14, 1 995.

[2] SPINO J., VENNIX K., COQUERELLE M., Detailed characterisation of the rim microstructure in PWR fuels in the burnup range 40-67 GWd/tM, Journal.of Nucl. Mater., vol 231, pp 149190, 1996.

[3] HERMITTE B., Etude et Modelisation du Rim dans le combustible des crayons REP, PhD thesis, Universite Marseille II, may 1996.

[4] BARON D., Compte rendu de reunion technique du 26/02196 sur l'etude de la zone peripherique du combustible, 17 April 1996.

[5] RICE J.R., Inelastic constitutive relations for solids: an internal-variable theory and its application to metal plasticity, J. Mech. Phys. Solids, 19, 433-455, 1971.

[6] GERMAIN P., NGUYEN Q.S., SUQUET P., Continuum thermodynamics, J. Appl. Mech., Transactions of the ASME, 50, 1010-1020, 1983.

[7] OLANDER D.R., Fundamental aspects of nuclear reactor fuel elements, Technical Information Center, Office of Public Affairs, Energy Research and Development Administration, 1976.

[8] LEMAÎTRE J., CHABOCHE J.L., Mécanique des Matériaux Solides, Dunod, 1985.

[9] MURAKAMI Y., MATSUDA K., Analysis of Vickers Hardness by the Finite Element Method, Transactions of the ASME, vol 61, 822-828, December 1994.

DISCUSSION

(Questions are given in italics)

Is the vacuum in the test chamber not likely to influence the results, especially for high burnup specimens?

We are able to study material behavior in different atmospheres. Don't you think that by performing the micromechanical tests under vacuum you will modify mechanical properties of the irradiated fuel which might depend on the oxygen potential?

Indeed the measurement will not be performed under vacuum. The chamber will be first evacuated but then filled up with a gas mixture (i.e. CO/CO_2 mixture), in order to determine the mechanical properties under different oxygen potentials. In fact, the objective is to determine the creep and stress relaxation property as a function of O/M.

IN-REACTOR PERFORMANCE OF PROTOTYPE SBR MOX FUEL

C. BROWN, J. MULLEN
BNFL International Group,
British Nuclear Fuels Plc,
Sellafield, Seascale, Cumbria

I.D. PALMER
LWR Business Unit,
British Nuclear Fuels Plc,
Springfields

United Kingdom

Abstract

As part of the international Callisto experiment, BNFL have undertaken the base irradiation, ramp testing and post-irradiation examination of two fuel rods, manufactured by BNFL's Short Binderless Route (SBR) for MOX fuel. Although of only short (lm) length, the rods were in other respects of standard PWR geometry. Base irradiation was performed in the Callisto loop of the BR2 reactor and achieved burn-ups of 17 GWd/tM, 28 GWd/tM peak pellet, at moderate to high power levels. No problems were encountered during base irradiation, confirmed by intermediate examination.

In a separate BR2 capsule, a ramp test was then performed on one of the two rods. Again, the rod showed no problems and was discharged intact. The ramp test conditions employed were somewhat more onerous than the level corresponding to the best-estimate failure level for standard UO_2 fuel. The survival of the rod confirms the general observation that the PCI failure resistance of MOX fuel is superior to that of standard UO_2.

The irradiation has been followed by a detailed programme of non-destructive and destructive hot-cell examinations on both of the rods. Profilometry, ECT and gamma-scanning confirmed the overall satisfactory performance of the rods and the absence of incipient damage. Puncture testing and gas analysis showed the fission gas release levels in both the ramped and unramped rods to be in line with what would be expected for a UO_2 rod. The satisfactory microstructure of the fuel was confirmed via optical ceramography and autoradiography.

This paper will describe the fuel manufacture, base irradiation and ramp test conditions, and will provide a summary of the results of the PIE programme.

1. INTRODUCTION

The first fuel assemblies containing MOX fuel pellets made by BNFL's Short Binderless Route (SBR) were loaded into the Beznau 1 PWR in mid 1994. Since the loading, the fuel has been successfully irradiated through two cycles and is now under its third cycle at an average assembly burn-up of about 25 Gwd/tM. When the cycle is completed some fuel rods will be selected for destructive PIE to review the performance against prediction.

This paper provides a summary of the results of irradiation tests on the first SBR fuel produced in development facilities at Sellafield. Included is a brief summary of the irradiation conditions and PE results obtained. The test was part of the CALLISTO program managed by Belgonucleaire using the BR2 reactor. The BNFL ENIGMA fuel performance code is currently being used to analyse and interpret the results obtained.

Two rods, UK1 and UK2, one metre long but with otherwise standard 17×17 assembly dimensions were loaded into the CALLISTO rig of the BR2 reactor in October and August 1992 respectively. The two rods contained MOX fuel manufactured by BNFL in laboratory facilities using the Short Binderless Route. Following the base irradiation and non destructive examination of both rods, UK2 was selected for ramp testing in a Pressurised Water Capsule (PWC) in BR2 followed by non destructive examination. The fuel was irradiated to a peak pellet burn-up of ~29 GWd/tM and the measured peak power sustained by the rods was 456 W/cm. Both rods were then subjected to a number of destructive tests.

2. EXPERIMENTAL CONDITIONS

Fabrication

The fuel was produced in BNFL's laboratories via the short binderless route. The SBR uses a high energy attritor mill to blend the UO_2 and PuO_2 powders to achieve a homogeneous product at both the microscopic and macroscopic scales in a fraction of the time required for a conventional tumble ball mill. Following milling the mixture is spheroidised, pressed into pellets, sintered and the pellets checked to ensure that the stringent manufacturing specifications are satisfied prior to being sent for rod fabrication. The fuel fabrication data for UK1 and UK2 is given in Table 1. Figure 1 shows the fuel fabrication flow sheet.

Base irradiation conditions

The BR2/CALLISTO power history for the base irradiation of UK1 and UK2 is given in Figures 2 and 3, which show the mean and peak pellet powers sustained by the fuel during their 18 and 19 irradiation cycles respectively. The rods were irradiated to a calculated peak pellet burn-up of 27.0 GWd/tM (UKI) and 28.1 GWd/tM (UK2) and to a calculated mean burn-up of

TABLE I. FABRICATION DATA FOR RODS UK1 AND UK2

		UK1	UK2
Fuel:			
type	-	MOX	MOX
Pu_{fiss}/ U+Pu	w/o	4.0	4.0
U235 enrichment	w/o	0.282	0.282
Pellet:			
diameter	mm	8.179-8.204	8.179-8.204
length	mm	8.560-11.099	8.560-11.099
dish - diameter	mm	4.70-5.20	4.70-5.20
- depth	mm	0.191-0.292	0.191-0.292
chamfer - length	mm	0.051-0.203	0.051-0.203
- width	mm	0.508	0.508
Cladding:			
material	-	Zry 4	Zry 4
diameter - outer	mm	9.462-9.537	9.462-9.537
- inner	mm	8.319-8.394	8.319-8.394
wall thickness	mm	≥0.526	≥0.526

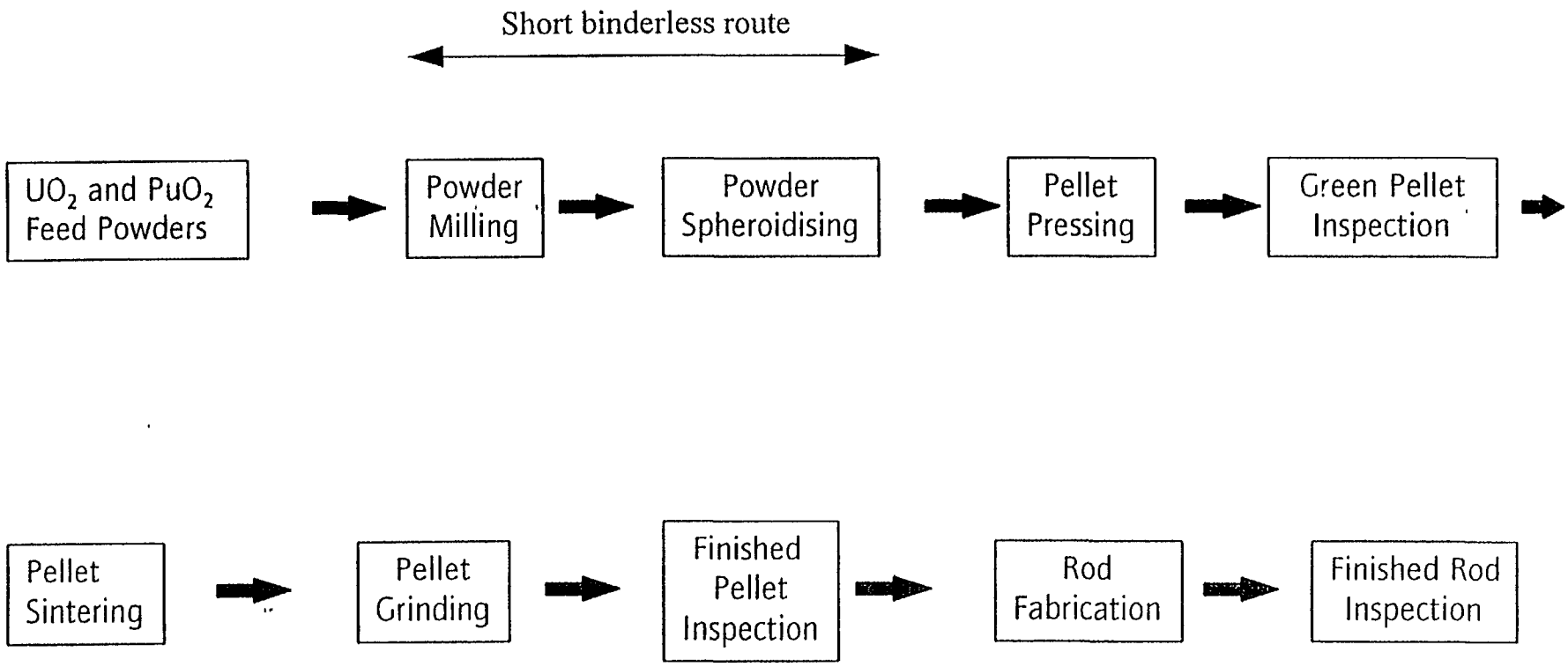

FIG. 1. Fabrication of MOX fuel using SBR

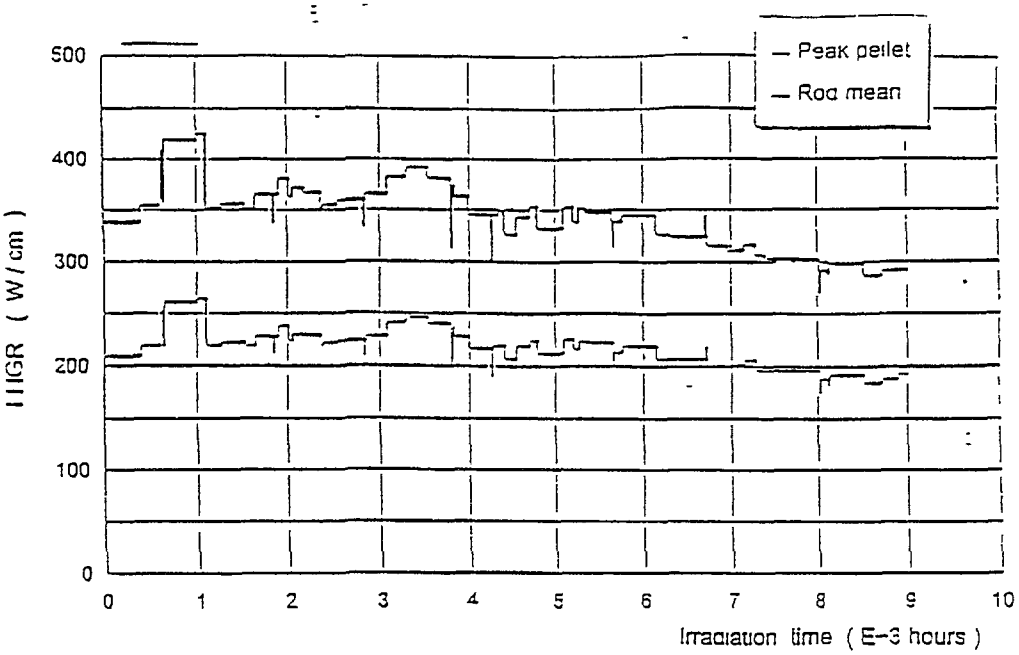

FIG. 2. Power history for UK1

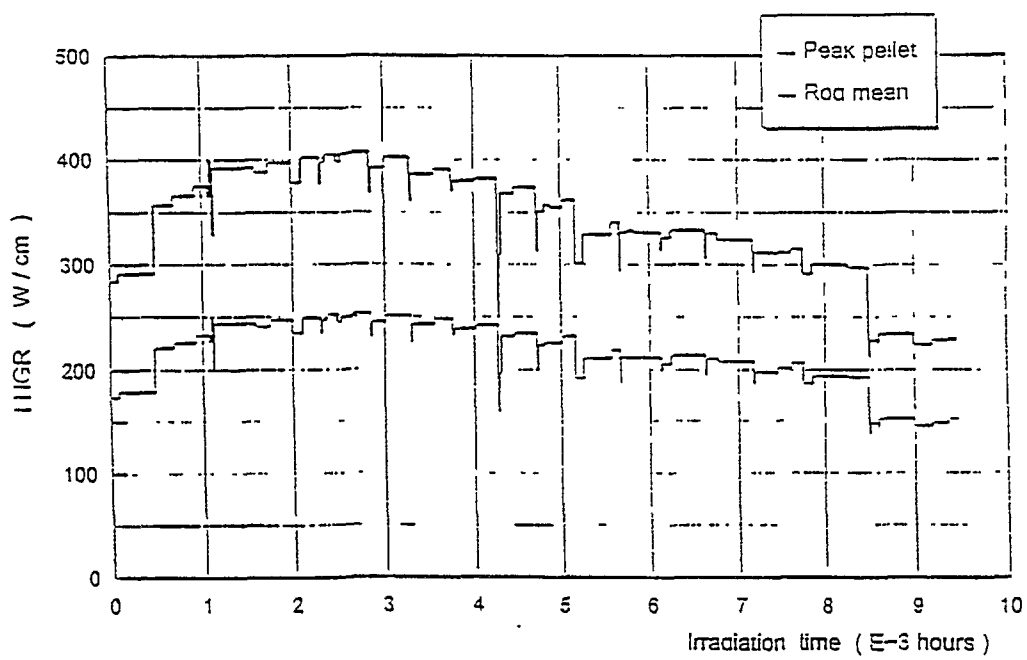

FIG. 3. Power history for UK2

17.1 GWd/tM and 17.8 GWd/tM respectively. Figure 4 shows the calculated base irradiation burn-up profiles for UK1. From the power history profiles the rod peak and average ratings obtained for UK1 were 425 and 217 W/cm and those for UK2 were 407 and 215 W/cm respectively.

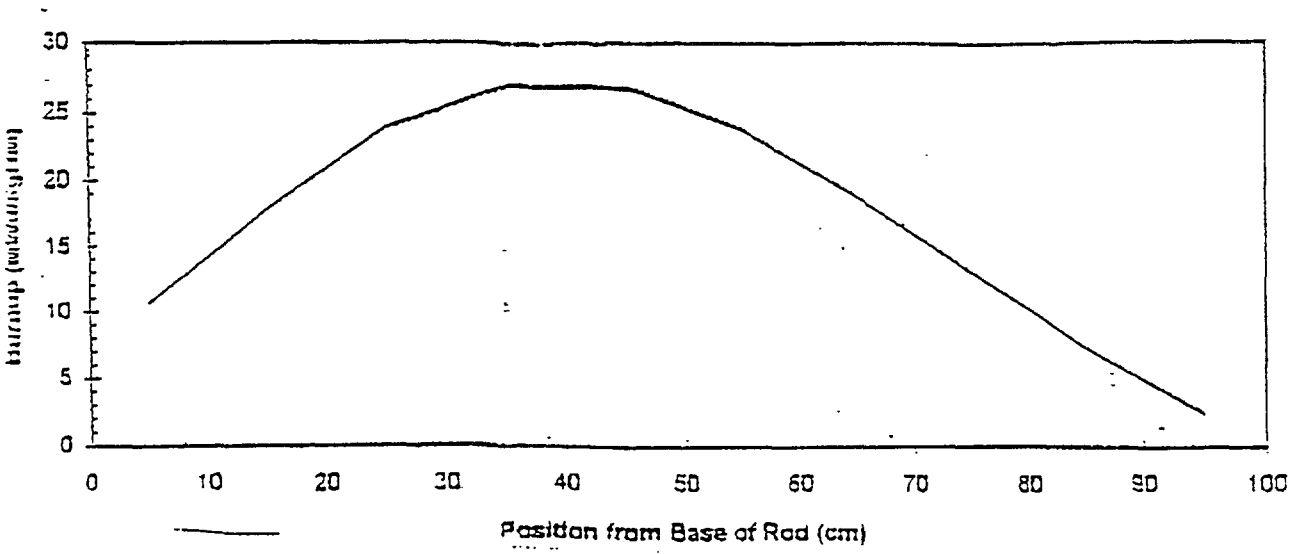

FIG. 4. End of life burn up profile for UK1

Ramp testing of UK2

The BR2/Pressurised Water Capsule ramp conditions were chosen to be slightly more onerous than the level corresponding to the best - estimate failure level for standard UO_2 fuel and consisted of the following:

- Preconditioning for 52 hours at 257 W/cm
- Fast ramp rate of 97 W/cm/min
- Hold for 12 hours at a peak power level of 418 W/cm
- Reactor shut down at 50 W/cm min

Post- irradiation examination

The PIE programme includes:

- Visual inspection - to confirm rod integrity.
- Diameter profile measurements - to determine the fuel swelling behaviour.
- Gamma scanning - to give information on the fuel column stability. The gross gamma profile is used to evaluate the axial burn-up distribution.
- Neutron radiography - to give information on the fuel column stability.
- Eddy current testing - to provide information about any clad defects present and the external oxide thickness on the fuel rod cladding.
- Puncture tests - to determine the fission gas release (FGR) from the total amount of Xe and Kr gases collected and gives the free volume inside the rod.
- Ceramography - to characterise the fuel and cladding microstructurally (fuel crack pattern, fuel porosity, fuel grain size, clad hydride distribution, fuel/clad interaction, etc.).
- Autoradiography - to show qualitatively any plutonium/uranium redistribution within the fuel and also the fission product distribution.
- Electron microscopy - to investigate the composition of the fuel and any bonding layer present.
- Density measurements

Samples were cut from each of the rods for ceramography, metallography, α/β autoradiography, local γ-scanning and density determination. The density measurements have yet to be completed, whilst electron microscopy of the samples is not due to commence until mid-1997.

3. RESULTS AND DISCUSSION

Fuel column stability

Both fuel rods were irradiated successfully without any failure occurring. There was no significant change in the fuel column length of UK2 pre and post ramp. Figures 5 - 7 show the gross gamma profiles of unramped UKl, UK2 and ramped UK2. The maximum power was experienced in the area of 340-520 mm from the rod base for both rods.

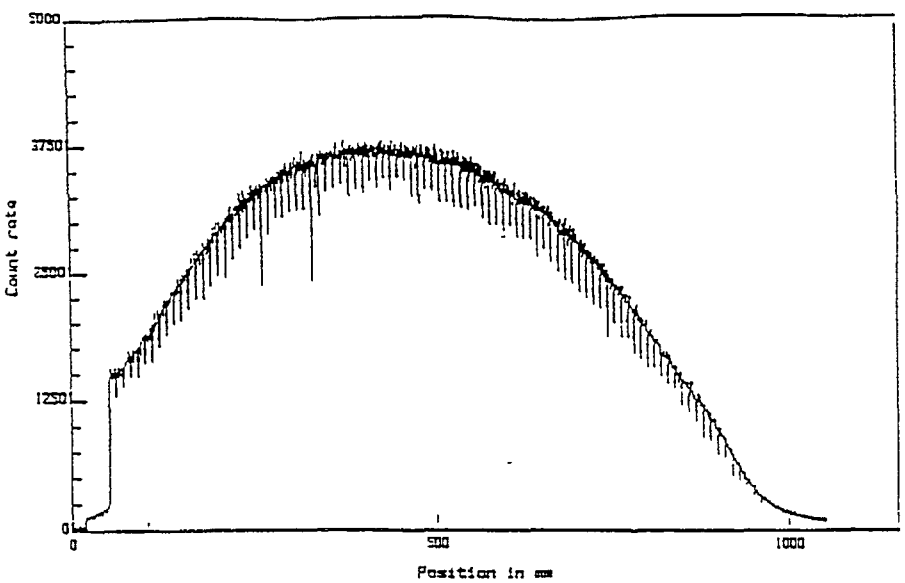

FIG. 5. Gross gamma activity scan of UKl

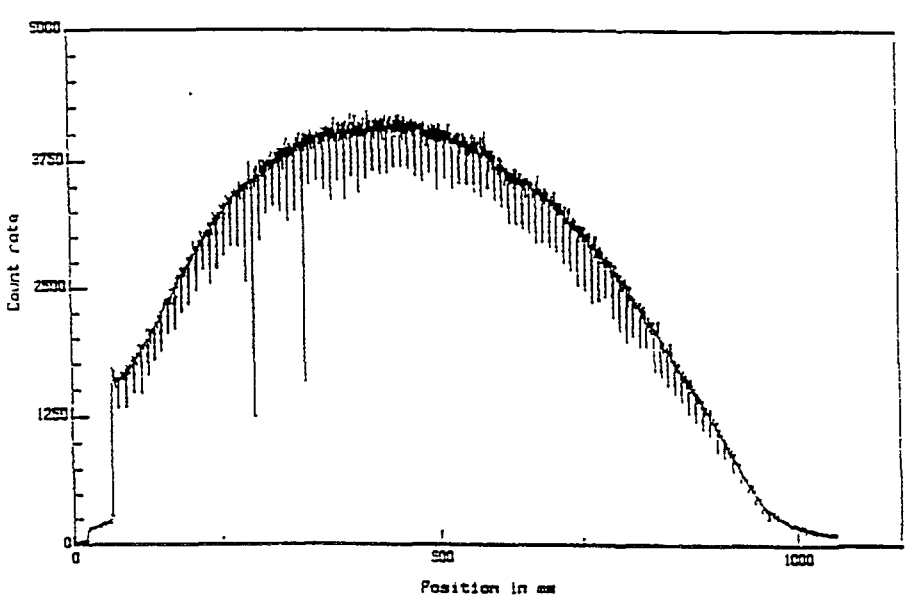

FIG. 6. Gross gamma activity scan of UK2 unramped

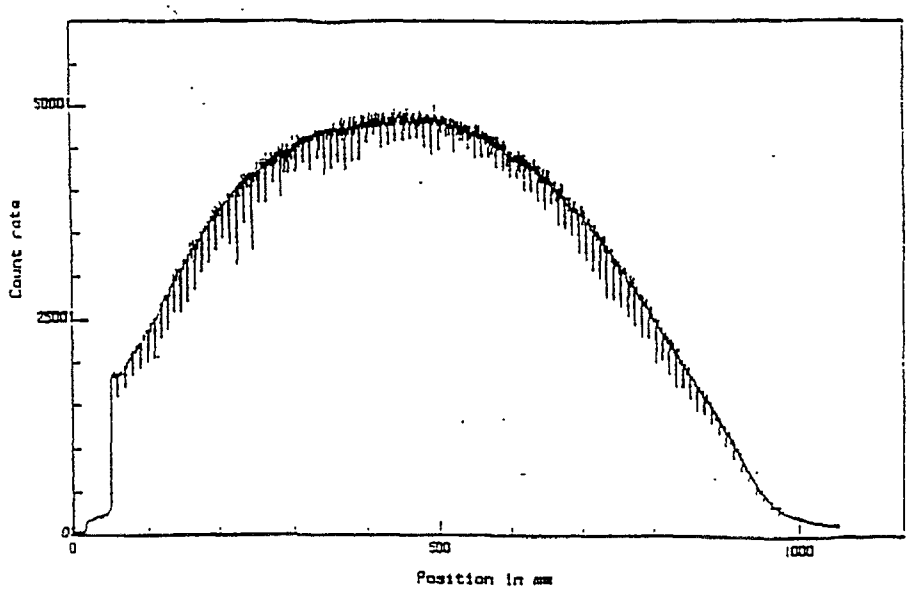

FIG. 7. Gross gamma activity scan of UK2 ramped

The gross gamma activity profiles after both the base irradiation and ramping were characteristic of LWR MOX fuel - no abnormal behaviour was observed. The pellets were well defined with some inter-pellet gaps visible in the lower part of the fuel column. The gross gamma activity scan of UK2 after the ramp test, however, with its shorter inter-pellet dips, implied that pellet separation was less pronounced due of fission product swelling.

Neutron radiography of unramped UK1, UK2 and ramped UK2 confirmed the gross gamma activity profiles; no abnormal features were observed. The fuel had undergone only slight fragmentation and some small inter-pellet gaps (< 0.5 mm) were seen in the bottom part of the fuel column. Slight dimple filling was observed in the hottest pellets in the ramped rod.

Fission gas release

The results of rod puncture testing and gas analysis were in good agreement with those predicted based on the power histories sustained by the rods. The fission gas release for UK1 (peak power rating of 425 W/cm and calculated peak pellet burn-up of 27 GWd/tM) was 4% and that for ramped UK2 (peak power rating of 407 W/cm and calculated peak pellet burn-up of 28.1 GWd/tM) was ~7 %; both values are consistent with other data available for LWR fuel irradiated under similar conditions.

Both rods experienced very high peak power levels, and therefore high peak temperatures, during the early stages of their base irradiation. While thermally activated release would be expected, the gas inventory at these low burn-ups would be so low that the absolute level of release would be small. The temperatures during these early stages would also be sufficiently high to promote significant fuel grain growth, and this was confirmed by the ceramography. The increase in grain size would be expected to lead to an improvement in the gas retention during the subsequent irradiation. These unusual irradiation conditions, for which modelling codes are not well tuned, make it difficult to assess whether the release levels observed during the base irradiation were significantly different from what would be expected for standard UO_2 fuel.

The increment of release due to the ramp test cannot be established precisely, but is clearly of the order of a few percent. This is consistent with the expectation for UO_2 fuel subjected to a similar ramp.

Fission product distribution and burn-up

The axial burn-up distribution of UK2 pre and post ramp was determined using the long lived Cs^{137} fission product profile. The local measurements confirmed that volatile fission products (Caesium, Iodine and Tellurium) had migrated to the pellet interfaces.

Axial distribution gamma spectroscopy profiles for the short lived isotopes were as expected for the end of life power experienced for UK1 and UK2. Following ramp testing of UK2 the axial distribution gamma spectroscopy profiles for the short lived Ba^{140}/La^{140} fission product isotopes were representative of the BR2/Pressurised Water Capsule power axial distribution.

The mean burn-up was determined using the Cs^{137} activity measurements and gave values of 18.1 GWd/tM for UKl, 18.4 GWd/tM for UK2 with peak pellet burn ups of 28.9 GWd/tM (UKl) and 29.4 GWd/tM (UK2). There was no difference between the values determined for the peak pellet and mean rod burn-up for UK2 pre and post ramp.

A total UK2 ramp rod power of 306.3W/cm was measured (with an accuracy of $< \pm$ 10%), with the measured peak power sustained by the rod during its ramp test being 456W/cm, which was in satisfactory agreement with the power determined by thermal balance.

Rod Swelling/ elongation

The rod elongation of UK1 was +0.24 % and +0.21 % for UK2 after base irradiation. After ramp testing and base irradiation the total rod elongation of UK2 was +0.25 %.

Diameter profiles for UK1, UK2 unramped and ramped were as expected for MOX fuel irradiated under such conditions. The profilometries showed an increase in the diameter of the fuel rods with some evidence of cladding creep down along the fuel column and of ridging, implying a degree of fuel clad interaction during irradiation. Primary ridges were observed at the bottom and top parts of the fuel column with secondary ridges seen in the mid to lower section of the rods. In the maximum power zone fuel swelling led to significant reduction of the cladding creep down effect. After the power ramp the mean diameter of the UK2 rod showed some creep out in the high power zone. The ridge height and aspect were not significantly modified by the ramp. Eddy current testing of the rods confirmed the results of the rod profilometries.

The rods were fabricated with a radial fuel-clad gap of 80 microns. For the cladding material used, and for the burn-up experienced, cladding creep-down would be expected to close this size of gap for only a small region near the peak power location. The observation from the profilometry is of some fuel-clad contact over a region of the rods, amounting to around half of the rod length. This is the case after the base irradiation of both UKI and UK2, and becomes even more pronounced after the ramping of UK2. All three profiles are indicative of appreciable fuel swelling in the hottest fuel regions. Superimposed on the overall profiles is clear evidence of both primary ridging (at pellet-pellet interfaces) and secondary ridging (at mid-pellet locations), throughout the regions of hard fuel-clad contact. Peak ridge heights are around 25 to 30 microns,

with no significant change caused by the ramping. Again these observations are consistent with those seen for other LWR MOX fuel irradiated under similar conditions.

Cladding Outer Oxidation

The cladding outer oxide layer thickness measured on the ceramographic samples from UK1 and UK2 was in the region of 2 to 10μm.

Structural changes

Macroscopic ceramographic examination of sections of the rods revealed fuel crack patterns which were characteristic of fuel which had been irradiated at the power levels achieved in this experiment. The modifications which occurred during irradiation were normal for the irradiation conditions experienced and are as follows:

- Both rods showed significant grain growth from the as-fabricated value.
- The as-fabricated fine porosity (typically $< 1\mu$m), disappeared early in life over the whole pellet radius by irradiation induced densification.
- Intergranular porosity of small size and similar density was observed in the central zone of the peak power sample of both the unramped and ramped rods. These were formed due to gaseous fission products precipitating when solubility limits were exceeded. The size and number of pores depend on the local enrichment, burn-up and temperature
- When the fuel temperature increased, i.e going towards the pellet centre, thermally activated phenomena were increasingly apparent:
  - plutonium diffusion in the (U, PU)O_2 matrix
  - grain growth
  - diffusion of gaseous fission products to the grain edge and the appearance of intergranular porosity
- The plutonium diffusion in the (U, PU)O_2 matrix intensified with temperature.

In the case of UK1 and UK2 rods it was observed that after irradiation significant grain growth had occurred at the centre of pellets which had experienced peak ratings of 425 W/cm.

The crack patterns in the α autoradiographs confirmed the optical micrographs and correlated well with the β/γ autoradiography

6. CONCLUSIONS

Two MOX fuel rods containing prototype SBR fuel have been irradiated in the CALLISTO experiment to peak pellet bum-ups of 27 and 28 Gwd/tM. One of the rods was ramp tested and

survived conditions slightly more severe than those expected to cause 50% of standard UO_2 rods to fail. The irradiation was complemented by an extensive PIE programme which showed:

- The rods remained intact with no abnormal features and no indications of incipient cladding damage.

- Fission gas release during the base irradiation was around 4% and accompanied by appreciable fuel grain growth (consistent with the high early-in-life power levels); the end-of-life gas release for the ramped rod was 7%, which was consistent with data obtained for other LWR fuel irradiated under similar conditions.

- Fuel-clad contact occurred over an extended region of the rods around the peak power location, accompanied by primary and secondary clad ridging. The fission gas bubble swelling in the hottest fuel regions showed the anticipated population of grain boundary bubbles, together with an additional population of intragranular bubbles.

The results show that the irradiation behaviour of the prototype SBR fuel was typical of other MOX fuels with no abnormal features being observed.

HIGH TEMPERATURE MECHANICAL TESTS PERFORMED ON DOPED FUELS

C. DUGAY, A. MOCELLIN, Ph. DEHAUDT, M. SLADKOFF
Nuclear Reactor Directorate,
Service for Fuel Behaviour Studies,
Grenoble, France

Abstract

The high-temperature compressive deformation of large-grained UO_2 doped with metallic oxides has been investigated and compared with that of pure UO_2 with a standard microstructure. All the specimens are made from a single batch of UO_2 powder. Tests with constant applied strain rate of $20\mu m.min^{-1}$ show that Cr_2O_3 additions cause a decrease in the flow stress of about 15 MPa compared with the reference material. When reduced in hydrogen at 1500°C the specimens present a peak stress close to the flow stress of the pure UO_2. Measurements of creep rates are made at 1500°C at applied stresses varying from 20 to 70 MPa. Cr_2O_3 additions increase the creep-rate, up to several orders of magnitude-change from the pure material to a doped one. All the doped materials exhibit power-law creep with exponents in the range of 4.9 to 6.3. The activation energy varies from 466 to 451 kJ/mol depending on the dopant concentration. The creep of the undoped material is divided into three regimes of deformation depending on stress. At low stresses the strain rate shows a second power dependence on stress. At high stress levels a higher stress dependence is observed. The creep power-law breaks down and an exponential law holds true at higher stresses. The activation energies are found to be 410 and 560 kJ/mol in the low- and high-stress regions respectively. The former value is in good agreement with the grain boundary diffusion energy in stoichiometric polycrystalline uranium dioxide and the latter corresponds to that found for self-diffusion energy of uranium. Creep behaviours are discussed in terms of deformation mechanisms.

1. INTRODUCTION

The current trend in research work on UO_2 fuel is towards increasing burnup and maintaining operational manoeuvrability. This assumes that the fuel rod is capable of resisting power ramps without failing. Care must be taken to ensure that, even at maximum operating temperatures, the direct contact between cladding and-fuel does not lead to excessively high tensions in the cladding or in the fuel.

The aim of UO_2 doping is to reduce fission gas release at high burnup and the pellet cladding mechanical interaction. By using appropriate additives, the fuel microstructure will be modified. The mechanical properties of UO_2, and its creep behaviour in particular, are sensitive to these modifications [1-3]. It is therefore necessary to characterize the doped fuel in order to be able to predict its in-pile behaviour.

Cr_2O_3 is a crystal growth activator and is among the various additives that could be envisaged in this context. It was therefore decided to study the influence of this additive on mechanical fuel behaviour.

2. EXPERIMENTAL TECHNIQUES

2.1 Sample characteristics

Five batches of PWR-geometry pellets, without dishing, were tested: one undoped batch serving as a reference and four doped batches. These pellets were manufactured from a single batch of dry route uranium dioxide supplied by FBFC[1]. Additions were made at levels of 0.025 to 0.2 wt % Cr_2O_3 in UO_2. The mixture of powders was dry blended by ball-milling. The mixture was then sintered under $H_2+1.7\%H_2O$ atmosphere at 1700°C, thereby restricting the hyperstoichiometric range of UO_2 to $x_{max} = 5.10^{-4}$ and promoting crystal growth. After grinding the cylindrical surface, the ends of the samples were ground parallel using a specially constructed jig. The physical characteristics of the sintered materials are given in Table I. Grain sizes were determined from linear intercept measurements on polished and etched sections of the specimens.

2.2 Deformation apparatus

All deformation tests were conducted by compression in a suitably adapted furnace on a screw-type Instron machine.

The furnace, with tungsten resistance and shields, is designed to operate under secondary vacuum or under an inert (argon) or reducing (hydrogenated- argon) atmosphere up to a temperature of the order of 1900°C. The temperature of the furnace and the sample is monitored by two WRe5%/WRe26% thermocouples to an accuracy of 0.5°C.

The specimen is placed between the rams of the machine at room temperature and a load of about 3 MPa is applied. The machine automatically maintains this load during the heating cycle. When the testing temperature is reached and stabilised, the test force is applied.

The crosshead movement is defined from a speed range of 0.5 μm to 1 $m.min^{-1}$. The testing machine is equipped with a load servo-system which drives the crosshead motion to ensure that a constant load is applied during the creep test.

The strain value is obtained by extensometric measurements (LVDT [2] direct measuring device), crosshead motion and measurement of sample height before and after the test. The variation in experimental parameters is recorded on a graphical recorder. A computer-based data logging and processing system then plots the strain curves.

3. RESULTS

Conventional compression tests were performed, during which the temperature, stress or strain rate parameters were kept constant. The tests were performed at 1500°C, except

---

[1] Franco Belge de Fabrication du Combustible

[2] Linear Variable Differential Transformer

TABLE I. PHYSICAL CHARACTERISTICS OF SINTERED SAMPLES

Cr2O3 content (wt %)	Theoretical density (%) ±0.2	Mean grain size (μm)
0	96.8	7
0.025	95.8	15
0.06	97.0	27
0.1	97.5	45
0.2	97.6	70

where otherwise indicated, under an atmosphere of argon with 5% hydrogen to maintain the samples at stoichiometry during the experiment.

3.1 Tests with constant applied strain rate

The tests were conducted at a crosshead speed of 20 $\mu m.min^{-1}$, corresponding to a strain rate of 9%/h.

The stress-strain curves (Fig.1) show that the addition of Cr_2O_3 lowers the fuel flow stress-by about 15 MPa.

Heat treatment for reducing the Cr^{3+} ions to Cr metal under H_2 atmosphere at 1500°C increases the maximum stress to a value close to that of the reference fuel, with the emergence of a stress peak, regardless of the additive content. This peak, occurring at a low strain level, increases with heat treatment duration. Figure 2 illustrates this phenomenon for the batch doped with 0.06 wt %Cr_2O_3.

The emergence of a strain peak is associated with the progressive transformation of the oxide to metal during reduction. A peak is generally observed when the initial density of mobile dislocations is not sufficient to allow deformation according to the imposed strain rate [4]. This phenomenon may occur when the dislocations are pinned and must be freed. A stress sufficient to pull dislocations away from pinning points is necessary to initiate deformation. Once sufficient dislocations are moving, the stress drops. This is probably the case here, where the metallic precipitates form potential pinning points for the dislocations.

3.2 Creep tests

Creep was studied between 20 and 70 MPa.

Generally, the creep rate $\dot{\varepsilon}$ is given by a law of the form: $\dot{\varepsilon} = A.\sigma^n .\exp(-Q / R.T)$, where A and n are constants, σ the applied stress and Q the creep activation energy. The values of the stress exponent $n = (\delta \ln\dot{\varepsilon} / \delta \ln\sigma)_T$ and the creep activation energy $Q = -(\delta \ln\dot{\varepsilon} / \delta(1/(R.T)))_\sigma$ were determined.

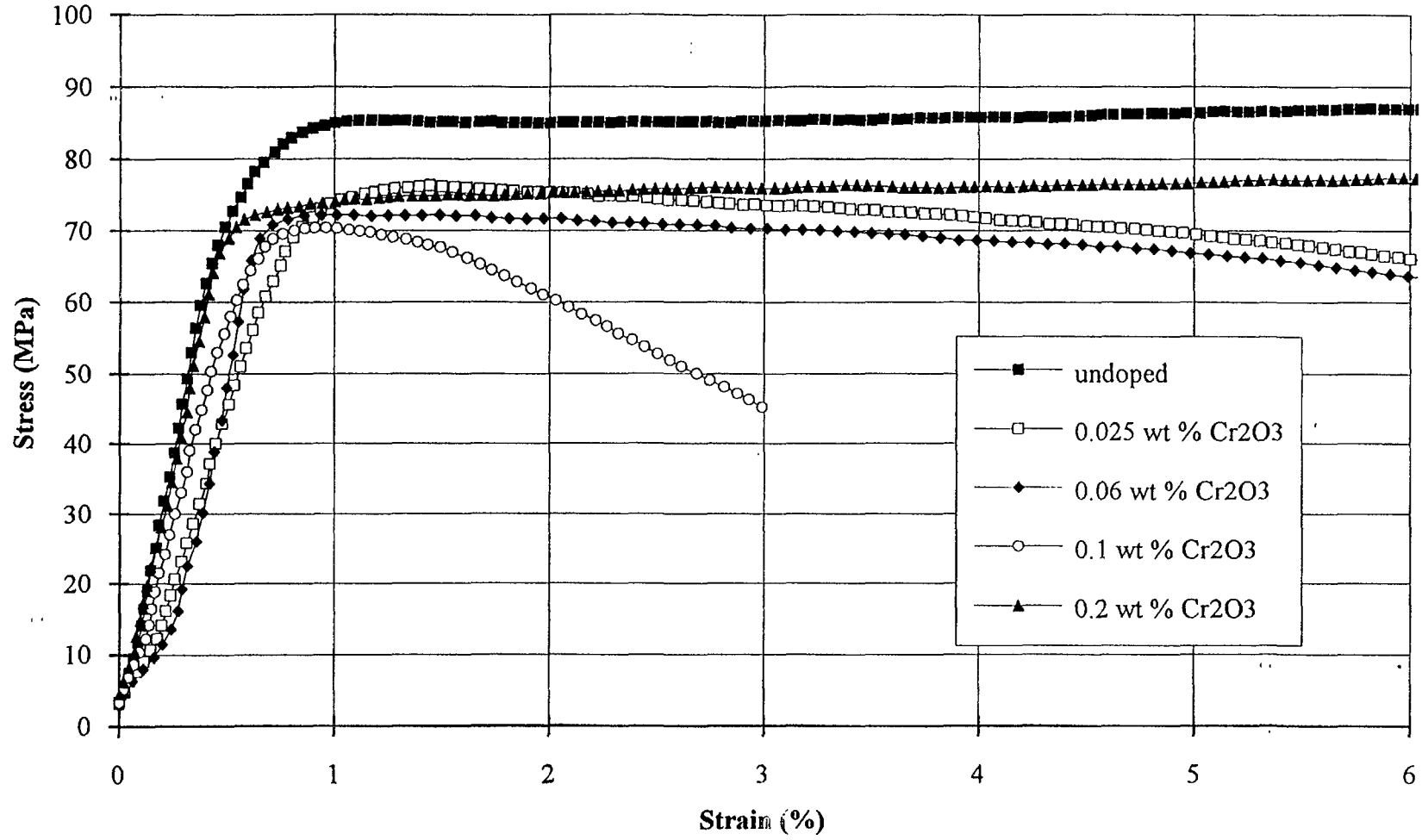

FIG. 1. Tests with constant applied strain rate of 20 μm/min at 1500 °C

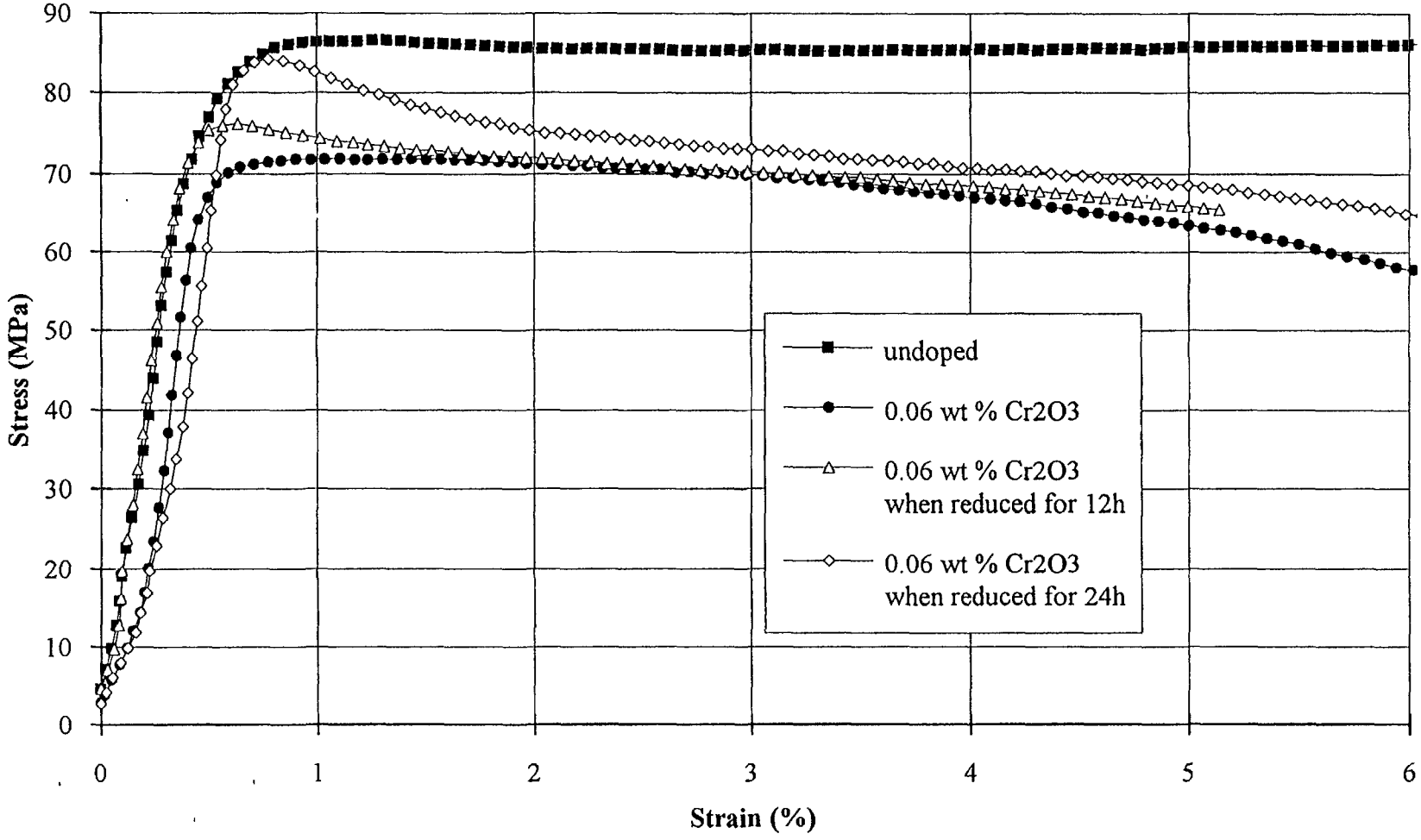

FIG. 2. Effect of reduction on the deformation of the batch doped with 0.06 wt% Cr203 at constant applied strain rate of 20 μm/min at 1500 °C.

3.2.1 Creep of the undoped fuel

Three creep regimes were highlighted (Fig.3):

- at low stresses ($\sigma < 45$ MPa), the strain rate is proportional to the square of the applied stress. The activation energy is found to be 410 kJ/mol. This value agrees well with 380 kJ/mol which corresponds to the grain boundary diffusion energy in stoichiometric polycrystalline uranium dioxide [5].
- at high stresses ($45 < \sigma < 60$ MPa), a power law with $n = 4.7$ is observed. The measured activation energy for creep is 560 kJ/mol which compares with the value of 540 kJ/mol reported for uranium self-diffusion energy [5].
- at higher stresses ($\sigma > 60$ MPa), the creep rate increases rapidly with stress ($n > 12$). The creep rate appears to increase with σ faster than a power law, possibly exponentially.

3.2.2 Creep of doped fuels

The addition of Cr_2O_3 increases the creep rate of the material up to a factor of 12 (Fig.5). However, it should be noted that the relative strain does not vary monotonously with the additive content, the highest strains being obtained for a doping with 0.1 wt %Cr_2O_3, regardless of the applied stress.

A single creep regime according to a power law is established in the explored stress range (Fig. 3) with stress exponents between 4.9 and 6.3. From tests carried out at 1600°C on the batch doped with 0.1 wt %Cr_2O_3 it has been checked that n is independent of temperature.

The creep activation energy varies from 466 to 551 kJ/mol, depending on dopant content (Fig. 4). Table II gives a summary of the creep parameters.

4. DEFORMATION MECHANISMS

4.1 Creep of the undoped fuel

This study reveals the existence of three regions of deformation. Authors generally predict two regimes of deformation [6, 7], at low and high stress levels, associated respectively with diffusion ($n=1$) and dislocation ($4 < n < 5$) creep mechanisms. However, some authors mention the existence of three, or even four, creep regimes [8-10]. This paper attempts to identify the mechanisms governing deformation in each domain.

At low stresses, the stress-dependence of the speed ($n=2$) associated with an activation energy close to the grain boundary diffusion energy in UO_2 is in accord with models based on diffusion-accommodated grain boundary sliding as the rate controlling mechanism [10,11]. This behaviour is often observed for materials with a small grain size, generally less than 10 μm, at low stresses.

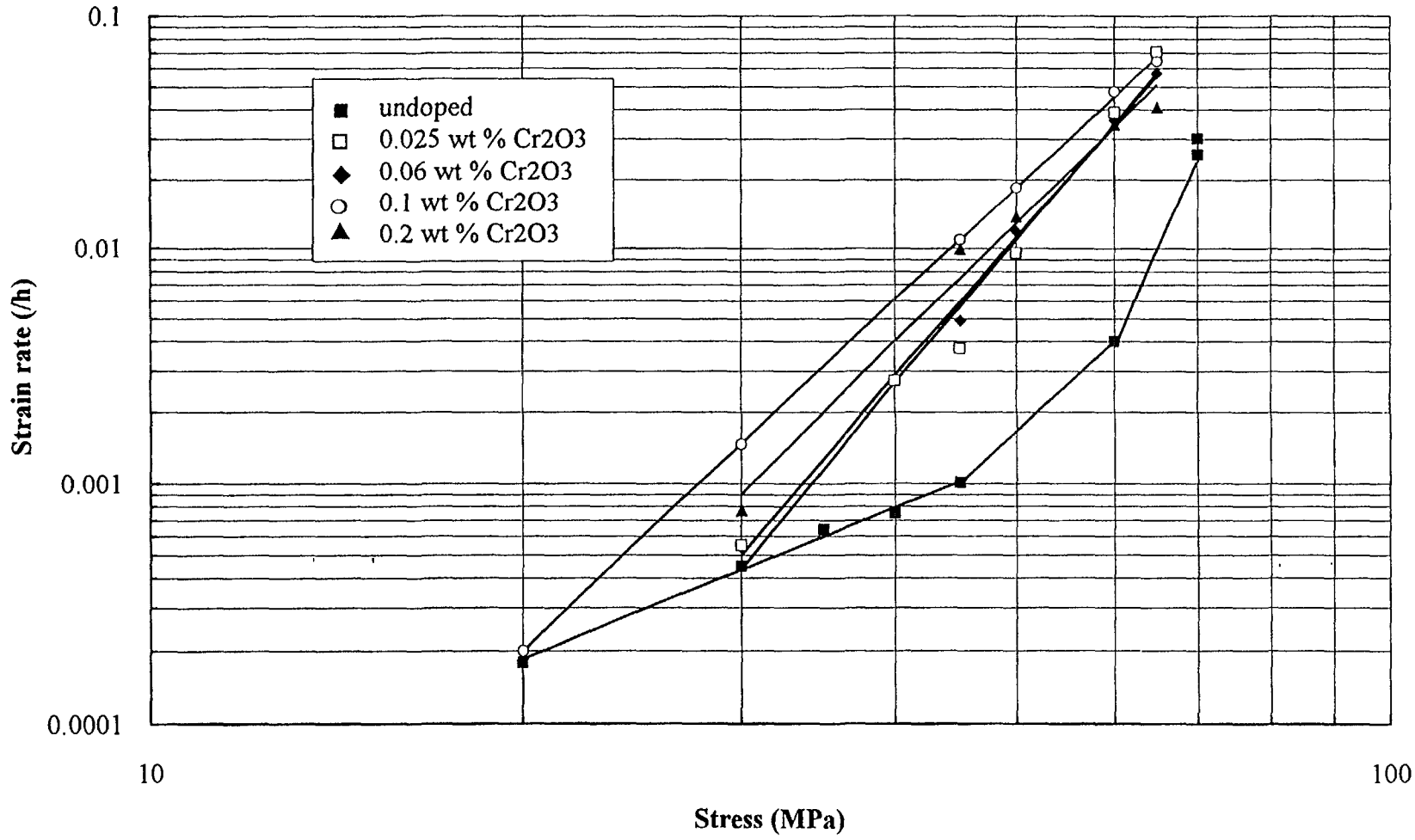

FIG. 3. Creep rate as a function of applied stress at 1500 °C.

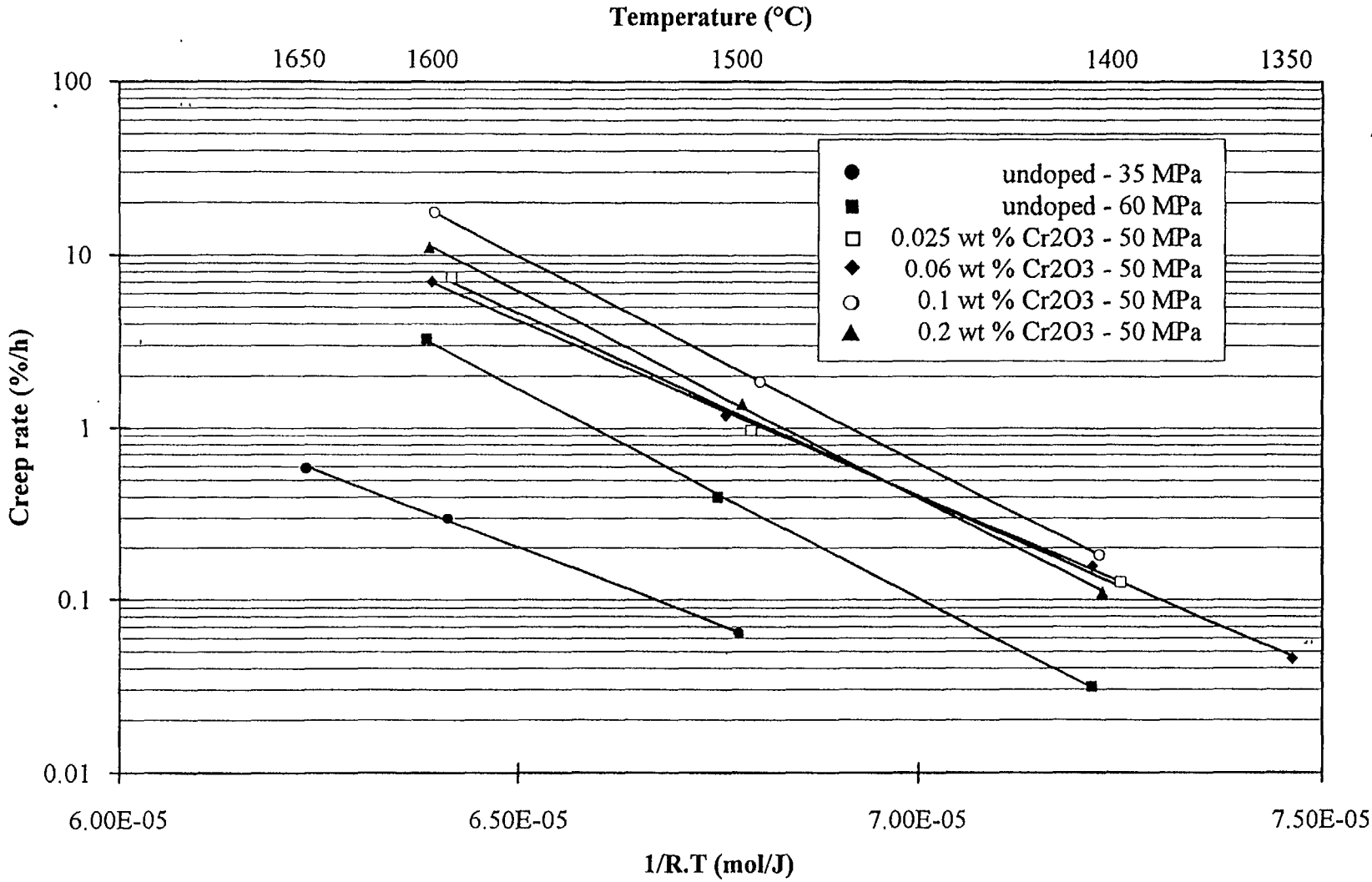

FIG. 4. Temperature dependence of creep rate.

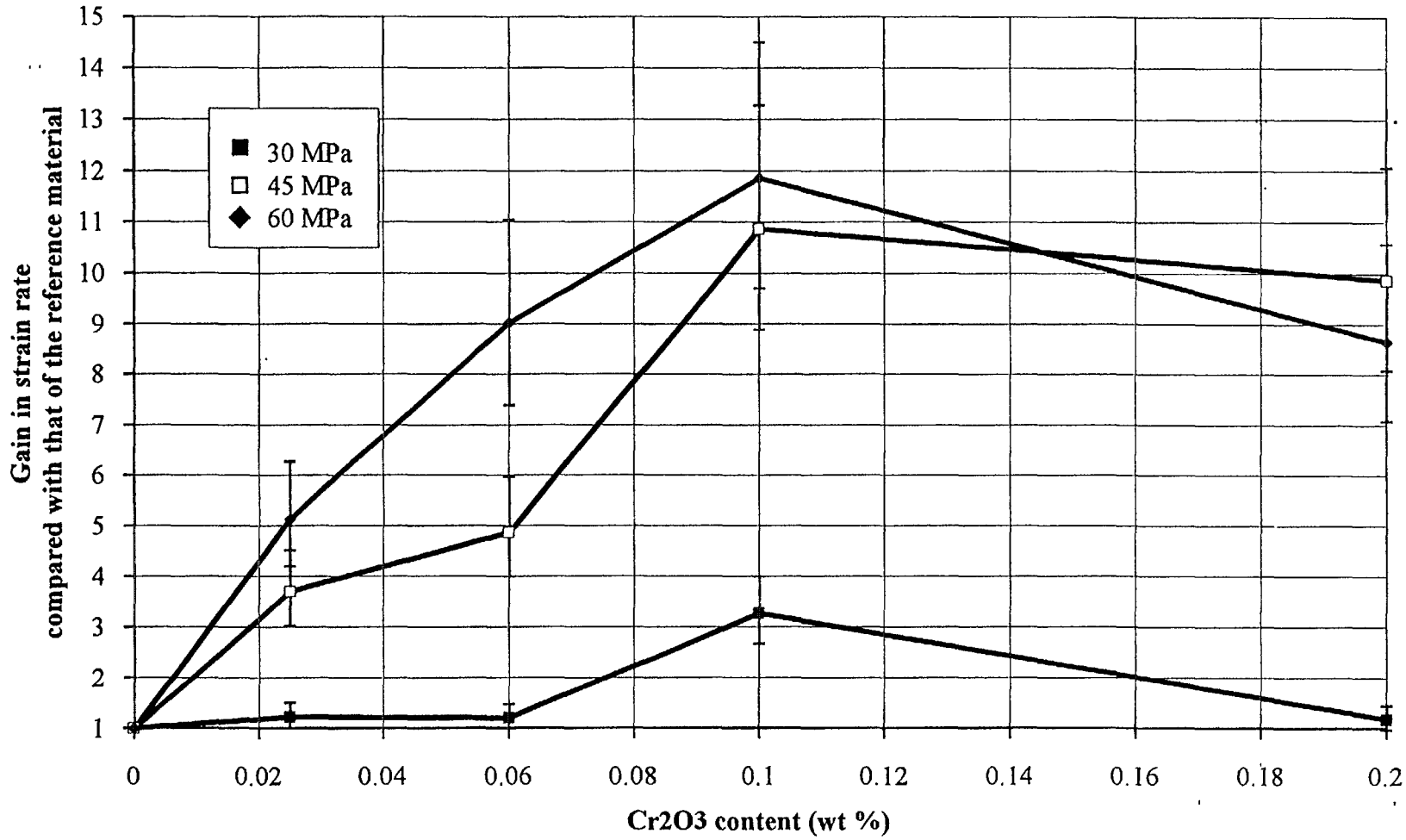

FIG. 5. Effect of composition on creep rate at 1500 °C.

TABLE II. CREEP PARAMETERS AT 1500°C

Cr2O3 content (wt %)	Stress range (MPa)	n	Q (kJ/mol)
0	20 to 45	2.1	410
	45 to 60	4.8	560
0.025	30 to 65	6.3	487
0.06	30 to 65	6.1	466
0.1	20 to 65	4.9	551
0.2	30 to 65	5.2	550

At intermediate stress levels, the apparent activation energy of creep, which is very close to the self-diffusion activation energy of U^{4+} ions in UO_2, and the value of the stress exponent indicate that UO_2 creep is due to the movement of dislocations. However it is not possible to define the rate controlling mechanism (climb or glide).

At very high stress levels, assuming an exponential creep law, the deformation could be governed by a mechanism of the same nature as in the previous domain.

4.2 Creep of doped fuels

In the doped state, dislocation creep extends over the entire stress range studied.

We have shown that creep rate and grain size increase with Cr_2O_3 content. The influence of grain size on the creep has not been studied yet.

It is likely that the additions affect the diffusion properties in UO_2. Indeed Peres [12] observed that Cr^{3+} bulk diffusion coefficient is increased of about six orders of magnitude compared with that of U^{4+} in undoped UO_2. Cr^{3+} is expected to enhance U^{4+} bulk diffusion. Hence a dislocation climb mechanism would be favoured.

Additions of Al_2O_3 result in similar observations. It would be interesting to investigate the creep of other corundum oxides (with Ti^{3+}, V^{3+}...) in order to confirm the trivalent cation influence.

5. CONCLUSION

This study compared compressive deformation at 1500°C of large-grained UO_2 doped with Cr_2O_3 and a reference fuel of standard microstructure. It was shown that doping improves the plasticity of the fuel.

At least three mechanisms govern the deformation of undoped UO_2 whereas a single one occurs in doped fuels, correlated to dislocation creep.

Doping with Al_2O_3 leads to similar observations. Other corundum oxides, insofar as they are grain growth promoters, could be very favourable and promising dopants. The use of such doped fuels is expected to reduce the pellet-cladding mechanical interaction and thus to improve the performances of the nuclear fuel.

REFERENCES

[1] SAWBRIDGE, P.T., REYNOLDS, G.L., BURTON, B., "The creep of UO_2 fuel doped with Nb_2O_5", J. Nucl. Mat. 97 (1981) 300-308.

[2] MOORE, D.A., MORROW, S.A.,"Thermally activated creep of undoped and magnesia doped large grain UO_2", Nuclear fuel performance, BNES, London (1985).

[3] ARMSTRONG, W.M., IRVINE, W.R., "Creep of urania base solid solutions", J. Nucl. Mat. 12 3 (1964) 261-270.

[4] GUERIN, Y., "Etude par compression à hautes températures de la déformation plastique du bioxyde et du monocarbure d'uranium", PhD Thesis, Université Claude Bernard, Lyon (1973).

[5] KNORR, D.B., CANNON, R.M., COBLE, R.L., "An analysis of diffusion and diffusional creep in stoichiometric and hyperstoichiometric uranium dioxide", Acta Metall. 37 8 (1989) 2103-2123.

[6] LANGDON, T.G., "Creep mechanisms in stoichiometric uranium dioxide", J. Nucl.Mat. 38 (1971) 88-92.

[7] HOUGH, A., "Compressive creep in nuclear oxides", AERE R 13232 (1988).

[8] ROBERTS, J.T.A., "Mechanical equation of state and high-temperature deformation ($\geq 0.5T_m$) of uranium dioxide", Acta Metall. 22 (1974) 873-878.

[9] MOHAMED, F.A., SOLIMAN, M.S., "On the Creep Behavior of Uranium Dioxide", Mat. Sci. Eng.53 (1982) 185-190.

[10] LANGDON, T.G., "Grain Boundary Sliding as a Deformation Mechanism during Creep", Phil. Mag. 22 (1970) 689-700.

[11] MUKHERJEE, A.K., "High Temperature Creep", Treatise on Materials Science and Technology, Vol. 6 Plastic Deformation of Materials (ARSENAULT, R.J., Ed.), Academic Press, London (1975) 163-224. -

[12] PERES, V., "Contribution à l'étude de la dispersion de particules de phases secondaires dans le dioxyde d'uranium polycristallin", PhD Thesis, INPG, Grenoble (1993).

LIST OF PARTICIPANTS

Amaya, M.	Nippon Nuclear Fuel Development Co. Ltd, 2613 Narita–cho, Oarai-machi, Higashi-Ibaraki-gun, Ibaraki-ken, 311-13 Japan
Anegawa, T.	Tokyo Electric Power Company, 1-3 Uchisaiwai-cho 1-chome, Chiyoda-ku, Tokyo, Japan
Bairiot, H.	FEX, Lijsterdreef 24, B-2400 MOL, Belgium
Balestrieri, D.	CEN Cadarache, DEC/SDC/LEMC Bt. 315, F-13108 Saint-Paul-lez-Durances, France
Baron, D.	Direction des études et recherches, Département MTC, B.P. 1, Electricité de France, F-77250 Moret-sur-Long, France
Bengtsson, S.	Hot Cell Laboratory, Studsvik Nuclear AB, S-611 82 Nyköping, Sweden
Bibilashvili, I.K.	Nuclear Fuel Department, A.A. Bochvar All Russia Research Institute of Inorganic Materials (VNIIM), St. Rogov 5, 123060 Moscow, Russian Federation
Brinsden, S.D.	MOX R&D Department, British Nuclear Fuels Plc, Sellafield, Seascale, Cumbria CA20 1PG, United Kingdom
Brown, C.	Thorp Division, BNFL International Group, Building 582, Sellafield, Seascale, Cumbria CA20 1PG, United Kingdom
Buchan, P.G.	Thorp Division Commercial Department, British Nuclear Fuels Ltd, 1st. Floor, Fleming House, Risley WA3 6AS, United Kingdom
Chantoin, P. *(Scientific Secretary)*	Division of Nuclear Power and the Fuel Cycle, International Atomic Energy Agency, Wagramer Strasse 5, P.O. Box 100, A-1400 Vienna, Austria
Chotard, A.	Framatome Nuclear Fuel, 10 rue Juliette Récamier, F-9456 Lyon Cedex 06, France

Combette, P.	CEA/STXN, 29 Rue de la Federation, Paris (15), France
Cook, T.	Office of Nuclear Energy, US Department of Energy, Washington D.C. 20585, United States of America
Davies, J. H.	Vallecitos Nuclear Center, GE Nuclear Electric, P.O. Box 460, Vallecitos Road, Pleasanton, California 94566, United States of America
Dehaudt, Ph.	CENG/SECC (CEA), 17 Rue des Martyrs, F-38054 Grenoble Cedex 9, France
Egorov, A.	Department of Nuclear Reactors, Ministry of the Russian Federation for Atomic Energy, Staromonetny 26, 109180 Moscow, Russian Federation
Fujishiro, T.	Japan Atomic Energy Research Institute, 2–4 Shirakata Shirane, Tokai-Mura, Naka-Gun, Ibaraki-ken, 319-11, Japan
Furuya, H.	Department of Nuclear Engineering, Kyushu University, 6-10-1 Hakozaki, Higashi-ku, Fukuoka-shi, Fukoka-ken, 812-81, Japan
Golovanov, V.N.	State Scientific Centre, RIAR, 433510 Dimitrovgrad-10, Ulyanovsk region, Russian Federation
Grapengieser, B.	ABB Atom AB, S-721 63 Västerås, Sweden
Hayashi, H.	Nuclear Power Engineering Corporation, Fujita Kanko Toranomom Building, 6F, 17-1, 3-chome Toranomon, Minato-ku, Tokyo 105, Japan
Hirai, M.	Nippon Nuclear Fuel Development Co. Ltd, 2613 Narita–cho, Oarai-machi, Higashi-Ibaraki-gun, Ibaraki-ken, 311-13 Japan
Ichikawa, M.	Japan Atomic Power Company, Ohtemachi Bldg., 6-1, 1-Chome, Ohtemachi, Chiyoda-ku, Tokyo 100, Japan
Ishikawa, H.	Nuclear Safety Research Association, 5-18-7, Shinbashi, Minato-ku, Tokyo 105, Japan
Itagaki, N.	Nuclear Fuel Industries Ltd., 3135-41 Muramatsu, Tokai-mura, Naka-gun, Ibaraki-ken 319-11, Japan

Kamath, H.S.	Advanced Fuel Fabrication Facility, Bhabha Atomic Research Centre, Tarapur, Mumbai, Dist. Thane, Maharashtra, India
Kato, M.	Power Reactor and Nuclear Fuel Development Corporation, 4–33 Muramatsu, Tokai-mura, Naka-gun, Ibaraki-ken,, 319-11 Japan
Khadeev, V.G.	Joint Stock Company, Ulba Metallurgical Plant, 102 Abay Avenue, Ust-Kamenogorsk, 492026 Kazakhstan
Kim, H.C.	Korea Institute of Nuclear Safety, 19 Kusong-dong, Yusong-ku, Taejon, Republic of Korea 305-338
Komine, I.	Nuclear Power Engineering Corporation, Fujita Kanko Toranomom Building, 6F, 17-1, 3-chome Toranomon, Minato-ku, Tokyo 105, Japan
Kondo, Y.	Nuclear Development Corporation, 622-12 Funaishikawa, Tokai-mura, Naka-gun, Ibaraki-ken 319-11, Japan
Konings, R.J.M.	Netherlands Energy Research Foundation, NL-1755 ZG Petten, Netherlands
Kosaka, Y.	Nuclear Development Corporation, 622-12 Funaishikawa, Tokai-mura, Naka-gun, Ibaraki-ken 319-11, Japan
Koukouchkine, I.A.	Concern TVEL, B. Ordynka str. 24/26, 101000 Moscow, Russian Federation
Kurosu, T.	Nuclear Fuel Department, Nuclear Power Engineering Corporation, Fujita Kanko Toranomom Building, 6F, 17-1, 3-chome Toranomon, Minato-ku, Tokyo 105, Japan
Loktev, I.	Novosibirsk Plant of Chemical Concentrates, Bogdan Khmelnitskij Str. 94, 630110 Novosibirsk, Russian Federation
Maki, H.	Hitachi Ltd, 1-1 Saiwai-cho 3, Chome, Hitachi-shi, Ibaraki-ken, 317, Japan
Manzel, R.	Fuel Irradiation Project, Siemens AG, Unternehmensbereich KWU, P.O. Box 3220, D-91050 Erlangen, Germany
Marajofsky, A.	Argentine Atomic Energy Commission, Av. del Libertador 8250, 1429 Buenos Aires, Argentina

Marsh, G.	Fuel Division, BNFL International Group, Springfields Works, Salwick, Preston, Lancs. PR4 0XJ, United Kingdom
Matsuda, T.	Nuclear Fuel Industries Ltd, 950, Noda, Kumatori-cho, Sennan-gun, Osaka-fu, 590-04, Japan
Medvedev, A.V.	A.A. Bochvar All Russian Research Institute of Inorganic Materials, VNIIM, St. Rogov 5, 123060 Moscow, Russian Federation
Milovanov, O.V.	A.A. Bochvar All Russian Research Institute of Inorganic Materials, VNIIM, St. Rogov 5, 123060 Moscow, Russian Federation
Morgan, H.G.	AEA Technology, B7 Windscale, Seascale, Cumbria CA20 1PF, United Kingdom
Mori, K.	Nuclear Fuel Industries Ltd, 23-5, Nishi-shinbashi 3-chome, Minato-ku, Tokyo 105, Japan
Nakamura, J.	Tokai Research Establishment, Japan Atomic Energy Research Institute, 2-4 Shirakata-shirane, Tokai-mura, Naka-gun, Ibiraki-ken 319-11, Japan
Nishida, T.	Japan Nuclear Fuel Co. Ltd, 2-3-1 Uchikawa, Yokosuka-shi, Kanagawa-ken, 239, Japan
Nogita, K.	Nippon Nuclear Fuel Development Co. Ltd, 2163 Narita-cho, Oarai-Machi, Higashi-Ibaraki-gun, Ibaraki-ken 311-13, Japan
Ohkubo, T.	Deptartment of Mechanical Engineering, 7-1 Kioi-cho, Chiyoda-ku, Tokyo, 102, Japan
Powell, D.	British Nucler Fuels Ltd, Fleming House, Risley, Warrington, Cheshire WA3 6AS, United Kingdom
Quecedo, M.	Uranio S.A. (ENUSA), Empresa Nacional de Santiago Rusinol 12, E-28040 Madrid, Spain
Rechetnikov, F.G.	A.A. Bochvar All Russian Research Institute of Inorganic Materials, VNIIM, St. Rogov 5, 123060 Moscow, Russian Federation

Sendo, T.	Kansai Electric Power Co., Inc., 3-3-22 Nakanoshima, Kita-ku, Osaka, 530-70, Japan
Sohn, D.S.	Advanced LWR Fuel Development Division, Korea Atomic Research Institute, P.O. Box 105, Yusung, Yusung-gu, Taejon 305-353, Republic of Korea
Smirnov, A.V.	Research Institute of Atomic Reactors, 433510 Dimitrovgrad-10, Ulyanovsk Region, Russian Federation
Sokolov, F.G.	A.A. Bochvar All-Russia Research, Institute of Inorganic Materials, VNIIM, St. Rogov 5, 123060 Moscow, Box 369, Russian Federation
Spino, J.	CEC Joint Research Centre, Institute for Transuranium Elements, Postfach 2340, D-76125 Karlsruhe, Germany
Tayal, M.	Atomic Energy of Canada Ltd, 2251 Speakman Drive, Mississauga, Ontario, L5K IB2, Canada
Trotabas, M.	COGEMA BC/CT, 2 rue Paul Dautier B.P. 4, 78141 Velizy Cedex, France
Tsiboulia, V.A.	Mashinostroitelny zavod, 12, Karl Marx Street Electrostal, Moscow Region 144001, Russian Federation
Uchida, H.	Nuclear Power Engineering Corporation, Fujita Kanko Building, 6F, 17-1, 3-chome Toranomon, Minato-ku, Tokyo 105, Japan
Uetsuka, H.	Japan Atomic Energy Research Institute, Tokai Research Establishment, 2-4 Shirakata-shirane, Tokai-Mura, Naka-Gun, Ibaraki-Ken, 319-11, Japan
Vitanza, C.	Institute for Energiteknikk, OECD Halden Reactor Project, OS Alle 13 P.O. Box 173, N-1751 Halden, Norway
Wood, G.A.	Fuel Division, BNFL International Group, Springfields Works, Salwick, Preston, Lancs. PR4 0XJ, United Kingdom
Yamawaki, M.	Nuclear Engineering Research Laboratory, University of Tokyo, 7-3-1, Hongo, Bunkyo-ku, Tokyo, 113, Japan